Monte Carlo simulations of hole transport and relaxation in the valence bands of a semiconductor quantum well

R.W. Kelsall

MONTE CARLO SIMULATIONS OF HOLE TRANSPORT AND RELAXATION IN THE VALENCE BANDS OF A SEMICONDUCTOR QUANTUM WELL

by

R. W. Kelsall, BSc (Dunelm)

A thesis

submitted in candidature for

the degree of Doctor of Philosophy

at the University of Durham

July 1989

DECLARATION

I hereby declare that the work reported in this thesis has not previously been submitted for any degree and is not being currently submitted in candidature for any other degree.

The work reported in this thesis was carried out by the candidate.

Blessed are those whose strength is in you,
who have set their hearts on pilgrimage.

As they pass through the Valley of Baca,
they make it a place of springs;
the autumn rains also cover it with pools.

They go from strength to strength
till each appears before God in Zion.

Psalm 84; 5–7

ACKNOWLEDGEMENTS

Firstly, I would like to thank my supervisor, Dr. R. A. Abram, for his patient encouragement over the last four years. I would like to thank Drs. M. J. Kirton and S. Monaghan for our discussions on the Monte Carlo program development, and Andrew Wood and Dr. Ian Taylor for their advice and the provision of software for use in developing the valence band model. I would like to acknowledge the assistance of: Kate Hewlett for proof reading and photocopying; Drs. Charles Newby and David Hughes for checking some of the algebra, and Brian Hunter for preparing the line drawings. I also wish to acknowledge financial support from the SERC.

In addition, I would like to express my grateful appreciation for the support, and practical help of:

Geoff and Grace Atkinson, Isobel Atkinson, Peter Clark, Ross and Jean Clifford, Kate Hewlett, Jonathan Lloyd, Edward Meanwell, Sue Neal, Charles Newby, Chrissie Newton, Sally Raynham, and, of course, my parents June and Arthur Brooks.

MONTE CARLO SIMULATIONS OF HOLE TRANSPORT AND RELAXATION IN THE VALENCE BANDS OF A SEMICONDUCTOR QUANTUM WELL

ABSTRACT

This thesis describes the development, from first principles, of a set of Monte Carlo programs to simulate the transport and relaxation of quantum confined holes. We have examined the particular case of hole dynamics in a 100Å GaAs/AlAs single quantum well. Information on the valence band energy dispersions and hole wavefunctions in the quantum well is obtained from a 4-band k.p calculation. We derive expressions for the quantum confined hole-phonon matrix elements and scattering rates which incorporate the 4-band k.p bandstructure, and present detailed results for intra- and inter-band scattering in the first four valence subbands of the quantum well. We consider scattering by acoustic (deformation potential), non-polar optical, polar optical and piezoelectric phonons. The scattering matrix elements in all cases show marked variations with the wavevectors of the scattering states, due to strong heavy - light hole mixing in the valence subbands. The phonon scattering rates show additional structure related to the regions of extremely large densities of states which exist in subband energy minima located away from the Brillouin zone centre.

We have carried out simulations of steady state electric field heating of the quantum confined holes. The structure in the scattering rates is reflected in the low energy portions of the carrier energy distributions, and large carrier populations are found in the off-zone-centre band minima. Using the high energy tails of these distributions, we have been able to define effective temperatures for carriers in each subband. The similarity of these temperatures indicates that intersubband scattering is important in carrier thermalisation. We have obtained values for the hole energy loss rates in the steady state, which we are able to compare with experimental results.

We have also undertaken a detailed study of the transient cooling of quantum confined holes, for a range of initial conditions. We use an approximate model of inelastic acoustic scattering, and include, in our results, the time dependent energy loss rates resolved into components due to intra- and inter-band scattering by optical and acoustic phonons. The relative efficiency of cooling via different numbers of subbands is compared, and the possibility of carrier trapping in the subband energy minima is critically investigated. The influence of features peculiar to the quantum well valence bandstructure, in particular, the presence of off-zone-centre energy minima, is also examined.

CONTENTS

Abstract i

List of Symbols v

Chapter 1 Introduction 1

Chapter 2 The Monte Carlo Method 4

2A Basic Monte Carlo Transport Simulation 5

2A.1 The Stochastic Model of Electronic Transport 5

2A.2 Monte Carlo Estimators 8

2A.3 Distribution Functions 10

2B Monte Carlo Algorithms 12

2B.1 Single Particle Algorithm 12

2B.2 Ensemble Algorithm 13

2C Further Refinements 18

2C.1 Improved Self Scattering Efficiency 18

2C.2 Variance Reduction 21

Chapter 3 Carrier-Phonon Scattering in Bulk Semiconductors 23

3A Fundamental Electron-Phonon Scattering Theory 23

3A.1 Basic Principles 24

3A.2 Coupling Coefficients

3B Electron-Phonon Scattering in a Simple Parabolic Band

3C Hole-Phonon Scattering in the GaAs Valence Bands

Chapter 4 Monte Carlo Simulations of Hole Transport in Bulk GaAs 42

4A 77K Hole-Phonon Scattering Rates 43

4B Angular Dependence of the Scattering Rates 45

4C Simulations 49

4C.1 77K Simulations 49

4C.2 300K Simulations 50

Chapter 5 Carrier-Phonon Scattering in Semiconductor Quantum Wells 52

5A Electron-Phonon Scattering in Quasi-2D Systems 52

5B 2D Electron-Phonon Scattering in the Confined Carrier / Bulk Phonon Approximation 54

5C 2D Hole-Phonon Scattering 58

5C.1 The Quantum Confined Valence Bandstructure 58
5C.2 2D Hole-Phonon Scattering Matrix Elements in the 4-Band k.p Scheme 59
5C.3 Calculation of the 2D Hole-Phonon Scattering Rates 62

Chapter 6 Quantum Confined Hole-Phonon Scattering Matrix Elements 68
6A Introduction 68
6B Overlap Integrals 70
6C Matrix Elements 72
6C.1 Matrix Elements for Optical Phonon Scattering 72
6C.2 Matrix Elements for Acoustic Phonon Scattering 77
6D Angular Dependence of the Matrix Elements 80
6E Screening of the Polar Optical and Piezoelectric Interactions 83

Chapter 7 Quantum Confined Hole-Phonon Scattering Rates 84
7A Densities of States 84
7A.1 Densities of States as derived from the Band Dispersions 84
7A.2 Analysis of the Densities of States around the Critical Points 85
7A.3 Broadening of the Densities of States 86
7B Scattering Rates 90
7B.1 Scattering Rate Parameters 90
7B.2 Scattering Rate Results 92
7C Inelastic Acoustic Scattering 94
7C.1 The Average Phonon Energy Approximation 94
7C.2 Detailed Balancing of the Scattering Rates 95

Chapter 8 Monte Carlo Implementation 97
8A Preliminary Details of the Simulation Codes 97
8B Bandstructure Routines 99
8C Scattering Rate Routines 101
8D Self Scattering 104
8E Scattering Process Selection 105
8F Angular Dependences for Polar Optical and Piezoelectric Processes 108
8G General Program Specifications 109

Chapter 9 Electric Field Heating of Quantum Confined Holes 111
9A Electric Field Dependence of the Basic Monte Carlo Estimators 112
9B Hole Energy Distributions 115

9C Carrier Temperatures 118
9D Energy Loss Rates 120
9E Hole Distributions in the 2D Wavevector Plane 125

Chapter 10 Cooling of Quantum Confined Holes 128
10A Introduction 128
10B Transient Hole Cooling Simulations 131
10B.1 Prototype Hole Cooling Simulation 131
10B.2 Dependence of Hole Cooling on the Number of Subbands present 135
10B.3 Cooling of Single- and Multi-band Heated Maxwellian Distributions 139
10B.4 Cooling of a Hole Population above the $2\times \hbar\omega_{op}$ Threshold 142
10B.5 Cooling of Hole Populations generated in the Lower Bands 145
10B.6 Maxwellian Hole Distributions in the Acoustic Dominated Cooling Regime 149
10B.7 Cooling of a Hole Population at the Lowest Optical Phonon Emission Threshold 151
10C Summary 153

Chapter 11 Conclusions 156

Appendices 161
Appendix 1 Rejection Techniques for the generation of Stochastic Variates 161
Appendix 2 Valence Band Deformation Potentials 163
Appendix 3 Critical Points in the Valence Band Energy Dispersions 168

References 170

LIST OF SYMBOLS

a	valence band deformation potential
a	label for $k > k_n(0)$ region of quantum well valence subbands (Chapter 6)
a_0	lattice constant
$a_{i,n}$	coefficients for parabolic extrapolation of quantum well valence bandstructure (Chapter 8)
$a_{\mathbf{q}}$, $a_{\mathbf{q}}^{\dagger}$	phonon annihilation and creation operators
A	label for electronic state in quantum well (Chapter 5)
A_i^{I}, A_i^{II}, A_i^{III}	coefficients of bulk basis functions (Chapter 5)
A	area of quantum well plane
b	valence band deformation potential
b	label for $k < k_n(0)$ region of quantum well valence subbands (Chapter 6)
$b_{n',n}$	effective length term in infinite square well phonon scattering rates (Chapter 5)
B	label for electronic state in quantum well (Chapter 5)
B_i^{I}, B_i^{II}, B_i^{III}	coefficients of bulk basis functions (Chapter 5)
c, c'	quantum numbers for lattice (crystal) states
c_{11}, c_{12}, c_{44}	elements of the crystal elastic tensor
$c_{\mathbf{g}}$, c_0	coefficients of Fourier expansions in reciprocal space; g = 0 coefficient
c_l, c_t	bulk spherically averaged crystal elastic constants
$C_{\mathbf{q}}$	coupling coefficient for carrier-phonon scattering
d	valence band deformation potential
d_{op}	fundamental optical deformation potential
$D(\epsilon)$	density of states
$\mathbb{D}_{\mathrm{op}}$, D_{op}	optical deformation potential constant
$\mathcal{D}_n(k)$, $\mathcal{D}_n(\epsilon)$	reduced density of states in the quantum confined valence subbands
e	electronic charge
e^*	effective charge
$\hat{e}_{\mathbf{q}}$, e_i	unit polarisation vector and Cartesian components
$E(\mathbf{k}, c)$	total energy of electron plus lattice system
E_{AC}	valence band acoustic deformation potential used in this work
E_1, E_1^0, $E_{\mathrm{AC,Wiley}}$	acoustic deformation potentials used by other authors (see Appendix 2)
$E_{1,\mathrm{op}}$, $E_{\mathrm{NPO,Wiley}}$	optical deformation potentials used by other authors (see Appendix 2)
$f(\epsilon)$	circularly symmetric carrier distribution function in 2D (Chapter 8)
$f'(\epsilon)$	2D as-sampled carrier energy distribution from Monte Carlo simulations (Chapter 8)
$f(\mathbf{k})$	3D carrier distribution function (Chapter 2)
$f_n(\epsilon)$	coefficient of spherical harmonic expansion of 3D distribution function (Chapter 2)
F	electric field
$F(\epsilon, \theta)$	3D carrier distribution function (Chapter 2)
$F(\epsilon, \beta)$, $F(\mathbf{k})$	2D carrier distribution function (Chapters 8,9)
$F_{ii}(k_f, k)$, $F_{fi}(k_f, k)$	integral terms in 3D scattering rate calculations (Chapter 3)
$\mathcal{F}^2(\cos\beta)$	angular dependence of quantum confined hole-phonon scattering rates
$\mathbf{g}$,g, $\mathbf{g}_{\parallel}$,$g_{\parallel}$, g_z	3D reciprocal lattice vector and modulus; 2D in-plane vector and modulus, and z-component.
$g(x)$, $g(\cos\beta)$	approximating functions for probability distributions (Chapter 4, Appendix 1)
$G(\mathbf{k}', \mathbf{k})$	overlap integral
$G^2_{0_{n',n}}(k)$	overlap integrals with zone centre states in quantum well (Chapter 6)
$\mathbf{h}$, h_{ijk}	piezoelectric tensor and components
h_{14}	non-zero component of the piezoelectric tensor for cubic crystals,

	in symmetric notation
$\hbar$	reduced Planck's constant
H_{ep}	electron-phonon interaction Hamiltonian
I, II, III	labels for well and barrier regions of quantum well (Chapter 5)
$I(\mathbf{k}',\mathbf{k})$	electronic part of carrier-phonon scattering matrix element
$\mathcal{I}(k_BT_c)$	remnant temperature dependence of steady state hole energy loss rate (Chapter 9)
$J_{n'n}(q_z)$, $J_{k'n',kn}(q_z)$	envelope function integrals (Chapter 5)
$\mathbf{k}$,k	electron/hole wavevector and modulus
$\mathbf{k}_\parallel$,$k_\parallel$	2D in-plane electron/hole wavevector and modulus (Chapter 5 only)
k_{acr}	wavevectors of anticrossing points in the quantum confined valence bandstructure
k_B	Boltzmann constant
$k_n(0)$	wavevectors of off-zone-centre minima in the quantum confined valence bandstructure
$K_{\rm av}$	average electromechanical coupling constant
L	quantum well width
$\mathcal{L}(\epsilon)$	Lorentzian broadening function (Chapter 7)
m_0	free electron mass
m^*	relative effective mass of electrons or holes
M'	lattice oscillator mass
M_1, M_2	atomic masses
$\overline{M}$	reduced mass of a diatomic unit cell
$\mathcal{M}_{k'n',kn}$	quantum confined carrier-phonon scattering matrix element
n	electron concentration
n, n'	quantum well subband indices
$\overline{n}$	fractional population
$\overline{n}_1 \ldots \overline{n}_4$	fractional population of the quantum well subbands
$\overline{n}_l$	fractional population of bulk light hole band
$n_{\rm sys}$	total carrier population of system
N	number of unit cells in crystal lattice
N_A, N_B	normalisation coefficients for quantum confined carrier wavefunctions (Chapter 5)
$N_{\rm ens}$	number of carriers in an ensemble Monte Carlo simulation
$\mathcal{N}_{\rm ac}$, $\mathcal{N}_{\rm op}$	thermal equilibrium populations of acoustic and optical phonons
$\mathcal{N}_{\mathbf{q}}$	thermal equilibrium population (occupation number) of phonon mode $\mathbf{q}$
p	hole concentration
$\mathbf{p}$	crystal momentum of electron or hole
$P(\mathbf{k})$	carrier-phonon scattering rate
$\mathbf{P}(\mathbf{r})$, P_i	polarisation and Cartesian components
$P_n(\cos\theta)$	Legendre polynomials
$\mathcal{P}(t)$	probability distribution of electronic free flights (Chapter 2)
$\mathbf{q}$,q, $\mathbf{q}_\parallel$,$q_\parallel$, q_z	3D phonon wavevector and modulus; 2D in-plane wavevector and modulus, and z-component
q_0	reciprocal Debye screening length
$Q_{\mathbf{q}}$	normal coordinate for lattice vibrations of mode $\mathbf{q}$
r	random number generated from an even distribution in the range [0,1]
$\mathbf{r}$, $\mathbf{r}_\parallel$	3D real space position vector, and 2D in-plane vector
R_i	position vector of the $i^{\rm th}$ lattice site
$s(\mathbf{k})$	self scattering rate
S	$rP(\mathbf{k})$ or $r\Gamma$ (Chapters 2 and 8)
S, S_{ij}	strain tensor and components
S_k	number of electronic states

$S_{k,c}$	number of states in the electron/lattice system
t	time
$t_{\rm obs}$	time at which an observation is made in an ensemble Monte Carlo simulation
t_r	stochastic free flight time
$t_{\rm sim}$	total simulation time in a single particle (steady state) Monte Carlo simulation
$t_{\rm step}$	interval between successive observations in an ensemble simulation
T	total duration of an electron 'history' (Chapter 2) ($\equiv t_{\rm sim}$)
T_c	carrier temperature
T_L	lattice temperature
$u_0(\mathbf{r})$	periodic part of a zone-centre bulk Bloch function
$u_{\rm ac}$	equivalent acoustic displacement for an optical vibration in a diatomic crystal
$u_{\rm k}(\mathbf{r})$	periodic part of a bulk Bloch function for state $\|\mathbf{k}\rangle$
$\mathbf{u}(\mathbf{r})$	atomic displacement function in continuous lattice approxmation
$\mathbf{u}_i$	atomic displacement of lattice site i
$U(\mathbf{r})$	crystal potential
$U_{ij}^{\rm I}$, $U_{ij}^{\rm II}$, $U_{ij}^{\rm III}$	coefficients in plane wave expansions of bulk basis functions (Chapter 5)
v_a, v_b	electron velocity at the beginning and end of a free flight (Chapter 2)
$v_{\rm Bens}$, $v_{\rm FBS}$	estimates of the steady state carrier drift velocity obtained from Monte Carlo simulations
v_d, $v_{\rm av}$	carrier drift velocity; overall average drift velocity in 3D or 2D
v_h, v_l	bulk heavy and light hole drift velocities
v_s, v_l, v_t	sound velocity, and longitudinal and transverse values
$\overline{v}^2$	mean square sound velocity
V	crystal volume
$V_{\rm cell}$	unit cell volume
$V_{ij}^{\rm I}$, $V_{ij}^{\rm II}$, $V_{ij}^{\rm III}$	coefficients in plane wave expansions of bulk basis functions (Chapter 5)
x,y,z	space coordinates
x_r	randomly generated value of a variate x
X, Y, Z	stochastic parameters (Chapter 2)
α, α_0	$\alpha = \alpha_0/m^*$, $\alpha_0 = \hbar^2/2m_0$
β	scattering angle (angle of $\mathbf{k}'$ relative to $\mathbf{k}$), polar angle in 2D wavevector plane
β	c_l/c_t
β_r	stochastically generated scattering angles (Chapter 4)
γ	azimuthal angle of $\mathbf{k}'$ relative to $\mathbf{k}$ (3D only)
Γ	total scattering rate in a Monte Carlo simulation, including self scattering
Γ_i	values of Γ in a piecewise-constant (stepped) total scattering rate profile
δU	carrier-phonon interaction energy
Δ	determinant of second derivatives of 2D energy dispersion functions (Appendix 3)
$\Delta\epsilon$	linewidth for Lorentzian broadening function
$\epsilon(\mathbf{k})$, $\epsilon(k_\parallel, n)$	electron/hole (kinetic) energy
ϵ_c	energy of a critical point in the bandstructure
ϵ_n	energies of the subband minima in a quantum well
$\epsilon_n(0)$	zone centre (k=0) energies
ϵ_{ph}, $\epsilon_{\rm ac}$	phonon energy; fixed value acoustic phonon energy
ϵ_{xx}, ϵ_{xy}, *etc.*	second derivatives of $\epsilon(\mathbf{k})$ with respect to the Cartesian components of the 2D wavevector $\mathbf{k}$
ε_0	free space permittivity
$\varepsilon_{\rm pol}$	$(1/\varepsilon_s - 1/\varepsilon_\infty)^{-1}$
ε_s, ε_∞	static and high frequency dielectric constants
ζ	energy term (Chapter 7)

η	energy term: $\sqrt{(\epsilon-\epsilon_c)^2+(\Delta\epsilon/2)^2}$ (Chapter 7)
θ	angle between $\mathbb{k}$ and F (Chapter 2), angle between $\mathbb{k}$ and k_z (Chapter 3), scattering angle (Chapter 8) only
$\theta(\epsilon)$	unit step function
$\kappa_z^{A_{\rm I}}$, $\kappa_z^{B_{\rm I}}$, $\kappa_z^{A_{\rm III}}$, $\kappa_z^{B_{\rm III}}$	$(\pm)$ imaginary parts of complex wavevector components k_z in barrier regions of quantum well (Chapter 5)
μ_p	lattice mobility of holes
Ξ, Ξ_{ij}	deformation potential tensor and components
Ξ	scalar deformation potential for electrons
$\Xi_{\rm eff}$	'effective' valence band acoustic deformation potential (see Appendix 2)
ρ	crystal density
$\rho(\mathbf{r})$	space charge density
σ	standard deviation
σ_i	direction cosines
$\sigma_\parallel$	azimuthal average of $\sigma_1\sigma_2$ in quantum well plane: $\sigma_\parallel^4 = 8\sigma_1^2\sigma_2^2$ (Chapter 5)
τ	scattering lifetime
$\tau_{\rm POP}$	average lifetime for scattering by polar optical phonons
$\tau_{\rm ac}$	effective lifetime for scattering by acoustic (deformation potential) phonons
ϕ	azimuthal angle in 3D kspace
$\phi(\mathbf{r})$	electrostatic potential
$\phi_{\mathbf{q}}(Q)$	harmonic oscillator wavefunctions in the lattice
φ_i	bulk basis functions for calculating carrier wavefunctions in the quantum well
$\psi_{\mathbb{k}}(\mathbf{r})$	one-electron wavefunction (Chapter 3), also quantum well carrier wavefunction (Chapter 5)
$\omega_{\mathbf{q}}$	phonon frequency
$\omega_{\rm LO}$, $\omega_{\rm TO}$	longitudinal and transverse optical phonon frequencies
$\omega_{\rm op}$	optical phonon frequency in dispersionless, single frequency approximation

CHAPTER 1
INTRODUCTION

In recent years it has become possible to fabricate semiconductor devices which include extremely narrow layers. Within these layers, charge carriers are subject to quantum mechanical effects; their motion being restricted by confining potentials at the layer interfaces (Dingle 1975). Transport in these so-called 'quantum well' devices is therefore termed two-dimensional (2D) or quasi-2D. A great deal of research activity has been devoted to the properties of carriers in these devices, most of which has concentrated on GaAs material systems; in particular, the $GaAs/Al_xGa_{1-x}As$ family of quantum wells.

Interest in the transport properties of these devices has centered on the possibility of creating a large carrier density in the active (GaAs) layer, by introducing dopant atoms into the confining layers only (modulation doping). This means that the carrier mobility is not reduced by ionised impurity scattering, as is the case in extrinsic bulk semiconductors, and very high values for the 2D electron mobility have been reported (Dingle *et al.* 1978). New transport effects, such as a negative differential mobility due to real space transfer, where the carriers aquire sufficient energy to surmount the potential barriers and escape into the confining layers, have also been investigated (Hess *et al.* 1979).

More recently, a number of experiments have been designed to investigate the relaxation or cooling properties of quantum confined carriers excited to high energy states by optical or electrical means, using absorption or luminescence measurements to probe the energy spectra of the excited carrier populations in both the transient and steady state regimes (see, for example; Lyon 1986; Shah 1986). The results of these observations can be used to deduce effective temperatures with which to characterise the non-equilibrium carrier distributions, and the average rates of energy loss from the carriers to the lattice.

In most of the work to date, attention has been primarily directed towards the electrons; relatively little information is currently available on the properties of quantum confined holes. It is clear that the effects of quantum confinement on the valence band system of a semiconductor such as GaAs are much more complicated than for the conduction band, since both heavy and light hole states are present, and a considerable degree of mixing will occur between these states (Chang and Schulman 1983). This will modify the form of the fundamental processes by which holes are scattered in a quantum well, with consequent implications for all transport and relaxation properties.

Theoretical studies of quantum confined carriers have, in general, used simple approximations for both the energy band dispersions and carrier wavefunctions,

and, in most cases, deal with only a single subband in the quantum well. This description works reasonably well for electrons, but cannot be used with any confidence for holes, for the reasons given above.

Therefore it is our aim, in this thesis, to describe the development of a model for the investigation of quantum confined hole dynamics which includes the detailed effects of confinement on the GaAs valence band system. We have chosen the specific case of a single lattice matched GaAs/AlAs quantum well; however, our results will also be applicable, to a good approximation, to most of the $GaAs/Al_xGa_{1-x}As$ family of quantum wells, and the method is applicable to any materials system.

For the study of carrier transport and relaxation in a system of such complexity, the traditional approach, involving explicit solution of the Boltzmann equation (see, for example, Conwell (1967)), represents a formidable problem, and we have chosen, instead, to use the Monte Carlo method. This method was first applied to the study of electronic transport by Kurosawa (1966), and was subsequently developed by Fawcett and co-workers (see Fawcett *et al.* 1970). The principal advantages of the Monte Carlo method are that it allows a quite general description of the carrier states, gives direct information on the carrier distribution function, and can be used to study transient phenomena with little extra effort.

We have developed our own Monte Carlo simulations from first principles, and we will begin discussion of our work in Chapter 2, by setting out the details of the Monte Carlo method, with reference to these algorithms.

Essential to any study of carrier transport properties is an understanding of the interaction between the carrier and lattice systems (carrier-phonon scattering). In Chapter 3 we will briefly review the essential features of carrier-phonon scattering, and give the derivations of expressions for the scattering of both electrons and holes in GaAs by the principal phonon modes. Then, in Chapter 4 we will show some results from our prototype simulation of hole transport in *bulk* GaAs.

In Chapter 5 we will consider the scattering of carriers by phonons in a quasi-2D system, and will develop expressions for the scattering matrix elements and rates for quantum confined hole-phonon scattering, based on a realistic (4 band k.p) description of the valence bandstructure. Detailed results for the quantum confined hole-phonon scattering matrix elements in a GaAs/AlAs quantum well will be shown in Chapter 6. These results represent the database for our quantum well Monte Carlo simulations. In Chapter 7 we will examine the form of the densities of states in the GaAs quantum confined valence bands, which we will use to obtain numerical results for hole-phonon scattering rates in the quantum well. In Chapter 8 we will explain how we have modified our basic Monte Carlo algorithms in order to incorporate the detailed model of the quantum well valence

band system.

The results of our Monte Carlo simulations will be shown in chapters 9 and 10. In Chapter 9 we will consider the electric field heating of the quantum confined holes, and will demonstrate the versatility of our Monte Carlo simulations by examining a range transport parameters. In Chapter 10 we will describe a systematic study of transient hole cooling in the GaAs quantum confined valence band system, designed to provide a qualitative and quantitative understanding of the influence of confinement effects on hole transport.

Finally, in Chapter 11 we will summarise the achievements of the work, discuss some of the approximations involved, and offer some suggestions for future research in this subject area. Much of the work described in this thesis is unpublished at present. We will include, in the Appendix to the thesis, a paper (Kelsall *et al.* 1989) which constitutes a preliminary report of this research activity.

CHAPTER 2
THE MONTE CARLO METHOD

The Monte Carlo method is a general purpose computational tool for solving problems associated with a wide variety of disciplines. Rather than solving the problem using postulates and analytical methods, we *model* the 'environment' of the problem and *simulate* the evolution of the relevant parameters in a manner described by a set of random numbers.

The Monte Carlo method can be applied to *probabilistic* problems, in which a particular 'result' is not, in general, repeatable on re-creation of the same environmental conditions. Examples include the simulation of military or business/commercial environments, in which decisions made by key personnel are *biased* by the current 'state' of the environment, but are never an inevitable consequence of that given state.

The Monte Carlo method can also be used to solve problems of a *deterministic* nature, in which a result is expected to be repeatable, and which can therefore be described in a mathematical formulation. In this case, the Monte Carlo method is implemented by developing a description of the problem in terms of a random, or pseudorandom set of processes. The solution of problems of electronic transport belongs in this latter category.

Detailed reviews of the Monte Carlo method as applied to electronic transport can readily be found in the literature (*e.g.*, Price (1979); Jacoboni and Reggiani (1983)), and it is not intended to emulate these here. Rather, it is our intention to set out the important features of the method, and also, to draw attention to some details which are not commonly appreciated. In Section 2A we will describe the constituent elements of a basic Monte Carlo transport simulation; in Section 2B, we will discuss some of the key features of our Monte Carlo computer algorithms, and finally, in Section 2C, we will consider some of the suggested refinements for improving the computational efficiency of the method.

2A BASIC MONTE CARLO TRANSPORT SIMULATION

2A.1: The Stochastic Model of Electronic Transport

Let us consider the simplest case of electronic transport in a semiconductor; *i.e.*, that of an electron† subject to an applied electric field F. In a classical picture, we would expect the electron to travel ballistically under the influence of the field, until scattered, and we may write for the equation of motion:

$$\frac{d\mathbf{p}}{dt} = \hbar\frac{d\mathbf{k}}{dt} = eF, \tag{2.1}$$

where $\mathbf{p}$ is the crystal momentum of the electron, and $\mathbf{k}$, its crystal wavevector.

This ballistic trajectory would be terminated, at some time t, due to scattering of the electron by some mechanism such as interaction with the lattice, or another charge carrier, or some defect or impurity. Upon scattering, the energy and momentum/wavevector of the electron would, in general, be changed, and it would subsequently set off in some new direction to begin another period of ballistic travel. We may imagine a typical electron path to consist of a continuously repeated series of such events, as depicted in Fig. 2.1. In the steady state, the combination of trajectories like this, for all the electrons, would give rise to a resultant motion in the direction of the applied field, and a drift velocity v_d may be defined. Thus, we have satisfied the criterion stated above for the application of the Monte Carlo method to a deterministic problem; namely that the electronic transport phenomenon has been modelled by a set of random processes. We may identify three basic elements of randomness associated with the trajectory shown in Fig. 2.1, which, as we shall see, are all interdependent. The first element lies in the *duration* of each ballistic portion of the electron trajectory, the so called 'free flight time'. The second element is concerned with the identity of the process by which the electron is scattered at the end of each free flight, and the third lies in the choice of the new wavevector $\mathbf{k}'$ after each scattering event. These three random parameters each have an associated non-uniform probability distribution. We will now discuss how values for each parameter may be obtained from a set of random numbers r, evenly distributed in the range [0,1]. The parameter r represents the fundamental random variate in the Monte Carlo algorithm.

Determination of the Free Flight Time

The probability that an electron will be scattered within a time interval dt can be written as $P(\mathbf{k}(t))dt$, where $P(\mathbf{k}(t))$ is the total scattering rate in the semiconductor crystal. Then, the probability that an electron which was last

† Whilst, in this chapter, we will talk of electron transport, our discussion will apply equally well to (charge) carriers of either type — electrons or holes.

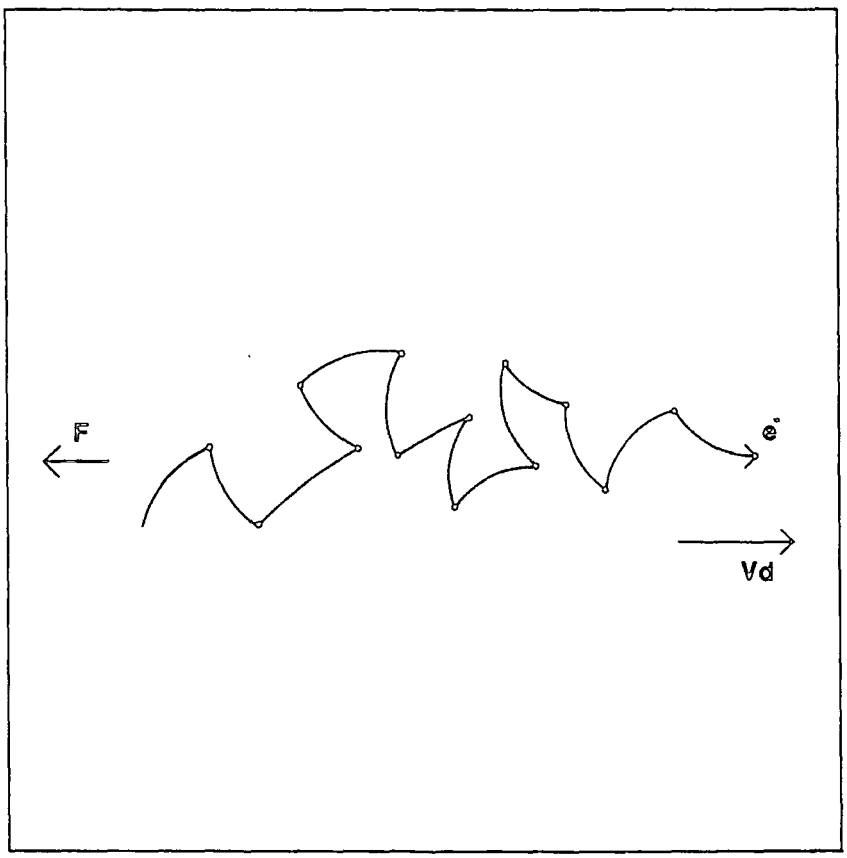

Fig. 2.1 Schematic real-space trajectory of an electron in an electric field F. v_d represents the resultant steady state drift velocity.

scattered at time $t = 0$ still remains unscattered after a time t is given by

$$\exp\left[-\int_0^t P(\mathbf{k}(t'))\,dt'\right],$$

and the probability that this electron will *next* be scattered within an interval dt around t is

$$\mathcal{P}(t)\,dt = P(\mathbf{k}(t))\exp\left[-\int_0^t P(\mathbf{k}(t'))\,dt'\right]dt. \tag{2.2}$$

The function $\mathcal{P}(t)$ therefore gives the probability distribution of the electronic free flights.

Now, the so-called direct technique (see Jacoboni and Reggiani 1983) for the generation of values of a stochastic variate x_r according to a probability distribution $f(x_r)$ in an interval $[a,b]$ is employed via the relation

$$r = \frac{\int_a^{x_r} f(x)\,dx}{\int_a^b f(x)\,dx}. \tag{2.3}$$

After evaluating the integrals, the equation must be inverted to obtain x_r in terms of r. However, unless the scattering rate $P(\mathbf{k}(t))$ has a particularly simple form, this approach leads to a very unwieldy relation between the stochastic flight time t_r and the random variate r, and, in many cases, the inversion of equation (2.3) cannot be achieved at all. This difficulty has been very neatly circumvented by the introduction of the self scattering scheme due to Rees (1968,1969).

Let the maximum value of $P(\mathbf{k}(t))$ encountered in the Monte Carlo simulation be Γ. Then, an additional, fictitious scattering process is introduced, having a scattering rate $s(\mathbf{k})$ such that

$$P(\mathbf{k}) + s(\mathbf{k}) = \Gamma \tag{2.4}$$

for all $\mathbf{k}$. This process is termed 'self scattering', because its occurrence in the simulation is *not* permitted to affect the current state of the electron, as will be discussed later in this section.

The advantage of the self scattering scheme is that the new total scattering rate Γ is independent of t: hence the integrals in equations (2.2) and (2.3) can readily be solved. We thus obtain, for the free flight distribution:

$$\mathcal{P}(t) = \Gamma\exp(-\Gamma t), \tag{2.5}$$

and for the stochastic free flight times;

$$t_r = -\frac{1}{\Gamma}\log_e(1-r). \tag{2.6}$$

Since r is evenly distributed in the interval [0,1], so too is the quantity $(1-r)$, and we may take

$$t_r = -\frac{1}{\Gamma}\log_e r. \tag{2.7}$$

Selection of a scattering process

At the end of each free flight, a scattering process must be selected from the set included in the simulation. This is readily achieved by use of a second random variate r_2. If $P(\mathbf{k})$ is the total scattering rate for an electron in state $\mathbf{k}$, then we should compare the product $S = r_2 P(\mathbf{k})$ successively with the cumulative sums of the rates for one, two, three, *etc.* processes. If $S \leq P_1(\mathbf{k})$, then process 1 should be selected; if $P_1(\mathbf{k}) < S \leq P_1(\mathbf{k}) + P_2(\mathbf{k})$, then process 2 should be selected, and in general, if $P_1 + P_2 + \ldots P_{i-1} < S \leq P_1 + P_2 + \ldots P_i$, then process i should be selected. This procedure is shown schematically in Fig. 2.2.

Of course, in the self scattering scheme, the total scattering rate is simply Γ. However, the self scattering rate $s(\mathbf{k})$ must be included in these cumulative sums, hence there exists a finite probability that the self scattering process will be selected.

Choice of the After-Scattering Electron Wavevector

This choice is made by identifying the angular dependence of the particular scattering process chosen. This can be represented in the form $P(\beta, \gamma)$, where β and γ are the polar and azimuthal angles of the after-scattering wavevector $\mathbf{k}'$ with respect to the before-scattering wavevector $\mathbf{k}$. In most cases of interest the scattering probability is independent of γ, and the angular dependence of the process is given simply by $P(\beta)$. Values for the stochastic β_r can be obtained from a random variate r by the direct technique, or, if the form of $P(\beta)$ precludes this, by one of the so-called rejection techniques. In Chapter 4 we will describe the generation of stochastic scattering angles β_r for specific hole-phonon scattering processes, using both direct and rejection techniques. Details of the rejection techniques are given in Appendix 1.

Values for the stochastic γ_r can be obtained simply from the formula $\gamma_r = 2\pi r$, and the magnitude of the after-scattering wavevector is given by energy conservation.

If a self scattering event is selected, then the energy and wavevector of the electron are not changed; the electron commences its next phase of ballistic motion occupying exactly the same state. The only effect of the self scattering events is therefore to subdivide the actual ballistic trajectories of an electron into a series of shorter paths, the duration of which follow the probability distribution of equation (2.5). Fawcett *et al.* (1970) give a mathematical proof which shows that the introduction of self scattering *does not alter* the distribution $P(t)$ of the duration of flights terminated by a real scattering event.

The disadvantage of the self scattering scheme is, of course, that the selection of a self scattering process in the Monte Carlo simulation represents wasted computer

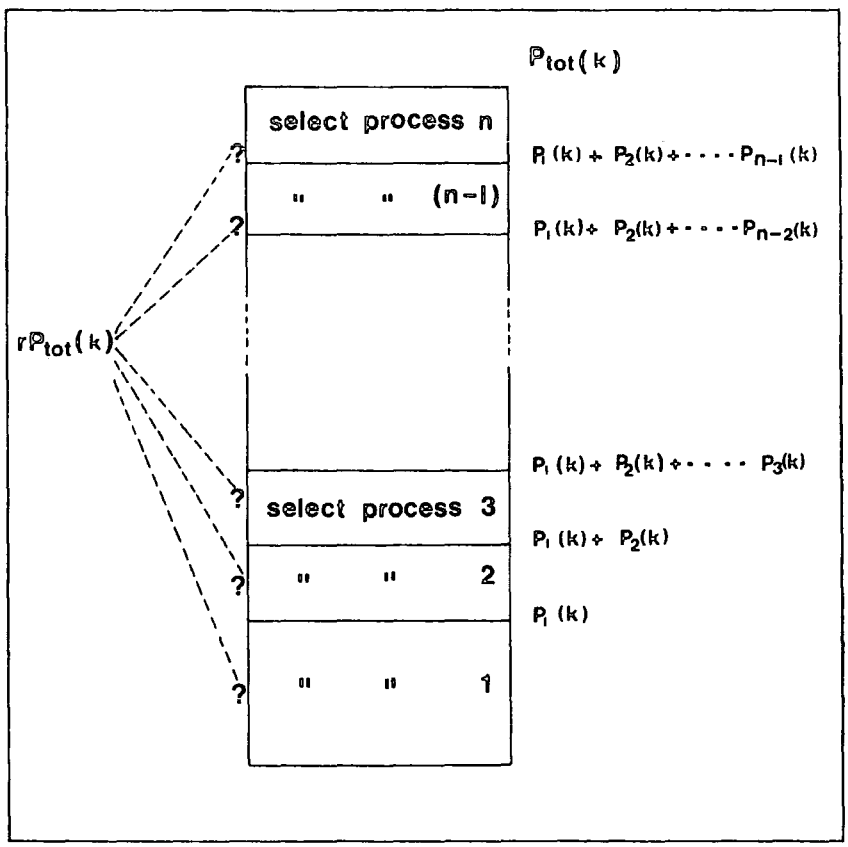

Fig. 2.2 Schematic representation of the scattering process selection algorithm in a Monte Carlo simulation.

processing time. It is therefore desirable to use the lowest possible value of Γ, in order to minimise the occurrence of such events. Where the proportion of self scattering events in a simulation is particularly large, further refinements can be used to improve the computational efficiency, as will be discussed in Section 2C.

2A.2: Monte Carlo Estimators

To simulate electronic transport in the steady state, it is simply necessary to repeat, a large number of times, the three steps described in the previous section. The values of drift velocity, mean energy *etc.* deduced from this 'history' of a single electron can then be taken as characteristic of the steady state values for the entire carrier system. This is the so-called single particle Monte Carlo simulation. The simulation time in this case is effectively a dummy parameter. If the study of time (or space) dependent effects is desired, then it is necessary to simulate, in parallel, the paths of a representative batch or 'ensemble' of electrons. This is known as an ensemble Monte Carlo simulation.

In both types of simulation, data pertaining to the electron state is sampled at frequent intervals, and this information is used to form expectation values of macroscopic parameters such as the electron drift velocity, mean energy *etc.* Such quantities are known as estimator values, or estimators, and will be denoted here by the use of angle brackets $\langle\rangle$. In this section, we will describe the methods for obtaining estimator values in both ensemble and single particle simulations. An important advantage of the Monte Carlo method over other approaches for solving problems of electronic transport is that detailed information on the electron distribution function in wavevector and energy space can be directly obtained. This feature will also be discussed.

Ensemble Estimators

In an ensemble simulation, it is usually required to obtain estimator values at regular time intervals Δt. The expectation value of a parameter x at a time $t_{\rm obs}$ is simply the ensemble average

$$\langle x(t_{\rm obs})\rangle = \frac{1}{N_{\rm ens}} \sum_{i=1}^{N_{\rm ens}} x_i(t_{\rm obs}), \tag{2.8}$$

where the subscript i indexes the electrons in the ensemble, and the total number of electrons is $N_{\rm ens}$.

This approach can be used to obtain the electron drift velocity $\langle v_d\rangle$, the mean energy $\langle\epsilon\rangle$, and, for a multiband system, the fractional population of a given band $\langle\overline{n}\rangle$. These three quantities represent the basic estimators used in our Monte Carlo simulations.

Steady State Estimators

There are two different approaches to calculating estimator values in a steady state simulation. In the first approach, as exemplified by Fawcett *et al.* (1970), the expectation value of a parameter x is obtained as a time average over the entire set of free flights:

$$\langle x \rangle = \frac{1}{T}\int_0^T x\,dt = \frac{1}{T}\sum_{i=1}^{n}\int_0^{t_r} x\,dt, \tag{2.9}$$

where T is the duration of the electron 'history' and the sum is taken over all free flights in the electron path.

Then, for the steady state drift velocity we may write

$$\begin{aligned}\langle v_d \rangle &= \frac{1}{T}\sum_{i=1}^{n}\frac{1}{\hbar}\int_0^{t_r}\frac{\partial \epsilon}{\partial \mathbf{k}}\,dt \\ &= \frac{1}{eFT}\sum_{i=1}^{n}\int_{\mathbf{k}_a}^{\mathbf{k}_b}\frac{\partial \epsilon}{\partial \mathbf{k}}\,d\mathbf{k}\end{aligned} \tag{2.10}$$

where ϵ is the electron energy, $\mathbf{k}_a$ and $\mathbf{k}_b$ are the electron wavevectors at the beginning and end of each free flight, and we have used equation (2.1) to change the variable of integration.

Irrespective of the form of the dispersion relation $\epsilon(\mathbf{k})$, this expression reduces to

$$\langle v_d \rangle = \frac{1}{eFT}\sum_{i=1}^{n}(\epsilon_b - \epsilon_a), \tag{2.11}$$

where ϵ_a and ϵ_b are the electron energies corresponding to the wavevectors $\mathbf{k}_a$ and $\mathbf{k}_b$. The estimator $\langle v_d \rangle$ as defined in equation (2.11) will be referred to as the FBS drift velocity estimator (after Fawcett, Boardmann and Swain (1970)).

The second method of obtaining estimator values in a steady state simulation is based on the so-called before-scattering-ensemble (B-ensemble) theorem of Price (1968,1970) (see also Jacoboni and Reggiani (1983)). The theorem states that, in the steady state, the before-scattering electron distribution $f_b(\mathbf{k})$ — defined as the probability that an electron will be found in a state $\mathbf{k}$ immediately before a scattering event — is related to the actual distribution $f(\mathbf{k})$ according to

$$f(\mathbf{k}) \propto \frac{f_b(\mathbf{k})}{P(\mathbf{k})}. \tag{2.12}$$

This means that the distribution $f(\mathbf{k})$, and indeed any other parameter, may be obtained by sampling data *at the end* of each free flight and weighting the samples by the scattering rate $P(\mathbf{k})$. In particular, when self scattering is included the total rate is Γ, which is independent of $\mathbf{k}$, and hence

$$f(\mathbf{k}) \propto f_b(\mathbf{k}). \tag{2.13}$$

This correlation between $f_b(\mathbb{k})$ and $f(\mathbb{k})$ may be understood by reference to Fig. 2.3, which shows schematic trajectories for an ensemble of electrons relative to a common time origin. If a line AA' is drawn through the time axes, to represent the observation of the ensemble at some time t_{obs}, then the distribution of the lengths of the set of partial flights, each beginning on the line AA' and each terminating at some time $t_i > t$, will be identical to the distribution of a set of N_{ens} ordinary flights. Then, the average length of of the partial flights to the RHS of the line AA' will be $\tau = 1/P(\mathbb{k})$, and similarly, the average length of the partial flights to the LHS of AA' will also be τ.

Now this shows that, in an ensemble simulation, when an observation is made at any time t, the *average* time since an electron was last scattered is τ. In a single particle simulation, we must accurately model the conditions which apply in a large ensemble of electrons. This means that the appropriate point for collecting data is at the *end* of every free flight, because only this choice of points will reproduce the value τ as the average time elapsed between a scattering and a data collection event.

Expectation values of any parameter may therefore be obtained by the B-ensemble method using the simple formula

$$\langle x \rangle = \frac{1}{N} \sum_{i=1}^{N} x_{b_i}, \tag{2.14}$$

where N is the total number of scatterings, and the x_{b_i} are values of x sampled immediately before each scattering event. The B-ensemble method is particularly useful for generating distribution functions, since no time averaging procedure is necessary.

2A.3: Distribution Functions

When an electric field is applied to a semiconductor, the electron distribution can be represented by a function $F(\epsilon, \theta)$, where θ is the angle between the electron wavevector $\mathbf{k}$ and the field direction. In a Monte Carlo simulation, the energy distribution function can be obtained directly by setting up a mesh in energy space. For a single particle simulation in the B-ensemble scheme, it is simply necessary to increment a tally corresponding to the energy cell occupied by the electron (in a given band) immediately before each scattering event. The distribution function can then be normalised at the end of the simulation by dividing the tally for each cell by the total number of scattering events which occurred within the given band. For an ensemble simulation, an identical energy mesh is used, but each distribution function is compiled in its entirety by identifying the energy cell occupied by every electron in the ensemble at the observation time t_{obs}.

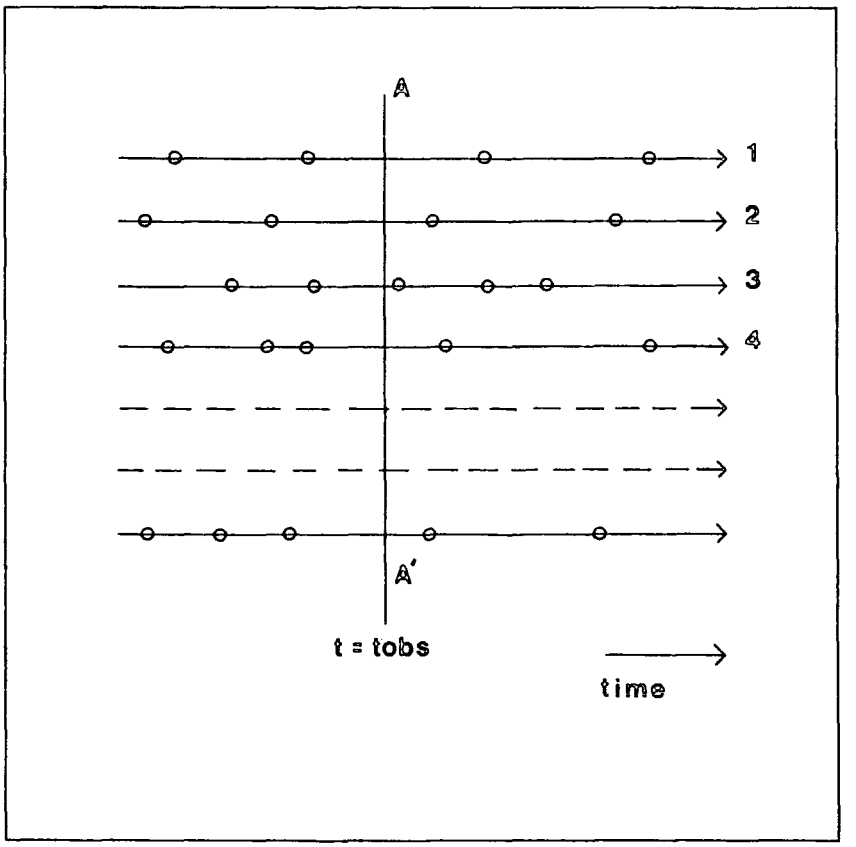

Fig. 2.3 Schematic trajectories of an ensemble of electrons, shown on a common time axis. The open circles represent scattering events, and the line AA' represents an observation of the ensemble made at time $t = t_{obs}$.

This direct sampling approach entails (for 3D systems) an implicit integration over $\cos\theta$, and therefore yields an energy distribution of the form

$$f(\epsilon) = \int_{-1}^{1} F(\epsilon,\theta)D(\epsilon)\,d(\cos\theta), \tag{2.15}$$

where $D(\epsilon)$ is the density of states, which, for a parabolic band in a bulk semiconductor, is proportional to $\epsilon^{1/2}$.

Now, the distribution function $F(\epsilon,\theta)$ may be expanded in a spherical harmonic series (see Conwell 1967):

$$\begin{aligned} F(\epsilon,\theta) &= \sum_{n=0}^{\infty} f_n(\epsilon)P_n(\cos\theta) \\ &= f_0(\epsilon) + f_1(\epsilon)\cos\theta + f_2(\epsilon)\,\tfrac{1}{2}(3\cos^2\theta - 1) + \cdots \end{aligned} \tag{2.16}$$

where the $P_n(\cos\theta)$ are Legendre polynomials.

It is possible to obtain any of the components $f_n(\epsilon)$ from the Monte Carlo simulation. The orthogonality property of the Legendre polynomials gives

$$\begin{aligned} \int_{-1}^{1} P_m(\cos\theta)F(\epsilon,\theta)\,d(\cos\theta) &= \sum_{n=0}^{\infty} f_n(\epsilon)\int_{-1}^{1} P_m(\cos\theta)P_n(\cos\theta)\,d(\cos\theta) \\ &= \frac{2}{2m+1}f_m(\epsilon). \end{aligned} \tag{2.17}$$

Thus, comparison of the LHS of equation (2.17) and the RHS of equation (2.15) shows that, if each tally increment in the Monte Carlo simulation is weighted, firstly by $1/\epsilon^{1/2}$ to remove the density of states contribution, and secondly by 1, $\cos\theta$, or $(3\cos^2\theta - 1)/2$, we should obtain the coefficients of the zeroth, first or second spherical harmonics of the distribution function respectively. We have used this method to successfully reproduce the results obtained by Fawcett and Rees (1969) for the harmonic components of the electron distribution function in the Γ valley of GaAs (Fig. 2.4). In most cases however, only the zeroth, or spherically symmetric component of the distribution function is of interest.

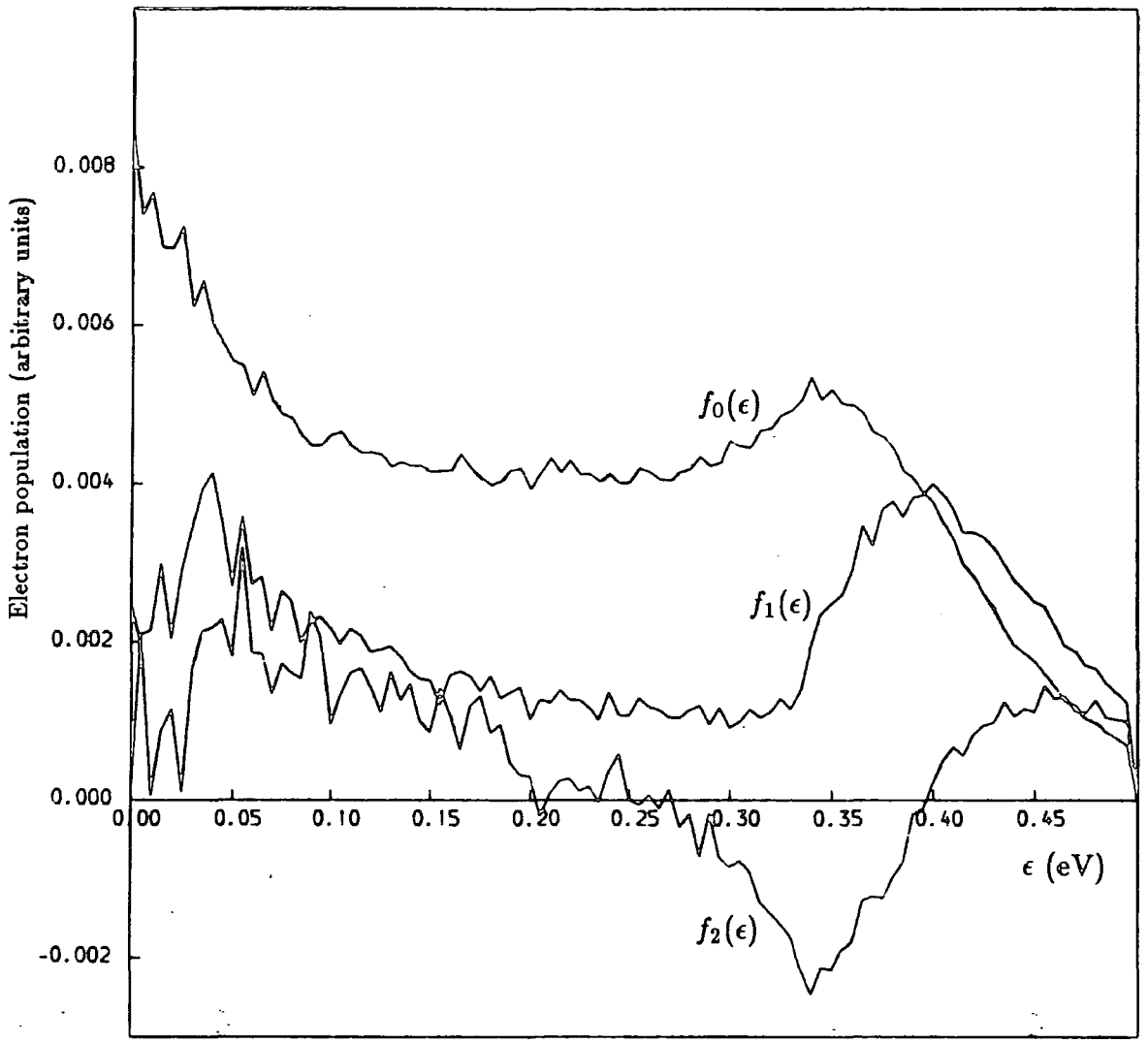

Fig. 2.4 Coefficients of the first three harmonic components, $f_0(\epsilon)$, $f_1(\epsilon)$ and $f_2(\epsilon)$ of the electron distribution in the Γ valley of GaAs at a field of 15kVcm^{-1} (after Fawcett and Rees 1969). The results were obtained from a two valley steady state simulation including acoustic, polar optical and intervalley scattering, at a lattice temperature of 300K.

2B MONTE CARLO ALGORITHMS

2B.1: Single Particle Algorithm

We have used the principles described in the previous section to write prototype single particle and ensemble Monte Carlo programs to simulate electronic transport in a bulk semiconductor. Fig. 2.5 shows the flow diagram for our single particle program. The program was written in standard FORTRAN77, and where appropriate, we have shown the names of FORTRAN subroutines. We have also shown the principal FORTRAN variables sent and returned from the routines. These include the 'state variables' of the electron — the energy $\epsilon \equiv$ EI, and the wavevector components $k_x \equiv$ VIX, $k_y \equiv$ VIY and $k_z \equiv$ VIZ. The suffix 'I' in the FORTRAN variable names denotes quantities measured at the beginnning of a free flight, those measured at the end of a flight have 'I' replaced by 'F' (*i.e.*, EF, VFX, VFY, VFZ). In a simulation involving more than one energy band (or valley), the band index IBAND is also a state variable of the electron.

The main simulation loop contains the three stochastic elements of the Monte Carlo algorithm, as described in section 2A.1. The free flight time and the energy and wavevector components at the end of the flight are calculated in the subroutine DRIFT. A scattering process is then selected in subroutine SMECH, which, in turn, calls the one of the subroutines K1, K2, or K3, in which the after-scattering wavevector is generated according to an angular probability distribution appropriate to the particular process. If self scattering is selected, then the subroutine KSELF is called, which simply returns the same values for the after-scattering state variables as those which pertained immediately before scattering.

The scattering rates are calculated for a wide range of energies at the initialisation stage of the program; *i.e.*, before the main simulation loop. This approach makes for faster program execution time than if the relevant scattering rates were to be calculated upon each call to the scattering process selection routine SMECH. Also, it allows the code pertaining to the calculation of the scattering rates to be contained within a separate set of subroutines, which can readily be modified, or transferred to another program, without affecting the rest of the code.

In the process selection routine SMECH, it is not the scattering rates themselves, but the *cumulative sums* of the scattering rates for 1,2,3 *etc.*, processes which must be successively compared with the random variate $r\Gamma$, in order to make a selection (see Fig. 2.2). Indeed, during the simulation the individual scattering rates are never used; only these cumulative sums are required. Therefore these sums are formed at the initialisation stage of the simulation and are stored in a single 3D array SCLAD(M,J,K), where the index M gives the energy at which the rates are calculated, K indexes the energy band, and J gives the number of

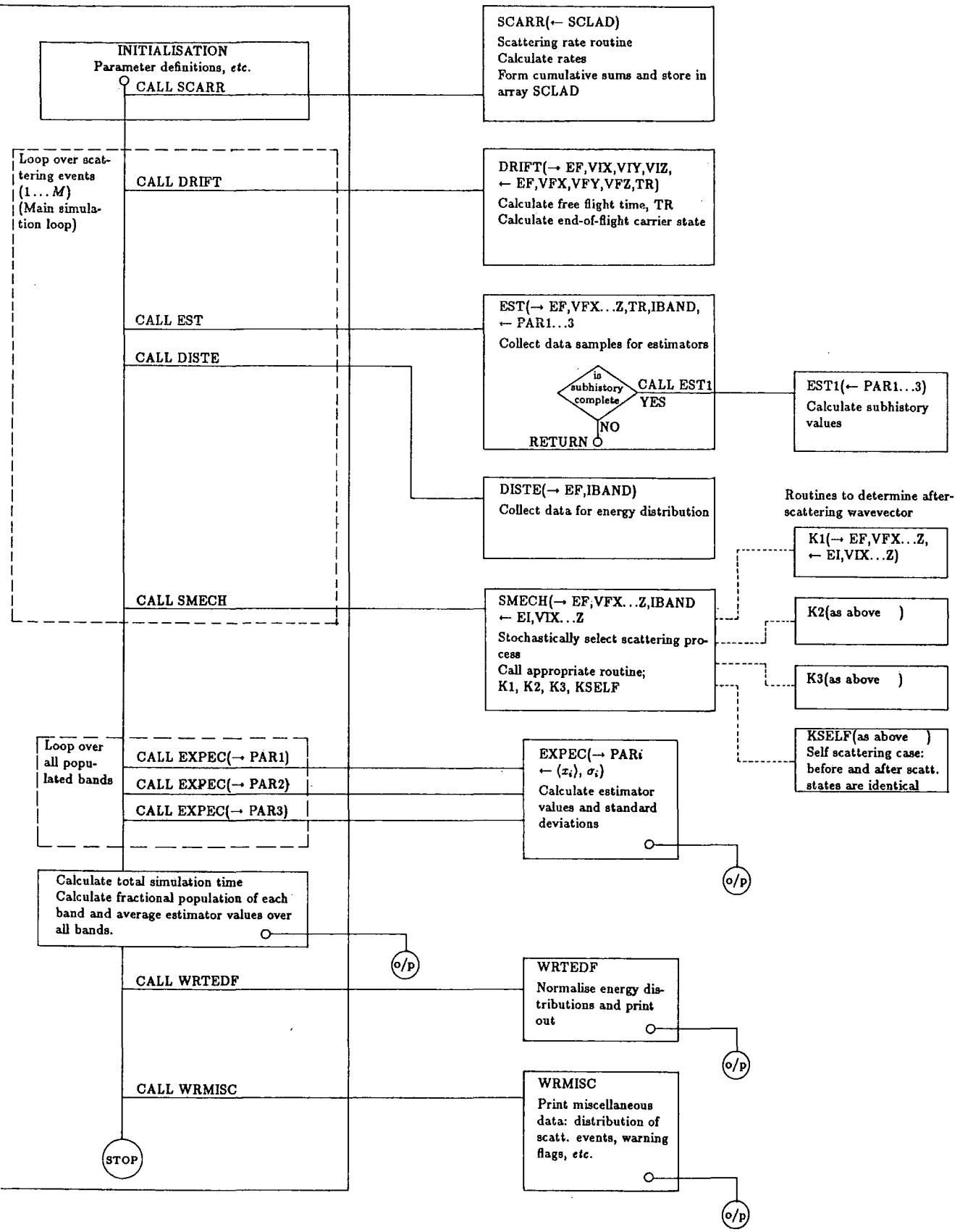

Fig. 2.5 Flow diagram for single particle Monte Carlo program, showing principal FORTRAN subroutine and variable names. '→' indicates variables passed to routines; '←' indicates variables for which new values are returned.

terms in the cumulative sum. The process selection algorithm depicted in Fig. 2.2 can then be readily implemented as a cascade of IF...THEN...ELSE clauses, as shown in Fig. 2.6. In this example, the angular dependence of the first, second and third scattering processes is contained within the subroutines K1, K2, and K3 respectively, and the third process is an interband transition.

Information on the current electronic state is collected by a subroutine EST, which is called at the end of each free flight. We have used the method of Alberigi Quaranta *et al.* (1971) in which the total simulation is divided into 'subhistories', with estimator values obtained in each such period. At the end of the simulation, the actual estimators are obtained as averages of these subhistory values. The method enables evaluation of the statistical error in the final estimator values, as deduced from the standard deviation of each set of subhistory values, since, for purely random fluctuations, the standard deviation decreases as $1/\sqrt{N}$, where N is the sample size. The subroutine EST1 is used to calculate subhistory values, whenever a subhistory is complete, and these values are stored in arrays PAR1, PAR2 and PAR3. At the end of the program, the final estimators are obtained from the subhistory values by use of a subroutine EXPEC, which also gives the estimated tolerance of each parameter.

Data for the compilation of an electron distribution function is also collected at the end of each free flight (B-ensemble scheme). The subroutine DISTE increments the appropriate element of an array representing the energy mesh. The increments can be weighted to obtain the required harmonic component of the distribution function.

The total simulation time in each energy band is obtained from the sum of the subhistory durations. These quantities are used to calculate the fractional population in each band, and to form averages of the estimator values over the whole system.

2B.2: Ensemble Algorithm

In developing an ensemble Monte Carlo program, we may take advantage of the features which are common to both single particle and ensemble simulations. In particular, the subroutines associated with the calculation of scattering rates may be transferred unmodified between the two programs, and, provided that the calling subprogram is appropriately designed, the subroutines K1, K2, K3 and KSELF will also be compatible with both types of simulation. This use of common sets of subroutines for the single particle and ensemble simulations is an important aid to program development.

In Fig. 2.7 we have shown the flow diagram for our prototype ensemble Monte Carlo program. Obviously, the main differences between this program and the

```
SUBROUTINE SMECH (EF,VFX,VFY,VFZ, EI,VIX,VIY,VIZ)
IMPLICIT REAL*8 (A-H, O-Z)
DIMENSION SCLAD (0:1000,20,2)

COMMON /LADDER/ SCLAD
COMMON /SIM/      GAM(2)
COMMON /VALP/     IBAND

IE = IDINT(EF*1000)
S = GAM(IBAND) * G05CAF(1)

IF (S .LE. SCLAD(IE, 1, IBAND) THEN
  CALL K1(VFX,VFY,VFZ,EF, VIX,VIY,VIZ,EI)
ELSEIF (S .LE. SCLAD(IE, 2, IBAND) THEN
  CALL K2(VFX,VFY,VFZ,EF, VIX,VIY,VIZ,EI)
ELSEIF (S .LE. SCLAD(IE, 3, IBAND) THEN
  CALL K3(VFX,VFY,VFZ,EF, VIX,VIY,VIZ,EI)
  IBAND = 2
ELSEIF. . .
.
.
ELSE
  CALL KSELF(VFX,VFY,VFZ,EF, VIX,VIY,VIZ,EI)
ENDIF

RETURN
END
```

Fig. 2.6 FORTRAN code for an example version of the scattering process selection subroutine SMECH in a single particle Monte Carlo program. The function G05CAF is the basic Numerical Algorithms Group (NAG) random number generator (NAG 1987).

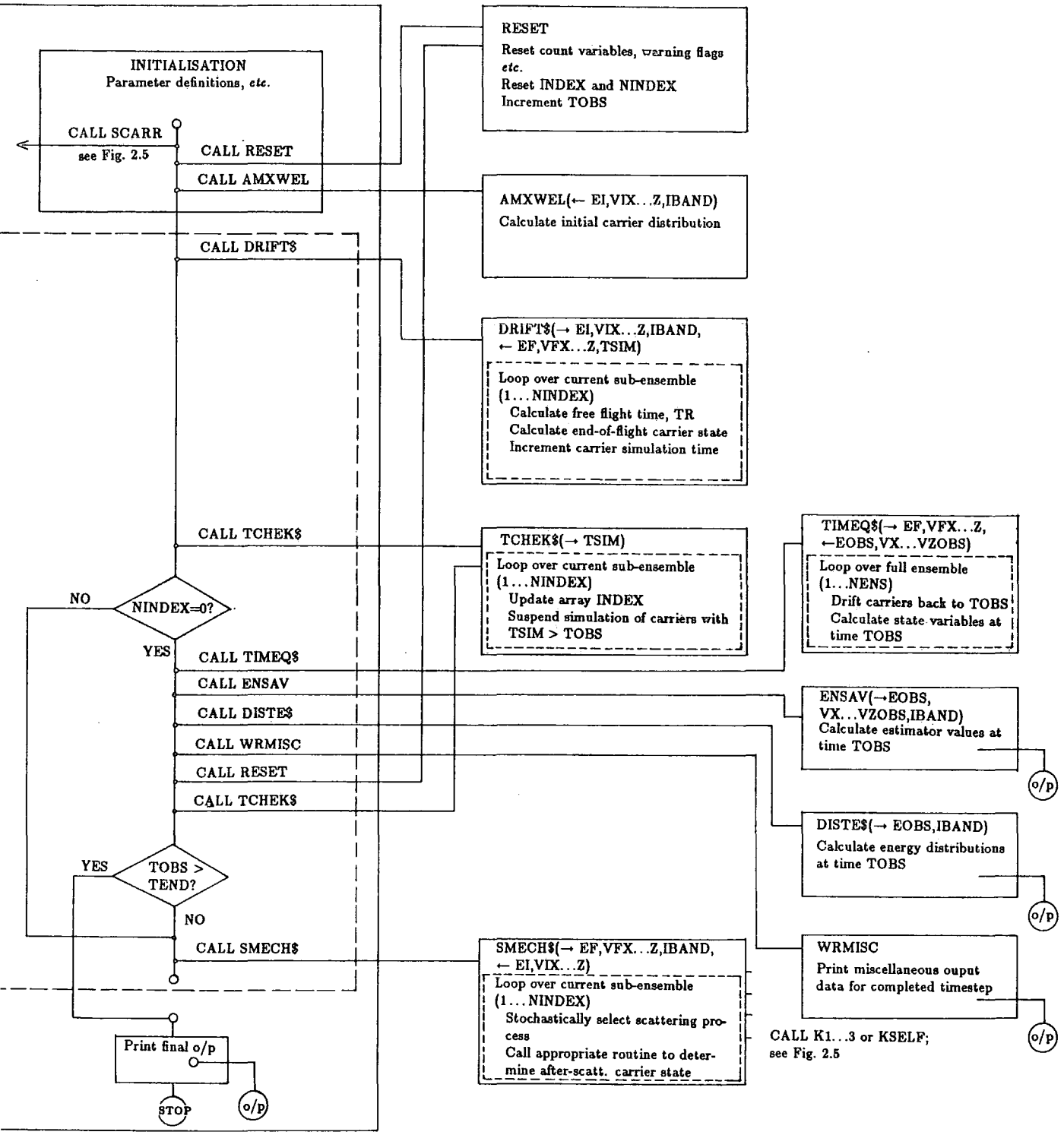

Fig. 2.7 Flow diagram for ensemble Monte Carlo program using backdrifting method (see text). Principal FORTRAN subroutine and variable names are shown.

single particle program are, firstly, that in the ensemble case a large number ($N_{\text{ens}} \equiv$ NENS) of electron trajectories are simulated 'in parallel', and secondly, that the simulation time is a real, rather than a dummy variable. In certain programming languages, such as APL, the inherent parallelism of the ensemble Monte Carlo algorithm may be translated directly into parallel (vector) processing instructions. However, in FORTRAN only serial processing is available. This means that the implementation of a particular operation on a whole batch of electrons must be achieved in the simulation either by a very large number of calls to a subroutine which operates on just one electron, or by a single call to a routine which contains a loop over the whole batch. The former approach is expensive in computer processing time, since the subroutine CALL instruction entails a number of processing steps. Therefore, we have adopted the latter approach, using what we will call 'ensemble-handling' routines, which we will label by the suffix \$. Thus, for example, the subroutine DRIFT\$ in Fig. 2.7 calculates the free flight times and subsequent energies and wavevectors for a whole batch of electrons, in contrast to the routine DRIFT in Fig. 2.5, which performs the same operations on a single electron.

The state variables of the ensemble of electrons are stored in a set of ensemble (sized) arrays which are passed between the various ensemble-handling routines. We have named these arrays EI, VIX, VIY, VIZ *etc.*, corresponding to the state variables in the single particle program. An ensemble array IBAND is used to store the band indices of all the electrons.

In a single particle simulation, the state of the electron at the beginning of the simulation is of no consequence; its effect on the final estimator values is negligible due to the averages taken over the entire simulation duration. However, in an ensemble simulation, the initial *distribution* of the ensemble of electrons represents an important initial condition in the transient transport problem. Our ensemble program allows the form of the initial electron distribution to be freely altered. In Fig. 2.7 we have indicated, as an example, the use of a subroutine AMXWEL, to generate a Maxwell-Boltzmann distribution of electrons at $t=0$. However, in Chapter 10 we describe simulations which use a variety of predetermined initial carrier distributions.

Now, the main difficulty in the ensemble simulation is that, whilst the electrons begin at a common time origin, as soon as the first set of free flights is generated the simulation time (as given by the cumulative flight time) is different for each electron, and this situation will prevail throughout the simulation. Therefore, a separate record of the simulation time for each electron is stored in the elements of an ensemble array TSIM. However, in an ensemble simulation it is usually required

to obtain estimator values at specific time intervals, which involves interrogation of the state variables for each electron at the *same* observation time $t_{obs} \equiv$ TOBS, relative to the common origin. There are two methods of achieving this, which we will refer to as backdrifting and forward drifting.

In the backdrifting method (Kirton 1987), the simulation of each electron is continued until its simulation time *exceeds* the observation time t_{obs}. Thereafter, the simulation of this electron is suspended until all electrons in the ensemble have passed the observation time. This means that, whilst in the first execution of the simulation loop of Fig. 2.7 trajectories for the whole ensemble of electrons are simulated, in subsequent loop executions some of the electrons will have exceeded the current observation time, and so the operand batch is some remnant-sub-set of the ensemble. The ensemble algorithm must determine not only the size of this 'sub-ensemble' but also its exact composition; *i.e.*, it is necessary to keep an exact record of those electrons which still require further simulation. This is achieved by use of an ensemble array INDEX and an associated integer variable NINDEX. The electrons are indexed by an integer between 1 and NENS, and the array INDEX contains the indices of those electrons still requiring further simulation in any given execution of the simulation loop. The variable NINDEX gives the total number of such electrons, *i.e.*, the current size of the sub-ensemble. Thus, most of the ensemble-handling subroutines employ a loop of the form

```
      DO 100 N = 1,NINDEX
         NP = INDEX(N)
         .
         .
100   CONTINUE
```

In this loop, the index number NP of each electron in the sub-ensemble is obtained in turn; this index can then be used to access the state variables of the NP*th* electron from the ensemble arrays EI, VIX, VIY, VIZ, *etc.* The sub-ensemble, as described by the array INDEX, is modified by the routine TCHEK$ (Fig. 2.8a) which is called immediately following drifting of the ensemble. The sub-ensemble size NINDEX is then tested, and, if this is zero, then the complete ensemble of electrons have now passed the observation time t_{obs}. The ensemble is then drifted *back* to the observation time by use of a subroutine TIMEQ$ (Fig. 2.8b). This simply involves tracing back along the last ballistic trajectory of each electron for a time period (TSIM(N) - TOBS), where TSIM(N) is the current simulation time for the N*th* electron in the ensemble. The state variables of the ensemble at the observation time are stored in the arrays EOBS, VXOBS, VYOBS and VZOBS,

```
      SUBROUTINE TCHEK$
      IMPLICIT REAL*8(A-H,O-Z)
      DIMENSION  TSIM(10000)
      INTEGER*2  IBAND(10000), INDEX(10000)
      COMMON /SIM/   GAM(2), TOBS, NENS,NINDEX, TSIM,IBAND,INDEX

      NNEW = 0                                                    (a)
      DO 10 N = 1,NINDEX
         NP = INDEX(N)
         IF (TSIM(NP)  .GE.  TOBS)  GOTO 10
         NNEW = NNEW + 1
         INDEX(NNEW) = NP
10    CONTINUE

      NINDEX = NNEW
      RETURN
      END



      SUBROUTINE TIMEQ$(EF,VFX,VFY,VFZ,  EOBS,VXOBS,VYOBS,VZOBS)
      IMPLICIT REAL*8(A-H,O-Z)
      DIMENSION  VFX(10000), VFY(10000), VFZ(10000), EF(10000),
     *                  VXOBS(10000), VYOBS(10000), VZOBS(10000),
     *                    EOBS(10000), TSIM(10000)
      INTEGER*2  IBAND(10000), INDEX(10000)
      COMMON /FUND/   ALPHA0, BLSTC, PI                           (b)
      COMMON /SIM/      GAM(2), TOBS, NENS,NINDEX, TSIM,IBAND,INDEX
      COMMON /MAT/      BM(2)

C     Variable ALPHA0 = hbar*hbar/(2m0)
C     Variable BLSTC = F * hbar/e

      DO 10 N = 1,NENS
         IBN = IBAND(N)
         VXOBS(N) = VFX(N)
         VYOBS(N) = VFY(N)
         VZOBS(N) = VFZ(N)  + BLSTC*(TOBS-TSIM(N))
         EOBS(N)  = (VXOBS(N)*VXOBS(N) + VYOBS(N)*VYOBS(N)
     *              + VZOBS(N)*VZOBS(N)) * ALPHA0 / BM(IBN)
10    CONTINUE

      RETURN
      END
```

Fig. 2.8 FORTRAN code for subroutines TCHEK$ (a), and TIMEQ$ (b) in the backdrifting ensemble Monte Carlo program. In subroutine TIMEQ$, the electron energies EOBS(N) are calculated for parabolic bands of effective masses BM(IBN); IBN = 1 or 2.

which are subsequently used to calculate the estimator values in a subroutine ENSAV. After the observation has been made, the subroutine RESET is called to refill the array INDEX with the complete set of electron indices 1...NENS, and to assign to NINDEX the value NENS. The observation time TOBS is also incremented.

However, even after the increment of TOBS, it is still possible that some of the electrons have simulation times greater than this new observation time. The simulation of these electrons must be suspended *immediately*, before any scattering takes place. Thus, an extra call to subroutine TCHEK$ is necessary following the call to subroutine RESET (see Fig. 2.7). This is the main disadvantage of the backdrifting method; *i.e.*, that electrons are allowed to drift well beyond the current observation time.

In the forward drifting method (Price 1979), the simulation times of individual electrons are not allowed to exceed the current observation time; the electrons are drifted, one by one, up to the time TOBS. This is achieved by the simulation loop shown in Fig. 2.9. The subroutine FFT$ simply calculates free flight times for the current sub-ensemble, and these are returned in the ensemble array TR. The subroutine SIFT$ (Fig. 2.10) is essentially an amalgamation of the subroutines DRIFT$, TCHEK$ and TIMEQ$ used in the backdrifting program. In this subroutine, the extrapolated simulation time for each electron (TSIM(NP)+TR(NP)) is compared with the observation time TOBS. If a free flight of duration TR(NP) would take the NP*th* electron beyond TOBS, then it is simply drifted right up to TOBS. The electron state at TOBS is stored, and the electron is removed from the sub-ensemble. On the other hand, if the proposed free flight does not take the electron beyond the observation time, then drifting is performed as normal, and the electron is retained in the new sub-ensemble. In both cases, in the code shown in Fig. 2.10, drifting is performed by calling a single-particle-handling subroutine DRIFT. When NINDEX = 0, the estimator values can be obtained immediately by a call to subroutine ENSAV, since the electron states at time TOBS have already been determined for the whole ensemble. After the observation has been made, the ensemble must once more be drifted. It is not valid to proceed by scattering the electrons, since the time point TOBS does not represent the end point of a free flight on any of the electron trajectories.

At first sight, it would seem necessary to store both the simulation times TSIM(NP) for each electron at the end of the last complete free flight before TOBS, and the free flight durations TR(NP) which take each electron across the observation point, in order to continue the simulation, after the observation, using the correct set of flight times. However, Price (1979) has pointed out that this is

```
      .
      .
      DO 100 M = 1, MSIM
         CALL FFT$(TR)
         CALL SIFT$(EI,VIX,VIY,VIZ,TR,  EF,VFX,VFY,VFZ,
     *                    EOBS,VXOBS,VYOBS,VZOBS)

         IF (NINDEX .EQ. 0) THEN
            CALL ENSAV(EOBS,VXOBS,VYOBS,VZOBS)
            CALL DISTE$(EOBS)
            CALL WRMISC(M)
            CALL RESET
            IF (TOBS .GT. TEND) GOTO 200
         ELSE
            CALL SMECH$(EF,VFX,VFY,VFZ,  EI,VIX,VIY,VIZ)
         ENDIF

  100    CONTINUE
  200    CONTINUE
      .
      .
```

Fig. 2.9 FORTRAN code for the main simulation loop of the forward drifting ensemble Monte Carlo program. The definitions of subroutines ENSAV, DISTE$, WRMISC, RESET AND SMECH$ are as given in Fig. 2.7.

not necessary. Rather, the simulation time of every electron can be set to TOBS, and the simulation recommenced after the observation by generating a completely new set of free flight times. The justification for this can be found in our discussion of the B-ensemble principle in section 2A.2. We pointed out that the distribution of the the set of remnant portions of free flights following an observation at time t_{obs} is equivalent to the distribution of any normal set of randomly generated flight times. Therefore, such a new set may be directly substituted for the remnant portions, with no loss of statistical integrity in the simulation.

When the above simplification is utilised there is little to choose between the forward and back-drifting methods. The back-drifting method makes for a more elegant program architecture, and a faster execution time than the forward drifting approach, due to the use of a single-particle-handling DRIFT routine in the latter case. The forward drifting method may, however, be more convenient when obtaining values for other estimators, such as the real space electron displacement, where the extrapolation of sample data up to the observation time entails a more complex dependence on time.

Finally, we should point out that in both cases the simulation is terminated when the next observation time exceeds some preset value TEND. Therefore, in contrast to the single particle simulation, the simulation loop variable M is a dummy parameter; it is related neither to the timescales in the simulation, nor to the number of scattering events. Its upper limit should be set sufficiently high so that loop execution is not terminated before the time TEND is reached.

```
      SUBROUTINE SIFT$(EI,VIX,VIY,VIZ,TR, EF,VFX,VFY,VFZ,
     *                          EOBS,VXOBS,VYOBS,VZOBS)
      IMPLICIT REAL*8(A-H,O-Z)
      DIMENSION VIX(10000), VIY(10000), VIZ(10000),EI(10000),TR(10000),
     *          VFX(10000), VFY(10000), VFZ(10000), EF(10000), TSIM(10000),
     *          VXOBS(10000), VYOBS(10000), VZOBS(10000), EOBS(10000)
      INTEGER*2 IBAND(10000), INDEX(10000)

      COMMON /FUND/  ALPHA0, BLSTC, PI
      COMMON /SIM/     GAM(2), TOBS, NENS,NINDEX, TSIM,IBAND,INDEX
      COMMON /VALP/  IBNP

      NNEW = 0

      DO 10 N = 1,NINDEX
         NP = INDEX(N)
         IBNP = IBAND(NP)
         TRNP = TR(NP)
         TSIMNP = TSIM(NP)

         IF (TSIMNP+TRNP .GE. TOBS) THEN
            CALL DRIFT(TOBS-TSIMNP,VIX(NP),VIY(NP),VIZ(NP),
     *                          EOBS(NP),VXOBS(NP),VYOBS(NP),VZOBS(NP))
C           Set carrier simulation time to TOBS;  P.J. Price method.
            TSIM(NP) = TOBS
         ELSE
            CALL DRIFT(TRNP,VIX(NP),VIY(NP),VIZ(NP),
     *                          EF(NP),VFX(NP),VFY(NP),VFZ(NP))
            TSIM(NP) = TSIMNP + TRNP
            NNEW = NNEW + 1
            INDEX(NNEW) = NP
         ENDIF
10    CONTINUE

      NINDEX = NNEW
      RETURN
      END
```

Fig. 2.10 FORTRAN code for the subroutine SIFT$ in the forward drifting ensemble Monte Carlo program.

2C FURTHER REFINEMENTS

Having discussed, in the previous sections, the basic features of the Monte Carlo simulation of electronic transport, we will now consider some of the ways in which the algorithms can be improved. The simulations described suffer from two main drawbacks: firstly, the proportion of self scattering events can be quite large, representing inefficient use of computer processing time, and secondly, the stochastic nature of the simulation can give rise to large fluctuations in the estimator values. The first problem can be alleviated by using some modification of the self scattering scheme, as we will discuss in section 2C.1. The second problem can be countered by some form of variance reduction, a possibility which we will examine in section 2C.2.

2C.1: Improved Self Scattering Efficiency

Several methods have been proposed for reducing the proportion of self scattering events in a Monte Carlo simulation; see, for example, Yorston (1986). All these methods aim, in some way, to reduce the discrepancy between the total scattering rate $P(\mathbf{k})$ and the value of Γ over various portions of the range of ϵ or $\mathbb{k}$ considered. The two most widely used methods are the stepped, or piecewise-constant gamma method (Borsari and Jacoboni 1972), and the iterative gamma method (Hockney and Eastwood 1981)

Stepped Gamma Method

In this method, the constant term Γ ($> P(\mathbf{k})$ for all k) is replaced by a piecewise-constant (stepped) function, as shown in Fig. 2.11. The difference between the area under the stepped profile and that under the largest fixed value Γ_n in the figure represents the reduction in the proportion of self scattering events achieved using this method. Now, if an electron begins a free flight with a wavevector of magnitude $k_a < k_1$, and ends it with a wavevector k_b $(k_{n-1} < k_b < k_n)$, a stochastic flight time may be generated as follows.

From equations (2.2) and (2.3) it can be shown that, for a general form of the scattering rate $P(\mathbf{k})$, the free flight time t_r is related to the random variate r according to

$$r = 1 - \exp\left[-\int_0^{t_r} P(\mathbf{k}(t))\,dt\right], \tag{2.18}$$

whence

$$-\log_e r = \int_0^{t_r} P(\mathbf{k}(t))\,dt \tag{2.19}$$

(where we have replaced $(1 - r)$ with r as in section 2A.1). So, for a stepped gamma profile we may write

$$-\log_e r = \int_0^{t_1} \Gamma_1\,dt + \int_{t_1}^{t_2} \Gamma_2\,dt + \cdots \int_{t_{n-1}}^{t_r} \Gamma_n\,dt, \tag{2.20}$$

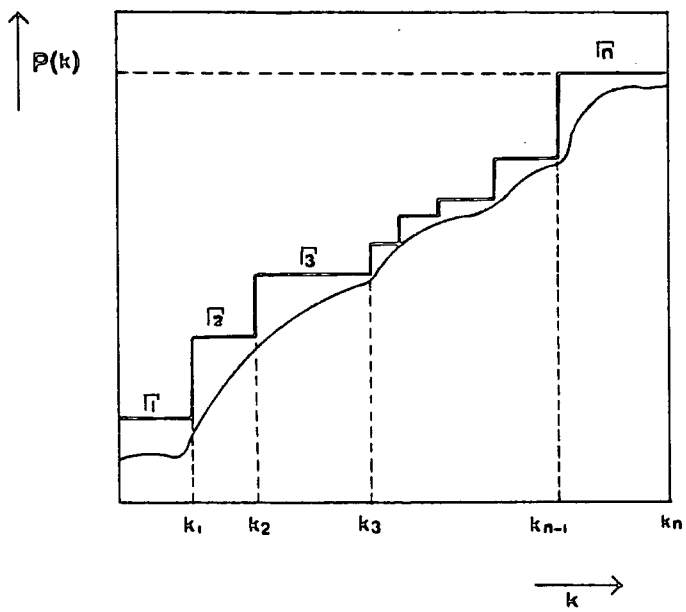

Fig. 2.11 Schematic representation of the stepped gamma method. The bold line represents the piecewise constant fit to the curve giving the total real scattering rate $P(\mathbf{k})$.

where the t_i are the times at which the electron passes the steps at k_1, k_2, *etc.* The free flight time is then obtained as

$$t_r = t_{n-1} - \frac{1}{\Gamma_n}\{\log_e r + t_1\Gamma_1 + \Gamma_2(t_2 - t_1) + \cdots \Gamma_{n-1}(t_{n-1} - t_{n-2})\}. \qquad (2.21)$$

For an electric field applied in the x direction, the times t_i will be given from equation (2.1) as

$$t_i = \frac{\hbar}{eF}(k_{x_i} - k_a); \qquad k_{x_i} = \sqrt{k_i - (k_y^2 + k_z^2)}. \qquad (2.22)$$

At first sight, it might be considered sufficient to calculate the free flight time using the value Γ_1 appropriate to the initial wavevector k_a and, if this gives rise to a final electron wavevector k_b, where $k_{n-1} < k_b < k_n$, then to recalculate the free flight time using each of $\Gamma_1, \Gamma_2 \ldots \Gamma_n$ as in equation (2.21) above. However, since all the subsequent values $\Gamma_2 \ldots \Gamma_n$ will be greater than Γ_1, the new free flight time will be less than that originally calculated, and there is no guarantee that the new value of k_b will be greater than k_{n-1}. Therefore, an algorithm must be employed in which the free flight time is calculated using one, two, three *etc.* values of gamma until the final wavevector k_b obtained corresponds to the upper value of gamma used.

We have shown an example of the implementation of the stepped gamma method in Fig. 2.12. We have used a variable INGAM to index the step positions VSTG, and the corresponding gamma values GAM for each energy band. The index INGAM must be made available to the scattering process selection subroutine SMECH, which must be modified to ensure that the value of gamma appropriate to the end-of-flight (before scattering) state is used in the selection algorithm. In an ensemble simulation, a record of gamma indices must be maintained for the entire ensemble, in which case the scalar variable INGAM must be replaced by an ensemble array.

In a single particle simulation the use of a stepped gamma profile also affects the calculation of B-ensemble estimator values. Equation (2.12) shows that, in general, it is the quotient $f_b(\mathbf{k})/P(\mathbf{k})$, rather than merely $f_b(\mathbf{k})$ which is proportional to the actual electron distribution. Therefore, it is necessary to weight all the data samples for B-ensemble estimators by $1/\Gamma_i$, where Γ_i is the value of gamma appropriate to the before-scattering electron state in each case. The estimator value is then obtained at the end of the simulation by dividing the sum of all such data samples by the quantity $n_1/\Gamma_1 + n_2/\Gamma_2 + \cdots n_n/\Gamma_n$, where, in general, n_i represents the number of flights which ended in the range where the scattering rate $P(\mathbf{k})$ was approximated by Γ_i. When calculating B-ensemble distribution functions within the stepped gamma approach, this $1/\Gamma_i$ weighting must be used in addition to any of the weighting factors described in section 2A.2.

```
      SUBROUTINE  DRIFT6(EI,VIX,VIY,VIZ,  EF,VFX,VFY,VFZ,TFLT)
C     6-stepped Gamma
      IMPLICIT REAL*8(A-H,O-Z)
      COMMON /FUND/   ALPHA0, BLSTC, PI
      COMMON /SIM/      INGAM
      COMMON /MAT/      BM(2)
      COMMON /STGAM/  VSTG(6,2), GAM(6,2), NSTEPS
      COMMON /VALP/    IBNP

C     Find & record index of initial wavevector range,  and select initial Gamma
      V2PERP = VIY*VIY + VIZ*VIZ
      VINIT = DSQRT(VIX*VIX + V2PERP)
      IF (VINIT .LE. VSTG(1,IBNP)) THEN
         INGAM = 1
      ELSEIF (VINIT .LE. VSTG(2,IBNP)) THEN
         INGAM = 2
      ELSEIF (VINIT .LE. VSTG(3,IBNP)) THEN
         INGAM = 3
      ELSEIF (VINIT .LE. VSTG(4,IBNP)) THEN
         INGAM = 4
      ELSEIF (VINIT .LE. VSTG(5,IBNP)) THEN
         INGAM = 5
      ELSE
         INGAM = NSTEPS
      ENDIF

C     Calculate free flight time using initial value of Gamma.
C     (Variable BLSTC = F * hbar/e )
      R1 = G05CAF(1)
      DLNR = DLOG(R1)
      TFLT = -DLNR / GAM(INGAM,IBNP)
      VFX = VXINIT  + BLSTC*TFLT
      VFY = VIY
      VFZ = VIZ
      VMOD = DSQRT(VX*VX + V2PERP)

      IF (VMOD  .GT.  VSTG(INGAM,IBNP)) THEN
C        Set up iterative loop to calculate TFLT using 2,3 etc. values of Gamma.
         TERM = DLNR
         TINIT = VXINIT / BLSTC
         TCURR = TINIT
10       CONTINUE
            INGAM = INGAM + 1
            VSTEP = VSTG(INGAM-1,IBNP)
            VXSTP = DSQRT(VSTEP*VSTEP - V2PERP)
            TLAST = TCURR
            TCURR = VXSTP / BLSTC
            TERM = TERM + GAM(INGAM-1,IBNP) * (TCURR-TLAST)
            TFLT = TCURR - TINIT - TERM/GAM(INGAM,IBNP)
C           Recalculate final state.
            VFX  = VIX + BLSTC*TFLT
            VMOD = DSQRT(VX*VX + V2PERP)
         IF ((VMOD .GT. VSTG(INGAM,IBNP)) .AND. (INGAM .LT. NSTPS))  GOTO 10
      ENDIF

      EF = (VFX*VFX + V2PERP) * ALPHA0 / BM(IBNP)
      RETURN
      END
```

Fig. 2.12 FORTRAN code showing the implementation of the stepped gamma method in a modified version of the single particle routine DRIFT.

Iterative Gamma Method

In this method, a free flight time is first calculated assuming a fixed value of $\Gamma_1 \equiv P(k_a)$, where k_a is the initial electron wavevector. Thus,

$$t_r = \frac{-\log_e r}{\Gamma_1}. \tag{2.23}$$

The end-of-flight wavevector k_b is then obtained, and, if $\Gamma_1 > P(k_b)$ the flight time t_r is accepted, otherwise t_r is recalculated using a new constant value $\Gamma_2 = m\Gamma_1$, where m is a multiplier marginally greater than unity. This process is repeated until a value $\Gamma_i > P(k_b)$ is obtained.

With this method, a new value of Γ is used for each free flight. Yorston (1986) points out that, whilst the scattering function used to generate free flight times must *not* be modified by the occurrence of self scattering events, once a *real* scattering has occurred the value of Γ may be freely altered. Whilst this fact allows iteration of gamma between real scatterings, it would appear that if a self scattering event is selected, it is *not* valid to obtain, by iteration, a new value of gamma in the calculation of the next free flight. It may be argued that, in the iterative gamma scheme, the probability of selecting a self scattering event is so small that this discrepancy will not be of any consequence. This will be true if the scattering rate is a monotonically increasing function of k, whence the value of gamma selected by iteration will always be very close to $P(k_b)$. However, for a general form of the scattering rate, the maximum value of $P(\mathrm{k})$ may not occur at the end of the free flight; hence the choice of $\Gamma > P_{\max}(\mathrm{k})$ may be significantly larger than $P(k_b)$, with a consequent increased probability of self scattering.

A further concern over the iterative gamma method is that, in certain circumstances, the same value of t_r can be obtained using two different values of Γ (Yorston 1986). This means that the function $\Gamma(t)$ is essentially double-valued in certain time ranges, and this will distort the distribution of free flight times. Again, it may be argued that this discrepancy will have only a minor effect on any Monte Carlo simulation; however, it must be concluded that the iterative gamma method gives only an *approximation* (albeit a good one in most circumstances) to the true free flight time distribution.

Rockett (1987) has proposed a so-called linear search technique for generating stochastic free flight times, which is essentially a hybrid of the stepped gamma and iterative gamma methods. This method is reported to give a very small proportion of self scatterings, however, it will still contain the discrepancies associated with the basic iterative gamma method.

2C.2: Variance Reduction

Several general methods have been proposed for reducing the variance associated with parameter values estimated in stochastic simulations (see, for example, Hammersley and Handscomb (1964); Law and Kelton (1982)). In this section we will consider two such methods; those of antithetic and control variates.

Let X and Y be two parameters which are a function of of a set of random numbers r_i, and have the same variance σ^2. If no correlation exists between X and Y, then the variance of each of the quantities $X+Y$ and $X-Y$ is the same as that of X and Y alone. However, if a positive correlation exists between X and Y, then the variance of $X-Y$ will be less than that of X or Y, and, conversely, if a negative correlation exists, then the variance of $X+Y$ will be less than that of X or Y alone.

In the antithetic variate method, we must look for a way of calculating the expectation value of the required parameter which involves the association of quantities having a degree of negative correlation. This approach is based on a theorem (Hammersley and Morton 1956; Hammersley and Mauldon 1956) which states that, to obtain an expectation value for the parameter $X(r_1, r_2, \ldots r_n)$ we may freely rearrange the order of the random variates in the simulation, provided that $X(r_1, r_2, \ldots r_n) \equiv X_1(r_1) + X_2(r_2) + \ldots X_n(r_n)$. Therefore, we may *group together* pairs of the terms $X_i(r_i)$ between which a negative correlation exists: the variance of the expectation value calculated from values for these grouped pairs will be less than that deduced from the $X_i(r_i)$ in isolation.

In the control variate method, the variance of a parameter $X(r_1, r_2, \ldots r_n)$ is reduced by identifying a second parameter $Y(r_1, r_2, \ldots r_n)$ which is positively correlated with X, and whose expectation value $\langle Y \rangle$ is exactly determined. Then

$$X'(r_1, r_2, \ldots r_n) = X(r_1, r_2, \ldots r_n) - Y(r_1, r_2, \ldots r_n) + \langle Y \rangle \qquad (2.24)$$

gives an estimate of $\langle X \rangle$ which will have a lower variance than that associated with $X(r_1, r_2, \ldots r_n)$ alone.

For Monte Carlo simulations of electronic transport, one method of variance reduction which has been cited several times in the literature is that due to Hammar (1971). Hammar's method is essentially an implementation of the antithetic variate technique. He points out that the expectation value of the electron drift velocity in a Monte Carlo simulation may be written as

$$\langle v_d \rangle = \tfrac{1}{2}\langle v_b - v_a \rangle + \langle v_a \rangle, \qquad (2.25)$$

where v_a and v_b are the electron velocities at the beginning and end of a free flight. Most of the statistical fluctuations in the drift velocity are contained within the

term $\langle v_a \rangle$. To combat this, Hammar suggests that after each scattering event *two* electron trajectories are simulated, beginning with equal and opposite after-scattering wavevectors $\mathbf{k}_a$ and $-\mathbf{k}_a$. The same random number is used to generate the free flight times for both trajectories and, at the end of the flights, one of the electron states is chosen at random to continue the simulation. Data samples for the Monte Carlo drift velocity estimator are taken from averages of the electron states for each pair of trajectories (Price 1979): these averaged pairs should give rise to a reduced variance for the final result, since the large fluctuations associated with the quantity $\langle v_a \rangle$ will be smoothed out.

The method is only applicable in the above form if the scattering processes involved have no dependence on the scattering angle ('isotropic' or 'wavevector-randomising' scattering). If this is not the case, then the contribution to the drift velocity estimator from trajectories with initial wavevectors $\mathbf{k}_a$ and $-\mathbf{k}_a$ must be weighted according to the ratio of the scattering probabilities $P(\mathbf{k}_a, \mathbf{k})$ and $P(-\mathbf{k}_a, \mathbf{k})$.

For the case of isotropic scattering, we have devised an alternative approach for obtaining a reduced-variance estimate of the electron drift velocity, based on the control variate method. Our approach has the advantage that the simulation of extra flights, as described above, is not necessary.

If we collect data for the drift velocity estimator around *real* scattering events only, then the expectation value of v_a in equation (2.25) must be zero. From the equation, it is clear that the statistical fluctuations in v_a will be positively correlated with those in v_d; therefore, we can apply the control variate method to calculate

$$\langle v_d \rangle = \langle v_d - v_a \rangle + \langle v_a \rangle \tag{2.26}$$

where $\langle v_a \rangle \equiv 0$.

We have successfully used this method to reduce the variance associated with both FBS and B-ensemble drift velocity estimators. Fig. 2.13 shows the correlation between v_{FBS}, v_{Bens} and v_a, and the effect of applying our control variate method, in a simulation with isotropic scattering. It should be noted that when calculating $\langle v_{\mathrm{Bens}} \rangle$, since data is collected around real scattering events only, the sampled values of before-scattering electron velocity must be weighted by the total real scattering rate $P(\mathbf{k})$, rather than Γ.

The restriction of this method to the case of isotropic scattering precludes its use in the simulations of carrier transport in GaAs and GaAs quantum wells described later in this thesis. However, it may find application in the study of transport in non-polar semiconductors, where the principal scattering processes can be treated in an isotropic (velocity randomising) approximation.

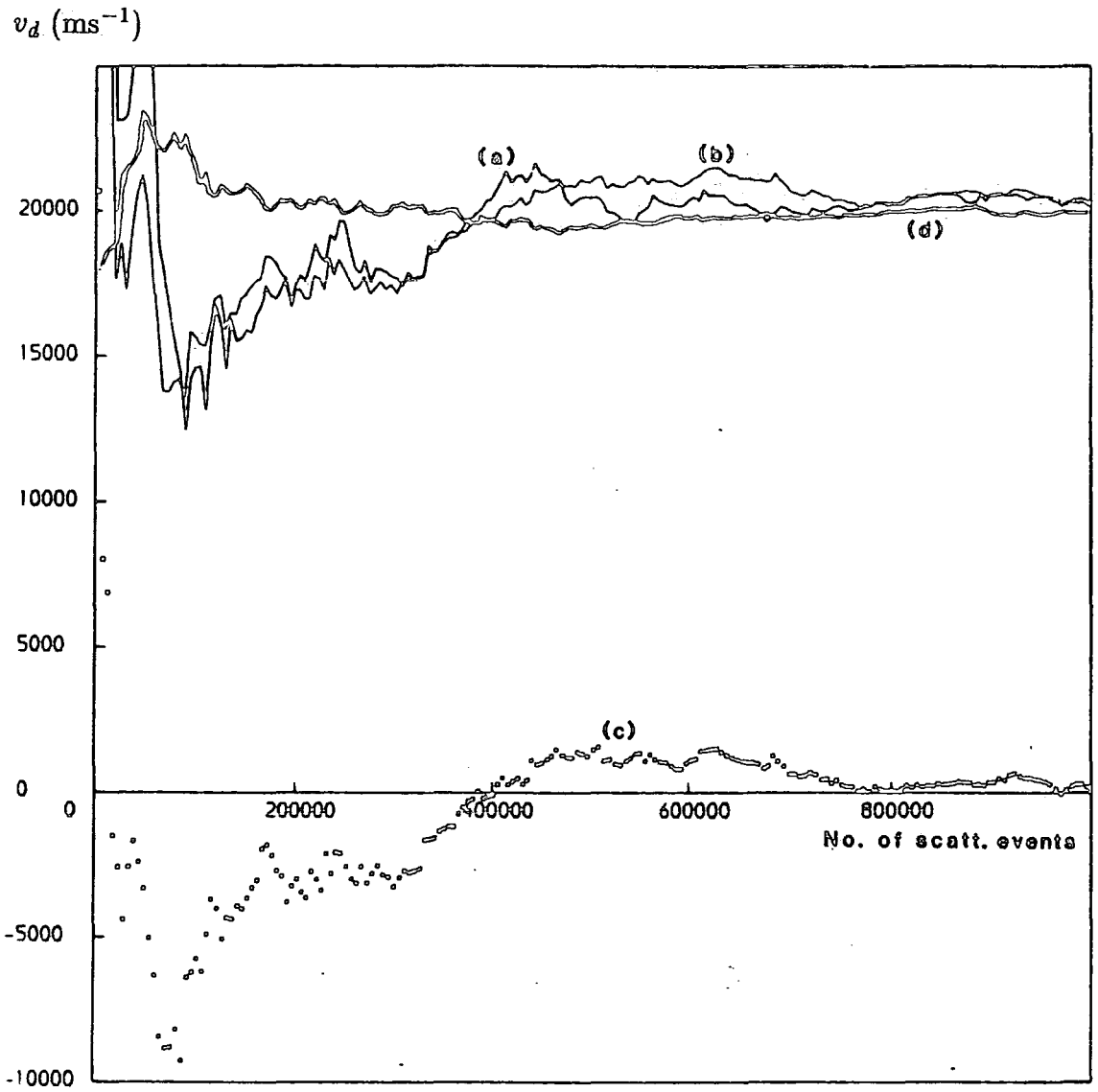

Fig. 2.13 Application of the control variate variance reduction method in a single particle simulation with isotropic scattering, in which data is collected around real scattering events only. Plots (a) and (b) represent the values of v_{FBS} and v_{Bens} obtained without variance reduction, as a function of the total number of scattering events in the simulation. Plot (c) gives the actual values of v_a obtained, and (d) gives the reduced variance estimate of v_{Bens}: $\langle v_{\mathrm{Bens}} - v_a \rangle + \langle v_a \rangle$, where $\langle v_a \rangle \equiv 0$ — see text.

CHAPTER 3
CARRIER-PHONON SCATTERING IN BULK SEMICONDUCTORS

In this chapter we will outline some of the basic principles of the theory of carrier-phonon scattering in a semiconductor. We will derive expressions for the scattering rates of electrons in a single parabolic band, and also for holes in the heavy and light hole valence bands of a III-V semiconductor such as GaAs, for the principal phonon scattering processes.

The purpose of this work is twofold. Firstly, it is necessary to gain an understanding of the physics of phonon scattering in bulk materials, before embarking on any investigation of scattering in quantum confined systems. Secondly, we will use the scattering rate expresssions for holes, derived in Section 3C, to form the basis of a preliminary Monte Carlo simulation of hole transport in bulk GaAs, which we will describe in Chapter 4.

3A FUNDAMENTAL ELECTRON-PHONON SCATTERING THEORY

In this section, some of the fundamental ideas and assumptions of the theory are outlined (section 3A.1). It is then indicated how these can be used to create a generalised phenomenological expression for the electron-phonon scattering rate, in which the details of the interaction due to a particular process are contained within a coupling coefficient term, C_q (see Ridley 1988). In section 3A.2 we will give general expressions for the coupling coefficients for scattering by four different phonon processes:

(i) acoustic phonons via the deformation potential interaction, which we will refer to simply as acoustic scattering,

(ii) optical phonons via the deformation potential interaction, which we will refer to as non-polar optical scattering,

(iii) optical phonons via the polar interaction, which we will call polar optical scattering,

(iv) acoustic phonons via the piezoelectric interaction, which we will refer to as piezoelectric scattering.

These four scattering processes will also be labelled by the abbreviations AC, NPO, POP and PZ respectively. The expressions for the coupling coefficients for these interactions can then be used in the derivation of the scattering rates for electrons in a single parabolic band (Section 3B), and for holes in the heavy and light hole valence bands of GaAs (Section 3C). The same coupling coefficients will also be used in the work on quantum confined carrier-phonon scattering described in Chapter 5.

3A.1: Basic Principles

The adiabatic approximation

The scattering of electrons by phonons involves the interaction of a lattice of ions, disturbed by some vibration, with a gas of conduction electrons. The adiabatic approximation is essential to any practical treatment of this problem. In this approximation, the electrons are assumed to respond almost instantaneously to any change in the lattice configuration (Born and Huang 1954; Ziman 1960) such that the change in the electronic configuration is quasi-continuous, and does not involve transitions to new eigenstates. This means that an eigenvalue equation for the electrons can be solved by assuming the lattice to be frozen in position at any instant of time, in which case the Schrödinger equation is separable and wavefunctions can be separately defined for the electron and lattice systems.

The possibility of electron-phonon scattering can then be considered as a first order correction to the adiabatic picture. A non-adiabatic (coupling) term can be identified in the Hamiltonian for the electron plus lattice system, which operates on both electronic and lattice wavefunctions. This can be regarded as a small perturbation, introducing transitions between states in both the electron and lattice systems.

The transition rate can be obtained using Fermi's Golden Rule:

$$P(\mathbf{k},c) = \frac{2\pi}{\hbar} \int |\langle \mathbf{k}', c'|H_{ep}|\mathbf{k},c\rangle|^2 \delta\Big(E(\mathbf{k}',c') - E(\mathbf{k},c)\Big)\, dS_{\mathbf{k}',c'}, \qquad (3.1)$$

where we have labelled the lattice part of the states by the quantum number c, and the electronic part by the electron wavevector $\mathbf{k}$. The term $E(\mathbf{k},c)$ represents the total energy of the lattice plus electron system in the state $|\mathbf{k},c\rangle$. The final states are denoted by primes, and the integral is taken over all final states $S_{\mathbf{k}',c'}$.

The interaction Hamiltonian H_{ep} is best described in the Bloch formulation (Ziman 1960; Sham and Ziman 1963), in which the effect on the electronic system of a change in atomic displacement is simulated by a change δU in the lattice energy, which scatters the electrons into new states. In this formulation, the electronic states appearing in the scattering matrix element can be taken as stationary states of the undistorted lattice, which means that the particular 'frozen' configuration of the lattice is unimportant.

The continuous lattice approximation

For simple harmonic vibrations of the lattice, the atomic displacement operator at lattice site i is given by (Kittel 1963):

$$\mathbf{u}_i = \frac{1}{2\sqrt{N}} \sum_{\mathbf{q}} \hat{\mathbf{e}}_{\mathbf{q}} \left(Q_{\mathbf{q}} \exp(i\mathbf{q}.\mathbb{R}_i) + Q_{\mathbf{q}}^* \exp(-i\mathbf{q}.\mathbb{R}_i) \right) \tag{3.2}$$

where N is the number of unit cells, $\mathbb{R}_i$ is the position vector of the i^{th} site, $Q_{\mathbf{q}}$ is the normal coordinate for vibrations of mode $\mathbf{q}$, $\hat{\mathbf{e}}_{\mathbf{q}}$ is the unit polarisation vector for the mode, and the sum is taken over all modes $\mathbf{q}$.

In all cases of interest, the perturbing potential δU is proportional to the atomic displacement or its derivative. Therefore, in the simplest treatments, the lattice is assumed to be a continuous medium, so that δU is derived everywhere in the lattice from a smooth, continuous displacement function $\mathbf{u}(\mathbf{r})$. $\mathbf{u}(\mathbf{r})$ is chosen to coincide with the discrete atomic displacements $\mathbf{u}_i$ at the lattice sites. That is

$$\mathbf{u}(\mathbb{R}_i) = \mathbf{u}_i \tag{3.3}$$

and, for long wavelength excitations, it is a good approximation to take

$$\mathbf{u}(\mathbf{r}) = \frac{1}{2\sqrt{N}} \sum_{\mathbf{q}} \hat{\mathbf{e}}_{\mathbf{q}} \left(Q_{\mathbf{q}} \exp(i\mathbf{q}.\mathbf{r}) + Q_{\mathbf{q}}^* \exp(-i\mathbf{q}.\mathbf{r}) \right) \tag{3.4}$$

throughout the lattice. This idea is fundamental to the deformation potential theorem of Bardeen and Shockley (1950), and is also a basic assumption of the analysis of polar scattering by Frohlich (1937). In the continuous lattice approximation, the Bloch formula for the interaction potential can be written as (Seitz 1948; Harrison 1956)

$$\delta U = \mathbf{u}(\mathbf{r}).\nabla U(\mathbf{r}), \tag{3.5}$$

where $U(\mathbf{r})$ is the unperturbed crystal potential.

Lattice part of the scattering matrix element

The normal coordinates $Q_{\mathbf{q}}$ can be expressed in terms of phonon annihilation and creation operators, $a_{\mathbf{q}}$ and $a_{\mathbf{q}}^\dagger$:

$$Q_{\mathbf{q}} = \sqrt{\frac{\hbar}{2M'\omega_{\mathbf{q}}}} (a_{\mathbf{q}} + a_{\mathbf{q}}^\dagger), \tag{3.6}$$

where $\omega_{\mathbf{q}}$ is the angular frequency of the lattice vibration (the phonon frequency). M' is the mass of the unit harmonic oscillator in the lattice, which, in the following cases, is either the atomic mass, or the reduced mass of the two different atoms in the unit cell of a diatomic semiconductor.

Then

$$\mathrm{u}(\mathrm{r}) = \sum_{\mathrm{q}} \hat{\mathrm{e}}_{\mathrm{q}} \sqrt{\frac{\hbar}{2M'N\omega_{\mathrm{q}}}} \left(a_{\mathrm{q}} \exp(i\mathrm{q}.\mathrm{r}) + a_{\mathrm{q}}^{\dagger} \exp(-i\mathrm{q}.\mathrm{r}) \right). \tag{3.7}$$

The wavefunction for the lattice system can be written as a product of harmonic oscillator wavefunctions $\phi_{\mathrm{q}}(Q)$, in the normal mode representation. The operators a_{q} and $a_{\mathrm{q}}^{\dagger}$ each act on just one function in the product, changing the occupation number $\mathcal{N}_{\mathrm{q}}$ of the lattice state $|\mathcal{N}_{\mathrm{q}}\rangle$ by -1 or $+1$ respectively. Thus, by the definition of a_{q} and $a_{\mathrm{q}}^{\dagger}$, the lattice part of the scattering matrix element is

$$\langle \mathcal{N}_{\mathrm{q}} - 1 | a_{\mathrm{q}} | \mathcal{N}_{\mathrm{q}} \rangle = \sqrt{\mathcal{N}_{\mathrm{q}}}, \qquad \text{or} \tag{3.8a}$$

$$\langle \mathcal{N}_{\mathrm{q}} + 1 | a_{\mathrm{q}}^{\dagger} | \mathcal{N}_{\mathrm{q}} \rangle = \sqrt{\mathcal{N}_{\mathrm{q}} + 1}. \tag{3.8b}$$

Equation (3.8a) represents absorption, and (3.8b), emission, of a single phonon of energy $\hbar\omega_{\mathrm{q}}$. Note that, in equation (3.7) the annihilation (absorption) operator a_{q} is associated with the factor $\exp(i\mathrm{q}.\mathrm{r})$, and the creation (emission) operator $a_{\mathrm{q}}^{\dagger}$ with $\exp(-i\mathrm{q}.\mathrm{r})$.

Electronic part of the matrix element

The electronic wavefunction for the carrier system may be expressed as a product of one electron wavefunctions $\psi_{\mathrm{k}}(\mathrm{r})$. For all the cases of interest, the term operating on these wavefunctions is just the plane wave factor $\exp(\pm i\mathrm{q}.\mathrm{r})$ in the interaction described by equations (3.4) and (3.5). Then, the electronic part of the matrix element is given by

$$I(\mathrm{k}', \mathrm{k}) = \int_V \psi_{\mathrm{k}'}^*(\mathrm{r}) \exp(\pm i\mathrm{q}.\mathrm{r}) \psi_{\mathrm{k}}(\mathrm{r})\, d\mathrm{r}, \tag{3.9}$$

where V is the cavity (crystal) volume. The electron wavefunctions are Bloch functions of the form

$$\psi_{\mathrm{k}}(\mathrm{r}) = \frac{1}{\sqrt{V}} u_{\mathrm{k}}(\mathrm{r}) \exp(i\mathrm{k}.\mathrm{r}) \tag{3.10}$$

with the periodic parts $u_{\mathrm{k}}(\mathrm{r})$ normalised to the unit cell volume. Thus

$$I(\mathrm{k}', \mathrm{k}) = \frac{1}{V} \int_V u_{\mathrm{k}'}^*(\mathrm{r}) u_{\mathrm{k}}(\mathrm{r}) \exp\left(i(\mathrm{k} - \mathrm{k}' \pm \mathrm{q}).\mathrm{r} \right) d\mathrm{r}. \tag{3.11}$$

The product $u_{\mathrm{k}'}^*(\mathrm{r}) u_{\mathrm{k}}(\mathrm{r})$ in the above equation can be expanded as a Fourier series over reciprocal lattice vectors g:

$$u_{\mathrm{k}'}^*(\mathrm{r}) u_{\mathrm{k}}(\mathrm{r}) = \sum_{\mathrm{g}} c_{\mathrm{g}} \exp(i\mathrm{g}.\mathrm{r}), \tag{3.12}$$

where

$$c_{\mathrm{g}} = \frac{1}{V_{\mathrm{cell}}} \int_{\mathrm{cell}} u_{\mathrm{k}'}^*(\mathrm{r}') u_{\mathrm{k}}(\mathrm{r}') \exp(-i\mathrm{g}.\mathrm{r}')\, d\mathrm{r}'. \tag{3.13}$$

The integral is evaluated over the volume of a single unit cell, given by V_{cell}. This gives, for $I(\mathbb{k}', \mathbb{k})$:

$$I(\mathbb{k}, \mathbb{k}) = \sum_{\mathbb{g}} c_{\mathbb{g}} \delta_{\mathbb{k}-\mathbb{k}'\pm\mathbb{q},\,\mathbb{g}}. \tag{3.14}$$

In practice, the electron wavevectors $\mathbb{k}$ and $\mathbb{k}'$, and the phonon wavevector $\mathbb{q}$ are usually much smaller than the smallest non-zero reciprocal lattice vectors $\mathbb{g}$. Therefore, only the $\mathbb{g} = 0$ term normally contributes to the sum in equation (3.14). We thus obtain

$$I(\mathbb{k}', \mathbb{k}) = \delta_{\mathbb{k}-\mathbb{k}'\pm\mathbb{q},\,0}\, G(\mathbb{k}', \mathbb{k}), \tag{3.15}$$

where

$$G(\mathbb{k}', \mathbb{k}) = \frac{1}{V_{\text{cell}}} \int_{\text{cell}} u^*_{\mathbb{k}'}(\mathbb{r}) u_{\mathbb{k}}(\mathbb{r})\, d\mathbb{r}, \tag{3.16}$$

the overlap integral.

The Kronecker delta imposes momentum conservation. It gives, for the phonon absorption term:

$$\mathbb{k}' = \mathbb{k} + \mathbb{q}, \tag{3.17a}$$

and for the emission term;

$$\mathbb{k}' = \mathbb{k} - \mathbb{q}. \tag{3.17b}$$

A phenomenological scattering rate formula

The expresssions derived above can now be collected together to give a phenomenological expression for the scattering of carriers by interaction with phonons of any mode. Substituting equations (3.7), (3.8), and (3.15) into equation (3.1), we obtain, for the modulus squared of the scattering matrix element:

$$|\langle \mathbb{k}', \mathcal{N}_{\mathbb{q}} \mp 1^{\ddagger} | H_{\text{ep}} | \mathbb{k}, \mathcal{N}_{\mathbb{q}} \rangle|^2 = \frac{\hbar}{2M'N\omega_{\mathbb{q}}} \begin{bmatrix} \mathcal{N}_{\mathbb{q}} \\ \mathcal{N}_{\mathbb{q}} + 1 \end{bmatrix}^{\ddagger} C_{\mathbb{q}}^2\, G^2(\mathbb{k}', \mathbb{k}) \delta_{\mathbb{k}\pm\mathbb{q},^{\ddagger}\,\mathbb{k}'}, \tag{3.18}$$

taking at ‡, the upper case for absorption, and the lower case for emission. $C_{\mathbb{q}}$ is the coupling coefficient which contains the detailed form of the interaction Hamiltonian for each particular scattering process. The scattering rate for a carrier in state $|\mathbb{k}\rangle$ is then

$$\begin{aligned} P(\mathbb{k}) = \frac{2\pi}{\hbar} \frac{V}{(2\pi)^3} \delta_{\mathbb{k}\pm\mathbb{q},^{\ddagger}\,\mathbb{k}'} \int \frac{\hbar}{2M'N\omega_{\mathbb{q}}} \begin{bmatrix} \mathcal{N}_{\mathbb{q}} \\ \mathcal{N}_{\mathbb{q}} + 1 \end{bmatrix}^{\ddagger} C_{\mathbb{q}}^2\, G^2(\mathbb{k}', \mathbb{k}) \\ \times\, \delta\left(\epsilon(\mathbb{k}') - \epsilon(\mathbb{k}) \mp^{\ddagger} \hbar\omega_{\mathbb{q}}\right) d\mathbb{k}', \end{aligned} \tag{3.19}$$

where $\epsilon(\mathbb{k})$ and $\epsilon(\mathbb{k}')$ are the energies of the initial and final electron states, and the the integral is taken over all final states $|\mathbb{k}'\rangle$.

3A.2: Coupling Coefficients

Acoustic (deformation potential) scattering

The deformation potential theorem of Bardeen and Shockley (1950) states that, for long wavelength acoustic modes in semiconductors, the interaction potential δU can be taken as

$$\delta U(\mathbf{r}) = \sum_{i,j} \Xi_{ij} S_{ij}, \tag{3.20}$$

where S is the strain tensor, with components

$$S_{ij} = \frac{1}{2}\left(\frac{\partial u_i}{\partial r_j} + \frac{\partial u_j}{\partial r_i}\right), \qquad (i,j = 1\ldots 3), \tag{3.21}$$

and Ξ is the so called deformation potential tensor.

Equation (3.20) is merely a variant of the Bloch formulation of equation (3.5). The principal advantage of the theorem is that the deformation potentials Ξ_{ij} can be identified with the rigid shifts in energy bands observed upon application of uniaxial stress.

Substituting equations (3.7) and (3.21) into equation (3.20), we obtain

$$\begin{aligned}\delta U(\mathbf{r}) = \frac{1}{2}\sum_{\mathbf{q}} \sqrt{\frac{\hbar}{2M'N\omega_{\mathbf{q}}}} \sum_{i,j} \Xi_{ij}(e_i q_j + e_j q_i) \\ \times i\left(a_{\mathbf{q}} \exp(i\mathbf{q}.\mathbf{r}) - a_{\mathbf{q}}^{\dagger} \exp(-i\mathbf{q}.\mathbf{r})\right),\end{aligned} \tag{3.22}$$

where the e_i and q_i are Cartesian components of the polarisation vector and phonon wavevector respectively.

Then, by comparison of equation (3.22) with equations (3.8), (3.15) and (3.18), the details of the deformation potential interaction can be summarised in a coupling coefficient (squared) of the form

$$C_{\mathbf{q}}^2 = \left(\frac{1}{2}\sum_{i,j} \Xi_{ij}(e_i q_j + e_j q_i)\right)^2. \tag{3.23}$$

Non-Polar Optical Scattering

In a semiconductor crystal lattice, there are two atoms per unit cell. When the lattice vibrates in an optical mode, these atoms are displaced in opposite directions. The optical displacement is defined as the relative displacement of the two atoms. The oscillator mass M' in this case is the *reduced* mass $\overline{M}$ of the unit cell, which is given by

$$\overline{M} = \left(\frac{1}{M_1} + \frac{1}{M_2}\right)^{-1}, \tag{3.24}$$

where M_1 and M_2 are the two atomic masses.

For intravalley scattering, $\mathbb{q}$ is restricted to small values, hence only long wavelength modes are important. For such modes, the interaction energy δU can be approximated by (Seitz 1948; Harrison 1956; Meyer 1958)

$$\delta U(\mathbb{r}) = \mathbb{D}_{\text{op}}.\mathbb{u}(\mathbb{r}). \tag{3.25}$$

$\mathbb{D}_{\text{op}}$ is an optical deformation potential constant, and is a vector, rather than a second rank tensor, as in the case of acoustic scattering. There is, however, some inconsistency in the definition of $\mathbb{D}_{\text{op}}$ for diatomic crystals. Ridley (1988) suggests that $\mathbb{D}_{\text{op}}$ should be regarded as the change of energy per unit 'equivalent acoustic' displacement u_{ac}, where u_{ac} is defined as the displacement of the whole unit cell having the same elastic energy as the optical displacement u: *i.e.*,

$$(M_1 + M_2)u_{\text{ac}}^2 = \overline{M}u^2. \tag{3.26}$$

This gives

$$\delta U(\mathbb{r}) = \sqrt{\frac{\overline{M}}{M_1 + M_2}}\,\mathbb{D}_{\text{op}}.\mathbb{u}(\mathbb{r}), \tag{3.27}$$

and this is the form of the non-polar interaction which we will adopt in this work. The coupling coefficient for a mode travelling in a particular direction is then

$$C_{\mathbb{q}} = \frac{\overline{M}}{M_1 + M_2} D_{\text{op}}^2 \sigma_{\mathbb{q}}, \tag{3.28}$$

where $\sigma_{\mathbb{q}}$ is the direction cosine of the polarisation vector of the mode relative to $\mathbb{D}_{\text{op}}$.

Polar Optical Scattering

In a polar crystal, the contrary displacement of adjacent, oppositely charged atoms creates a polarisation, and hence an electric field, resulting in strong scattering of electrons (Frohlich 1937; Callen 1949).

The polarisation in a unit cell is

$$\mathbb{P}(\mathbb{r}) = \frac{e^*\mathbb{u}(\mathbb{r})}{V_{\text{cell}}}, \tag{3.29}$$

where e^* is an effective charge (see below).

The electrostatic potential $\phi(\mathbb{r})$ due to the polarisation is obtained from Poisson's equation:

$$\nabla^2\phi(\mathbb{r}) = \frac{-\rho(\mathbb{r})}{\varepsilon_0}, \tag{3.30}$$

where $\rho(\mathbf{r})$ is the space charge density;

$$\rho(\mathbf{r}) = -\mathrm{div}\mathbb{P}(\mathbf{r}). \tag{3.31}$$

Thus

$$\rho(\mathbf{r}) = \frac{-ie^*}{V_{\mathrm{cell}}} \sum_{\mathbf{q}} \hat{\mathbf{e}}_{\mathbf{q}}.\mathbf{q} \sqrt{\frac{\hbar}{2M'N\omega_{\mathbf{q}}}} \left(a_{\mathbf{q}} \exp(i\mathbf{q}.\mathbf{r}) - a_{\mathbf{q}}^{\dagger} \exp(-i\mathbf{q}.\mathbf{r})\right). \tag{3.32}$$

The dot product indicates that only longitudinal modes will contribute to the electrostatic potential. For such modes, this potential is given by

$$\phi(\mathbf{r}) = \frac{-e^*}{\varepsilon_0 V_{\mathrm{cell}}} \sum_{\mathbf{q}} \frac{1}{q} \sqrt{\frac{\hbar}{2M'N\omega_{\mathbf{q}}}} \left(a_{\mathbf{q}} \exp(i\mathbf{q}.\mathbf{r}) - a_{\mathbf{q}}^{\dagger} \exp(-i\mathbf{q}.\mathbf{r})\right). \tag{3.33}$$

The interaction energy is given by

$$\delta U(\mathbf{r}) = e\phi(\mathbf{r}). \tag{3.34}$$

Thus, by comparison of equations (3.33) and (3.34) with equations (3.8), (3.15) and (3.18), the coupling coefficient (squared) can be written as

$$C_{\mathbf{q}}^2 = \left(\frac{ee^*}{\varepsilon_0 V_{\mathrm{cell}}}\right)^2 \frac{1}{q^2}. \tag{3.35}$$

The effective charge e^* appearing in this expression was first defined by Callen (1949) (see also Ehrenreich (1957)). Expressed in SI units, the effective charge is given by

$$(e^*)^2 = \overline{M} V_{\mathrm{cell}} \omega_{\mathbf{q}}^2 \varepsilon_0 \left(\frac{1}{\varepsilon_\infty} - \frac{1}{\varepsilon_s}\right), \tag{3.36}$$

where ε_s and ε_∞ are the static and high frequency dielectric constants respectively.

Piezoelectric scattering

In a polar crystal with no inversion symmetry, a long wavelength acoustic vibration produces an additional, second order polarisation. That is, $\mathbb{P}(\mathbf{r})$ is proportional to acoustic strain, rather than displacement. The i^{th} Cartesian component of $\mathbb{P}(\mathbf{r})$ is given by

$$P_i = \frac{1}{\varepsilon_s} \sum_{j,k} h_{ijk} S_{jk}, \tag{3.37}$$

where $\mathbb{h}$ is the piezoelectric tensor. $\mathbf{h}$ is symmetric, and is therefore usually written in the reduced notation $h_{ijk} \rightarrow h_{im}$, $m = 1 \ldots 6$. For zincblende crystals, $\mathbb{h}$ has only three non-zero components, and these are all equal: $h_{14} = h_{25} = h_{36}$ (Mason 1950). This means that only shear strain components contribute to the polarisation. Using equations (3.7) and (3.21) we obtain

$$P_1 = \frac{h_{14}}{\varepsilon_s} \sum_{\mathbf{q}} \sqrt{\frac{\hbar}{2M'N\omega_{\mathbf{q}}}}\, i(e_2 q_3 + e_3 q_2) \left(a_{\mathbf{q}} \exp(i\mathbf{q}.\mathbf{r}) - a_{\mathbf{q}}^{\dagger} \exp(-i\mathbf{q}.\mathbf{r})\right). \tag{3.38}$$

Analagous expressions can be written for P_2 and P_3. Then, the space charge density is given by

$$\rho(\mathbf{r}) = -\mathrm{div}\mathbb{P}(\mathbf{r}) = \frac{h_{14}}{\varepsilon_s}\sum_{\mathbf{q}}\sqrt{\frac{\hbar}{2M'N\omega_{\mathbf{q}}}} \times 2\left(e_1q_2q_3 + e_2q_1q_3 + e_3q_1q_2\right) \times \left(a_{\mathbf{q}}\exp(i\mathbf{q}.\mathbf{r}) - a_{\mathbf{q}}^{\dagger}\exp(-i\mathbf{q}.\mathbf{r})\right). \tag{3.39}$$

Solving Poisson's equation gives the electrostatic potential, and hence the interaction energy:

$$\delta U(\mathbf{r}) = \frac{eh_{14}}{\varepsilon_0\varepsilon_s}\sum_{\mathbf{q}}\sqrt{\frac{\hbar}{2M'N\omega_{\mathbf{q}}}} \times \frac{2}{q^2}\left(e_1q_2q_3 + e_2q_1q_3 + e_3q_1q_2\right) \times \left(a_{\mathbf{q}}\exp(i\mathbf{q}.\mathbf{r}) - a_{\mathbf{q}}^{\dagger}\exp(-i\mathbf{q}.\mathbf{r})\right). \tag{3.40}$$

Then, comparison with equations (3.8), (3.15) and (3.18) shows that the coupling coefficient (squared) takes the form

$$C_{\mathbf{q}}^2 = \left(\frac{eh_{14}}{\varepsilon_0\varepsilon_s}\right)^2\frac{4}{q^4}(e_1q_2q_3 + e_2q_1q_3 + e_3q_1q_2)^2. \tag{3.41}$$

The piezoelectric interaction clearly has a complicated directional dependence and most practical treatments have involved some averaging over direction. The simplest approach is to separate the contributions from longitudinal and transverse modes, and take a spherical average in each case (Hutson 1961; Zook 1964). The appropriate values of the e_i for each of the three modes of polarisation are obtained by means of a transformation to a coordinate frame in which the $z(3)$ axis lies parallel to $\mathbf{q}$ (see Zook 1964; also Jones 1975). For longitudinal modes, the coupling coefficient (squared) then reduces to

$$C_{\mathbf{q},l}^2 = \left(\frac{eh_{14}}{\varepsilon_0\varepsilon_s}\right)^2 \times 36\sigma_1^2\sigma_2^2\sigma_3^2 \tag{3.42}$$

where the σ_i are the direction cosines of $\mathbf{q}$. The coupling coefficient for the combined effect of the two transverse modes is given by

$$C_{\mathbf{q},t}^2 = \left(\frac{eh_{14}}{\varepsilon_0\varepsilon_s}\right)^2 \times 4(\sigma_1^2\sigma_2^2 + \sigma_2^2\sigma_3^2 + \sigma_3^2\sigma_1^2 - 9\sigma_1^2\sigma_2^2\sigma_3^2). \tag{3.43}$$

Taking spherical averages of these two quantities gives

$$C_{\mathbf{q},l}^2 = \frac{12}{35}\left(\frac{eh_{14}}{\varepsilon_0\varepsilon_s}\right)^2, \tag{3.44a}$$

$$C_{\mathbf{q},t}^2 = \frac{16}{35}\left(\frac{eh_{14}}{\varepsilon_0\varepsilon_s}\right)^2. \tag{3.44b}$$

If no screening effects are included, then the piezoelectric scattering expression has a singularity at $q = 0$ (see equation (3.68) in Section 3B), and a finite scattering rate cannot be obtained (Rode 1970). The effect of screening by free carriers can be included by writing

$$P_i\left(\frac{q^2+q_0^2}{q^2}\right) = \frac{1}{\varepsilon_s}\sum_{j,k} h_{ijk}S_{jk} \tag{3.45}$$

in place of equation (3.37), where q_0 is the reciprocal Debye screening length (Hutson 1961). The coupling coefficients (squared) then become

$$C_{q,l}^2 = \frac{12}{35}\left(\frac{eh_{14}}{\varepsilon_0\varepsilon_s}\right)^2 \frac{q^4}{(q^2+q_0^2)^2}, \tag{3.46a}$$

$$C_{q,t}^2 = \frac{16}{35}\left(\frac{eh_{14}}{\varepsilon_0\varepsilon_s}\right)^2 \frac{q^4}{(q^2+q_0^2)^2}. \tag{3.46b}$$

3B ELECTRON-PHONON SCATTERING IN A SIMPLE PARABOLIC BAND

Most common semiconductors have a bandstructure profile in which the lowest valleys can be well approximated by a parabolic dispersion relation. In this section, we will show how the results derived above can be used to write down scattering rate expressions for electrons in such a parabolic band. We will also assume that the band is isotropic in $\mathbb{k}$-space, and furthermore, that the overlap integral $G^2(\mathbb{k}', \mathbb{k})$ can be taken as unity — as is a common approximation for electron transport in the conduction band of a semiconductor. The results will therefore be applicable to any of the Γ, L, or X valleys in GaAs (see Fawcett *et al.* 1970) — except where a particular scattering process is forbidden. However, the main purpose of presenting these expressions is to show the simplest case of carrier-phonon scattering, for comparison with the results of Section 3C for holes in the GaAs valence bands, and with those of Chapter 5 for scattering in two dimensional systems.

We will write the energy dispersion relation in the form

$$\epsilon(\mathbf{k}) \equiv \epsilon(k) = \alpha k^2, \tag{3.47}$$

where

$$\alpha = \frac{\alpha_0}{m^*} \quad \text{and} \quad \alpha_0 = \frac{\hbar^2}{2m_0}, \tag{3.48}$$

with m_0 the free electron mass and m^* the relative effective mass in the band.

Acoustic (deformation potential) scattering

If only dilational strains produce any shift in the energy band (as, for example, in the Γ valley of GaAs), then the coupling coefficient for acoustic scattering becomes (from equation (3.23))

$$C_{\mathbf{q}}^2 = (\Xi \hat{\mathbf{e}}_{\mathbf{q}}.\mathbf{q})^2 \equiv \Xi^2 q^2. \tag{3.49}$$

We will assume, as is usual for acoustic modes, that scattering is elastic, and that the energy equipartition approximation is valid. This gives

$$\mathcal{N}_{\mathbf{q}} + 1 \approx \mathcal{N}_{\mathbf{q}} \approx \frac{k_B T_L}{\hbar\omega_{\mathbf{q}}}, \quad \left(\frac{\hbar\omega_{\mathbf{q}}}{k_B T_L} \ll 1\right), \tag{3.50}$$

where

$$\mathcal{N}_{\mathbf{q}} = \frac{1}{\exp(\hbar\omega_{\mathbf{q}}/k_B T_L) - 1} \tag{3.51}$$

and T_L is the lattice temperature. The acoustic phonon frequency is given by

$$\omega_{\mathbf{q}} = v_s q, \tag{3.52}$$

where v_s is the appropriate sound velocity.

The oscillator mass M' for acoustic modes is equal to the total mass of the unit cell; thus $M'N = \rho V$, where ρ is the crystal density. Then, with reference to equation (3.19), the scattering rate is given by:

$$P(\epsilon(k)) = 2 \times \frac{2\pi}{\hbar} \frac{V}{(2\pi)^3} \frac{k_B T_L \Xi^2}{2\rho V v_s^2} \int \delta_{\mathbf{k}\pm\mathbf{q},\mathbf{k}'} \delta\big(\epsilon(k') - \epsilon(k)\big)\, d\mathbf{k}'. \tag{3.53}$$

An extra factor of two has been included, compared to equation (3.19), to give the combined rate for phonon absorption and emission. The remaining integral may readily be evaluated to give, for the scattering rate:

$$P(\epsilon(k)) = \frac{k_B T_L \Xi^2 \epsilon^{1/2}(k)}{2\pi\hbar\rho v_s^2 \alpha^{3/2}}. \tag{3.54}$$

Non-Polar Optical scattering

We have seen, in equation (3.28), that the coupling coefficient for non-polar optical phonon scattering is dependent on the direction of the polarisation vector of the phonon mode. This means that the LO and TO modes, which have different frequencies, ought to be considered separately. However, in most III-V semiconductors, the difference between the LO and TO phonon frequencies is relatively small, and a single frequency approximation is usually adopted. The coupling coefficient for the combination of the one LO and two TO modes is then given by

$$C_{\mathbf{q}}^2 = \frac{\overline{M}}{M_1 + M_2} D_{\mathrm{op}}^2. \tag{3.55}$$

For optical modes, $\omega_{\mathbf{q}}$ is only weakly dependent on $\mathbf{q}$, and hence can be replaced by a fixed frequency ω_{op}. The scattering rate, from equation (3.19), is then

$$P(\epsilon(k)) = \frac{2\pi}{\hbar} \frac{V}{(2\pi)^3} \frac{\hbar D_{\mathrm{op}}^2}{2\rho V \omega_{\mathrm{op}}} \begin{bmatrix} \mathcal{N}_{\mathrm{op}} \\ \mathcal{N}_{\mathrm{op}} + 1 \end{bmatrix} \times \int \delta_{\mathbf{k}\pm\mathbf{q},\mathbf{k}'} \delta\big(\epsilon(k') - \epsilon(k) \mp \hbar\omega_{op}\big)\, d\mathbf{k}', \tag{3.56}$$

where $\mathcal{N}_{\mathrm{op}} = (\exp(\hbar\omega_{\mathrm{op}}/k_B T_L) - 1)^{-1}$ and we have used $M' = \overline{M}$ and $(M_1 + M_2)N = \rho V$. Evaluating the integral over $\mathbf{k}'$ gives the result

$$P(\epsilon(k)) = \frac{D_{\mathrm{op}}^2}{4\pi\rho\omega_{\mathrm{op}}\alpha^{3/2}} \begin{bmatrix} \mathcal{N}_{\mathrm{op}} \\ \mathcal{N}_{\mathrm{op}} + 1 \end{bmatrix} (\epsilon(k) \pm \hbar\omega_{\mathrm{op}})^{1/2}. \tag{3.57}$$

Polar Optical scattering

Using equations (3.19), (3.35) and (3.36) we obtain, for the polar optical scattering rate:

$$P(\epsilon(k)) = \frac{2\pi}{\hbar}\frac{V}{(2\pi)^3}\frac{\hbar}{2M'N\omega_{\rm op}}\begin{bmatrix} \mathcal{N}_{\rm op} \\ \mathcal{N}_{\rm op}+1 \end{bmatrix}\left(\frac{e}{\varepsilon_0 V_{\rm cell}}\right)^2 \times \overline{M}V_{\rm cell}\omega_{\rm op}^2\frac{\varepsilon_0}{\varepsilon_{\rm pol}}\int \delta_{\mathbf{k}\pm\mathbf{q},\,\mathbf{k}'}\frac{1}{q^2}\delta\left(\epsilon(k') - \epsilon(k) \mp \hbar\omega_{op}\right)\, d\mathbf{k}', \quad (3.58)$$

where $\varepsilon_{\rm pol} = (1/\varepsilon_\infty - 1/\varepsilon_s)^{-1}$ and $\omega_{\rm op}$ is again independent of q. M' is equal to the reduced mass $\overline{M}$, as for non-polar optical scattering, and $NV_{\rm cell} = V$. Then

$$P(\epsilon(k)) = \frac{e^2\omega_{\rm op}}{8\pi^2\varepsilon_0\varepsilon_{\rm pol}}\begin{bmatrix} \mathcal{N}_{\rm op} \\ \mathcal{N}_{\rm op}+1 \end{bmatrix} \times \int \delta_{\mathbf{k}\pm\mathbf{q},\,\mathbf{k}'}\frac{1}{q^2}\delta\left(\epsilon(k') - \epsilon(k) \mp \hbar\omega_{op}\right)\, d\mathbf{k}'. \quad (3.59)$$

The integral over all final states can be evaluated by writing

$$d\mathbf{k}' = k'^2\, dk'\, d\cos\theta\, d\phi. \quad (3.60)$$

If the direction of $\mathbf{k}$ is taken as the z direction, then the momentum conserving Kronecker delta gives, for q:

$$q^2 = k^2 + k'^2 - 2kk'\cos\theta. \quad (3.61)$$

Changing the variables in the delta function then gives

$$\delta\left(\epsilon(k') - \epsilon(k) \mp \hbar\omega_{op}\right) = \frac{\delta(k' - k_f)}{|\partial\epsilon/\partial k'|}, \quad (3.62)$$

where, for a parabolic band

$$\frac{\partial\epsilon}{\partial k'} = 2\alpha k' \quad \text{and} \quad k_f = \sqrt{k^2 \pm \hbar\omega_{\rm op}/\alpha}. \quad (3.63)$$

Then, a little straightforward algebra leads to the result

$$P(k) = \frac{e^2\omega_{\rm op}}{8\pi\alpha\varepsilon_0\varepsilon_{\rm pol}}\begin{bmatrix} \mathcal{N}_{\rm op} \\ \mathcal{N}_{\rm op}+1 \end{bmatrix}\frac{1}{k}\log_e\left|\frac{k+k_f}{k-k_f}\right|, \quad (3.64)$$

or

$$P(\epsilon(k)) = \frac{e^2\omega_{\rm op}}{8\pi\alpha^{1/2}\varepsilon_0\varepsilon_{\rm pol}}\begin{bmatrix} \mathcal{N}_{\rm op} \\ \mathcal{N}_{\rm op}+1 \end{bmatrix}\frac{1}{\epsilon^{1/2}}\log_e\left|\frac{\epsilon^{1/2}+\epsilon_f^{1/2}}{\epsilon^{1/2}-\epsilon_f^{1/2}}\right|. \quad (3.65)$$

Piezoelectric scattering

Within the elastic and equipartition approximations, described above for acoustic scattering, the piezoelectric scattering rate for a given polarisation mode may be written as

$$P(\epsilon(k)) = \frac{2\pi}{\hbar}\frac{V}{(2\pi)^3}\frac{k_B T_L}{2\rho V v_{s,\mathrm{mode}}^2}\int \delta_{\mathbf{k}\pm\mathbf{q},\,\mathbf{k}'}\frac{C_{\mathrm{mode}}^2}{q^2}\,\delta\big(\epsilon(k') - \epsilon(k)\big)\,d\mathbf{k}', \tag{3.66}$$

where $v_{s,\mathrm{mode}}$ is the sound velocity for the particular mode (longitudinal or transverse). Zook (1964) describes the derivation of spherically averaged elastic constants c_l and c_t, where

$$\rho v_{s,l}^2 = c_l, \tag{3.67a}$$

$$\rho v_{s,t}^2 = c_t. \tag{3.67b}$$

These quantities can be used to derive a combined rate for scattering via longitudinal and transverse modes:

$$P(\epsilon(k)) = \frac{e^2 k_B T_L}{8\pi^2\hbar}\left(\frac{K_{\mathrm{av}}^2}{\varepsilon_0\varepsilon_s}\right)\int \delta_{\mathbf{k}\pm\mathbf{q},\,\mathbf{k}'}\frac{q^2}{(q^2+q_0^2)^2}\,\delta\big(\epsilon(k') - \epsilon(k)\big)\,d\mathbf{k}', \tag{3.68}$$

where K_{av} is the dimensionless so called average electromechanical coupling constant (Ridley 1988);

$$K_{\mathrm{av}}^2 = \frac{h_{14}^2}{\varepsilon_0\varepsilon_s}\left(\frac{12}{35c_l} + \frac{16}{35c_t}\right). \tag{3.69}$$

The integrals are evaluated as for polar optical scattering, by use of equations (3.60–61) and the final result, including a factor of 2 to account for both absorption and emission processes, can be written as

$$P(k) = \frac{e^2 k_B T_L}{4\pi\hbar\alpha}\left(\frac{K_{\mathrm{av}}^2}{\varepsilon_0\varepsilon_s}\right)\frac{1}{k}\times\frac{1}{2}\left[\log_{\mathrm{e}}\left(1+\frac{4k^2}{q_0^2}\right) - \frac{4k^2}{(4k^2+q_0^2)}\right]. \tag{3.70}$$

3C HOLE-PHONON SCATTERING IN THE GaAs VALENCE BANDS

In this section we will consider the scattering of holes in the heavy and light hole valence bands of GaAs by the four processes described in the previous sections. Whilst the valence bands in GaAs are reasonably parabolic near the zone centre, their energy surfaces are known to be somewhat warped (Dresselhaus *et al.* 1955; see also Wiley 1975). However, as a first approximation, we will assume both heavy and light hole bands to be isotropic and parabolic. The energy dispersions of the bands are then of the form $\epsilon(k) = \alpha_i k^2$, where $\alpha_i = \alpha_0/m_i^*$ and $m_i^* = m_h^*$ or m_l^* is the effective mass in the band.

The p-type symmetry of the valence band wavefunctions means that the overlap integrals $G(\mathbf{k}', \mathbf{k})$ can no longer be taken as unity. Wiley (1971) has shown that, for states $|\mathbf{k}\rangle$ and $|\mathbf{k}'\rangle$ which are both in the heavy hole, or both in the light hole band, $G^2(\mathbf{k}', \mathbf{k})$ can be approximated by

$$G^2(\mathbf{k}', \mathbf{k}) = \frac{1}{4}(1 + 3\cos^2\beta), \tag{3.71}$$

where β is the angle between $\mathbf{k}$ and $\mathbf{k}'$. When the two states are in different bands, the corresponding result is

$$G^2(\mathbf{k}', \mathbf{k}) = \frac{3}{4}\sin^2\beta. \tag{3.72}$$

These modifications are important in any Monte Carlo model of hole transport, since they affect not only the total scattering rate out of a given state, but also the angular dependence of scattering, and therefore the stochastic selection of the wavevector $\mathbf{k}'$ in the Monte Carlo algorithm. The angular dependences of the hole-phonon scattering processes will be discussed in Section 4B.

Acoustic Scattering

In the valence bands of GaAs, acoustic scattering occurs via both longitudinal and transverse modes. The effect of acoustic strain is described by three deformation potentials a, b and d (Pikus and Bir 1960; Bir and Pikus 1961; Lawaetz 1968). a is associated with dilational strain, giving the shift of the band edge on application of hydrostatic pressure. b and d give the splitting of the heavy and light hole bands due to uniaxial shear strains in the $\langle 100 \rangle$ and $\langle 111 \rangle$ directions respectively. However, Lawaetz (1968) has shown that the effects of acoustic strain in the valence bands can be summarised, to a reasonable approximation, by a single deformation potential parameter. Therefore, we will write the coupling coefficient (squared) in a similar form to that in Section 3B:

$$C_{\mathbf{q}}^2 = E_{\mathrm{AC}}^2 q^2, \tag{3.73}$$

where E_{AC} is a 'phenomenological' deformation potential whose derivation will be discussed in Appendix 2.

For the sound velocity appearing in equation (3.52), we will take the mean square of the longitudinal and transverse values:

$$v_s^2 \rightarrow \overline{v}^2 = \tfrac{1}{3}(v_l^2 + 2v_t^2). \tag{3.74}$$

Then, within the elastic and equipartition approximations, the acoustic scattering rate, from equations (3.19), (3.50–51) and (3.73), is

$$P(\epsilon(k)) = \frac{E_{AC}^2 k_B T_L}{4\pi^2 \rho \overline{v}^2} \iiint G^2(\mathbf{k}', \mathbf{k}) \delta\big(\epsilon(\mathbf{k}') - \epsilon(\mathbf{k})\big)\, k'^2 dk'\, d\cos\theta\, d\phi. \tag{3.75}$$

If we take the z direction of the coordinate frame for $\mathbf{k}'$ to be parallel to $\mathbf{k}$, then the scattering angle β becomes interchangeable with θ. The integral over θ is then, for intraband scattering,

$$\frac{1}{4}\int_{-1}^{1} (1 + 3\cos^2\theta)\, d\cos\theta = \frac{1}{2}, \tag{3.76}$$

and, for interband scattering,

$$\frac{3}{4}\int_{-1}^{1} \sin^2\theta\, d\cos\theta = \frac{1}{2}. \tag{3.77}$$

So, the effect of the overlap integral, in both cases, is to reduce the acoustic scattering rate by a factor of two. Therefore, with reference to equation (3.54), we can write the result for absorption plus emission immediately as

$$P(\epsilon(k)) = \frac{k_B T_L E_{AC}^2\, \epsilon^{1/2}(k)}{4\pi\hbar\rho\overline{v}^2 \alpha_f^{3/2}}, \tag{3.78}$$

where $\alpha_f = \alpha_h$ for scattering into the heavy hole band, and α_l for scattering into the light hole band. This result has been previously derived by Costato and Reggiani (1973a).

Non-Polar Optical Scattering

As in Section 3B, we will consider NPO scattering of carriers by a combination of LO and TO modes, assuming a common frequency for both, and hence using a single deformation potential constant D_{op} which represents an average over optical strains in all directions. Lawaetz (1968) has shown that such an averaged deformation potential constant is given by

$$D_{op}^2 = \frac{3}{2}\frac{d_0^2}{a_0^2} \tag{3.79}$$

where a_0 is the lattice constant and d_0 is the 'fundamental' optical deformation potential introduced by Bir and Pikus (1961).

As in the case of acoustic scattering, the only angular dependence in the NPO rate is that due to the overlap integral $G(\mathbf{k}',\mathbf{k})$ which, again, serves to reduce the total rate for both intra- and inter-band scattering by a factor of two. Hence we can write, for NPO scattering in the heavy and light hole bands:

$$P(\epsilon(k)) = \frac{D_{\rm op}^2}{8\pi\rho\omega_{\rm op}\alpha_f^{3/2}} \begin{bmatrix} \mathcal{N}_{\rm op} \\ \mathcal{N}_{\rm op}+1 \end{bmatrix} (\epsilon(k) \pm \hbar\omega_{\rm op})^{1/2}, \tag{3.80}$$

where $\alpha_f = \alpha_h$ or α_l for scattering into the heavy or light hole band respectively. This result was also given by Costato and Reggiani (1973a).

Polar Optical Scattering

From equations (3.19), (3.35) and (3.36), the polar optical scattering rate is given as

$$P(\epsilon(k)) = \frac{e^2\omega_{\rm op}}{8\pi^2\varepsilon_0}\left(\frac{1}{\varepsilon_\infty}-\frac{1}{\varepsilon_s}\right)\begin{bmatrix} \mathcal{N}_{\rm op} \\ \mathcal{N}_{\rm op}+1 \end{bmatrix} \times \iiint \delta_{\mathbf{k}\pm\mathbf{q},\mathbf{k}'} \frac{G^2(\mathbf{k}',\mathbf{k})}{q^2} \delta\left(\epsilon(\mathbf{k}') - \epsilon(\mathbf{k}) \mp \hbar\omega_{op}\right) d\mathbf{k}', \tag{3.81}$$

where $G(\mathbf{k}',\mathbf{k})$ is dependent only on the scattering angle β. We can write $d\mathbf{k}' = k'^2 dk'\, d\cos\theta\, d\phi$, and the Kronecker delta gives $q^2 = k^2 + k'^2 - 2kk'\cos\beta$. We may again take the k_z direction as being parallel to $\mathbf{k}$, and hence identify β with θ. Then, the integral over ϕ gives a factor of 2π, and the integral over k' can be evaluated, as in previous cases, by changing the variables in the Dirac delta function. We thus obtain

$$P(\epsilon(k)) = \frac{e^2\omega_{\rm op}}{4\pi\varepsilon_0}\left(\frac{1}{\varepsilon_\infty}-\frac{1}{\varepsilon_s}\right)\begin{bmatrix} \mathcal{N}_{\rm op} \\ \mathcal{N}_{\rm op}+1 \end{bmatrix} \times \frac{k_f}{2\alpha_f}\int_{-1}^{1} \frac{G^2(\mathbf{k}_f,\mathbf{k})}{(k^2+k_f^2-2kk_f\cos\theta)}\, d\cos\theta, \tag{3.82}$$

where k_f satisfies

$$\alpha_f k_f^2 = \alpha_i k^2 \pm \hbar\omega_{\rm op} \tag{3.83}$$

and the subscripts i and f denote the initial and final bands.

The remaining integral can be written in the form

$$F_{ii}(k_f,k) = \frac{1}{4}\int_{-1}^{1} \frac{(1+3x^2)}{(a-bx)}\, dx \tag{3.84}$$

for intraband scattering, and

$$F_{fi}(k_f,k) = \frac{3}{4}\int_{-1}^{1} \frac{(1-x^2)}{(a-bx)}\, dx \tag{3.85}$$

for interband scattering: where $a = k^2 + k_f^2$ and $b = 2kk_f$. The evaluation of these integrals is relatively straightforward, and leads to the results

$$F_{ii}(k_f, k) = \frac{1}{4b}\left[\left\{1 + 3\left(\frac{a}{b}\right)^2\right\} \log_e\left(\frac{a+b}{a-b}\right) - 6\left(\frac{a}{b}\right)\right], \tag{3.86}$$

and

$$F_{fi}(k_f, k) = \frac{3}{4b}\left[\left\{1 - \left(\frac{a}{b}\right)^2\right\} \log_e\left(\frac{a+b}{a-b}\right) + 2\left(\frac{a}{b}\right)\right]. \tag{3.87}$$

The polar optical scattering rate is then obtained as

$$P(k) = \frac{e^2\omega_{\text{op}}}{8\pi\varepsilon_0\alpha}\left(\frac{1}{\varepsilon_\infty} - \frac{1}{\varepsilon_s}\right)\begin{bmatrix}\mathcal{N}_{\text{op}} \\ \mathcal{N}_{\text{op}} + 1\end{bmatrix} \times \frac{1}{4k}\left[\left\{1 + \frac{3(k^2 + k_f^2)^2}{4k^2k_f^2}\right\} \log_e\left|\frac{k + k_f}{k - k_f}\right| - \frac{3(k^2 + k_f^2)}{2kk_f}\right] \tag{3.88}$$

for intraband scattering, and

$$P(k) = \frac{e^2\omega_{\text{op}}}{8\pi\varepsilon_0\alpha_f}\left(\frac{1}{\varepsilon_\infty} - \frac{1}{\varepsilon_s}\right)\begin{bmatrix}\mathcal{N}_{\text{op}} \\ \mathcal{N}_{\text{op}} + 1\end{bmatrix} \times \frac{3}{4k}\left[\left\{1 - \frac{(k^2 + k_f^2)^2}{4k^2k_f^2}\right\} \log_e\left|\frac{k + k_f}{k - k_f}\right| + \frac{(k^2 + k_f^2)}{2kk_f}\right] \tag{3.89}$$

for interband scattering. Similar results have been derived by Costato *et al.* (1972) and Costato and Reggiani (1973b), although the latter publication contains several typographical errors.

Piezoelectric Scattering

From equation (3.68) it can be seen that the combined rate for scattering via longitudinal and transverse piezoelectric modes in the presence of free carrier screening is given, within the elastic and equipartition approximations, by

$$P(\epsilon(k)) = \frac{e^2k_BT_L}{8\pi^2\hbar}\left(\frac{K_{\text{av}}^2}{\varepsilon_0\varepsilon_s}\right)\int \delta_{\mathbf{k}\pm\mathbf{q},\,\mathbf{k}'}\frac{q^2}{(q^2 + q_0^2)^2}G^2(\mathbf{k}', \mathbf{k})\,\delta\big(\epsilon(k') - \epsilon(k)\big)\,d\mathbf{k}', \tag{3.90}$$

where $G^2(\mathbf{k}', \mathbf{k})$ is given by equations (3.71) and (3.72) for intra- and inter-band processes respectively. We may write $d\mathbf{k}' = k'^2 dk'\, d\cos\theta\, d\phi$ and proceed as for polar optical scattering, to obtain

$$P(k) = \frac{e^2k_BT_L}{8\pi\hbar\alpha_f}\left(\frac{K_{\text{av}}^2}{\varepsilon_0\varepsilon_s}\right)k_fF(k_f, k) \tag{3.91}$$

where, for intraband scattering, $k_f = k$, and for interband scattering, $\alpha_i k^2 = \alpha_f k_f^2$, with the subscripts i and f denoting the initial and final states. The term $F(k_f, k)$ is given by

$$F_{ii}(k_f, k) = \frac{1}{4}\int_{-1}^{1}\frac{(a - bx)(1 + 3x^2)}{(c - bx)^2}\,dx \tag{3.92}$$

for intraband scattering, and

$$F_{fi}(k_f,k)=\frac{3}{4}\int_{-1}^{1}\frac{(a-bx)(1-x^2)}{(c-bx)^2}\,dx \tag{3.93}$$

for interband scattering, with $a=k^2+k_f^2$, $b=2kk_f$, and $c=a+q_0^2$.

The evaluation of these integrals is straightforward, but lengthy. The total scattering rates, for absorption plus emission, are eventually obtained in the form

$$P(k)=\frac{e^2k_BT_L}{4\pi\hbar\alpha}\left(\frac{K_{\rm av}^2}{\epsilon_0\epsilon_s}\right)\times\frac{(4k^2+3q_0^2)}{8k^3}\left[\frac{(4k^2+3q_0^2)}{4k^2}\log_{\rm e}\left(1+\frac{4k^2}{q_0^2}\right)-\frac{(10k^2+3q_0^2)}{(4k^2+q_0^2)}\right] \tag{3.94}$$

for intraband scattering, and

$$P(k)=\frac{e^2k_BT_L}{4\pi\hbar\alpha_f}\left(\frac{K_{\rm av}^2}{\epsilon_0\epsilon_s}\right)\times\frac{3}{8k}\left[\frac{(k^2+k_f^2+3q_0^2)}{kk_f}-\frac{\left((k^2-k_f^2)^2+q_0^2(4k^2+4k_f^2+3q_0^2)\right)}{4k^2k_f^2}\log_{\rm e}\left(\frac{q_0^2+(k+k_f)^2}{q_0^2+(k-k_f)^2}\right)\right] \tag{3.95}$$

for interband scattering. As far as we are aware, these results have not been reported previously.

For interband scattering, the overlap integral $G(\mathbf{k}',\mathbf{k})$ acts to remove the singularity associated with the case $k_f=k$ in the unscreened piezoelectric scattering rates. We obtain, for interband scattering in the limit $q_0=0$,

$$P(k)=\frac{e^2k_BT_L}{4\pi\hbar\alpha_f}\left(\frac{K_{\rm av}^2}{\epsilon_0\epsilon_s}\right)\times\frac{3}{8k}\left[\frac{(k^2+k_f^2)}{kk_f}-\frac{(k^2-k_f^2)^2}{2k^2k_f^2}\log_{\rm e}\left|\frac{k+k_f}{k-k_f}\right|\right]. \tag{3.96}$$

Now, for elastic scattering at an energy ϵ, we may write $k^2=m_i^*\epsilon/\alpha_0$ and $k_f^2=m_f^*\epsilon/\alpha_0$ and substitute for k and k_f in the above equation, to obtain

$$P(k)=\frac{e^2k_BT_L}{4\pi\hbar\alpha_f}\left(\frac{K_{\rm av}^2}{\epsilon_0\epsilon_s}\right)\times\frac{3}{8k}\left[\frac{(m_i^*+m_f^*)}{(m_i^*m_f^*)^{\frac{1}{2}}}-\frac{(m_i^*-m_f^*)^2}{2m_i^*m_f^*}\log_{\rm e}\left|\frac{m_i^{*\frac{1}{2}}+m_f^{*\frac{1}{2}}}{m_i^{*\frac{1}{2}}-m_f^{*\frac{1}{2}}}\right|\right]. \tag{3.97}$$

This expression shows clearly that, in the absence of screening, the effect of the overlap integral $G(\mathbf{k}',\mathbf{k})$ is merely to introduce a constant multiplying factor; hence the rate is proportional to $1/k$ as for the unity overlap case (equation (3.70)). This means that a singularity still occurs at $k=0$, and, for elastic interband scattering, this is the only case where $k_f=k$. However, in any inelastic treatment of the piezoelectric scattering of holes, the $k_f=k$ transitions would occur *away* from the zone centre, and therefore the associated scattering rate would be finite, even in the absence of screening.

CHAPTER 4
MONTE CARLO SIMULATIONS OF HOLE TRANSPORT IN BULK GaAs

In the previous chapter, we derived expressions for the scattering of holes in a semiconductor by acoustic (deformation potential), non-polar optical, polar optical and piezoelectric phonons. Prior to that, in Chapter 2, we set out the basic principles of the Monte Carlo method for the simulation of electronic transport. Therefore we may, in this chapter, take the opportunity to report on the development of a Monte Carlo simulation of hole transport in bulk GaAs, based on the foregoing descriptions. This work is potentially very useful in its own right, as very few theoretical studies of hole transport exist in the literature. However, the main purpose of the simulation described here is to serve as a precursor of the simulations of quantum confined hole dynamics which will be described in chapters 8–10.

We will use a two band model of the GaAs valence band system, with both the heavy and light hole bands assumed isotropic and parabolic, as described in Section 3C. We have included intra- and inter-band scattering via the four phonon modes, AC, NPO, POP and PZ, discussed in that section. Other processes, such as impurity and carrier-carrier scattering, have not been included. This means that the results from our simulations will represent the limiting case of a high purity and low carrier density sample.

We will present results obtained at a lattice temperature of 77K, to enable comparison with our subsequent work on quantum confined holes. At this temperature, the elastic and equipartition approximations for acoustic (AC and PZ) scattering still hold good. In addition, we will show hole drift velocities obtained from simulations at $T_L = 300$K, to enable some comparison with other published work. Only results for the steady state case (single particle simulation) will be shown.

Before presenting these results (Section 4C), we will show firstly, in Section 4A, the energy dependences of the hole-phonon scattering rates derived in the previous chapter, for the case $T_L = 77$K. Then, in Section 4B, we will discuss the angular dependence of the various scattering processes, and the determination of stochastic scattering angles in the Monte Carlo simulation.

4A 77K HOLE-PHONON SCATTERING RATES

In Table 4.1 we have shown values of the material parameters, for GaAs, to be used in the scattering rate expressions of Section 3C. In particular, we have used an optical phonon energy $\hbar\omega_{\rm op}$ of 36.4meV for both polar scattering (LO modes only) and non-polar scattering (LO and TO modes combined). This value corresponds to that for LO phonons for temperatures in the range of $T_L = 77$K. Whilst the TO phonon energy is somewhat less than the LO value — the Lyddane-Sachs-Teller relation $(\omega_{\rm LO}/\omega_{\rm TO})^2 = \varepsilon_s/\varepsilon_\infty$ gives, for GaAs, $\hbar\omega_{\rm TO} \approx 0.93\hbar\omega_{\rm LO}$ — the discrepancy is sufficiently small as to have very little effect on hole transport. The values of the deformation potentials $E_{\rm AC}$ and $D_{\rm op}$ are our own, as discussed in Appendix 2.

In Fig. 4.1 we have shown the acoustic scattering rates for heavy hole band – heavy hole band (h–h), and heavy hole band – light hole band (h–l) transitions, as a function of the energy of the initial state. The energy dependence is of the form $\epsilon^{1/2}$ (see equation (3.78)), corresponding to the 3D density of states function, and the much lower value for (h–l) scattering is simply due to the smaller density of states in the light hole band. We saw in Section 3C that, for acoustic scattering in the elastic and equipartition approximations, the overlap integral term $G^2(\mathbf{k}',\mathbf{k})$ does not modify the form of the scattering rate, but merely contributes a constant factor of 1/2. Since the rate is dependent only on the density of *final* states, the (h–h) curve also gives the rate for (l–h) scattering, and the (h–l) curve also corresponds to the (l–l) result.

Figs. 4.2 and 4.3 show the scattering rates for NPO phonon absorption and emission respectively. The energy dependence again follows an $\epsilon^{1/2}$ law, as for acoustic scattering; the only differences being, of course, that the absorption rate is non-zero at $\epsilon = 0$, and the emission process has a threshold energy of $\hbar\omega_{\rm op}$. The large difference in the scales for the absorption and emission rates is due to the small value of $N_{\rm op}$ at 77K. In this case also, the overlap integral term $G^2(\mathbf{k}',\mathbf{k})$ simply contributes a constant multiplying factor to the scattering rates, and the comments made above concerning the equivalence of the (h–h) and (l–h), and (h–l) and (l–l) rates also apply here.

Figs. 4.4 and 4.5 show the rates for POP absorption and emission. For polar scattering, as demonstrated in Section 3C, the overlap integrals exert considerable influence on the energy dependence of the transition rates. In Fig. 4.6 we have shown, for comparison, the POP emission rate for heavy holes calculated with the exclusion of the $G^2(\mathbf{k}',\mathbf{k})$ term, as is the case for electrons in GaAs (see equation 3.65).

Of particular note is the fact that the dominant contribution is provided by

$\hbar\omega_{\rm op}$	36.4 meV
m_h^*	0.50
m_l^*	0.068
a_0	5.6533 Å
ρ	5.32×10^3 kgm^{-3}
v_l	4.7265×10^3 ms^{-1}
v_t	3.3436×10^3 ms^{-1}
$\overline{v}$	3.860×10^3 ms^{-1}
ε_s	12.74
ε_∞	10.94
h_{14}	0.160 Cm^{-2} [a,b,c]
c_{11}	11.88×10^{10} Nm^{-2}
c_{12}	5.38×10^{10} Nm^{-2}
c_{44}	5.94×10^{10} Nm^{-2}
c_l	14.032×10^{10} Nm^{-2} [e]
c_t	4.864×10^{10} Nm^{-2} [e]
a	2.7 eV [b]
b	−1.7 eV [a,b]
d	4.55 eV [a,b]
d_0	41.0 eV [a,b,d]
$E_{\rm AC}$	5.07 eV [e]
$D_{\rm op}$	8.88×10^{10} eVm^{-1} [e]

Table 4.1: Values of the Material Parameters used in the Simulations of Hole Transport in Bulk GaAs

Values unmarked, or marked *a* were taken from Landolt-Börnstein (1982); those marked *b*, from Adachi (1985); *c*, Rode (1970); *d*, Wiley (1970), and for those marked *e*, see Appendix 2.

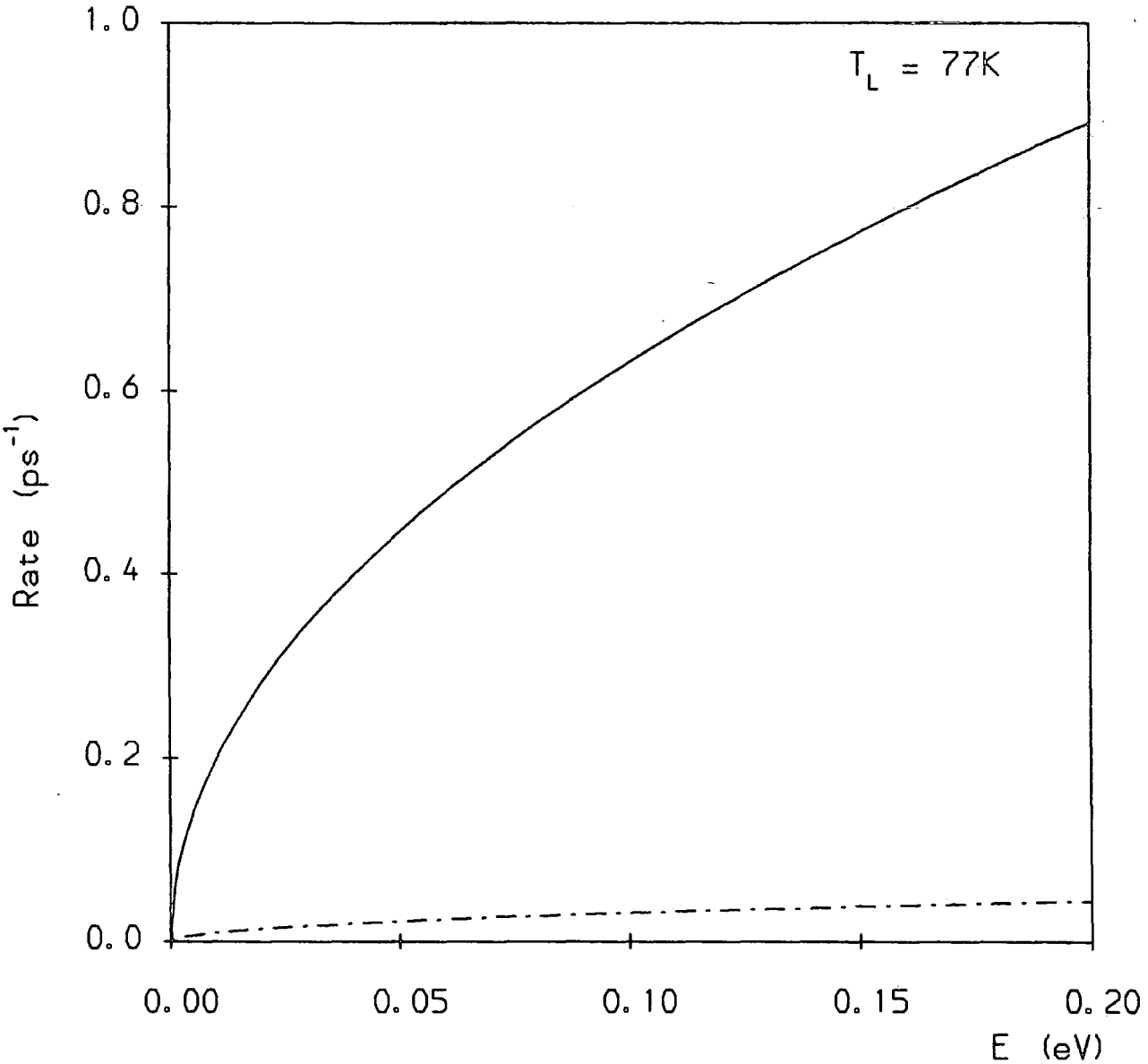

Fig. 4.1 Acoustic (AC) scattering rates for holes in the heavy (h) and light (l) hole bands of GaAs at $T_L = 77$K. — (h–h) and (l–h); · – · (h–l) and (l–l).

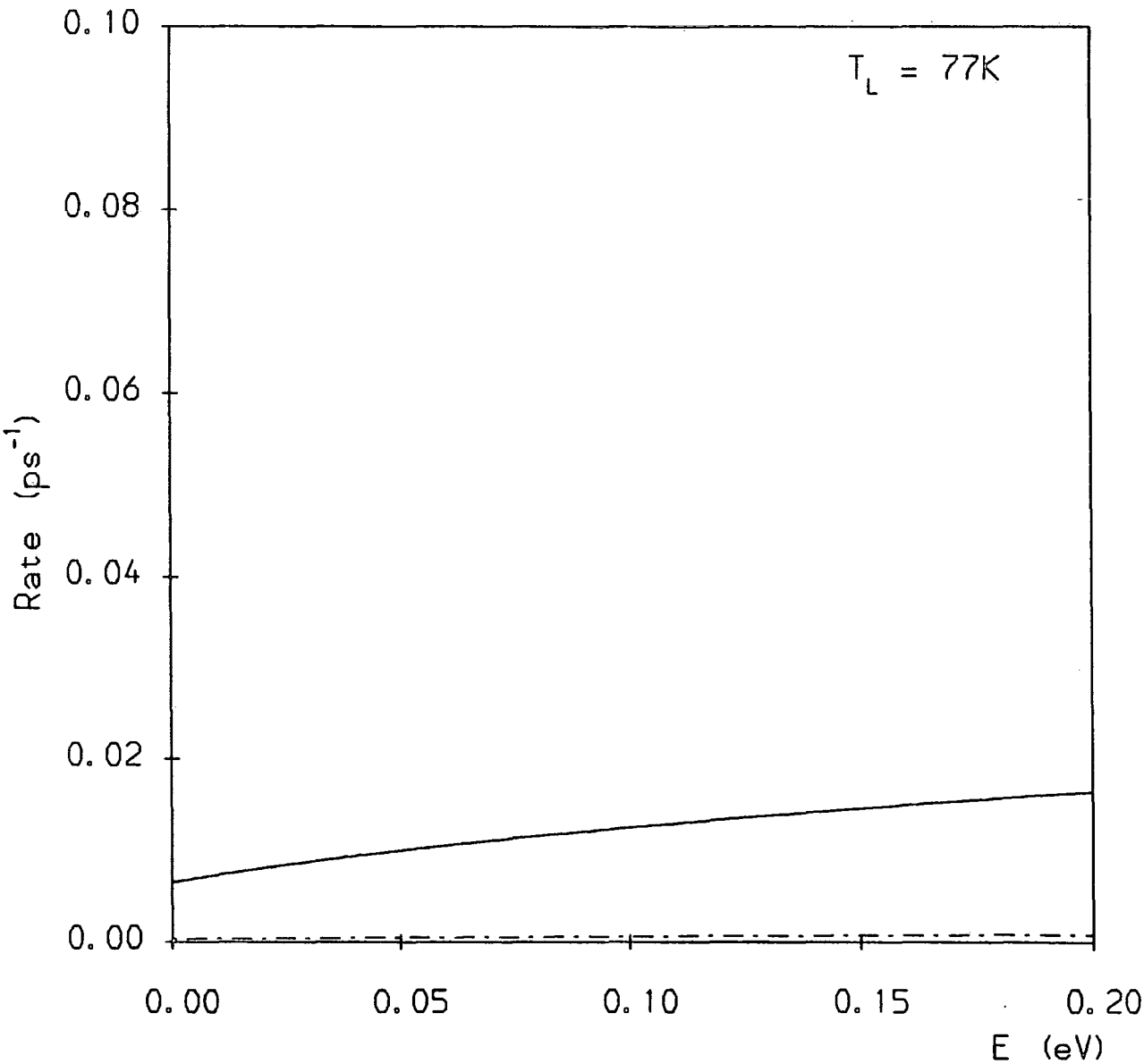

Fig. 4.2 Scattering rates for NPO phonon absorption by holes in GaAs. — (h–h) and (l–h); · – · (h–l) and (l–l).

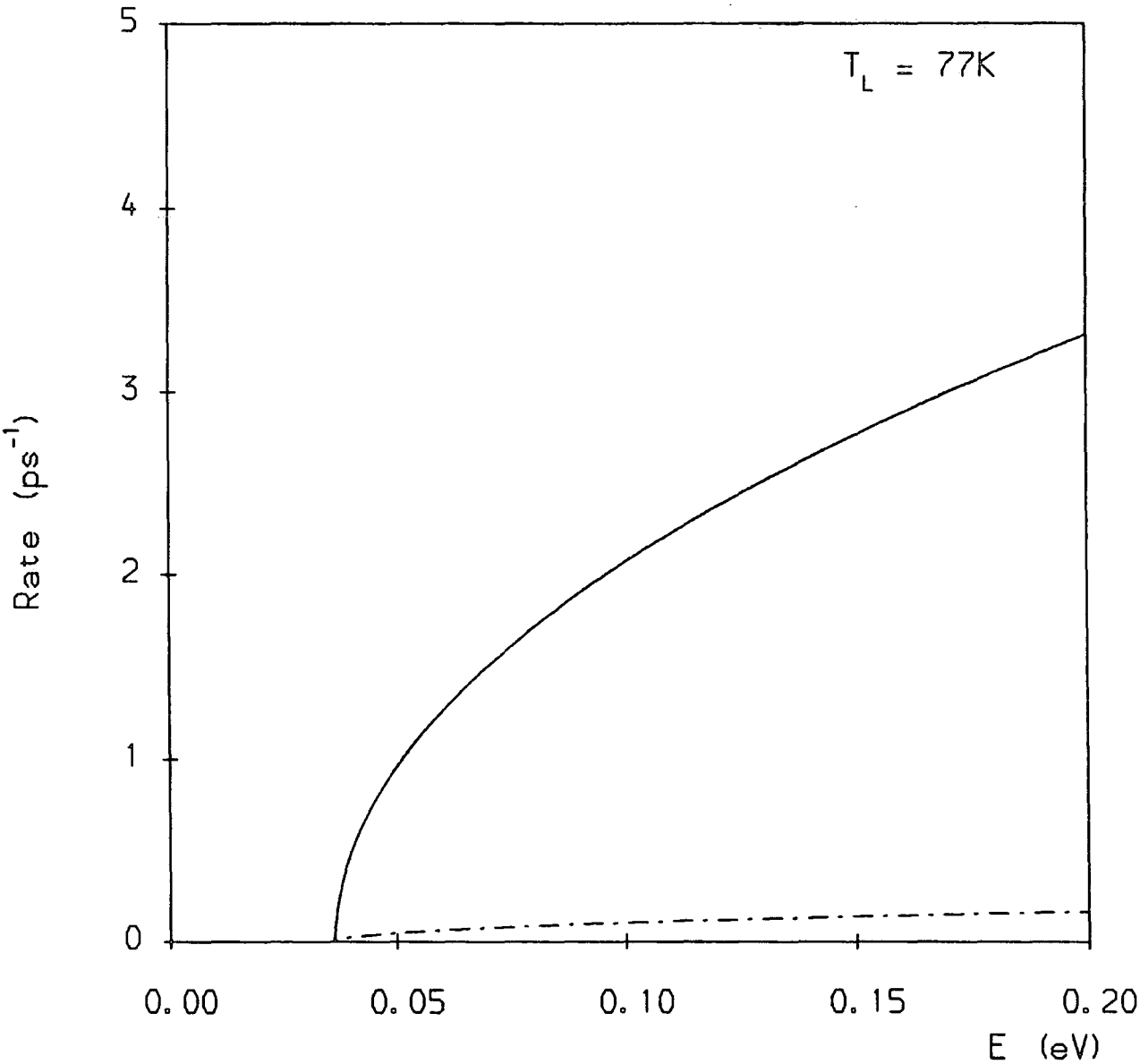

Fig. 4.3 Scattering rates for NPO phonon emission by holes in GaAs. — (h–h) and (l–h); · – · (h–l) and (l–l).

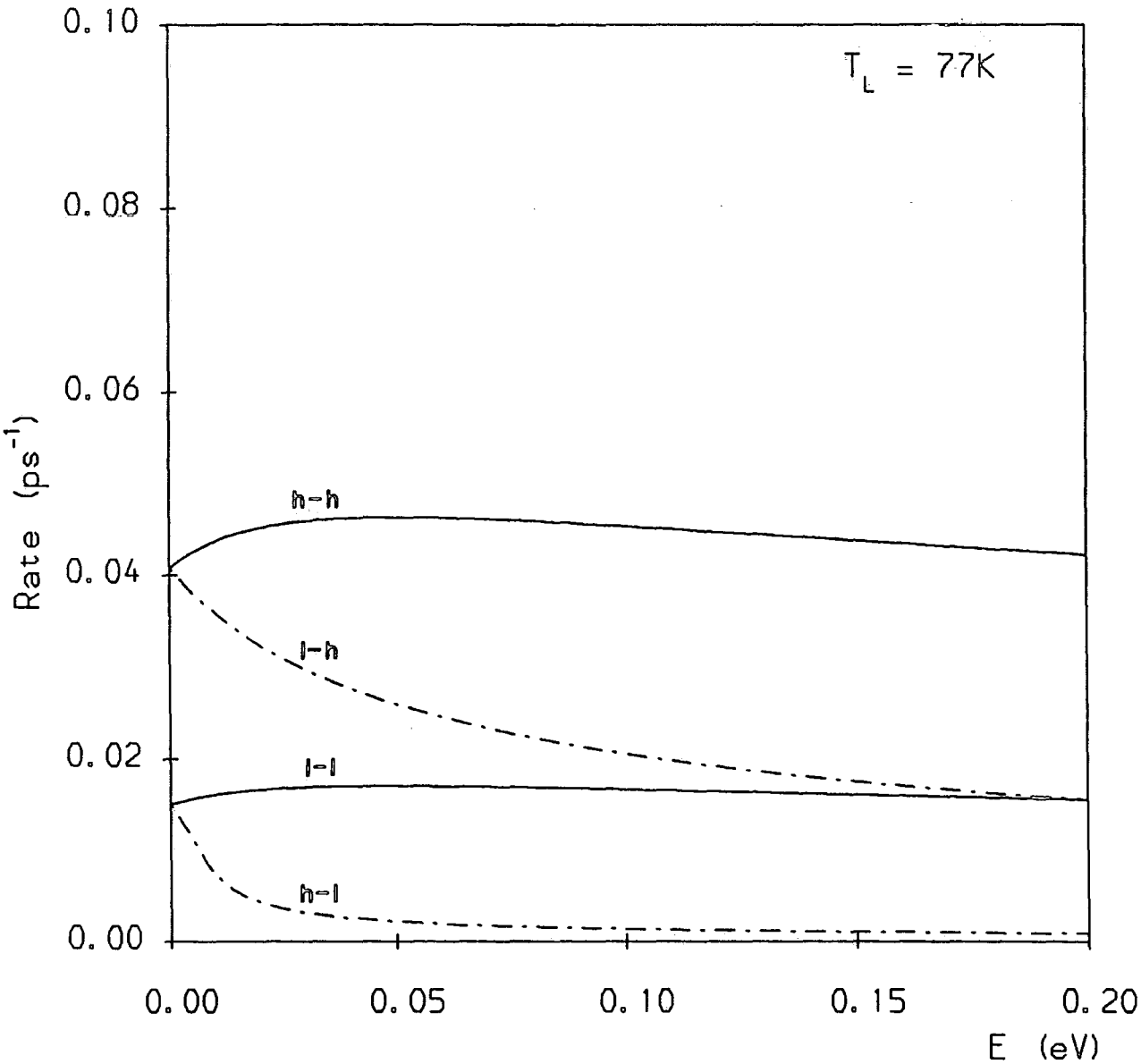

Fig. 4.4 Scattering rates for POP phonon absorption by holes in GaAs.

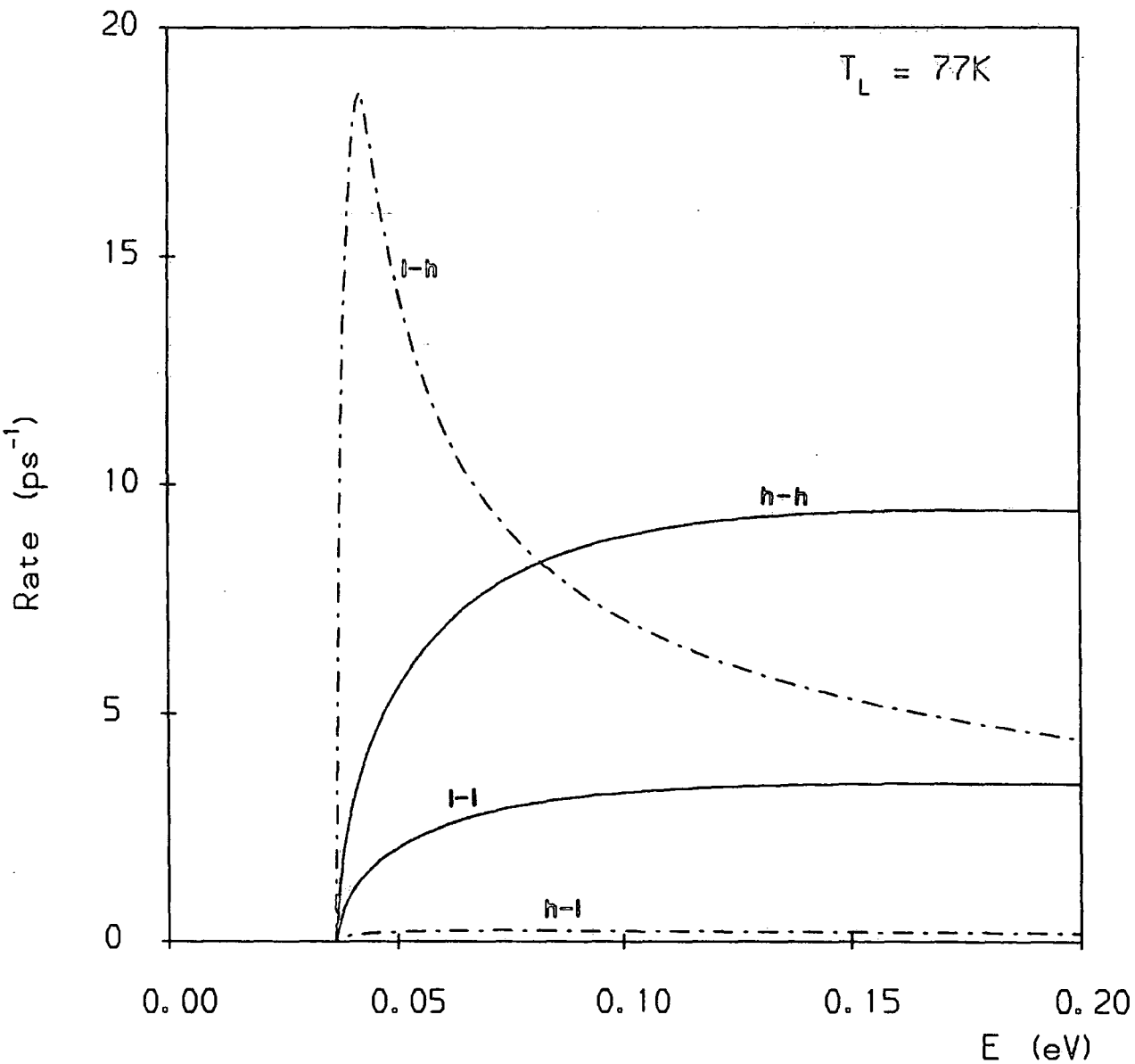

Fig. 4.5 Scattering rates for POP phonon emission by holes in GaAs.

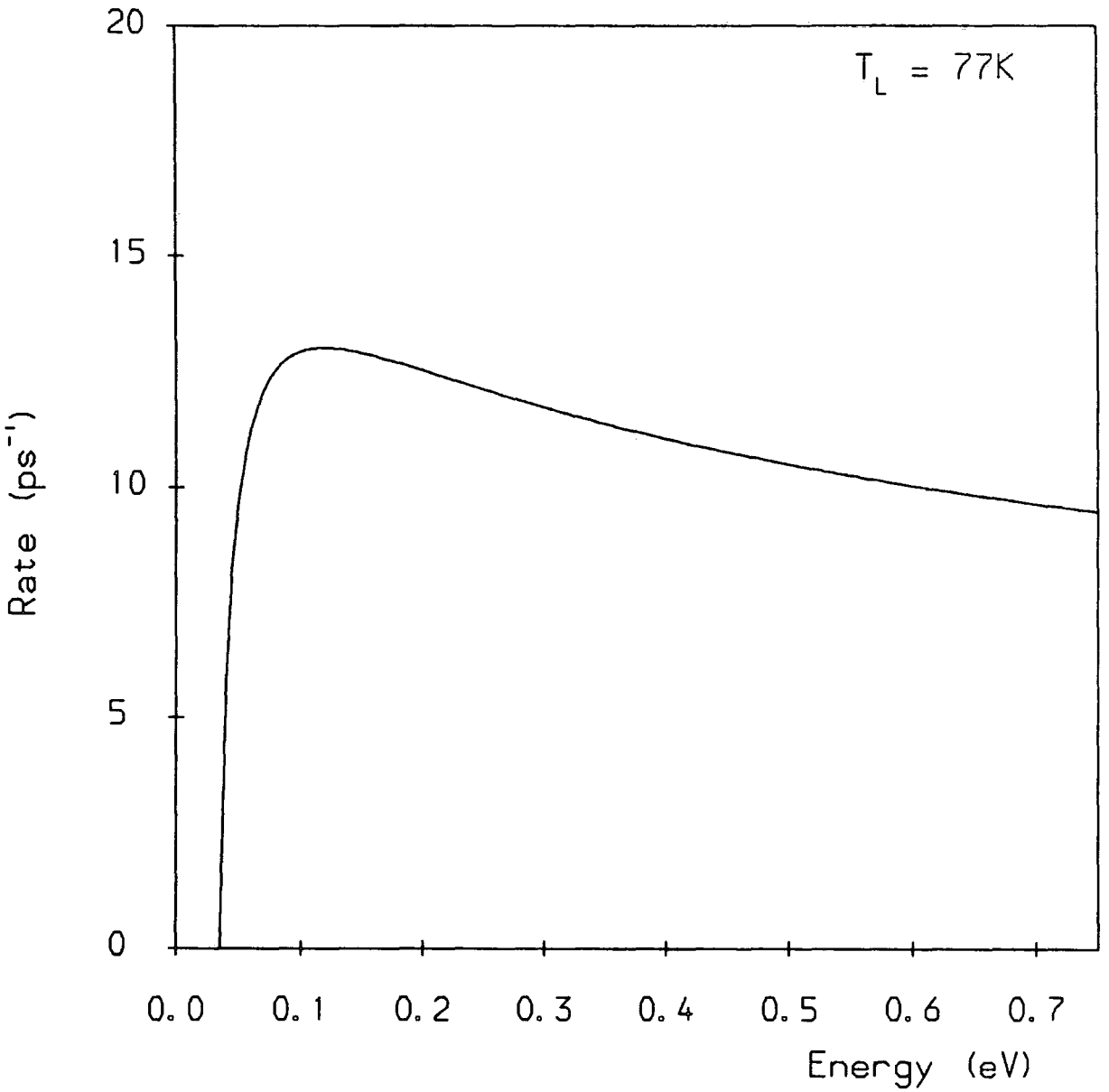

Fig. 4.6 Scattering rate for POP phonon emission by heavy holes in GaAs, calculated excluding overlap integral effects.

the interband (l–h) rate, which is strongly peaked soon after threshold. This indicates that coupling of the valence bands is an important aspect of polar phonon scattering. However, the (h–l) polar emission rate is much lower, due again to the smaller density of states in the light hole band. Costato and Reggiani (1973b) have also pointed out that, for interband scattering, the overlap integral term $G^2(\mathbf{k}', \mathbf{k})$ serves to remove the singularities which would otherwise occur at vertical ($\mathbf{q} = 0$) transitions.

In Figs. 4.7–8 we have shown the rates for intraband (h–h) and interband (l–h) PZ scattering, for a range of reciprocal screening lengths q_0. We have assumed that screening is due a non-degenerate population of free carriers at the lattice temperature T_L, in which case q_0 is related to the carrier density p by (see Ridley 1988)

$$q_0^2 = \frac{e^2 p}{\epsilon_0 \epsilon_s k_B T_L}. \tag{4.1}$$

For interband scattering, we have also shown the unscreened $q_0 = 0$ case, which, as mentioned in the previous chapter, diverges as $\epsilon \to 0$. The curve for $p = 10^{16}\text{cm}^{-3}$ lies very close to that for $q_0 = 0$, and thus represents the case of relatively weak screening, although we still expect to obtain zero rate at $\epsilon = 0$ as with higher values of p.

Figs. 4.9–10 show the intraband (h–h) and interband (l–h) rates compared with those calculated excluding overlap integral effects. For interband scattering, at the upper end of the energy range shown the reduction in the rate due to overlap integral effects is relatively small, whereas for (l–h) scattering, this reduction is close to a factor of two (*cf.* AC and NPO scattering) for each of the different values of q_0.

As the purpose of this chapter is to present only a representative, rather than a comprehensive set of results for bulk hole transport, we will report on simulations using only one value of q_0. We will take the case $q_0 = 4.6266 \times 10^{-3}\text{Å}^{-1}$, appropriate to $p = 10^{16}\text{cm}^{-3}$, for the sake of consistency with our model of quantum confined hole transport described later in this thesis (see Section 6E). Fig. 4.11 shows the scattering rates for all four PZ processes ((h–h), (l–h), (l–l) and (h–l)) for the case $p = 10^{16}\text{cm}^{-3}$. The rates for scattering into the heavy hole band are again dominant, but are still substantially smaller than those for the corresponding AC processes. Finally, in Fig. 4.12 we have shown the total scattering rates for holes in the heavy and light hole bands. The light hole rate is dominated by the contribution from (l–h) polar scattering, giving much larger values near the optical phonon emission threshold than for heavy holes, with a peak value in excess of 20ps^{-1}.

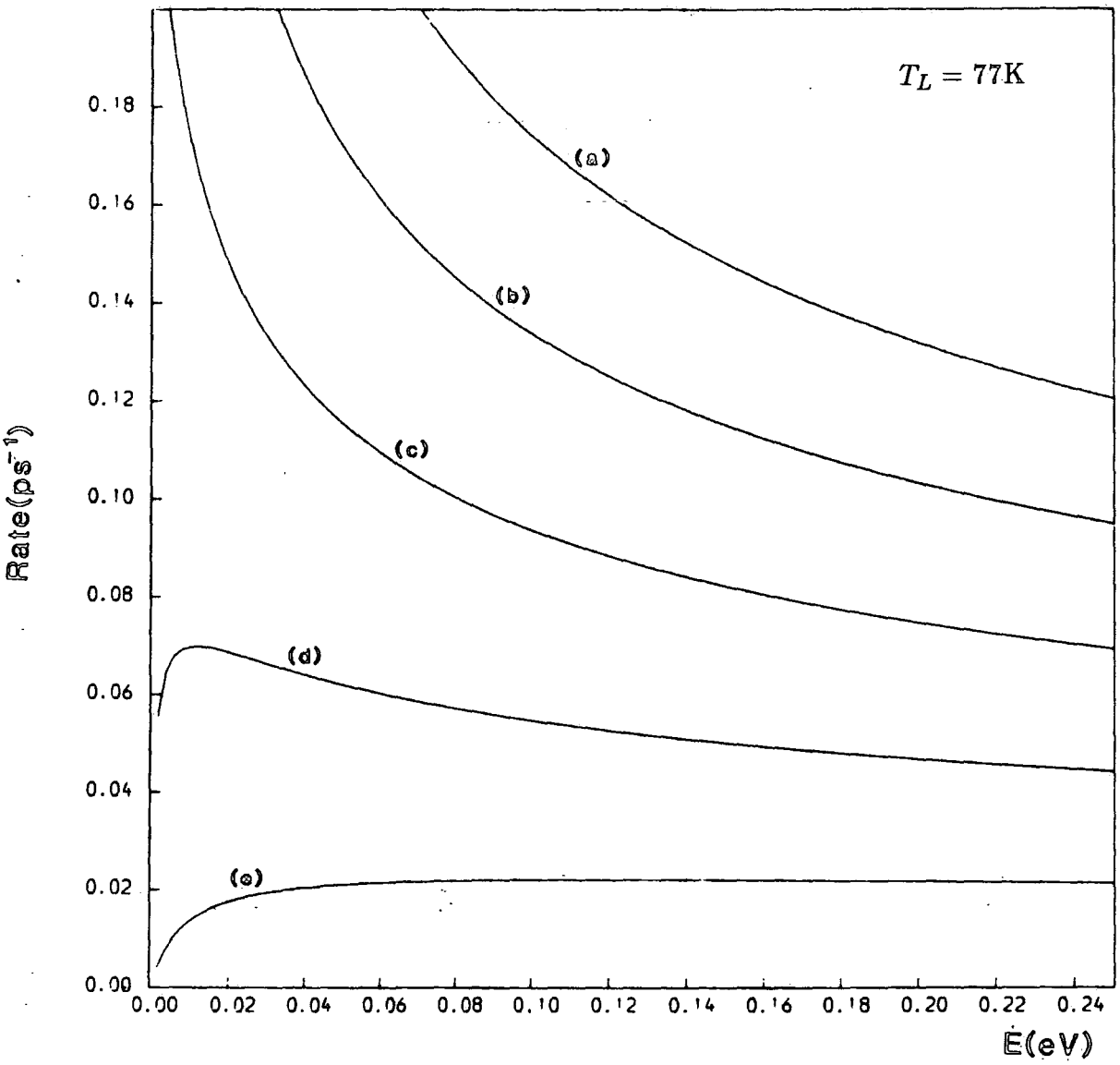

Fig. 4.7 Rates for (h–h) PZ scattering in GaAs, with free carrier screening. (a) $q_0 = 4.6266\times10^{-4}$Å^{-1} ($p = 10^{14}$cm^{-3}); (b) $q_0 = 1.4631\times10^{-3}$Å^{-1} ($p = 10^{15}$cm^{-3}); (c) $q_0 = 4.6266\times10^{-3}$Å^{-1} ($p = 10^{16}$cm^{-3}); (d) $q_0 = 1.4631\times10^{-2}$Å^{-1} ($p = 10^{17}$cm^{-3}); (e) $q_0 = 4.6266\times10^{-2}$Å^{-1} ($p = 10^{18}$cm^{-3}).

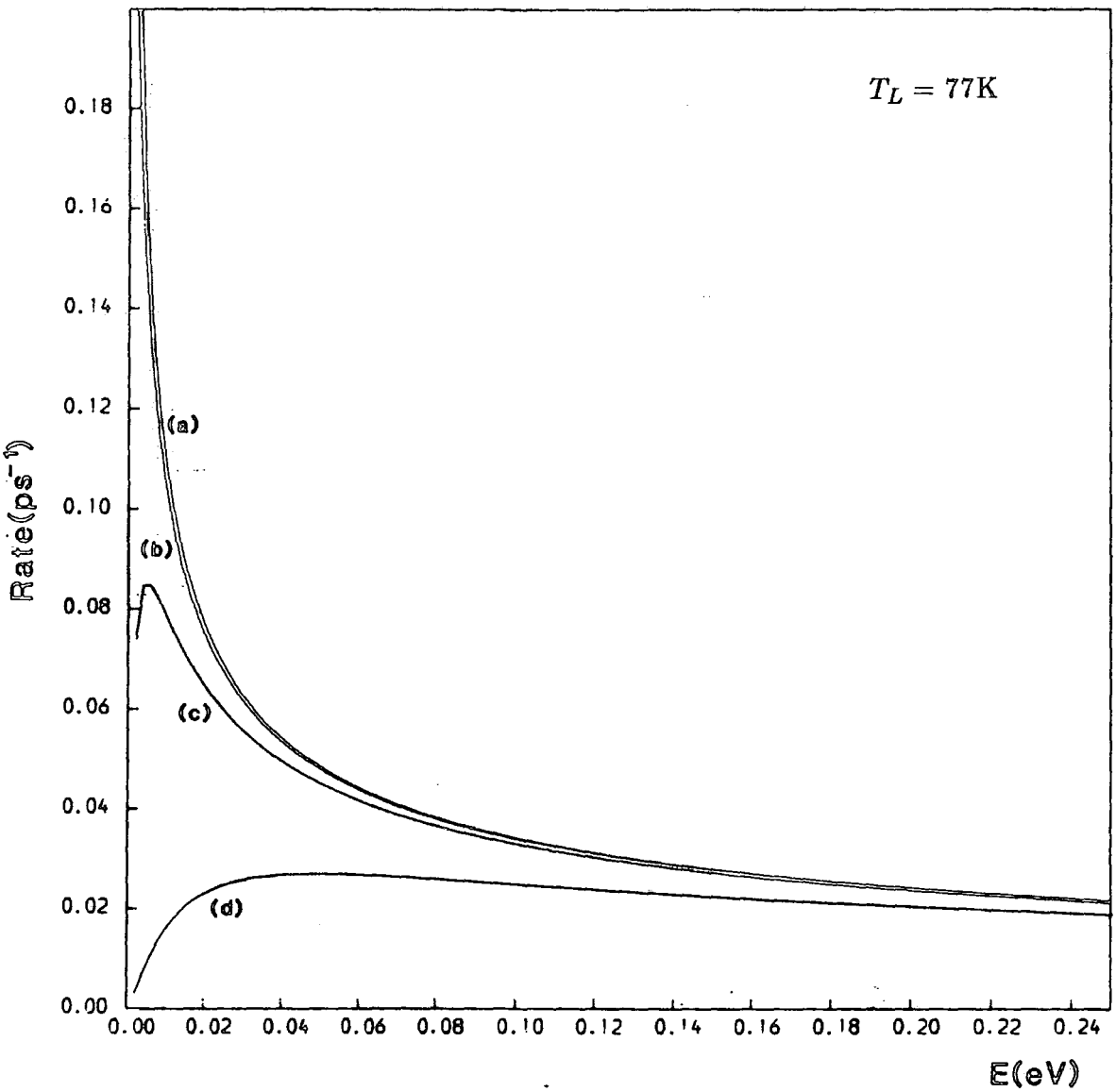

Fig. 4.8 Rates for (l–h) PZ scattering in GaAs, with free carrier screening. (a) $q_0 = 0$; (b) $q_0 = 4.6266 \times 10^{-3}$Å^{-1} ($p = 10^{16}$cm^{-3}); (c) $q_0 = 1.4631 \times 10^{-2}$Å^{-1} ($p = 10^{17}$cm^{-3}); (d) $q_0 = 4.6266 \times 10^{-2}$Å^{-1} ($p = 10^{18}$cm^{-3}).

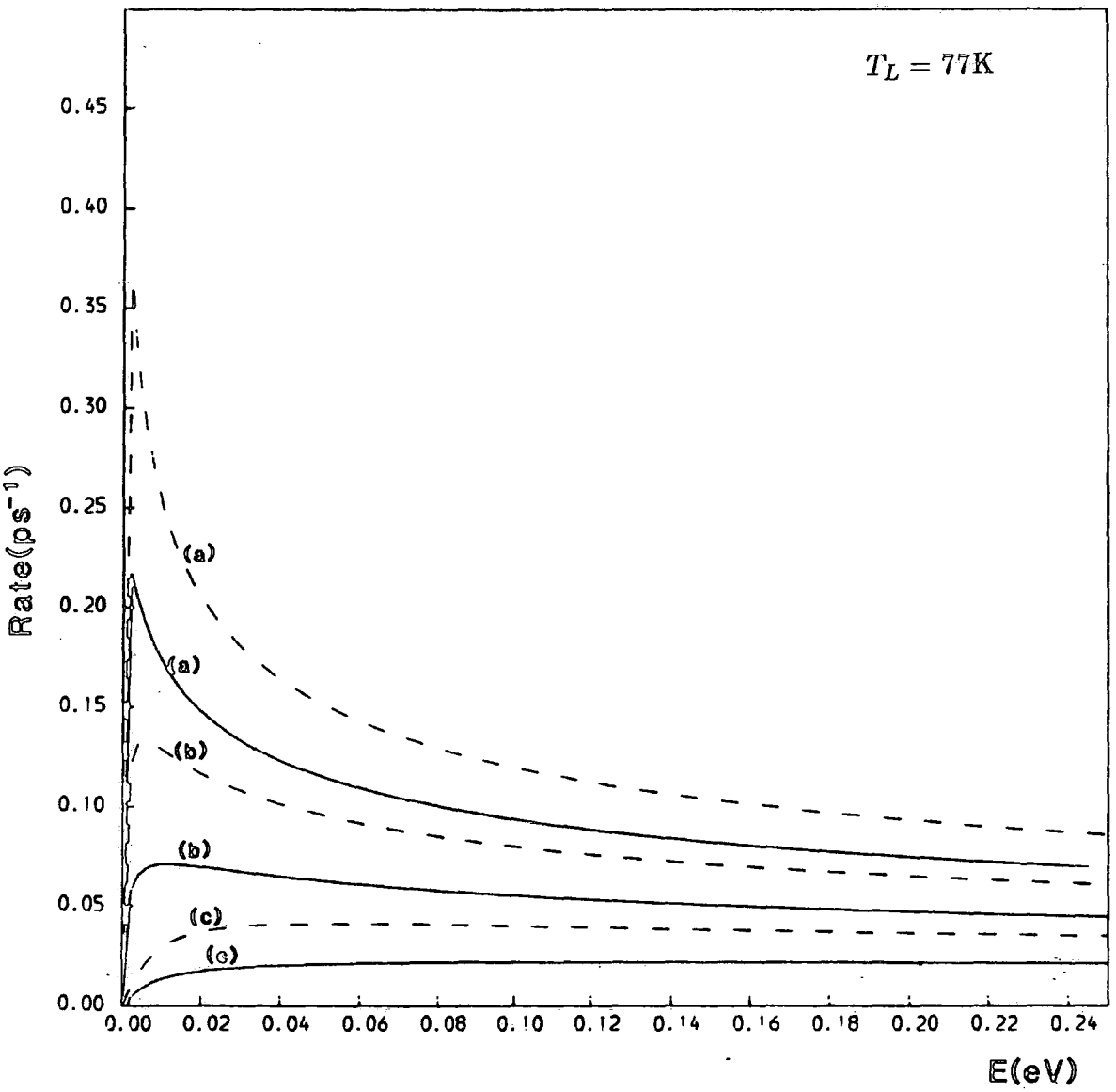

Fig. 4.9 Rates for (h–h) PZ scattering in GaAs. — Full rates; · – · rates calculated with the exclusion of overlap integral effects. (a) $q_0 = 4.6266\times10^{-3}$Å^{-1} ($p = 10^{16}$cm^{-3}); (b) $q_0 = 1.4631\times10^{-2}$Å^{-1} ($p = 10^{17}$cm^{-3}); (c) $q_0 = 4.6266\times10^{-2}$Å^{-1} ($p = 10^{18}$cm^{-3}).

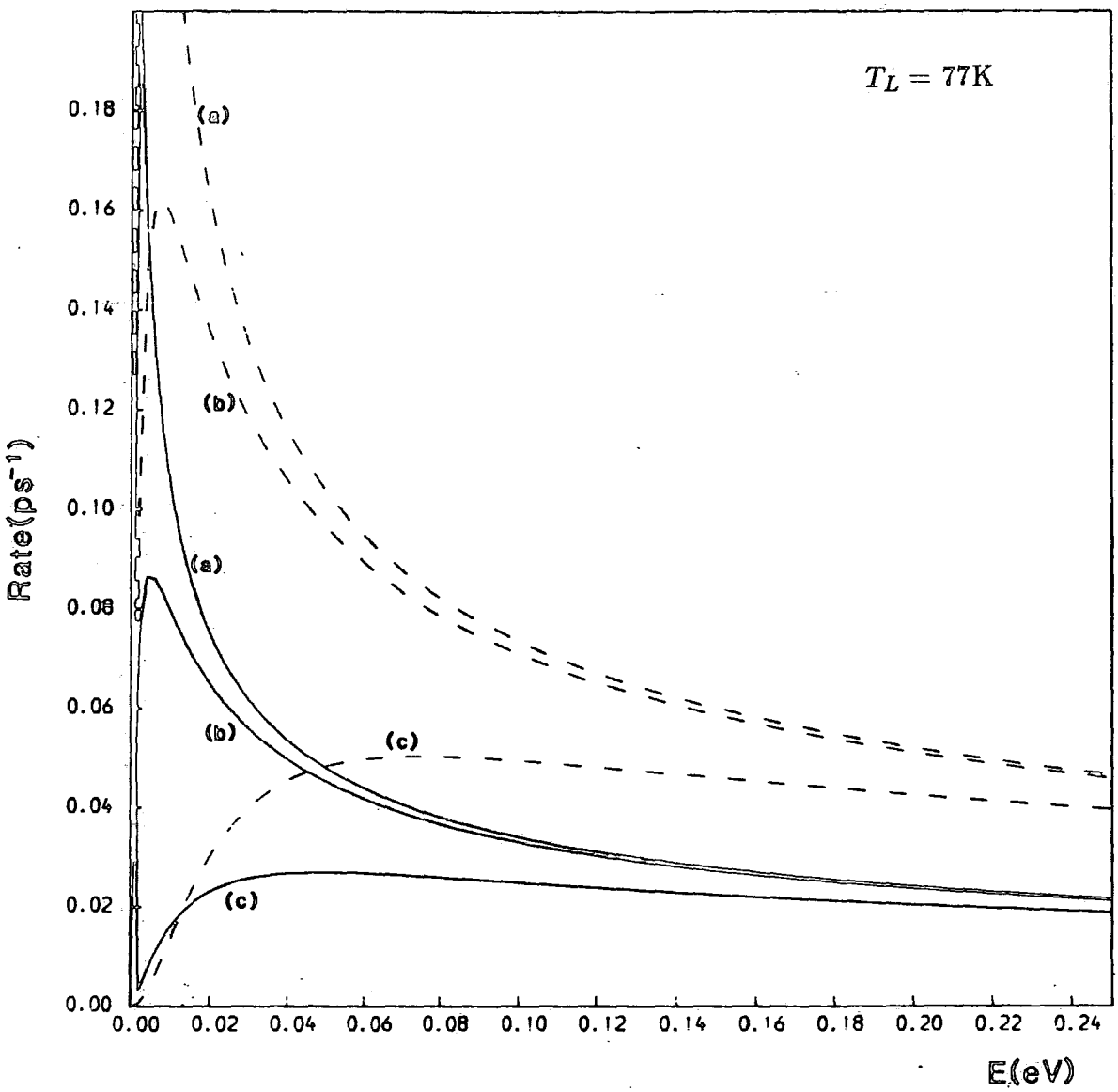

Fig. 4.10 Rates for (l–h) PZ scattering in GaAs. — Full rates; · – · rates calculated with the exclusion of overlap integral effects. (a) $q_0 = 4.6266\times10^{-3}$Å^{-1} ($p = 10^{16}$cm^{-3}); (b) $q_0 = 1.4631\times10^{-2}$Å^{-1} ($p = 10^{17}$cm^{-3}); (c) $q_0 = 4.6266\times10^{-2}$Å^{-1} ($p = 10^{18}$cm^{-3}).

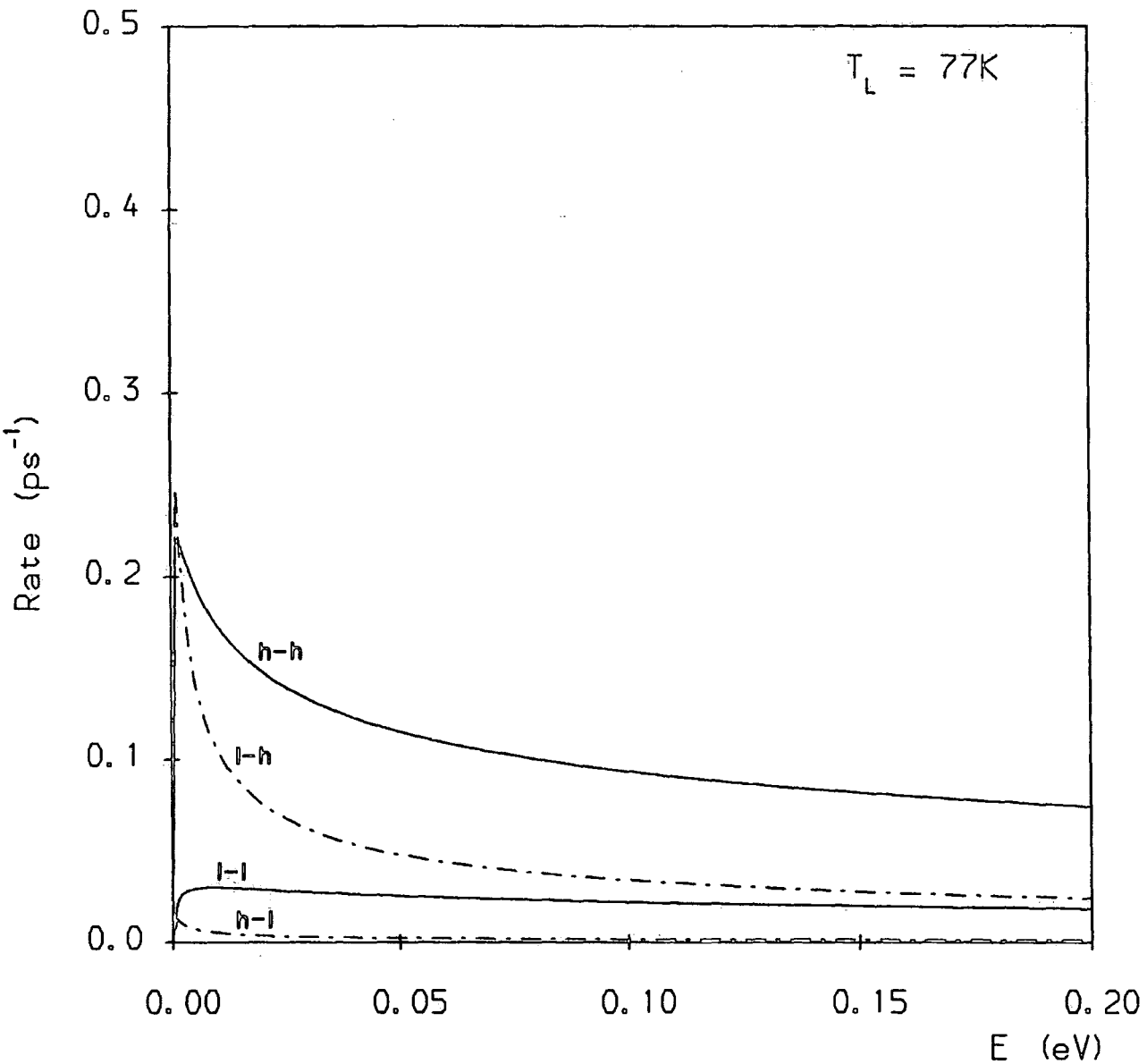

Fig. 4.11 PZ scattering rates for holes in GaAs: $q_0 = 4.6266 \times 10^{-3}$Å^{-1} ($p = 10^{16}$cm^{-3}); $T_L = 77$K.

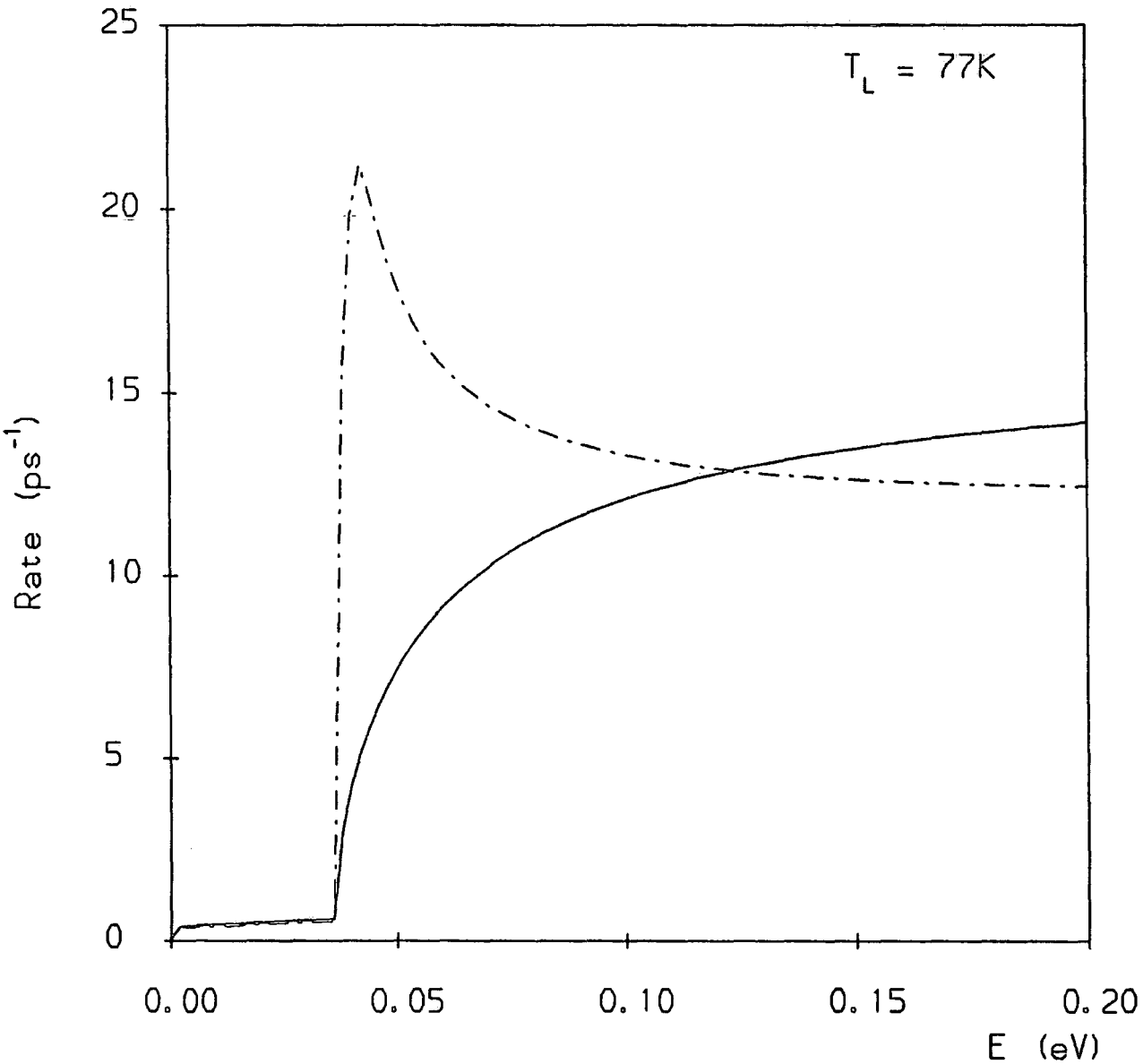

Fig. 4.12 Total scattering rates for holes in the heavy (—) and light (· – ·) hole bands of GaAs, including AC, NPO, POP and PZ processes.

4B ANGULAR DEPENDENCE OF THE SCATTERING RATES

We have seen, in Chapter 2, that an important aspect of any Monte Carlo simulation of electronic transport is the computation of stochastic scattering angles appropriate to each particular scattering process. This requires the isolation of the angular dependence $P(\theta,\phi)$ of the transition probability in each case. These expresssions can then be used to generate scattering angles, and hence the components of the after-scattering wavevector $\mathbb{k}'$, by one of the techniques described in section 2A.1 and Appendix 1.

AC and NPO scattering

The angular dependence of these processes is solely that of the overlap term $G^2(\mathbb{k}',\mathbb{k})$. Since, in the forms given in equations (3.71) and (3.72), $G^2(\mathbb{k}',\mathbb{k})$ is a function of the scattering angle β only, we may, from the outset, choose our coordinate frame such that the polar angle θ is identical to β. Then, for intraband scattering, the angular dependence of the transition probability is given by

$$P(\theta,\phi) \rightarrow P(\cos\beta) = \frac{1}{4}(1+3\cos^2\beta), \tag{4.2}$$

and, for interband scattering, by

$$P(\theta,\phi) \rightarrow P(\cos\beta) = \frac{3}{4}(1-\cos^2\beta). \tag{4.3}$$

It is possible to use these equations to obtain expressions for the stochastic scattering angles β_r as a function of the random variate r. However, for both intra- and inter-band scattering, the calculation entails solving a cubic equation in $\cos\beta$. This is a rather tedious process, and the resulting expression involves exponentiation operations which, when repeated a large number of times, will cause a notable increase in the computer processing time required by the Monte Carlo simulation. A more attractive and efficient approach is to use the basic rejection technique of Appendix 1. It can readily be shown that the method yields an acceptance ratio of 50% for both intra- and inter-band scattering, and hence the amount of processing time wasted in the simulation is relatively small.

Polar optical scattering

From equation (3.82), making use of the interchangeability of θ and β, the angular dependence of the intraband polar scattering rate can be obtained as

$$P(\cos\beta) = \frac{1}{4}\frac{(1+3\cos^2\beta)}{(k^2+k_f^2-2kk_f\cos\beta)}. \tag{4.4}$$

To obtain an expression for the stochastic β_r as a function of r by the direct technique involves the integration of the above expression with respect to $\cos\beta$,

and the subsequent inversion of the result (see section 2A.1). It is clear, from the work in Section 3C, that the latter operation would not be feasible in the present case. Therefore, a rejection technique must be used.

The function $P(\cos\beta)$ may be rewritten in the form

$$P(x) = \frac{1}{4a}\frac{(1+3x^2)}{(1-\lambda x)}, \tag{4.5}$$

where $a = k^2 + k_f^2$, $b = 2kk_f$, and $\lambda = b/a$, so that $\lambda \leq 1$. The function $P(x)$ is obviously dominated by the behaviour of the denominator, giving a sharp increase in $P(x)$ as $x \to 1$, and, indeed, a singularity at $x = 1$ if $\lambda = 1$, though this case will not occur for intraband scattering.

To make use of the improved efficiency of the combined rejection technique, as compared with the basic method (see Appendix 1), it is necessary to identify a function which is similar in value, yet greater than $P(x)$, throughout the allowed range of x, and which is sufficiently simple in form to enable its use in the generation of random values of x by the direct technique. For x restricted to the range $[-1, 1]$, the denominator of equation (4.5) has a minimum value when $x = 1$, and therefore we can take for the above described function:

$$g(x) = \frac{1}{a(1-\lambda x)}. \tag{4.6}$$

Now, with $x = \cos\beta$, this function gives the angular dependence for polar optical scattering of carriers assuming unity overlap integral, and it has been shown by Fawcett *et al.* (1970) that, for this case, stochastic scattering angles β_r can be generated using the direct technique.

Writing

$$r_1 = \int_{\cos\beta_r}^{1} \frac{dx}{a(1-\lambda x)} \Big/ \int_{-1}^{1} \frac{dx}{a(1-\lambda x)}, \tag{4.7}$$

we obtain, for β_r derived from the random variate r_1:

$$\cos\beta_r = \frac{(1+f) - (1+2f)^{r_1}}{f} \tag{4.8}$$

where $f = \lambda/(1-\lambda) = 2kk_f/(k-k_f)^2$ (*cf.* Fawcett *et al.* 1970). Then, the selected value of β_r is accepted if

$$r_2 g(\cos\beta_r) < P(\cos\beta_r), \tag{4.9}$$

where r_2 is a second random variate. Thus, the acceptance criterion is:

$$r_2 < \frac{1}{4}(1 + 3\cos^2\beta_r). \tag{4.10}$$

For interband polar scattering, the angular dependence is given by (see equation (3.82)):

$$P(\cos\beta) = \frac{(1-\cos^2\beta)}{(k^2+k_f^2-2kk_f\cos\beta)}, \tag{4.11}$$

where we have omitted the factor of 3/4 associated with the overlap integral term $G^2(\mathbb{k}',\mathbb{k})$. This equation can then be written in the form

$$P(x) = \frac{(1-x^2)}{a(1-\lambda x)}, \tag{4.12}$$

with $x \equiv \cos\beta$ and a, b and λ defined as above.

We may proceed exactly as for intraband scattering; approximating $P(x)$ by the function $g(x)$ of equation (4.6), from which stochastic scattering angles β_r can be generated according to equation (4.8). Then, equation (4.9) gives the acceptance criterion for the interband case as

$$r_2 < 1-\cos^2\beta_r. \tag{4.13}$$

Since the angular dependence of the polar interaction in the unity overlap integral case gives a bias to forward scattering ($\cos\beta \rightarrow 1$), the acceptance ratio for the intraband case here can be expected to be very high, whilst that for interband scattering will be considerably lower.

Piezoelectric scattering

The angular dependence of the screened piezoelectric interaction is given by (see equation (3.90)):

$$P(\cos\beta) = \frac{q^2}{(q^2+q_0^2)^2}G^2(\cos\beta) \tag{4.14}$$

where $q^2 = k^2+k_f^2-2kk_f\cos\beta$ and $G^2(\cos\beta)$ is the overlap integral term, which we shall normalise to a maximum value of unity; $G^2(\cos\beta) = 1/4(1+3\cos^2\beta)$ for intraband scattering, and $(1-\cos^2\beta)$ for interband scattering.

The complexity of this function again precludes the use of the direct technique for generating stochastic scattering angles β_r in a Monte Carlo simulation. Also, because of the strongly peaked nature of the term $q^2/(q^2+q_0^2)^2$, use of the basic rejection technique would lead to very a low acceptance ratio for the β_r. However, it is possible to make use of the combined technique, in a similar manner to that described for polar scattering.

Since, in equation (4.14), $G^2(\cos\beta) \leq 1$, we may write

$$P(x) \leq \frac{(a-bx)}{(c-bx)^2} \tag{4.15}$$

where $x \equiv \cos\beta$, $a = k^2 + k_f^2$, $b = 2kk_f$ and $c = a + q_0^2$. Then, since $c > a$; $(a - bx)/(c - bx) < 1$ for all x. Therefore

$$P(x) \leq \frac{1}{(c - bx)} \quad \text{for all } x. \tag{4.16}$$

This result is analogous to that of equation (4.6). It is clear that we can generate stochastic scattering angles β_r from the function $g(\cos\beta) = 1/(c - b\cos\beta)$ using the direct technique. We again obtain

$$\cos\beta_r = \frac{(1+f) - (1+2f)^{r_1}}{f} \tag{4.17}$$

where, in this case, $f = b/(c - b) = 2kk_f/\{(k - k_f)^2 + q_0^2\}$. Then, from equation (4.9), the acceptance criterion is given by

$$r_2 < \frac{(a - b\cos\beta_r)}{(c - b\cos\beta_r)} G^2(\cos\beta_r) \tag{4.18}$$

where $G^2(\cos\beta_r)$ takes one of the forms given above for intra- or inter-band scattering.

4C SIMULATIONS

4C.1: 77K Simulations

In this section we will show the electric field dependence of the basic Monte Carlo estimators; the drift velocity $\langle v \rangle$, mean energy $\langle \epsilon \rangle$ and fractional population $\langle \overline{n} \rangle$, to demonstrate the operation of our simulation of hole transport in the heavy and light valence bands of GaAs.

In Fig. 4.13 we have shown the drift velocities of heavy and light holes ($\langle v_h \rangle$ and $\langle v_l \rangle$), and the overall average drift velocity $\langle v_{\rm av} \rangle$, as a function of an applied electric field F. The curves for $\langle v_{\rm av} \rangle$ and $\langle v_h \rangle$ lie very close together, since most of the carriers occupy the heavy hole band, whilst the values for $\langle v_l \rangle$ are much larger, due to the smaller effective mass in the light hole band.

Fig. 4.14 shows the overall average drift velocity $\langle v_{\rm av} \rangle$ for a larger range of electric fields, estimated with and without the inclusion of piezoelectric scattering. It is clear that, even at 77K, piezoelectric scattering has relatively little effect on bulk hole transport; whereas Rode (1970) found this process to be quite important in electron transport at similar temperatures.

In Fig. 4.15 we have shown the low field (ohmic) portion of the $\langle v_{\rm av} \rangle$ *vs.* field plot, from which we estimate a lattice mobility of $\mu_p = 9400 {\rm cm}^2{\rm V}^{-1}{\rm s}^{-1}$. This compares well with experimental estimates of μ_p for low doped samples at 77K. Zschauer (1973) gives $\mu_p \approx 1.15 \times 10^4 {\rm cm}^2{\rm V}^{-1}{\rm s}^{-1}$, whilst Mears and Stradling (1971) give $\mu_p \approx 8000 {\rm cm}^2{\rm V}^{-1}{\rm s}^{-1}$, both for samples with carrier concentrations $p < 10^{15} {\rm cm}^{-3}$.

Fig. 4.16 shows the mean energies of the heavy and light holes, and the overall average energy. At low fields, the values in all three cases correspond to the thermal equilibrium result $(3/2)k_B T_L = 9.95 {\rm meV}$ at 77K, for a parabolic band. For fields greater than $F \approx 15 {\rm kVcm}^{-1}$ the mean energies increase significantly. This indicates the onset of the so called 'polar runaway' effect, whereby the rate of energy dissipation to polar phonon modes *decreases* with increasing field, because the scattering rates fall off. Hence, for sufficiently high fields, a steady state situation cannot be attained.

In Fig. 4.17 we have shown the fraction of the carrier population occupying the light hole band, $\langle \overline{n}_l \rangle$, as a function of electric field. The zero field result corresponds closely to the ratio of the density of states in the light hole band to the total density of states, a factor which reduces to $(m_l^*)^{3/2}/\{(m_h^*)^{3/2} + (m_l^*)^{3/2}\} \approx 0.048$ (*cf.* Costato *et al.* 1972). At low fields, scattering from the light to the heavy hole band is dominant, due to the larger density of states in the latter case, and to the peak in the (l–h) POP emission rate for energies immediately above the threshold. Also, because of the large density of states, most of the carriers in the heavy hole

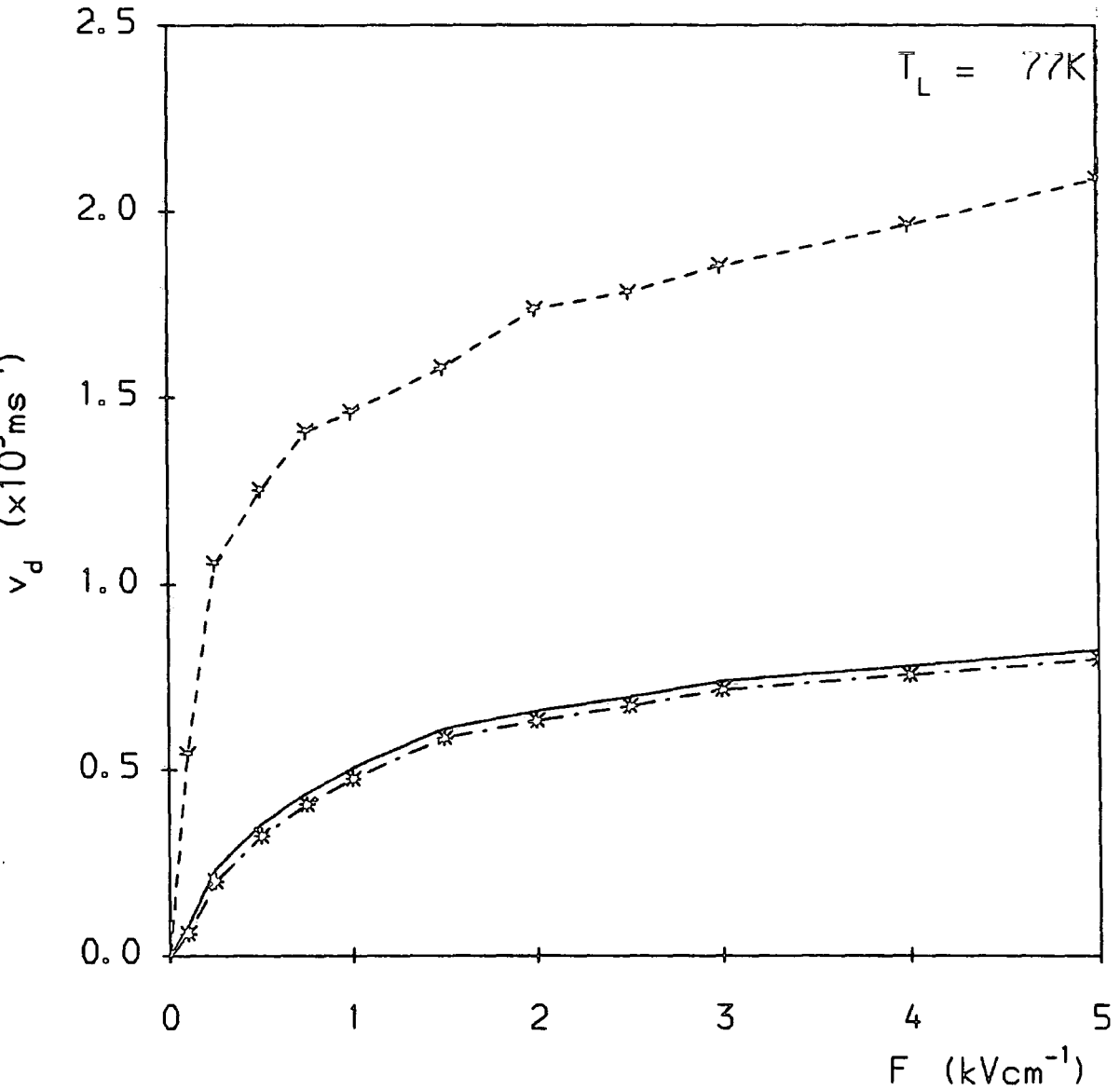

Fig. 4.13 Mean drift velocity of heavy (· – ·) and light (- - -) holes, and the overall average drift velocity (—) in GaAs, as a function of applied electric field.

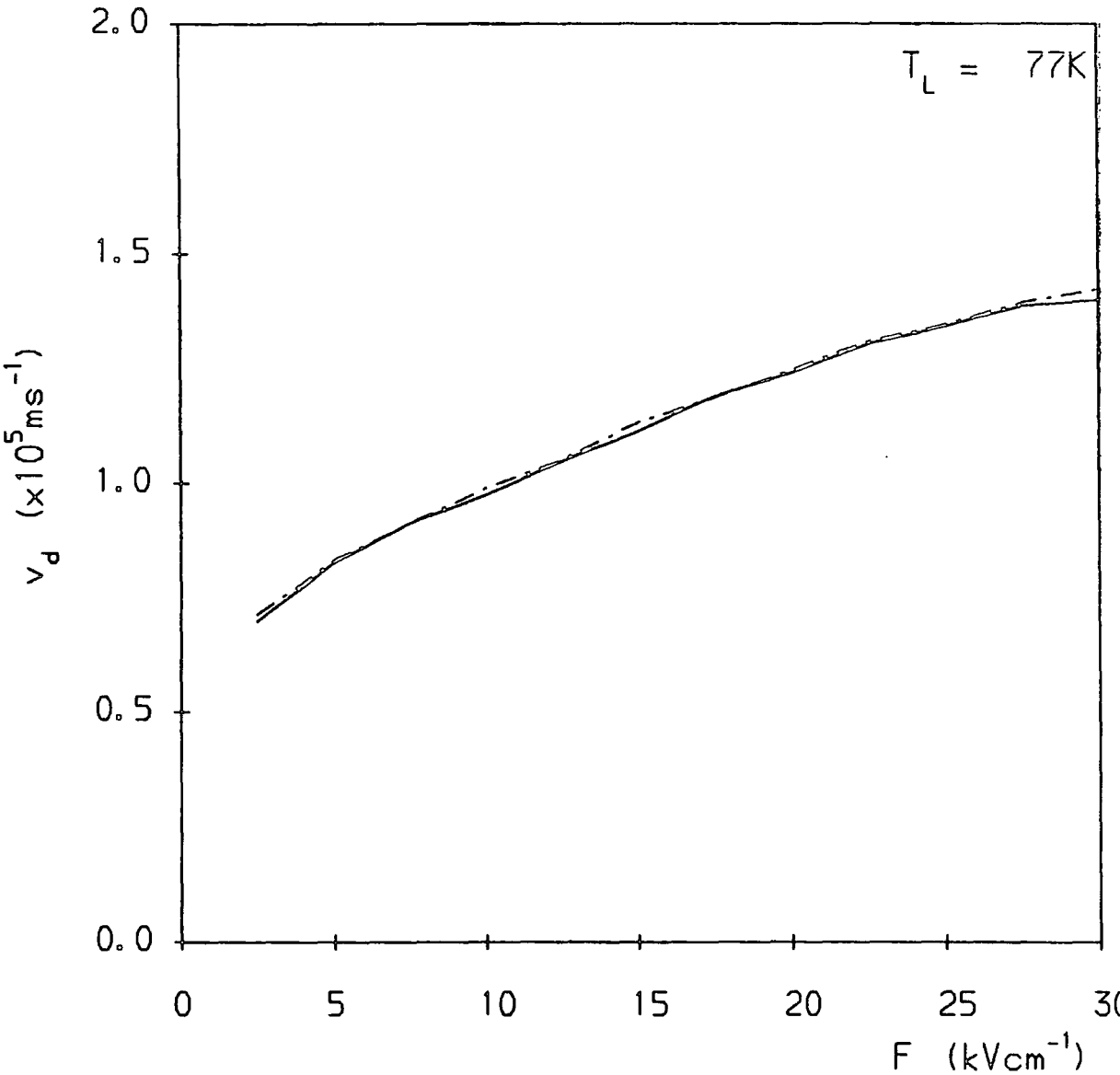

Fig. 4.14 Overall average hole drift velocity in GaAs, *vs.* electric field. — including PZ scattering; · – · excluding PZ scattering.

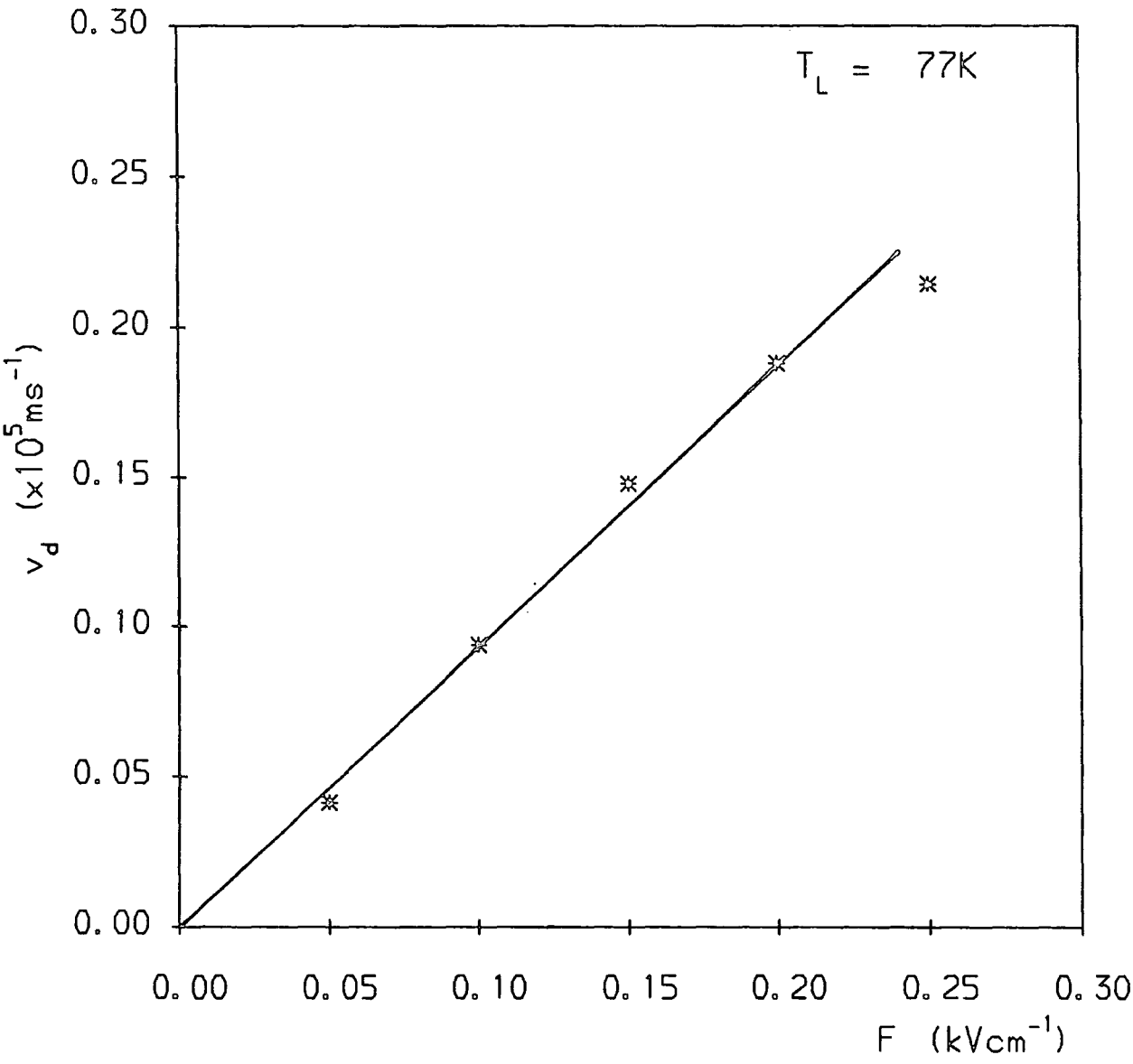

Fig. 4.15 Overall average hole drift velocity in GaAs, *vs.* electric field in the ohmic regime. The straight line fit gives a value for the low field lattice mobility of $\mu_p = 9400 \text{cm}^2\text{V}^{-1}\text{s}^{-1}$.

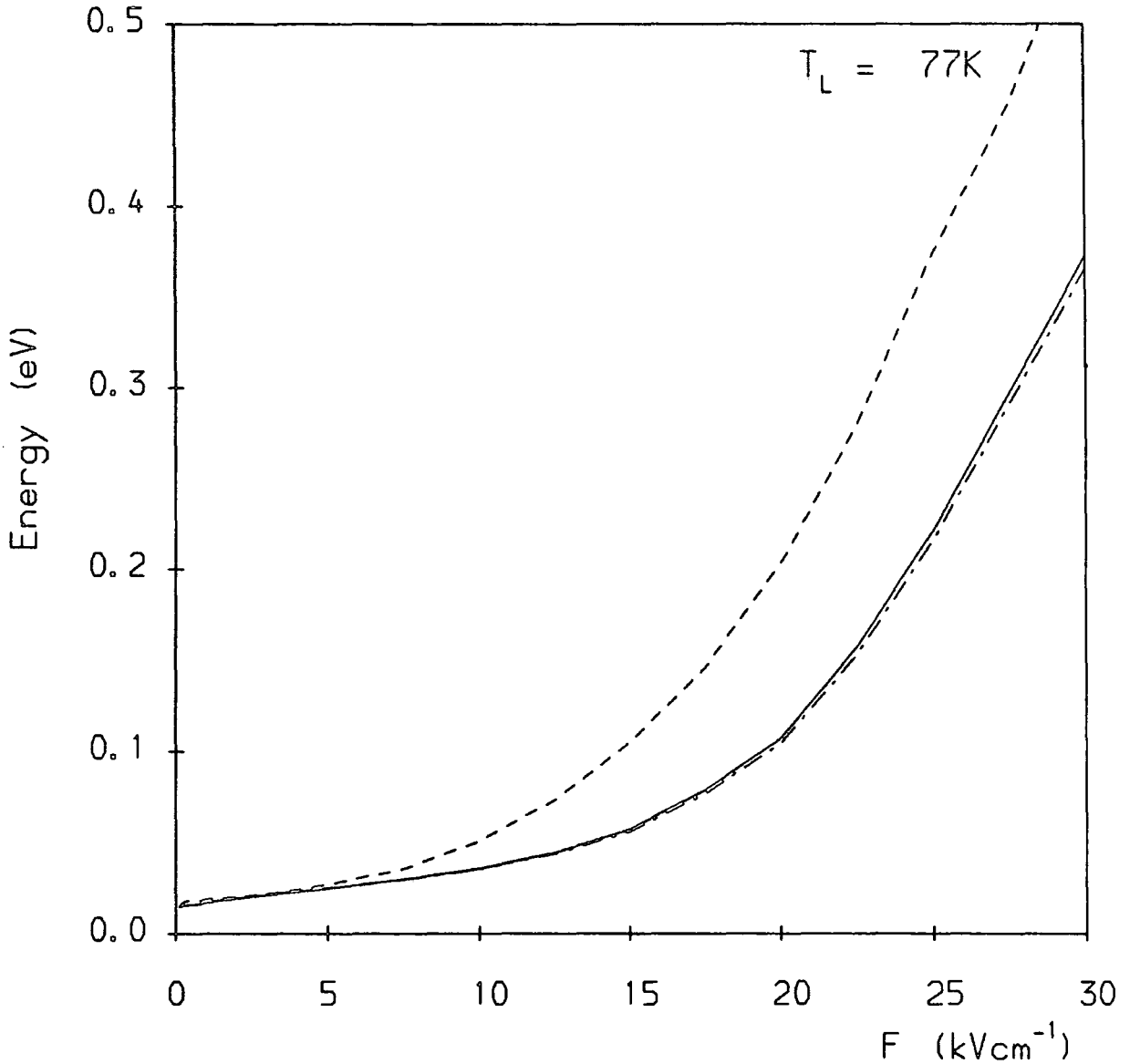

Fig. 4.16 Mean energies of heavy (· – ·) and light (- - -) holes in GaAs, and the overall average energy (—), as a function of electric field.

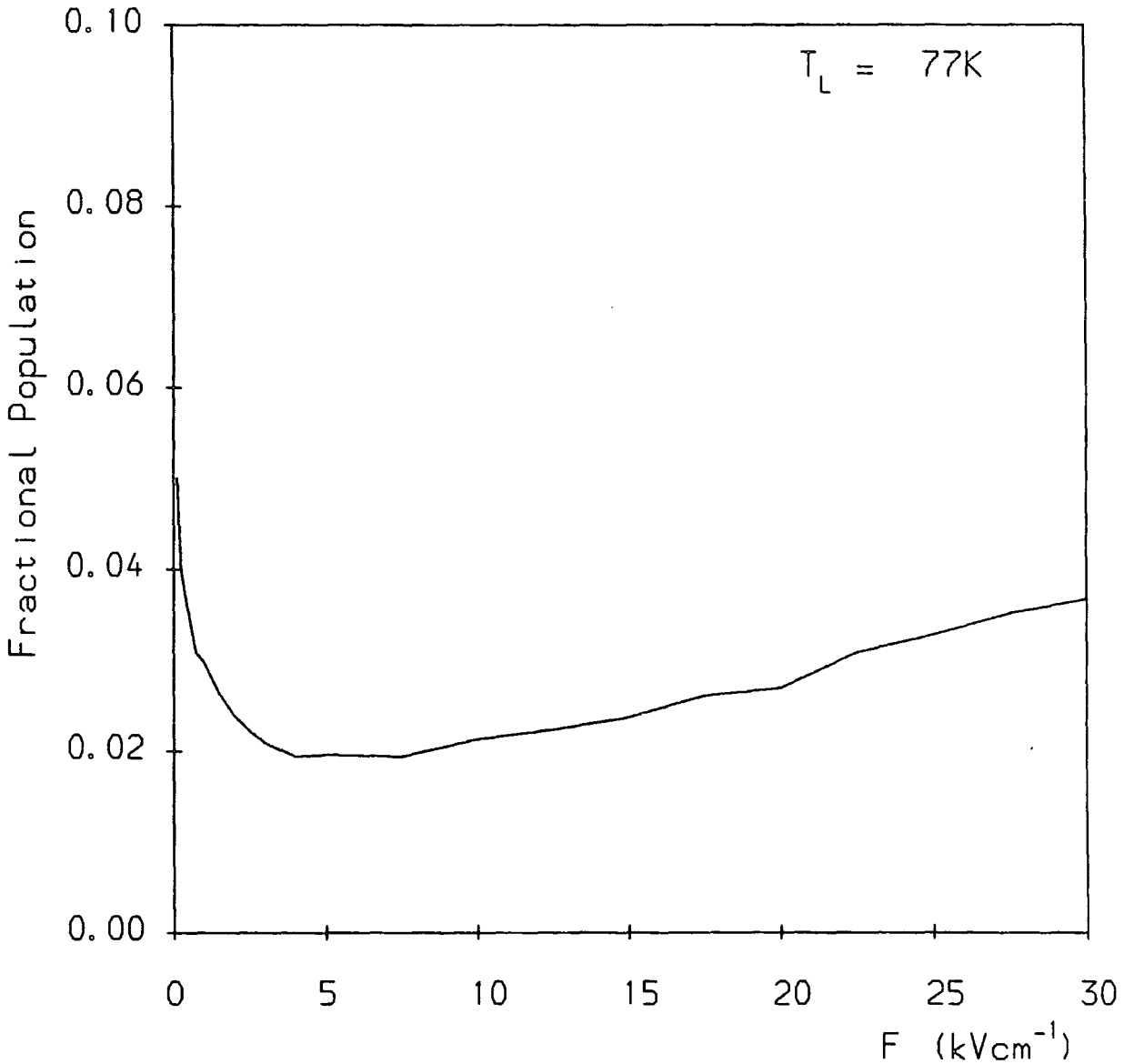

Fig. 4.17 Fractional population of the light hole band in GaAs, as a function of electric field.

band remain near the band edge, hence (h–l) scattering via optical phonon emission is suppressed. Therefore, the population of the light hole band *decreases* when the electric field is initially turned on. However, a minimum light hole population is attained for $F \approx 5\text{kVcm}^{-1}$, and for higher fields $\langle \overline{n}_l \rangle$ increases. This is principally due to the fall off of the (l–h) POP emission rate at higher energies, and to the heating of the large heavy hole population to energies where (h–l) polar emission scattering is effective. Thus, a transition from net (l–h) scattering to net (h–l) scattering occurs. It would appear that this phenomenon has not been previously reported.

4C.2: 300K Simulations

As mentioned at the beginning of this chapter, our main purpose in carrying out simulations at $T_L = 300\text{K}$ was to obtain some comparison between our results and those from the few other experimental and theoretical studies of hole transport available. In calculating the hole-phonon scattering rates at 300K we have assumed that the temperature dependence of the relevant material parameters is negligible, so that the values given in Table 4.1 can be used. The energy dependence of the scattering rates at 300K is broadly similar to that observed at 77K, and therefore need not be shown here. We can expect optical phonon scattering to be more important at 300K than at 77K: firstly, since a larger proportion of the carrier population will lie above the phonon emission threshold, even at low fields, and secondly, because the rates for optical phonon absorption are considerably increased, due to the larger value of N_{op}.

In Fig. 4.18 we have shown our results for the average hole drift velocity $\langle v_{\text{av}} \rangle$, compared with those obtained by other workers. We would expect our results to be somewhat larger than the typical experimental values, due to our neglect of any impurity scattering. However, whilst our results are significantly higher than those of Holway *et al.* (1979), we obtain much closer correspondence with the data of Dalal *et al.* (1971) measured on a p-type sample of carrier concentration $p = 10^{16}\text{cm}^{-3}$. Of the three other sets of results obtained by Monte Carlo simulation, those of Costato *et al.* (1972) were calculated with the inclusion of polar scattering only, and hence are inevitably overestimates of the true values. The simulation of Brennan and Hess (1984) is considerably more detailed, accounting for the anisotropy and non-parabolicity of the valence bands by use of k.p bandstructure data. They also make use of the calculation of inelastic acoustic phonon scattering described by Canali *et al.* (1975). Impurity scattering, however, is not considered. Hinckley and Singh (1988) also incorporate a k.p description of the valence bandstructure in their simulations, but treat acoustic scattering as elastic. Neither pair of authors considers piezoelectric scattering, but its omission is not

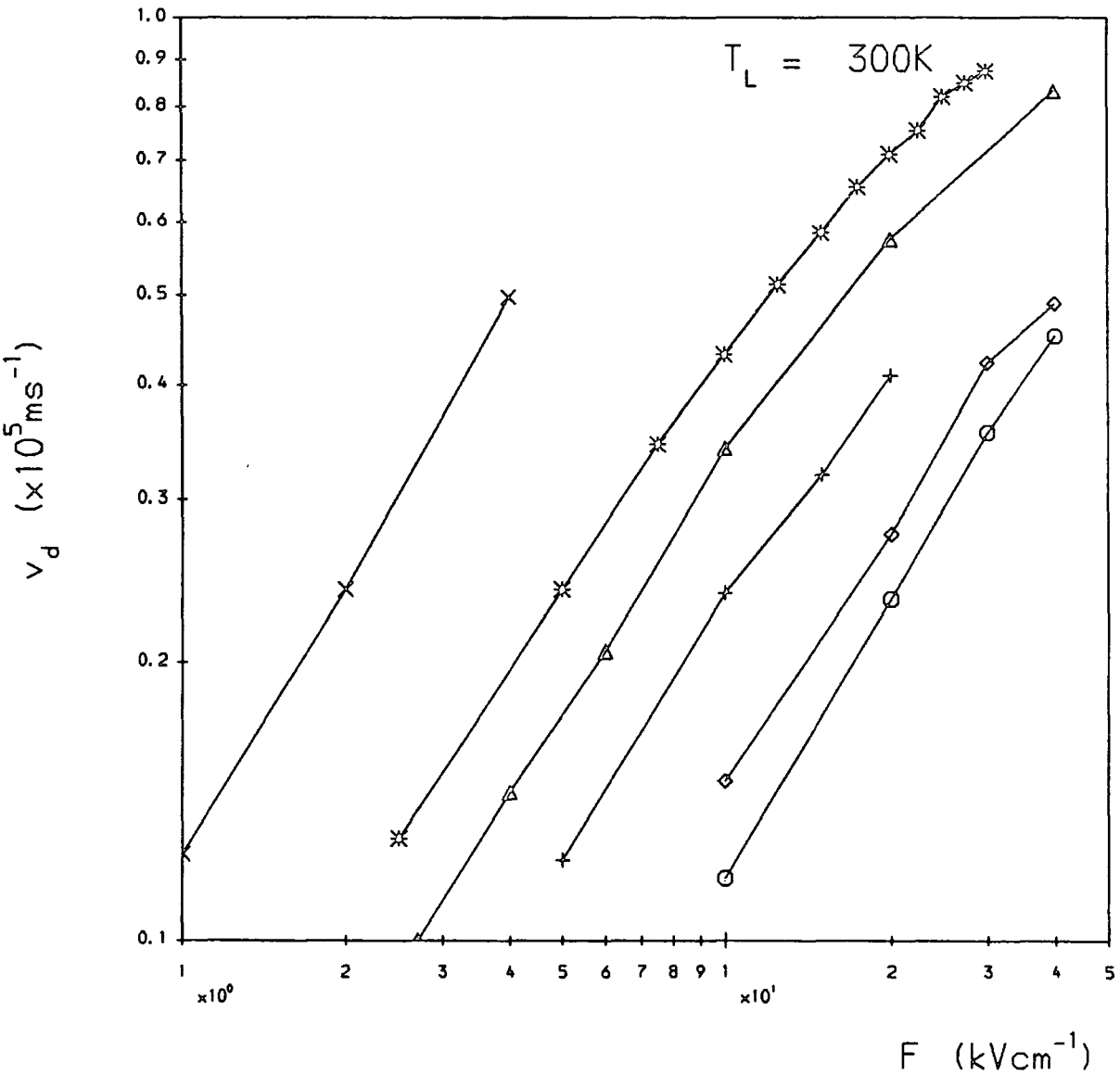

Fig. 4.18 Overall average hole drift velocity in GaAs at $T_L = 300K$

* Our Monte Carlo simulations.

Experimental results:

△ Dalal *et al.* (1971);

◯ Holway *et al.* (1979).

Other Monte Carlo simulations:

× Costato *et al.* (1972);

◇ Brennan and Hess (1984);

\+ Hinckley and Singh (1988).

expected to be noticeable at 300K.

We may conclude, from the results shown on Fig. 4.18, that, despite the simplicity of our model, a reasonable description of hole transport can still be obtained. Of the approximations used, the neglect of the anisotropy of the valence bands is likely to lead to the largest discrepancies; the use of parabolic band dispersions, and of the elastic and equipartition approximations for acoustic scattering should lead to little error in the results, in the range of fields considered, at both 77K and 300K.

CHAPTER 5

CARRIER-PHONON SCATTERING IN SEMICONDUCTOR QUANTUM WELLS

5A ELECTRON-PHONON SCATTERING IN QUASI-2D SYSTEMS

In a quantum well, confinement of the electronic states occurs, and the motion of carriers becomes essentially two dimensional. The energy bands split into sets of discrete subbands, and the density of states function assumes a step like form in contrast to the smooth $\epsilon^{\frac{1}{2}}$ dependence for the bulk material. The phonon states are also modified by confinement effects.

The first reported calculations of electron-phonon scattering in a two dimensional (2D) system included those by Ferry (1978) and Hess (1979), who considered scattering within a spherical parabolic subband, assuming bulk-like phonon modes and neglecting the effects of the quantum confined electron wavefunction envelopes on the scattering matrix element. Hess considered scattering by acoustic and polar optical phonons, whilst Ferry dealt with polar optical scattering only. Both authors obtained rates which were inversely proportional to the quantum well width, and slightly larger than the bulk rates.

These reports were followed by publications by Price (1981), Ridley (1982) and Riddoch and Ridley (1983), in which the wavefunction envelopes were assumed to have the sinusoidal form appropriate to a single band and an infinite square potential well. This consideration modified the scattering matrix elements and permitted resolution of intraband and interband scattering rates. (The symmetry of the zone centre Bloch states was assumed to be the same for the different subbands.) Ridley, and Riddoch and Ridley considered deformation potential and polar optical scattering, whilst Price additionally investigated (unscreened) piezoelectric scattering. These works have become virtually a standard for use in Monte Carlo simulations of 2D electron transport and for fits to experimental data. However the intense interest in, and considerable controversies arising from, work on 2D electron dynamics has demanded attempts at more sophisticated calculations of electron-phonon scattering.

Mason and Das Sarma (1987) have calculated polar optical scattering rates in quantum wells and heterojunctions using a many-body formalism in which the scattering rate is obtained from the electronic self-energy. Their approach allows screening and degeneracy effects to be included, and also involves the more complex variational type wavefunction encountered in a single heterostructure.

Several authors have endeavoured to relax the bulk-like phonon mode approximation. Riddoch and Ridley (1985) calculated rates for polar optical scattering via phonon modes appropriate to a thin ionic slab, finding that scattering was

weakened, with the correction factor being largest for small slab widths. A continuum theory of phonon modes in quantum wells and superlattices developed by Babiker and co-workers (Babiker 1986; Babiker and Ridley 1986; Chamberlain 1987; Babiker *et. al.* 1989) has yielded, for intersubband polar optical scattering, a rate which increases with increasing well width, and the occurrence of resonance peaks associated with the contribution of each new confined phonon mode to scattering. Chamberlain (1987) reports that the intersubband scattering rate for a GaAs/AlGaAs quantum well is about an order of magnitude lower than the bulk GaAs rate, which is also true of the intersubband rate obtained using bulk-like phonon modes; whilst Babiker *et al.* (1989) show an intrasubband scattering rate around 60% of that obtained from the confined electron / bulk phonon model. Their result was obtained for a short period (40Å) superlattice, in which case the discrepancy between bulk and confined phonon mode calculations is likely to be greatest. Thus, the evidence currently available suggests that the bulk phonon approximation will give a reasonable estimate of scattering rates in a quantum well, provided that the well width is not too small.

In the following section (5B) we will set out the confined carrier / bulk phonon model of 2D scattering, and its application to the case of electrons in an infinite square potential well with parabolic subbands. Then in section 5C, we will turn our attention to hole-phonon scattering; showing our calculation of scattering matrix elements in a quantum well using a 4-band **k.p** scheme (section 5C.2), and the derivation of associated scattering rates (section 5C.3).

5B 2D ELECTRON-PHONON SCATTERING IN THE CONFINED CARRIER / BULK PHONON APPROXIMATION

Following the treatment of carrier-phonon scattering in bulk materials, presented in Chapter 3, we first obtain the scattering rate for an electron in state $|\mathbf{k}\rangle$ from Fermi's Golden Rule (equation (3.1)):

$$P(\mathbf{k}) = \frac{2\pi}{\hbar} \int |\langle \mathbf{k}', c'|H_{ep}|\mathbf{k}, c\rangle|^2 \, \delta\Big(E(\mathbf{k}', c') - E(\mathbf{k}, c)\Big) \, dS_{\mathbf{k}'}. \tag{5.1}$$

Definitions for the symbols appearing in this and the following equations can be found in Chapter 3. Since we are considering bulk phonon modes, the atomic displacement is just the sum over plane waves given in equation (3.7):

$$\mathbf{u}(\mathbf{r}) = \sum_{\mathbf{q}} \hat{\mathbf{e}}_{\mathbf{q}} \sqrt{\frac{\hbar}{2M'N\omega_{\mathbf{q}}}} \left(a_{\mathbf{q}} \exp(i\mathbf{q}.\mathbf{r}) + a_{\mathbf{q}}^{\dagger} \exp(-i\mathbf{q}.\mathbf{r})\right). \tag{5.2}$$

Then the scattering rate expression becomes

$$P(\mathbf{k}) = \frac{2\pi}{\hbar} \sum_{\mathbf{q}} \int \left(\frac{\hbar}{2M'N\omega_{\mathbf{q}}}\right) C_{\mathbf{q}}^2 \begin{bmatrix} \mathcal{N}_{\mathbf{q}} \\ \mathcal{N}_{\mathbf{q}} + 1 \end{bmatrix} |I(\mathbf{k}', \mathbf{k})|^2 \, \delta\Big(\epsilon(\mathbf{k}') - \epsilon(\mathbf{k}) \mp \epsilon_{ph}\Big) \, dS_{\mathbf{k}'}, \tag{5.3}$$

where

$$I(\mathbf{k}', \mathbf{k}) = \int \psi_{\mathbf{k}'}^*(\mathbf{r}) \exp(\pm i\mathbf{q}.\mathbf{r}) \psi_{\mathbf{k}}(\mathbf{r}) \, d\mathbf{r} \tag{5.4}$$

and $C_{\mathbf{q}}$ is the coupling coefficient for the interaction. In equations (5.3) and (5.4) the upper cases give the rate for phonon absorption, and the lower cases, the rate for emission.

For an infinite square well, the carrier wavefunctions in a one-band model of the semiconductor can be expressed as

$$\psi_{\mathbf{k}}(\mathbf{r}) = \left(\frac{2}{\mathcal{A}L}\right)^{\frac{1}{2}} u_{\mathbf{k}}(\mathbf{r}) \exp(i\mathbf{k}_{\|}.\mathbf{r}_{\|}) \sin(k_{n,z} z) \tag{5.5}$$

where $\mathcal{A}$ is the area of the well plane, L is the well width, z is the direction perpendicular to the well plane, $k_{n,z} = n\pi/L$ with n the subband index, $\mathbf{k}_{\|}$ and $\mathbf{r}_{\|}$ are 2-dimensional vectors in the plane of the well, and $u_{\mathbf{k}}(\mathbf{r})$ is the periodic part of the bulk Bloch function.

This gives, for $I(\mathbf{k}', \mathbf{k})$:

$$I(\mathbf{k}', \mathbf{k}) = \frac{2}{\mathcal{A}L} \int u_{\mathbf{k}'}^*(\mathbf{r}) u_{\mathbf{k}}(\mathbf{r}) \exp\left(i(\mathbf{k}_{\|} - \mathbf{k}'_{\|} \pm \mathbf{q}_{\|}).\mathbf{r}_{\|}\right) \sin(k_{n',z} z) \sin(k_{n,z} z) \exp(\pm i q_z z) \, d\mathbf{r}. \tag{5.6}$$

We now expand $u_{\mathbf{k}'}^*(\mathbf{r}) u_{\mathbf{k}}(\mathbf{r})$ as a Fourier series over reciprocal lattice vectors:

$$u_{\mathbf{k}'}^*(\mathbf{r}) u_{\mathbf{k}}(\mathbf{r}) = \sum_{\mathbf{g}} c_{\mathbf{g}} \exp(i\mathbf{g}.\mathbf{r}) \tag{5.7}$$

where

$$c_{\mathrm{g}} = \frac{1}{V_{\mathrm{cell}}} \int_{\mathrm{cell}} u^*_{\mathrm{k}'}(\mathrm{r}') u_{\mathrm{k}}(\mathrm{r}') \exp(-i\mathrm{g}.\mathrm{r}')\, d\mathrm{r}'. \tag{5.8}$$

Then, writing $d\mathrm{r} = d\mathrm{r}_{\|} dz$ and integrating over $\mathrm{r}_{\|}$, we obtain

$$I(\mathrm{k}', \mathrm{k}) = \sum_{\mathrm{g}} c_{\mathrm{g}} \frac{(2\pi)^2}{\mathcal{A}} \delta(\mathrm{k}_{\|} - \mathrm{k}'_{\|} \pm \mathrm{q}_{\|} + \mathrm{g}_{\|}) \times \frac{2}{L} \int \sin(k_{n',z} z) \sin(k_{n,z} z) \exp\left(i(\pm q_z + g_z) z\right)\, dz. \tag{5.9}$$

We make the usual approximation that only the term with $\mathrm{g} = 0$ contributes to the sum over g (see Section 3A). This is quite reasonable since the smallest non zero value of $\mathrm{g}_{\|}$ will be much greater than the values of $\mathrm{k}_{\|}$ and $\mathrm{q}_{\|}$, hence the delta function argument is only ever likely to be zero for the case $\mathrm{g} = 0$. The scattering rate is then obtained as

$$P(\mathrm{k}) = \frac{2\pi}{\hbar} \sum_{\mathrm{q}} \int \left(\frac{\hbar}{2M' N \omega_{\mathrm{q}}}\right) \begin{bmatrix} \mathcal{N}_{\mathrm{q}} \\ \mathcal{N}_{\mathrm{q}} + 1 \end{bmatrix} C_{\mathrm{q}}^2 |G(\mathrm{k}', \mathrm{k})|^2 \times \frac{(2\pi)^2}{\mathcal{A}} \delta(\mathrm{k}_{\|} - \mathrm{k}'_{\|} \pm \mathrm{q}_{\|}) |J_{n',n}(q_z)|^2 \delta\left(\epsilon(\mathrm{k}') - \epsilon(\mathrm{k}) \mp \epsilon_{ph}\right)\, dS_{\mathrm{k}'} \tag{5.10}$$

where $G(\mathrm{k}', \mathrm{k})$ is the overlap integral;

$$G(\mathrm{k}', \mathrm{k}) = \frac{1}{V_{\mathrm{cell}}} \int_{\mathrm{cell}} u^*_{\mathrm{k}'}(\mathrm{r}') u_{\mathrm{k}}(\mathrm{r}')\, d\mathrm{r}', \tag{5.11}$$

$J_{n',n}(q_z)$ is the envelope function integral;

$$J_{n',n}(q_z) = \frac{2}{L} \int_0^L \sin(k_{n',z} z) \sin(k_{n,z} z) \exp(\pm i q_z z)\, dz, \tag{5.12}$$

and we have used the fact that

$$\delta^2(\mathrm{k}_{\|} - \mathrm{k}'_{\|} \pm \mathrm{q}_{\|}) = \frac{\mathcal{A}}{(2\pi)^2} \delta(\mathrm{k}_{\|} - \mathrm{k}'_{\|} \pm \mathrm{q}_{\|}). \tag{5.13}$$

The wavevector delta function can be rewritten as a Kronecker delta

$$\frac{(2\pi)^2}{\mathcal{A}} \delta(\mathrm{k}_{\|} - \mathrm{k}'_{\|} \pm \mathrm{q}_{\|}) = \delta_{\mathrm{k}_{\|} \pm \mathrm{q}_{\|}, \mathrm{k}'_{\|}} \tag{5.14}$$

which selects a single value of $\mathrm{q}_{\|}$ from the sum over phonon modes q for a given absorption or emission process. Thus momentum conservation is imposed in the plane of the well. However, momentum is *not* conserved in the direction perpendicular to the well plane. Whilst k'_z is fixed for each specific transition, q_z may vary without restriction. Consequently

$$\sum_{\mathrm{q}} \int \frac{(2\pi)^2}{\mathcal{A}} \delta(\mathrm{k}_{\|} - \mathrm{k}'_{\|} \pm \mathrm{q}_{\|}) \ldots dS_{\mathrm{k}'} \;\rightarrow\; \delta_{\mathrm{k}_{\|} \pm \mathrm{q}_{\|}, \mathrm{k}'_{\|}} \frac{V}{(2\pi)^3} \int \ldots d\mathrm{k}'_{\|} dq_z. \tag{5.15}$$

We assume that the functions $u_{\mathbb{k}}(\mathbb{r})$ can be approximated by the zone centre Bloch functions $u_0(\mathbb{r})$, and that these functions have the same symmetry for the different subbands. Then the term $|G(\mathbb{k}',\mathbb{k})|^2$ can be taken as unity for both intra- and inter-subband scattering.

For acoustic (deformation potential) scattering we have, in the elastic equipartition approximation (Section 3B)

$$\mathcal{N}_q \approx \mathcal{N}_q + 1 \approx \frac{k_B T}{\hbar\omega_q} \qquad (\omega_q = v_s q) \tag{5.16}$$

and, from equation (3.49)

$$C_q^2 = \Xi^2 q^2, \tag{5.17}$$

giving

$$P_{n',n}(\mathrm{k}_{\|}) = \frac{k_B T \Xi^2}{8\pi^2\hbar\rho v_s^2} \int |J_{n'n}(q_z)|^2 dq_z \int \delta_{\mathrm{k}_{\|}\pm\mathrm{q}_{\|},\mathrm{k}'_{\|}} \delta\left(\epsilon(\mathrm{k}'_{\|},n') - \epsilon(\mathrm{k}_{\|},n)\right) d\mathrm{k}'_{\|}. \tag{5.18}$$

Since the scattering rate contains no dependence on $\mathrm{q}_{\|}$, it can be assumed that $\mathrm{q}_{\|}$ may take any value required to achieve momentum conservation, and hence the Kronecker delta $\delta_{\mathrm{k}_{\|}\pm\mathrm{q}_{\|},\mathrm{k}'_{\|}}$ need not be included in the scattering rate expression.

Following Price (1981) we write

$$\int |J_{n'n}(q_z)|^2 dq_z = \frac{\pi}{b_{n',n}} \tag{5.19}$$

where $b_{n',n} = L/3$ for $n' = n$, and $L/2$ otherwise. The integral over $\mathrm{k}'_{\|}$ simply represents the density of final states in the 2D system, and gives (for a parabolic subband) a factor of π/α, where α is defined in Section 3B.

Then, multiplying by two to give the total rate for absorption plus emission, we obtain for acoustic scattering between subbands n' and n:

$$P_{n',n}(k_{\|}) = \frac{k_B T \Xi^2}{4\pi\hbar\rho v_s^2 \alpha}\left(\frac{\pi}{b_{n',n}}\right), \tag{5.20}$$

which is the result obtained by both Price (1981) and Ridley (1982). The scattering rate is independent of energy, since the 2D density of states is energy independent, and is inversely proportional to the well width (through $b_{n',n}$), as pointed out in Section 5A.

For non-polar optical scattering, with $C_q^2 = \overline{M}D_{\mathrm{op}}^2/(M_1 + M_2)$ (equation (3.55)), and ω_q independent of q as in the bulk, we obtain

$$P_{n',n}(k_{\|}) = \frac{D_{\mathrm{op}}^2}{8\pi\rho\omega_{\mathrm{op}}\alpha}\left(\frac{\pi}{b_{n',n}}\right)\begin{bmatrix}\mathcal{N}_{\mathrm{op}} \\ \mathcal{N}_{\mathrm{op}}+1\end{bmatrix}. \tag{5.21}$$

The polar optical scattering case is rather more involved. The coupling coefficient takes the form given by equations (3.35–6):

$$C_{\mathbf{q}}^2 = \frac{e^2\overline{M}}{V_{\text{cell}}\varepsilon_0}\omega_{\text{op}}^2\left(\frac{1}{\varepsilon_\infty} - \frac{1}{\varepsilon_s}\right) \times \frac{1}{q^2}. \tag{5.22}$$

With $\omega_{\mathbf{q}}$ independent of $\mathbb{q}$ the scattering rate becomes

$$P_{n'n}(k_{\|}) = \frac{e^2\omega_{\text{op}}}{8\pi^2\varepsilon_0}\left(\frac{1}{\varepsilon_\infty} - \frac{1}{\varepsilon_s}\right)\begin{bmatrix} \mathcal{N}_{\text{op}} \\ \mathcal{N}_{\text{op}}+1 \end{bmatrix} \tag{5.23}$$
$$\times \iint \frac{|J_{n',n}(q_z)|^2}{q_{\|}^2+q_z^2}\delta_{\mathbf{k}_{\|}\pm\mathbf{q}_{\|},\mathbf{k}'_{\|}}\,\delta\left(\epsilon(\mathbf{k}'_{\|},n') - \epsilon(\mathbb{k}_{\|},n) \mp \hbar\omega_{op}\right)\, d\mathbb{k}'_{\|}dq_z$$

where $q_{\|}^2+q_z^2 = q^2$. Riddoch and Ridley (1983) have given the result of the integration over q_z; however the remaining integrations must be performed numerically.

Consideration of piezoelectric scattering in 2D will be deferred until our treatment of quantum confined hole-phonon scattering in section 5C.3.

We have shown in Figs. 5.1 and 5.2 the energy dependence of the rates for acoustic (deformation potential) and non-polar optical scattering respectively; for an electron in the lowest subband of a 100Å quantum well, with material parameters as for bulk GaAs. The rate for any given process is constant, and the total rate displays an abrupt increment whenever a new subband contributes to scattering. The bulk rates are also shown and it can be seen that the constant contributions from different subbands accumulate to form a total rate of similar magnitude to that in the bulk material.

Fig. 5.3 shows the total and intrasubband rates for polar optical scattering in the lowest subband of a 100Å quantum well (parameters as for bulk GaAs), with the bulk rate shown for comparison. Clearly the main difference between the bulk and 2D rates is that the 2D optical phonon emission threshold is abrupt, whereas the bulk rate rises smoothly to a maximum beyond the threshold energy. Much has been made of this abrupt optical emission threshold in terms of electronic transport: specifically, the suggestions of a negative differential mobility arising purely from scattering effects (Ridley 1982). It suffices to say here that the abruptness of threshold, and the enhanced magnitude of the rate at threshold over that in the bulk, are both logical consequences of the form of the 2D density of states. At higher energies, where more subbands are involved in scattering, the total rate comes very close to the bulk rate. It should also be noted that the intersubband contributions shown are all considerably smaller than the intrasubband rate in band 1.

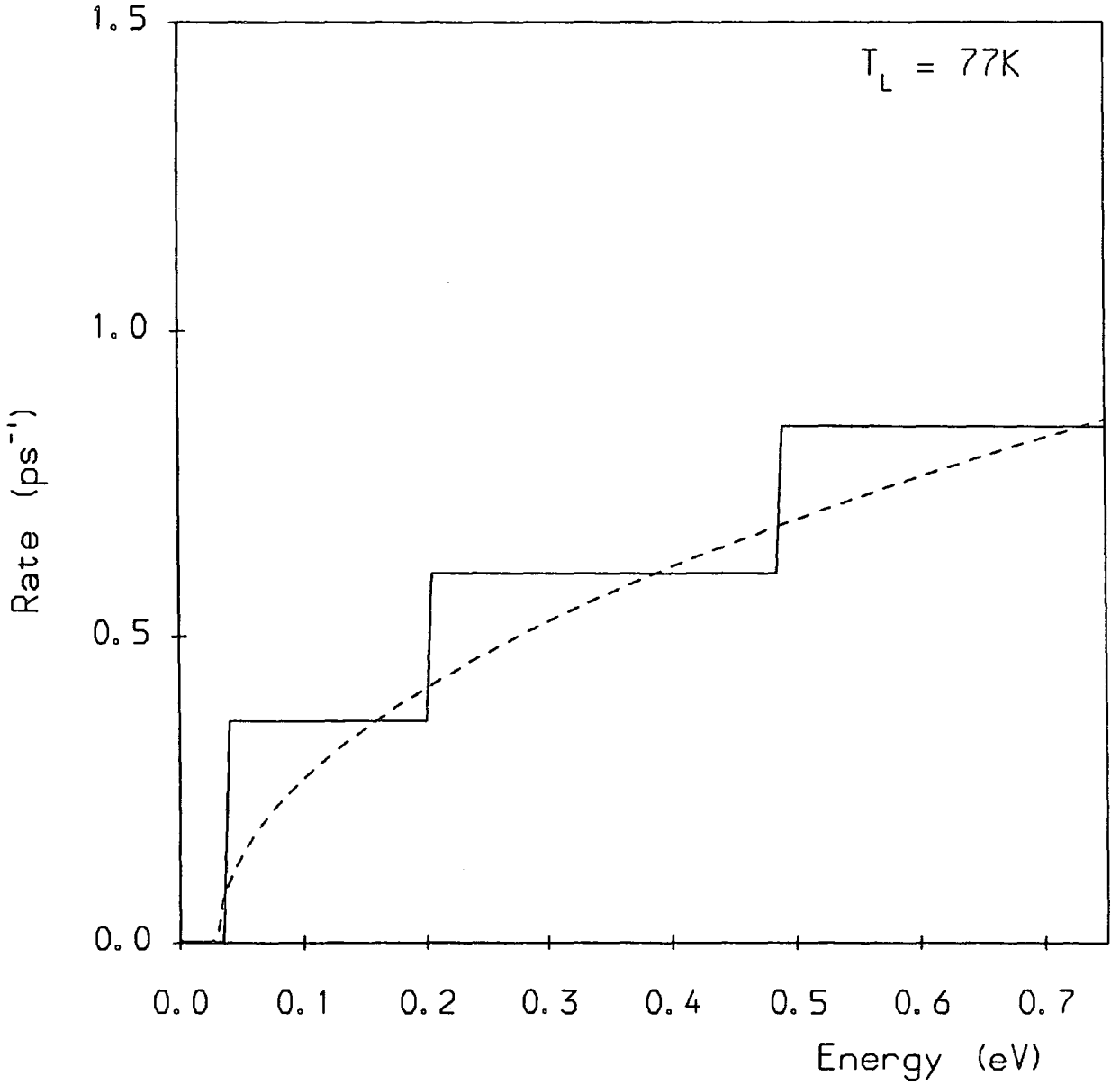

Fig. 5.1 Rates for acoustic deformation potential scattering (absorption plus emission): — electron in the lowest subband of a 100Å GaAs quantum well; - - - electron in bulk GaAs. $\Xi = 8.6$eV; $m^* = 0.067$.

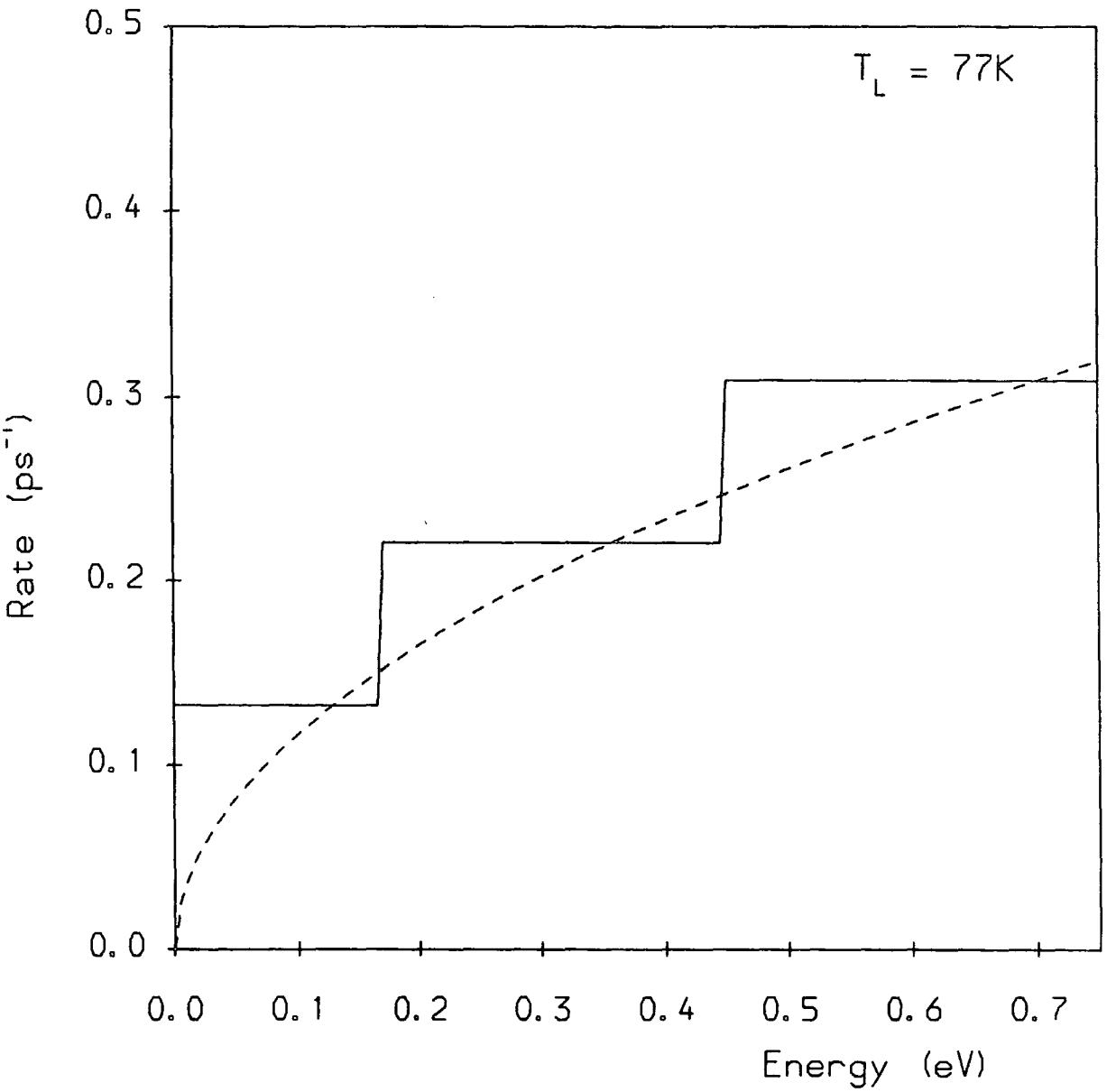

Fig. 5.2 Rates for non-polar optical scattering scattering (absorption plus emission combined): — electron in the lowest subband of a 100Å GaAs quantum well; - - - electron in bulk GaAs (*e.g.* for non-equivalent intervalley scattering into the Γ valley — Γ–Γ scattering is forbidden by symmetry (Birman *et al.* 1966)). $D_{\rm op} = 10^{11}{\rm eVm}^{-1}$; $m^* = 0.067$; $\hbar\omega_{\rm op} = 36.4{\rm meV}$.

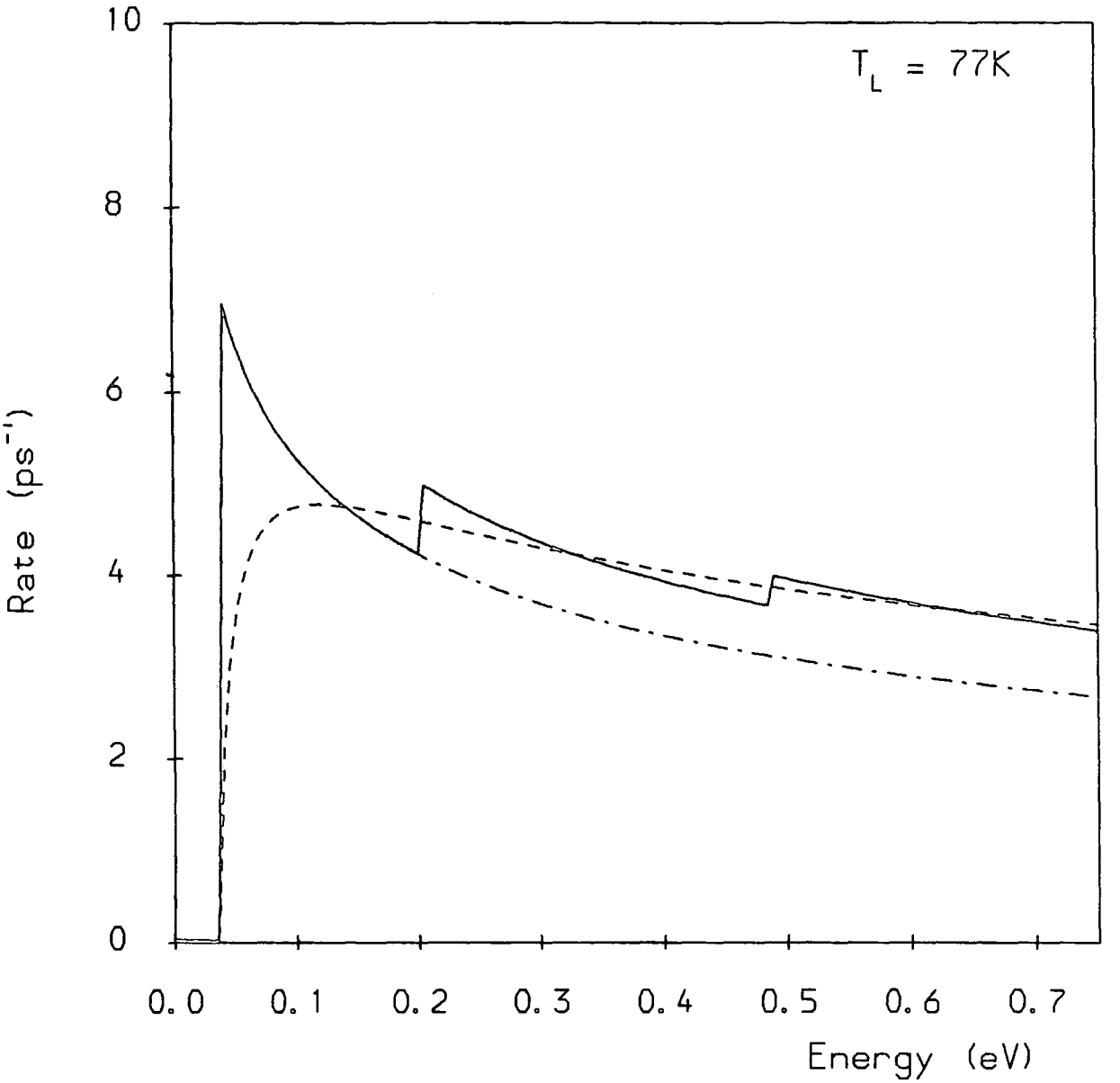

Fig. 5.3 Rates for polar optical scattering scattering (absorption plus emission combined):
— electron in the lowest subband of a 100Å GaAs quantum well;
· – · intrasubband rate in the lowest subband;
- - - electron in bulk GaAs. $m^* = 0.067$; $\hbar\omega_{op} = 36.4$meV.

5C 2D HOLE-PHONON SCATTERING

5B.1 The Quantum Confined Valence Bandstructure

In the valence band system of a quantum well, subbands arise from splitting of both light and heavy hole bands (the spin split off band is usually above the top of the well, and its effects on transport can be neglected). A mixing of these confined heavy and light hole states occurs (Chang and Schulman 1983, 1985; Sanders and Chang 1985), such that a description of the wavefunctions by a simple one band effective mass model, as employed above, is no longer possible. The mixing of states also distorts the subband energy dispersions, with repulsion effects evident between bands. These repulsions result in so called anticrossing features; regions where an exchange of character occurs between two adjacent subbands. In Fig. 5.4 we have shown the in-plane dispersion of the first four valence subbands in a 100Å GaAs/AlAs quantum well. In this system, an anticrossing occurs between the first and second subbands at $k_{||} \approx 0.02\text{Å}^{-1}$, and between the third and fourth subbands at $k_{||} \approx 0.0275\text{Å}^{-1}$. The subbands are usually labelled according to the character of the pure (unmixed) zone centre states. In Fig. 5.4 therefore, the labelling HH1, HH2, LH1 and HH4 indicates that the first, second and fourth subbands all have heavy hole character at the zone centre, with wavefunctions appropriate to the ground, and first and second excited states respectively of the quantum well. Similarly, the third subband is light hole like at the zone centre, with a wavefunction corresponding to a ground state of the well. Beyond the anticrossing regions, we expect both the two lower and the two upper subbands to exchange character. This means that the third subband will become heavy hole like at large k, and the fourth subband will become light hole like. In practice the mixing is such that all states with $\mathbf{k}_{||} > 0$ are a hybrid of zone centre states of all neighbouring subbands. Therefore, no symmetry rules can be deduced for either inter- or intra-subband phonon scattering — the matrix elements are dependent on the specific nature of the initial and final states involved.

The energy dispersions and wavefunctions for quantum well valence band states have been calculated by several different methods: tight binding (Schulman and Chang 1985); pseudopotential (Ninno *et al.* 1986), and k.p perturbation (Schuurmans and t'Hooft 1985). For this work we have used the 4-band k.p scheme described by Schuurmans and t'Hooft, and extended to include spin effects (Eppenga *et al.* 1987). Calculations of the subband energy dispersions were performed by Wood (1987), who also supplied a computer program for calculation of the hole wavefunctions.

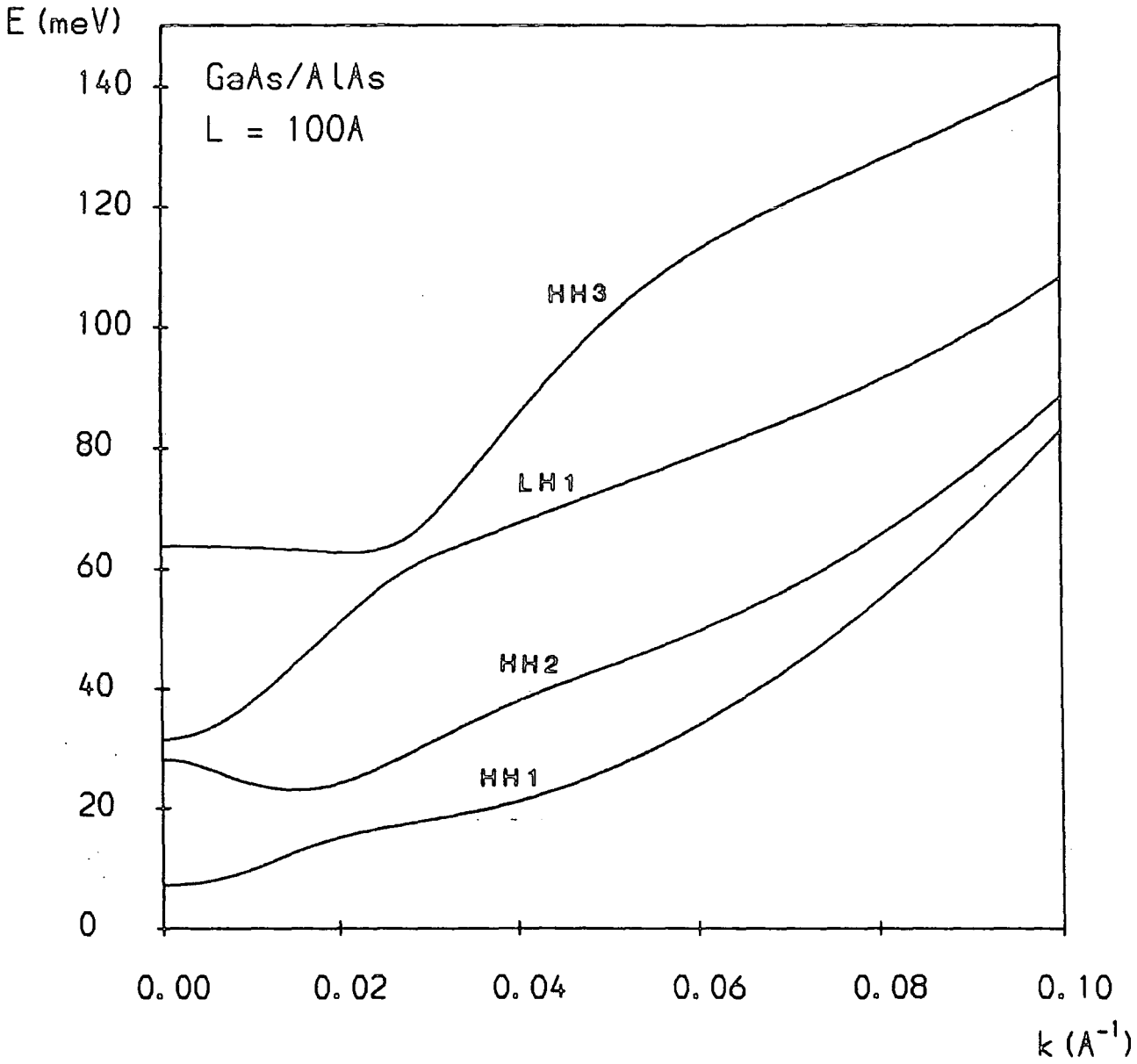

Fig. 5.4 In-plane energy dispersion of the first four valence subbands of a 100Å GaAs/AlAs quantum well. The subbands are labelled according to the character of the zone-centre states (see text). The energy scale is shown inverted relative to its usual form: zero energy corresponds to the base of the valence band quantum well, and energy is measured as positive in the direction of increasing subband indices. This convention will be used throughout this thesis.

5C.2: 2D Hole-Phonon Scattering Matrix Elements in the 4-Band k.p Scheme

This calculation was written down, in preliminary form, by Taylor (1987) for use in this project. The following is a completely rewritten and modified version which can be used in the subsequent calculation of scattering rates (section 5C.3).

The quantum well wavefunctions ψ are taken as linear combinations of bulk wavefunctions φ;

$$\psi = \sum_i A_i \varphi_i. \tag{5.24}$$

The φ_i are sums over plane waves

$$\varphi_i = \sum_j U_{ij} \exp(i\mathbf{k}_i.\mathbf{r}) u_j(\mathbf{r}) \tag{5.25}$$

where the $u_j(\mathbf{r})$ are a basis set consisting of zone centre Bloch states for the lowest conduction band, the heavy, light and spin split off hole bands, for both spin parities; 8 basis states in all.

The Schrödinger equation is solved for ψ in the three regions of the quantum well; $[-\infty, L/2]$, region I; $[-L/2, L/2]$, region II, and $[L/2, \infty]$, region III, with ψ and $\partial\psi/\partial z$ matched at the interfaces. Continuity of ψ means that $\mathbf{k}_{||}$ must be the same in all three regions ($\mathbf{k}_{||}$ is thus a good quantum number of the state), and hence the quantum well wavefunction in region I can be written as

$$\psi_{\mathrm{I}}(\mathbf{r}) = \exp(i\mathbf{k}_{||}.\mathbf{r}_{||}) \sum_{ij} A_i^{\mathrm{I}} U_{ij}^{\mathrm{I}} u_j(\mathbf{r}) \exp(ik_{z,i}^{\mathrm{I}} z). \tag{5.26}$$

ψ_{II} and ψ_{III} take exactly the same form, with the basis states $u_j(\mathbf{r})$ assumed to be the same in both well and barrier regions. The $k_{z,i}$ are in general complex, but $\mathbf{k}_{||}$ can be taken as real, since evanescent solutions are not expected in the plane of the well.

Calculation of the phonon scattering matrix element requires first evaluating the integral of equation (5.4):

$$I(\mathbf{k}', \mathbf{k}) = \int \psi_{\mathbf{k}'}^*(\mathbf{r}) \exp(\pm i\mathbf{q}.\mathbf{r}) \psi_{\mathbf{k}}(\mathbf{r}) d\mathbf{r}. \tag{5.27}$$

We will include, in the calculation of $I(\mathbf{k}', \mathbf{k})$ interactions between the hole wavefunction and the phonon modes in the barrier regions I and III. However, we assume that in all three regions, the wavefunction interacts with bulk GaAs phonon modes. Thus $I(\mathbf{k}', \mathbf{k})$ consists of three terms, I_{I}, I_{II} and I_{III}, each similar in form to equation (5.27), but with the limits of integration defined by the boundaries of regions I, II, and III as given above.

We will consider firstly the term I_{II}, with initial and final states

$$\psi_{A,\text{II}}(\mathbf{r}) = \exp(i\mathbf{k}_{\|}^{A}.\mathbf{r}_{\|}) \sum_{ij} A_i^{\text{II}} U_{ij}^{\text{II}}\, u_j(\mathbf{r}) \exp(ik_{z,i}^{A_{\text{II}}} z), \tag{5.28a}$$

$$\psi_{B,\text{II}}(\mathbf{r}) = \exp(i\mathbf{k}_{\|}^{B}.\mathbf{r}_{\|}) \sum_{lk} B_l^{\text{II}} V_{lk}^{\text{II}}\, u_k(\mathbf{r}) \exp(ik_{z,l}^{B_{\text{II}}} z). \tag{5.28b}$$

Substituting equations (5.28a) and (5.28b) into equation (5.27) gives

$$I_{\text{II},BA} = \sum_{ijlk} A_i^{\text{II}} U_{ij}^{\text{II}} B_l^{*\text{II}} V_{lk}^{*\text{II}} \times \int_{z=-L/2}^{z=L/2} \exp\left(i(\mathbf{k}_{\|}^{A} - \mathbf{k}_{\|}^{*B} \pm \mathbf{q}_{\|}).\mathbf{r}_{\|}\right) \times u_j(\mathbf{r}) u_k^*(\mathbf{r}) \exp\left(i(k_{z,i}^{A_{\text{II}}} - k_{z,l}^{*B_{\text{II}}} \pm q_z)z\right)\, d\mathbf{r}. \tag{5.29}$$

Let

$$u_j(\mathbf{r}) u_k^*(\mathbf{r}) = \sum_{\mathbf{g}} c_{\mathbf{g},jk} \exp(i\mathbf{g}.\mathbf{r}) \tag{5.30}$$

and make the approximation, as in Section 5B, that only the term with $\mathbf{g} = 0$ contributes. This term,

$$c_{0,jk} = \frac{1}{V_{\text{cell}}} \int_{\text{cell}} u_j(\mathbf{r}) u_k^*(\mathbf{r})\, d\mathbf{r} = \delta_{j,k}, \tag{5.31}$$

since the bulk basis states form an orthogonal set.

We write $d\mathbf{r} = d\mathbf{r}_{\|}\, dz$ and integrate over $\mathbf{r}_{\|}$ to obtain

$$I_{\text{II},BA} = (2\pi)^2 \delta(\mathbf{k}_{\|}^{A} - \mathbf{k}_{\|}^{*B} \pm \mathbf{q}_{\|}) \sum_{ijl} A_i^{\text{II}} U_{ij}^{\text{II}} B_l^{*\text{II}} V_{lj}^{*\text{II}} \times \int_{-L/2}^{L/2} \exp\left(i(k_{z,i}^{A_{\text{II}}} - k_{z,l}^{*B_{\text{II}}} \pm q_z)z\right)\, dz. \tag{5.32}$$

Then, integrating over z gives the result

$$I_{\text{II},BA} = L(2\pi)^2 \delta(\mathbf{k}_{\|}^{A} - \mathbf{k}_{\|}^{*B} \pm \mathbf{q}_{\|}) \sum_{ijl} A_i^{\text{II}} U_{ij}^{\text{II}} B_l^{*\text{II}} V_{lj}^{*\text{II}} \times \frac{\sin(k_{z,i}^{A_{\text{II}}} - k_{z,l}^{*B_{\text{II}}} \pm q_z)L/2}{(k_{z,i}^{A_{\text{II}}} - k_{z,l}^{*B_{\text{II}}} \pm q_z)L/2}. \tag{5.33}$$

Secondly, we will consider I_{I}. The form of the wavefunctions is the same as for I_{II}. However we know that the real parts of the wavevectors $k_i^{A_{\text{I}}}$ and $k_l^{B_{\text{I}}}$ will always be zero, since no oscillatory solutions are allowed in the barrier regions. Furthermore, for region I, only those wavevectors with *negative* imaginary parts are allowed (to ensure $\psi \to 0$ as $z \to \infty$). Thus we can write the wavefunctions in region I in the form

$$\psi_{A,\text{I}}(\mathbf{r}) = \exp(i\mathbf{k}_{\|}^{A}.\mathbf{r}_{\|}) \sum_{ij} A_i^{\text{I}} U_{ij}^{\text{I}}\, u_j(\mathbf{r}) \exp(\kappa_{z,i}^{A_{\text{I}}} z) \tag{5.34a}$$

$$\psi_{B,\text{I}}(\mathbf{r}) = \exp(i\mathbf{k}_{\|}^{B}.\mathbf{r}_{\|}) \sum_{lk} B_l^{\text{I}} V_{lk}^{\text{I}}\, u_k(\mathbf{r}) \exp(\kappa_{z,l}^{B_{\text{I}}} z), \tag{5.34b}$$

where $\kappa_{z,i}^{A_\mathrm{I}} = -\Im m(k_{z,i}^{A_\mathrm{I}})$, $\kappa_{z,l}^{B_\mathrm{I}} = -\Im m(k_{z,l}^{B_\mathrm{I}})$, and the A_i^I and B_l^I each represent a subset of exactly half the bulk basis states in region I. We then obtain for I_I:

$$I_{\mathrm{I},BA} = L(2\pi)^2\delta(\mathbb{k}_\parallel^A - \mathbb{k}_\parallel^{*B} \pm \mathbb{q}_\parallel) \sum_{ijl} A_i^\mathrm{I} U_{ij}^\mathrm{I} B_l^{*\mathrm{I}} V_{lj}^{*\mathrm{I}} \times \frac{1}{2} \frac{\exp\left(-(\kappa_{z,i}^{A_\mathrm{I}} + \kappa_{z,l}^{B_\mathrm{I}} \pm iq_z)L/2\right)}{(\kappa_{z,i}^{A_\mathrm{I}} + \kappa_{z,l}^{B_\mathrm{I}} \pm iq_z)L/2}. \tag{5.35}$$

For region III, again the real parts of the $k_{z,i}^{A_\mathrm{III}}$, $k_{z,l}^{B_\mathrm{III}}$ will be zero, but this time only wavevectors with positive imaginary parts are allowed. Thus

$$I_{\mathrm{III},BA} = L(2\pi)^2\delta(\mathbb{k}_\parallel^A - \mathbb{k}_\parallel^{*B} \pm \mathbb{q}_\parallel) \sum_{ijl} A_i^\mathrm{III} U_{ij}^\mathrm{III} B_l^{*\mathrm{III}} V_{lj}^{*\mathrm{III}} \times \frac{1}{2} \frac{\exp\left(-(\kappa_{z,i}^{A_\mathrm{III}} + \kappa_{z,l}^{B_\mathrm{III}} \mp iq_z)L/2\right)}{(\kappa_{z,i}^{A_\mathrm{III}} + \kappa_{z,l}^{B_\mathrm{III}} \mp iq_z)L/2} \tag{5.36}$$

where $\kappa_{z,i}^{A_\mathrm{III}} = \Im m(k_{z,i}^{A_\mathrm{III}})$ and $\kappa_{z,l}^{B_\mathrm{III}} = \Im m(k_{z,l}^{B_\mathrm{III}})$.

Normalisation

The 4-band k.p wavefunctions must be normalised to the form $\frac{1}{\sqrt{N_A}}\psi_A$ where

$$N_A = \int \psi_A^* \psi_A \, d\mathbf{r}. \tag{5.37}$$

This gives, for $|I_{BA}|^2$:

$$|I_{BA}|^2 = \frac{|I_{\mathrm{I},BA} + I_{\mathrm{II},BA} + I_{\mathrm{III},BA}|^2}{N_A N_B} \tag{5.38}$$

with

$$N_A = \left|I_{\mathrm{I},AA} + I_{\mathrm{II},AA} + I_{\mathrm{III},AA}\right|_{\mathbb{q}=0}^2. \tag{5.39}$$

Thus N_A and N_B can be obtained from the same calculation as for I_{BA}. It should be noted, however, that in calculating $I_{\mathrm{II},AA}$, the case $k_{z,i}^{A_\mathrm{II}} = k_{z,l}^{*A_\mathrm{II}}$ should be treated separately. The z integral of equation (5.32) becomes, for $B = A$ and $\mathbb{q} = 0$:

$$\int_{-L/2}^{L/2} \exp\left(i(k_{z,i}^{A_\mathrm{II}} - k_{z,l}^{*A_\mathrm{II}})z\right) dz = L\frac{\sin(k_{z,i}^{A_\mathrm{II}} - k_{z,l}^{*A_\mathrm{II}})L/2}{(k_{z,i}^{A_\mathrm{II}} - k_{z,l}^{*A_\mathrm{II}})L/2} \quad \text{for } k_{z,i}^{A_\mathrm{II}} \neq k_{z,l}^{*A_\mathrm{II}},$$
$$= L \quad \text{for } k_{z,i}^{A_\mathrm{II}} = k_{z,l}^{*A_\mathrm{II}}. \tag{5.40}$$

The integral over $\mathbb{r}_{\|}$ in each of the three terms in N_A simply gives the normalisation area $\mathcal{A}$, and hence we can write

$$|I_{BA}|^2 = \frac{(2\pi)^2}{\mathcal{A}}\delta(\mathbb{k}_{\|}^A - \mathbb{k}_{\|}^{*B} \pm \mathbb{q}_{\|})\frac{\left|J_{\mathrm{I},BA}(q_z) + J_{\mathrm{II},BA}(q_z) + J_{\mathrm{III},BA}(q_z)\right|^2}{\overline{N}_A\overline{N}_B}, \quad (5.41)$$

where $J_{\mathrm{I},BA}(q_z)$, $J_{\mathrm{II},BA}(q_z)$ and $J_{\mathrm{III},BA}(q_z)$ are the q_z dependent parts of $I_{\mathrm{I},BA}$, $I_{\mathrm{II},BA}$ and $I_{\mathrm{III},BA}$ as given in equations (5.35), (5.33) and (5.36) respectively, and $\overline{N}_A = N_A/\mathcal{A}$. Finally we may write:

$$|I_{BA}|^2 = \frac{(2\pi)^2}{\mathcal{A}}\delta(\mathbb{k}_{\|}^A - \mathbb{k}_{\|}^{*B} \pm \mathbb{q}_{\|})|J_{BA}(q_z)|^2 \quad (5.42)$$

where $|J_{BA}(q_z)|^2$ contains all the details of the interaction of the quantum confined hole states with the phonon mode in the z direction, (*cf.* the function $|J_{n',n}(q_z)|^2$ of equation (5.10)).

5C.3: Calculation of the 2D Hole-Phonon Scattering Rates

We will consider phonon scattering via four different processes; acoustic (deformation potential) (AC), non-polar optical (NPO), polar optical (POP) and piezoelectric (PZ) — as in Chapter 3. The case of piezoelectric scattering in 2D is of particular interest; the detailed nature of the piezoelectric coupling coefficient raises additional problems which have thus far not been mentioned.

We will assume that the quantum well valence subbands are isotropic in $\mathbb{k}_{\|}$ space, so that the hole energy $\epsilon(\mathbb{k})$ may be written as $\epsilon(k_{\|}, n)$, with n the subband index. For isotropic subbands, $J_{\mathbb{k}',\mathbb{k}}(q_z)$ will also be independent of the directions of $\mathbb{k}'_{\|}$ and $\mathbb{k}_{\|}$, and hence can be written as $J_{k'_{\|}n',k_{\|}n}(q_z)$. Then, substituting equation (5.42) into equation (5.3) and using equation (5.15), we obtain the general expression

$$P_{n',n}(\mathbb{k}_{\|}) = \frac{2\pi}{\hbar}\frac{V}{(2\pi)^3}\iint \delta_{\mathbb{k}_{\|}\pm\mathbb{q}_{\|},\mathbb{k}'_{\|}}\left(\frac{\hbar}{2M'N\omega_{\mathbb{q}}}\right)\begin{bmatrix}\mathcal{N}_{\mathbb{q}}\\ \mathcal{N}_{\mathbb{q}}+1\end{bmatrix}C_{\mathbb{q}}^2$$
$$\times |J_{k'_{\|}n',k_{\|}n}(q_z)|^2\delta\left(\epsilon(k'_{\|},n') - \epsilon(k_{\|},n) \mp \epsilon_{ph}\right)\, d\mathbb{k}'_{\|}dq_z. \quad (5.43)$$

Acoustic (deformation potential) scattering

For AC scattering, we will once again make use of the elastic and equipartition approximations (see Section 3B) Equation (5.43), together with equations (5.16) and (5.17) then gives

$$P_{n',n}(\mathbb{k}_{\|}) = \frac{k_BTE_{\mathrm{AC}}^2}{8\pi^2\hbar\rho v_s^2}\iint \delta_{\mathbb{k}_{\|}\pm\mathbb{q}_{\|},\mathbb{k}'_{\|}}|J_{k'_{\|}n',k_{\|}n}(q_z)|^2\delta\left(\epsilon(k'_{\|},n') - \epsilon(k_{\|},n)\right)\, d\mathbb{k}'_{\|}dq_z \quad (5.44)$$

where E_{AC} is the acoustic deformation potential in the quantum well. The choice of a suitable value for E_{AC} will be discussed in Chapter 7. For v_s^2 we will take the mean square of the longitudinal and transverse sound velocities, $\overline{v}^2$, as in Section 3C (equation (3.74)).

The above equation differs from equation (5.18) in that $|J_{k_\parallel' n', k_\parallel n}(q_z)|^2$ must be included in the integration over $\mathbf{k}_\parallel'$. As mentioned in section 5B we may omit the Kronecker delta $\delta_{\mathbf{k}_\parallel \pm \mathbf{q}_\parallel, \mathbf{k}_\parallel'}$ since we have no interest in, and assume no dependence of $P_{n',n}(\mathbf{k}_\parallel)$ on, the value which $\mathbf{q}_\parallel$ takes in order to conserve momentum. We now write $d\mathbf{k}_\parallel' = k_\parallel' dk_\parallel' d\beta$, where β is the polar angle in the 2D k-space plane. Integration over β merely gives a factor of 2π. We may now change the variables in the energy delta function to find

$$\begin{aligned}\iiint |J_{k_\parallel' n', k_\parallel n}(q_z)|^2 \delta\big(\epsilon(k_\parallel', n') - \epsilon(k_\parallel, n)\big)\, k_\parallel' dk_\parallel' d\beta dq_z \\ = 2\pi \iint |J_{k_\parallel' n', k_\parallel n}(q_z)|^2 \frac{\delta(k_\parallel' - k_\parallel^f)}{\left|\partial\epsilon/\partial k_\parallel'\right|}\, k_\parallel' dk_\parallel' dq_z \\ = 2\pi \mathcal{D}_{n'}(k_\parallel^f) \int |J_{k_\parallel^f n', k_\parallel n}(q_z)|^2\, dq_z \end{aligned} \tag{5.45}$$

where $k_\parallel^f$ is the final state in-plane wavevector;

$$\mathcal{D}_{n'}(k_\parallel^f) = \left| \frac{k_\parallel'}{\partial\epsilon/\partial k_\parallel'} \right|_{k_\parallel' = k_\parallel^f} \tag{5.46}$$

and $2\pi \mathcal{D}_{n'}(k_\parallel^f)$ gives the density of final states in subband n'. We will call $\mathcal{D}_{n'}(k_\parallel^f)$ the reduced density of states. Then the AC scattering rate, for absorption plus emission, is

$$P_{n',n}(k_\parallel) = \frac{k_B T E_{AC}^2}{2\pi\hbar\rho\overline{v}^2} \mathcal{D}_{n'}(k_\parallel^f)\, M^2_{k_\parallel^f n', k_\parallel n} \tag{5.47}$$

where

$$M^2_{k_\parallel^f n', k_\parallel n} = \int |J_{k_\parallel^f n', k_\parallel n}(q_z)|^2\, dq_z. \tag{5.48}$$

Hence the description of the 4-band **k.p** matrix element is contained within the term $M^2_{k_\parallel^f n', k_\parallel n}$. For isotropic subbands, the scattering rate has no angular dependence. This means that for most initial states $|\mathbf{k}_\parallel, n\rangle$, for scattering into a given subband n', $k_\parallel^f$ is uniquely defined (by energy conservation). However, some of the valence subbands (such as the second and fourth subbands in Fig. 5.4), are doubly valued in $k_\parallel$ for energies near the subband edge. For scattering into these regions, two values of $k_\parallel^f$ are possible for scattering from the same state $|k_\parallel, n\rangle$. Throughout this work, we will treat all such cases as two distinct processes, so that $P_{n',n}(k_\parallel)$ always gives the scattering rate between initial and final states each located on a single equi-energy circle in $\mathbf{k}_\parallel$ space.

Non-Polar Optical scattering

For NPO scattering we will adopt the same approach as in Section 3C; considering scattering by a combination of bulk LO and TO phonons assumed to have a common frequency $\omega_{\rm op}$. The coupling coefficient is then given by $C_{\rm q} = \overline{M} D_{\rm op}^2/(M_1 + M_2)$ (equation (3.55)), and, substituting into equation (5.43) we obtain:

$$P_{n',n}(k_{\|}) = \frac{D_{\rm op}^2}{8\pi^2\rho\omega_{\rm op}} \begin{bmatrix} \mathcal{N}_{\rm op} \\ \mathcal{N}_{\rm op}+1 \end{bmatrix} \times \iint \delta_{\mathbf{k}_{\|}\pm\mathbf{q}_{\|},\mathbf{k}'_{\|}} |J_{k'_{\|}n',k_{\|}n}(q_z)|^2 \delta\big(\epsilon(k'_{\|},n') - \epsilon(k_{\|},n) \mp \hbar\omega_{op}\big)\, d\mathbb{k}'_{\|} dq_z \tag{5.49}$$

The analysis then proceeds exactly as for acoustic scattering, giving

$$P_{n',n}(k_{\|}) = \frac{D_{\rm op}^2}{4\pi\rho\omega_{\rm op}} \begin{bmatrix} \mathcal{N}_{\rm op} \\ \mathcal{N}_{\rm op}+1 \end{bmatrix} \mathcal{D}_{n'}(k_{\|}^f)\, \mathcal{M}^2_{k_{\|}^f n',k_{\|}n}, \tag{5.50}$$

where $k_{\|}^f$ satisfies

$$\epsilon(k_{\|}^f, n') = \epsilon(k_{\|}, n) \pm \hbar\omega_{\rm op}. \tag{5.51}$$

Again $k_{\|}^f$ in subband n' will be uniquely defined for scattering out of state $|k_{\|}^f, n\rangle$, except for the special cases described above.

Polar Optical scattering

For polar optical scattering we will take the coupling coefficient $C_{\rm q}^2$ from equation (5.22). Then, substituting into equation (5.43), with $\omega_{\rm q}$ independent of $\mathbb{q}$, we obtain

$$P_{n',n}(k_{\|}) = \frac{e^2\omega_{\rm op}}{8\pi^2\varepsilon_0}\left(\frac{1}{\varepsilon_\infty} - \frac{1}{\varepsilon_s}\right) \begin{bmatrix} \mathcal{N}_{\rm op} \\ \mathcal{N}_{\rm op}+1 \end{bmatrix} \times \iiint \delta_{\mathbf{k}_{\|}\pm\mathbf{q}_{\|},\mathbf{k}'_{\|}} \frac{|J_{k'_{\|}n',k_{\|}n}(q_z)|^2}{q_{\|}^2 + q_z^2} \delta\big(\epsilon(k'_{\|},n') - \epsilon(k_{\|},n) \mp \hbar\omega_{op}\big)\, k'_{\|} dk'_{\|} d\beta dq_z. \tag{5.52}$$

We may perform the integration over $k'_{\|}$ by using the delta function, as for acoustic scattering, to find:

$$P_{n',n}(k_{\|}) = \frac{e^2\omega_{\rm op}}{8\pi^2\varepsilon_0}\left(\frac{1}{\varepsilon_\infty} - \frac{1}{\varepsilon_s}\right) \begin{bmatrix} \mathcal{N}_{\rm op} \\ \mathcal{N}_{\rm op}+1 \end{bmatrix} \mathcal{D}_{n'}(k_{\|}^f)\, \mathcal{M}^2_{k_{\|}^f n',k_{\|}n}, \tag{5.53}$$

where

$$\mathcal{M}^2_{k_{\|}^f n',k_{\|}n} = \iint \delta_{k_{\|}\pm q_{\|},k_{\|}^f} \frac{|J_{k_{\|}^f n',k_{\|}n}(q_z)|^2}{q_{\|}^2 + q_z^2}\, dq_z d\beta. \tag{5.54}$$

The Kronecker delta $\delta_{k_{\|}\pm q_{\|},k_{\|}^f}$ requires $q_{\|}^2 = k_{\|}^2 + {k_{\|}^f}^2 - 2k_{\|}k_{\|}^f\cos\beta$, where $k_{\|}^f$ is the in-plane wavevector of the allowed final states. The integration over β is actually quite straightforward. The β integral is of the form

$$\int_0^{2\pi} \frac{d\beta}{(a - b\cos\beta)} = \frac{2\pi}{\sqrt{a^2 - b^2}}, \tag{5.55}$$

with $a = k_{\|}^2 + k_{\|}^{f\,2} + q_z^2$, and $b = 2k_{\|}k_{\|f}$. Thus

$$\mathcal{M}^2_{k_{\|}^f n',k_{\|}n} = 2\pi \int \frac{|J_{k_{\|}^f n',k_{\|}n}(q_z)|^2}{\sqrt{q_z^4 + 2(k_{\|}^2 + k_{\|}^{f\,2})q_z^2 + (k_{\|}^2 - k_{\|}^{f\,2})^2}}\, dq_z. \tag{5.56}$$

However, it is also desirable to examine the angular dependence of the scattering rate. This is given by

$$\mathcal{F}^2_{k_{\|}^f n',k_{\|}n}(\cos\beta) = \int \frac{|J_{k_{\|}^f n',k_{\|}n}(q_z)|^2}{q_{\|}^2 + q_z^2}\, dq_z, \tag{5.57}$$

whence $\mathcal{M}^2_{k_{\|}^f n',k_{\|}n}$ is given by

$$\mathcal{M}^2_{k_{\|}^f n',k_{\|}n} = \int \delta_{k_{\|}\pm q_{\|},k_{\|}^f}\, \mathcal{F}^2_{k_{\|}^f n',k_{\|}n}(\cos\beta)\, d\beta. \tag{5.58}$$

Piezoelectric scattering

The case of piezoelectric scattering in 2D must be examined with some care, as the coupling coefficient $C_{\mathbf{q}}$ contains a detailed dependence on the direction of the phonon wavevector $\mathbf{q}$, as was shown in Section 3B.

Using the elastic, equipartition approximation we obtain, from equation (5.43):

$$P_{n',n}(k_{\|}) = \frac{k_B T}{8\pi^2 \hbar \rho v^2_{s,\mathrm{mode}}} \iiint \delta_{k_{\|}\pm q_{\|},k'_{\|}} \frac{C^2_{\mathbf{q},\mathrm{mode}}}{q^2} \times |J_{k'_{\|}n',k_{\|}n}(q_z)|^2 \delta\Big(\epsilon(k'_{\|},n') - \epsilon(k_{\|},n)\Big)\, k'_{\|}\, dk'_{\|}\, d\beta\, dq_z. \tag{5.59}$$

This expression gives the rate for scattering by either longitudinal or transverse piezoelectric phonons, with $v_{s,\mathrm{mode}}$ and $C_{\mathbf{q},\mathrm{mode}}$ taking appropriate values in each case.

We have seen that when free carrier screening is included, the coupling coefficients for the longitudinal and (the two combined) transverse modes are (from equations (3.42–3)):

$$C^2_{\mathbf{q},\mathrm{long}} = \frac{e^2 h_{14}^2}{\varepsilon_0^2 \varepsilon_s^2} \frac{q^4}{(q^2 + q_0^2)^2} \times 36\sigma_1^2\sigma_2^2\sigma_3^2, \tag{5.60a}$$

$$C^2_{\mathbf{q},\mathrm{trans}} = \frac{e^2 h_{14}^2}{\varepsilon_0^2 \varepsilon_s^2} \frac{q^4}{(q^2 + q_0^2)^2} \times 4(\sigma_1^2\sigma_2^2 + \sigma_2^2\sigma_3^2 + \sigma_3^2\sigma_1^2 - 9\sigma_1^2\sigma_2^2\sigma_3^2), \tag{5.60b}$$

where h_{14} is an element of the piezoelectric tensor, and σ_1, σ_2 and σ_3 are the direction cosines of the phonon wavevector $\mathbf{q}$; $\sigma_1 = q_x/q$, $\sigma_2 = q_y/q$ and $\sigma_3 = q_z/q$. Since we are not concerned with orientation of $\mathbf{q}$ in the plane of the well we can take

an average of $\sigma_1\sigma_2$ over all azimuthal angles in the q_xq_y plane; finding $\sigma_1^2\sigma_1^2 = \sigma_\parallel^4/8$, where $\sigma_\parallel = q_\parallel/q$. Then

$$C^2_{\mathbf{q},\text{long}} = \frac{e^2h_{14}^2}{\epsilon_0^2\epsilon_s^2}\frac{q^4}{(q^2+q_0^2)^2} \times \frac{9}{2}\sigma_\parallel^4\sigma_3^2, \tag{5.61a}$$

$$C^2_{\mathbf{q},\text{trans}} = \frac{e^2h_{14}^2}{\epsilon_0^2\epsilon_s^2}\frac{q^4}{(q^2+q_0^2)^2} \times \frac{1}{2}(\sigma_\parallel^4 + 8\sigma_\parallel^2\sigma_3^2 - 9\sigma_\parallel^4\sigma_3^2). \tag{5.61b}$$

Nevertheless it is clear that the inclusion of these coupling coefficients in equation (5.59) would render the triple integral quite intractable, given the complexity of the envelope function term $J_{k'_\parallel n',k_\parallel n}(q_z)$. Price (1981), in his treatment of electron scattering by piezoelectric phonons in 2D, proceeded by omitting the envelope function term entirely, saying that $|J_{k'_\parallel n',k_\parallel n}(q_z)|^2$ varied with q_z only slowly compared to the other terms in the integrand, and therefore could be taken as unity. This allowed him to perform the integration over q_z including the directional dependence of $C^2_{\mathbf{q},\text{long}}$ and $C^2_{\mathbf{q},\text{trans}}$. This approach, in the absence of screening, leads to an average electromechanical constant K_{av} (see section 3B) of the form

$$K^2_{\text{av}} = \frac{h_{14}^2}{\epsilon_0\epsilon_s}\left(\frac{9}{32c_l} + \frac{13}{32c_t}\right). \tag{5.62}$$

The first term gives the contribution from longitudinal modes, and the second, from the two sets of transverse modes, with $c_{\text{mode}} = \rho v^2_{s,\text{mode}}$. This result differs little from that for the bulk electromechanical constant (equation (3.69)), obtained by taking spherical averages of the directionally dependent parts of the piezoelectric coupling coefficients. Therefore we believe it a reasonable approximation, for the quantum confined holes calculation, to replace the directionally dependent terms of $C^2_{\mathbf{q},\text{long}}$ and $C^2_{\mathbf{q},\text{trans}}$ with the bulk spherical averages. This approach is consistent with the assumption of bulk-like phonon modes, and also with the fact that the elastic constants c_l and c_t are themselves spherical averages over crystal direction (Zook 1964). The 2D scattering rate, for longitudinal and transverse modes combined, is then

$$P_{n',n}(k_\parallel) = \frac{e^2k_BT}{8\pi^2\hbar}\left(\frac{K^2_{\text{av}}}{\epsilon_0\epsilon_s}\right)\iiint \delta_{\mathbf{k}_\parallel \pm \mathbf{q}_\parallel, \mathbf{k}'_\parallel}|J_{k'_\parallel n',k_\parallel n}(q_z)|^2\frac{q_\parallel^2+q_z^2}{(q_\parallel^2+q_z^2+q_0^2)^2} \times \delta\Big(\epsilon(k'_\parallel,n') - \epsilon(k_\parallel,n)\Big)\, k'_\parallel dk'_\parallel d\beta dq_z, \tag{5.63}$$

with K^2_{av} given by (equation (3.69);

$$K^2_{\text{av}} = \frac{h_{14}^2}{\epsilon_0\epsilon_s}\left(\frac{12}{35c_l} + \frac{16}{35c_t}\right). \tag{5.64}$$

The integration over $k'_\parallel$ is performed as above, by changing the variables in the Dirac delta function. Multiplying by two to account for both absorption and

emission processes, we obtain:

$$P_{n',n}(k_{\|}) = \frac{e^2 k_B T}{4\pi^2 \hbar}\left(\frac{K_{\mathrm{av}}^2}{\varepsilon_0 \varepsilon_s}\right) D_{n'}(k_{\|}^f)\mathcal{M}^2_{k_{\|}^f n',k_{\|}n}, \tag{5.65}$$

where

$$\mathcal{M}^2_{k_{\|}^f n',k_{\|}n} = \iint \delta_{k_{\|}\pm q_{\|},k_{\|}^f} |J_{k_{\|}^f n',k_{\|}n}(q_z)|^2 \frac{q_{\|}^2 + q_z^2}{(q_{\|}^2 + q_z^2 + q_0^2)^2}\, d\beta dq_z \tag{5.66}$$

and the Kronecker delta gives $q_{\|}^2 = k_{\|}^2 + {k_{\|}^f}^2 - 2k_{\|}k_{\|}^f \cos\beta$.

If screening effects are omitted (by setting $q_0 = 0$), the matrix element has the same form as that for (unscreened) polar optical scattering (equation (5.54)). However, without screening the RHS of equation (5.66) diverges as $q_z \to 0$ and $q_{\|} \to 0$. This means that a finite rate cannot be obtained for intrasubband scattering, since, within the elastic approximation, $k_{\|} = k_{\|}^f$ and so the case $q_{\|} = 0$ always contributes. The lack of momentum conservation in the z direction allows for a form of screening due to q_z. However, in most cases the envelope function term $|J_{k_{\|}^f n',k_{\|}n}(q_z)|^2$ was found to be peaked at $q_z = 0$; thus a singularity in the unscreened $q_0 = 0$ scattering rate is not avoided. Note also that screening may readily be included in the polar optical scattering rate by taking, for $\mathcal{M}^2_{k_{\|}^f n',k_{\|}n}$ in equation (5.53), the form given in equation (5.66) above, rather than that in equation (5.54).

We can proceed, as for polar optical scattering, by solving the β integral. This is of the form

$$\int_0^{2\pi} \frac{(a - b\cos\beta)}{(c - b\cos\beta)^2}\, d\beta = 2\pi \frac{(ac - b^2)}{(c^2 - b^2)^{3/2}}, \tag{5.67}$$

where $a = k_{\|}^2 + {k_{\|}^f}^2 + q_z^2$, $b = 2k_{\|}k_{\|}^f$, and $c = a + q_0^2$.

This result may be substituted into equation (5.66) to give an expression for the remaining integral over q_z, which must be performed numerically. Alternatively, the angular dependence of the scattering rate can be obtained in the form

$$\mathcal{F}^2_{k_{\|}^f n',k_{\|}n}(\cos\beta) = \int |J_{k_{\|}^f n',k_{\|}n}(q_z)|^2 \frac{q_{\|}^2 + q_z^2}{(q_{\|}^2 + q_z^2 + q_0^2)^2}\, dq_z, \tag{5.68}$$

in which case $\mathcal{M}^2_{k_{\|}^f n',k_{\|}n}$ is given by equation (5.58).

CHAPTER 6
QUANTUM CONFINED HOLE-PHONON SCATTERING MATRIX ELEMENTS

6A INTRODUCTION

In Chapter 5, a method of calculating matrix elements for the hole-phonon interaction in a quantum well was described. In this chapter, detailed results of these calculations will be presented: to demonstrate the influence of the quantum confined valence bandstructure on phonon scattering, and to form a database for use in the Monte Carlo simulations of 2D hole dynamics described in later chapters.

We have studied the specific case of a 100Å lattice matched GaAs/AlAs single quantum well. The in-plane valence bandstructure for this system was shown in Fig. 5.4, for the $\langle 100 \rangle$ direction. We will assume, as mentioned in Chapter 5, that the bandstructure is isotropic in $\mathbf{k}_{\|}$-space. Anisotropy in this system is expected to lead to shifts of the order of 10% in the subband energies over the range of $k_{\|}$ concerned ($k_{\|} < 0.12\text{Å}^{-1}$).

The effect of anisotropy on the scattering matrix elements is rather more difficult to estimate. The valence band wavefunctions will always change with direction, due to their p-like symmetry. In bulk GaAs, this effect gives rise to overlap integrals $G(\mathbf{k}',\mathbf{k})$ which exhibit a strong directional dependence (Wiley 1971), and therefore the phonon scattering matrix elements are similarly affected (see Section 3C). Preliminary work by Taylor (1987) indicates that, whilst the overlap integrals of quantum confined hole states show some directional dependence, the variation in $G(\mathbf{k}',\mathbf{k})$ is not, in general, as marked as in the bulk. Therefore, we have decided not to consider anisotropy effects any further here; preferring to examine the basic influence of band mixing on hole-phonon scattering in a quantum well. In any case, in any Monte Carlo model of quantum confined hole dynamics, the important parameters will be the scattering rates from a given state $|\mathbf{k}\rangle$ into all possible final states: in these quantities, any anisotropy effects will inevitably be averaged out by integration over direction in the $\mathbf{k}_{\|}$-plane.

We will consider scattering between states in the first four subbands of the well: four will serve as a sufficient number to give a representative picture of carrier dynamics in a multisubband system. In Fig. 6.1 we have shown again the in-plane dispersion of these subbands, which we will now label simply as bands 1–4. We will also drop the $\|$ subscript on the hole wavevectors $\mathbf{k}_{\|}$ and $k_{\|}$; all vectors $\mathbf{k}$ and their moduli k can henceforth be taken as 2D in-plane quantities. Marked on Fig. 6.1 are the band minima and zone centre energies, the band minima wavevectors (bands 2 and 4 only), and the points of closest approach (anticrossings). Values for these quantities can be found in Table 6.1. For kinetic energies less than the zone centre

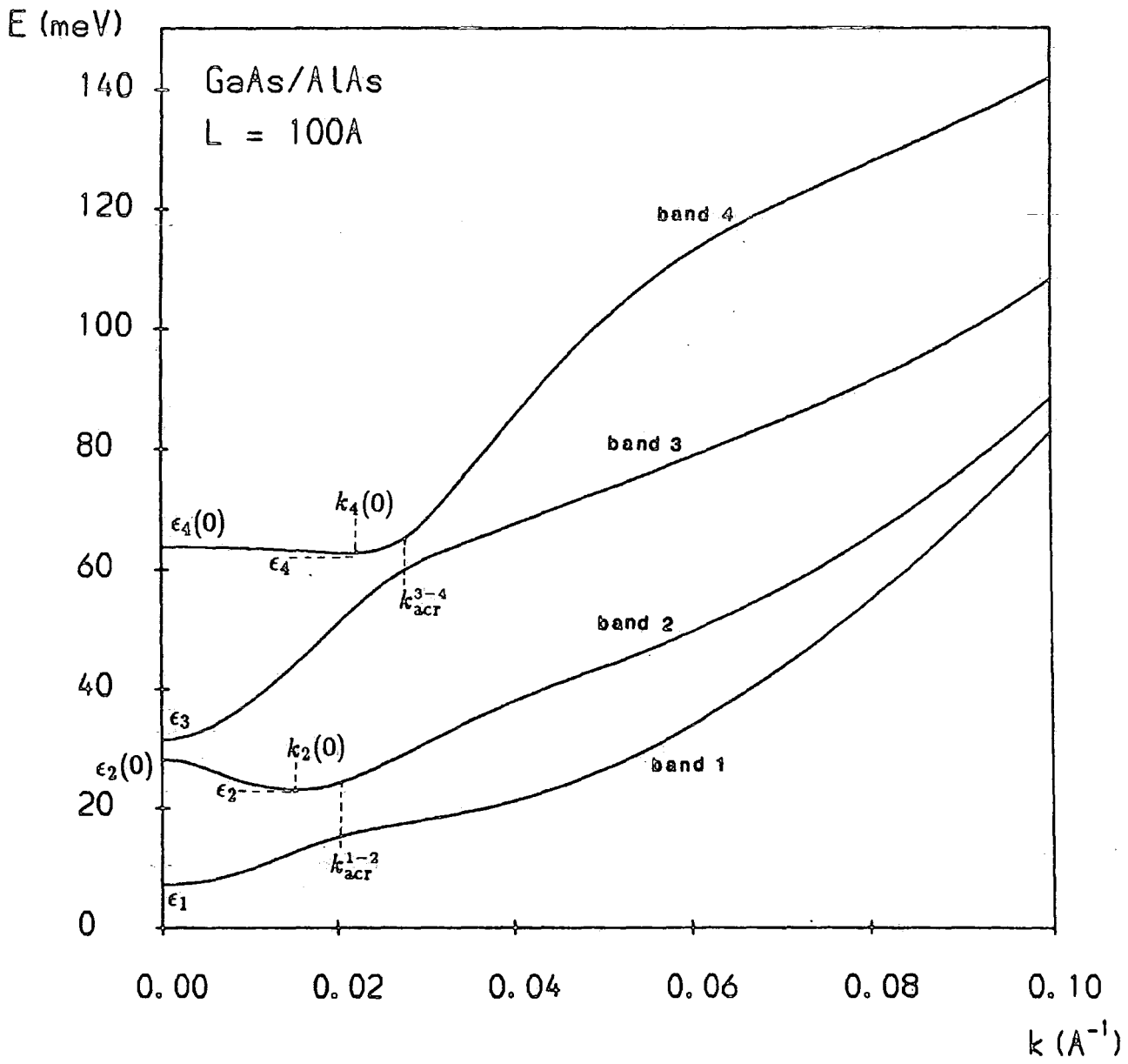

Fig. 6.1 In-plane energy dispersion of the first four valence subbands of a 100Å GaAs/AlAs quantum well. The energy and wavevector points marked are defined in Table 6.1.

ϵ_1	7.18655meV
ϵ_2	23.0854meV
ϵ_3	31.5272meV
ϵ_4	62.7394meV

Table 6.1a: Energies of the band minima relative to the bottom of the quantum well

$\epsilon_2(0)$	5.0563meV
$\epsilon_4(0)$	1.0796meV

Table 6.1b: Band 2 and 4 zone centre energies relative to the band minima

$k_2(0)$	0.01500Å^{-1}
$k_4(0)$	0.02125Å^{-1}

Table 6.1c: Wavevectors of the band 2 and 4 minima

bands:	k_{acr}
1/2	0.01975Å^{-1}
3/4	0.02750Å^{-1}

Table 6.1d: Points of closest approach (anticrossing points)

energies, bands 2 and 4 are doubly valued in wavevector. We will refer to states for which $k < k_n(0)$ as 'b' states, and those for which $k \geq k_n(0)$ as 'a' states, and consider scattering into states of each type separately.

Before presenting the scattering matrix elements for this system we will examine, in Section 6B, the overlap integrals involving zone centre states. These give an insight into the way in which the character of the valence band states is modified by band mixing effects for $k > 0$. In Section 6C, we will show the matrix elements for scattering by optical (non-polar and polar), and acoustic (deformation potential and piezoelectric) phonons (sections 6C.1 and 6C.2 respectively). We will then examine the angular dependence of some of the polar optical and piezoelectric processes (Section 6D), and finally, we will discuss the effect of screening on polar scattering (Section 6E).

6B OVERLAP INTEGRALS

We have calculated overlap integrals of the form

$$G^2(k'n', kn) = \left| \int \psi^*_{k'n'}(\mathbb{r}) \psi_{kn}(\mathbb{r})\, d\mathbb{r} \right|^2, \tag{6.1}$$

which are obtained from the calculation of $|I_{BA}|^2$ (equation (5.41)), with $\mathbb{q} = 0$. Specifically, we have considered the overlap of states $|k, n\rangle$ in a given band n, over a range of k, with the zone centre states $|0, n'\rangle$ of each of the four bands $n' = 1 \ldots 4$. This shows the extent of mixing within a particular band, as described by the proportions of zone centre states of neighbouring bands which constitute a state at a given k.

Figs. 6.2–5 show these overlap integrals (squared), which we will refer to as $G^2_{0_{n',n}}(k)$, for bands 1 to 4 respectively. (We have used an offset of $k = 10^{-4}\text{Å}^{-1}$ in locating the zone centre states to avoid the numerical difficulties associated with the point $k = 0$.) In each case, at the zone centre only the term $G^2_{0_{n,n}}(k)$ contributes, having value unity. This confirms that the zone centre states are unmixed, as we would expect by definition.

Fig. 6.2 shows that as k nears the region of anticrossing between bands 1 and 2 ($k \approx 0.02\text{Å}^{-1}$), the character of band 1 becomes much less $|0, 1\rangle$ like, taking on the character of $|0, 2\rangle$ and $|0, 3\rangle$. Beyond the anticrossing point the $|0, 1\rangle$ contribution is less than 25%, with the $|0, 3\rangle$ contribution greatest. The $|0, 3\rangle$ state is LH1 like (see Fig. 5.4); hence, band 1 can be said to have assumed predominantly light hole character beyond the anticrossing. The $|0, 4\rangle$ contribution remains negligible throughout the range of k shown.

Figs. 6.3–4 show a strong degree of mixing between bands 2 and 3 even at small wavevectors ($k \approx 0.005\text{Å}^{-1}$). This is clearly because the bands are so close together at the zone centre. Indeed, if the quantum well width were to be reduced slightly, it would be expected that the character of the two bands at $k = 0$ would be exchanged: *i.e.*, $|0, 2\rangle$ would become LH1 like; and $|0, 3\rangle$, HH2 like (Eppenga *et al.* 1987; Wood 1987). It can be seen from Fig. 6.3 that the character of band 2 is again exchanged on anticrossing with band 1. For $k > 0.02\text{Å}^{-1}$ the band gains substantial $|0, 1\rangle$ character and loses virtually all of its $|0, 3\rangle$ character. A small contribution from $|0, 4\rangle$ is also visible at larger wavevectors.

Band 3 anticrosses with band 4 at $k = 0.0275\text{Å}^{-1}$. Fig. 6.4 shows, at this point, a distinct exchange of $|0, 2\rangle$ and $|0, 3\rangle$ character for that of $|0, 4\rangle$. In a similar manner, the $|0, 4\rangle$ content of states in band 4 falls sharply as $k \to 0.0275\text{Å}^{-1}$. Beyond the anticrossing region, the band 4 states consist of a fairly balanced mixture of all four zone centre states considered, with no dominant contribution from any one.

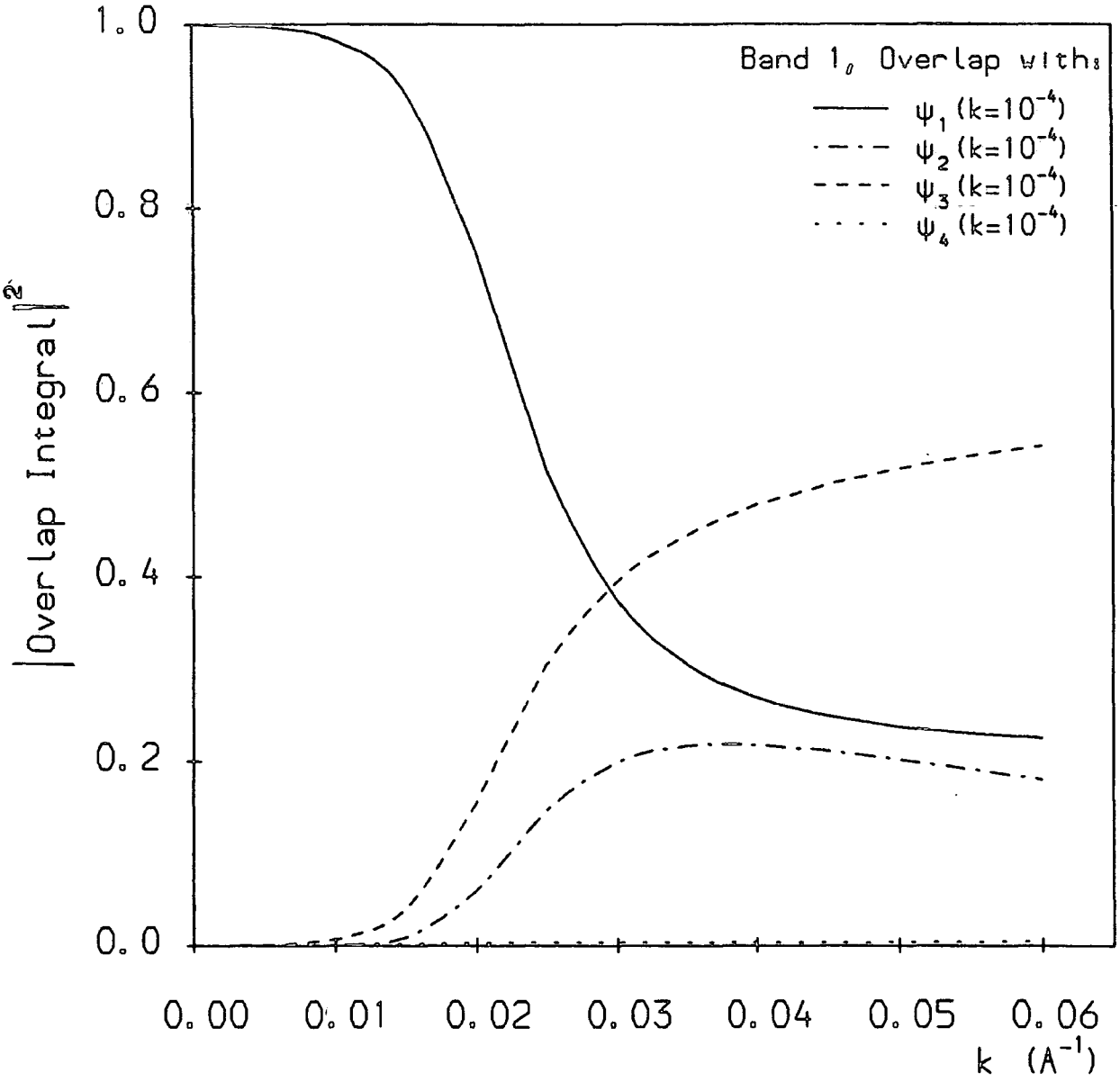

Fig. 6.2 Band 1. Moduli squared of the overlap integrals between state $|k\rangle$ and the zone centre states of bands 1–4.

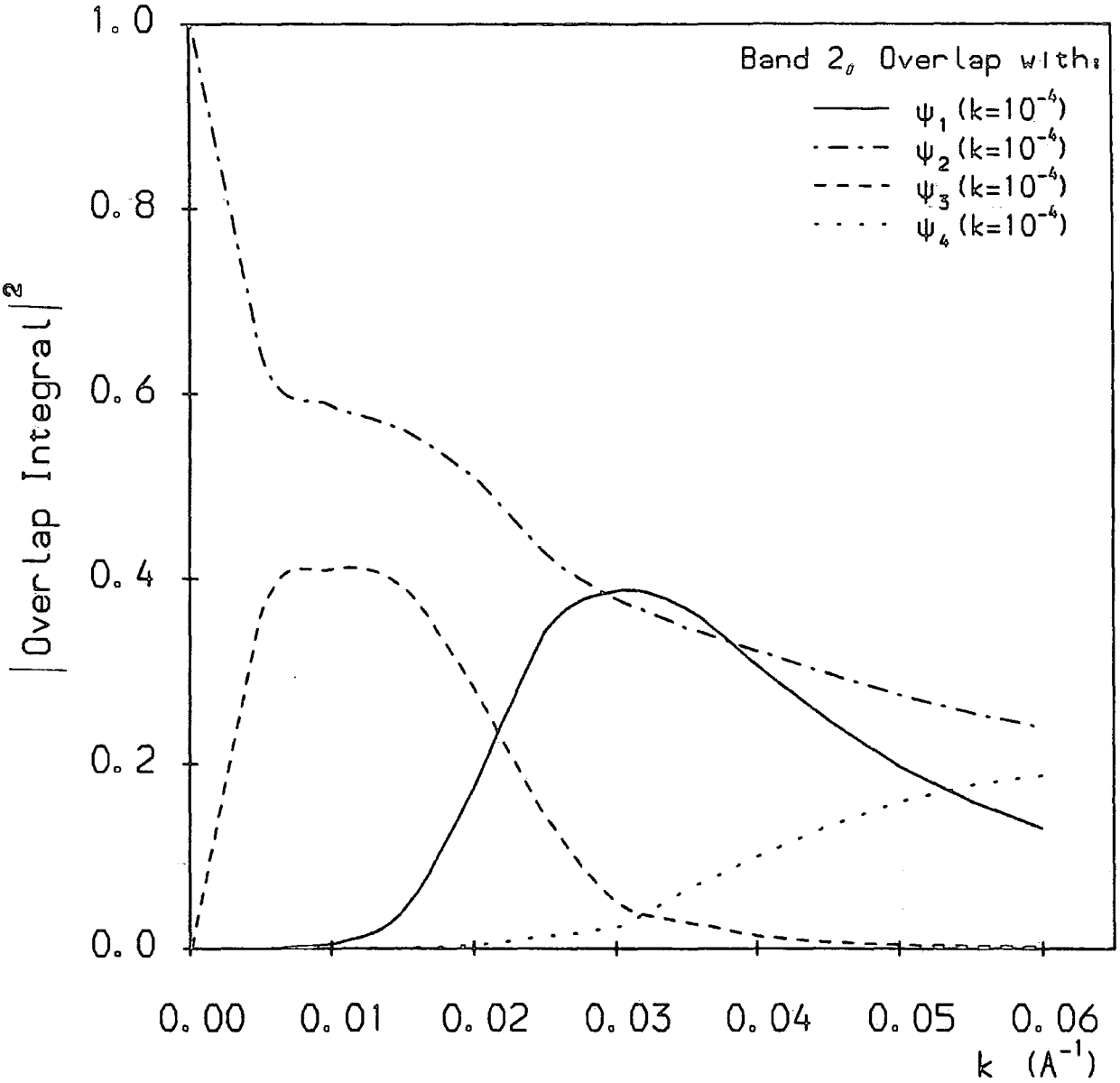

Fig. 6.3 Band 2. Moduli squared of the overlap integrals between state $|k\rangle$ and the zone centre states of bands 1–4.

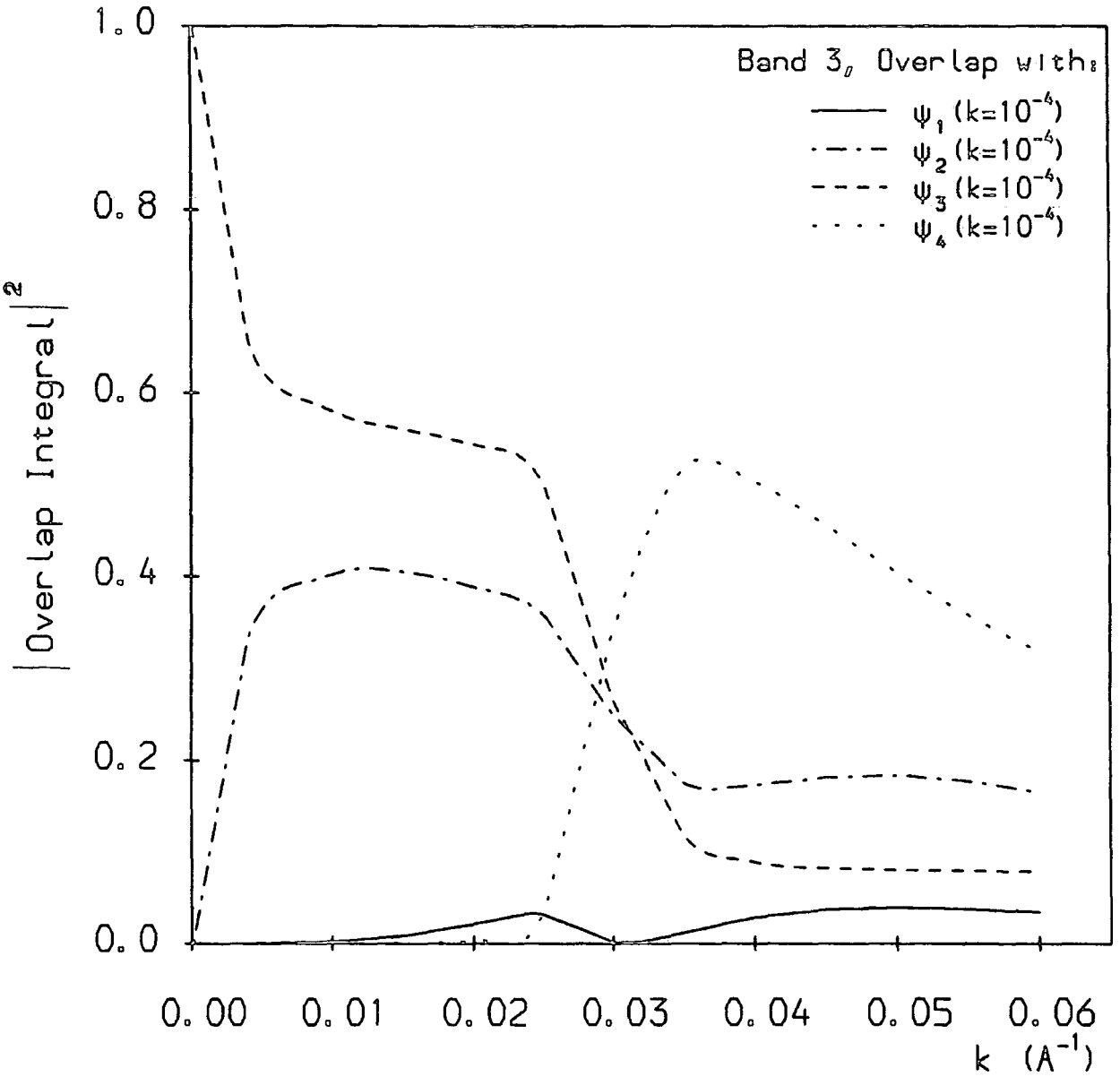

Fig. 6.4 Band 3. Moduli squared of the overlap integrals between state $|k\rangle$ and the zone centre states of bands 1–4.

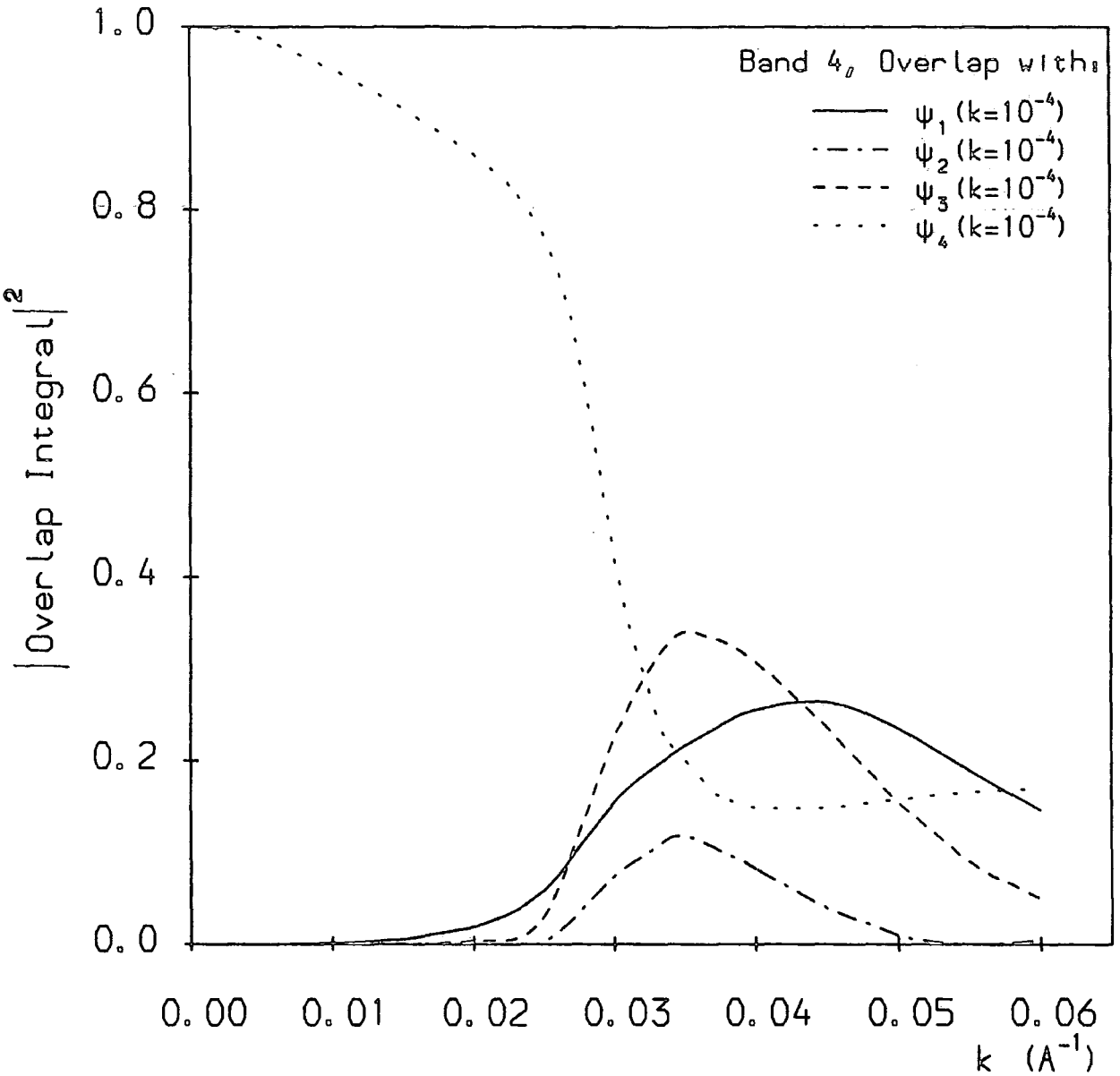

Fig. 6.5 Band 4. Moduli squared of the overlap integrals between state $|k\rangle$ and the zone centre states of bands 1–4.

Thus, by studying these overlap integrals alone, we can make some broad predictions concerning scattering between states in the four bands.

We expect that intraband scattering between two states on opposite sides of an anticrossing region will be *low* compared to scattering between states both lying before, or both lying beyond, the anticrossing. This will lead to intraband scattering matrix elements which vary markedly with k as the anticrossing region is traversed.

Where an exchange of character between two adjacent states is apparent, we expect a complementary effect for interband scattering. For example, a large scattering matrix element may be predicted for band $1 \leftrightarrow 2$ transitions which straddle the band 1/2 anticrossing region; and similarly for $3 \leftrightarrow 4$ transitions which straddle the band 3/4 anticrossing region.

We may also predict: especially weak scattering between band 1 and the zone centre states of band 4, and between band 3 and the zone centre states of band 1; and strong scattering between states near $k = 0$ in bands 2 and 3 (assuming such processes are allowed).

6C MATRIX ELEMENTS

The calculation of hole-phonon scattering matrix elements in the 4-band k.p scheme involves the numerical evaluation of the terms $\mathcal{M}^2_{k'n',kn}$, as defined in equations (5.48), (5.54) and (5.66) for the various scattering processes. This task involves considerable computational effort, since the 4-band k.p wavefunctions must be calculated in full for every pair of initial and final states considered. We have used a modified version of Wood's 4-band k.p wavefunction program (Wood 1987), together with programs written to evaluate the integrals over q_z, and a program which determines the energies and wavevectors of the scattering states. We have calculated matrix elements for all permutations of intra- and inter-band scatterings, including separate transitions to *a* and *b* states in bands 2 and 4, by acoustic (deformation potential) (AC); non polar optical (NPO); polar optical (POP), and piezoelectric (PZ) phonons. For the optical processes we have used a fixed phonon energy of $\hbar\omega_{op} = 36.4$meV (Landolt-Börnstein 1982), which is appropriate to scattering at a lattice temperature T_L of 77K. For acoustic processes we will take scattering to be elastic, selecting initial and final states of equal energy; although we have also examined the effect on the matrix elements of introducing an energy shift between the scattering states.

In Tables 6.2–4 we have shown the threshold energies and wavevectors for optical and acoustic processes. For scatterings into *b* states (which will be termed *b* processes) an upper limit is also imposed on the energy and wavevector of the initial state, since the energy of the *b* state cannot exceed the zone centre energy. These upper limits are also given in the tables. Where no upper limit is enforced on k, we have restricted the value of the larger wavevector of k and k' to $< 0.12\text{Å}^{-1}$, which is close to the upper limit (typically 10% of the Brillouin zone) beyond which the k.p method ceases to be reliable.

6C.1: Matrix elements for optical phonon scattering

Figs. 6.6–9 show the matrix elements for optical phonon absorption (abs) processes in bands 1–4 respectively. In each case, figures (a)–(d) show NPO matrix elements, and (e)–(h), POP matrix elements. The quantity plotted for NPO processes is the matrix element squared in dimensionless form, $(L/4)\mathcal{M}^2_{k'n',kn}$; and that for POP processes, $(1/4L)\mathcal{M}^2_{k'n',kn}$, where L is the quantum well width. The prefactors are merely a by-product of the numerical integration process used, in which q_z was substituted for the dimensionless variable $q_z L/2$. Thus, on the scales shown in the figures, the matrix elements $|I_{n',n}|^2$ obtained by Price (1981) for AC and NPO scattering in a 1-band infinite square well calculation would have values $L/4 \times (\pi/b_{n',n}) = \pi/2$ and $3\pi/4$ for inter- and intra-band transitions respectively, where $b_{n',n}$ is defined in Section 5B. It is important to note that the definition of

Process (NPO/POP)	Threshold Kinetic Energy (meV)	Threshold Wavevector 10^{-2}Å^{-1}	Max. Kinetic Energy (meV)	Max. Wavevector 10^{-2}Å^{-1}
			b processes only	
1–4abs	19.15	4.978	20.23	5.145
2–4abs	3.254	2.389	4.334	2.545
			all 2*b* abs processes forbidden	
			3–4*b* abs and 4–4*b* abs forbidden	
	no restriction on remaining abs processes			

Table 6.2: Energy Restrictions for Optical Phonon Absorption

Process (NPO/POP)	Threshold Kinetic Energy (meV)	Threshold Wavevector 10^{-2}Å^{-1}	Max. Kinetic Energy (meV)	Max. Wavevector 10^{-2}Å^{-1}
			b processes only	
1–1em	36.40	7.030		
1–2em	52.30	8.380	57.36	8.758
1–3em	60.74	9.000		
1–4em	91.95	10.958	93.03	11.019
2–1em	20.50	4.979		
2–2em	36.40	7.359	41.46	7.918
2–3em	44.84	8.260		
2–4em	76.05	10.722	77.13	10.792
3–1em	12.06	1.477		
3–2em	27.96	2.731	33.01	3.486
3–3em	36.40	4.082		
3–4em	67.61	9.035	68.69	9.159
4–1em				
4–2em			1.802	2.702
4–3em	5.188	3.006		
4–4em	36.40	4.856	37.48	4.931

Table 6.3: Energy Restrictions for Optical Phonon Emission

Process (Ac/PZ)	Threshold Kinetic Energy (meV)	Threshold Wavevector 10^{-2}Å^{-1}	Max. Kinetic Energy (meV)	Max. Wavevector 10^{-2}Å^{-1}
			b processes only	
1–1				
1–2	15.90	4.406	20.95	5.251
1–3	24.34	5.712		
1–4	55.55	8.625	56.63	8.705
2–1				
2–2			5.056	2.645
2–3	8.442	3.096		
2–4	39.65	7.726	40.73	7.842
3–1				
3–2			3–2*b* forbidden	
3–3				
3–4	31.21	3.173	32.29	3.359
4–1				
4–2			4–2*b* forbidden	
4–3				
4–4			1.080	2.592

Table 6.4: Energy Restrictions for Acoustic Processes

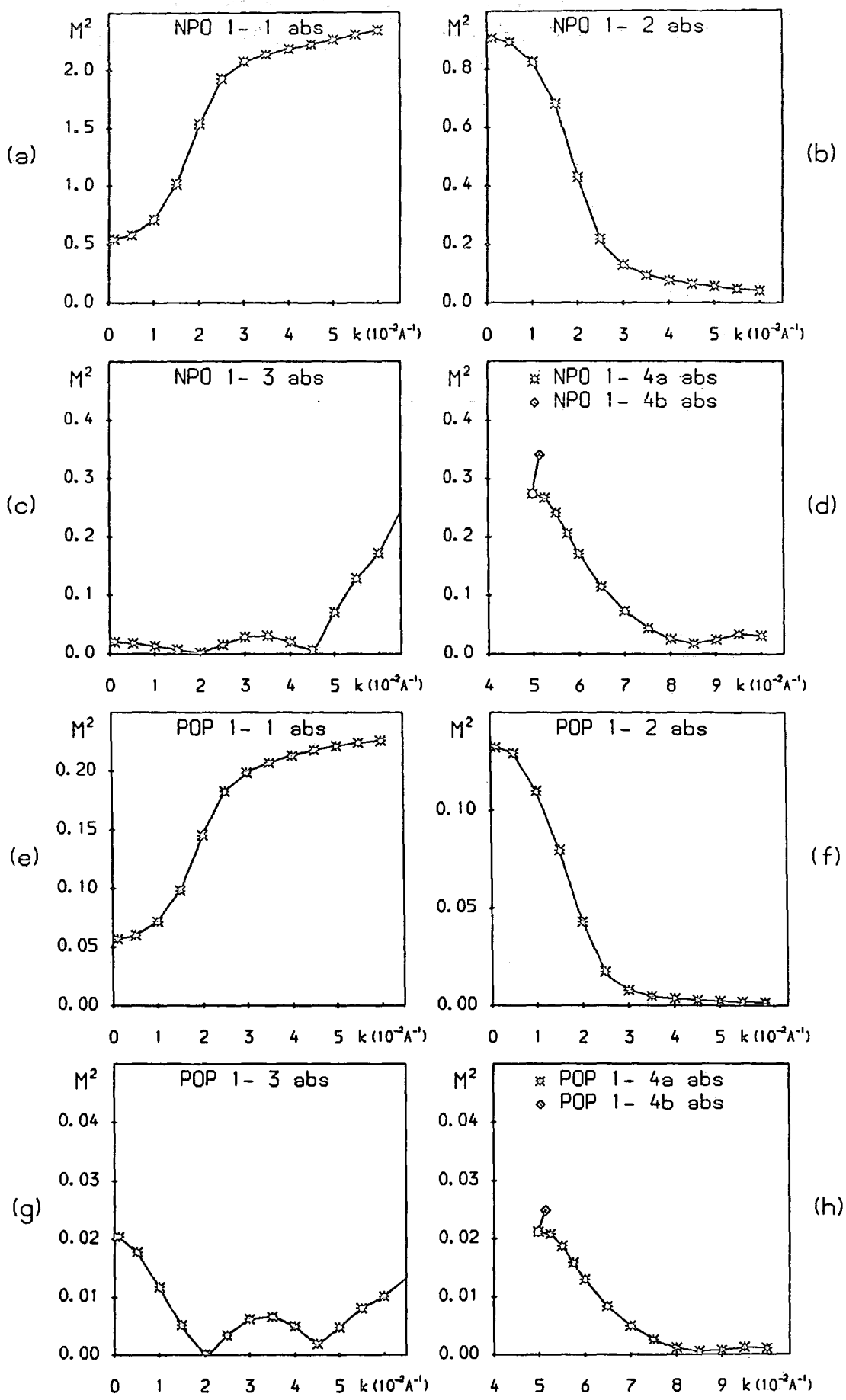

Fig. 6.6 Matrix elements for optical phonon absorption processes for a hole in state $|k\rangle$ in band 1.

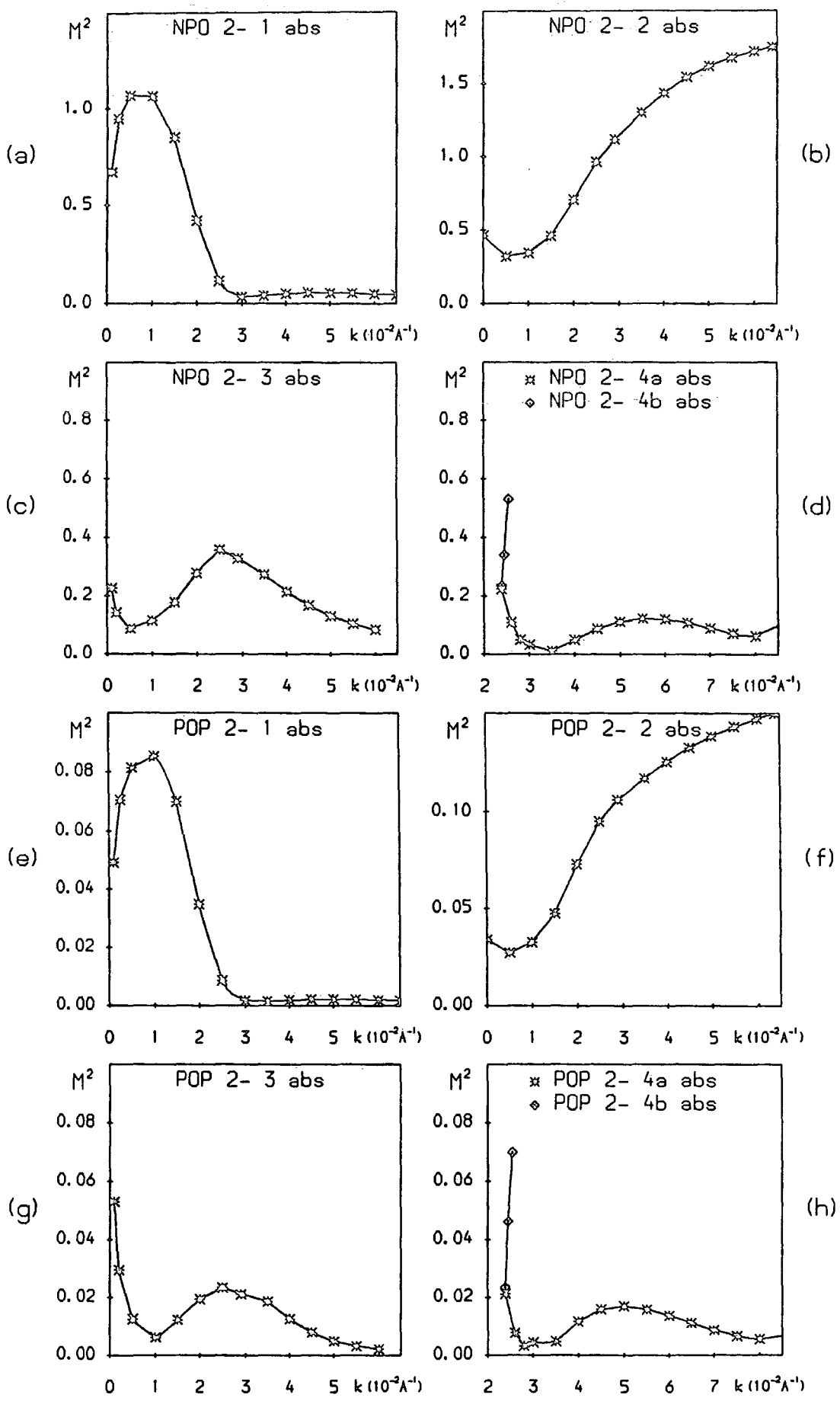

Fig. 6.7 Matrix elements for optical phonon absorption processes for a hole in state $|k\rangle$ in band 2.

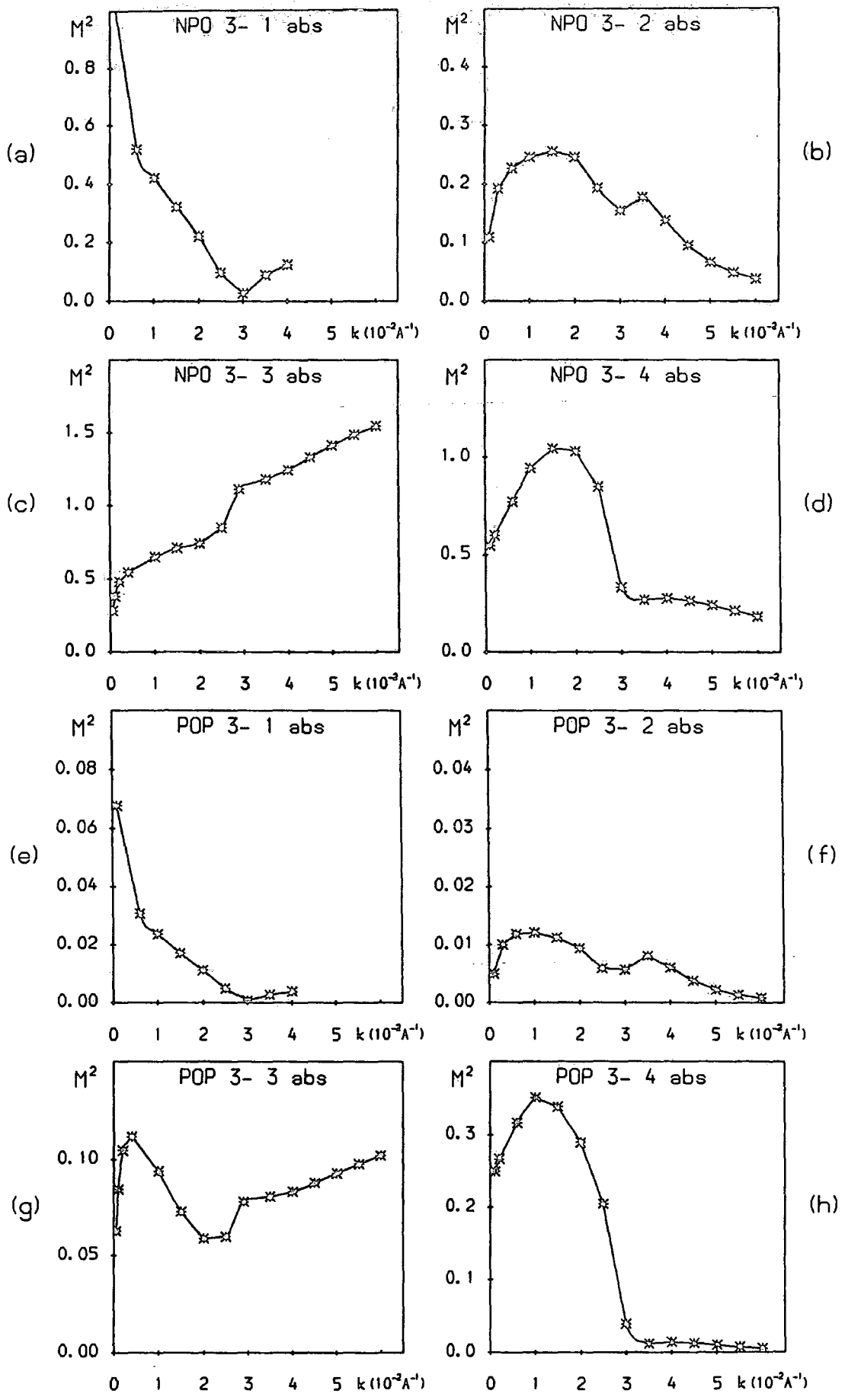

Fig. 6.8 Matrix elements for optical phonon absorption processes for a hole in state $|k\rangle$ in band 3.

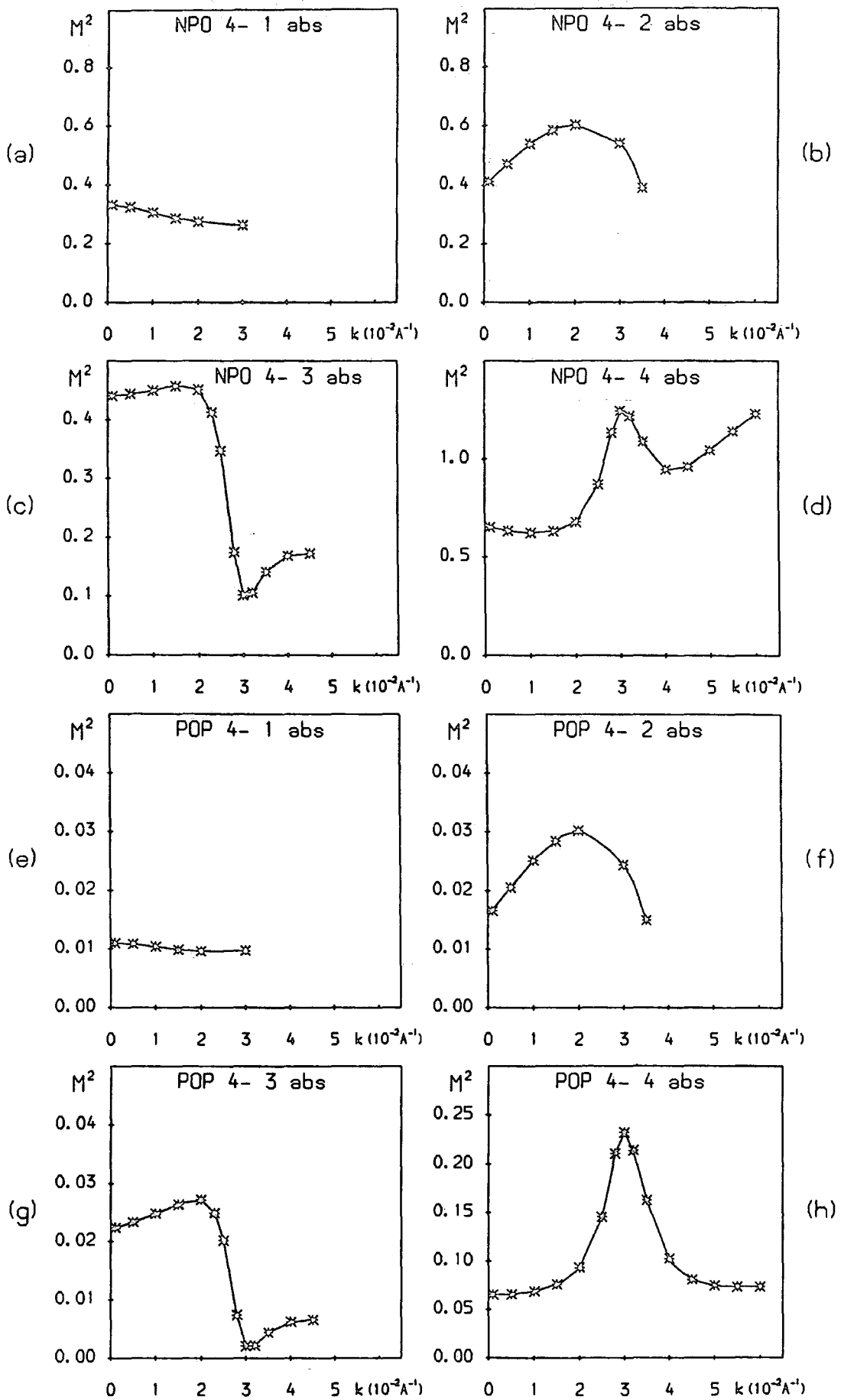

Fig. 6.9 Matrix elements for optical phonon absorption processes for a hole in state $|k\rangle$ in band 4.

$\mathcal{M}^2_{k'n',kn}$ for POP scattering (section 5C.3) includes an integration over polar angle β. Therefore, the plots for POP processes represent the cumulative effect of scattering to all final states on the energy conserving circle in 2D k-space. For NPO scattering the matrix element has no angular dependence (in our model), and so the NPO plots simply give the matrix elements for scattering between two states, with integration over the energy conserving circle contributing a factor of 2π to the results shown. For brevity, we shall refer to the plots of both $(L/4)\mathcal{M}^2_{NPO}$ and $(1/4L)\mathcal{M}^2_{POP}$ simply as 'matrix elements', and will label both merely as '$\mathcal{M}^2$' on the figures shown in this chapter.

Looking at the intraband NPO matrix elements (Figs. 6.6a, 6.7b, 6.8c and 6.9d); we see that the 4-band k.p results approach the infinite square well result ($3\pi/4 \approx 2.36$) at large wavevectors. However in all cases the matrix element is considerably smaller at small wavevectors. This is a clear manifestation of the effect predicted in Section 6B. For small wavevectors, the final state $|k', n\rangle$ lies beyond the anticrossing region in the given band n; hence the states $|k, n\rangle$ and $|k', n\rangle$ have markedly different character and the matrix element is small. As k approaches the anticrossing region ($k = 0.02\text{Å}^{-1}$ in bands 1 and 2, $k = 0.0275\text{Å}^{-1}$ in bands 3 and 4) the matrix element increases, since the initial state loses the zone centre state character and becomes much more mixed. Beyond anticrossing, the character of the states changes relatively little with k, and the matrix element is large. According to this description, the k dependence of the NPO 1–1abs matrix element (Fig. 6.6a) may be regarded as the model case of intraband scattering in a quantum confined valence band system. The NPO 2–2abs matrix element (Fig 6.7b) is modified only by a minimum at small k which reflects the turning point in energy in band 2. In band 3 (Fig. 6.8c), the effect is not quite so dramatic, but is manifested by a sharp kink in the matrix element at $k \approx 0.0275\text{Å}^{-1}$. Fig. 6.9d shows rather unpredictable behaviour in the NPO 4–4abs matrix element, with a peak at $k \approx 0.03\text{Å}^{-1}$ which corresponds to peaks in the $|0, 2\rangle$ and $|0, 3\rangle$ character in states near that point.

The corresponding POP intraband matrix elements (Figs. 6.6e, 6.7f, 6.8g and 6.9h) are modified only by the $1/q^2$ dependence of polar scattering, which is here averaged out by integration over β. This results in little change from the NPO case for 1–1abs and 2–2abs. For 3–3abs however (Fig. 6.8g), we see an enhancement of the matrix element at small k. This is due to the shape of band 3, which has a large curvature at the zone centre, but is 'bent over' by repulsion from band 4, and so rises much less steeply for larger k. This means that for k near the zone centre the minimum value of $q_{\|}$ ($q_{\text{min}} = |k' - k|$) for optical processes is fairly small. As k increases, q_{min} must also increase, due to the change in band dispersion, in order

to maintain a fixed energy separation $\hbar\omega_{op}$ between the scattering states. Thus, the $1/q^2$ factor gives a larger contribution to scattering at small k.

An even more drastic effect is visible for POP 4–4abs (Fig. 6.9h). Band 4 is almost flat up to the anticrossing point. Hence, q_{min} for optical phonons decreases sharply to a minimum at $k \approx 0.0275\text{Å}^{-1}$. Thus, the peak which appears in the NPO 4–4abs matrix element is significantly enhanced by $1/q^2$ weighting for polar scattering. That the two effects should contribute at the same wavevector is obviously no coincidence, since both are direct consequences of the anticrossing between bands 3 and 4.

For interband NPO scattering we note that the matrix elements are, in general, smaller than those for intraband transitions, and that a wide range of magnitudes is displayed. Firstly we will examine the case of NPO 1–2abs (Fig. 6.6b), since this represents the model case of scattering between two anticrossing bands as described in Section 6B. For small k the final state $|k', n'\rangle$ lies beyond the anticrossing region, hence the initial and final states have *similar* character and the matrix element is large. As k traverses the anticrossing region the character of state $|k, n\rangle$ becomes less like that of $|k', n'\rangle$ until, at large k, the character of the two states is quite dissimilar and the matrix element is small. A similar trend can be seen for NPO 2–1abs, 3–4abs, and 4–3abs (Figs. 6.7a, 6.8d, and 6.9c respectively). The 2–1 process is dominated by the exchange of $|0, 3\rangle$ character between bands 1 and 2 (see Figs. 6.2 and 6.3), which also accounts for the initial rise in the matrix element, as band 2 rapidly gains $|0, 3\rangle$ character at small k. The NPO 3–4abs matrix element shows a reduced value at small k, because k' is still too close to the anticrossing region for the model description to apply. In the case of NPO 4–3abs, the final states in band 3 are so far from the anticrossing region that the form of the matrix element reflects solely the variation of character with k of states in band 4. Comparing the matrix elements for these four cases with those for the remaining NPO processes, we see that the transitions between adjacent, anticrossing bands (the 'inter-anticrossing-band processes') represent the principal form of interband NPO scattering.

The matrix elements for inter-anticrossing-band POP transitions, 1–2, 2–1, 3–4 and 4–3abs, are shown in Figs. 6.6f, 6.7e, 6.8h and 6.9g. It can be seen that the variation of each matrix element with k is very similar to that for the corresponding NPO process. However, for POP phonons, the dominance of these processes in interband scattering is lost. Whilst the POP 1–2abs matrix element has approximately the same magnitude as the intraband POP matrix elements, the 2–1 matrix element is rather smaller, the 4–3abs matrix element almost an order of magnitude smaller, and the 3–4abs matrix element considerably larger

than the intraband values. From the dispersion curves in Fig. 6.1 we see that the initial and final states for POP 2–1abs must be well separated in k-space in order to satisfy energy conservation, and that those for POP 4–3abs must be still further apart. Consequently $q_{\min}$ is very large for POP 4–3abs for all k; diminishing the matrix element considerably. Conversely, for POP 3–4abs at small k, both k and k' are on portions of the band which rise very steeply with k, so that $q_{\min}$ remains small and the matrix element is enhanced. Indeed, this $1/q^2$ coupling gives, for POP 3–4abs, the largest of all the POP matrix elements.

The remaining matrix elements for optical phonon absorption need only be discussed briefly. The $1 \leftrightarrow 3$ and $2 \leftrightarrow 3$ matrix elements display considerable oscillatory structure, due to interactions between strongly mixed initial and final states whose characters are not correlated in any simple way. A general point concerning the POP matrix elements, compared with their NPO counterparts, is that the former tend to show a steeper fall-off at large k. This is a consequence of the integration over polar angle, which results in all values of $q_{\|}$ between $q_{\min} = |k' - k|$ and $q_{\max} = k' + k$ contributing to the matrix element. For large k, $q_{\max}$ will be very large, and, irrespective of the value of $q_{\min}$, this will tend to reduce the value of the matrix element.

Figs. 6.10–13 show the matrix elements for optical phonon emission (em). These contain no new information concerning the effect of the quantum confined bandstructure on optical scattering, since the processes represented here involve the same pairs of states for any given transition, but with their rôles as 'initial' and 'final' scattering states reversed. However, we show the optical phonon emission matrix elements here: firstly, because POP emission is the dominant scattering process in bulk GaAs, and so it is instructive to see how the matrix elements vary with the wavevector of the emitting (initial) state; and secondly, to demonstrate that our 4-band k.p calculation is, indeed, invariant upon reversal of the scattering states.

The complicated nature of the band dispersions does introduce significant differences between the forms of the matrix elements when viewed as a function of the wavevector of the upper (energy) state (as for emission), compared to their forms when plotted against the lower state wavevector (as for absorption). For example: the NPO and POP 1–1em matrix elements rise sharply immediately following threshold (Figs. 6.10(a) and (d)); whereas the complementary (1–1abs) processes change little between $k = 0$ and $k \approx 0.01\text{Å}^{-1}$ (Figs. 6.6(a) and (e)). This is simply because band 1 is flatter near the zone centre than at large k. A more emphatic example is the case of the POP 4–4 processes. The POP 4–4a em matrix element rises extremely rapidly to a maximum just beyond threshold (Fig 6.13h), whereas

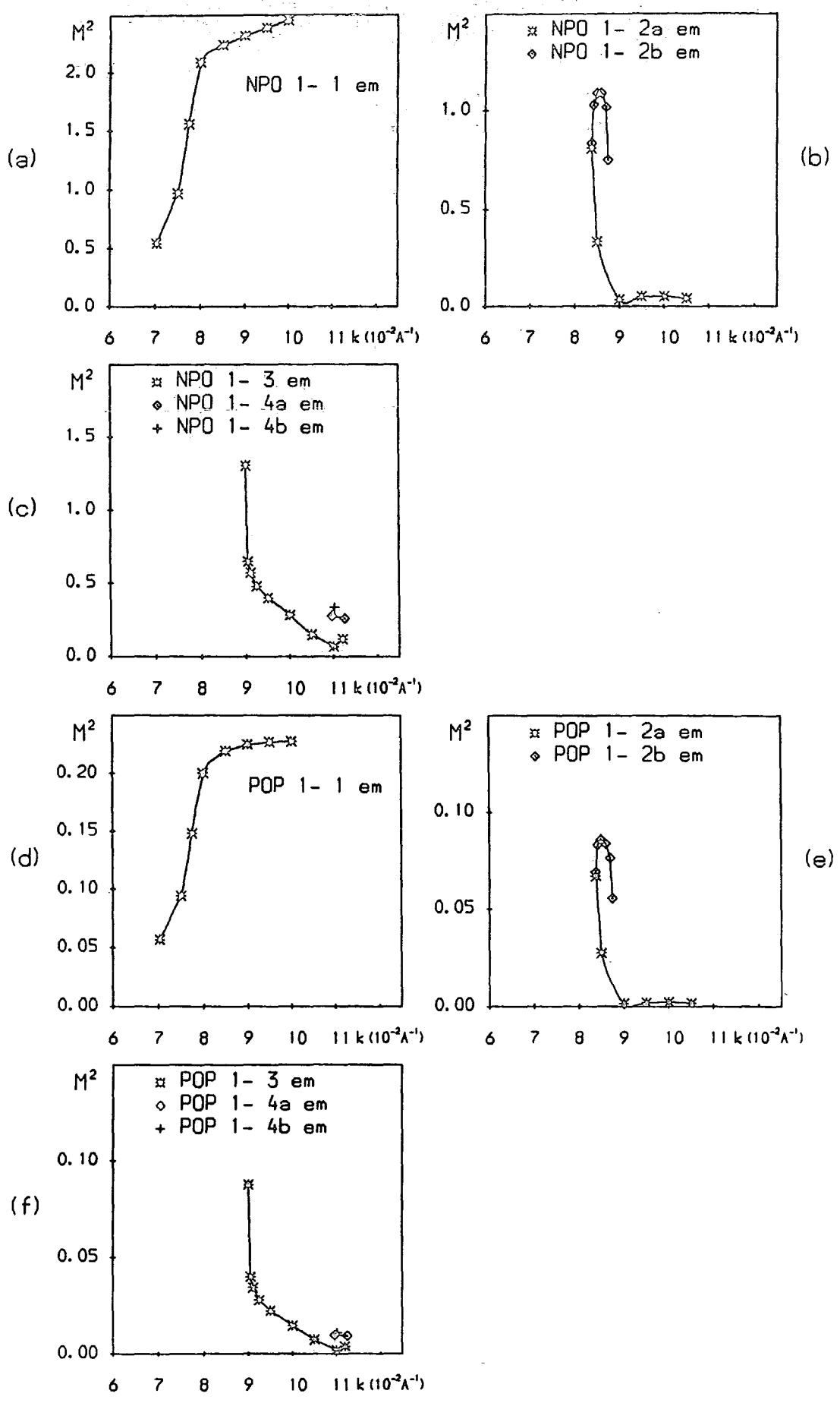

Fig. 6.10 Matrix elements for optical phonon emission processes for a hole in state $|k\rangle$ in band 1.

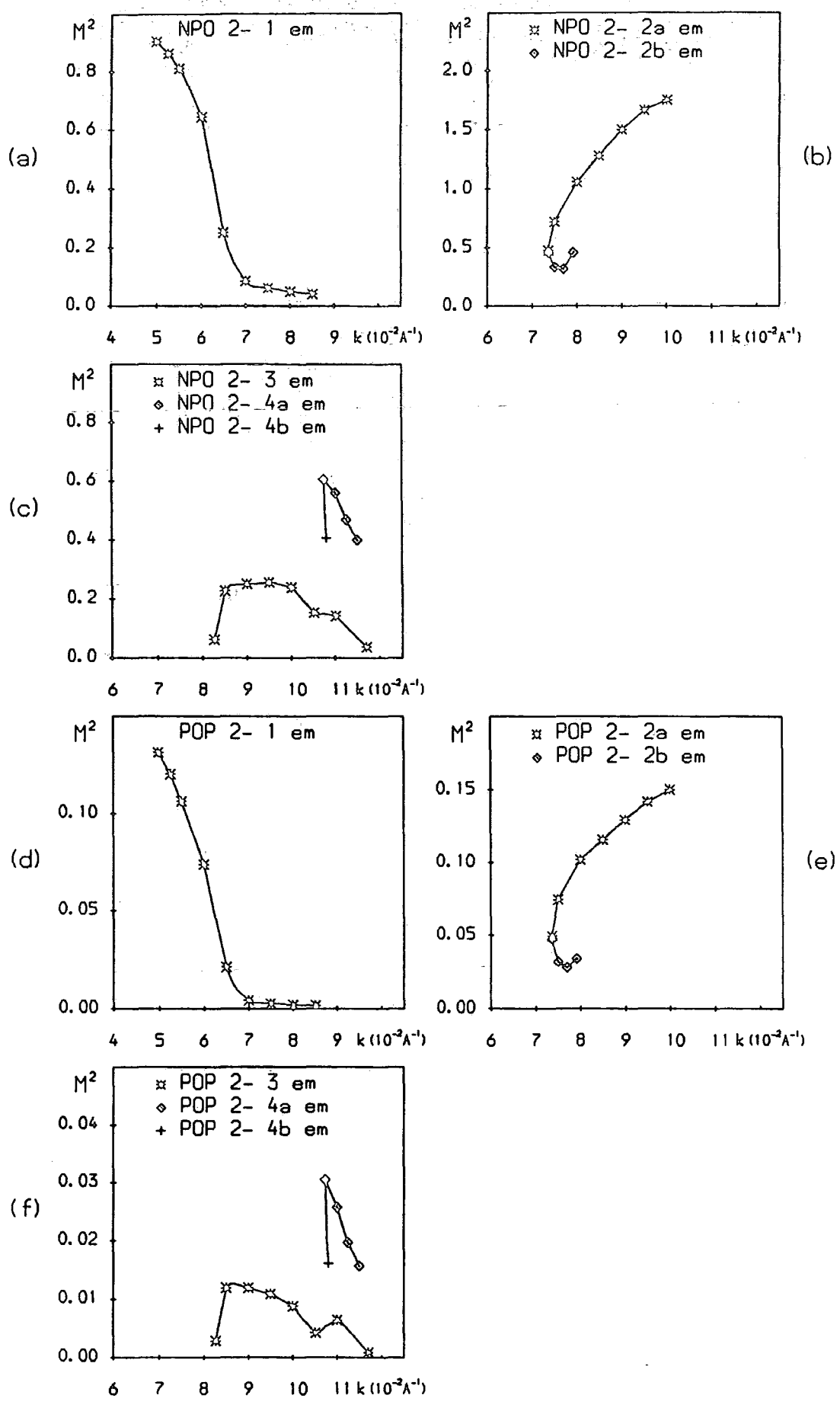

Fig. 6.11 Matrix elements for optical phonon emission processes for a hole in state $|k\rangle$ in band 2.

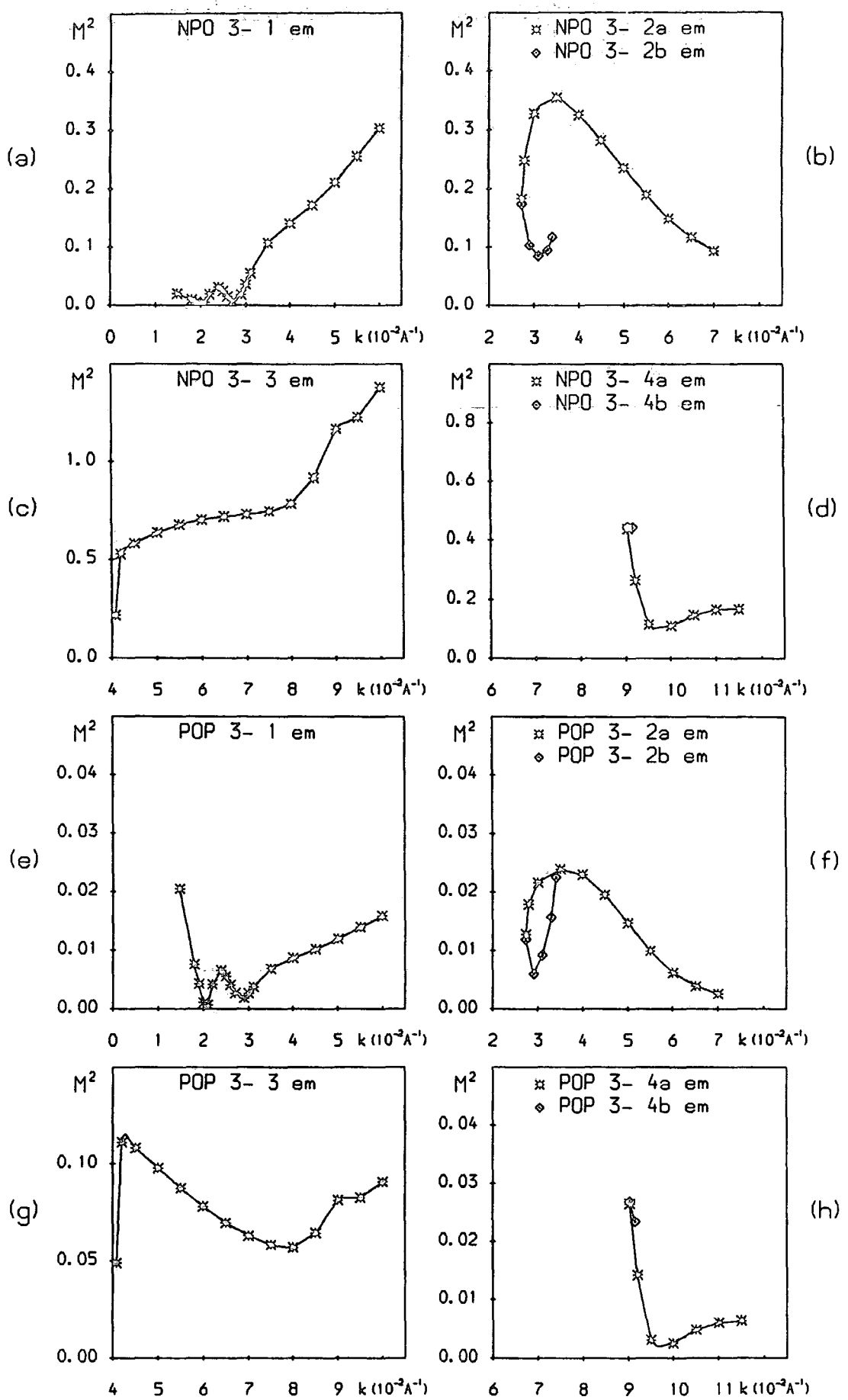

Fig. 6.12 Matrix elements for optical phonon emission processes for a hole in state $|k\rangle$ in band 3.

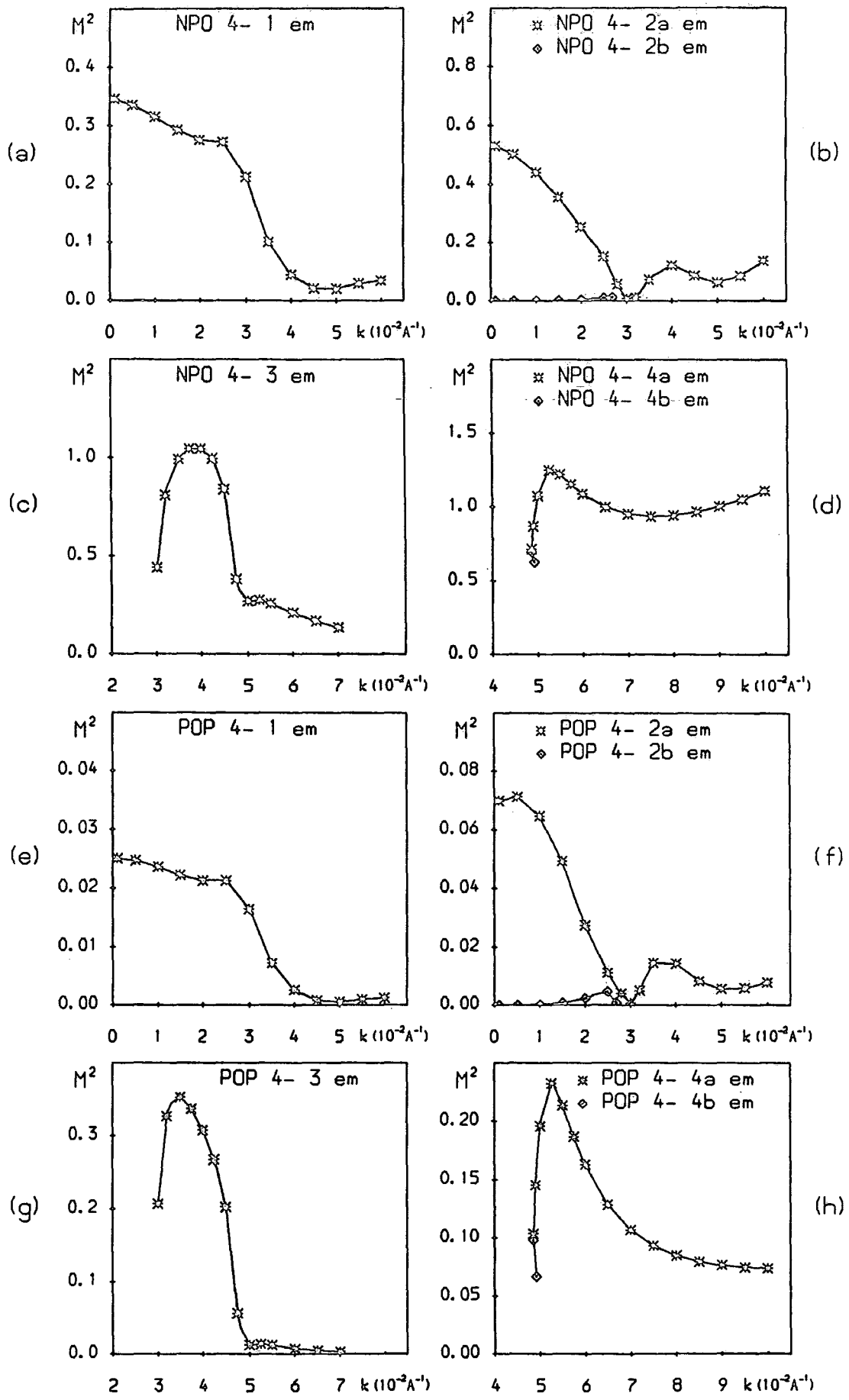

Fig. 6.13 Matrix elements for optical phonon emission processes for a hole in state $|k\rangle$ in band 4.

the POP 4–4abs matrix element is relatively invariant for $k < 0.015\text{Å}^{-1}$, and does not peak until $k \approx 0.032\text{Å}^{-1}$ (Fig. 6.9h). The difference between the two plots here arises because, at the emission threshold, the final state for both *a* and *b* processes lies at the band 4 minimum ($k = 0.02125\text{Å}^{-1}$). Thus, the transitions represented by the portion of the POP 4–4abs matrix element plot for $k < 0.02125\text{Å}^{-1}$ are, in Fig. 6.13h, represented by the POP 4–4*b* em curve, which spans only a very small range of wavevectors since the *b* region of band 4 is so flat. The same effect can be observed for other processes where the lower energy state is in band 4. In the case of POP 2–4 em (Fig. 6.11f), the near vertical line for 2–4*b* em represents the range of transitions covered by the POP 4–2abs curve (Fig. 6.9f) for all $k < 0.02125\text{Å}^{-1}$.

These dispersion effects have much less influence on processes in which the lower energy state is in band 2 (2*b* processes), since the *b* region of band 2 is not nearly so flat. However, distinctive features also occur in these cases, as a result of band mixing. The 1–2*b*, 2–2*b*, and 3–2*b* optical emission matrix elements all show cup-like or inverted cup-like features (Figs. 6.10(b) and (e); 6.11(b) and (e); 6.12(b) and (f)). These appear because the matrix element changes rapidly, both at threshold (due to the changing character of the final (2*b*) states near the band minimum), and at the upper wavevector limit for the process (due to the changing character of the 2*b* states near the zone centre). Thus, a general characteristic of the *b* processes is that the matrix elements display rather abrupt features.

The matrix elements for all pairs of *a* and *b* processes should coincide at threshold, since the final (lower energy) state then lies at the band minimum, which represents the intersection of the *a* and *b* regions of the band. In this sense, the 4–2*b* optical emission process is anomalous. The *b* process matrix element is small throughout, and at no point meets the curve for the *a* process (Figs. 6.13(b) and (f)). This is simply because there is no threshold. 4–2 optical emission is allowed at $k = 0$, but the *a* and *b* final states are well separated in *k*-space. The *b* state lies very close to the zone centre for all allowed initial *k*, and, because of the lack of $|0,4\rangle$ character in this region, the 4–2*b* matrix element remains very small.

6C.2: Matrix Elements for Acoustic Phonon Scattering

The matrix elements for acoustic (AC and PZ) phonon scattering are shown in Figs. 6.14–17. The quantity plotted for AC processes is $(L/4)\mathcal{M}^2_{k'n',kn}$, as for NPO scattering; and that for PZ, $(1/4L)\mathcal{M}^2_{k'n',kn}$, as for POP scattering. The PZ matrix elements include an integration over polar angle β, from the definition of $\mathcal{M}^2_{\rm PZ}$, as was the case for the POP matrix elements.

We consider first the intraband AC matrix elements AC 1–1 and AC 3–3 (Figs. 6.14a and 6.16c). The matrix elements are large (compared to the NPO results), with values approaching the 1-band infinite square well result of $3\pi/4$, and are relatively invariant with k. These features are to be expected, since here we are considering matrix elements involving identical initial and final states (within the approximation of elastic scattering). We will check whether these features are preserved on displacement of the scattering states later in this section.

For AC 2–2 and 4–4 scattering we have adopted a slightly different convention. Rather than plotting on one curve, the matrix element for scattering into a states, and on the other, that for scattering into b states; we have shown one curve for 'identical state scattering', and a second for 'cross valley' scattering. The 'identical state' curve is analogous to the curves for the AC 1–1 and AC 3–3 processes; giving the matrix element between states of the same energy and wavevector magnitude. These states will be b type for $k < k_n(0)$ and a type for $k \geq k_n(0)$; hence the labelling '*b*-*b* & *a*-*a*' on Figs. 6.15b and 6.17d. The 'cross valley' curve gives the matrix element between states of the same energy in band 2 or 4, but lying on opposite sides of the band minimum. Thus, the curve shows the matrix element for $b \rightarrow a$ transitions for $k < k_n(0)$ and $a \rightarrow b$ transitions for $k \geq k_n(0)$. The upper energy limit for such processes is the zone centre energy, as for the other b processes. This modified convention is preferable for intraband acoustic scattering, since the identical state processes form a distinct set which should be shown together. Similarly, the cross valley transitions represent another category, having common properties different from those of the identical state processes.

We see that for AC 2–2 and 4–4 identical state processes (Figs. 6.15b and 6.17d), the matrix elements are large and flat, as was found for AC 1–1 and 3–3 scattering. The cross valley matrix elements coincide with the identical state plots at the wavevectors of the band minima, as expected. At this point, the cross valley matrix elements are at a maximum value, and decrease as k either increases or decreases; since the scattering states move in opposite directions along the band, and become progressively less alike in character. The 4–4 cross valley process actually remains quite large, away from the band minimum, because all states below the band 4 zone centre energy retain substantial $|0,4\rangle$ character.

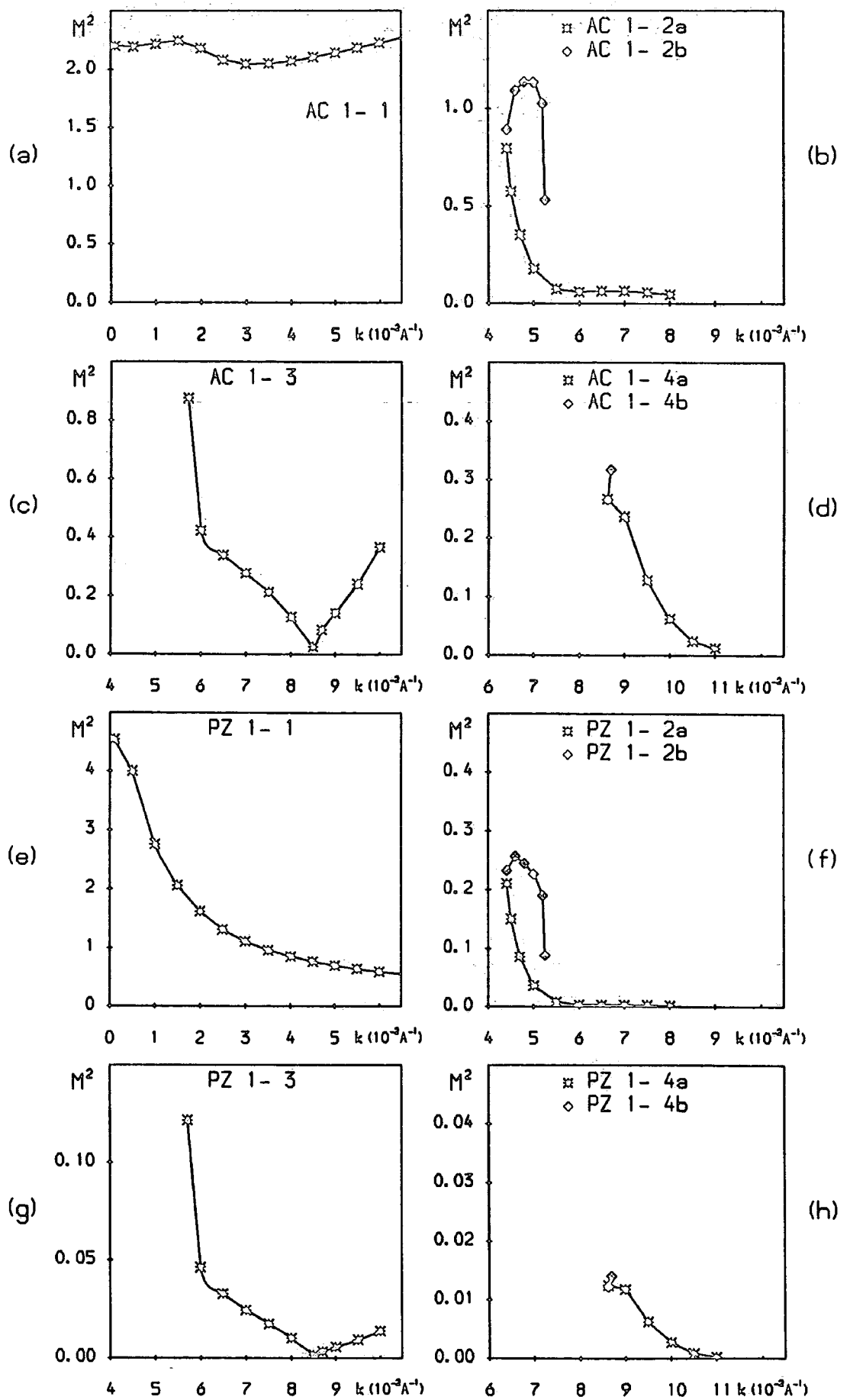

Fig. 6.14 Matrix elements for acoustic scattering processes for a hole in state $|k\rangle$ in band 1.

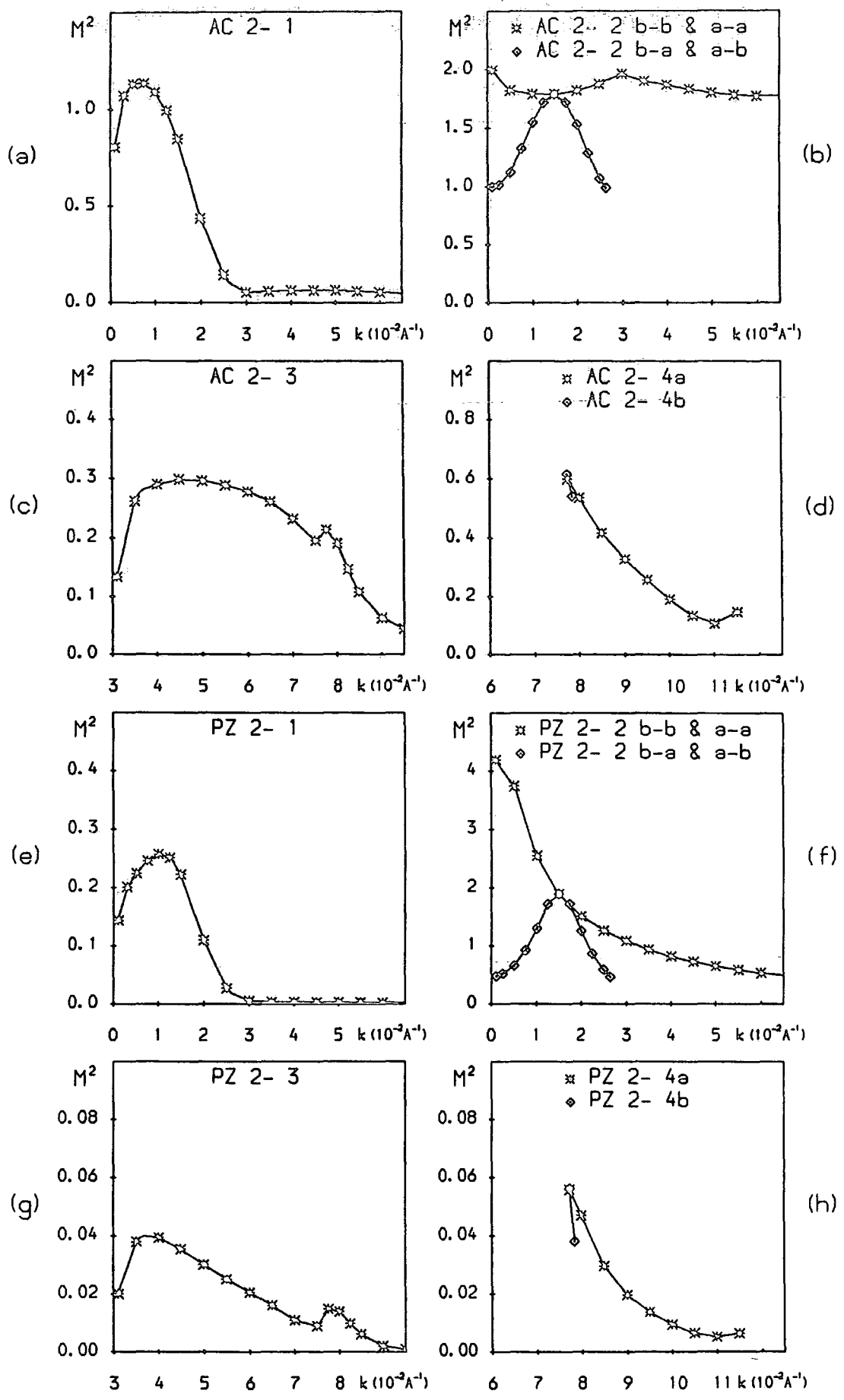

Fig. 6.15 Matrix elements for acoustic scattering processes for a hole in state $|k\rangle$ in band 2.

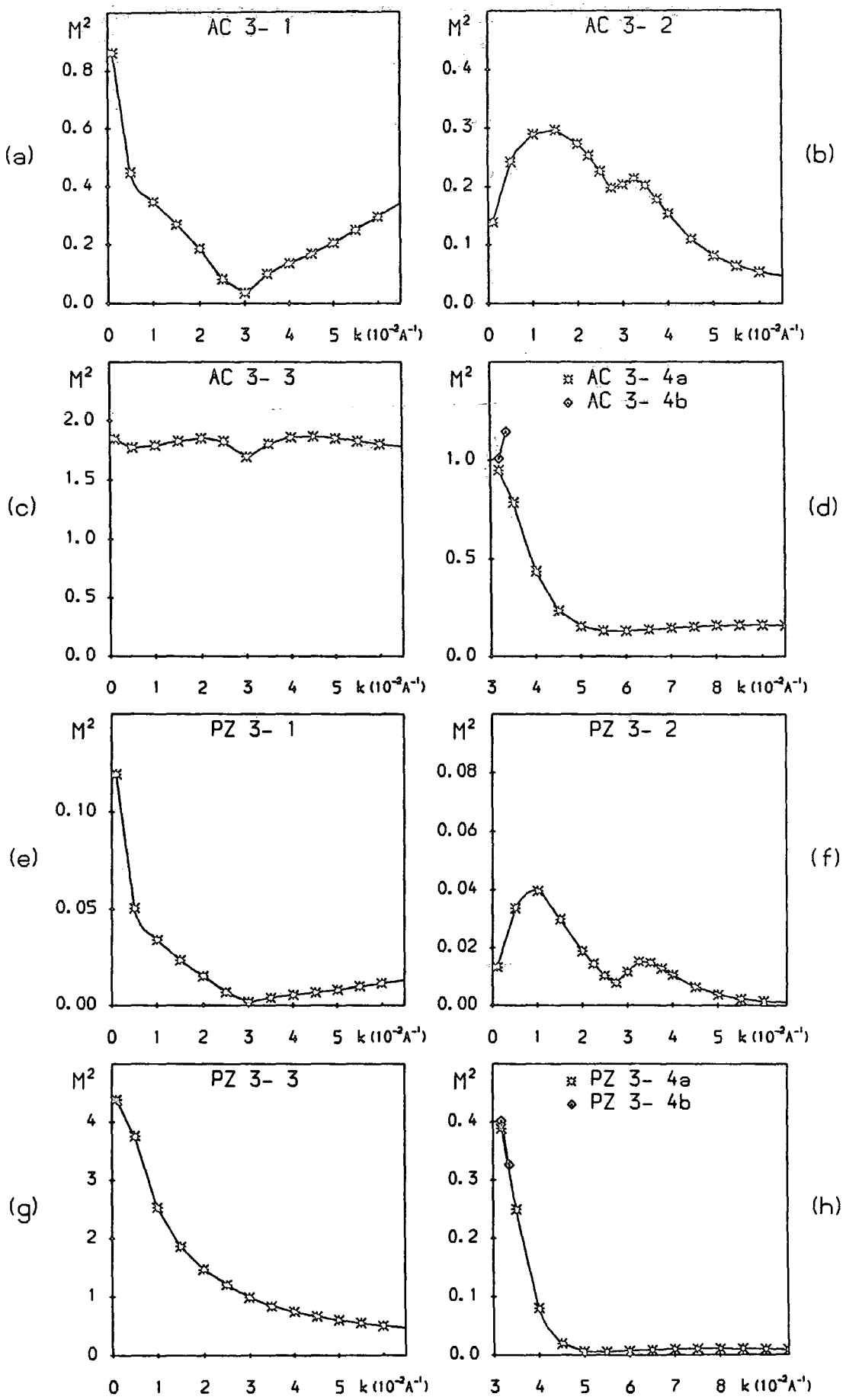

Fig. 6.16 Matrix elements for acoustic scattering processes for a hole in state $|k\rangle$ in band 3.

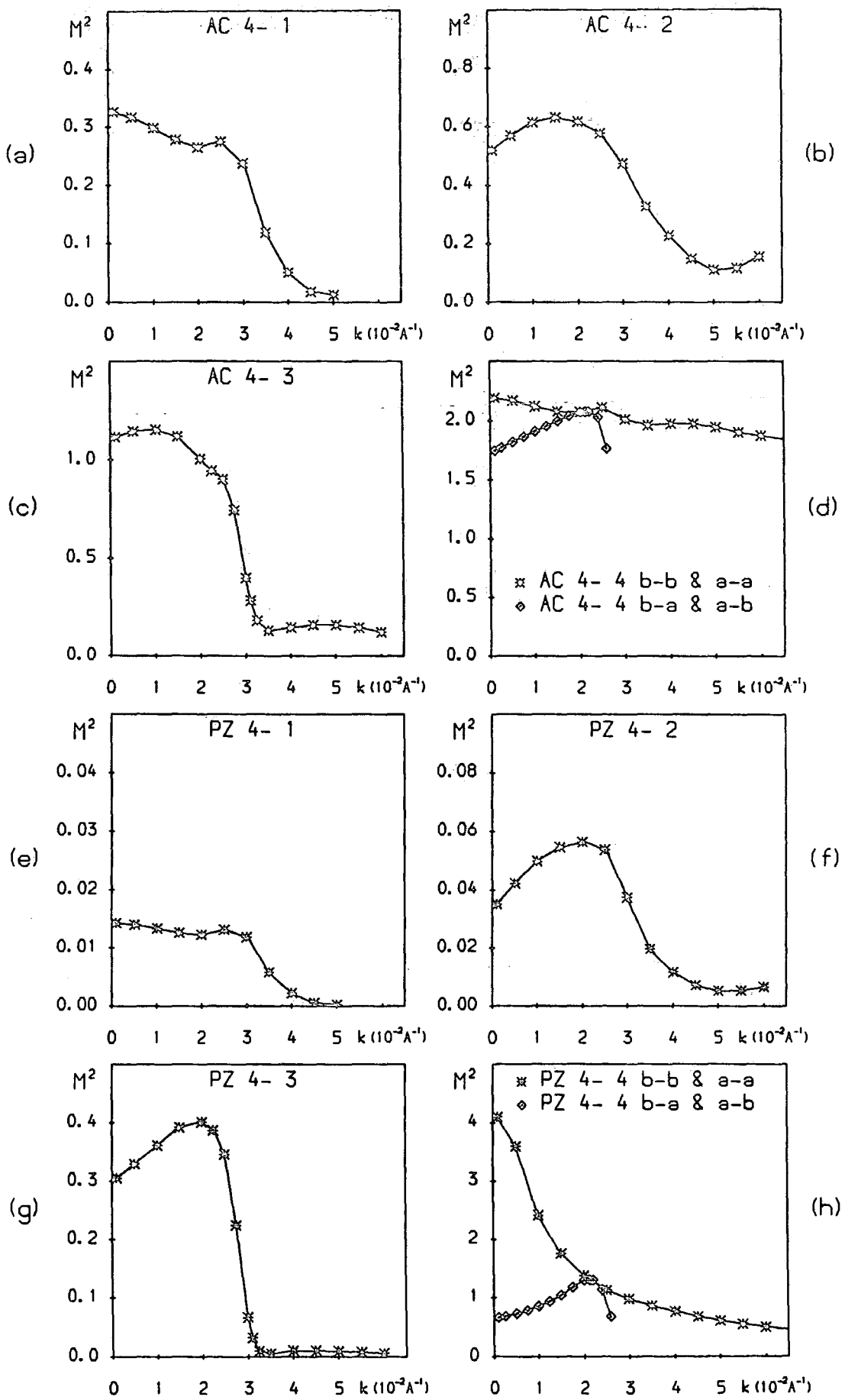

Fig. 6.17 Matrix elements for acoustic scattering processes for a hole in state $|k\rangle$ in band 4.

For interband scattering, we can recognise several types of feature which were previously observed in the optical phonon matrix elements. The inter-anticrossing-band matrix elements, AC 1–2, 2–1, 3–4, 4–3 (Figs. 6.14b, 6.15a, 6.16d, and 6.17c), all show a distinctive fall-off as either k or k' traverses the anticrossing region. In this case of course, with scattering taken as elastic, AC 1–2 and 2–1, and AC 3–4 and 4–3, are actually complementary processes (*i.e.*; processes involving the same pairs of initial and final states). The differences in the form of the matrix elements are only due to taking, in the the one case, k in band n, and in the other, k in band n', as the independent variable in the graphs. As in the case of NPO scattering, these inter-anticrossing-band matrix elements are notably larger than those for the remaining processes. The only interband b process covering a significant wavevector range is AC 1–2b, and this shows the inverted cup-like shape previously identified as typical for a 2b process.

We have calculated PZ matrix elements in the presence of free carrier screening (see section 5C.3) and have used a reciprocal screening length q_0 appropriate to a free carrier density of 10^{16}cm^{-3}. This choice will be discussed in section 6E.

The intraband PZ matrix elements (Figs. 6.14e, 6.15f, 6.16g, and 6.17h) are all extremely large (over an order of magnitude larger than most of the interband matrix elements), and are virtually identical in form. Clearly the matrix elements are dominated by the $1/q^2$ dependence of PZ scattering, which gives rise to the characteristic fall-off as q_{max} increases with k. The size of the matrix elements is largely dictated by the value of q_0, since, with no screening ($q_0 = 0$), the intraband PZ matrix elements would be infinite for all k. For PZ 2–2 and 4–4 scattering, we have plotted matrix elements for identical state and cross valley transitions, as described for the AC case. The identical state matrix elements clearly bear the same characteristics as those for the 1–1 and 3–3 processes, whilst the cross valley matrix elements are considerably smaller at small k due to the non-zero value of q_{min}. It is interesting to note that for both PZ 2–2 and 4–4 scattering, the cross valley matrix element exceeds the identical state value for k just beyond the band minimum. This occurs because, at this point, q_{max} for the cross valley process is actually less than that for identical state scattering (since in the former case, $k' < k_n(0)$).

Turning to the interband PZ matrix elements, we find that the dominance of the inter-anticrossing-band processes PZ 1–2, 2–1, 3–4, 4–3 (Figs. 6.14f, 6.15e, 6.16h, and 6.17g), survives in the presence of $1/q^2$ weighting. This is because, at small k, the (equal energy) scattering states are not widely separated in k-space, as was found for optical scattering states. Therefore q_{min} remains small. Indeed, for PZ 4–3 scattering, near the anticrossing point the scattering states

are very close together, and this serves to enhance the PZ 4–3 matrix element in this region (Fig. 6.17g). (At large wavevectors, the equal energy scattering states in bands 1 and 2 are also very close together in k-space, but the consequent reduction in $q_{\min}$ is overshadowed by the large value of $q_{\max}$ at large k, hence the matrix element as presented here remains small.) As was observed for POP scattering, the $1/q^2$ dependence serves in general to diminish all the PZ matrix elements considerably at large k. For processes involving remote bands, such as PZ 1–4 and 4–1 (Figs. 6.14h and 6.17e), the separation of scattering states in k-space is so large that the matrix element is small throughout the range of k. The PZ 1–4 and 4–1 matrix elements are over an order of magnitude less than the inter-anticrossing-band matrix elements, and over two orders of magnitude less than the intraband PZ matrix elements.

Energy Dissipation in Acoustic Processes

We commented earlier in this section that, for intraband acoustic (AC and PZ) scattering, the approximation of elastic scattering results in the selection of initial and final states which are identical. Obviously this leads to very large matrix elements as were shown in Figs. 6.14–17. It would be instructive to ascertain whether these large values survive when the scattering states are displaced by typical acoustic phonon energies.

The acoustic phonon energy in 3D is given by $\epsilon_{ph} = \hbar v_s q$. Here, we will assume that $\epsilon_{ph} = \hbar v_s q_{\|}$, and therefore, that the maximum value of ϵ_{ph} for a given k is $2\hbar v_s k$. Taking $v_s = \overline{v} = 3.860\text{ms}^{-1}$ (see Table 4.1), we obtain $\epsilon_{ph,\max} \approx 50{\times}k\,\text{meV}$, for k in units of Å^{-1}.

We have considered the case of AC 1–1 scattering, and calculated matrix elements for several different values of k, with the final state displaced in energy by $\pm\epsilon_{ph,\max}$ with respect to the initial state. The results of these calculations are shown in Table 6.5, and it is clear that the changes in the matrix elements introduced are very small (typically 1%), especially when compared to the difference in the size of the matrix elements for intra- and inter-band scattering.

It may be concluded, therefore, that these large matrix elements represent a genuine result for intraband acoustic scattering in the quantum confined valence band system. The initial and final states for such scatterings will lie sufficiently close together on the energy band that their characters will be very similar, giving a large enhancement of the matrix elements over those for interband scattering. This effect may also prevail when anisotropy of the bands is taken into account, provided that the shift introduced in the band energies at different orientations is of no greater order than the typical acoustic phonon energies discussed above.

k_i ($\times 10^{-2}$Å^{-1})	ϵ_i (meV)	ϵ_{ph} (meV)	$(L/4)\mathcal{M}^2$
0.5	7.804	0.0	2.196
		0.25	2.196
		-0.25	2.196
1.0	9.775	0.0	2.217
		0.5	2.220
		-0.5	2.212
1.5	12.63	0.0	2.243
		0.75	2.233
		-0.75	2.238
2.0	15.12	0.0	2.177
		1.0	2.094
		-1.0	2.165
2.5	16.76	0.0	2.079
		1.25	2.017
		-1.25	2.035
3.0	18.04	0.0	2.044
		1.5	2.032
		-1.5	1.999
4.0	21.22	0.0	2.068
		2.0	2.081
		-2.0	2.051
6.0	33.86	0.0	2.223
		3.0	2.237
		-3.0	2.207

Table 6.5: Matrix Elements for AC 1–1 scattering

The matrix elements are shown for elastic scattering ($\epsilon_{ph} = 0$), and for the displacement of the scattering states by $\pm(\epsilon_{ph,\max} = 2\hbar v_s k_i)$ — see text. k_i and ϵ_i give the wavevector and energy, respectively, of the initial state.

6D ANGULAR DEPENDENCE OF THE MATRIX ELEMENTS

It was shown in section 5C.3 that, in the isotropic approximation, the AC and NPO matrix elements were independent of polar angle β. For POP scattering, the angular dependence of the matrix element is given by the term $\mathcal{F}^2_{k'n',kn}(\cos\beta)$ of equation (5.57):

$$\mathcal{F}^2_{k'n',kn}(\cos\beta) = \int \frac{|J_{k'n',kn}(q_z)|^2}{q_{||}^2 + q_z^2}\, dq_z, \tag{6.2}$$

where $q_{||}^2 = k^2 + k'^2 - 2kk'\cos\beta$.

Since, in the isotropic approximation, the envelope function term $J_{k'n',kn}(q_z)$ contains no dependence on β, the angular dependence of the POP scattering rate arises entirely from the polar weighting factor $1/(q_{||}^2+q_z^2)$. Therefore, we expect an angular dependence akin to that derived from a $1/q_{||}^2$ law, but somewhat weakened by the contribution from q_z, which is averaged over all q_z without restriction.

In Fig. 6.18 we have shown the angular dependence, $(1/4)L\mathcal{F}^2_{k'n',kn}(\cos\beta)$, of the POP 1–1abs scattering rate for a range of k. The dotted curves show the unmodified $1/q_{||}^2$ dependence for scattering between the same states, normalised to the $\mathcal{F}^2_{k'n',kn}(\cos\beta)$ curves at $\cos\beta = 1$. The POP 1–1abs matrix element, integrated over all polar angles, is small at small k and large at large k — see Fig. 6.6e. This is reflected by the ascending order of the curves with k at $\cos\beta = 1$. The curves for all values of k fall off as β increases; however the reduction in $\mathcal{F}^2_{k'n',kn}(\cos\beta)$ is much greater for the largest wavevector considered ($k = 0.04\text{Å}^{-1}$). This is simply due to the larger range of $q_{||}$ involved. The $1/q_{||}^2$ curves show the same trends, but as expected they give too strong a dependence on β, especially for the case $k = 0.04\text{Å}^{-1}$.

Fig. 6.19 shows the same information for the POP 1–2abs process. Here the matrix element is large at small k and small at large k (Fig. 6.6f). This is again reflected by the ordering of the curves at $\cos\beta = 1$. The fall off of the curves with increasing polar angle is much less marked than for POP 1–1abs, because at large wavevectors the matrix element is small due to mixing, and at small wavevectors the range of $q_{||}$ is small. Again the $1/q_{||}^2$ curves show a similar trend, but with a stronger dependence on $\cos\beta$ than the $\mathcal{F}^2_{k'n',kn}(\cos\beta)$. We may surmise that the form of the angular dependence for the other POP processes could be reasonably well approximated by the simple $1/q_{||}^2$ response. It may also be concluded that the intraband POP processes will exhibit the strongest angular dependence, since only these have large matrix elements at large k. This is an important result, since we have seen that the intraband matrix elements represent the dominant contribution to polar scattering.

The angular dependence of the screened PZ scattering rate has been given by

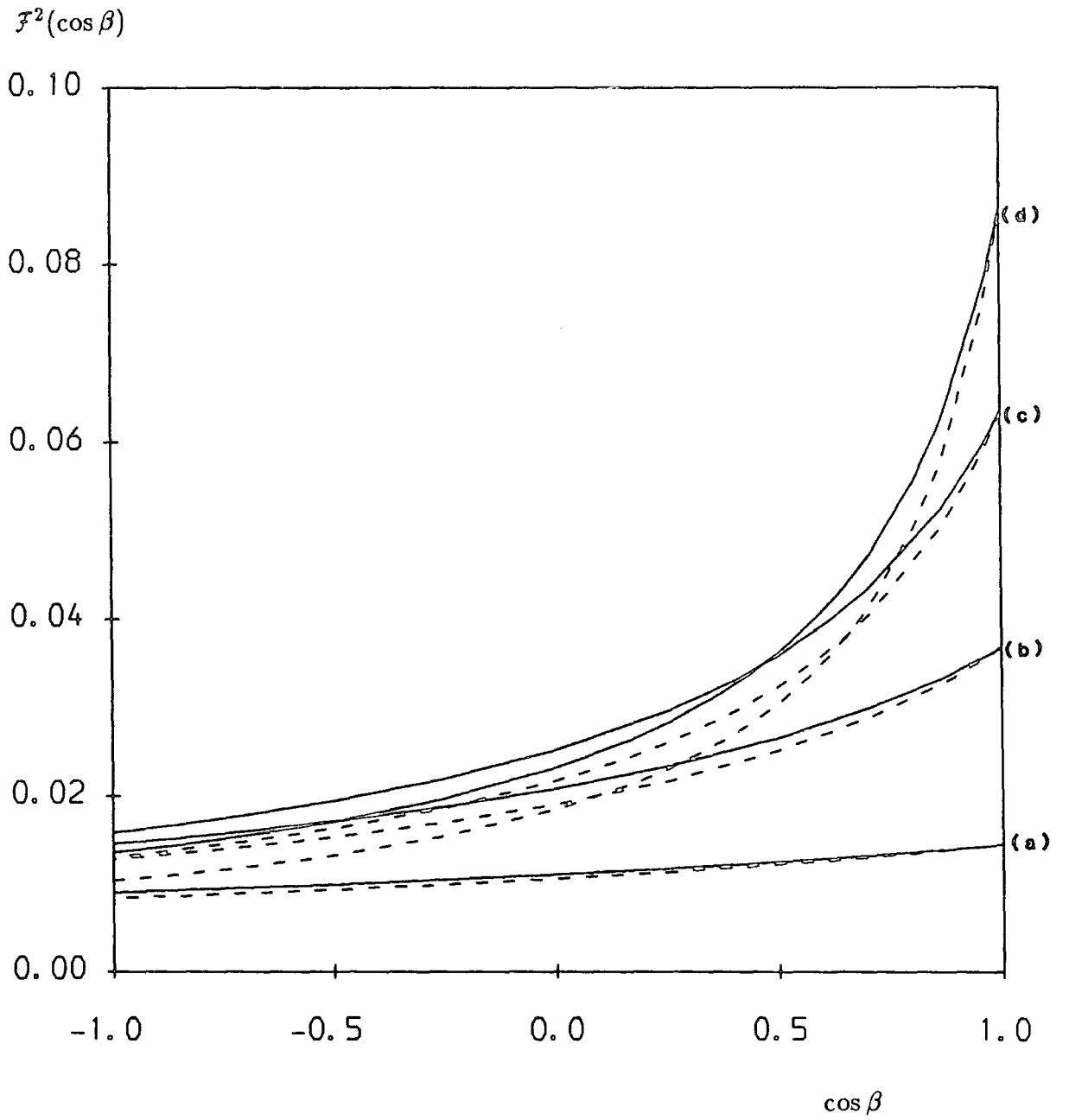

Fig. 6.18 Angular dependence of the POP 1–1abs scattering rate. — full 4-band k.p result; $(1/4L)\mathcal{F}^2_{k'n',kn}(\cos\beta)$. - - - $1/q_{\|}^2$, normalised to the full curves at $\cos\beta = 1$. (a) $k = 0.01\text{Å}^{-1}$; (b) 0.02Å^{-1}; (c) 0.03Å^{-1}; (d) 0.04Å^{-1}.

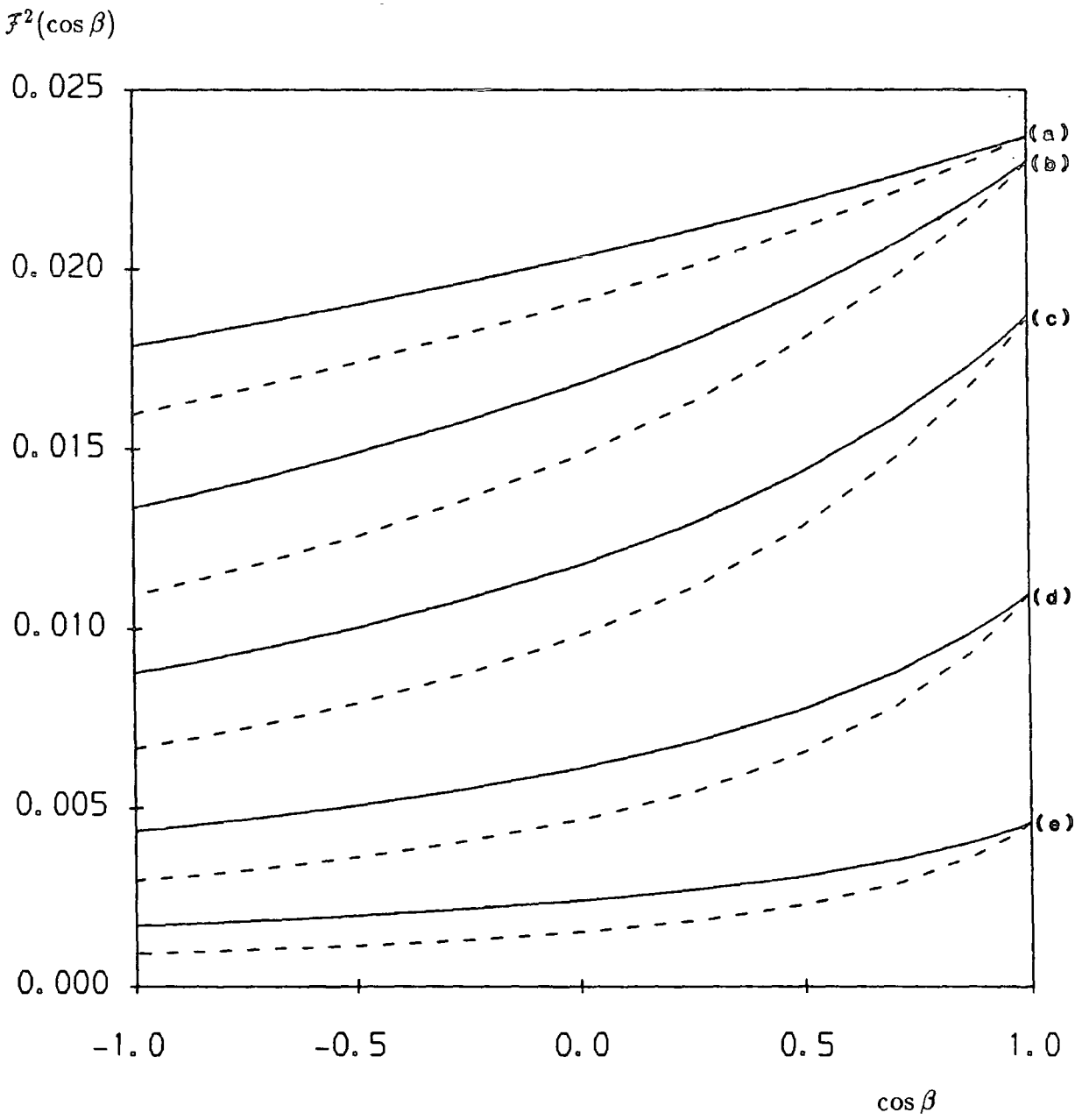

Fig. 6.19 Angular dependence of the POP 1–2abs scattering rate. — full 4-band k.p result; $(1/4L)\mathcal{F}^2_{k'n',kn}(\cos\beta)$. - - - $1/q_{\|}^2$, normalised to the full curves at $\cos\beta = 1$. (a) $k = 0.005\text{Å}^{-1}$; (b) 0.01Å^{-1}; (c) 0.015Å^{-1}; (d) 0.02Å^{-1}; (e) 0.025Å^{-1}.

equation (5.68):

$$\mathcal{F}^2_{k'n',kn}(\cos\beta) = \int |J_{k'n',kn}(q_z)|^2 \frac{(q_{||}^2 + q_z^2)}{(q_{||}^2 + q_z^2 + q_0)^2}\, dq_z, \tag{6.3}$$

where, as for POP scattering, only $q_{||}$ varies with $\cos\beta$. In Fig. 6.20 we have plotted $(1/4L)\mathcal{F}^2_{k'n',kn}(\cos\beta)$, for intraband (1–1) scattering over a range of k values. The striking feature of these curves is that the function is non-zero at $\beta = 0$, and furthermore, that its value at this point is almost independent of k. This is a consequence of the lack of momentum conservation in the z direction. When $\beta = 0$, $q_{||} = 0$ also (for elastic scattering), but the contribution to scattering from non-zero values of of q_z gives a non-zero value for the matrix element. For 3D piezoelectric scattering, momentum conservation holds in all directions, giving $q = 0$ at zero scattering angle (elastic case), and hence a zero valued matrix element. The invariance of the $\beta = 0$ matrix element with k arises because, for elastic intraband scattering involving identical states, the term $|J_{k'n',kn}(q_z)|^2$ is near-unity and changes little with k. Using this fact we can take the $|J(q_z)|^2$ term outside the integral of equation (6.3) and write, as an approximation for intraband PZ scattering:

$$\mathcal{F}^2_{k'n,kn}(\cos\beta) \propto \int_{-\infty}^{\infty} \frac{(q_{||}^2 + q_z^2)}{(q_{||}^2 + q_z^2 + q_0^2)^2}\, dq_z. \tag{6.4}$$

This integral can readily be evaluated to give

$$\mathcal{F}^2_{k'n,kn}(\cos\beta) \propto \frac{\pi}{2} \frac{(2q_{||}^2 + q_0^2)}{(q_{||}^2 + q_0^2)^{3/2}}. \tag{6.5}$$

This result reduces to $\pi/2q_0$ at $q_{||} = 0$ ($\beta = 0$) — a fixed (k-independent), non-zero value, as required. In Fig. 6.20 we have compared this approximate angular dependence with the full numerical result; finding good agreement for small k. Fig. 6.21 shows $(1/4L)\mathcal{F}^2_{k'n',kn}(\cos\beta)$ compared with the angular dependence for 3D piezoelectric scattering; $q^2/(q^2+q_0^2)^2$, with $q^2 = k^2 + k'^2 - 2kk'\cos\beta$ (unity overlap case; see Sections 3B and 4B). The curves for the 3D approximation are normalised to the values of $(1/4L)\mathcal{F}^2_{k'n',kn}(\cos\beta)$ at $\cos\beta = -1$. Besides the difference in values at $\beta = 0$, the 3D function has a large peak corresponding to the point $q = q_0$, which does not appear in the 2D case. In contrast, the approximate intraband 2D angular dependence (equation (6.5) above) has a maximum at $q_{||} = q_0/2$ of magnitude $\approx 0.544\pi/q_0$; which represents only a small magnification of the $q_{||} = 0$ value. Thus the lack of z direction momentum conservation also serves to dampen the $q \approx q_0$ peak in screened PZ scattering. We may say that the contribution to 2D scattering from non-zero values of q_z provides an extra degree of screening of the piezoelectric interaction.

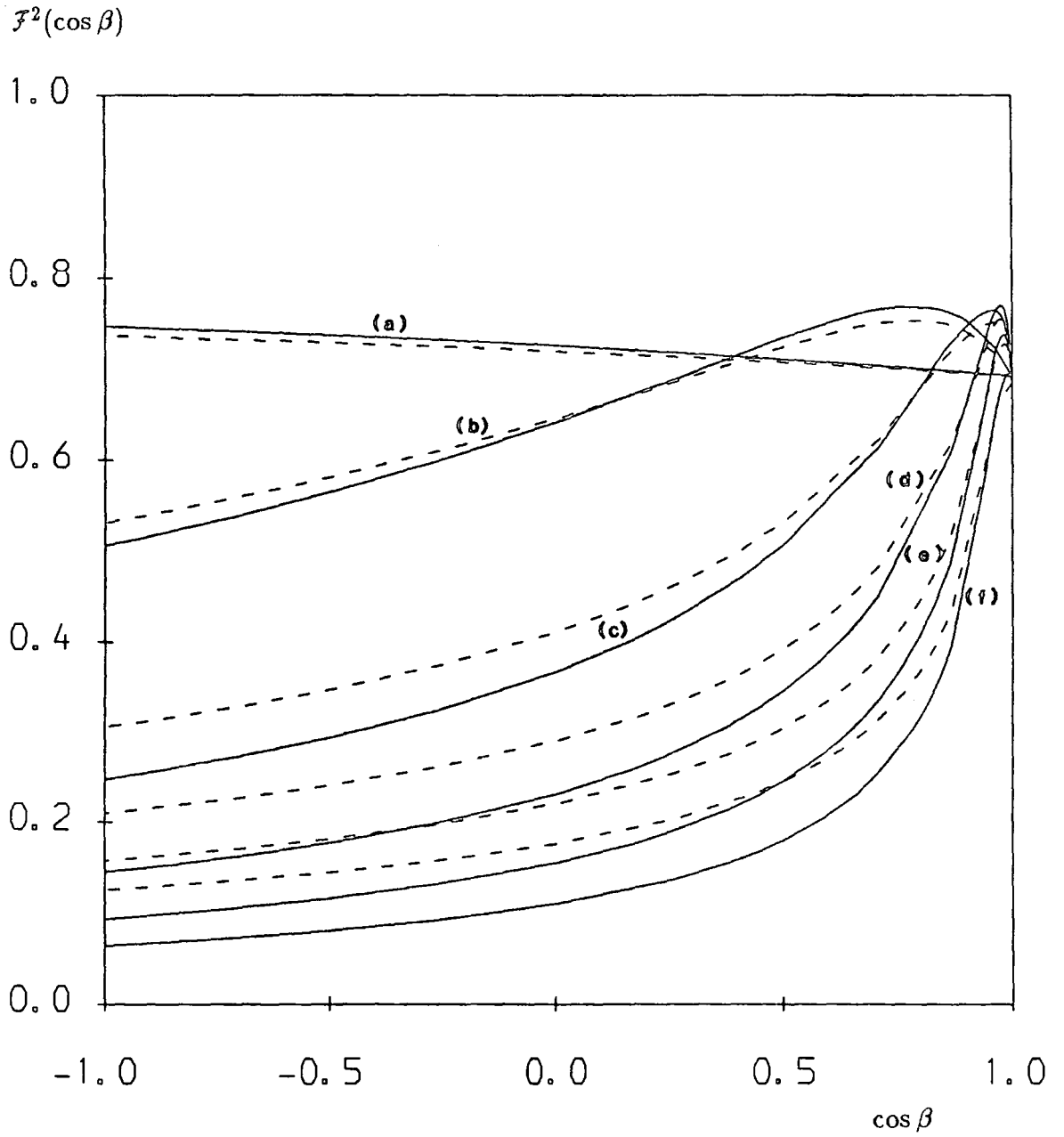

Fig. 6.20 Angular dependence of the PZ 1–1abs scattering rate. — full 4-band **k.p** result; $(1/4L)\mathcal{F}^2_{k'n',kn}(\cos\beta)$. - - - approximate 2D result; $(2q_{\|}^2 + q_0^2)/(q_{\|}^2 + q_0^2)^{3/2}$ (see equation (6.5)), normalised to the full curves at $\cos\beta = 1$. (a) $k = 0.001\text{Å}^{-1}$; (b) 0.005Å^{-1}; (c) 0.01Å^{-1}; (d) 0.015Å^{-1}; (e) 0.02Å^{-1}; (f) 0.025Å^{-1}.

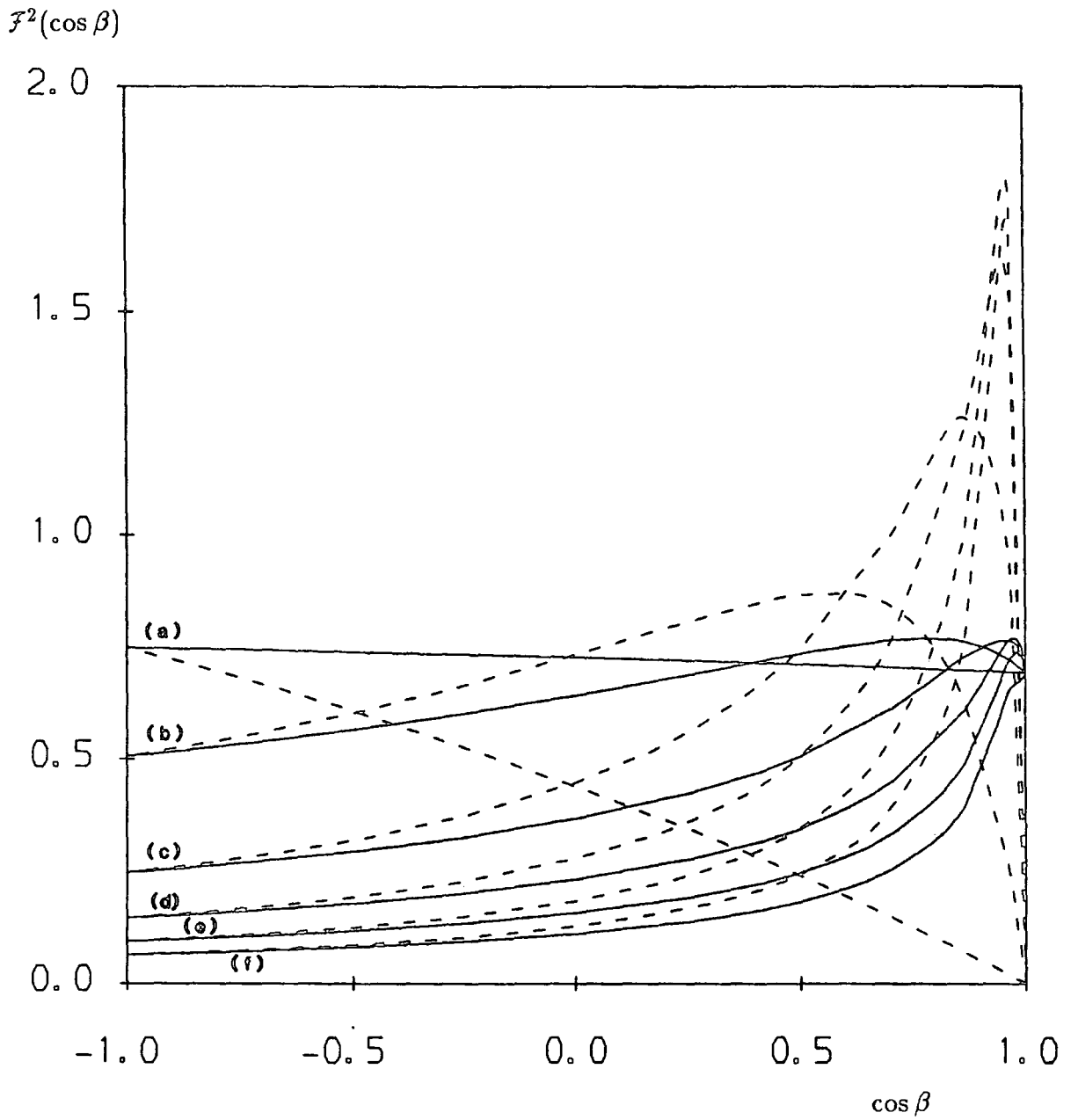

Fig. 6.21 Angular dependence of the PZ 1–1abs scattering rate. — full 4-band **k.p** result, as in Fig. 6.20. - - - approximate 3D result; $q_{\|}^2/(q_{\|}^2+q_0^2)^2$, normalised to the full curves at $\cos\beta=-1$. (a)-(e) as for Fig. 6.20.

Fig. 6.22 shows the angular dependence for interband (1–2) PZ scattering. For interband processes $q_{\|}$ is non-zero at $\beta = 0$, and thus we find that the bulk-like angular dependence $q^2/(q^2+q_0^2)^2$ (dotted curves) gives a reasonable approximation to $\mathcal{F}^2_{k'n',kn}(\cos\beta)$ of equation (6.3).

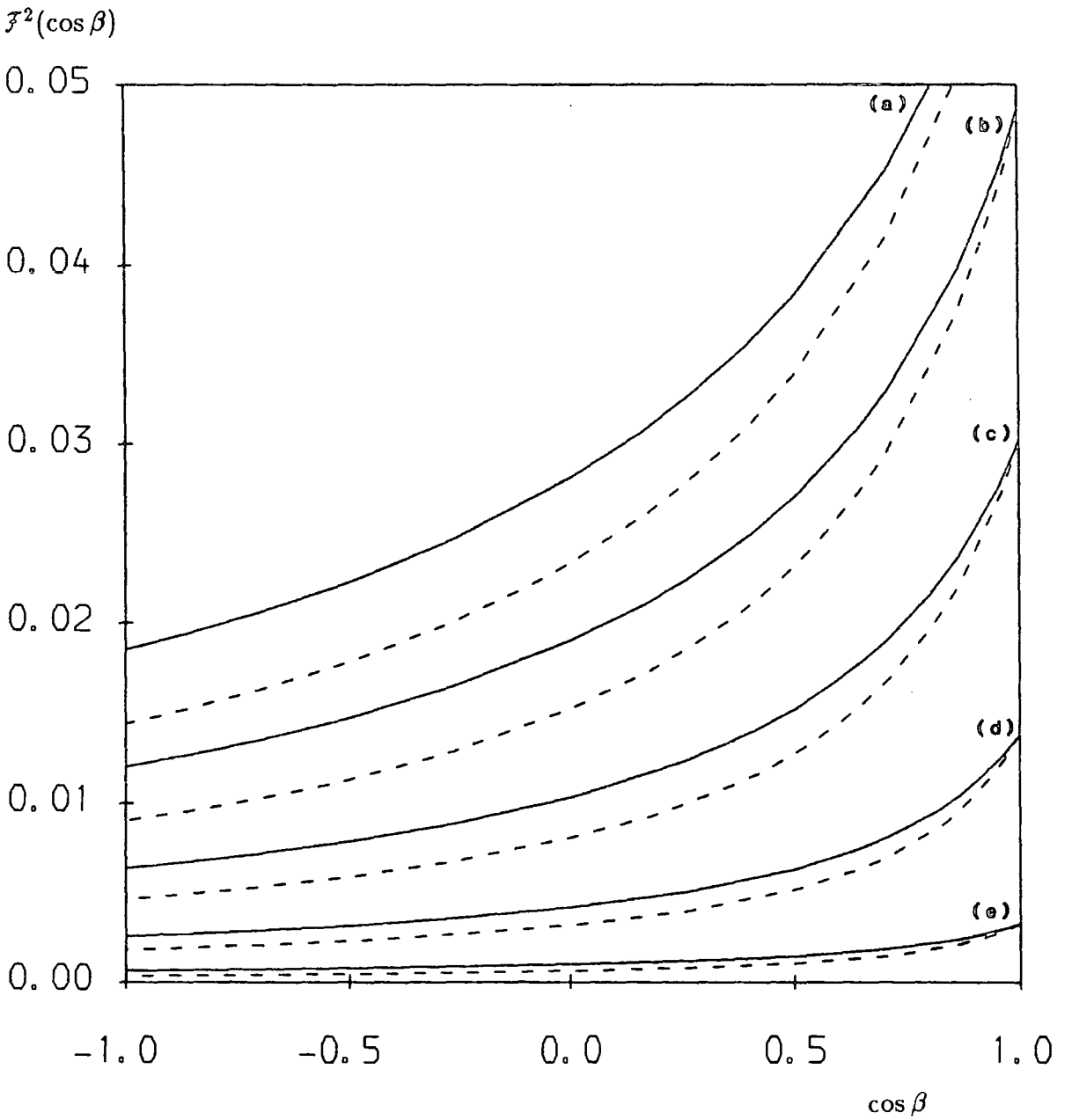

Fig. 6.22 Angular dependence of the PZ 1–2abs scattering rate. — full 4-band **k.p** result; $(1/4L)\mathcal{F}^2_{k'n',kn}(\cos\beta)$. - - - approximate 3D result; $q_\parallel^2/(q_\parallel^2+q_0^2)^2$, normalised to the full curves at $\cos\beta = 1$. (a) $k = 0.0441\text{Å}^{-1}$; (b) 0.045Å^{-1}; (c) 0.047Å^{-1}; (d) 0.05Å^{-1}; (e) 0.055Å^{-1}.

6E SCREENING OF THE POLAR OPTICAL AND PIEZOELECTRIC INTERACTIONS

The matrix elements for PZ scattering shown in Figs. 6.14–17 were calculated assuming the presence of free carrier screening appropriate to a carrier density of $p = 10^{16}\text{cm}^{-3}$. Using equation (4.1), this value gives a reciprocal screening length $q_0 = 4.6266 \times 10^{-3}\text{Å}^{-1}$. This form of screening was included in the PZ calculation purely to allow a finite scattering rate to be obtained. In the Monte Carlo simulations described in the following chapters the carrier density will be assumed to be low: effects such as Pauli exclusion and phonon-plasmon coupling, important at high carrier densities, will not be considered.

The choice of $p = 10^{16}\text{cm}^{-3}$ was made on the basis of our work on PZ scattering of electrons and holes in 3D (Chapters 3 and 4). In this work, PZ scattering for carrier densities greater than 10^{16}cm^{-3} was found to be significantly dampened by screening (Figs. 4.7–10), to the extent that, at $p = 10^{18}\text{cm}^{-3}$, no peak whatsoever was observed in the rate at low energies. Obviously, as p is reduced below 10^{16}cm^{-3}, the scattering rate is further enhanced, since the forward scattering contribution increases according to $1/q_0^4$. Therefore, we took $p = 10^{16}\text{cm}^{-3}$ as the highest free carrier density at which PZ scattering is not heavily damped by screening. This means that the $p = 10^{16}\text{cm}^{-3}$ matrix element is representative of the form of PZ scattering at low carrier densities, but is not magnified to unrealistically large values.

At $p = 10^{16}\text{cm}^{-3}$ it is assumed that POP scattering of holes is unaffected by screening (Lyon 1986). We can readily test this assumption for the case of quantum confined holes by introducing free carrier screening into some of the POP matrix elements. Figs. 6.23–5 show the POP 1–1, 1–2, and 1–3abs matrix elements respectively, with $q_0 = 0$ and $q_0 = 4.6266 \times 10^{-3}\text{Å}^{-1}$. For 1–1 and 1–2abs, screening at $p = 10^{16}\text{cm}^{-3}$ introduces virtually no difference in the matrix elements, and for 1–3abs, where the matrix element is much smaller, the difference between unscreened and screened results is less than 10%.

The concern over a suitable choice of q_0 arises because, given the computational intensity of the calculation of the 4-band k.p matrix elements, it is not feasible to recalculate (or store) all the PZ matrix element data for a range of values of q_0. Certainly, for the purposes of our Monte Carlo simulations, q_0 is not a sufficiently important parameter to warrant such a multiplicity of matrix element calculations: the use of the single value $q_0 = 4.6266 \times 10^{-3}\text{Å}^{-1}$ will prove quite adequate for the work on quantum confined hole dynamics described in Chapters 9 and 10.

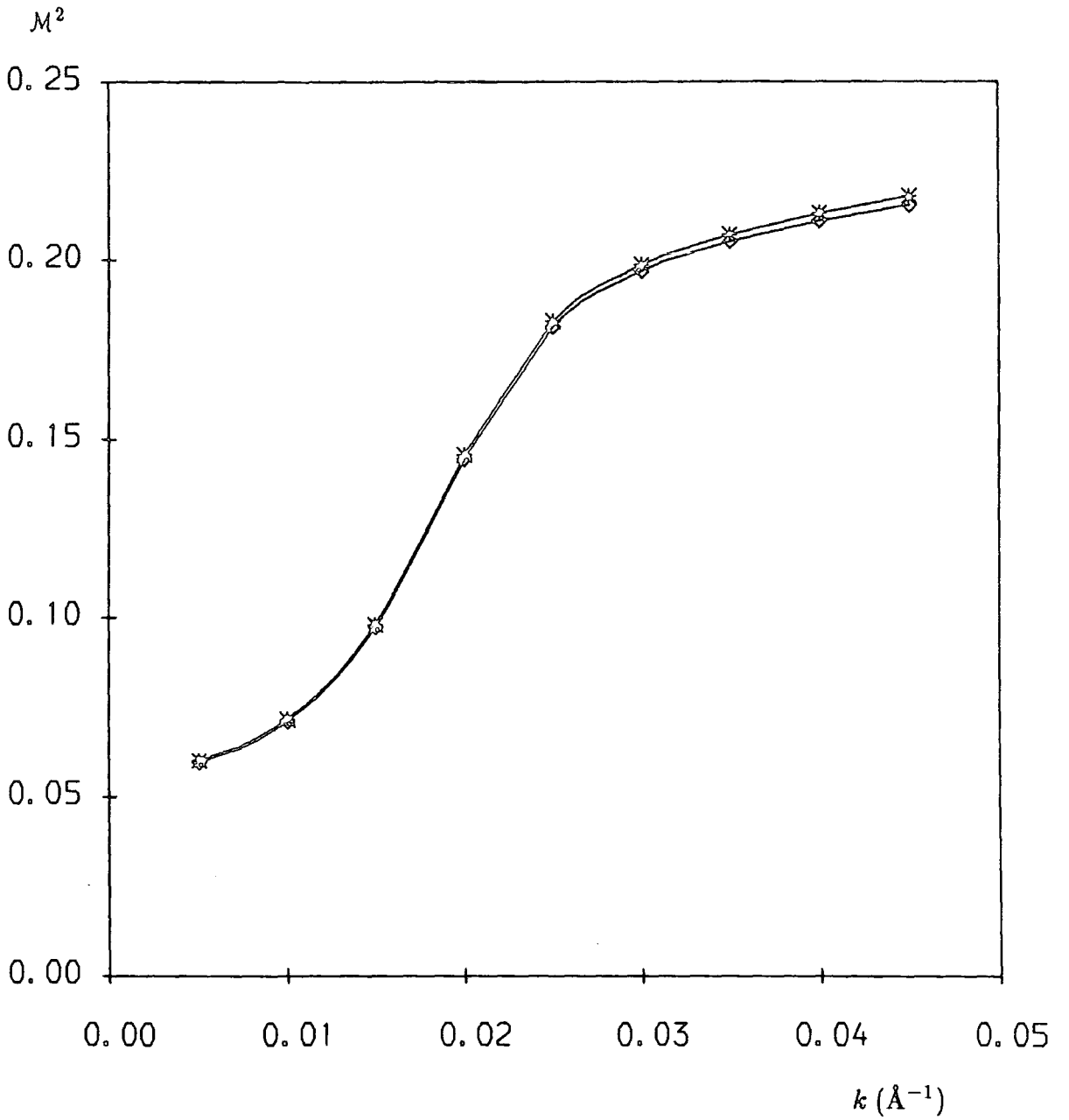

Fig. 6.23 POP 1–1abs matrix element; $(1/4L)\mathcal{M}^2_{k'n',kn}$ *vs.* k. $*$ unscreened; $q_0 = 0$. $\diamond$ screened; $q_0 = 4.6266 \times 10^{-3}$Å^{-1} ($p = 10^{16}$cm^{-3}).

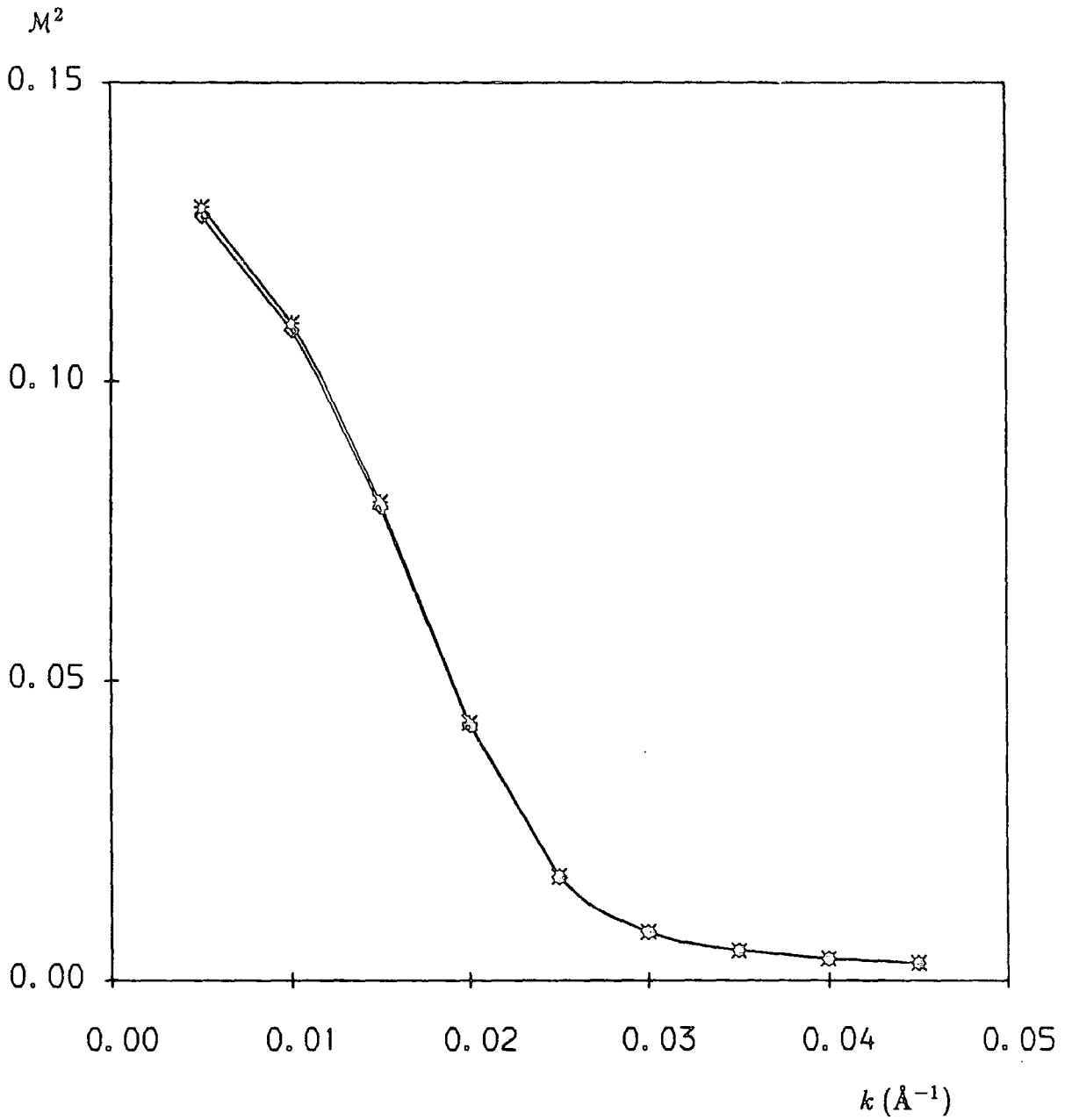

Fig. 6.24 POP 1–2abs matrix element; $(1/4L)\mathcal{M}^2_{k'n',kn}$ *vs.* k. $*$ unscreened; $q_0 = 0$. $\diamond$ screened; $q_0 = 4.6266 \times 10^{-3}$Å^{-1} ($p = 10^{16}$cm^{-3}).

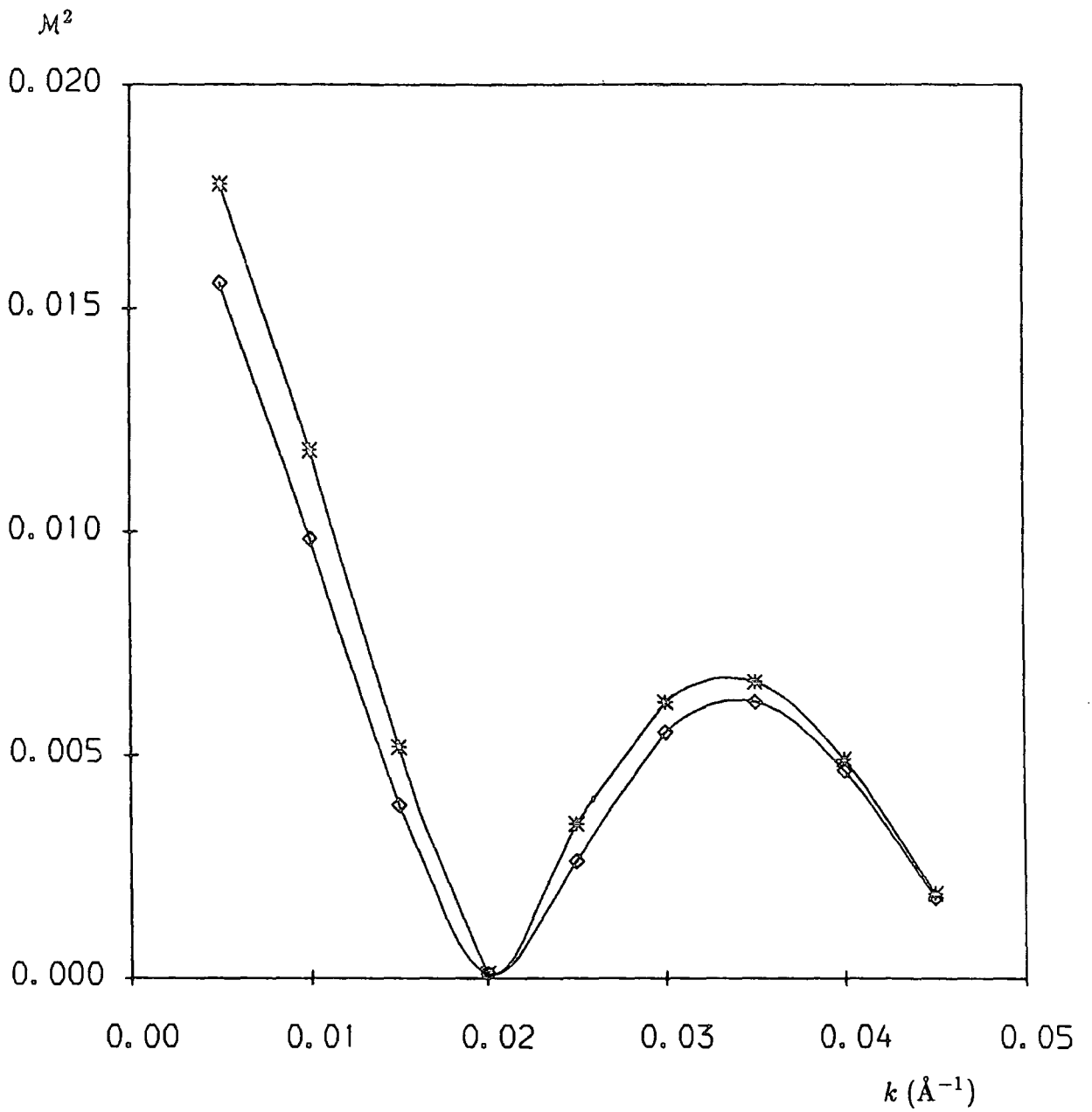

Fig. 6.25 POP 1–3abs matrix element; $(1/4L)\mathcal{M}^2_{k'n',kn}$ *vs.* k. $*$ unscreened; $q_0 = 0$. $\diamond$ screened; $q_0 = 4.6266 \times 10^{-3}$Å^{-1} ($p = 10^{16}$cm^{-3}).

CHAPTER 7
QUANTUM CONFINED HOLE-PHONON SCATTERING RATES

In the previous chapter, we presented detailed results for the quantum confined hole-phonon matrix elements, calculated within a 4-band k.p scheme. These results will form the basis of our description of scattering in, and hence our Monte Carlo model of, the quantum well valence band system. In this chapter, we will present numerical results for the principal phonon scattering rates (Section 7B). This first requires derivation of the density of states functions for the quantum confined valence bands, which we will describe in Section 7A. Finally, in Section 7C, we will give details of a scheme by which energy dissipation may be introduced into our model of acoustic scattering.

7A DENSITIES OF STATES

7A.1: Densities of States as derived from the Band Dispersions

In the isotropic approximation to the quantum confined valence bandstructure, the energy dispersions $\epsilon(\mathbf{k})$ in each band (where $\mathbf{k}$ is a vector in the 2D wavevector plane) become circularly symmetric functions, dependent only on the 2D radial wavevector k. The reduced densities of states $D_n(\mathbf{k})$ also have circular symmetry in the 2D wavevector plane, taking the form $D_n(k) = k/|\partial\epsilon/\partial k|$ in each band n. Thus, the derivation of the densities of states reduces to an essentially one-dimensional problem, and values for $\partial\epsilon/\partial k$, and hence $D_n(k)$, can be readily obtained from the band dispersions of Fig. 6.1.

Figs. 7.1 and 7.2 show $\partial\epsilon/\partial k$ and $D_n(k)$ respectively, as a function of the radial wavevector k, in each of the four bands. These results were obtained by forming a cubic spline fit to the $\epsilon(k)$ data for each band. A derivative of the spline curve could then be obtained at any value of k. We identified as an optimum fit in each case, a curve which closely matched the $\epsilon(k)$ data, but did not give rise to any spurious structure in the derivative function $\partial\epsilon/\partial k$.

Fig. 7.1 is of interest in its own right, since $1/\hbar(\partial\epsilon/\partial k)$ gives the group velocity of carriers in the given band. It can be seen that $\partial\epsilon/\partial k$ is negative in the b regions of bands 2 and 4 ($k < k_n(0)$). This, of course, is an expected result since these regions have a curvature of the opposite sense to that normally found near the zone centre in valence bands — these are the so called 'negative effective mass' regions. In bands 3 and 4, $\partial\epsilon/\partial k$ is significantly enhanced by band distortion near the anticrossing region. At large wavevectors, the derivative curves become near-linear in all four bands, indicating that the bands themselves become essentially parabolic.

The reduced densities of states shown in Fig. 7.2 represent a substantial devi-

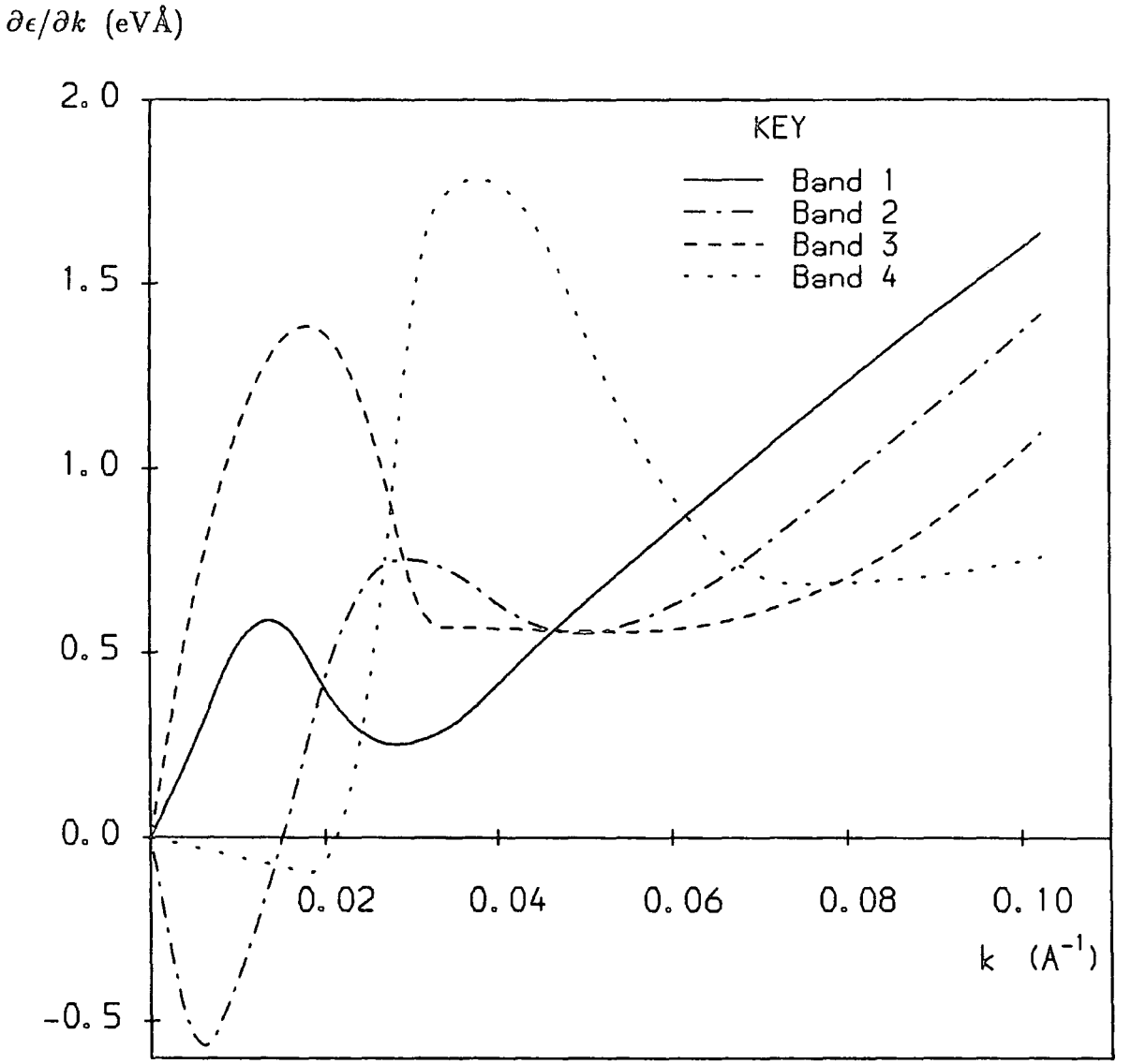

Fig. 7.1 Variation of $\partial\epsilon/\partial k$ with radial wavevector k in the first four valence bands of a 100Å GaAs/AlAs quantum well. The bands are assumed to be isotropic in 2D k-space.

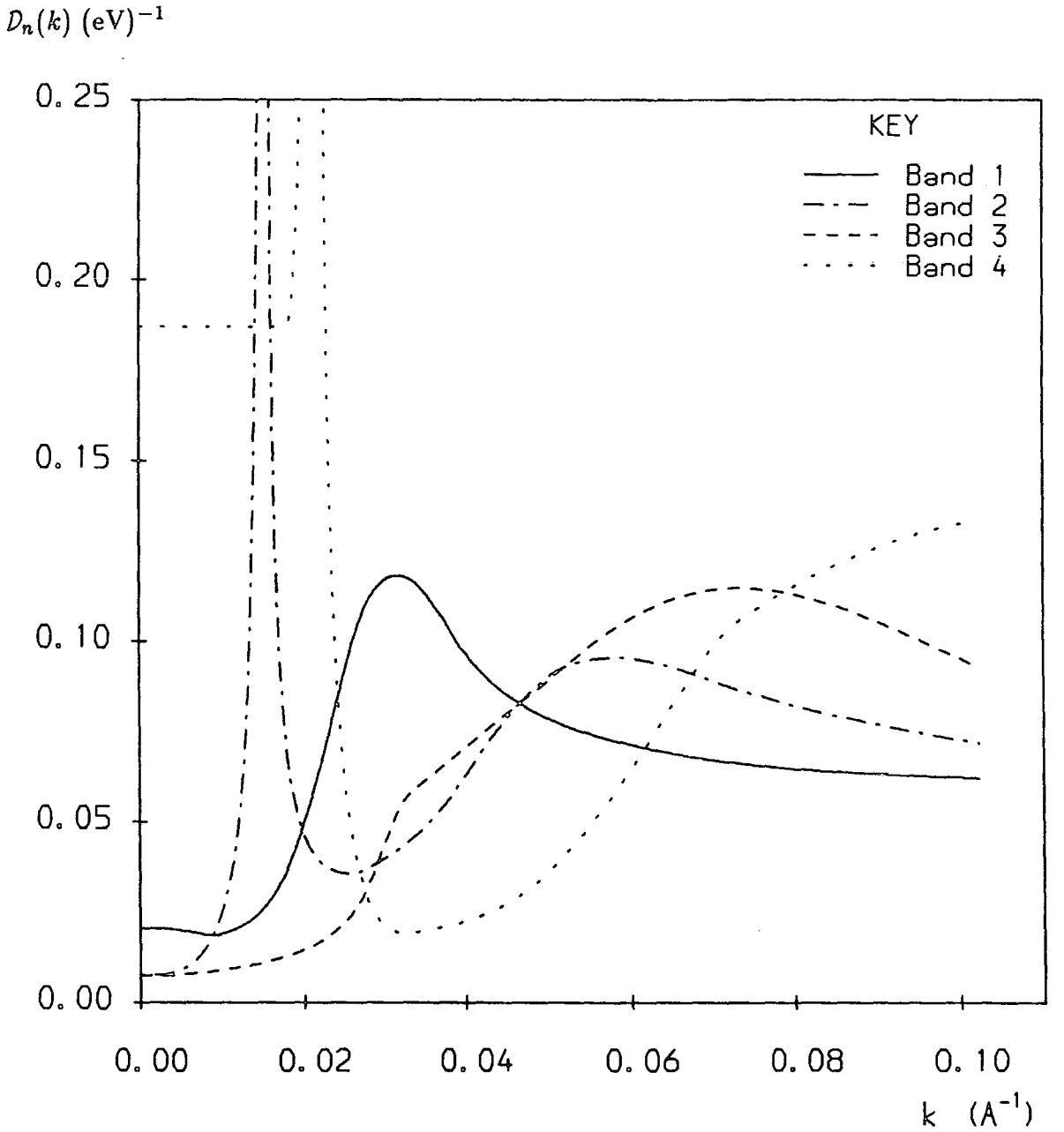

Fig. 7.2 Reduced density of states $D(k)$ *vs.* radial wavevector k in the first four valence bands of a 100Å GaAs/AlAs quantum well.

ation from the case of a parabolic band, where $\mathcal{D}_n(k)$ is independent of k. Similar results have been published by Eppenga *et al.* (1987) and Colak *et al.* (1987) for GaAs/AlGaAs quantum wells, though in neither case were the densities of states of the individual bands shown. Fig. 7.2 shows a maximum in the band 1 density of states at $k = 0.03175\text{Å}^{-1}$; a very high density of states in the b region of band 4 (because $|\partial\epsilon/\partial k|$ is so small here), and singularities in the band 2 and band 4 densities of states at the band minima. The singularities arise, in our derivation of $\mathcal{D}_n(k)$ from the isotropic $\epsilon(k)$, simply from the zero value of $\partial\epsilon/\partial k$ at these points. However, it must be appreciated that, since the $\mathcal{D}_n(k)$ are circularly symmetric quantities in the 2D wavevector plane, the singularities in $\mathcal{D}_2(k)$ and $\mathcal{D}_4(k)$ shown in Fig. 7.2 each represent a continuous ring of states (with $k = k_n(0)$; $n = 2$ or 4) where the density of states is infinite. In Figs. 7.3a and b we have shown 3-dimensional plots of $\epsilon(k)$ and $\mathcal{D}_n(k)$ for band 2, in the 2D k-space plane. Fig. 7.3a shows the ring of states where $\partial\epsilon/\partial k = 0$, and Fig. 7.3b shows the corresponding ring around which the density of states exhibits singular behaviour. The form of the function $\epsilon(k)$ of Fig. 7.3a is examined further in Appendix 3.

7A.2: Analysis of the Densities of States around the Critical Points

Points on a dispersion curve where $\nabla_{\mathbf{k}}(\epsilon) = 0$ are known as critical points or Van Hove singularities (Van Hove 1953; Phillips 1956). In 2D systems these have been shown to lead to discontinuities (steps) in the density of states, for a maximum or minimum in $\epsilon(\mathbf{k})$, or a logarithmic singularity in the density of states, for a saddle point in $\epsilon(\mathbf{k})$ (Van Hove 1953; Bassani and Parravicini 1975). However, the continuous ring of critical points described above does not fit into either category, and must be treated as a special case. Van Hove mentions such a continuous family of critical points in relation to the case $\epsilon_{xx}\epsilon_{yy} - \epsilon_{xy}\epsilon_{yx} = 0$, where ϵ_{xx} *etc.* are second derivatives of $\epsilon(\mathbf{k})$ with respect to the Cartesian components of $\mathbf{k}$, and this is exactly the condition which pertains here (see Appendix 3 for more details). The behaviour of the density of states around a critical point may be examined by expanding the energy to second order in $\mathbf{k}$. Remembering that $\epsilon(\mathbf{k})$ is independent of the polar angle β, and that the linear term in the expansion must be zero, since $\partial\epsilon/\partial k = 0$ at the critical point, we may write

$$\epsilon(k_c) \approx \epsilon_c + \alpha(k - k_c)^2, \tag{7.1}$$

where k_c is the (radial) wavevector of the ring of critical points, and ϵ_c, their energy. Then, the density of states $D_n(k)$ around the whole ring is given by

$$\lim_{h\to 0} D_n(k_c + h) = \int_0^{2\pi}\int_{k_c}^{k_c+h} \delta(\zeta - \epsilon(k))\, k dk d\beta, \tag{7.2}$$

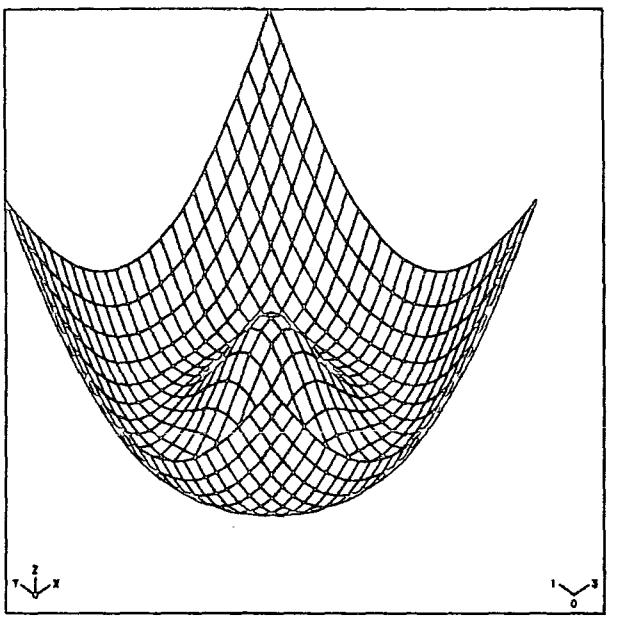

(a)

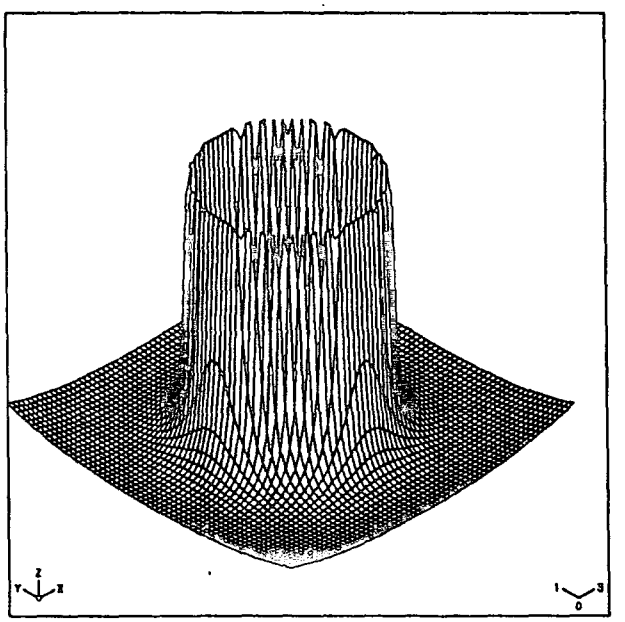

(b)

Fig. 7.3 (a) Energy dispersion $\epsilon(k)$ (z axis) for band 2, in the 2D wavevector plane (xy). The spacing between adjacent grid lines is $\Delta k = 2 \times 10^{-3}$Å^{-1}.

(b) Reduced density of states $\mathcal{D}_n(k)$ (z axis) for band 2, in the 2D wavevector plane (xy). The spacing between adjacent grid lines is $\Delta k = 10^{-3}$Å^{-1}.

where $\varsigma \rightarrow \epsilon_c$ as $h \rightarrow 0$. The integration over β simply contributes a factor of 2π, and, on substituting for $\epsilon(k)$ from equation (7.1), we obtain:

$$\lim_{h\to 0} D_n(k_c + h) = 2\pi \int_{k_c}^{k_c+h} \delta(\varsigma - \epsilon_c - \alpha(k - k_c)^2)\, k dk. \tag{7.3}$$

We may now make the substitution $q = k - k_c$ and change the variables in the delta function, whereupon:

$$\lim_{h\to 0} D_n(k_c + h) = 2\pi \int_0^h \frac{(k_c + q)\delta(q_c - q)}{2\alpha q}\, dq \tag{7.4}$$

where $q_c = \sqrt{(\varsigma - \epsilon_c)/\alpha}$. Evaluating the final integral then gives

$$\lim_{h\to 0} D_n(k_c + h) = \frac{\pi}{\alpha} + \frac{2\pi k_c}{\sqrt{\alpha(\varsigma - \epsilon_c)}}. \tag{7.5}$$

The first term in this expression is the density of states appropriate to a parabolic 2D band. The second term diverges according to $(\varsigma - \epsilon_c)^{-1/2}$ as $\varsigma \rightarrow \epsilon_c$. This is the behaviour expected of the density of states near a critical point in a 1D system (Bassani and Parravicini 1975). The physical interpretation of our result is that, since we have assumed the quantum well bandstructure to be isotropic, the energy $\epsilon(k)$ is a function of only one variable, and therefore, we can expect the form of the density of states around the critical points to be characteristic of a 1D system.

In reality, the quantum well valence band system will have a degree of anisotropy, and this will cause both the wavevectors $k_n(0)$ and the energies ϵ_n of the off-zone-centre minima to vary with angle β. The critical points may then be either minima or saddle points, depending on the local topology of the function $\epsilon(\mathbf{k})$. However, the critical points associated with an off-zone-centre minimum in a given band will still form a continuous and closed loop. The overall effect of anisotropy will thus be to produce a broadened annular region, of inner and outer radii $k = k_n(0) - h$ and $k = k_n(0) + h$ $(h \rightarrow 0)$, within which the density of states diverges.

7A.3: Broadening of the Densities of States

The inclusion, in a Monte Carlo simulation, of density of states data containing divergent critical points clearly presents a problem. The infinities in the densities of states cannot be represented in any computer code, and neither would this represent a physically realistic situation. Irrespective of the anisotropy of the band, the singularites in the densities of states will also be smeared out by lifetime broadening effects. With these points in mind, we have chosen to modify the form of the density of states around the critical points by the inclusion of a form of

'phenomenological' broadening. This gives for the density of states, a well defined function for all values of k.

We have taken, as our broadening function, a Lorentzian:

$$\mathcal{L}(\epsilon) = \frac{A}{\epsilon^2 + (\Delta\epsilon/2)^2} \tag{7.6}$$

where $\Delta\epsilon$ is the linewidth (full width at half maximum) and A is a constant multiplier. The broadened density of states $\mathcal{D}'_n(\epsilon)$ can now be obtained by forming the convolution of $\mathcal{D}_n(\epsilon)$ with $\mathcal{L}(\epsilon)$:

$$\mathcal{D}'_n(\epsilon) = \int_{-\infty}^{\infty} \mathcal{D}_n(\epsilon - \epsilon')\mathcal{L}(\epsilon')\, d\epsilon', \tag{7.7}$$

where, for this calculation, we have written the density of states as a function of energy rather than wavevector ($\mathcal{D}_n(\mathrm{k}(\epsilon)) \rightarrow \mathcal{D}_n(\epsilon)$). The important property of the convolution operation is that the product of the areas under the two functions $\mathcal{D}_n(\epsilon)$ and $\mathcal{L}(\epsilon)$ is conserved. Thus, by defining $\mathcal{L}(\epsilon)$ to enclose unit area, we will obtain, for $\mathcal{D}'_n(\epsilon)$, a function which encloses the same area as the unbroadened $\mathcal{D}_n(\epsilon)$. This definition requires that $A = \Delta\epsilon/2\pi$.

Our analysis of the density of states around the critical points at the off-zone centre band minima has shown that $\mathcal{D}_n(\epsilon)$ diverges as $(\epsilon - \epsilon_c)^{-1/2}$. We may therefore write, as an approximation for $\mathcal{D}_n(\epsilon)$ near a critical point ϵ_c:

$$\mathcal{D}_n(\epsilon - \epsilon_c) \approx B\frac{\theta(\epsilon - \epsilon_c)}{\sqrt{\epsilon - \epsilon_c}} \tag{7.8}$$

where $\theta(\epsilon - \epsilon_c)$ is the unit step function and B is some constant prefactor. This allows algebraic solution of the convolution integral, which now takes the form:

$$\mathcal{D}'_n(\epsilon - \epsilon_c) = B\frac{\Delta\epsilon}{2\pi}\int_{-\infty}^{\infty} \frac{\theta(\epsilon - \epsilon_c - \epsilon')}{\sqrt{\epsilon - \epsilon_c - \epsilon'}} \times \frac{1}{(\epsilon')^2 + (\Delta\epsilon/2)^2}\, d\epsilon'. \tag{7.9}$$

Evaluation of this integral gives the result:

$$\mathcal{D}'_n(\epsilon - \epsilon_c) = \frac{B\sqrt{\eta + \epsilon - \epsilon_c}}{\sqrt{2\eta}}, \tag{7.10}$$

where $\eta = \sqrt{(\epsilon - \epsilon_c)^2 + (\Delta\epsilon/2)^2}$. Since the critical points lie at the band minima, $\epsilon_c = 0$. Therefore, in our Monte Carlo simulations, we may take for the density of states in bands 2 and 4: the Lorentzian broadened $\mathcal{D}'_n(\epsilon)$ at very small energies, and the unbroadened $\mathcal{D}_n(\epsilon)$ elsewhere. The constant B is chosen to match up the values of $\mathcal{D}'_n(\epsilon)$ and $\mathcal{D}_n(\epsilon)$ at some small energy near the band minimum.

Figs. 7.4–5 show the broadened densities of states near $\epsilon = 0$ in both the *a* and *b* regions of bands 2 and 4, with the unbroadened $\mathcal{D}_n(\epsilon)$ shown for comparison.

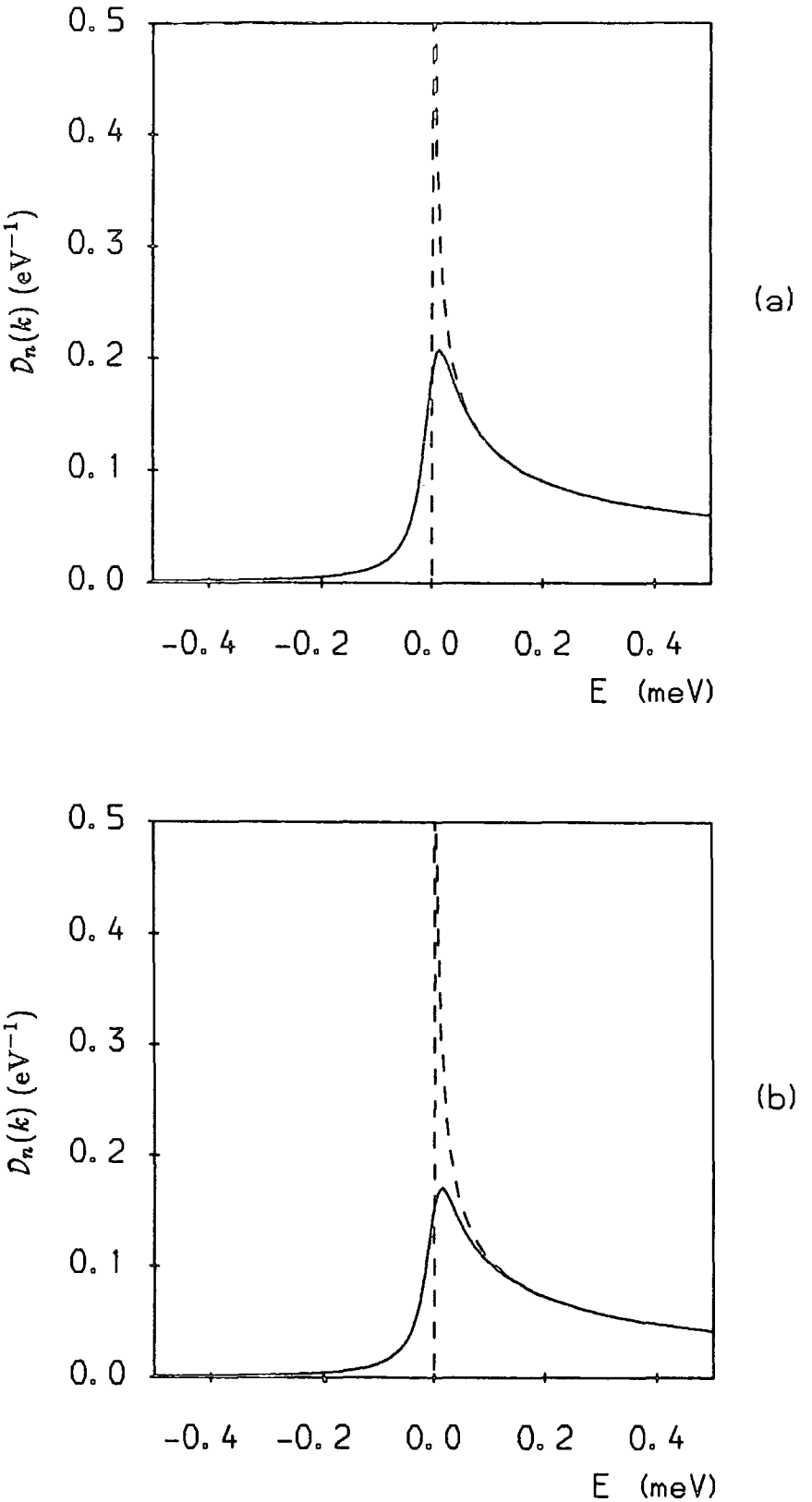

Fig. 7.4 Lorentzian broadened (—) and unbroadened (- - -) densities of states in the *a* and *b* regions of band 2. Values for the broadened and unbroadened curves are matched at $\epsilon = 0.15$meV, and the Lorentzian linewidth $\Delta\epsilon = 0.05$meV.

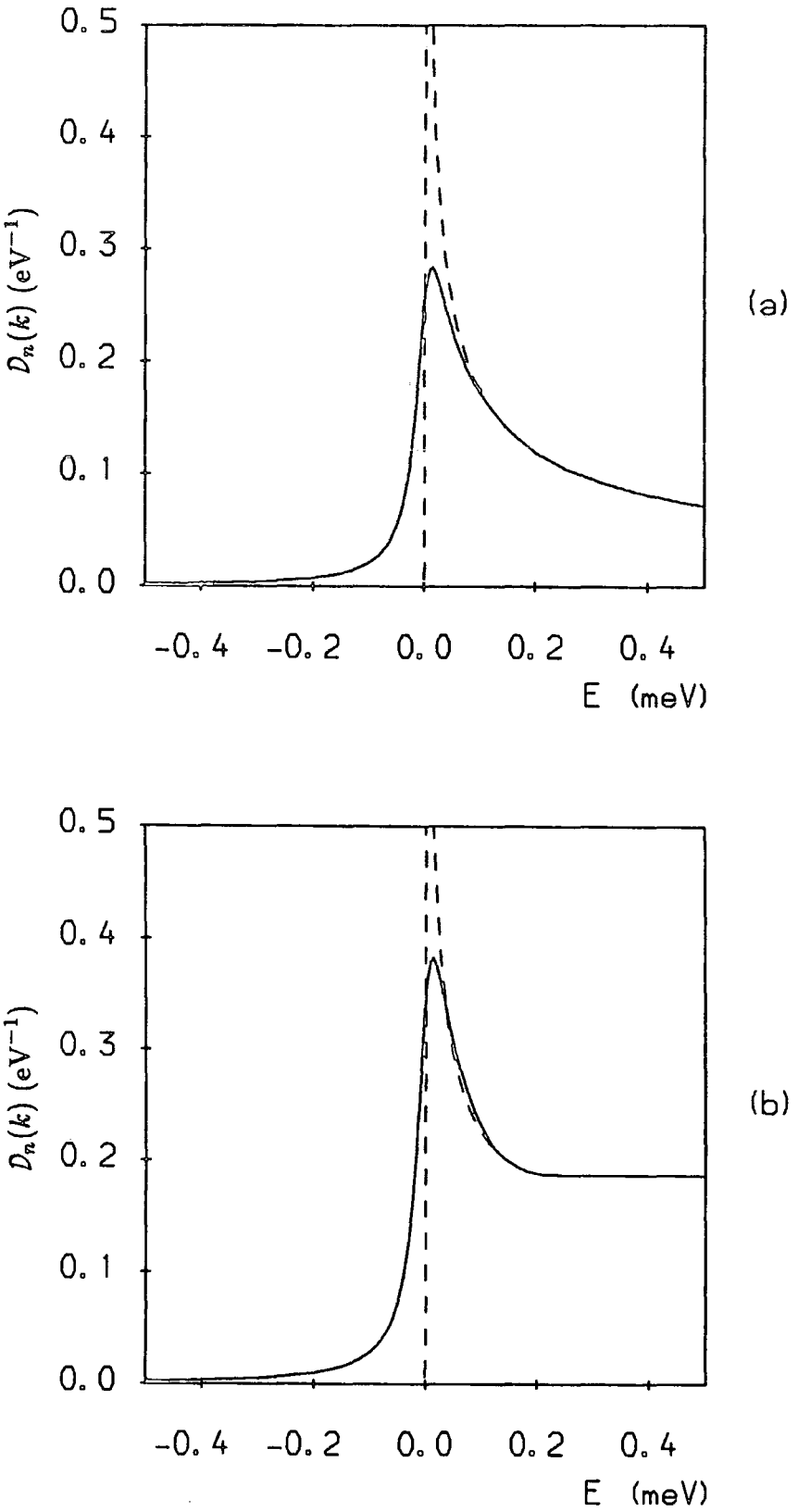

Fig. 7.5 Lorentzian broadened (—) and unbroadened (- - -) densities of states in the *a* and *b* regions of band 4. Values for the broadened and unbroadened curves are matched at $\epsilon = 0.125$meV, and $\Delta\epsilon = 0.05$meV.

We have taken $\Delta\epsilon = 0.05$meV, and matched the broadened and unbroadened densities of states at $\epsilon = 0.15$meV in band 2, and $\epsilon = 0.125$meV in band 4. The striking feature of the graphs is that the densities of states now extend *below* the band minima. This is a consequence of using a broadening function which is symmetrical about $\epsilon = 0$. The effect is physically valid, since any lifetime (or other) broadening of the densities of states will cause a loss in definition of the band edge, allowing a tail of electronic states to penetrate into the energy gaps between bands.

The linewidth associated with lifetime broadening is $\Delta\epsilon \sim \hbar/\tau$, where τ is the average lifetime of a carrier in a given state. We will see in Section 7B that the phonon scattering rates in the band 2 and 4 minima are of the order of 1ps^{-1} and 3ps^{-1} respectively. If we derive values for $\Delta\epsilon$ from the carrier lifetimes against phonon scattering, we will obtain $\Delta\epsilon \approx 0.7$meV in the band 2 minimum, and $\Delta\epsilon \approx 2.0$meV in the band 4 minimum. However, if these linewidths are used in equation (7.10), then the peaks in the densities of states are almost completely removed. In particular, the value of 2.0meV for $\Delta\epsilon$ in the band 4 minimum is greater than the zone centre energy of the band. This means that the contribution to the density of states at the band minimum would be redistributed right across the *b* region. It is clearly undesirable to use such a strong degree of broadening in the Monte Carlo simulation. We consider it preferable to use a value of linewidth sufficiently small that the densities of states still display large peaks at the band 2 and 4 minima. After having investigated the effect on carrier dynamics of such prominent structure in the densities of states, we could, if appropriate, increase $\Delta\epsilon$ and so reduce the peaks. It should be remembered that the primary motivation for including broadening effects in the calculation of the densities of states in this work was to avoid numerical difficulties in the Monte Carlo simulations. The choice of $\Delta\epsilon = 0.05$meV represents, in this context, the optimum for the attainment of density of states functions which are well behaved, but which are still strongly peaked around the critical points.

It is not clear, from the experimental work published to date, whether such structure in the densities of states at off-zone-centre valence band minima does, in fact, survive the various broadening effects which may be operative. Sanders and Chang (1987) have published calculated absorption spectra, which they compare with the experimental results of Miller *et al.* (1985) and Miller and Kleinmann (1985). Peaks in the spectra corresponding to transitions involving the off-zone-centre minima are observed; but the band-band and exciton transition are not resolved in the experimental data and the contribution of the densities of states at the band minima cannot be isolated.

It should be explained that, by applying the broadening prescription independently to the densities of states in the a and b regions of each of bands 2 and 4, a small discrepancy will arise in the values of the densities of states at $\epsilon = 0$. This does not lead to any major inconsistencies in the Monte Carlo simulations, since the a and b regions are always treated as separate entities. There is no need to match the a and b region densities of states at $\epsilon = 0$. Further details of the implementation of the density of states broadening scheme within the Monte Carlo simulations will be given in Chapter 8.

Finally, we note that a method of introducing broadening effects into the density of states around singular points has also been described by Briggs and Leburton (1988), in their work on electronic transport in quantum well wires. However, they considered a broadening of the *phonon* energies, in which case the appropriate lifetime τ is that of the phonons in the system. Any broadening of the phonon energies will affect the form of the density of states only indirectly; in particular, the density of states will not be seen to extend below the band edge. We prefer our direct approach to broadening, considering it more physically transparent, and physically defensible, than the Briggs-Leburton method.

7B SCATTERING RATES

7B.1: Scattering Rate Parameters

We are now in a position to obtain numerical results for the quantum confined hole-phonon scattering rates, as given by equations (5.47), (5.50), (5.53) and (5.68). We will consider scattering at a lattice temperature of 77K, and will use, for the values of the relevant material parameters, those quoted in Table 4.1 for bulk GaAs. The use of the bulk values is, in most cases, the logical choice; however, for the acoustic and optical deformation potentials, some degree of explanation is necessary.

The acoustic deformation potential: E_{AC}

When an acoustic phonon passes through the lattice, the energy perturbation experienced by a given state $|\mathbf{k}\rangle$ due to acoustic strain is, in general, a function of $\mathbf{k}$. However, if the valence bands are assumed to be isotropic and parabolic, then the energy perturbation is given by the term Ξ_{eff} of equation (A.3) in Appendix 2, which is simply an amalgamation of the rigid shifts in the bands prescribed by the fundamental valence band deformation potentials a, b and d (Lawaetz 1968; see Appendix 2 for more details). The deformation potentials a, b and d are also valid for describing the response of the quantum confined valence band system to strain. a gives the shift in the valence band edge upon application of hydrostatic pressure (dilational strain), as in the bulk, and, whilst the heavy hole - light hole degeneracy in the quantum well is already broken by band mixing effects, the *relative* shift of the heavy and light hole subbands is still given by the deformation potentials b and d. (Subbands of the same type (HH or LH) will not show any shift relative to each other, since the symmetry of their zone centre states is the same.)

Therefore, it seems entirely reasonable to use the approximation of a $\mathbf{k}$ independent energy perturbation in our description of acoustic scattering in a quantum well. Clearly, we do not wish our quantum well deformation potentials to include any modifications due to overlap integral effects, since, in our calculations in Chapter 5, such effects were entirely contained within the matrix element terms $\mathcal{M}^2_{k'n',kn}$. Therefore, we may make use of the derivation of the acoustic deformation potential given in Appendix 2. Using equations (A.3) and (A.8–9), we obtain:

$$\begin{aligned} E^2_{AC} &= \left(\frac{\overline{v}^2}{v_l^2}\right)\Xi^2_{\text{eff}} \\ &= \left(\frac{\beta+2}{3\beta}\right)\left[a^2 + \left(\frac{c_l}{c_t}\right)(b^2 + d^2/2)\right], \end{aligned} \tag{7.11}$$

where $\beta = c_l/c_t$.

Using the bulk spherically averaged elastic constants c_l and c_t, we obtain $E_{AC} = 5.07$eV, as for bulk GaAs. There are very few experimental results with which to compare this value. Leo, Rühle, and co-workers have deduced values of $E_{AC} = 5.5$eV and 7.0eV for GaAs/AlGaAs quantum wells of width 200Å and 90Å respectively (Leo *et al.* 1988): whilst an alternative report suggests $E_{AC} = 5.9$eV for both 50Å and 90Å wells (Rühle *et al.* 1988). These deductions were based on effective mass model fits to hole cooling data, and therefore the resultant value of E_{AC} represents little more than a fitted parameter into which all the effects of quantum confinement have been absorbed.

The Optical Deformation Potential Constant: D_{op}

In Section 3C it was reported that the optical deformation potential constant D_{op} was related to the optical deformation potential d_0 by (equation 3.79):

$$D_{op}^2 = \frac{3}{2}\frac{d_0^2}{a_0^2}. \tag{7.12}$$

d_0 is a phenomenological term introduced in the original calculation of Bir and Pikus (1961) to represent the energy shift of the valence bands at $\mathbf{k} = 0$ due to optical strain. As in the case of acoustic scattering, if anisotropy and nonparabolicity of the valence bands are neglected, then the energy perturbation experienced by a state $|\mathbf{k}\rangle$ upon interaction with a non-polar optical phonon is independent of $\mathbf{k}$. Consequently, we can again use the bulk value of the optical deformation potential constant; $D_{op} = 8.88 \times 10^{10}$eVm^{-1} — calculated with the exclusion of overlap integral effects (see Appendix 2). No experimentally deduced values for D_{op} in quantum wells are available, presumably because resolution of the contributions of polar and non-polar scattering to carrier dynamics is very difficult to achieve.

For polar optical and piezoelectric scattering, the perturbation energy is related to polarisation rather than strain effects, and these are independent of the details of the bandstructure. Hence, the calculation of both polar optical and piezoelectric scattering rates requires no further approximations concerning the nature of the quantum-confined valence band system, other than those set out in Chapters 5 and 6.

7B.2: Scattering Rate Results

In Figs. 7.6–9 we have shown the total rates for acoustic (deformation potential) (AC), non-polar optical (NPO), polar optical (POP), and piezoelectric (PZ) scattering, via all intra- and inter-band processes for a carrier in state $|\mathbf{k}\rangle$ in each of bands 1–4 respectively. It is clear that POP scattering is the dominant process throughout. The POP scattering rate is especially large in band 1, as a result of a large contribution from POP 1–1em scattering. An important feature concerning POP 1–1em is that the scattering rate is relatively small ($\approx 1\text{ps}^{-1}$) at threshold ($k = 0.070\text{Å}^{-1}$), but rises steeply to a maximum of around 16ps^{-1}. This steep shoulder is due to the combined effect of increases in the POP 1–1em matrix element (Fig. 6.10d) and the density of final states. The peak in the scattering rate at $k = 0.081\text{Å}^{-1}$ corresponds to the density of states maximum at $k = 0.032\text{Å}^{-1}$ in band 1 (Fig. 7.2). Thus, whilst POP emission does not 'switch on' so suddenly at threshold, as predicted for quantum confined electrons in the infinite square well approximation (Section 5B), the valence band mixing effects give rise to a very strong scattering rate for states of slightly larger wavevectors. The increase in the rate is almost sharp enough to define a secondary 'pseudo' threshold for POP 1–1em at $k \approx 0.081\text{Å}^{-1}$.

The structure in the POP rates at larger wavevectors corresponds to the thresholds for 1–2, 1–3 and 1–4 optical emission. The densities of final states for the 1–2 and 1–4 threshold processes are strongly peaked, as manifested by the spike-like features on the graph. Below the (1–1) optical emission threshold scattering is dominated by AC processes, with the PZ rates somewhat smaller throughout. The contribution from optical phonon absorption processes is very small, since $\mathcal{N}_{\text{op}} \ll 1$.

In band 2, the first optical emission threshold is that for 2–1 scattering, at $k = 0.050\text{Å}^{-1}$. The POP 2–1em scattering rate is largest at threshold ($\approx 2\text{ps}^{-1}$), and subsequently decays. This is due to the sharp decrease of the POP 2–1em matrix element with k (Fig. 6.11d). The key point to note is that there is no large contribution apparent from the density of final (band 1) states. Its effect has been almost completely negated by the fall-off in the matrix element. Thus, we see here the converse of the phenomenon observed for POP 1–1em. The strong k dependences of the matrix element and the density of states, which arise from band mixing, act to oppose, rather than reinforce each other.

The dominant structure in the POP rate in band 2 arises from 2–2em scattering. The spike at threshold ($k = 0.074\text{Å}^{-1}$) and the subsequent strong increase in the rate both reflect the form of the band 2 density of states. The spike at $k = 0.107\text{Å}^{-1}$ marks the POP 2–4em threshold.

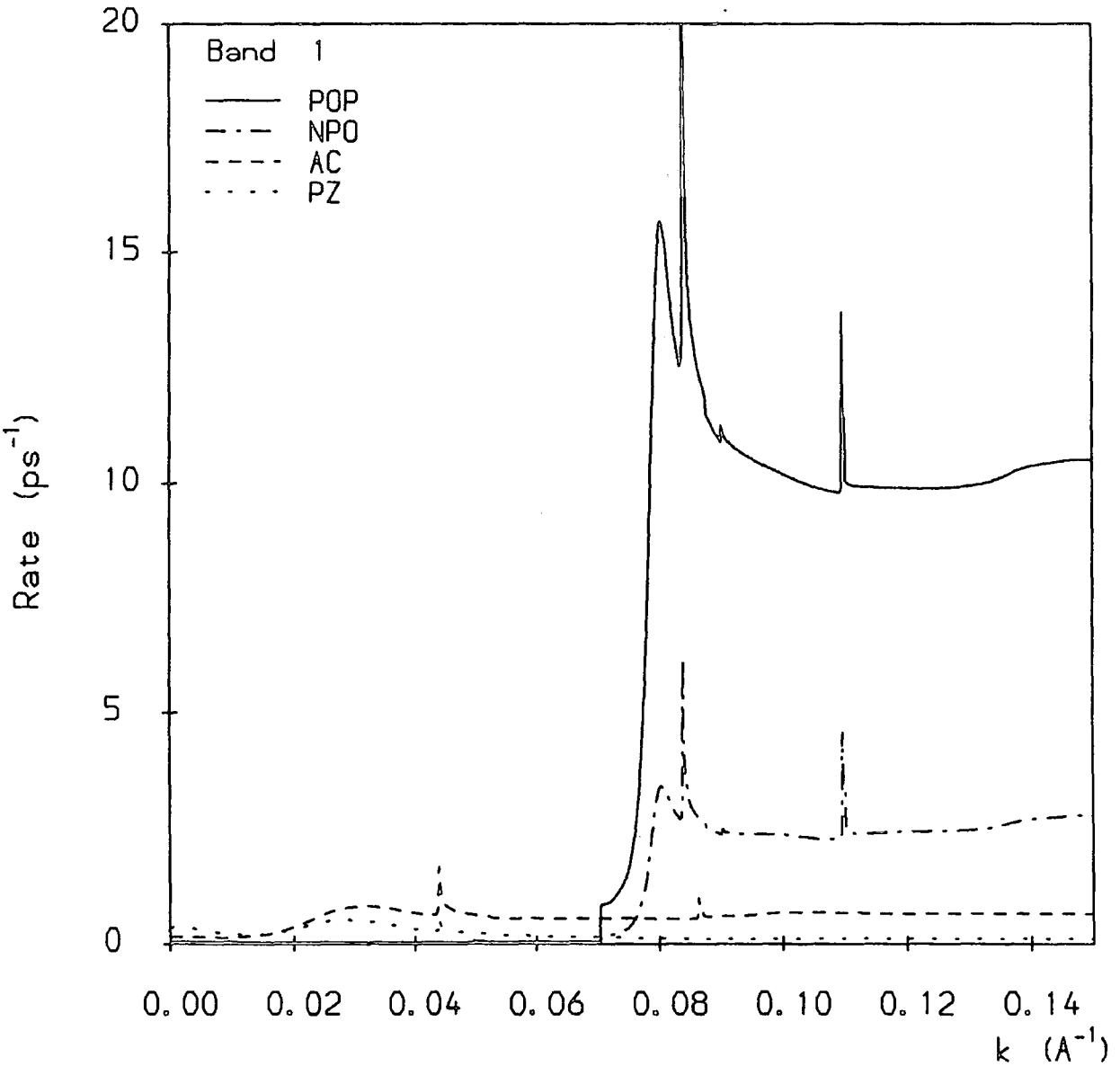

Fig. 7.6 Total scattering rate for a hole in state $|\mathbf{k}\rangle$ in band 1, via all possible intra- and inter-band processes, resolved into components due to scattering by POP, NPO, AC and PZ phonons. $T_L = 77$K.

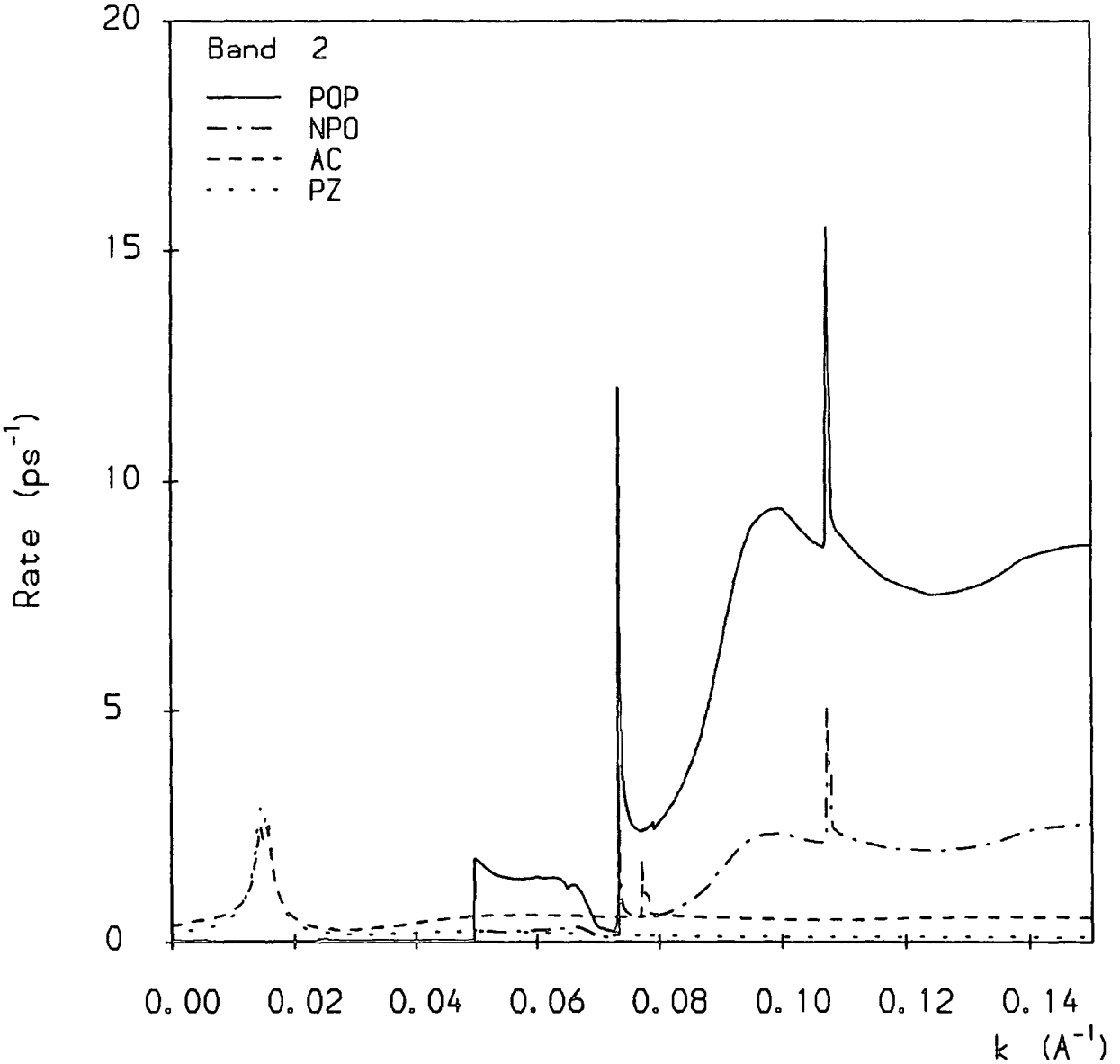

Fig. 7.7 Total scattering rate for a hole in state $|\mathbf{k}\rangle$ in band 2, via all possible intra- and inter-band processes, resolved into components due to scattering by POP, NPO, AC and PZ phonons. $T_L = 77$K.

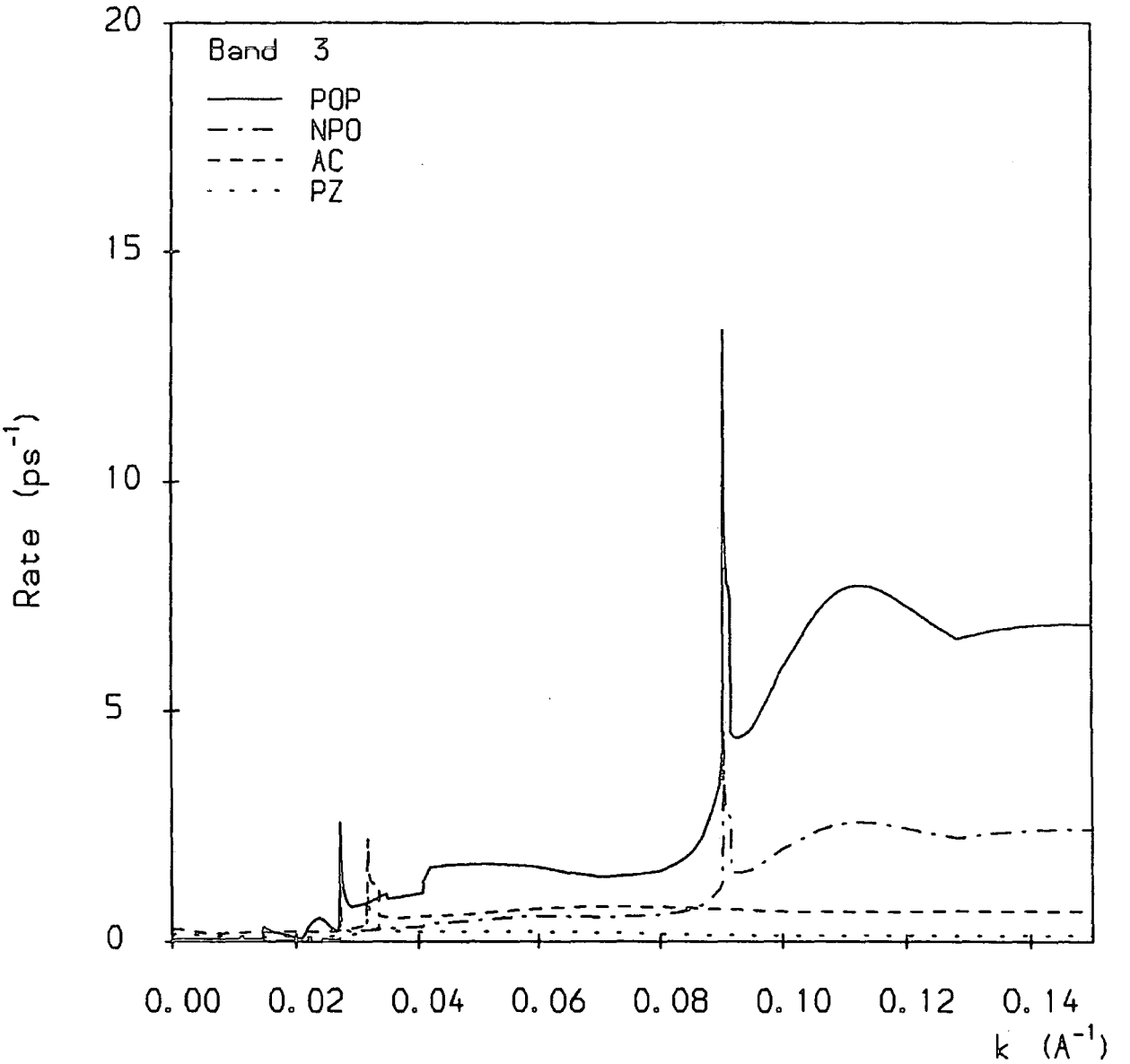

Fig. 7.8 Total scattering rate for a hole in state $|\mathbf{k}\rangle$ in band 3, via all possible intra- and inter-band processes, resolved into components due to scattering by POP, NPO, AC and PZ phonons. $T_L = 77$K.

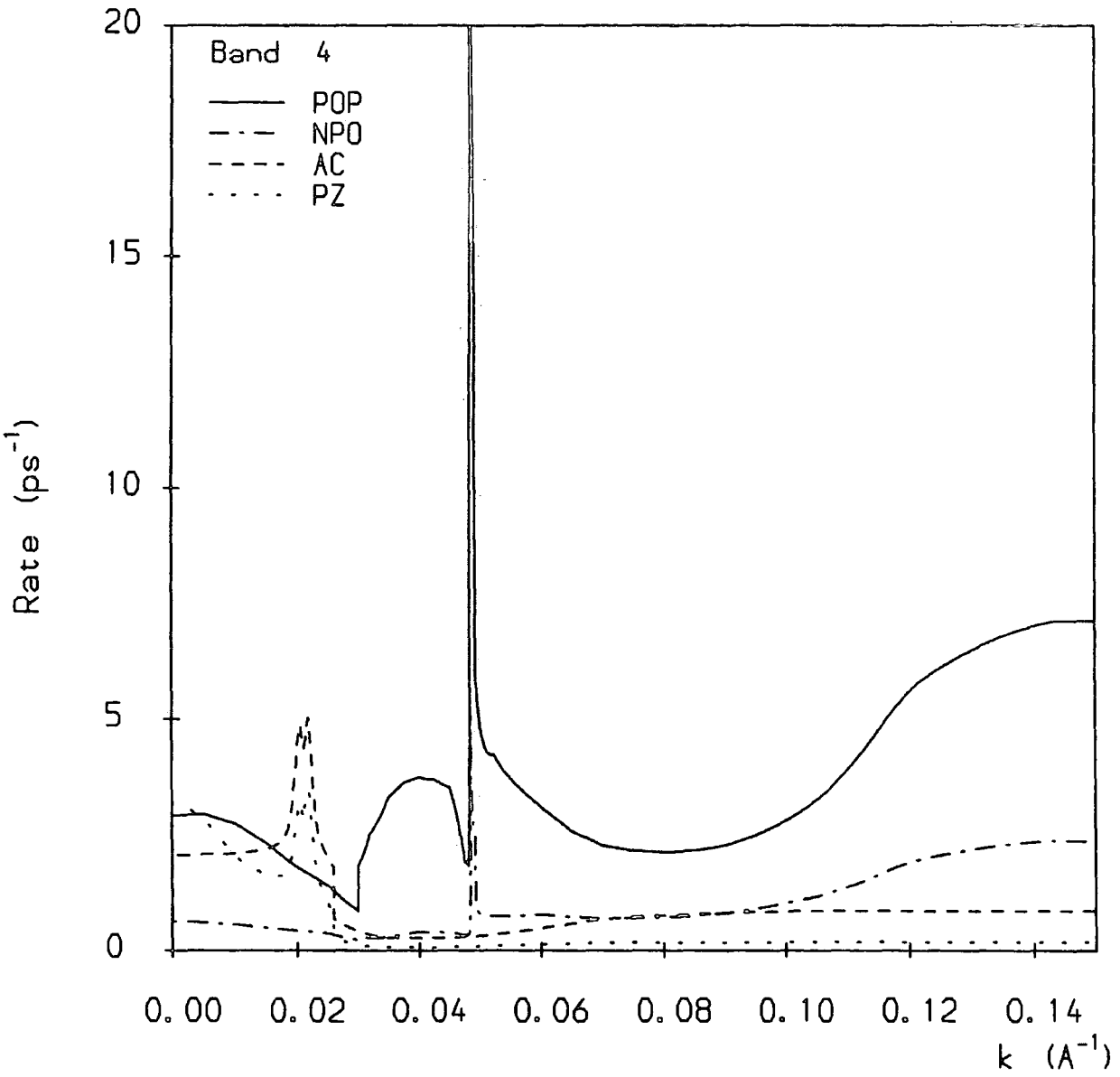

Fig. 7.9 Total scattering rate for a hole in state $|\mathbf{k}\rangle$ in band 4, via all possible intra- and inter-band processes, resolved into components due to scattering by POP, NPO, AC and PZ phonons. $T_L = 77$K.

The band 3 scattering rates are generally smaller than those for the other bands. As we have discussed in section 6C.1, the POP 3–1 and 3–2 matrix elements are small, and the POP 3–3em scattering rate is low up to $k \approx 0.08\text{Å}^{-1}$ due to the small density of final states.

In band 4, we note that the POP rate is unusually large ($\approx 2.5\text{ps}^{-1}$) at $k = 0$. This is because two emission processes, POP 4–1em and 4–2em, are allowed here. More significant is the fact that the AC rate at $k = 0$ is comparable with the POP rate, and the PZ rate is actually slightly larger. This is due to the abnormally large density of states at the band 4 zone centre (Fig. 7.2), and also, for PZ scattering, to an extremely large 4–4 matrix element (Fig. 6.17h). The AC and PZ rates also exhibit spikes at $k = 0.021\text{Å}^{-1}$ due to elastic scattering in the band 4 minimum. The contribution to POP scattering for $k > 0.03\text{Å}^{-1}$ is due to POP 4–3em, which, being an inter-anticrossing-band process (see section 6C.1), is relatively strong. The 4–4 optical emission threshold is marked by the spike at $k = 0.049\text{Å}^{-1}$.

With reference to Figs. 5.1 and 5.2, we find that the POP rate for quantum confined electrons in the infinite square well approximation is around $8\text{–}10\text{ps}^{-1}$. Thus, our results predict larger POP scattering rates in bands 1 and 2, but smaller rates in bands 3 and 4. The intraband POP emission rate for heavy holes in bulk GaAs (Fig. 4.5) is around 9ps^{-1}, whilst the light - heavy hole rate has a peak value of $\approx 18\text{ps}^{-1}$. Thus, our 1–1 and 2–2 POP rates have values similar to that for the principal bulk intraband rate. However, as was shown in Chapter 6, the band mixing effects weaken interband scattering considerably. Consequently, none of the quantum confined interband POP rates are of the same order as the light - heavy hole bulk rate, except for scattering into the off-zone-centre band minima.

7C INELASTIC ACOUSTIC SCATTERING

7C.1: The Average Phonon Energy Approximation

Thus far we have considered acoustic (AC and PZ) scattering only within the elastic and equipartition approximations. With phonon energies typically of the order of 1meV (see section 6C.2), these approximations are expected to be quite reasonable at 77K ($k_B T_L$ = 6.6meV). However, in Monte Carlo simulations of carrier relaxation (cooling), with no electric field bias, it would be desirable to include the effects of energy dissipation from acoustic phonon scattering; since optical scattering can only dissipate large, fixed quantities of energy.

The acoustic phonon energy is proportional to the phonon wavevector; $\epsilon_{\text{ph}} = \hbar v_s q$. If we substitute this result into the the general expression for 2D scattering (equation (5.43)), we obtain:

$$P_{n',n}(\mathbf{k}) = \frac{E_{\text{AC}}^2}{8\pi^2\rho}\iint \delta_{\mathbf{k}\pm\mathbf{q}_{\|},\mathbf{k}'}\frac{q^2}{\omega_q}\begin{bmatrix}\mathcal{N}_{\mathbf{q}}\\ \mathcal{N}_{\mathbf{q}}+1\end{bmatrix}\left|J_{k'n',kn}(q_z)\right|^2 \times \delta\Big(\epsilon(k',n') - \epsilon(k,n) \mp \hbar v_s q\Big)\, d\mathbf{k}'dq_z. \tag{7.13}$$

This expression cannot be further simplified without introducing some approximation. Since q appears in the energy delta function, the location of the final scattering states, and hence the value of $J(q_z)$, are dependent on q. It is certainly not feasible to recalculate the 4-band k.p envelope terms $|J(q_z)|^2$ for every required value of phonon energy. Instead, we decided to use a single, *average* value of ϵ_{ph}, to model the typical energy dissipation occurring for each acoustic phonon scattering. Alternatively, we may say that we have located a point on the acoustic phonon dispersion curve (ω_q *vs.* q) which represents the average value of q involved in acoustic scattering. The dominant contributions to the average value ϵ_{ac} will be made by phonon energies which are small, compared to $k_B T_L$, and so both $\mathcal{N}_q$ and $\mathcal{N}_q + 1$ can still be well approximated by $k_B T_L/\hbar v_s q$. It should be emphasised that we do *not* write $\mathcal{N}_q$ and $\mathcal{N}_q + 1 \approx k_B T_L/\epsilon_{\text{ac}}$, since this would alter the q dependence of the scattering rate expression. For the same reason, we will also substitute for ω_q: $v_s q$, rather than $\epsilon_{\text{ac}}/\hbar$. This ensures that the *linear* form of the dispersion curve is preserved. The substitution $\omega_q = \epsilon_{\text{ac}}/\hbar$ would imply that the dispersion curve is flat; an approximation which we do not wish to introduce.

Thus, equation (7.13) may now be simplified to obtain:

$$P_{n',n}(\mathbf{k}) = \frac{k_B T_L E_{\text{AC}}^2}{8\pi^2\hbar\rho v_s^2}\iint \delta_{\mathbf{k}\pm\mathbf{q}_{\|},\mathbf{k}'}\left|J_{k'n',kn}(q_z)\right|^2 \times \delta\Big(\epsilon(k',n') - \epsilon(k,n) \mp \epsilon_{\text{ac}}\Big)\, d\mathbf{k}'dq_z. \tag{7.14}$$

The remaining integrals can be evaluated as described in section 5C.3, to give the

scattering rate for absorption or emission as:

$$P^{\text{abs}}_{n',n}(\mathbb{k}) = \frac{k_B T_L E_{\text{AC}}^2}{4\pi\hbar\rho v_s^2}\, \mathcal{D}_{n'}(k^{\prime})\, \mathcal{M}^2_{k^{\prime}n',kn}, \tag{7.15}$$

where $k^{\prime} = k(\epsilon \pm \epsilon_{\text{ac}})$ and $\mathcal{M}^2_{k^{\prime}n',kn}$ is defined in equation (5.48).

To reduce the amount of data needed for the Monte Carlo simulation, we assume that the term $|J_{k^{\prime}n',kn}(q_z)|^2$, and hence $\mathcal{M}^2_{k^{\prime}n',kn}$, can be approximated by values calculated for $\epsilon_{\text{ac}} = 0$, as in section 6C.2. We have seen that this approximation is very good for intraband AC scattering, and, for small phonon energies, it is not expected to introduce any serious error in the rates for other acoustic processes.

The above expression is very similar to that obtained in the basic elastic and equipartition approximations. We have shown that it is also valid when an average, non-zero phonon energy is assumed: however, further amendments are necessary before this prescription for inelastic acoustic scattering can be included in a Monte Carlo simulation.

7C.2: Detailed Balancing the Scattering Rates

Whilst equation (7.15) gives a good approximation to the rates for both absorption and emission of acoustic phonons, it cannot be used in a simulation involving non-zero acoustic phonon energies. The equation yields the same scattering rate for both absorption and emission processes, a result which will not achieve the necessary detailed balance of these events. Irrespective of the accuracy of the approximation used, the scattering rates for absorption and emission transitions between two states must differ by a factor involving the ratio of the densities of initial and final states, and the ratio $\mathcal{N}_{\text{ac}}/(\mathcal{N}_{\text{ac}}+1) \equiv \exp(-\epsilon_{\text{ac}}/k_B T_L)$, where $\mathcal{N}_{\text{ac}} = 1/(\exp(\epsilon_{\text{ac}}/k_B T_L) - 1)$. The first term, giving the ratio of the numbers of initial and final states available, is already accounted for in equation (7.15) — provided that $\mathcal{D}_{n'}(k^{\prime})$ is always evaluated at $k^{\prime} = k(\epsilon \pm \epsilon_{\text{ac}})$. The second term, which gives the ratio of the probabilities of the phonon (lattice) system gaining or losing energy ϵ_{ac}, must be explicitly introduced into the scattering expressions. This requires modification of the absorption rate by a factor $2\mathcal{N}_{\text{ac}}/(2\mathcal{N}_{\text{ac}}+1)$, and the emission rate by a factor $2(\mathcal{N}_{\text{ac}}+1)/(2\mathcal{N}_{\text{ac}}+1)$. Consequently, using the definition of $\mathcal{N}_{\text{ac}}$ above, we obtain for inelastic AC scattering:

$$P^{\text{abs}}_{n',n}(k) = \frac{k_B T_L E_{\text{AC}}^2}{2\pi\hbar\rho v_s^2}\left[\frac{1}{\exp(\pm\epsilon_{\text{ac}}/k_B T_L)+1}\right] \mathcal{D}_{n'}(k^{\prime})\, \mathcal{M}^2_{\text{el},kn}, \tag{7.16}$$

where the subscript 'el' indicates that we will take the value of $\mathcal{M}^2_{k^{\prime}n',kn}$ appropriate to elastic scattering from the state $|k,n\rangle$.

To illustrate the use of the inelastic acoustic phonon energy scheme we have shown, in Figs. 7.10a and b, the total AC scattering rates for a carrier in state $|\mathbb{k}\rangle$ in bands 1 and 2 respectively, calculated for the case ϵ_{ac} = 1meV. The rates obtained within the elastic and equipartition approximations (ϵ_{ac} = 0meV) are also shown for comparison. Clearly, there is little difference in the magnitudes of the rates: the main point to note is that the spike features corresponding to scattering into the band 2 and 4 minima are split into doublets for the ϵ_{ac} = 1meV case, showing the separate contributions from absorption and emission processes. The value of ϵ_{ac} can be altered as desired; this will merely alter the separation of the doublet spikes.

For PZ scattering, we may follow exactly the same argument as above. Using an average phonon energy ϵ_{ac}, we obtain, in place of equation (5.65), the PZ rate for absorption or emission:

$$P^{\substack{\text{abs}\\ \text{em}}}_{n',n}(k) = \frac{e^2 k_B T_L}{4\pi^2\hbar}\left(\frac{K^2_{av}}{\varepsilon_0\varepsilon_s}\right)\left[\frac{1}{\exp(\pm\epsilon_{ac}/k_BT_L)+1}\right]\mathcal{D}_{n'}(k')\mathcal{M}^2_{el,kn}, \qquad (7.17)$$

where $\mathcal{M}^2_{el,kn}$ refers to the appropriate value of the term $\mathcal{M}^2_{k'n',kn}$ define in equation (5.66), as calculated in the elastic approximation.

Finally, in Figs. 7.11–14 we have shown the total scattering rates for all processes (AC, NPO, POP and PZ combined), in each of bands 1–4, with the AC and PZ contributions calculated as described above, for the case ϵ_{ac} = 1meV. These represent a typical set of scattering rate profiles for use in the Monte Carlo simulations described in the following chapters.

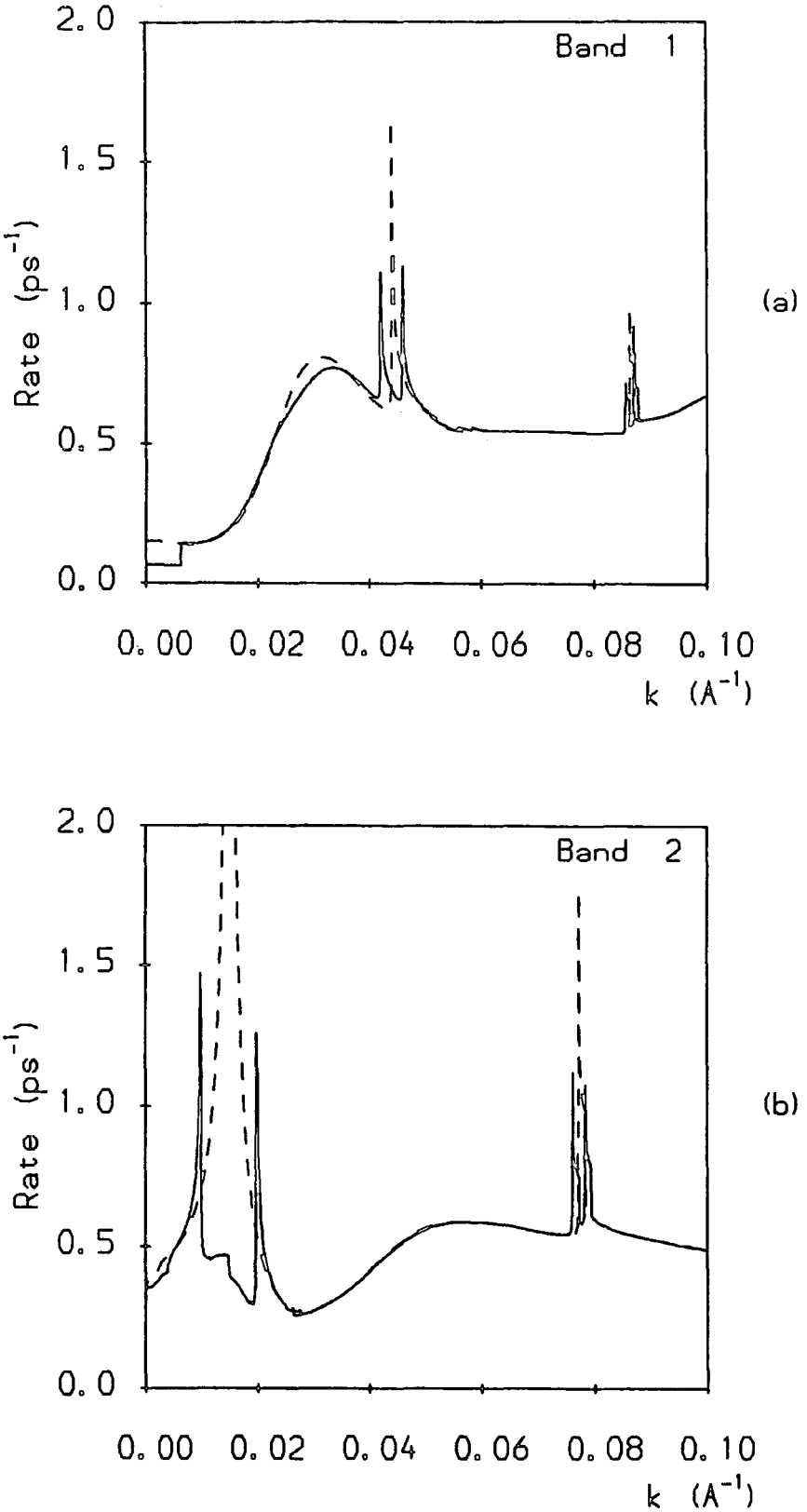

Fig. 7.10 Acoustic (deformation potential) scattering rates in bands 1 and 2, including all possible intra- and inter-band processes. — $\epsilon_{ac} = 1$meV; - - - $\epsilon_{ac} = 0$meV.

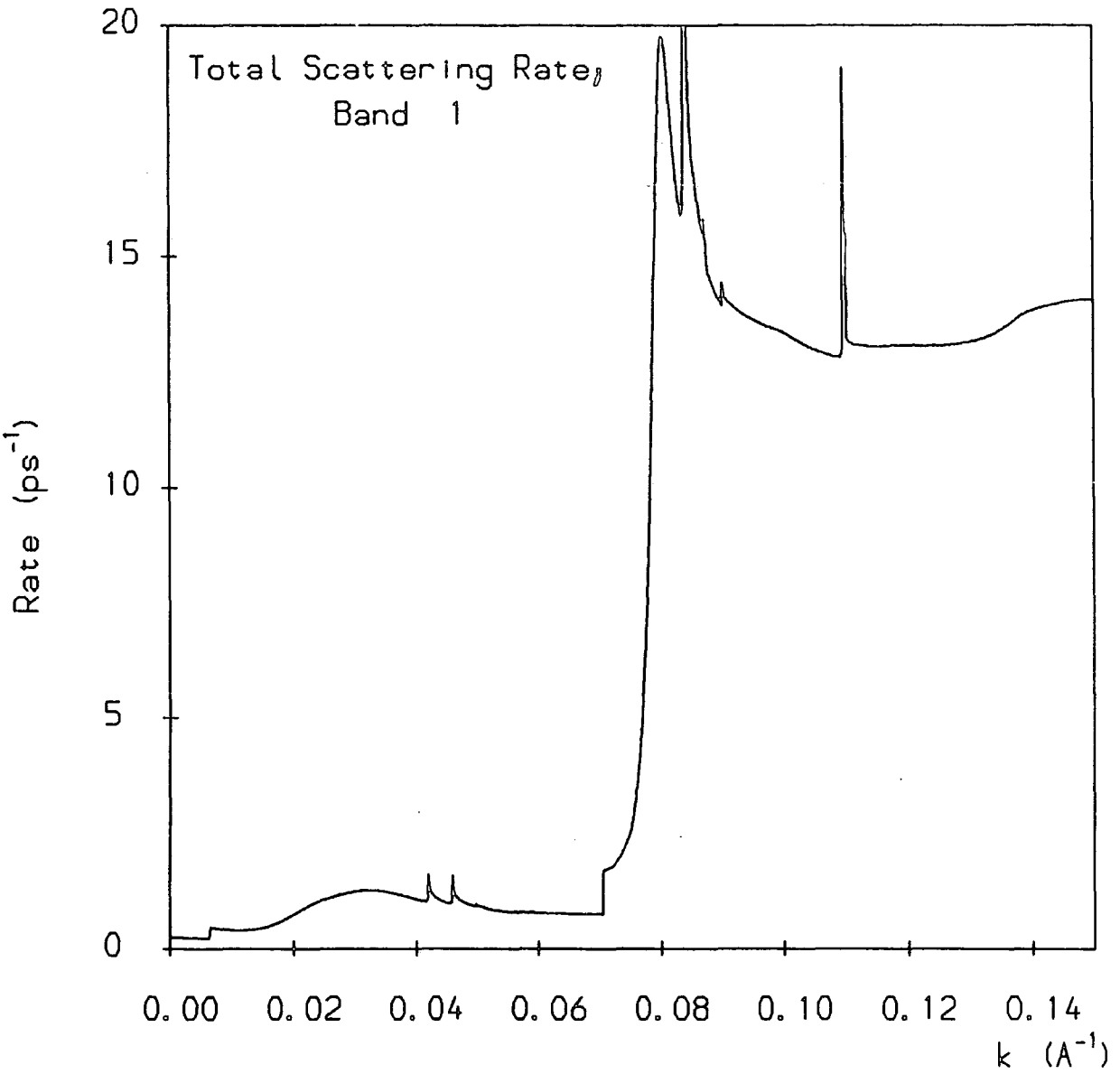

Fig. 7.11 Total phonon scattering rate for a hole in state $|\mathbf{k}\rangle$ in band 1, including all possible POP, NPO, AC and PZ processes. $T_L = 77K$; $\epsilon_{ac} = 1.0$meV.

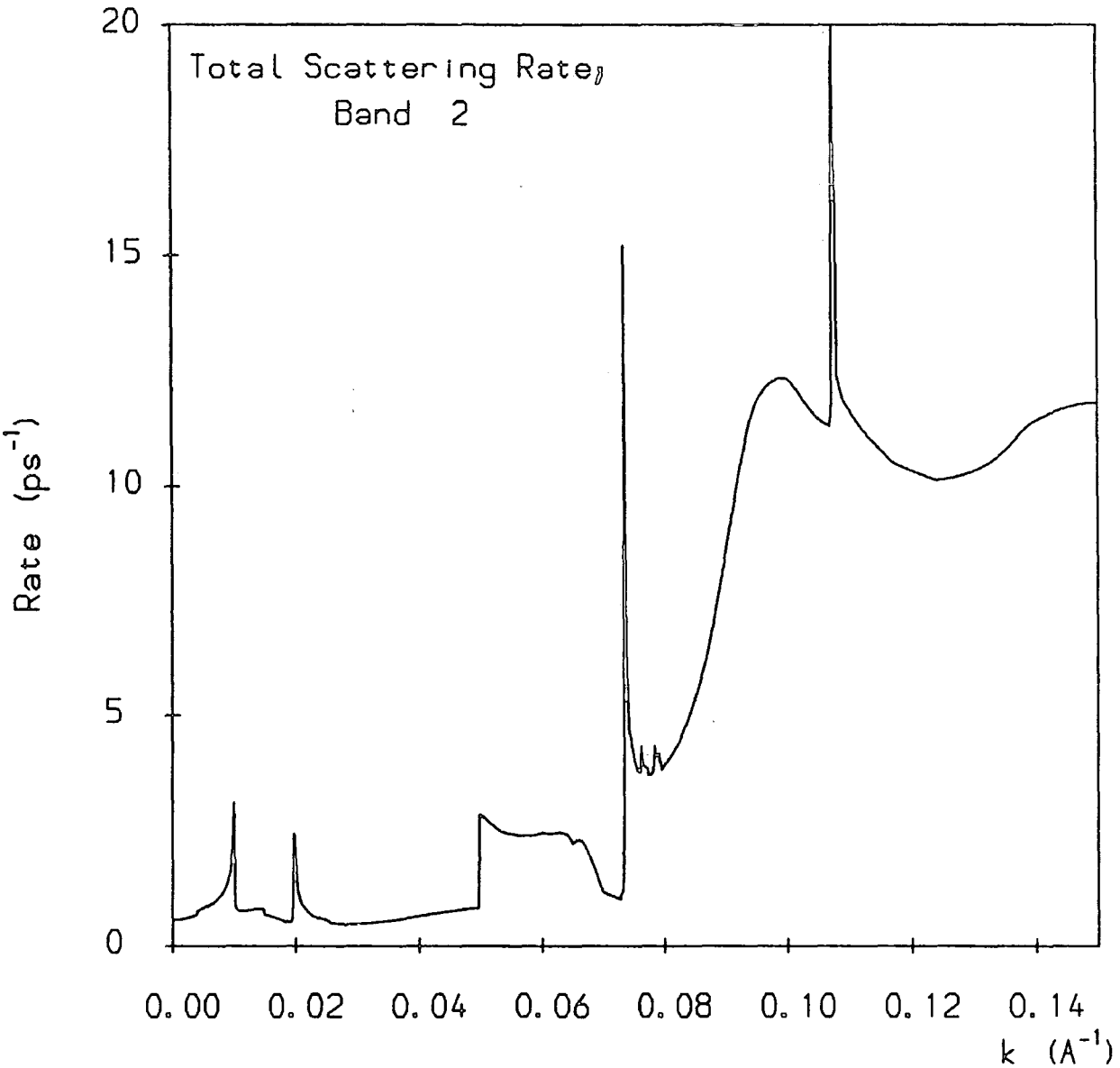

Fig. 7.12 Total phonon scattering rate for a hole in state $|\mathbf{k}\rangle$ in band 2, including all possible POP, NPO, AC and PZ processes. $T_L = 77K$; $\epsilon_{ac} = 1.0\text{meV}$.

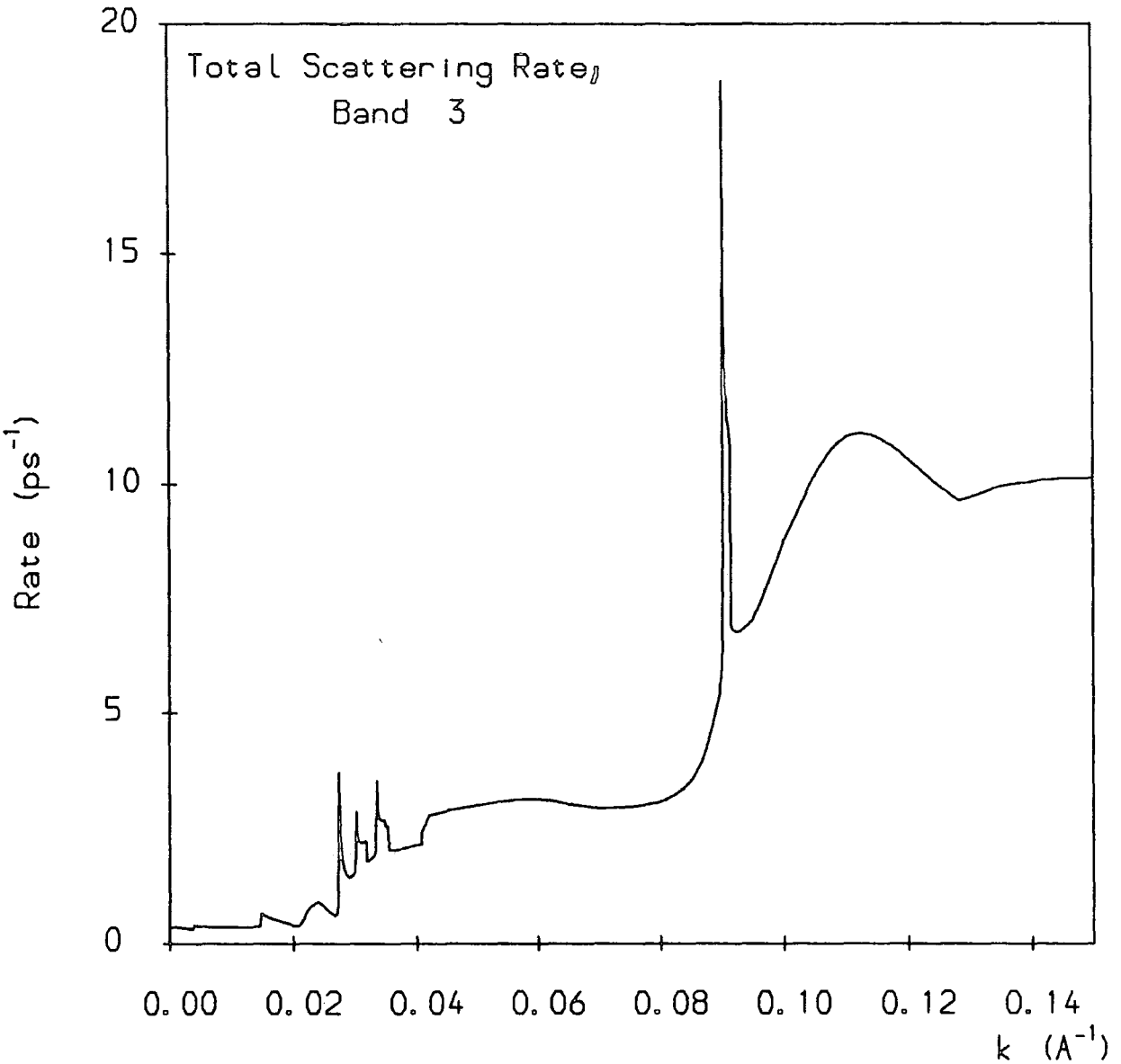

Fig. 7.13 Total phonon scattering rate for a hole in state $|\mathbf{k}\rangle$ in band 3, including all possible POP, NPO, AC and PZ processes. $T_L = 77K$; $\epsilon_{ac} = 1.0\text{meV}$.

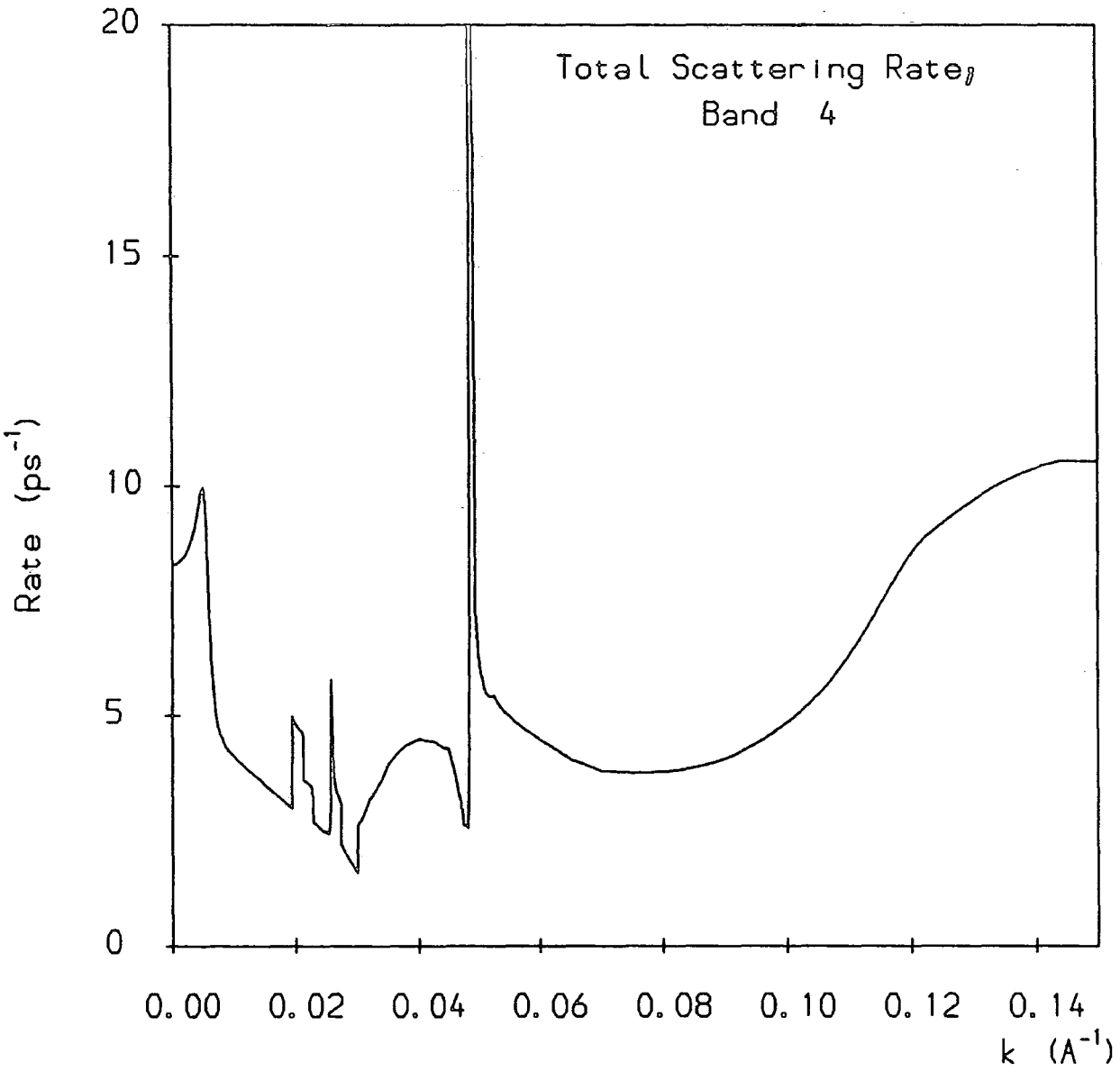

Fig. 7.14 Total phonon scattering rate for a hole in state $|\mathbf{k}\rangle$ in band 4, including all possible POP, NPO, AC and PZ processes. $T_L = 77K$; $\epsilon_{ac} = 1.0\text{meV}$.

CHAPTER 8
MONTE CARLO IMPLEMENTATION

In Chapter 2 we described the basic principles of the Monte Carlo method and gave some details of our prototype simulation programs. In this chapter, we will discuss some of the important additions and modifications necessary in order to incorporate, in the simulation, the detailed model of the quantum well valence band system as described in the previous three chapters.

8A PRELIMINARY DETAILS OF THE SIMULATION CODES

We have developed Monte Carlo programs for both single particle and ensemble simulations of quantum confined hole dynamics. As discussed in Chapter 2, the program design was such that the two simulations share large portions of code, and so it will not be necessary to discuss each program separately here. The programs were written in standard FORTRAN77. It is not intended to include in this thesis a complete listing of the source codes. Such a listing would occupy an inordinate amount of space, and would not, by itself, prove very informative to the reader. Rather, our objective is to set out the details of those key elements of the program which were developed especially for the inclusion of the quantum confined valence band model. Listings of individual portions of code are presented where this is considered necessary, but the length and frequency of such listings has been kept to a minimum. The reference to specific FORTRAN variable names in the text has been similarly minimised, although the use of certain variable names is essential in achieving clarity in explanation. In this chapter, we will use both 'physical' variables (ϵ, k, *etc.*) and FORTRAN variable names, and will make clear the equivalences between the two notations. We have not shown any flow diagrams for the programs: whilst many new features are described here, the basic program structures can still be represented by the flow diagrams given in Figs. 2.5 and 2.7.

In the simulations, hole transport is considered to be two dimensional, with the effects on confinement in the third dimension described by the form of the quantum confined hole wavefunctions. Transport in the plane of the well is assumed to be classical. We can therefore identify a set of 'state variables' for the carriers in the simulation. These are: the wavevector components $k_x \equiv$ VIX, $k_y \equiv$ VIY; the modulus of k, VIMOD, and the energy $\epsilon \equiv$ EI. As in Chapter 2, the suffix 'I' in the FORTRAN variable names denotes quantities measured at the beginning of a particle free flight, with those measured at the *end* of a flight having 'I' replaced by 'F'. A corresponding convention used in this chapter uses the suffices 'BS' and 'AS' to denote variables measured before and after a scattering event. Thus EBS corresponds to EF, and EAS corresponds to EI.

The band index ($n \equiv$ IBNP) is also a state variable and, in the ensemble

simulation, so is the cumulative particle flight time TSIM(NP) for the carrier of index NP.

8B BANDSTRUCTURE ROUTINES

In the work described in Chapters 2–4, the energy bands occupied by the carriers were taken to be parabolic. Thus, ϵ, k, the carrier group velocity $v_{gp} = (1/\hbar)\nabla_k\epsilon$, and the density of states $D(\epsilon)$ were all related by simple algebraic formulae. However, in the quantum well valence band system no simple relation between these parameters exists, due to the irregular form of the band dispersions. We chose to tabulate ϵ, $\partial\epsilon/\partial k$ and $\mathcal{D}_n = k/|\partial\epsilon/\partial k|$ against k. This data is loaded into the simulation at its initial stage, and stored in a 3D array BSK(L,M,N). The first index, L, gives the value of k, the second, M, the choice of parameter; k, ϵ, $\partial\epsilon/\partial k$ or $\mathcal{D}_n$, and the third, N, the band index IBNP. This information is made available to the various parts of the simulation via a set of subprograms BSENGY, BSVGRP, BSWAVE and BSEDOS.

The subprograms BSENGY and BSVGRP (Fig. 8.1) are functions which return the value of ϵ and v_{gp} (strictly $v_{gp}/\hbar \equiv \partial\epsilon/\partial k$) respectively, for a given value of k in a given band. Within the range of the tabulated data, a simple linear interpolation between datapoints is employed. Beyond the range of the data $\epsilon(k)$ is obtained by parabolic extrapolation, and $v_{gp}(k)$ by linear extrapolation. The parameters $a_{i,n} \equiv$ A(I,IBNP); I = 1...3 which define the extrapolation functions are themselves defined at an earlier stage of simulation initialisation.

BSWAVE and BSEDOS (Figs. 8.2–3) are subroutines which return values for k and $\mathcal{D}_n$ respectively, for a given energy ϵ in a given band. Both operations involve a search procedure through the energy (M = 2) column of the BSK array. The search obtains the energy entry closest to the supplied value ϵ, and the corresponding value of k or $\mathcal{D}_n$ (from column 1 or 4) is then returned.

The specification of BSWAVE and BSEDOS is complicated by the fact that, in each of bands 2 and 4, two values of k and $\mathcal{D}_n$ exist for energies below that of the zone centre. When this condition occurs, two searches must be performed: one through *decreasing* values of energy between the $k = 0$ and $k = k_n(0)$ (see Table 6.1c) entries in the BSK array, and the other through *increasing* values of energy, from the $k = k_n(0)$ entry upwards. These searches are implemented by two subroutines SEARCH and DNSRCH, which have not been shown here. Both subroutines use an algorithm which repeatedly halves the search interval, and both employ linear interpolation between adjacent data points.

Thus, BSWAVE and BSEDOS each return two values, corresponding to k and $\mathcal{D}_n$ in the a and b regions of the given band. Where the supplied value of energy is out of the range of the b region, the b-variable is set to zero. For supplied energy values beyond the range of the tabulated data, the wavevector k is obtained by taking the positive root of the extrapolation equation $\epsilon = a_{1,n} + a_{2,n}k + a_{3,n}k^2$.

```
      DOUBLE PRECISION FUNCTION  BSENGY(VMOD,IBNP)
      IMPLICIT REAL*8(A-H, O-Z)
      COMMON /BSTRUC/  BSK(0:409,4,4)
      COMMON /MAT/       EOP, WOP, E1, E2, E3, E4, E2K0, E4K0, DELK
      COMMON /BSXPAR/  A(3,4), NMAX

      VNORM = VMOD/DELK
      IV = IDINT(VNORM)

      IF (IV  .LT.  0) THEN                                          (a)
         BSENGY = 0.0
       ELSEIF (IV+1  .GT.  NMAX) THEN
C        Use parabolic extrapolation.
         BSENGY = A(1,IBNP) + A(2,IBNP)*VMOD + A(3,IBNP)*VMOD*VMOD
      ELSE
         ENGY1 = BSK(IV,2,IBNP)
         ENGY2 = BSK(IV+1,2,IBNP)
         BSENGY = ENGY1 + (VNORM - IV)*(ENGY2-ENGY1)
         IF (BSENGY .LT. 1E-9)  BSENGY = 0.0E00
      ENDIF

      RETURN
      END
```

```
      DOUBLE PRECISION FUNCTION  BSVGRP(VMOD,IBNP)
      IMPLICIT REAL*8(A-H, O-Z)
      COMMON /BSTRUC/  BSK(0:409,4,4)
      COMMON /MAT/       EOP, WOP, E1, E2, E3, E4, E2K0, E4K0, DELK
      COMMON /BSXPAR/  A(3,4), NMAX

      VNORM = VMOD/DELK
      IV = IDINT(VNORM)

                                                                     (b)
      IF (IV  .LT.  0) THEN
         BSVGRP = 0.0
      ELSEIF (IV+1  .GT.  NMAX) THEN
C        Use linear extrapolation
         BSVGRP =  A(2,IBNP) + 2.0*A(3,IBNP)*VMOD
      ELSE
         VEL1 = BSK(IV,3,IBNP)
         VEL2 = BSK(IV+1,3,IBNP)
         BSVGRP = VEL1 + (VNORM - IV)*(VEL2 - VEL1)
      ENDIF
      RETURN
      END
```

Fig. 8.1 FORTRAN code for the functions BSENGY (a) and BSVGRP (b). The variable NMAX gives the number of wavevector points in the bandstructure database (contained within array BSK), and DELK gives the wavevector increment between adjacent points.

```
      SUBROUTINE BSWAVE(E,IBNP, VA,VB)
      IMPLICIT REAL*8(A-H, O-Z)
      COMMON /BSTRUC/ BSK(0:409,4,4)
      COMMON /MAT/      EOP, WOP, E1, E2, E3, E4, E2K0, E4K0, DELK
      COMMON /MAT2/     V2E0, V4E0
      COMMON /BSXPAR/ A(3,4), NMAX

      VB = 0.0

      IF (E .GT. BSK(NMAX,2,IBNP)) THEN
C        Use inverse parabolic extrapolation.
         VA = ( -A(2,IBNP) +
     *          DSQRT( A(2,IBNP)*A(2,IBNP) - 4.0*A(3,IBNP)*(A(1,IBNP)-E) ))
     *          / (2.0*A(3,IBNP))

      ELSEIF (E .LT. 0.0E00) THEN
         IF (IBNP .EQ. 2) THEN
            VA = V2E0
            VB = V2E0
         ELSEIF (IBNP .EQ. 4) THEN
            VA = V4E0
            VB = V4E0
         ELSE
            VA = 0.0
         ENDIF

C     Use of search routines; arguments 2 & 3 define subset of tabulated
C     data in which search is performed.
C     ICOL gives index of column from which data is returned.
C     Search operation is always performed on energy column (index 2).
      ICOL = 1

      ELSEIF (IBNP .EQ. 2) THEN
         IF (E .LT. E2K0) THEN
            CALL DNSRCH(E,0,60,ICOL,IBNP, VB)
            CALL SEARCH(E,60,106,ICOL,IBNP, VA)
         ELSE
            CALL SEARCH(E,106,NMAX,ICOL,IBNP, VA)
         ENDIF

      ELSEIF (IBNP .EQ. 4) THEN
         IF (E .LT. E4K0) THEN
            CALL DNSRCH(E,0,85,ICOL,IBNP, VB)
            CALL SEARCH(E,85,104,ICOL,IBNP, VA)
         ELSE
            CALL SEARCH(E,104,NMAX,ICOL,IBNP, VA)
         ENDIF

      ELSE
        CALL SEARCH(E,0,NMAX,ICOL,IBNP, VA)
      ENDIF

      RETURN
      END
```

Fig. 8.2 FORTRAN code for the subroutine BSWAVE. Variables E2K0 and E4K0 give the zone-centre energies in bands 2 and 4 ($\epsilon_2(0)$ and $\epsilon_4(0)$ respectively), and V2E0 and V4E0 give the wavevectors of the off-

```
      SUBROUTINE BSEDOS(E,IBNP, DOSA,DOSB)
      IMPLICIT REAL*8(A-H,O-Z)
      COMMON /BSTRUC/  BSK(0:409,4,4)
      COMMON /MAT/       EOP, WOP, E1, E2, E3, E4, E2K0, E4K0, DELK
      COMMON /BSXPAR/  A(3,4), NMAX
      COMMON /BROAD/   SCALA(4),SCALB(4),EMATCH(4), DELHF, ELOW, LBROAD
      LOGICAL   LBROAD

      DOSB = 0.0E00

      IF (E .GT. BSK(NMAX,2,IBNP)) THEN
C        Constant value extension for all bamds.
         DOSA = BSK(NMAX,4,IBNP)

C        Use of search routines; see BSWAVE.
         ICOL = 4

      ELSEIF (IBNP .EQ. 2) THEN
         IF (E .GT. E2K0) THEN
            CALL SEARCH(E,106,NMAX,ICOL,IBNP, DOSA)
         ELSE
            IF ((LBROAD) .AND. (E .LT. EMATCH(IBNP))) THEN
               CALL CONVOL(E,IBNP, DOSA,DOSB)
            ELSE
               CALL DNSRCH(E,0,60,ICOL,IBNP, DOSB)
               CALL SEARCH(E,60,106,ICOL,IBNP, DOSA)
            ENDIF
         ENDIF

      ELSEIF (IBNP .EQ. 4) THEN
         IF (E .GT. E4K0) THEN
            CALL SEARCH(E,104,NMAX,ICOL,IBNP, DOSA)
         ELSE
            IF ((LBROAD) .AND. (E .LT. EMATCH(IBNP))) THEN
               CALL CONVOL(E,IBNP, DOSA,DOSB)
            ELSE
               CALL DNSRCH(E,0,85,ICOL,IBNP, DOSB)
               CALL SEARCH(E,85,104,ICOL,IBNP, DOSA)
            ENDIF
         ENDIF

      ELSE
C        Bands 1 & 3 only
         IF (E .LT. 0.0E00) THEN
            DOSA = 0.0
         ELSE
            CALL SEARCH(E,0,NMAX,ICOL,IBNP, DOSA)
         ENDIF
      ENDIF

      RETURN
      END
```

Fig. 8.3 FORTRAN code for the subroutine BSEDOS. If the logical variable LBROAD is assigned the value .TRUE. in the calling program, then broadening of the densities of states around the off-zone-centre band minima will be performed.

The density of states for out-of-range energies is again obtained by fixed value extrapolation.

The subroutine BSEDOS also includes a clause which invokes broadening of the density of states. As was discussed in section 7B.3, the Lorentzian broadened density of states around a critical point may be matched to the unbroadened density of states at some convenient value of energy. In the simulation, the matching energies in each of bands 2 and 4 (EMATCH(IBNP)) are set on initialisation. For supplied values of energy within the defined range, the tabulated density of states data is replaced by the function of equation (7.10), which is contained within the subroutine CONVOL (not shown).

8C SCATTERING RATE ROUTINES

Indexing of the Matrix elements

The database for the 4-band k.p matrix elements consists of sets of datapoints taken over a range of initial state wavevectors k, for each scattering process. Each data set contains up to twenty values of k; however, the actual k values, and the total number of points, vary from process to process. It is therefore necessary to make available to the simulation, information on the size and composition of the wavevector set for every process.

To this end we have indexed the processes for scattering from a given band n by a number between 1 and 48 (for the case of inelastic acoustic scattering). The matrix element data can then be stored in three sets of arrays:
ARMXA(I,J,K), VSETA(I,J,K) and NVPTSA(J,K) for AC processes;
ARMXN(I,J,K), VSETN(I,J,K) and NVPTSN(J,K) for NPO processes, and
ARMXIP(I,J,K), VSETP(I,J,K) and NVPTSP(J,K) for POP and PZ processes.
(It would be quite possible to store the AC and NPO data together in one set of arrays, as for the POP and PZ processes.) The index K then gives the band index $n \equiv$ IBNP $= 1 \ldots 4$. J gives the process index (JPROC), and I gives the index of the required datapoint for the process defined by J and K.

Then, the array element NVPTSA(J,K) gives the total number of datapoints in the data set for an AC process defined by J,K. VSETA(I,J,K) gives the wavevector of entry I in the data set for AC process J,K, and ARMXA(I,J,K) gives the matrix element evaluated at VSETA(I,J,K). Analogous definitions apply for the arrays for NPO, and POP and PZ processes.

The contents of the matrix element database are loaded into these arrays at the initialisation stage of the simulation, and made available to other subprograms as necessary via named COMMON blocks.

Compilation of the Scattering Rate Data

A complete set of scattering rates is calculated at the initialisation stage of the simulation, following the loading of bandstructure and matrix element data. The wavevector independent prefactors to the scattering rates are calculated by a short subroutine SCARR, after which the principal scattering rate subroutines SRATE1...4 are called from the main program.

The scattering rates are first stored in the form of a list of values for each of the 48 processes, for each value of k. (The wavevector increment is given by DELKSC $= 10^{-4}$Å^{-1}.) The calculation of a particular scattering rate mimics the basic form of the scattering rate expressions of equations (5.47), (5,50), (5.53) and (5.68). Fig. 8.4 shows extracts from subroutine SRATE1, from which it can be

```
      SUBROUTINE SRATE1(SCLIS1)
      IMPLICIT REAL*8(A-H, O-Z)
      COMMON /MAT/        EOP, WOP, E1, E2, E3, E4, E2K0, E4K0, WL, DELK
      COMMON /LADPAR/  DELKSC, LADSIZ, LADROW
      COMMON /SPREF/      P(8)
.
.
.
C     ********** BAND 1 **********
      DO 100 M = 0, LADROW
      VMOD  = DELKSC * FLOAT(M) + OFST
      E = BSENGY(VMOD,1)
.
.
.
.
.
C 7,8:  NPOab11, POPab11~~~~~~~~~~~~~~~~~~~~~~~~~~~~~~~~~~~~~~~~

      EAS = E+EOP
      CALL BSEDOS(EAS,1,  DOSA,DOSB)
      SCLIS1(M,7) = P(2) * DOSA * FMXELN(VMOD,7,1)
      SCLIS1(M,8) = P(3) * DOSA * FMXELP(VMOD,8,1)

C 9,10: NPOem11, POPem11~~~~~~~~~~~~~~~~~~~~~~~~~~~~~~~~~~~~~~~~

      EAS = E-EOP
      IF (EAS .LT. 0.0) THEN
         SCLIS1(M,9) = 0.0E00
         SCLIS1(M,10) = 0.0E00
      ELSE
         CALL BSEDOS(EAS,1,  DOSA,DOSB)
         SCLIS1(M,9)  = P(6) * DOSA * FMXELN(VMOD,9,1)
         SCLIS1(M,10) = P(7) * DOSA * FMXELP(VMOD,10,1)
      ENDIF
.
.
.
.
```

Fig. 8.4 Extracts from the FORTRAN code for subroutine SRATE1, showing the calculation of optical phonon (NPO and POP) scattering rates for intraband processes in band 1. The array P contains the wavevector-independent prefactors for the various scattering rates, and the variable EOP gives the optical phonon energy $\hbar\omega_{op}$.

seen that the scattering rate consists of only three terms:

(i) the appropriate prefactor;

(ii) the density of final states, and

(iii) a function FMXEL*(VMOD,J,K), where the suffix '*' represents 'A', 'N' or 'P' as described in the previous section.

The functions FMXEL* merely give the value of the matrix element at wavevector VMOD, for the process of index J in band K. The values are obtained from the arrays ARMX*, VSET* and NVPTS* described above, with linear interpolation between the datapoints. For wavevectors VMOD beyond the range for a given process, fixed value extrapolation is used. Fig 8.5 shows the function FMXELA; the functions FMXELN and FMXELP take exactly the same form.

The density of states is obtained by a call to subroutine BSEDOS, with the the appropriate after-scattering energy EAS as the supplied parameter.

The end product of the subroutines SRATE1...4 is a set of 2D arrays SCLIS1...4(M,J), which contain the scattering rates for all processes (indexed by J) for a regular set of initial state wavevectors indexed by M (k = M × DELKSCÅ^{-1}). Following our discussion in section 2B.1, we define the 3D array SCLAD(M,J,K) in which to store the cumulative sums of the scattering rates for 1,2,3 *etc.* processes (K represents the band index n). Then, for example, for the scattering rates in band 1 we have:

$$\begin{aligned}\text{SCLAD(M,J,1)} = \text{SCLIS1(M,1)} + \text{SCLIS1(M,2)} + \cdots \\ \cdots \text{SCLIS1(M,J}-1\text{)} + \text{SCLIS1(M,J)}.\end{aligned} \tag{8.1}$$

We refer to these sets of cumulative sums as scattering rate 'ladders'.

Detailed Balancing of the Acoustic Scattering Rates

As discussed in Section 7C, it was decided to adopt a scheme for acoustic scattering in which the scattering states were displaced by a predetermined phonon energy. The scattering rates, however, were to be calculated in the same manner as that prescribed by the elastic and equipartition approximations, but would be modified by a factor $2\mathcal{N}_{\text{ac}}/(2\mathcal{N}_{\text{ac}}+1)$ for absorption, and $2(\mathcal{N}_{\text{ac}}+1)/(2\mathcal{N}_{\text{ac}}+1)$ for emission — where $\mathcal{N}_{ac} = 1/\left(\exp(\epsilon_{\text{ac}}/k_B T_L) - 1\right)$ and ϵ_{ac} is the phonon energy. The density of states must be that appropriate to an energy $\epsilon = \epsilon_{\text{bs}} \pm \epsilon_{\text{ac}}$ (where ϵ_{bs} is the before-scattering energy), and this must be the value supplied in the call to subroutine BSEDOS.

However, on running the simulation, these two precautions were not found to be sufficient to achieve a detailed balance of acoustic phonon absorption and emission processes. This loss of balance was ascribed to the use of *different* values

```
      DOUBLE PRECISION FUNCTION  FMXELA(VMOD,IPROC,IBNP)
C     Gives values for Acoustic scattering matrix elements using
C     interpolation of envelope function data.
      IMPLICIT REAL*8(A-H, O-Z)
      COMMON /MXELA/  ARMXA(20,6,4), VSETA(20,6,4), NVPTSA(6,4)

      NVPTS = NVPTSA(IPROC,IBNP)
C     Out of range cases.
      IF (VMOD  .GE.  VSETA(NVPTS,IPROC,IBNP)) THEN
         FMXELA = ARMXA(NVPTS,IPROC,IBNP)
      ELSEIF (VMOD  .LE.  VSETA(1,IPROC,IBNP)) THEN
         FMXELA = ARMXA(1,IPROC,IBNP)
      ELSE
C        Repeated halving search, with linear interpolation.
         NL = 1
         NTOP = NVPTS
1        CONTINUE
            NU = (NL+NTOP)/2
            VU = VSETA(NU,IPROC,IBNP)
            IF (VMOD  .LT.  VU) THEN
               IF (NU-NL  .EQ.  1) THEN
                  VL = VSETA(NL,IPROC,IBNP)
                  DATU = ARMXA(NU,IPROC,IBNP)
                  DATL = ARMXA(NL,IPROC,IBNP)
                  FMXELA = DATL + (DATU - DATL)/(VU - VL)*(VMOD - VL)
                  GOTO 9
               ENDIF
               NTOP = NU
            ELSE
               IF (NTOP-NU  .EQ.  1) THEN
                  VT = VSETA(NTOP,IPROC,IBNP)
                  DATT = ARMXA(NTOP,IPROC,IBNP)
                  DATU = ARMXA(NU,IPROC,IBNP)
                  FMXELA = DATU + (DATT - DATU)/(VT - VU)*(VMOD - VU)
                  GOTO 9
               ENDIF
               NL = NU
            ENDIF
         GOTO 1
9        CONTINUE
      ENDIF

      RETURN
      END
```

Fig. 8.5 FORTRAN code for the function FMXELA, which returns a value for the acoustic (AC) scattering matrix element for the process of index IPROC, for a carrier of wavevector VMOD in band IBNP.

of matrix element to describe absorption and emission scatterings involving the same pair of states. The problem is summarised in Fig. 8.6. For scattering from state $|1^\circ\rangle$ to state $|2^+\rangle$ by absorption of an acoustic phonon, the correct matrix element would be $\langle 2^+|H|1^\circ\rangle$, for some Hamiltonian operator H. However, since our matrix elements are calculated in an *elastic* approximation, we would take, for the transition from $|1^\circ\rangle$, the matrix element $\langle 2^\circ|H|1^\circ\rangle$. For the complementary process — scattering from $|2^+\rangle$ to $|1^\circ\rangle$ by acoustic phonon emission — the correct matrix element is $\langle 1^\circ|H|2^+\rangle$; whence $|\langle 1^\circ|H|2^+\rangle|^2 \equiv |\langle 2^+|H|1^\circ\rangle|^2$, since H is Hermitian. However, the matrix element selected in the subroutines SRATE1...4 would be that for *elastic* scattering from state $|2^+\rangle$; *i.e.*, $\langle 1^+|H|2^+\rangle$.

Whilst the difference between the matrix elements $\langle 2^\circ|H|1^\circ\rangle$ and $\langle 1^+|H|2^+\rangle$ is expected to be small, errors of this kind, when reproduced consistently throughout the simulation, proved sufficient to displace the simulation from the true equilibrium state, at least for the zero field case. The obvious solution of the problem is to ensure that, in the scattering rate subroutines, all the acoustic rates are defined so that identical matrix elements are assigned to every pair of complementary transitions. We have adopted the convention that, for an absorption process from a state $|1^\circ\rangle$, the matrix element used is that evaluated at the wavevector of state $|1^+\rangle$; *i.e.*, the matrix element $\langle 2^+|H|1^+\rangle$. For an emission process, the elastic scattering matrix element appropriate to the given state is used, as before. This matrix element is given by $\langle 1^+|H|2^+\rangle$ as above, and so the matrix elements for complementary absorption and emission scatterings are now equal.

Special care must be taken for processes involving states in band 2 and 4 at energies below the zone centre, since there are some transitions of this type to which the general convention proposed above cannot be applied.

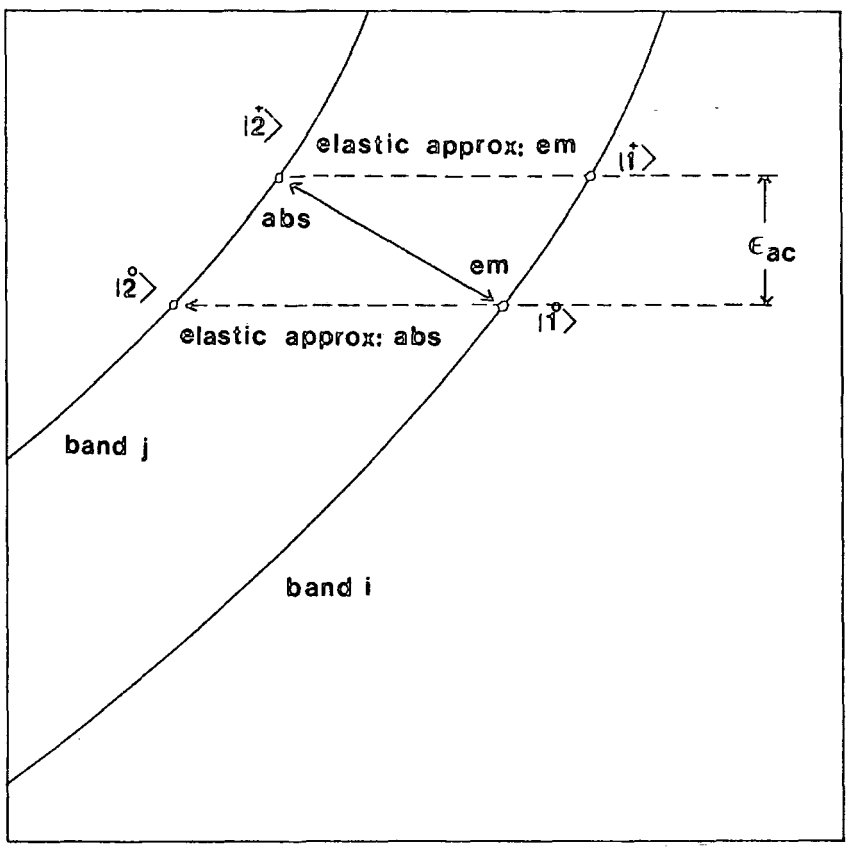

Fig. 8.6 Schematic diagram to show the difference between the true location of the after scattering states for interband acoustic processes, and those deduced within the elastic approximation.

8D SELF SCATTERING

The basic self scattering scheme used in a Monte Carlo simulation was described in section 2A.1. It involves the definition of a fixed scattering rate Γ, which is greater than the total real scattering rate $P(\mathbf{k})$, for all values of $\mathbf{k}$.

On examination of the quantum confined hole-phonon scattering rates of Figs 7.11–14, it can be seen that, if a fixed value of Γ were used for each band, then the percentage of self scatterings occurring in the Monte Carlo simulation would be very large. Clearly, the use of one of the methods described in section 2C.1, for improving the efficiency of the self scattering approach, is desirable. The scattering rates shown in Figs. 7.11–14 are quite general in form; in particular, they do not exhibit a monotonous increase with k. We mentioned in section 2C.1 that such cases introduce complications in the application of the iterative gamma method. Therefore, we preferred to adopt the stepped gamma approach. We have used the method in its simplest form, defining gamma profiles in each band which include a single step, located near the principal optical phonon emission threshold. This leads to a significant reduction in the proportion of self scattering events which occur in the simulation; however, if the upper values of Γ were set above the tops of the spike features in the scattering rates, then the proportion of self scatterings occurring would still be excessively large. To avoid this, we choose upper values of Γ in each band which are less than these peak values, but greater than the nearby values of $P(k)$. Such choices reduce the proportion of self scatterings considerably, but, in the absence of further intervention, would lead to a loss of the probability flux associated with the scattering rate spikes. This flux is restored to the simulation by the inclusion of a short clause, which compares the values of Γ and $P(k)$, prior to the selection of a scattering process. If $\Gamma < P(k)$, then the value of Γ to be used for the subsequent selection is *temporarily* raised above $P(k)$. This ensures that all valid contributions to the scattering rate are present when the selection is made. This clause appears at the beginning of the process selection subroutine SMECH (Fig. 8.7). The value of Γ to be used for the current selection (given by GAM(INGAM,IBNP); *cf.* Fig. 2.12) is duplicated in the local variable GAMMA; thus any change in this value is discarded on exit from the subroutine.

Of course, by using upper values of Γ less than the peak values of the scattering rate spikes, we will create a slight increase in the probability that a particle will escape scattering on drifting through regions in k-space where the spikes occur. However, since the spikes are very narrow, the discrepancy introduced is not expected to be serious.

```
      SUBROUTINE SMECH(EF,VFX,VFY, EI,VIX,VIY)
      IMPLICIT REAL*8(A-H,O-Z)

      COMMON /SIM/          VMAX(4), VSTG(4), GAM(2,4), BLSTC, INGAM
      COMMON /LADDER/  SCLAD
      COMMON /LADPAR/  DELKSC, LADSIZ, LADROW
      COMMON /MECHAR/  ECOL(48,4), KINDEX(48), NEWB(48)
      COMMON /VALP/       IBNP, IBNEW
      COMMON /COUNT/     NPUSH(2,4), NCOL(49,4), NCAP(4), NEG(4)

      GAMMA = GAM(INGAM,IBNP)
      JPROC = 0

      VFMOD = DSQRT(VFX*VFX + VFY*VFY)
C     W/v ceiling at VMAX
      IF (VFMOD  .GT.  VMAX(IBNP)) CALL ENCAP(VFX,VFY,VFMOD,EF)
C     1st cell is index 0; V = 1.0E-4 A-1
      IV = IDNINT(VFMOD/DELKSC)
C     Fixed value SCLAD extrapolation between top of ladder & VMAX.
      IF (IV  .GT.  LADROW) IV = LADROW

C     Temporary GAMMA 'push'.
      TSCAT = SCLAD(IV,LADSIZ,IBNP)
      IF (GAMMA  .LT.  TSCAT) THEN
         GAMMA = TSCAT*1.001
         NPUSH(INGAM,IBNP) = NPUSH(INGAM,IBNP) + 1
      ENDIF
      S = GAMMA * G05CAF(1)

10    CONTINUE
         JPROC = JPROC + 1
         IF (JPROC  .GT.  LADSIZ) THEN
C           "Top" of scatt. ladder had been reached; select self scattering.
C           Drop out of IF.. clause
            CALL KQWSLF (VFX,VFY,EF,  VIX,VIY,EI)

         ELSEIF (S  .LE.  SCLAD(IV,JPROC,IBNP)) THEN
C           Process has been selected;
C           Drop out of IF.. clause after appropriate action.
            EI = EF + ECOL(JPROC,IBNP)

            IF (EI  .LT.  0.0) THEN
C              -ve energy caused by dos tails; discard JPROC & self scatter.
               NEG(IBNP) = NEG(IBNP) + 1
               JPROC = LADSIZ + 1
               CALL KQWSLF (VFX,VFY,EF,  VIX,VIY,EI)
            ELSE
C              Real scatt: use JPROC to retrieve new band & select K** call.
               IBNEW = NEWB(JPROC)
               IF (KINDEX(JPROC)  .EQ.  1) THEN
                  CALL KQWISO (JPROC,VFX,VFY,VFMOD,  VIX,VIY,EI)
               ELSEIF (KINDEX(JPROC)  .EQ.  2) THEN
                  CALL KQWPOP (JPROC,VFX,VFY,VFMOD,  VIX,VIY,EI)
               ENDIF
            ENDIF
```

Fig. 8.7 *Continued overleaf ...*

```
      ELSE
C        No process selected; loop back to top of IF.. clause.
         GOTO 10
      ENDIF

C     Final parameter update on exit from IF.. clause.
      NCOL(JPROC,IBNP) = NCOL(JPROC,IBNP) + 1
      IBNP = IBNEW

      RETURN
      END
```

Fig. 8.7 FORTRAN code for the scattering process selection subroutine SMECH in the single particle Monte Carlo program.

8E SCATTERING PROCESS SELECTION

Loop Algorithm for Subroutine SMECH

In Chapter 2, we described the basic algorithm for the selection of a scattering process at the end of each free flight in the Monte Carlo simulation. We suggested that such an algorithm could be implemented as a simple cascade of IF...THEN...ELSE clauses. However, when the simulation includes such a large number of scattering processes as is used here, this method becomes impractical.

We have developed an alternative, loop algorithm for scattering process selection, which has the advantage of a high degree of flexibility, as well as being much more compact than the IF...THEN...ELSE cascade. The FORTRAN code for this algorithm is shown in Fig. 8.7.

The loop variable in the code is the scattering process index JPROC. If this exceeds the total number of processes in a given band (the size of the scattering ladder, LADSIZ), then a self scattering is selected. This is implemented by a call to a subroutine KQWSLF which assigns to the after-scattering state variables VIX, VIY and EI, the values of the before-scattering variables VFX, VFY and EF. Otherwise, the random variate $S \equiv r\Gamma$ (see section 2A.1) is compared with the JPROC*th* step of the scattering ladder SCLAD, in band IBNP. If S is less than the ladder entry, then the real process indexed by JPROC is selected.

At this point, three pieces of information are required before the after-scattering wavevector can be determined:

(i) the amount of energy gained or lost upon scattering;

(ii) the band into which the particle is scattered, and

(iii) the method by which the scattering angle must be chosen.

This information is contained within three arrays; ECOL(JPROC,IBNP), NEWB(JPROC) and KINDEX(JPROC), which are defined on initialisation.

The values of elements of array ECOL are simply given by the difference between the band edge energies of the initial and final bands plus or minus an optical or acoustic phonon energy. The first term ensures that the state variables EI and EF always give the particle energy relative to the band minimum; *i.e.*, EI and EF are 'kinetic' energies in the current band.

The array elements NEWB(JPROC) give the band into which the particle is scattered, for each process JPROC. For scattering into bands 2 or 4, the region of the band, *a* or *b*, must be explicitly stated. To this end, the *b* regions of bands 2 and 4 are indexed by NEWB(JPROC) = 21 and 41 respectively.

The array elements KINDEX(JPROC) are indices for the routines which determine the after-scattering wavevector. In this simulation, only two such routines

are required to cater for all real scatterings. These are: the subroutine KQWISO, in which VIX and VIY are chosen assuming an isotropic probability distribution of scattering angles, and the subroutine KQWPOP, in which an angular distribution is built up from a numerical data set for each process concerned. Subroutine KQWISO is used for AC and NPO scattering, and is assigned index 1, whilst subroutine KQWPOP is used for POP and PZ scattering, and is assigned index 2. Further details of subroutine KQWPOP are given in Section 8F.

The selection of either a self or a real scattering event causes program control to pass to the end of subroutine SMECH, where the array element NCOL(JPROC,IBNP) is incremented. Array NCOL thus contains the number of scattering events, of each of the 49 types (including self-scattering) in each of the four bands, which occur during the simulation. If no process is selected, which means that JPROC $\leq$ LADSIZ and S > SCLAD(IV,JPROC,IBNP) (see Fig. 8.7), then program control is passed back to the beginning of the loop, and JPROC is incremented.

Thus we have coded, in relatively few FORTRAN statements, a rather detailed algorithm involving a large number of possible paths and a variety of path-dependent variables. The flexibility of the code lies in the use of the arrays ECOL, NEWB and KINDEX to implement the choice of real scattering process. Processes may be swapped, simply by redefining the appropriate elements of these arrays, and new processes can be added by increasing the array sizes. Processes whose angular dependences do not fit into either of the two existing categories described above can be catered for by introducing new after-scattering wavevector determination subroutines, and indexing them by KINDEX(JPROC) = 3,4 ... *etc.*

Handling of Large k Values

The scattering ladders compiled during simulation initialisation extend to $k = 0.15\text{Å}^{-1}$. Beyond this limit, the subroutine SMECH provides for fixed value extrapolation of all columns in the array SCLAD. An upper wavevector limit in each band is imposed by the elements of the array VMAX. If the limit for the current band is exceeded, then a subroutine ENCAP is called, which sets the state variable VFMOD to the value of VMAX(IBNP), and resets VFX, VFY and EF accordingly. A tally of ENCAP calls for each band is recorded; these should not form a significant proportion of the total number of scattering events in the band.

Scattering Process Selection in the Ensemble Simulation

In the ensemble program, scattering process selection is implemented in a subroutine SMECH$ (Fig. 8.8). This is very similar in structure to the single particle routine SMECH, but operates on a complete batch (sub-ensemble) of carriers during each invocation (see section 2B.2). Thus we see, in Fig 8.8, that the entire algorithm is enclosed in a loop running up to the current sub-ensemble size NINDEX. The array element INDEX(N) gives the index number of the N*th* carrier to be scattered, and IBAND(NP) gives the current band for this carrier, as described in section 2B.2. The ensemble array INGAM contains the current values of the gamma indices (see section 2C.1) for the whole ensemble of carriers. Thus, IGNP = INGAM(NP) gives the Gamma index for the next carrier to be scattered, and GAMMA = GAM(IGNP,IBNP) gives its Gamma value.

SMECH$ contains the same process selection loop algorithm as that described above for the single particle routine SMECH. It involves calls to the same routines KQWSLF, KQWISO and KQWPOP, the only difference being that the state variables passed to these routines are now the array elements VIX(NP), VIY(NP) *etc.*, for the carrier of index NP. Thus the routines SMECH and SMECH$ give an excellent demonstration of the compatibility which exists between the single particle and ensemble simulation codes. The use of essentially the same variables, the same algorithm and the same (single particle handling) subroutines greatly increases the versatility of the programs, and disguises the extra complexity inherent in the ensemble code.

```
      SUBROUTINE SMECH$(EF,VFX,VFY, EI,VIX,VIY)
      IMPLICIT REAL*8(A-H,O-Z)
      DIMENSION  VIX(20000), VIY(20000), EI(20000), TR(20000),
     *                VFX(20000), VFY(20000), EF(20000), TSIM(20000)
      INTEGER*2  IBAND(20000), INDEX(20000), INGAM(20000), IBOLD(20000)

      COMMON /SIMENS/   VMAX(4), TDISC,NENS,NINDEX, TSIM,IBAND,INDEX,INGAM
      COMMON /STGAM/    VSTG(4),GAM(2,4)
      COMMON /LADDER/ SCLAD
      COMMON /LADPAR/ DELKSC, LADSIZ, LADROW
      COMMON /MECHAR/ ECOL(48,4), KINDEX(48), NEWB(48)
      COMMON /VALP/     IBNP, IBNEW
      COMMON /COUNT/    NPUSH(2,4), NCOL(49,4), NCAP(4), NEG(4)

      DO 100 N = 1,NINDEX
         NP = INDEX(N)
         IBNP = IBAND(NP)
         IGNP = INGAM(NP)
         GAMMA = GAM(IGNP,IBNP)
         JPROC = 0

        VFMOD = DSQRT(VFX(NP)*VFX(NP) + VFY(NP)*VFY(NP))

C        W/v ceiling at VMAX
         IF (VFMOD .GT. VMAX(IBNP))
     *    CALL ENCAP(VFX(NP),VFY(NP),VFMOD,EF(NP))
         IV = IDNINT(VFMOD/DELKSC)

C        Fixed value SCLAD extrapolation between top of ladder & VMAX.
         IF (IV .GT. LADROW) IV = LADROW

C        Temporary GAMMA 'push'.
         TSCAT = SCLAD(IV,LADSIZ,IBNP)
         IF (GAMMA .LT. TSCAT) THEN
            GAMMA = TSCAT*1.001
            NPUSH(IGNP,IBNP) = NPUSH(IGNP,IBNP) + 1
         ENDIF
         S = GAMMA * G05CAF(1)
.
.
.
```

Fig. 8.8 *Continued overleaf ...*

```
.
.
10      CONTINUE
          JPROC = JPROC + 1
          IF (JPROC  .GT.  LADSIZ) THEN
C           "Top" of scatt. ladder has been reached; select self scattering.
C           Drop out of IF.. clause
            CALL KQWSLF (VFX(NP),VFY(NP),EF(NP),
     *                                 VIX(NP),VIY(NP),EI(NP))
          ELSEIF (S  .LE.  SCLAD(IV,JPROC,IBNP)) THEN
C           Process has been selected;
C           Drop out of IF.. clause after appropriate action
            EI(NP) = EF(NP) + ECOL(JPROC,IBNP)

            IF (EI(NP)  .LT.  0.0) THEN
C             -ve energy caused by dos tails; discard JPROC & self scatter.
              NEG(IBNP) = NEG(IBNP) + 1
              JPROC = LADSIZ + 1
              CALL KQWSLF (VFX(NP),VFY(NP),EF(NP),
     *                                   VIX(NP),VIY(NP),EI(NP))
            ELSE
C             Real scatt; use JPROC to retrieve new band & select K** call.
              IBNEW = NEWB(JPROC)
              IF (KINDEX(JPROC)  .EQ.  1) THEN
                CALL KQWISO (JPROC,VFX(NP),VFY(NP),VFMOD,
     *                                          VIX(NP),VIY(NP),EI(NP))
              ELSEIF (KINDEX(JPROC)  .EQ.  2) THEN
                CALL KQWPOP (JPROC,VFX(NP),VFY(NP),VFMOD,
     *                                          VIX(NP),VIY(NP),EI(NP))
              ENDIF
              IBAND(NP) = IBNEW
            ENDIF

          ELSE
C           No process selected; loop back to top of IF.. clause.
            GOTO 10
          ENDIF

C       Final parameter updates on exit from IF.. clause.
        NCOL(JPROC,IBNP) = NCOL(JPROC,IBNP) + 1

100   CONTINUE
      RETURN
      END
```

Fig. 8.8 FORTRAN code for the scattering process selection subroutine SMECH$ in the ensemble Monte Carlo program.

8F ANGULAR DEPENDENCES FOR POLAR OPTICAL AND PIEZOELECTRIC PROCESSES

The selection of a stochastic scattering angle, and hence of the components of after-scattering wavevector, for POP and PZ processes, is accomplished by use of the subroutine KQWPOP (Fig. 8.9). Data on the angular dependences for all the POP and PZ processes is contained within the 4D array PTHETA(L,I,J,K). Indices I, J, and K have the same meanings as given in Section 8C. Index L gives the value of scattering angle $\theta = \pi L/12$. Thus, each row of PTHETA(L,I,J,K), L = 0...12 gives a set of 13 ordinates (values of $\mathcal{F}^2_{n',n}(\cos\theta)$) for the process of index J in band K, at the wavevector given by index I.

The scattering angle selection algorithm begins by identification of the appropriate wavevector index NSELCT (Fig. 8.9a). A simple repeated interval-halving search is employed. Then, the stochastic scattering angle θ is selected by a rejection technique using the probability distribution defined by the 13 ordinates (Fig. 8.9b). This operation first requires the identification of the largest ordinate in the relevant set. A linear interpolation scheme is used in the rejection algorithm. Finally, the sign of $\sin\theta$ is generated at random, in order to obtain scattering onto the full 2D k-plane, and the after-scattering wavevector components VIX and VIY are resolved.

The routine is quite general, with no restrictions on the form of the angular dependence or the numerical values used for the PTHETA entries. For convenience, we have calculated PTHETA values for the same complete set of wavevectors VSETP as those used in the tabulation of the matrix elements ARMXIP but, if this were not possible, a new wavevector set 'VSETP2' could be defined, along with a corresponding array to replace NVPTSP (see Section 8C).

```
      SUBROUTINE KQWPOP(JPROCF,VFX,VFY,VFMOD,  VIX,VIY)
      IMPLICIT REAL*8(A-H, O-Z)
      COMMON /FUND/      PI
      COMMON /VALP/      IBS,IAS
      COMMON /KQEFLG/  IPEXEP
      COMMON /MXELP/     PTHETA(0:12,20,36,4), ARMXIP(20,36,4),
     *                        VSETP(20,36,4), NVPTSP(36,4)
.
.
.
C     Array NVPTSP gives no. of w/v points (& corresponding PTHETA ordinate sets)
C     for each process.
      IVPTS = NVPTSP(JPROC,IBS)

C  1: Obtain NSELCT; index of nearest w/v point to VFMOD
C  1a: Out-of-range cases.
      IF (VFMOD .GE. VSETP(IVPTS,JPROC,IBS)) THEN
         NSELCT = IVPTS
      ELSEIF (VFMOD .LE. VSETP(1,JPROC,IBS)) THEN
         NSELCT = 1
      ELSE
C  1b:    Repeated halving search (monotonically increasing data set), with
C        resolution of nearest point.
         NL = 1
         NTOP = IVPTS

1        CONTINUE
         NU = (NL+NTOP)/2
         IF (VFMOD .LT. VSETP(NU,JPROC,IBS)) THEN
            IF (NU-NL .EQ. 1) THEN
               UDIST = VSETP(NU,JPROC,IBS) - VFMOD
               ALDIST = VFMOD - VSETP(NL,JPROC,IBS)
               IF (UDIST .LE. ALDIST) THEN
                  NSELCT = NU
               ELSE
                  NSELCT = NL
               ENDIF
               GOTO 9
            ENDIF
            NTOP = NU
         ELSE
            IF (NTOP-NU .EQ. 1) THEN
               TDIST = VSETP(NTOP,JPROC,IBS) - VFMOD
               UDIST = VFMOD - VSETP(NU,JPROC,IBS)
               IF (TDIST .LE. UDIST) THEN
                  NSELCT = NTOP
               ELSE
                  NSELCT = NU
               ENDIF
               GOTO 9
            ENDIF
            NL = NU
         ENDIF
         GOTO 1
      ENDIF
9     CONTINUE
```

Fig. 8.9a FORTRAN code for the after-scattering wavevector determination routine KQWPOP: identification of the wavevector index NSELCT.

```
C 2: Obtain scattering angle using rejection technique based on a probability
C    distribution defined by the 13 ordinates corresponding to the selected w/v point

C 2a: Determine highest ordinate (always 0 ordinate for POP, but not
C     necessarily so for PZ (esp. intraband for k=0))

      ISCAN = 0
      PISC = PTHETA(ISCAN,NSELCT,JPROC,IBS)
11    CONTINUE
      PISCP1 = PTHETA(ISCAN+1,NSELCT,JPROC,IBS)
      IF (PISC .GT. PISCP1) THEN
         PMAX = PISC
      ELSEIF (ISCAN .EQ. 11) THEN
         PMAX = PISCP1
      ELSE
         ISCAN = ISCAN + 1
         PISC = PISCP1
         GOTO 11
      ENDIF
      IF (ISCAN .GT. 0) IPEXEP = IPEXEP + 1

21    CONTINUE
C 2b: Obtain co-ordinates of trial point.
      RA = G05CAF(1)
      THINDX = RA * 12.0
      ITH = IDINT(THINDX)
      RP = G05CAF(1) * PMAX

C 2c: Obtain theta ordinates.
      PATITH = PTHETA(ITH,NSELCT,JPROC,IBS)
      PATIP1 = PTHETA(ITH+1,NSELCT,JPROC,IBS)

C 2d: Interpolate between ITH & ITH+1 ordinates, & test.
      PINTRP = PATITH + (PATIP1 - PATITH) * (THINDX - ITH)
      IF (RP .GT. PINTRP) GOTO 21
29    CONTINUE


C 3: Continue; define THETA & resolve a/s w/v.
      THETA = THINDX * PI / 12.0
      COSTA = DCOS(THETA)

C     Define sign associated with SINTA; The above process only defines THETA
C     in [0..PI]; need to allow all values in [0..2*PI].
      SIGN = 1.0E00
      IF (G05CAF(1) .LT. 0.5000) SIGN = -1.0E00
      SINTA = SIGN*DSIN(THETA)

      COSBS = VFX/VFMOD
      SINBS = VFY/VFMOD
      VIX = VIMOD * (COSBS*COSTA - SINBS*SINTA)
      VIY = VIMOD * (SINBS*COSTA + COSBS*SINTA)

      RETURN
      END
```

Fig. 8.9b FORTRAN code for the subroutine KQWPOP: selection of a stochastic scattering angle and resolution of the components of

8G GENERAL PROGRAM SPECIFICATIONS

Single Particle Simulation

Our single particle (steady state) simulation follows the basic form described in Chapter 2, with the inclusion of all the features described in this chapter. The program produces expectation values for the carrier drift velocity $\langle v_d \rangle$ by two different methods; FBS and B-ensemble (see section 2A.2), and the energy expectation value $\langle \epsilon \rangle$, for a supplied value of in-plane electric field. The simulation is divided into subhistories, as described in section 2B.1, so as to obtain estimates of the expected tolerance on $\langle v_d \rangle$ and $\langle \epsilon \rangle$ in each band. The fractional population $\langle \overline{n} \rangle$ in each band is obtained as the fraction of the total simulation time spent by the particle in that band.

Energy distributions can also be obtained, for carriers in individual bands, and for the complete four band system. The direct sampling technique described in section 2A.3 yields, for the 2D system, a distribution

$$f'(\epsilon) = \int F(\epsilon, \beta) \mathcal{D}(\epsilon)\, d\beta, \tag{8.2}$$

where $F(\epsilon, \beta) \equiv F(\mathbf{k})$ gives the probability of occupancy of a state $|\mathbf{k}\rangle$ of energy ϵ, and wavevector $\mathbf{k}$ directed at an angle β relative to the k_x direction. The direct sampling approach involves, in the Monte Carlo simulation, an implicit integration over the polar angle β (*cf.* the 3D case of section 2A.3). Thus the quantity $f'(\epsilon)d\epsilon$ gives the proportion of carriers in the simulation with energies between ϵ and $\epsilon + d\epsilon$. We will refer to $f'(\epsilon)$ as the as-sampled energy distribution of the carriers.

When obtaining distributions in each band separately, it is possible to remove the contribution from the density of states $\mathcal{D}(\epsilon)$, in order to obtain the distribution function proper:

$$f(\epsilon) = \int F(\epsilon, \beta)\, d\beta. \tag{8.3}$$

The distribution $F(\epsilon, \beta)$ may be expanded in a Fourier series (by analogy with the 3D case of section 2A.3), whereupon it may be seen that the distribution function $f(\epsilon)$ of equation (8.3) corresponds to the circularly symmetric component of the full 2D distribution. Higher moments of the distribution may also be obtained, as in 3D, but these will not be considered further here. It should be noted that the distribution function $f(\epsilon)$ only has meaning in the context of carriers in a single band; no corresponding quantity can be defined for the complete four band system.

It is also possible to look at the unmodified carrier distribution $F(\epsilon, \beta) \equiv F(\mathbf{k})$ as a function of position in the 2D wavevector plane, and some of these 'k-space' distributions will be shown in Chapter 9.

As mentioned in Section 8D, the simulation records a count of scattering events of every type, in every band. This unusually detailed breakdown of scattering in a Monte Carlo simulation is very useful in resolving the various contributions to the carrier energy loss rates, as will be described in Chapters 9 and 10.

Ensemble Simulation

The ensemble program is based on the basic backdrifting algorithm described in section 2B.2, with the inclusion of all the extensions described above. We have written subroutines to generate a variety of initial carrier distributions, as will be described in Chapter 10. Values for an in-plane electric field can also be supplied (though in most of our work the field has been set to zero). The simulation produces expectation values for drift velocity $\langle v_d \rangle$ and mean energy $\langle \epsilon \rangle$, in each band and for the complete system, at regular time intervals. The fractional population $\langle \overline{n} \rangle$ in each band is also given, as is a detailed breakdown of scattering events. The carrier energy distributions can be obtained on a timestep larger than that used for the expectation values, since these quantities are not needed at such regular time intervals.

Finally, we have shown, in Table 8.1, a summary of the program specifications for both the single particle and ensemble simulations.

No. of bands	4
No. of scatt. processes in each band	48
No. of particles (ensemble program)	typical; 20000
	max; 50000
Bandstructure:	
ϵ *vs.* k	tabulated; linear interpolation between adjacent points; parabolic extrapolation
v_{gp} *vs.* k	as above; linear extrapolation
D_n *vs.* k	" " fixed value extrapolation
k *vs.* ϵ	" " inverse parabolic extrapolation
D_n *vs.* ϵ	" " fixed value extrapolation with broadening around band 2 and 4 minima
Matrix Elements:	
AC, NPO, POP and PZ	tabulated, up to 20 wavevector points per process; linear interpolation between adjacent points; fixed value extrapolation beyond range of data.
Angular Dependences:	
AC, NPO	isotropic (wavevector randomising)
POP, PZ	tabulated probability distributions for each process
Scattering Rates:	
Optical phonon energies	single, fixed value — see Table 4.1
Acoustic phonon energies	single, operator-supplied value
Material parameters	see Table 4.1
No. of wavevector points in each band	1500 — fixed value extrapolation beyond range of stored data
Wavevector increment	10^{-4} Å^{-1}

Table 8.1: Simulation Specifications (part a)

Gamma Profile	singly stepped for each band
Upper limit of simulation	typically $k = 0.2\text{Å}^{-1}$ in each band
In-plane electric field (F)	operator supplied
Lattice Temperature (T_L)	operator supplied
Quantum well width (L)	fixed; 100Å
Steady state estimators	$\langle v_{\text{FBS}} \rangle$, $\langle v_{\text{Bens}} \rangle$, $\langle \epsilon \rangle$, $\langle \overline{n} \rangle$
Steady state carrier distributions	as-sampled energy distribution $f'(\epsilon)$ in each band distribution function $f(\epsilon)$ in each band as-sampled energy distribution for the complete system distribution of carriers in 2D k-space, in each band
Ensemble estimators	$\langle v \rangle$, $\langle \epsilon \rangle$ and $\langle \overline{n} \rangle$ *vs.* time
Timestep	operator supplied; typically $\geq$ 0.05ps
Simulation time	operator supplied; typically 1, 10, or 100ps
Ensemble distribution functions	$f'(\epsilon)$ and $f(\epsilon)$ in each band, at regular timesteps $f'(\epsilon)$ for the complete system, at regular timesteps
Timestep for distribution functions	operator supplied; typically 1/10 or 1/5 of simulation time

Table 8.1: Simulation Specifications (part b)

CHAPTER 9

ELECTRIC FIELD HEATING OF QUANTUM CONFINED HOLES

In the previous four chapters we have described various aspects of our model of the quantum confined valence band system and its incorporation in our Monte Carlo simulation programs. We are now in a position to present results obtained from the simulations, and will begin, in this chapter, by examining the response of quantum confined holes to an in-plane electric field. As far as we are aware, no other theoretical work has been published on this subject, and the experimental data thus far available on quantum confined hole dynamics contains very little detail. Therefore, although the model described in this thesis includes several approximations — neglect of: carrier-carrier scattering; plasmon effects; disturbance of the phonon population; degeneracy; real space transfer, and band anisotropy — it nonetheless allows a unique insight into the way in which the complexities of the quantum well valence bandstructure influence carrier dynamics. We will discuss the significance of the above approximations in Chapter 11.

In all the simulations described, the lattice temperature chosen was 77K. This value was preferred for three reasons:

(i) it is a temperature at which the elastic and equipartition approximations for acoustic scattering are valid;

(ii) it is a temperature at which heating of the quantum confined hole population can be readily observed, and

(iii) it is a commonly used temperature in experimental investigations, being the liquefaction temperature of nitrogen.

It would be quite possible to use our program to simulate hole transport at other lattice temperatures, within the range where the approximations stated in (i) above are valid. However, in this Chapter, we preferred to demonstrate the wide range of parameters which can be investigated by the Monte Carlo method and, for that purpose, we chose to restrict our study to the case $T_L = 77$K only.

9A ELECTRIC FIELD DEPENDENCE OF THE BASIC MONTE CARLO ESTIMATORS

We have used our single particle Monte Carlo program to simulate the steady state transport of holes in a 100Å GaAs/AlAs quantum well, for a range of in-plane electric fields. Figs. 9.1–3 show the expectation values of drift velocity $\langle v_d \rangle$, mean (kinetic) energy $\langle \epsilon \rangle$, and fractional population $\langle \overline{n} \rangle$ in each band, as a function of electric field F. Fig. 9.1 also shows the average drift velocity $\langle v_{\rm av} \rangle$ for the whole system, and Fig. 9.2 also gives the overall average energy $\langle \epsilon_{\rm av} \rangle$ for the system, *i.e.*, the average of hole energies in all four bands relative to the energy of the band 1 minimum.

From Fig. 9.3, we can see that most of the carriers reside in band 1 (more than 80% for $F < 10{\rm kVcm}^{-1}$). Consequently, the overall average drift velocity $\langle v_{\rm av} \rangle$ stays very close to the band 1 value (Fig. 9.1). On the other hand, the overall average energy $\langle \epsilon_{\rm av} \rangle$ deviates from the band 1 value at high fields (Fig. 9.2). This is because the high energy carriers in band 1 may be transferred to the upper bands via optical phonon emission (and acoustic phonon scattering), and hence are much more likely to be scattered out of band 1 than are the low energy carriers, which can only be transferred to higher bands via the very weak optical phonon absorption processes. Thus the band 1 mean energy is suppressed, relative to the overall average energy, at large fields.

Fig. 9.1 shows large values of drift velocity in bands 3 and 4, and a negative differential mobility (NDM) effect in both bands for intermediate fields. The large values in both cases are associated with unusually large group velocities for carriers near the energy minima (see Fig. 7.1), and with regions of relatively weak scattering in both bands (Figs. 7.13–14). The NDM effects are caused by the subsequent reduction in carrier group velocities at higher wavevectors/energies, and the eventual onset of stronger scattering in both bands. The NDM phenomena cannot be considered significant for transport applications, since the populations of bands 3 and 4 at intermediate fields are so small (Fig. 9.3).

In Fig. 9.2 it can be seen that, at low fields, the mean carrier energies in bands 2 and 4 remain below those in bands 1 and 3. This is a consequence of the extremely large densities of states at the minima of bands 2 and 4, which result in large populations of carriers in these low energy states (see, for example, Figs. 9.8 and 9.10). This effect is particularly marked in band 4, since the density of states is abnormally high throughout the *b* region of the band (see Fig. 7.2).

Carriers in band 3 have the highest mean energy for most of the field values shown. This is because the density of states in band 3 is very small near the zone centre (Fig. 7.2), and because scattering in band 3 is relatively weak, as mentioned

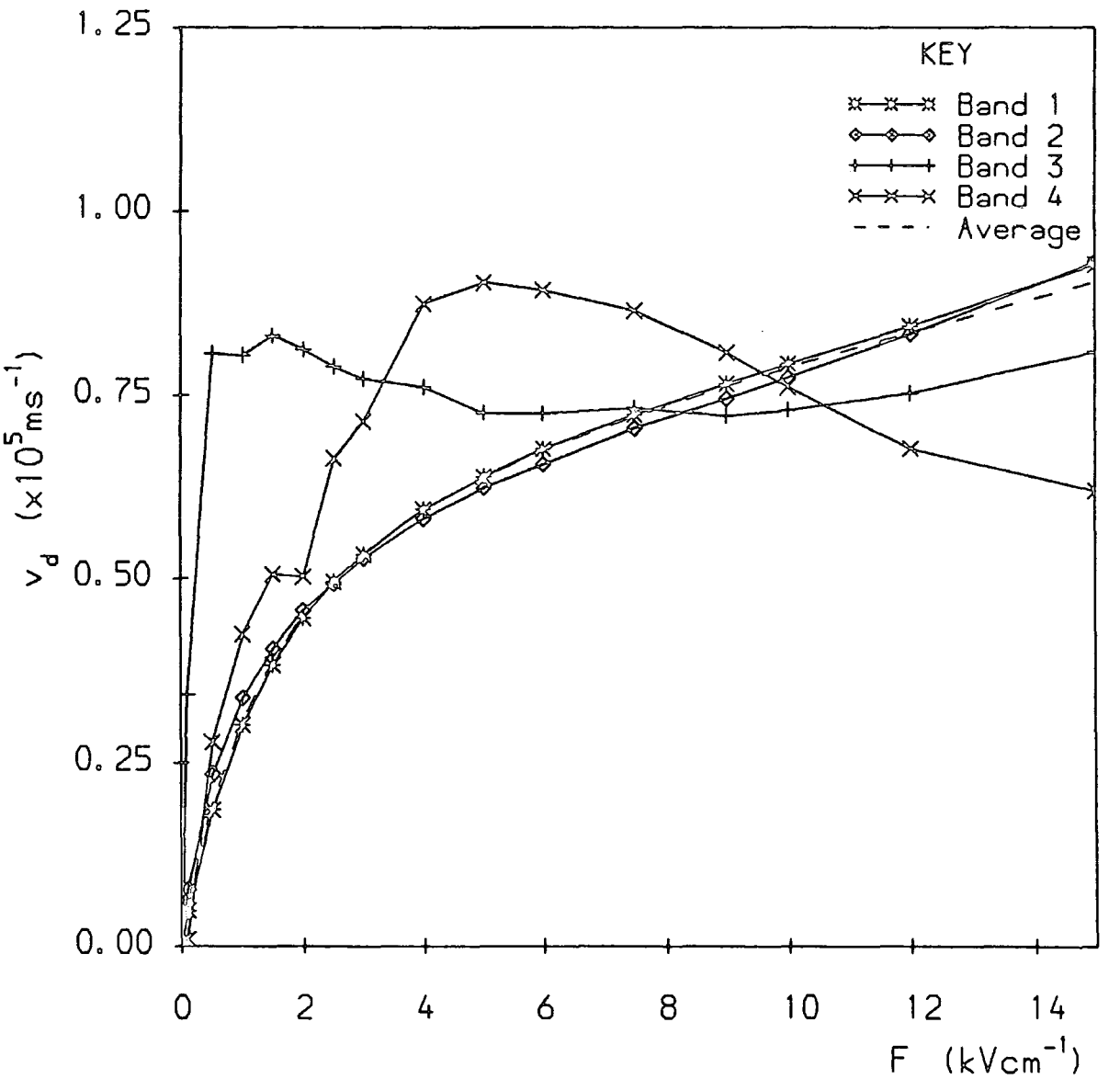

Fig 9.1 Mean drift velocities for holes in the first four valence bands of a 100Å GaAs/AlAs quantum well, and the overall average hole drift velocity, as a function of in-plane electric field. $T_L = 77$K; $\epsilon_{ac} =$ 1meV.

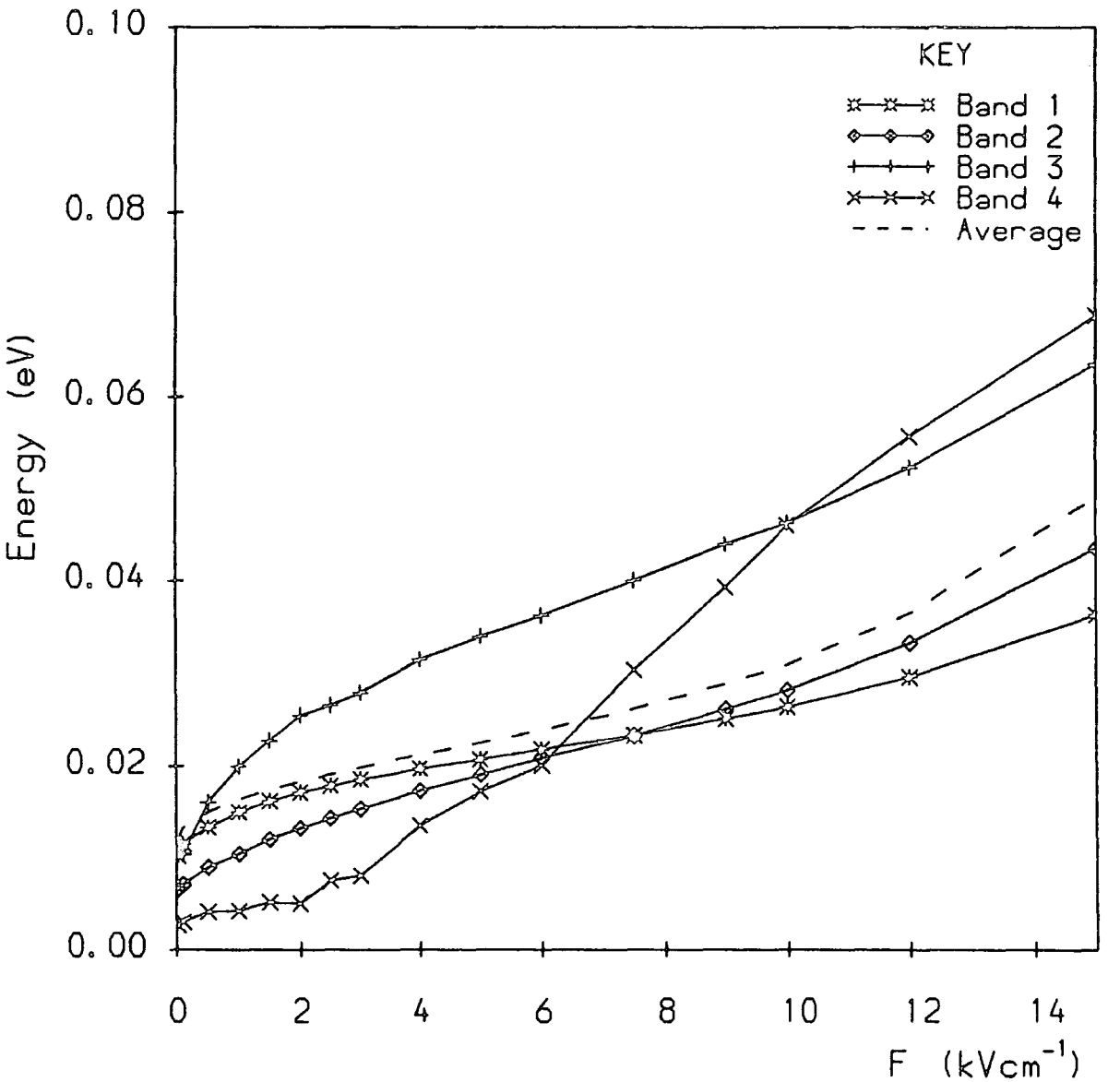

Fig. 9.2 Mean hole energies in bands 1–4 of a 100Å GaAs/AlAs quantum well, and the overall average energy, measured relative to the band 1 minimum, as a function of in-plane electric field. $T_L = 77$K; $\epsilon_{ac} =$ 1meV.

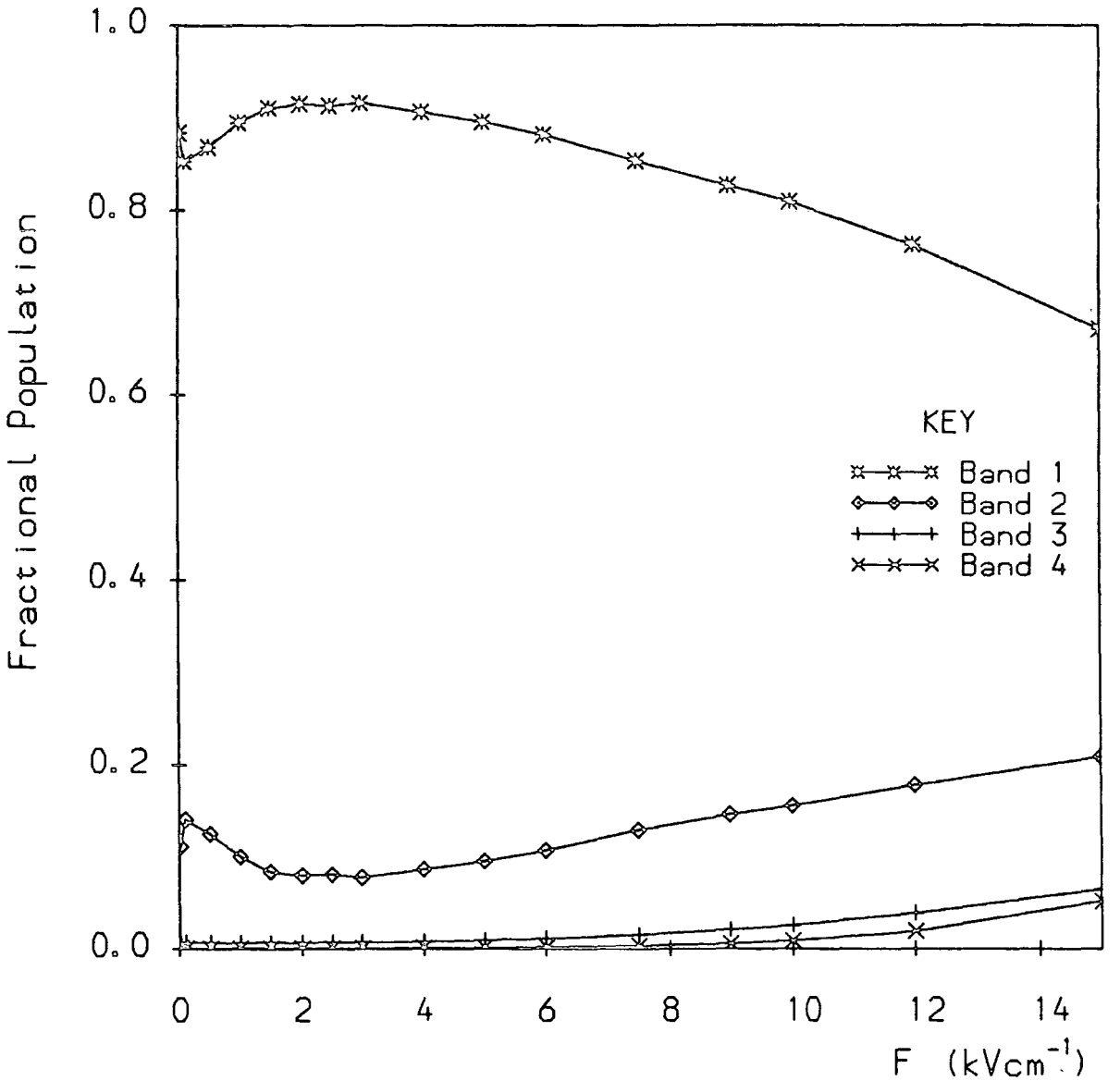

Fig. 9.3 Fractional population of holes in each of bands 1–4, as a function of in-plane electric field. $T_L = 77\text{K}$; $\epsilon_{ac} = 1\text{meV}$.

above. The band 4 mean carrier energy increases dramatically with field beyond $F \approx 2\text{kVcm}^{-1}$. This can be attributed to the region of low density of states corresponding to the very steep portion of the band beyond the energy minimum (see Fig. 6.1), and, as for band 3, to a region of relatively weak scattering. In particular, the mean carrier energies in bands 3 and 4 rise well above the optical phonon energy $\hbar\omega_{\text{op}}$ within the range of fields shown, indicating that, in both cases, intraband optical emission scattering is weak at energies near its threshold (see also Figs. 7.13–14). By contrast, the mean energies of carriers in bands 1 and 2 remain well below $\hbar\omega_{\text{op}}$ for most of the field range shown.

The thermal equilibrium energy for carriers in a 2D parabolic band at 77K is $k_B T_L = 6.6\text{meV}$. This is lower than both the band 1 mean energy, $\langle \epsilon_1 \rangle = 10.3\text{meV}$, and the overall average energy $\langle \epsilon_{\text{av}} \rangle = 11.93\text{meV}$ at zero field.

Fig. 9.3 shows a very peculiar response of the band 1 and 2 fractional populations to increasing electric field. After an initial decrease in population, band 1 experiences an anomalous repopulation, such that $\langle \overline{n}_1 \rangle$ exceeds its zero field value throughout the low field range. An explanation of this effect will be given in Section 9E.

In Fig. 9.4 we have shown the overall average drift velocity of the quantum confined holes, obtained using fixed acoustic phonon energies of $\epsilon_{\text{ac}} = 2\text{meV}$, 1meV and 0meV (elastic acoustic scattering). We have also shown the drift velocity obtained in the absence of piezoelectric scattering (for $\epsilon_{\text{ac}} = 1\text{meV}$), and our result for holes in bulk GaAs (from Section 4C). The bulk values exceed the 2D values (by typically 30%) throughout the range of electric fields shown. Remembering that bulk hole transport in GaAs is dominated by heavy holes (Section 4C), and that transport in the quantum confined system is dominated by the behaviour of carriers in band 1 (see above), it is apparent that the difference in the 3D and 2D drift velocities corresponds to the difference between the bulk heavy hole scattering rate (Fig. 4.12) and the quantum confined rate for holes in band 1 (Fig. 7.11). The biggest difference between the two rates occurs just above the optical phonon emission threshold, and this is exactly the region which will have the greatest influence on carrier transport throughout most of the range of electric fields considered. Above the threshold, the 2D rate rises steeply to around 20ps^{-1}, whereas the 3D rate displays a much slower, smoother increase, with none of the sharp structure present in the 2D case. Thus, the features in the 2D rate in this region will act to give a shorter average lifetime for phonon scattering for the quantum confined holes as compared with holes in the bulk material, and consequently the drift velocity and mobility will be reduced. The acoustic dominated scattering rate below the optical emission threshold is also larger in the 2D case, and therefore

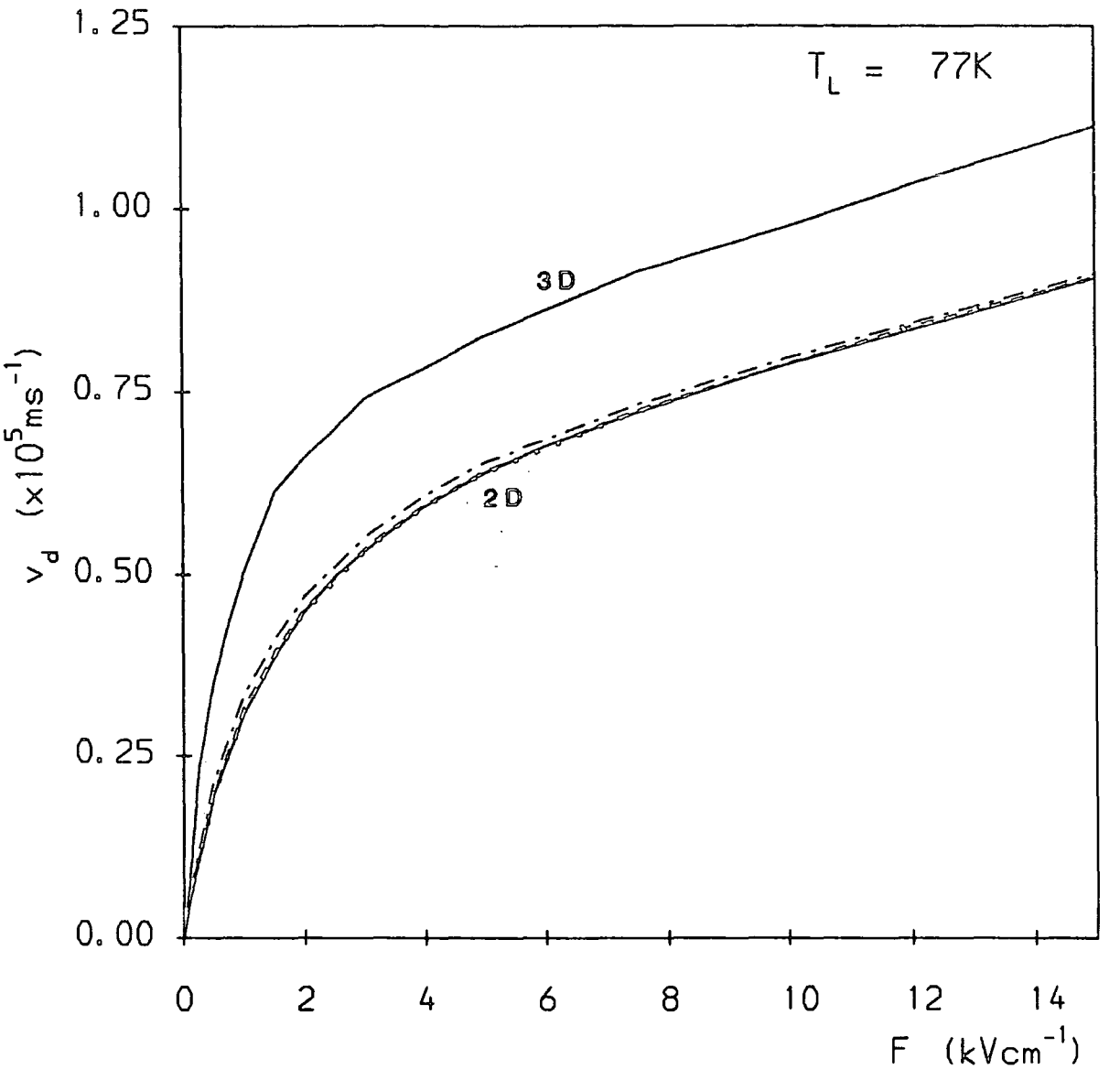

Fig. 9.4 Average hole drift velocities in 2D and 3D.

2D curves:

— $\epsilon_{ac} = 1meV$,

· – · $\epsilon_{ac} = 1meV$, excluding PZ scattering,

- - - $\epsilon_{ac} = 2meV$,

· · · $\epsilon_{ac} = 0meV$.

3D curve: elastic acoustic scattering.

the difference between the 2D and 3D drift velocities is preserved even at very low fields.

We found that, whilst the 3D drift velocity has a clearly identifiable ohmic (linear) region at low fields (see Fig. 4.15), it is much more difficult to identify a corresponding region on the 2D curve. This non-ohmic behaviour at low fields is a consequence of the complicated energy/wavevector dependence of scattering in the multiband quantum confined system, which results in a carrier lifetime which is, in all cases, dependent on electric field. We have estimated the upper limit of the quantum confined hole mobility in the GaAs/AlAs system to be approximately $5750\text{cm}^2\text{V}^{-1}\text{s}^{-1}$ (calculated at $\text{F} = 0.01\text{kVcm}^{-1}$). This is only around 60% of our value of $9400\text{cm}^2\text{V}^{-1}\text{s}^{-1}$ obtained for bulk holes at 77K (Section 4C). Our result confirms the predictions of Störmer *et al.* (1984) concerning the temperature dependence of the mobility of 2D hole systems. Their results indicate that the hole mobilities in modulation doped GaAs heterostructures are lower than those for high purity, low doped p-type bulk samples for a wide range of lattice temperatures, and they estimate 2D hole mobilities of the order of $4\text{–}6\times10^3\text{cm}^2\text{V}^{-1}\text{s}^{-1}$ at $T_L = 77\text{K}$.

A comparison of the various 2D curves on Fig. 9.4 shows, firstly that the omission of piezoelectric scattering from the simulation leads to a small overestimate of the drift velocity at all values of electric field. The discrepancy is around 10% for fields of 1kVcm^{-1} and less, but diminishes below 5% for higher fields. Secondly, it can be seen that the effect, on the drift velocity, of changing the value of acoustic phonon energy (ϵ_{ac}) supplied to the simulation is small — typically 1% discrepancy between the curves for $\epsilon_{\text{ac}} = 2$, 1, and 0meV. Fig. 9.5 shows the overall average energy *vs.* electric field for the same four sets of 2D simulations. For this quantity, the omission of piezoelectric scattering and the changing of ϵ_{ac} causes even less difference in the results.

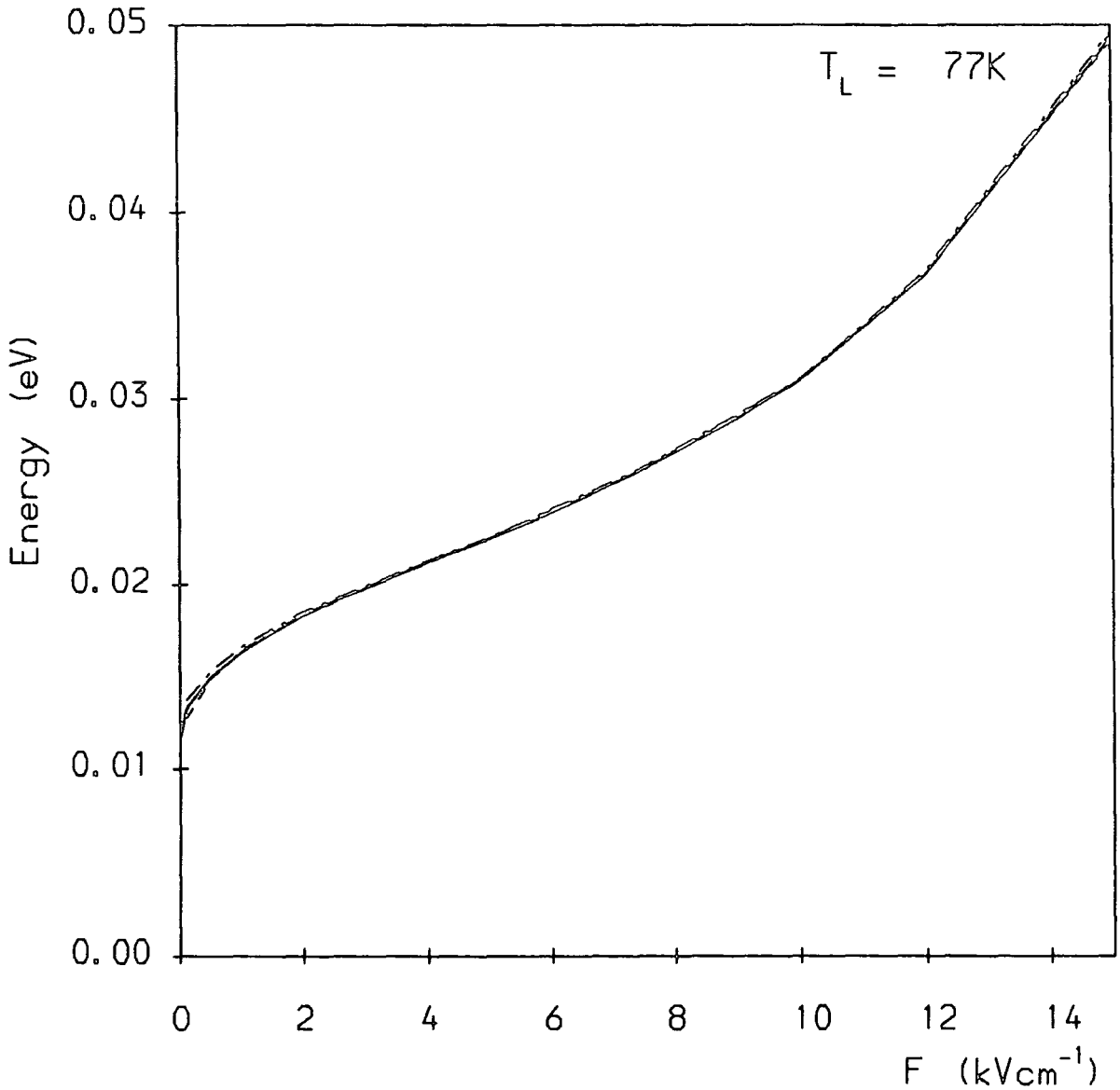

Fig. 9.5 Overall average hole energies in a 100Å GaAs/AlAs quantum well, measured relative to the band 1 minimum.
— with PZ scattering, · – · without PZ scattering; ϵ_{ac} = 1meV.

9B HOLE ENERGY DISTRIBUTIONS

As described in Section 8G, we have used our single particle Monte Carlo simulation to obtain the steady state as-sampled distribution of carrier energies $f'(\epsilon)$, and the distribution function $f(\epsilon)$, in each of the four bands of the quantum confined system. We have also obtained as-sampled distributions for the complete four band system, which we shall refer to as 'global' distributions.

Fig. 9.6 shows global distributions of hole energies obtained for a range of in-plane electric fields. Figs. 9.7–10 show the as-sampled energy distributions in bands 1–4, for the same set of field values. The global distributions exhibit structure at energies of around 10meV, 16meV and 55meV. Moreover, the maximum value of the distribution is not found at $\epsilon = 0$ for any of the field values shown. This feature is also seen in the band 1 as-sampled distributions (Fig. 9.7). It is a consequence of the form of the density of states in band 1, which is small at the band edge, and has a pronounced peak at $\epsilon = 11.3$meV ($k = 0.032\text{Å}^{-1}$; see Fig. 7.2). This peak corresponds to the structure observed in the global and band 1 distributions at around 10meV. The difference between the peak value of the distributions at $\epsilon \approx 10$meV and the $\epsilon = 0$ value *increases* with electric field. The explanation for this phenomenon is that, because of the large density of states at around 10meV in band 1, the depletion of carriers from this region upon electric field heating is less marked than that from the band edge.

The structure on the global distributions at $\epsilon = 16$meV represents the large carrier population located in the band 2 minimum due to the very large density of states in that region. This is clearly depicted in Fig. 9.8, which shows that the as-sampled distributions of carriers in band 2 are significantly enhanced at $\epsilon = 0$ throughout the range of fields shown. A similar effect is observed in the band 4 distributions of Fig. 9.10. The large carrier population in the band 4 minimum gives rise to the structure in the global distributions at $\epsilon \approx 55$meV. A similar degree of structure has been observed in the photoluminescence spectra from p-type modulation doped GaAs quantum wells (Da Costa *et al.* 1987).

Figs. 9.11–14 show the distribution functions $f(\epsilon)$ for the four bands, for the same set of electric fields as in the previous figures. With the contribution from the density of states removed, the functions $f(\epsilon)$ are relatively smooth at low energies, with the probability of state occupancy decreasing steadily from the $\epsilon = 0$ value in all cases. The remanent features of the curves are due to scattering effects. In particular, we observe shoulders in the distribution functions for bands 1, 2, and 3, corresponding to the principal optical phonon emission thresholds. In band 1, a shoulder occurs at $\epsilon \approx 40$meV, corresponding to the threshold for 1–1 optical emission. In band 2, the shoulder is found at $\epsilon \approx 20$meV, due to 2–1 optical

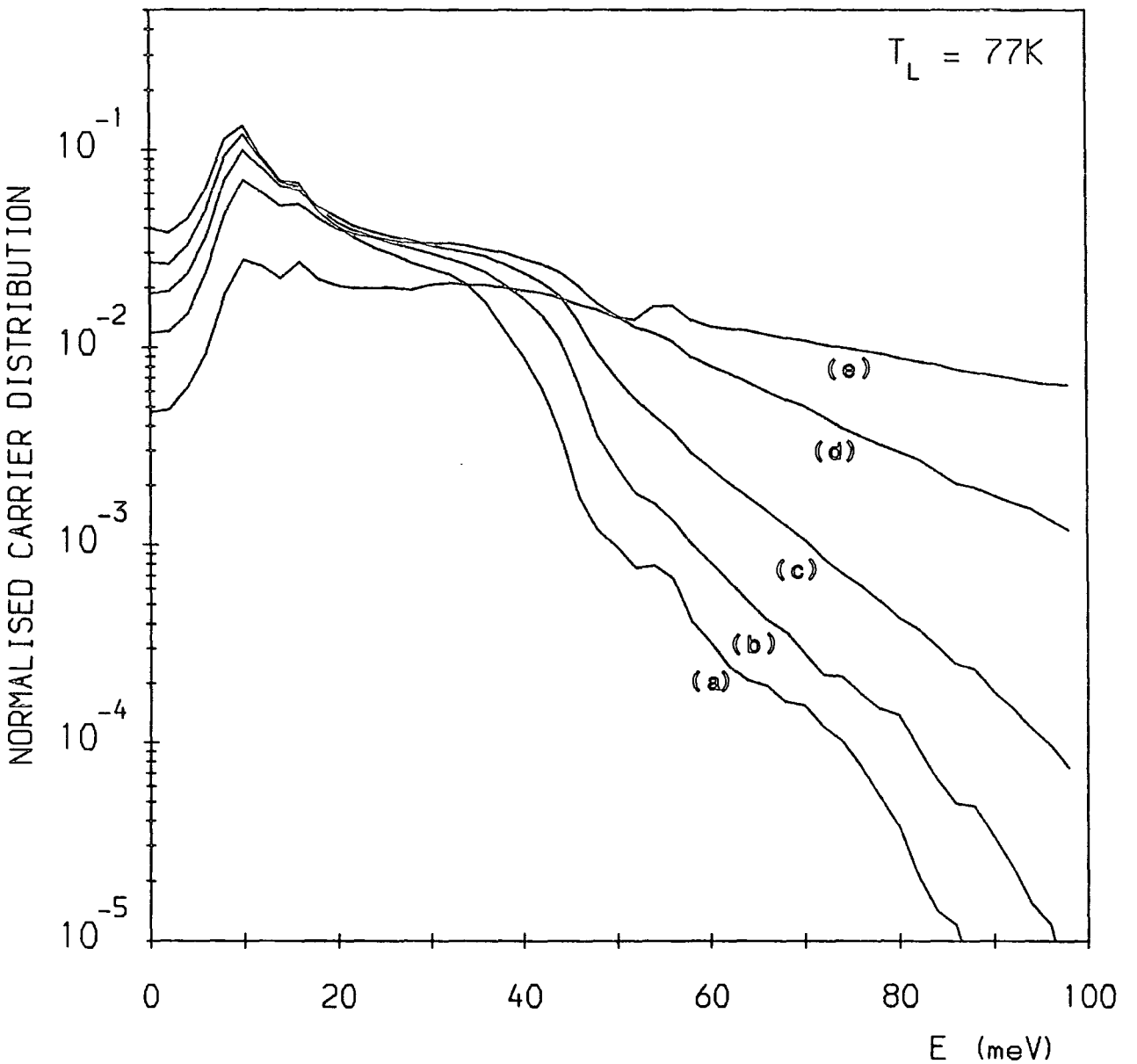

Fig. 9.6 Global hole energy distributions in a 100Å GaAs/AlAs quantum well for a range of in-plane electric fields: (a) $F = 1\text{kVcm}^{-1}$, (b) $F = 2.5\text{kVcm}^{-1}$, (c) $F = 5\text{kVcm}^{-1}$, (d) $F = 10\text{kVcm}^{-1}$ and (e) $F = 20\text{kVcm}^{-1}$. $\epsilon_{ac} = 1\text{meV}$.

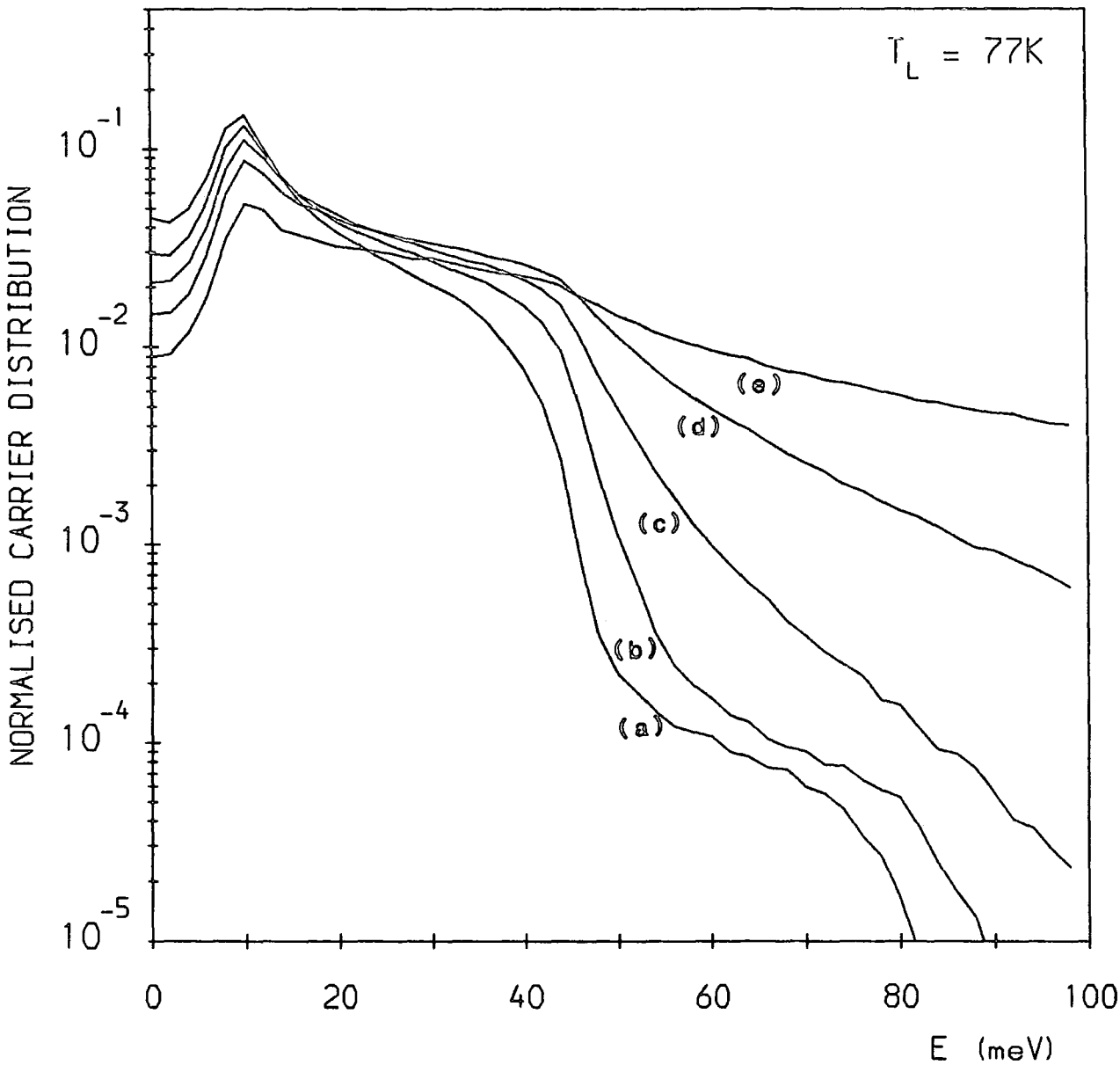

Fig. 9.7 Band 1 as-sampled hole energy distribution for in-plane electric fields of: (a) 1kVcm^{-1}; (b) 2.5kVcm^{-1}; (c) 5kVcm^{-1}; (d) 10kVcm^{-1}, and (e) 20kVcm^{-1}. $\epsilon_{ac} = 1\text{meV}$.

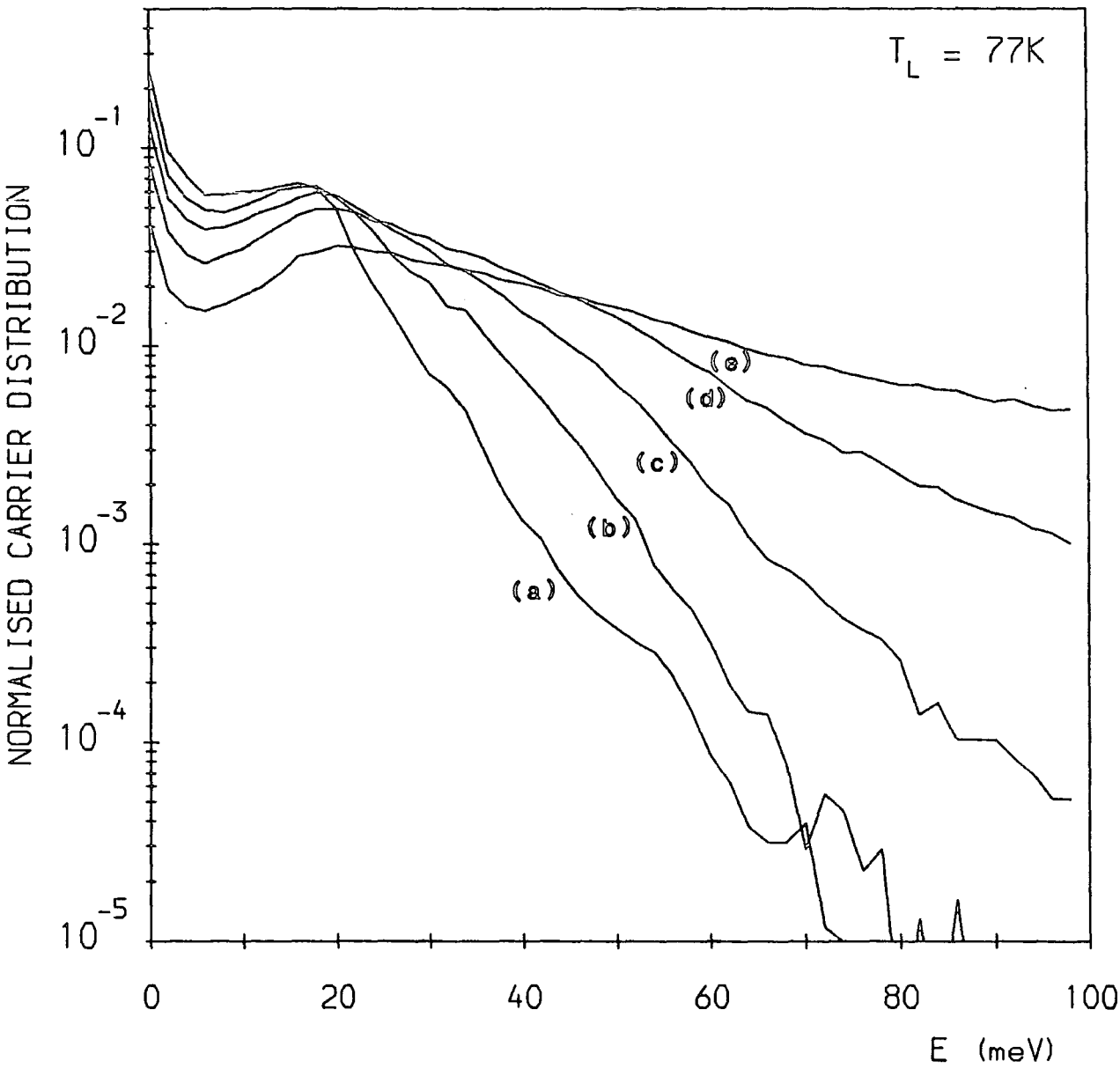

Fig. 9.8 Band 2 as-sampled hole energy distribution for in-plane electric fields of: (a) 1kVcm^{-1}; (b) 2.5kVcm^{-1}; (c) 5kVcm^{-1}; (d) 10kVcm^{-1}, and (e) 20kVcm^{-1}. ϵ_{ac} = 1meV.

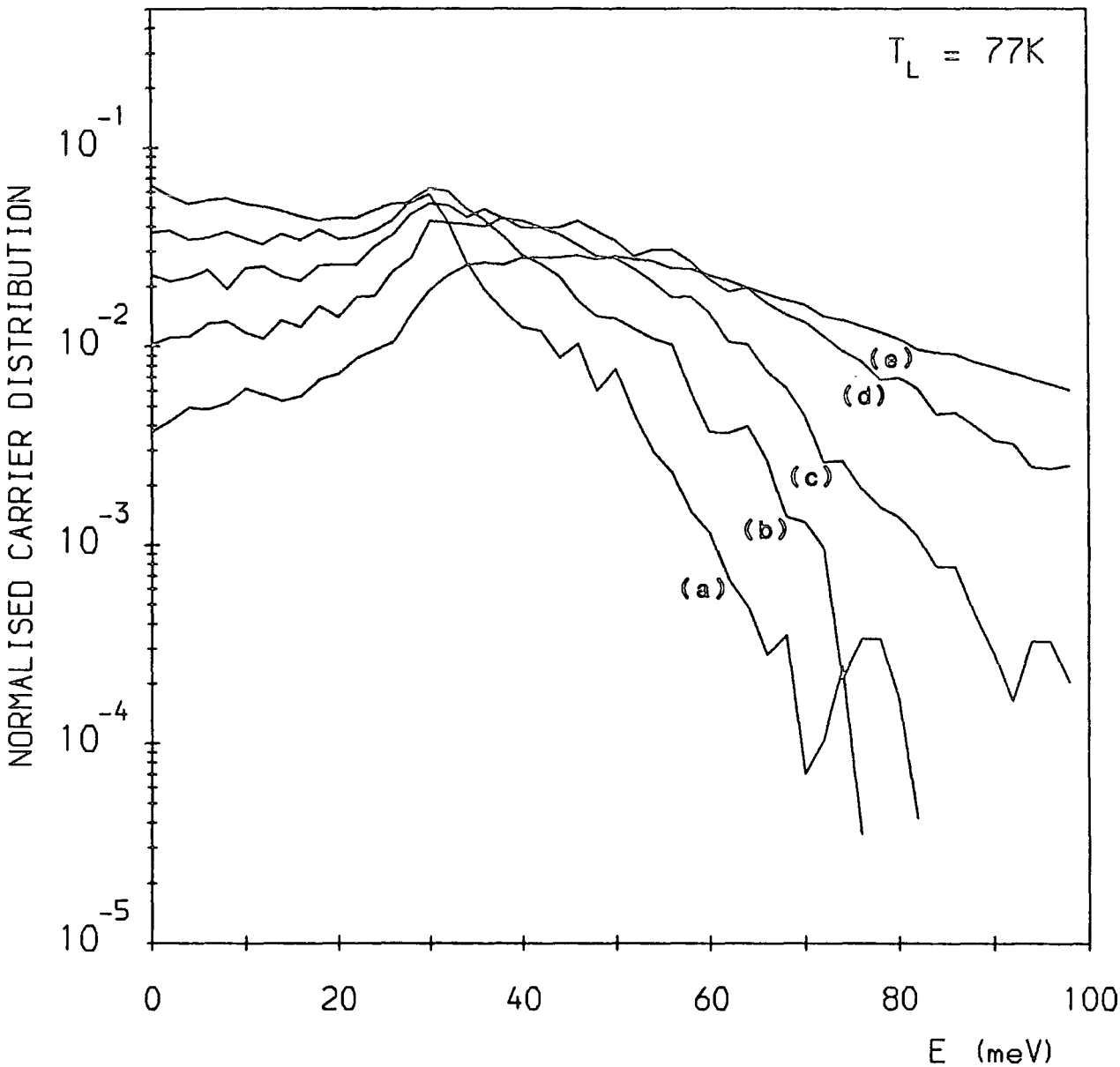

Fig. 9.9 Band 3 as-sampled hole energy distribution for in-plane electric fields of: (a) 1kVcm^{-1}; (b) 2.5kVcm^{-1}; (c) 5kVcm^{-1}; (d) 10kVcm^{-1}, and (e) 20kVcm^{-1}. $\epsilon_{ac} = 1$meV.

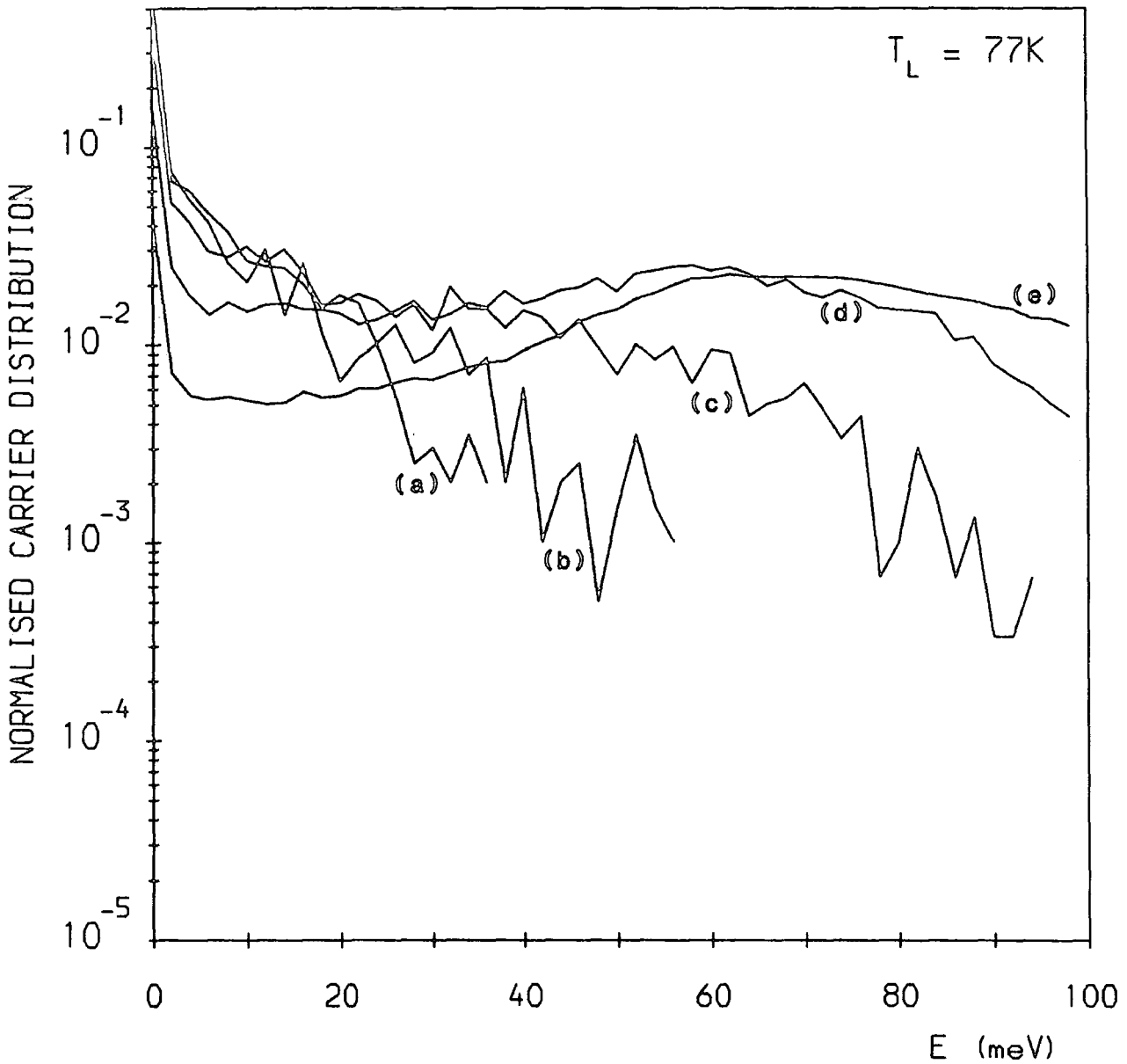

Fig. 9.10 Band 4 as-sampled hole energy distribution for in-plane electric fields of: (a) 1kVcm^{-1}; (b) 2.5kVcm^{-1}; (c) 5kVcm^{-1}; (d) 10kVcm^{-1}, and (e) 20kVcm^{-1}. ϵ_{ac} = 1meV.

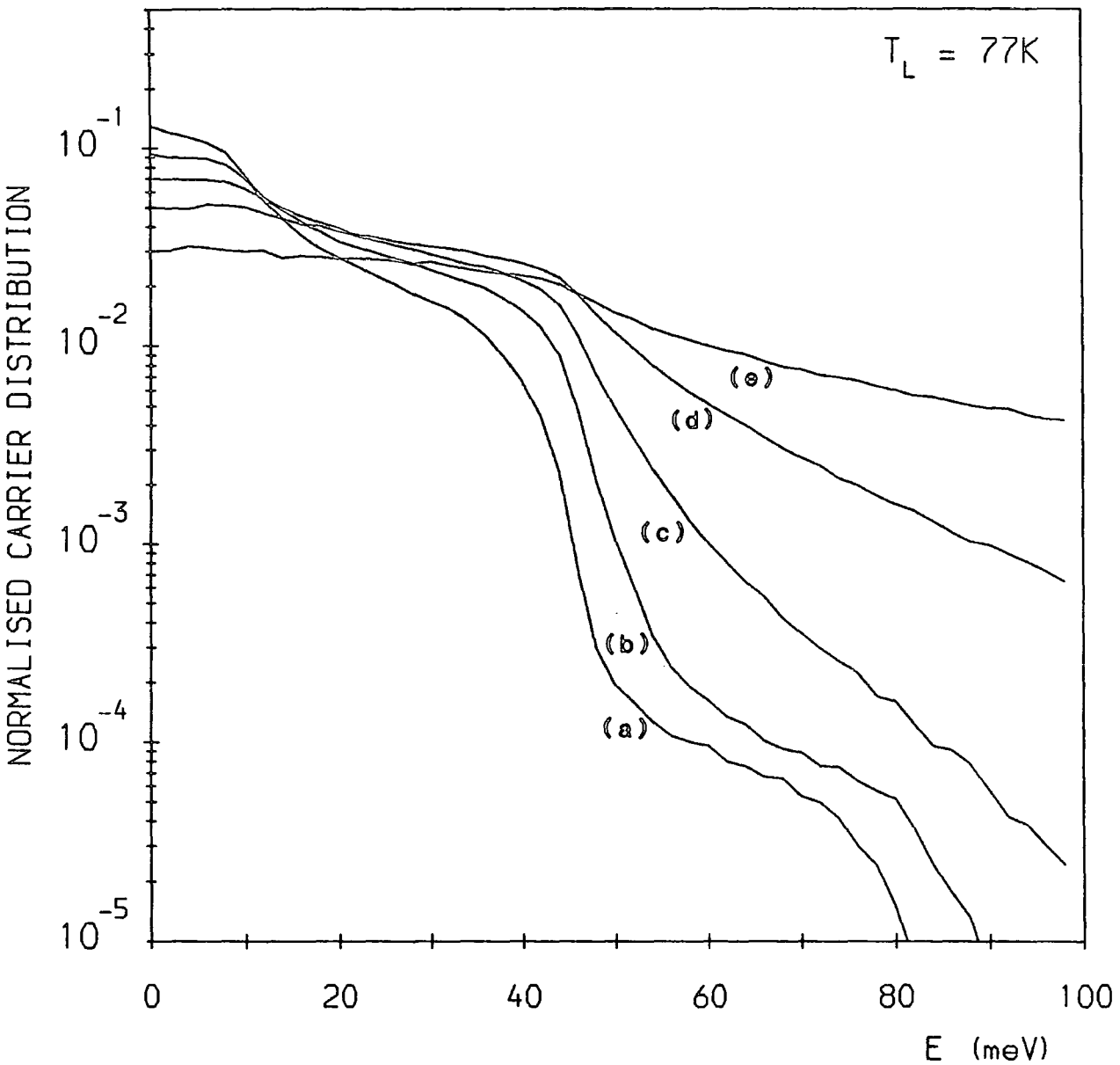

Fig. 9.11 Band 1 hole distribution function for in-plane electric fields of: (a) 1kVcm^{-1}; (b) 2.5kVcm^{-1}; (c) 5kVcm^{-1}; (d) 10kVcm^{-1}, and (e) 20kVcm^{-1}. $\epsilon_{ac} = 1$meV.

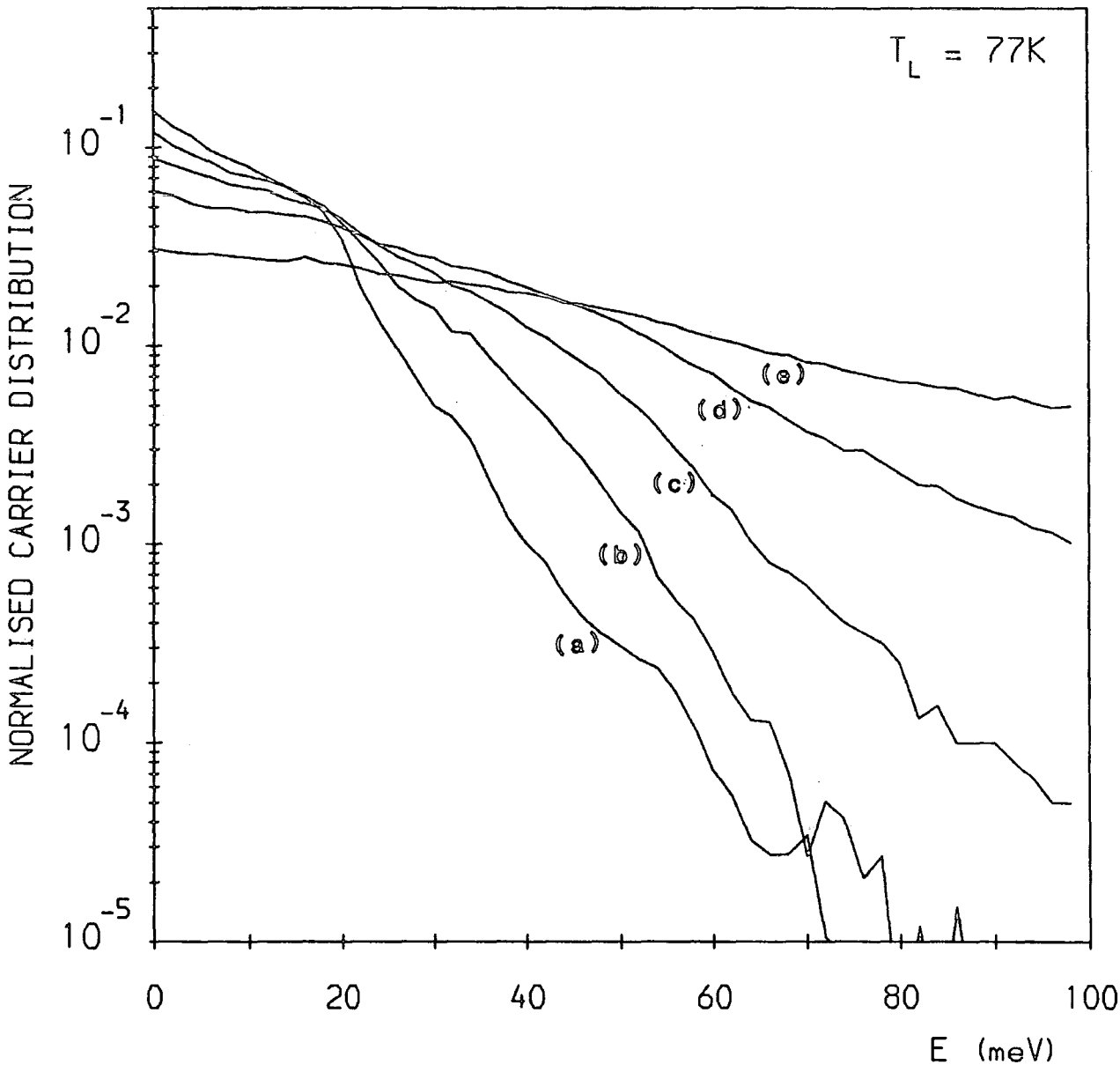

Fig. 9.12 Band 2 hole distribution function for in-plane electric fields of: (a) 1kVcm^{-1}; (b) 2.5kVcm^{-1}; (c) 5kVcm^{-1}; (d) 10kVcm^{-1}, and (e) 20kVcm^{-1}. $\epsilon_{ac} = 1$meV.

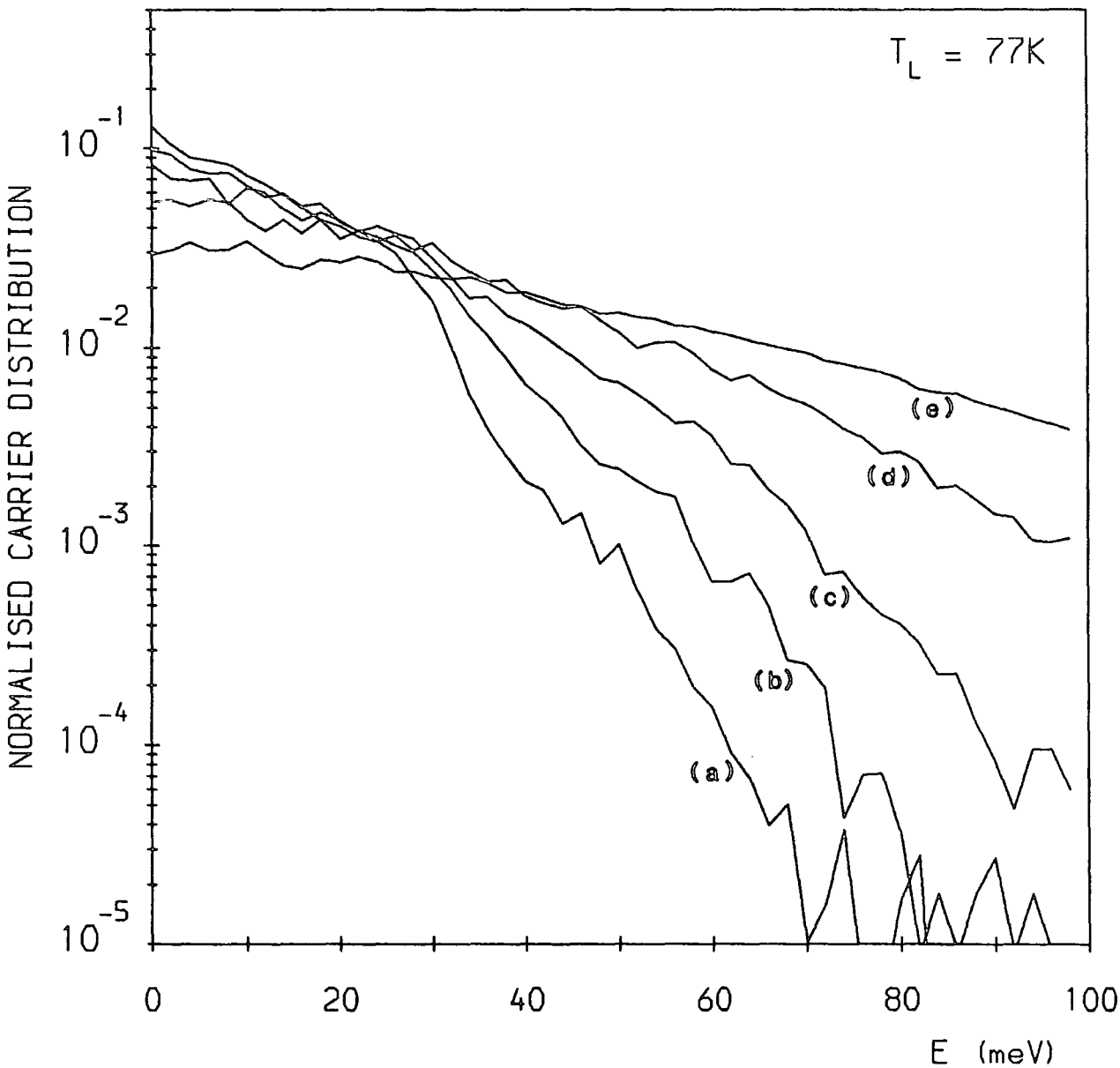

Fig. 9.13 Band 3 hole distribution function for in-plane electric fields of: (a) 1kVcm^{-1}; (b) 2.5kVcm^{-1}; (c) 5kVcm^{-1}; (d) 10kVcm^{-1}, and (e) 20kVcm^{-1}. $\epsilon_{ac} = 1$meV.

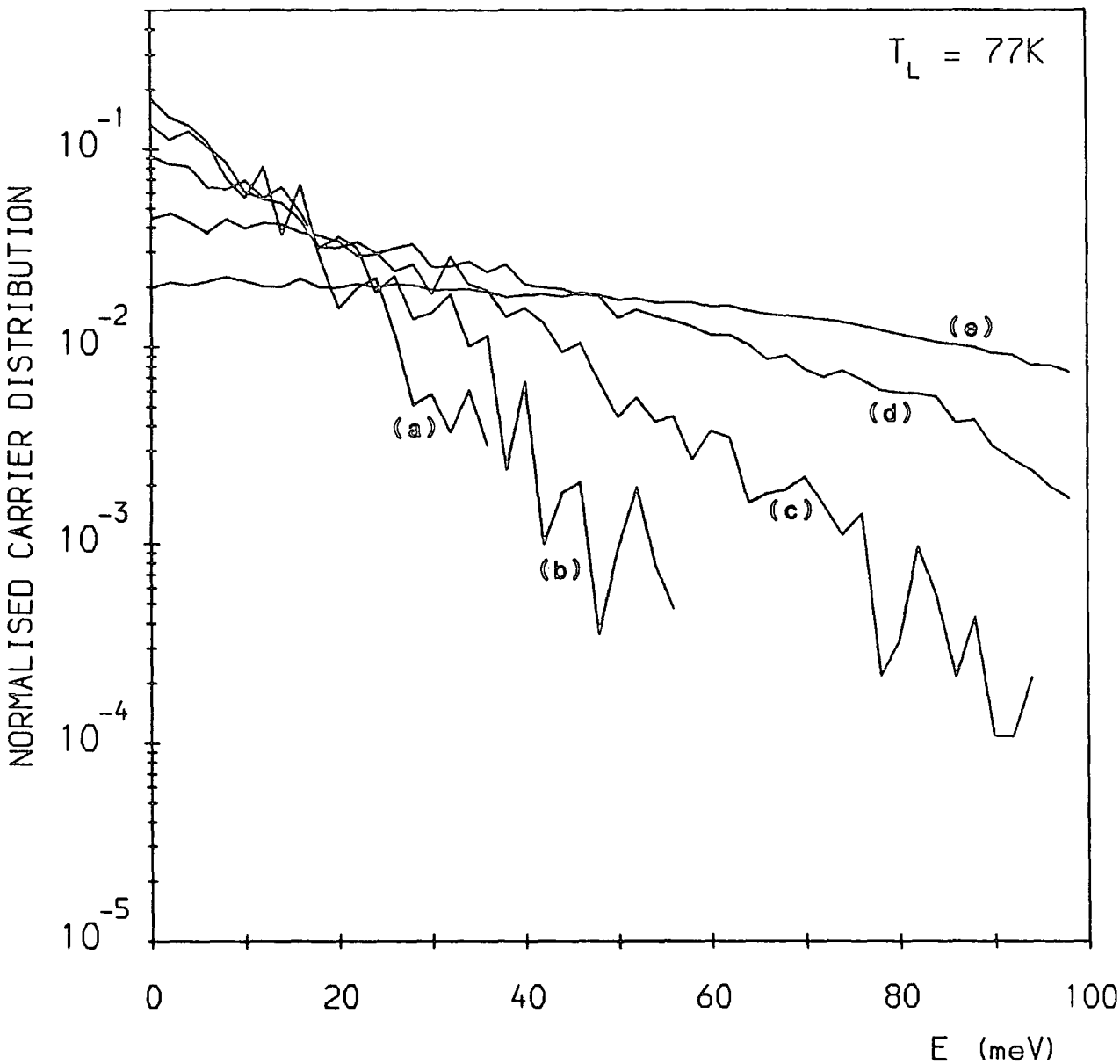

Fig. 9.14 Band 4 hole distribution function for in-plane electric fields of: (a) 1kVcm^{-1}; (b) 2.5kVcm^{-1}; (c) 5kVcm^{-1}; (d) 10kVcm^{-1}, and (e) 20kVcm^{-1}. ϵ_{ac} = 1meV.

emission, and in band 3, the shoulder at $\epsilon \approx 28$meV corresponds to the 3–2 optical emission threshold.

Whilst the shoulder in band 1 is particularly marked, its position is the least well defined of the three cases listed above. The position of the shoulder actually *increases* in energy as the electric field is increased. This is because the POP 1–1em rate is relatively small at threshold, and only becomes dominant for scattering from states of slightly higher energies (section 7B.2). Thus, as the field increases, a large carrier population persists beyond the primary optical emission threshold at $\hbar\omega_{op} = 36.4$meV, up to the 'pseudo' threshold described in section 7B.2, which occurs at $k \approx 0.081\text{Å}^{-1}$; $\epsilon = 48$meV.

In band 2, the 2–1 optical emission threshold is strong enough to cause carrier depletion sufficient that the 2–2 optical emission threshold is not manifested in the distribution functions. In band 3, the opposite effect occurs. POP 3–1em scattering is so weak as to have no visible effect on the distribution functions of Fig. 9.13. Consequently, the principal optical emission threshold for band 3 is that for 3–2 optical phonon emission, even though this does not occur until higher energies.

The only optical emission thresholds occurring in band 4 are those for 4–3 scattering, at 5meV, and 4–4 scattering, at 36meV (see Table 6.3). No structure is observed in the distribution functions in Fig. 9.14 near the 4–3 optical emission threshold, and, whilst we would expect some feature at $\epsilon \approx 36$meV associated with strong scattering into the band 4 minimum, the statistical fluctuations in the band 4 distribution functions away from $\epsilon = 0$ preclude the observation of any structure at this energy.

Reconsidering the distribution of carriers in band 1, it should be noted that both Figs. 9.7 and 9.11 show additional structure in the distribution at low fields ($F \leq 2.5\text{kVcm}^{-1}$). To investigate this further, we have obtained carrier distributions for a set of very low field values, including the zero field case. Fig. 9.15 shows the global distributions, Figs. 9.16–17, the as-sampled distributions for bands 1–2, and Figs. 9.18–19, the distribution functions for bands 1–2.

Figs. 9.18–19 show that at zero field, the distribution functions in bands 1 and 2 are Maxwellian, with slopes corresponding to the lattice temperature $T_L =$ 77K. The linearity of the zero field distribution function is particularly exact in the case of band 1, where the carrier population is largest. The attainment of these Maxwellian zero field (thermal equilibrium) distribution functions confirms that, despite all the complexities of phonon scattering in the quantum confined valence bands, our Monte Carlo model accurately maintains a detailed balance of absorption and emission scatterings for every process included (see Sections 7C

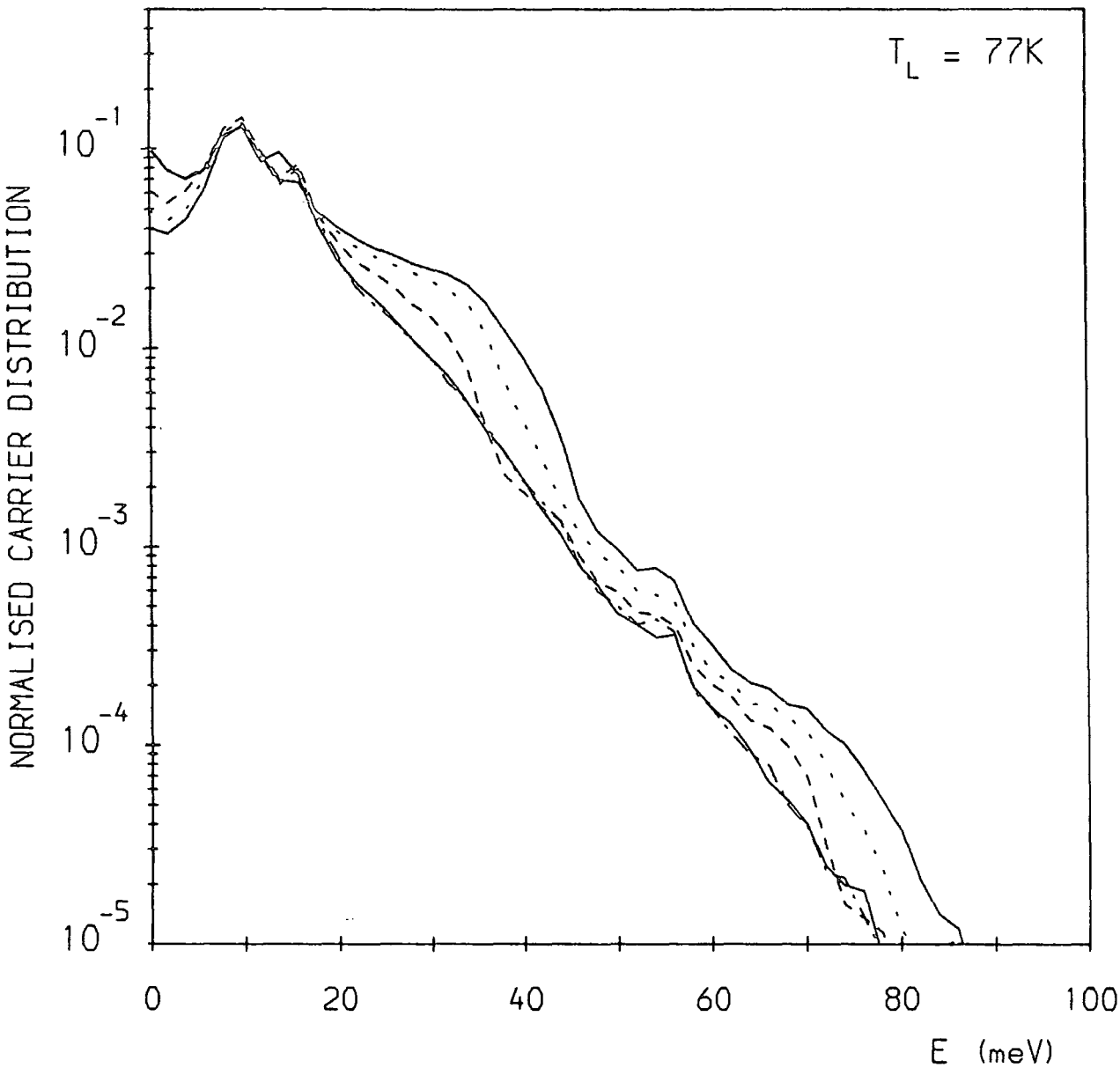

Fig. 9.15 Global hole energy distribution for in-plane electric fields of: — 0.0kVcm^{-1}; · – · 0.01kVcm^{-1}; - - - 0.1kVcm^{-1}; ··· 0.5kVcm^{-1}, and — 1.0kVcm^{-1}. $\epsilon_{ac} = 1.0\text{meV}$.

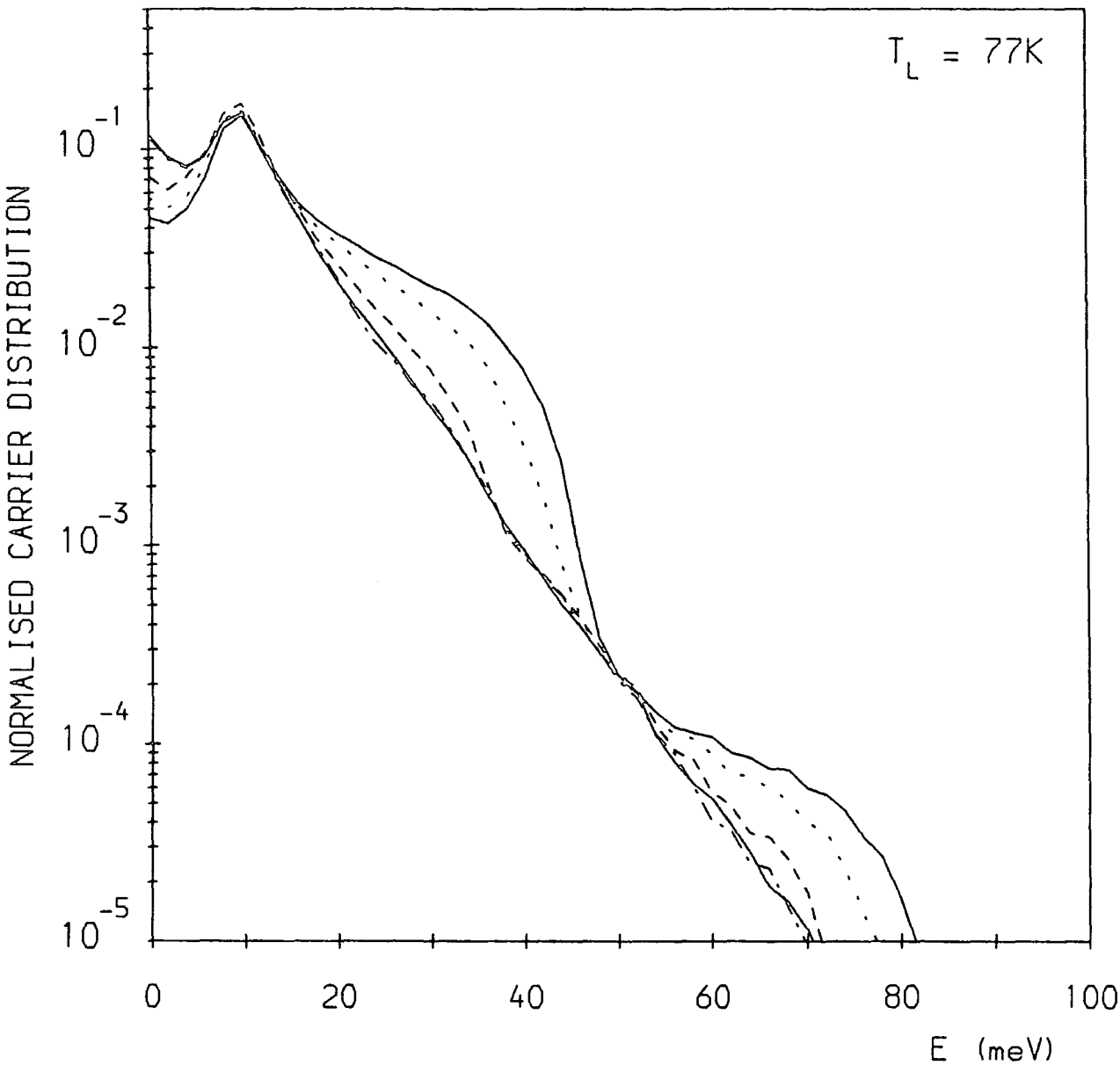

Fig. 9.16 Band 1 as-sampled hole energy distribution for in-plane electric fields of: — 0.0kVcm^{-1}; · - · 0.01kVcm^{-1}; - - - 0.1kVcm^{-1}; ··· 0.5kVcm^{-1}, and — 1.0kVcm^{-1}. $\epsilon_{ac} = 1.0$meV.

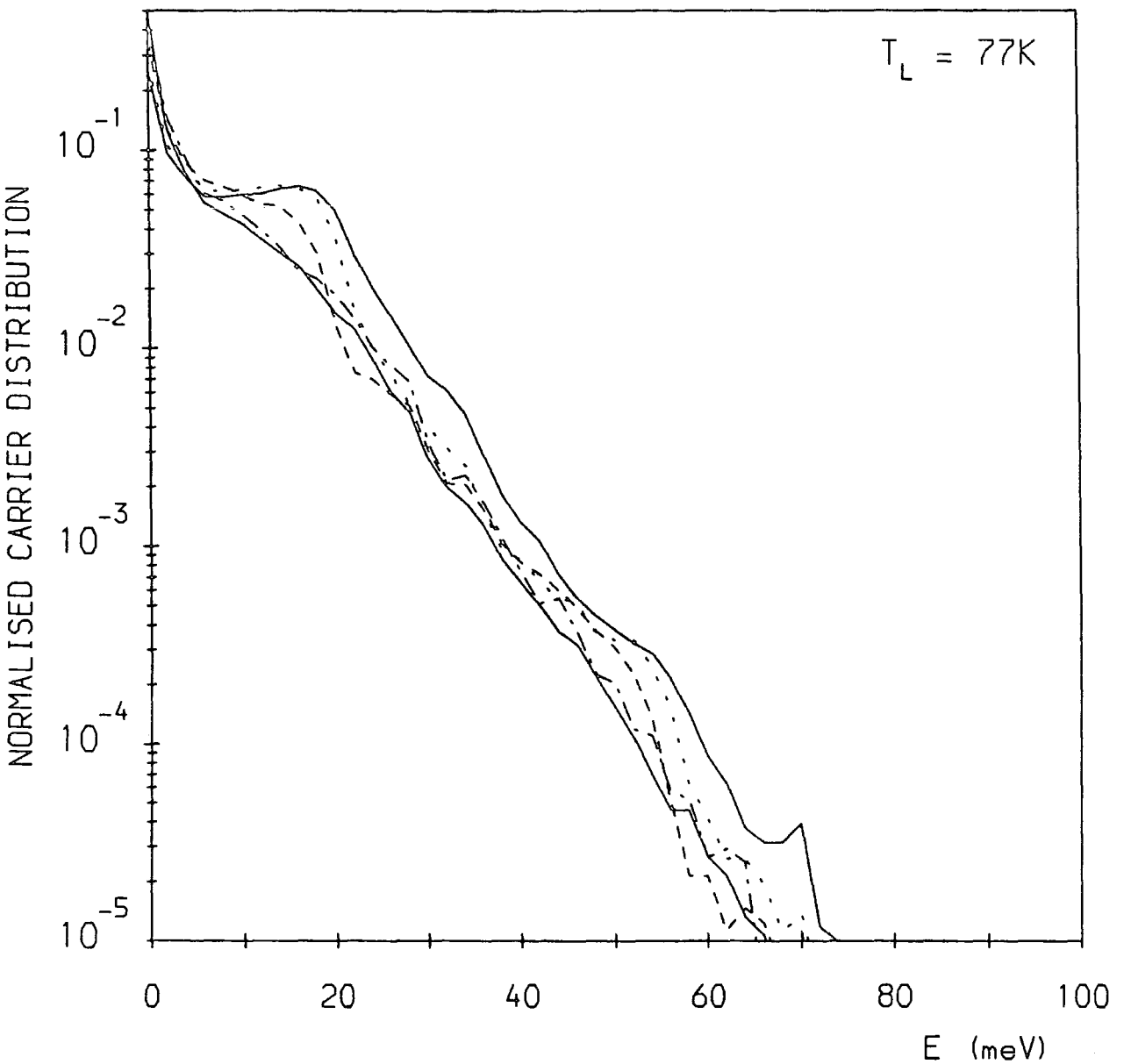

Fig. 9.17 Band 2 as-sampled hole energy distribution for in-plane electric fields of: — 0.0kVcm^{-1}; · – · 0.01kVcm^{-1}; - - - 0.1kVcm^{-1}; ··· 0.5kVcm^{-1}, and — 1.0kVcm^{-1}. ϵ_{ac} = 1.0meV.

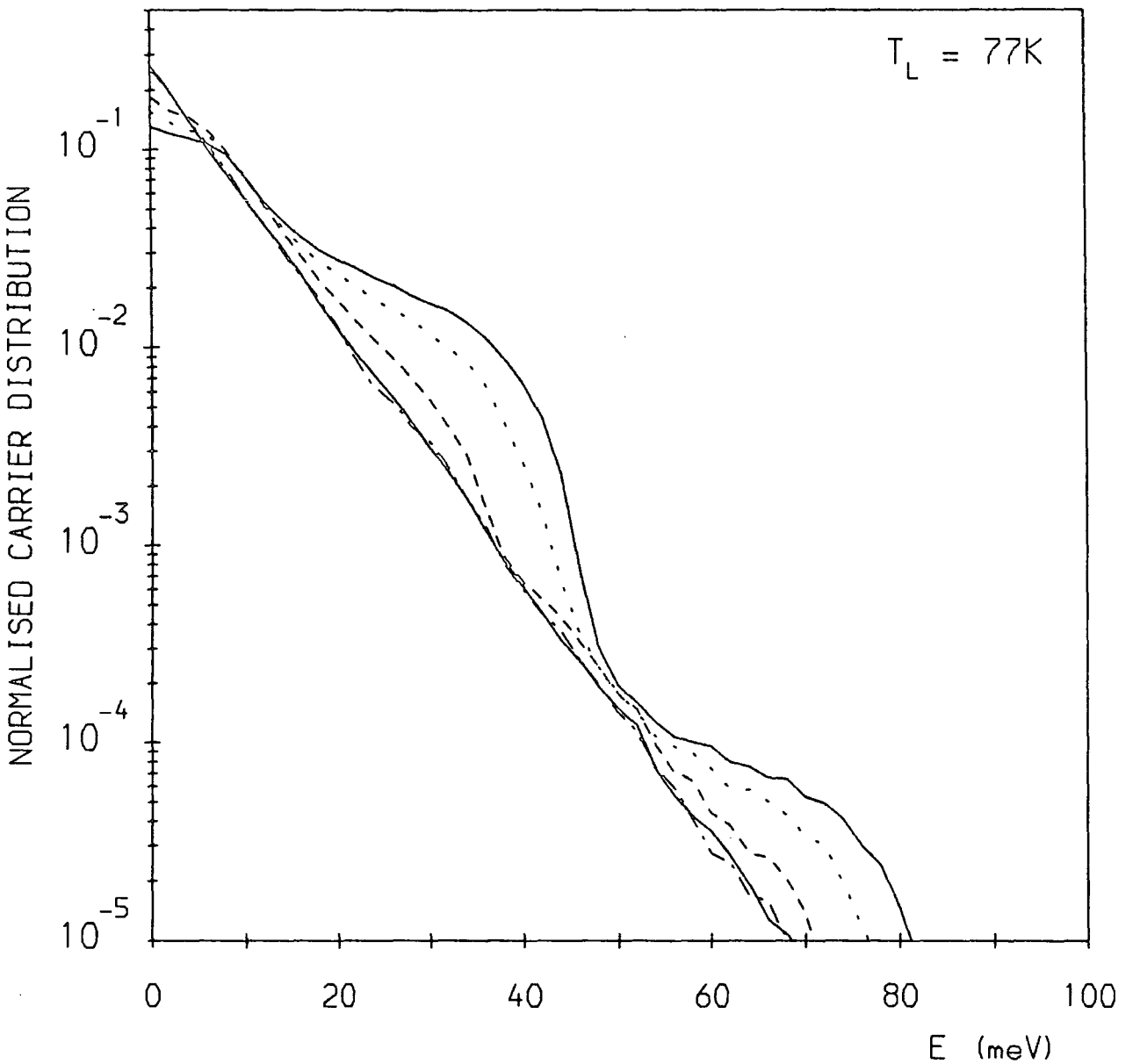

Fig. 9.18 Band 1 hole distribution function for in-plane electric fields of: — 0.0kVcm^{-1}; · – · 0.01kVcm^{-1}; - - - 0.1kVcm^{-1}; ··· 0.5kVcm^{-1}, and — 1.0kVcm^{-1}. $\epsilon_{ac} = 1.0\text{meV}$.

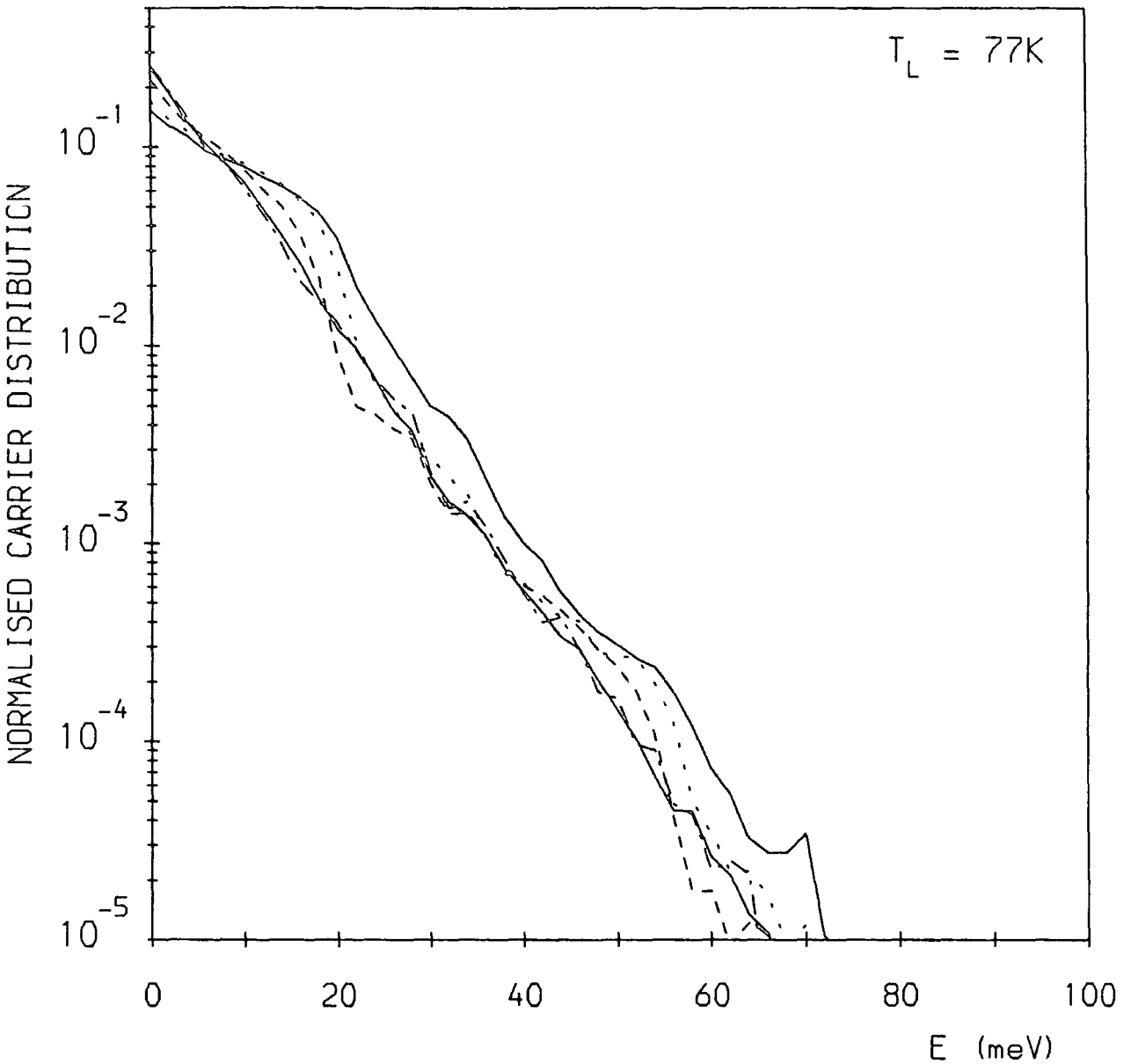

Fig. 9.19 Band 2 hole distribution function for in-plane electric fields of: — 0.0kVcm^{-1}; · – · 0.01kVcm^{-1}; - - - 0.1kVcm^{-1}; ··· 0.5kVcm^{-1}, and — 1.0kVcm^{-1}. $\epsilon_{ac} = 1.0\text{meV}$.

and 8C).

Fig. 9.18 shows that, as the electric field is turned on, the low energy states in band 1 begin to deplete, and a distinct repopulation of states at energies approaching the optical emission threshold occurs. For energies just above the 'pseudo' threshold at $\epsilon \approx 48\text{meV}$, the distribution function shows very little change with electric field, but, at higher energies, a second repopulation phenomenon is visible. This region extends up to $\epsilon \approx 48\text{meV} + \hbar\omega_{\text{op}}$, which represents the energy at which the total probability for scattering by the successive emission of two optical phonons is at a maximum. Thus the feature is essentially a 'phonon replica' of the pseudo-threshold at 48meV. Fig. 9.16 shows that the actual carrier population in band 1 (as given by the as-sampled distribution) develops as described above, but with the modifications associated with the density of states. It is interesting to note that, at zero field, a minimum appears in the as-sampled distribution between $\epsilon = 0$ and the position of the density-of-states maximum. As the field is turned on, the band edge population begins to deplete, and the position of the minimum shifts towards $\epsilon = 0$.

9C CARRIER TEMPERATURES

Referring to the distribution functions of Figs. 9.11–14, we see that whilst the low energy portions of the curves display various scattering-related features, at higher energies the curves are almost linear. The slopes of these upper energy tails decrease with increasing field; by measuring these slopes it should be possible to define a carrier temperature T_c in each band, where $T_c > T_L$ (*cf.* Conwell 1967; Shah 1978). Fig. 9.20 shows carrier temperatures derived from the distribution functions for each of the four bands, for a range of electric fields, and also the carrier temperatures derived from global distributions such as those in Fig. 9.6. Obviously, the values for these temperatures, particularly those in the upper bands, are subject to very large tolerances (probably ±50% in band 4) but the general trend of the data gives a useful insight into the equilibrium which is established in the multiband system.

The temperatures for carriers in bands 1,2 and 4 are broadly similar, whilst the band 3 temperatures are consistently lower throughout the range of fields shown. Unfortunately, due to the large tolerances on the data, it is not clear whether the reduced values in band 3 represent a physical effect, or are simply the consequence of some systematic error in estimating the temperatures. It is interesting to note that these results could not be predicted from the values of mean carrier energy in each band. For a parabolic band in 2D, the carrier temperatures would be given by $T_c = \langle\epsilon\rangle/k_B$. For our simulations, this assumption would lead to the prediction of higher temperatures in band 3 than in the other bands, and also of high temperatures in band 4 for fields greater than 6kVcm^{-1}. Furthermore, all the values predicted by the $\langle\epsilon\rangle/k_B$ approximation are considerably larger than those of Fig. 9.20. In Fig. 9.21 we have shown carrier temperatures obtained from the global distributions, compared with the overall average energy $\langle\epsilon_{\text{av}}\rangle$ expressed as a temperature. Clearly the discrepancy is substantial, and worsens with increasing field. Concerning the reliability of the T_c values obtained from the distribution functions in this context, it should be pointed out that these values are likely to be *overestimates*, rather than underestimates, of the true values, since the distribution functions include the effects of carrier drifting, as well as carrier heating. The drifting of the carriers will tend to further reduce the slope of the high energy tails of the distributions functions, leading to the prediction of higher temperatures.

Thus we may conclude that the values of $\langle\epsilon\rangle/k_B$ cannot be used, in isolation, to characterise the distribution functions of quantum confined holes. In particular, they lead to the suggestion of markedly different carrier temperatures in the different bands, and of especially large temperatures for carriers in band 3, neither of which, from the results of Fig. 9.20, appears to be the case. The similarity of

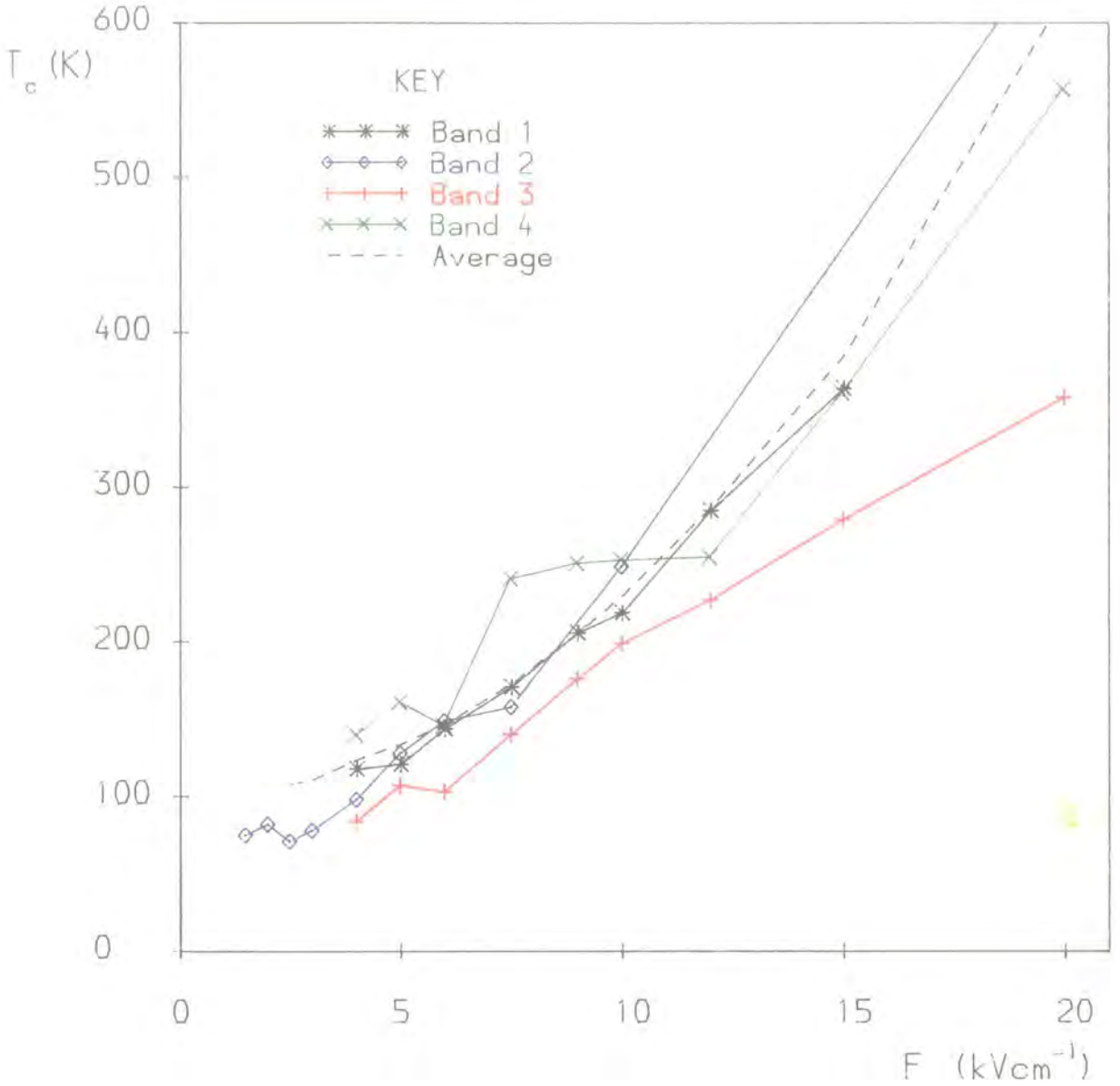

Fig. 9.20 Carrier temperatures in each of bands 1–4, and the overall average carrier temperature, as a function of in-plane electric field. T_L = 77K; ϵ_{ac} = 1meV.

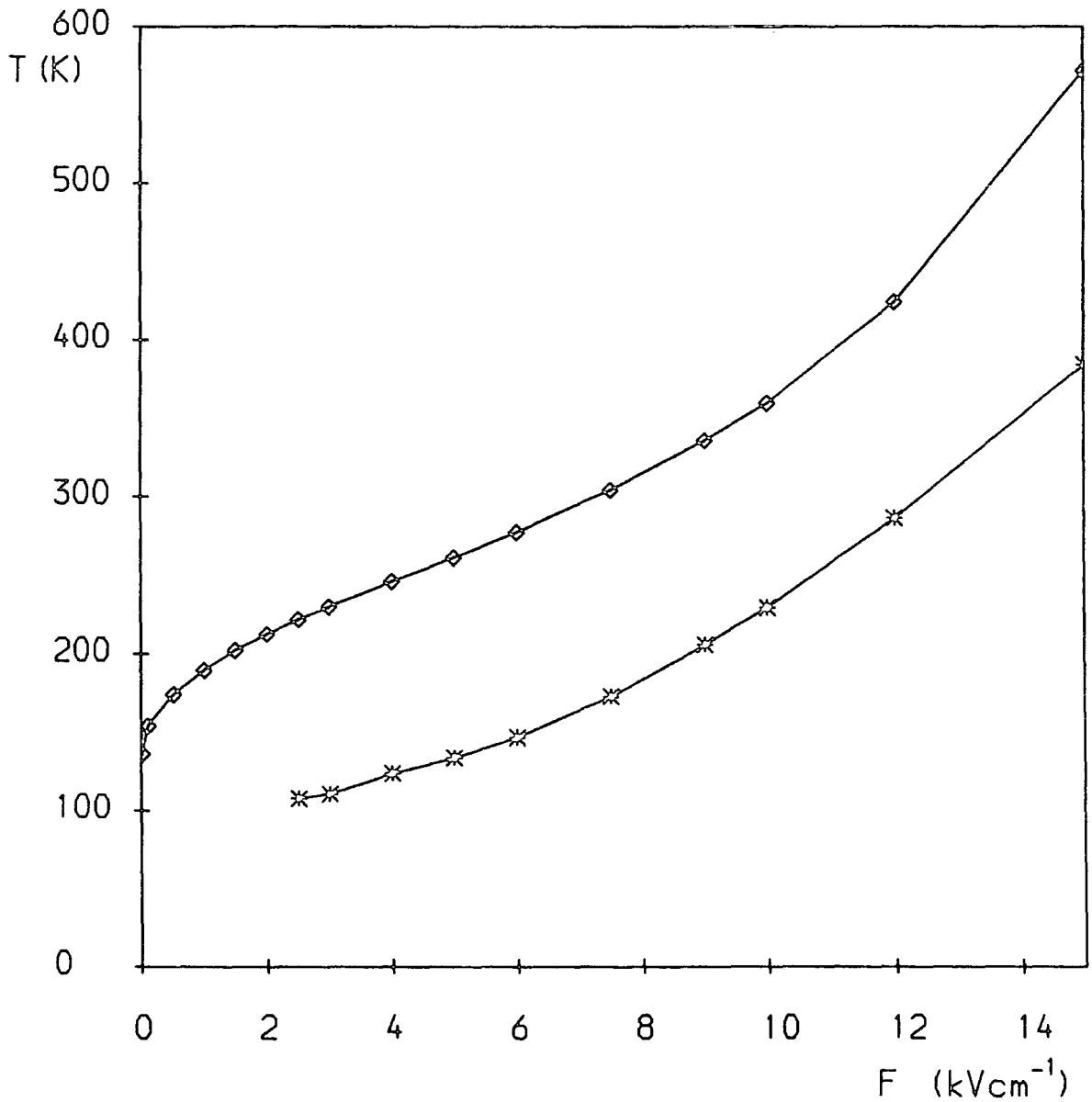

Fig. 9.21 Average carrier temperature (∗), and $\langle \epsilon_{av} \rangle / k_B$ (◇) *vs.* in-plane electric field. $T_L = 77$K; $\epsilon_{ac} = 1$meV.

carrier temperatures in bands 1,2, and 4 depicted in Fig. 9.20 indicates that, despite the general weakness of interband scattering in the quantum confined valence band system, a fair degree of communication exists between the bands; such that the carrier thermalisation process in any one band is not independent of that in the neighbouring bands. This was also suggested by Da Costa *et al.* (1987). Furthermore we may note that, at low fields ($F \leq 2.5\text{kVcm}^{-1}$), a temperature cannot be defined for carriers in band 1 (see Fig. 9.11), but a carrier temperature may be defined for the complete system (see Fig. 9.6). The high energy structure in the low field band 1 distribution functions is related to optical phonon scattering, as was discussed in the previous section. However, thermalisation of carriers across the whole system is sufficiently effective as to compensate for this effect, and to give rise to a global distribution which is near-Maxwellian at high energies.

9D ENERGY LOSS RATES

The power supplied to the carrier population by the electric field is given by eFv_d per carrier. In the steady state, this is equivalent to the average rate of energy loss per carrier due to scattering; *i.e.*,

$$\left\langle \frac{\partial \epsilon}{\partial t} \right\rangle = eFv_d \tag{9.1}$$

(see, for example, Conwell, 1967). This formula can be used to obtain the energy loss rate from the Monte Carlo simulations. However, an alternative and more powerful method is available. The energy loss rate via a particular phonon emission process is defined as:

$$\left\langle \frac{\partial \epsilon}{\partial t} \right\rangle = \frac{\int_0^\infty \hbar\omega P(\epsilon + \hbar\omega) f(\epsilon + \hbar\omega) D(\epsilon + \hbar\omega)\, d\epsilon}{\int_0^\infty f(\epsilon) D(\epsilon)\, d\epsilon}, \tag{9.2}$$

where $P(\epsilon)$ is the scattering rate for the given process, $\hbar\omega$ is the phonon energy, $f(\epsilon)$ is the carrier distribution function and $D(\epsilon)$ is the density of states. (A similar expression can be written for phonon absorption.) The denominator of the RHS of this equation simply gives the total carrier population of the system, n_{sys}. For a fixed phonon energy, the expression then reduces to:

$$\left\langle \frac{\partial \epsilon}{\partial t} \right\rangle = \frac{\hbar\omega}{n_{\text{sys}}} \int_0^\infty P(\epsilon + \hbar\omega) f(\epsilon + \hbar\omega) D(\epsilon + \hbar\omega)\, d\epsilon. \tag{9.3}$$

The integral represents the weighted average of the scattering rate $P(\epsilon)$ over the entire region of the distribution within which the particular phonon emission process is possible. This quantity is given in the single particle Monte Carlo simulations by N/t_{sim}, where N is the total number of scattering events via the given process and t_{sim} is the total simulation time. Then, the Monte Carlo estimate of the average energy loss rate per carrier via a given phonon mode is simply

$$\left\langle \frac{\partial \epsilon}{\partial t} \right\rangle = \frac{\hbar\omega N}{t_{\text{sim}}}. \tag{9.4}$$

Since we have used a fixed phonon energy for the acoustic modes, we may obtain the total energy loss rate per carrier by summing contributions of the above form for all the phonon scattering processes included in the simulation. This gives

$$\left\langle \frac{\partial \epsilon}{\partial t} \right\rangle = \frac{1}{t_{\text{sim}}} \sum_i \hbar\omega_i N_i \tag{9.5}$$

where i is an index for the phonon modes. However, the power of the method described above lies in its ability to resolve the total energy loss rate into all of its

constituent components, made possible in practice by the detailed breakdown of scattering events available from the Monte Carlo simulations.

Fig. 9.22 shows the energy loss rate per carrier due to POP, NPO, AC and PZ processes, and the total energy loss rate, as a function of electric field. As in the case of electrons in 2D, energy loss is dominated by POP scattering, with the NPO rate around a factor of five lower. The AC and PZ rates are typically three orders of magnitude below the POP rate, due to the much smaller phonon energy and the smaller scattering rates. The PZ energy loss rate is typically a factor of two lower than the AC rate. Fig. 9.23 shows the energy loss rates resolved into intra- and inter-band components. We find, as expected, that the intraband components dominate, with over an order of magnitude of difference between the intra- and inter-band rates for each of the four classes of phonons.

For quantum confined electrons, the predominance of POP scattering leads to a very simple dependence of the energy loss rate on carrier temperature. Assuming that POP absorption is negligible, and that an average scattering lifetime τ_{POP} may be defined:

$$\frac{1}{\tau_{\mathrm{POP}}} = \frac{\int_0^\infty P_{\mathrm{POP}}(\epsilon + \hbar\omega_{\mathrm{op}}) f(\epsilon + \hbar\omega_{\mathrm{op}}) D(\epsilon + \hbar\omega_{\mathrm{op}})\, d\epsilon}{\int_0^\infty f(\epsilon + \hbar\omega_{\mathrm{op}}) D(\epsilon + \hbar\omega_{\mathrm{op}})\, d\epsilon}, \tag{9.6}$$

we may write;

$$\left\langle \frac{\partial \epsilon}{\partial t} \right\rangle = \frac{\hbar\omega_{\mathrm{op}}}{\tau_{\mathrm{POP}}} \frac{\int_0^\infty f(\epsilon + \hbar\omega_{\mathrm{op}}) D(\epsilon + \hbar\omega_{\mathrm{op}})\, d\epsilon}{\int_0^\infty f(\epsilon) D(\epsilon)\, d\epsilon} \tag{9.7}$$

(see Lyon 1986). The ratio of integrals simply represents the proportion of the carrier population lying above the optical phonon emission threshold. For a Maxwellian distribution of carriers at a carrier temperature T_c, the energy loss rate becomes

$$\left\langle \frac{\partial \epsilon}{\partial t} \right\rangle = \frac{\hbar\omega_{\mathrm{op}}}{\tau_{\mathrm{POP}}} \exp\left(\frac{-\hbar\omega_{\mathrm{op}}}{k_B T_c}\right) I(k_B T_c) \tag{9.8}$$

where $I(k_B T_c) = \int f(\epsilon) D(\epsilon + \hbar\omega_{\mathrm{op}})\, d\epsilon / \int f(\epsilon) D(\epsilon)\, d\epsilon$.

For a parabolic band in 2D, $I = 1$, since the density of states is independent of energy. For the quantum confined valence bands $I(k_B T_c)$ cannot be determined algebraically; however, it is unlikely that this function will have a stronger temperature dependence than the exponential term $\exp(-\hbar\omega_{\mathrm{op}}/k_B T_c)$ for any of the POP scattering processes considered. Thus, the total energy loss rate for quantum confined holes may be expected to have an approximately exponential dependence on carrier temperature, as observed for electrons in 2D. In Fig. 9.24 we have plotted the total carrier energy loss rate on a logarithmic scale, as a function of $1/T_c$, using the values for T_c presented in the previous section.

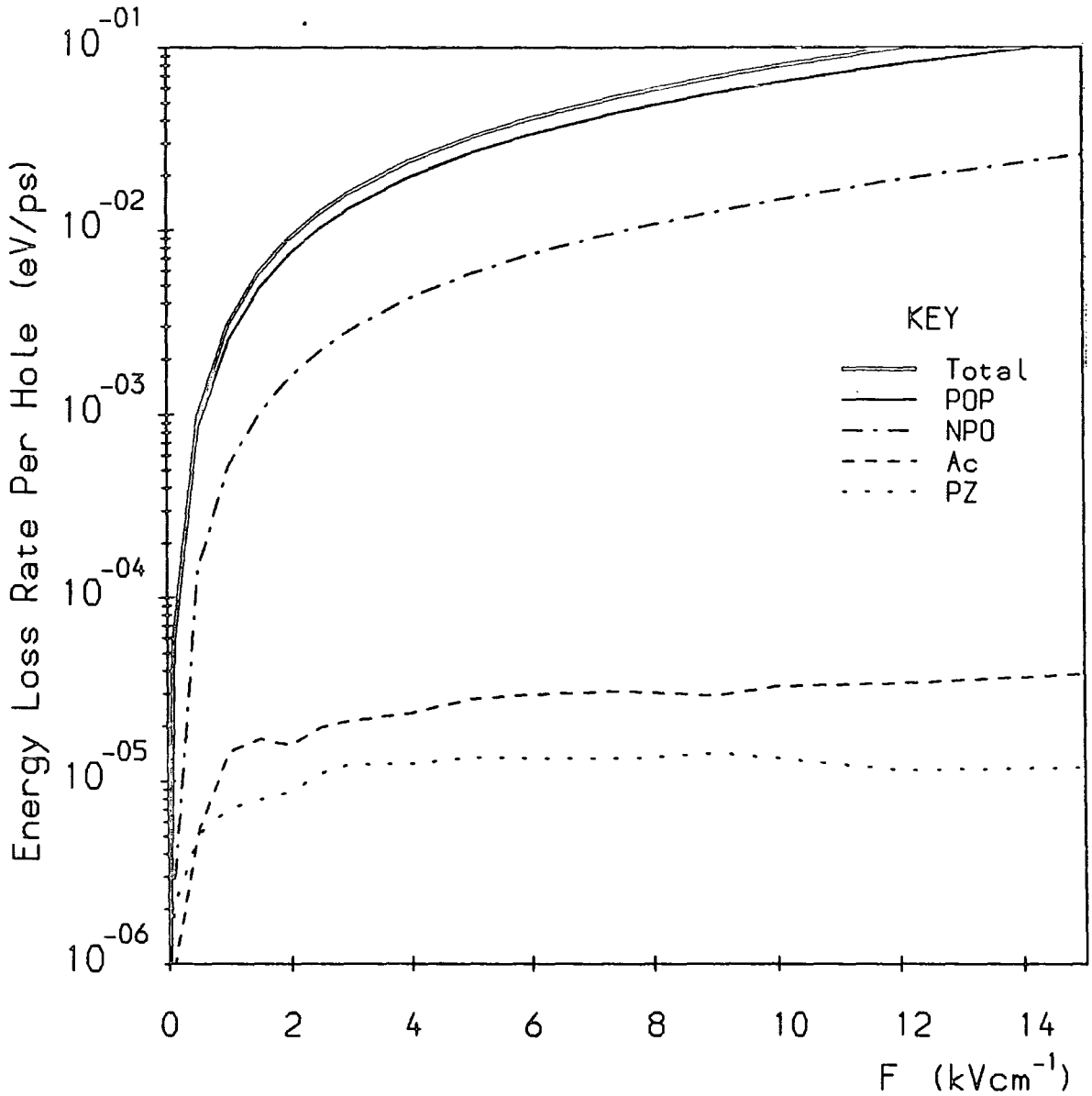

Fig. 9.22 Steady state 2D hole energy loss rate, resolved into components due to POP, NPO, AC and PZ scattering, as a function of in-plane electric field. $T_L = 77\text{K}$; $\epsilon_{ac} = 1\text{meV}$.

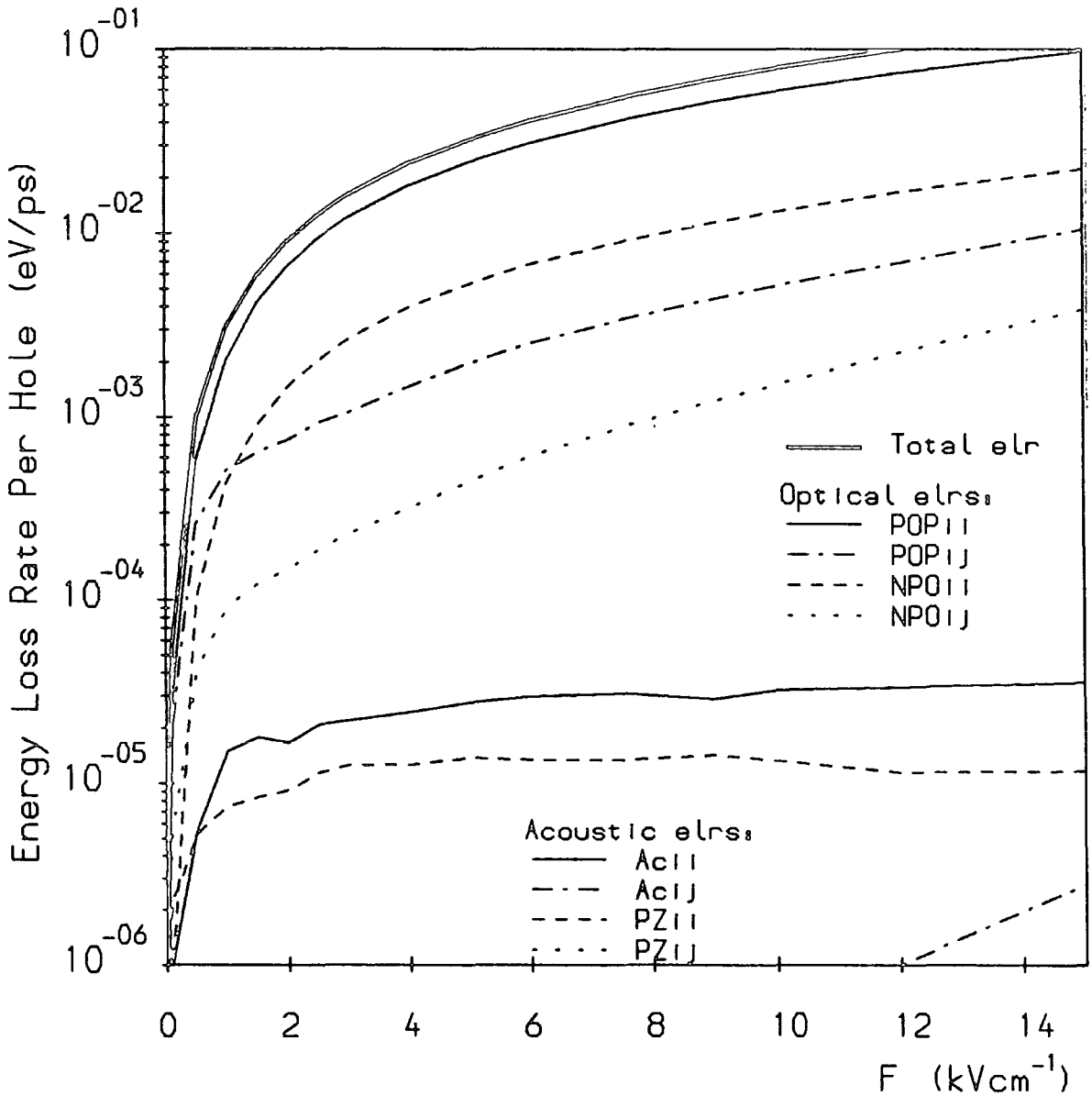

Fig. 9.23 Steady state 2D hole energy loss rate, resolved into components due to intra- and inter-band scattering. $T_L = 77\text{K}$; $\epsilon_{ac} = 1\text{meV}$.

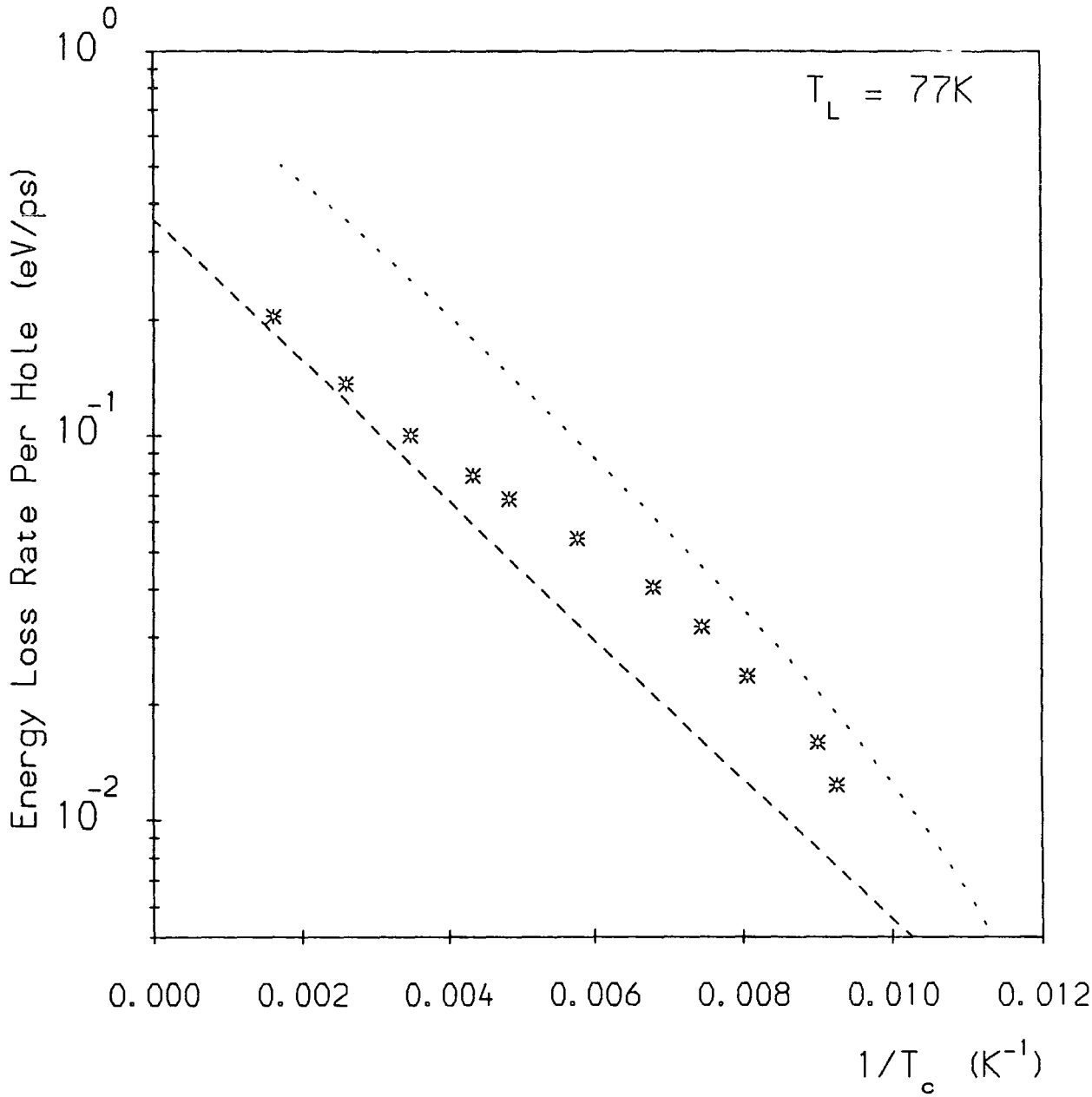

Fig. 9.24 Steady state hole energy loss rates *vs.* inverse carrier temperature.
* Monte Carlo simulation of quantum confined holes,
- - - line of slope $\hbar\omega_{op}/k_B$ (see text),
. . . calculated rate for heavy holes in bulk GaAs, due to POP scattering only (Conwell 1967).

It can be seen that, at high carrier temperatures (and therefore high electric fields) the energy loss rate follows quite closely the exponential law predicted above, with the datapoints asymptotic to the broken line of slope $-\hbar\omega/k_B$. There are three likely reasons for this high field response. Firstly, more carriers will be found in the higher energy states where the density of states varies relatively weakly with energy. Secondly, the scattering rate for carriers in these states is also nearly independent of energy, and thirdly, the high field distribution functions are closer to the Maxwellian form for a wide range of carrier energies (see Figs. 9.6 and 9.11).

At lower carrier temperatures (lower fields) the energy loss rate departs from, and is enhanced relative to the exponential form predicted by simple theory. The departure from the exponential law reflects the fact that, at low energies, the densities of states in the quantum confined valence bands are strongly dependent on energy. Also, at lower fields, the carrier distribution is dominated by the shoulder-like features caused by optical phonon scattering, so that the Maxwellian approximation does not hold good for the large population of carriers immediately above the (1–1) optical emission threshold. The enhancement of the rate relative to that for the simple model would appear to be due to the particularly large POP scattering rate near the 1–1 threshold. For carriers in this region, the average scattering time will be considerably shorter than that at higher energies. The quantity τ_{POP} defined in equation (9.6) cannot, in this case, be regarded as independent of carrier temperature. It is of interest to note that Shah *et al.* (1985) have conducted experiments on the steady state electric field heating of holes in a GaAs quantum well at $T_L = 1.8K$. Their results also indicates an exponential dependence of the hole energy loss rate on carrier temperature in the range of T_c where optical scattering is dominant. This trend would be expected to carry over to higher lattice temperatures, since the form and magnitude of the POP scattering rate should remain much the same. That Shah *et al.* do not observe any deviation from the exponential response of the energy loss rate in the low field regime may be due to the effect of carrier-carrier scattering in their sample, which will drive the carrier distribution towards the Maxwellian form.

Concerning the magnitude of the energy loss rate, the only relevant experimental data currently available is again that reported by Shah *et al.* (1985). The upper limit of their results predicts an energy loss rate of $1.4 \times 10^{-9}\mathrm{W} \equiv 9 \times 10^{-3}\mathrm{eVps}^{-1}$ at $T_c = 100\mathrm{K}$, which is very close to the low T_c end of our 77K data. The correlation between our results and those of Shah *et al.* confirms the common assumption that 2D hole cooling is not significantly affected by such phenomena as phonon reabsorption, which is supposed to reduce the cooling rate of electrons in 3D and

2D.

For carriers in bulk semiconductors, Conwell (1967) has derived an expression for the energy loss rate to polar phonon modes, assuming a Maxwellian carrier distribution. The dotted curve on Fig. 9.24 shows the rate given by her theory for heavy holes in GaAs, neglecting overlap integral effects. The values are close to, but always greater than those obtained from our 2D simulation. The reduction in energy loss rate in the 2D case may be attributed to the effects of band mixing on the scattering matrix elements.

The AC and PZ rates of Fig. 9.22 show a relatively weak dependence on electric field for most of the field range considered. This is probably a consequence of the fixed phonon energy approximation, which will lead to underestimates of the energy loss rates to acoustic modes at high fields when $\epsilon_{\mathrm{ph,max}} = 2\hbar v_s k$ can be quite large. For a 2D system, the rate of energy loss to acoustic (deformation potential) modes has been shown to be proportional to $(T_c - T_L)$ in the range of T_c where the equipartition approximation is valid (Hess and Sah 1974; Ferry 1977; Price 1982). However, for our fixed acoustic phonon energy scheme, the net energy loss rate due to a particular AC scattering process will be given by:

$$\left\langle \frac{\partial \epsilon}{\partial t} \right\rangle = \epsilon_{\mathrm{ac}} \int_0^\infty \Big(P_{\mathrm{em}}(\epsilon + \epsilon_{\mathrm{ac}}) f(\epsilon + \epsilon_{\mathrm{ac}}) D(\epsilon + \epsilon_{\mathrm{ac}}) - P_{\mathrm{abs}}(\epsilon) f(\epsilon) D(\epsilon) \Big) \, d\epsilon \times \left[\int_0^\infty f(\epsilon) D(\epsilon) \, d\epsilon \right]^{-1}. \tag{9.9}$$

We now introduce the quantity $P'(\epsilon)$, where

$$P_{\mathrm{em}}(\epsilon) = P'(\epsilon)(\mathcal{N}_{\mathrm{ac}} + 1), \tag{9.10a}$$

$$P_{\mathrm{abs}}(\epsilon) = P'(\epsilon)\mathcal{N}_{\mathrm{ac}}, \tag{9.10b}$$

with $\mathcal{N}_{\mathrm{ac}} = 1/(\exp(\epsilon_{\mathrm{ac}}/k_B T_L) - 1)$. Then, taking the carrier distribution to be Maxwellian with a temperature T_c, we may write for small ϵ_{ac}:

$$\left\langle \frac{\partial \epsilon}{\partial t} \right\rangle = \epsilon_{\mathrm{ac}} \left(\exp\left(\frac{-\epsilon_{\mathrm{ac}}}{k_B T_c} \right) (\mathcal{N}_{\mathrm{ac}} + 1) - \mathcal{N}_{\mathrm{ac}} \right) \times \frac{\int_0^\infty P'(\epsilon) f(\epsilon) D(\epsilon) \, d\epsilon}{\int_0^\infty f(\epsilon) D(\epsilon) \, d\epsilon}. \tag{9.11}$$

Defining

$$\frac{1}{\tau_{\mathrm{ac}}} = \frac{\int_0^\infty P'(\epsilon) f(\epsilon) D(\epsilon) \, d\epsilon}{\int_0^\infty f(\epsilon) D(\epsilon) \, d\epsilon} \tag{9.12}$$

in the same manner as for POP scattering, and taking $\mathcal{N}_{\mathrm{ac}} \approx k_B T_L / \epsilon_{\mathrm{ac}}$; we obtain

$$\left\langle \frac{\partial \epsilon}{\partial t} \right\rangle = \frac{\epsilon_{\mathrm{ac}}}{\tau'_{\mathrm{ac}}} \left(1 - \frac{T_L}{T_c} \right). \tag{9.13}$$

Thus, in our simulation, we may expect the energy loss rate due to the AC processes to saturate at high T_c. This is consistent with the very gradual increase of the AC energy loss rate with electric field shown in Fig. 9.22.

The actual magnitude of the acoustic energy loss rates are found to be quite strongly dependent on the value of phonon energy used. Fig. 9.25 shows the AC energy loss rate as a function of carrier temperature, for $\epsilon_{ac} = 1$ and 2meV. The 2meV rate is around five times larger than that for $\epsilon_{ac} = 1$meV. Obviously, a twofold increase in the rates is expected, since the energy exchange per scattering event has been doubled. The extra increase occurs because, as the phonon energy is increased, the ratio of emission to absorption events also increases. Whilst this increase is small, it is the *difference* between the numbers of emission and absorption events which gives the energy loss rate. This difference is generally much smaller than the actual number of scattering events for any given process, and can therefore change quite considerably when ϵ_{ac} is altered.

This susceptibility of the acoustic energy loss rates to changes in ϵ_{ac} means that we cannot make any definite predictions concerning the effects of quantum confinement on these quantities. Fig. 9.25 also shows the AC energy loss rate for holes in a 2D parabolic band, obtained from the expression derived by Hess and Sah (1974). The similarity between the range of values spanned by our results and those predicted by the simple model indicate that the fixed phonon energy approximation does give physically realistic values for the acoustic energy loss rates. At high fields, the choice of $\epsilon_{ac} = 2$meV should give the better approximation to the true energy loss rates, whilst, at low fields, the choice $\epsilon_{ac} = 1$meV may be more appropriate. It should be emphasised, of course, that had we adopted the usual elastic and equipartition approximations for acoustic scattering in our simulations, we would not have been able to obtain any information on the acoustic energy loss rates at all.

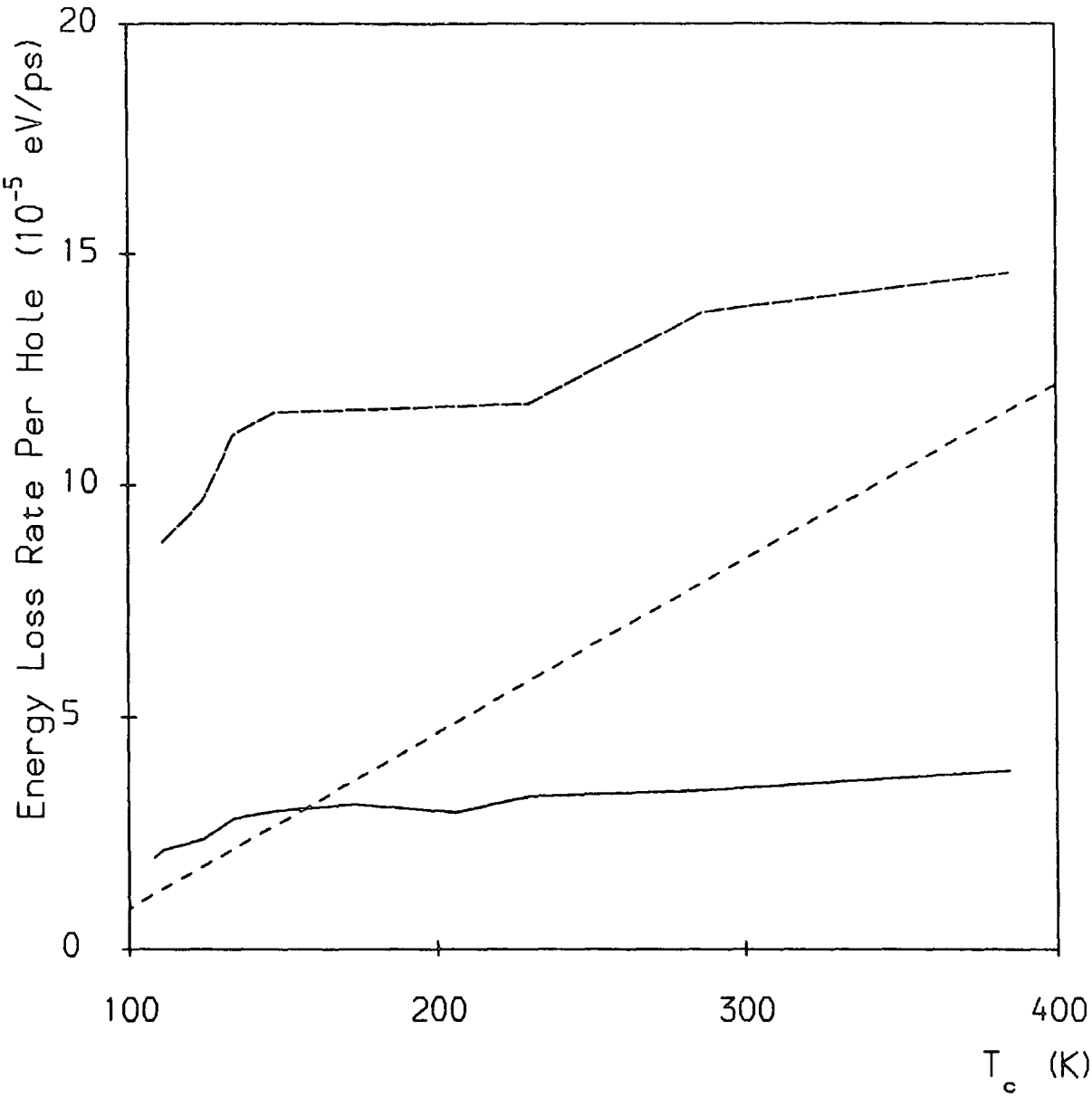

Fig. 9.25 Steady state energy loss rates to acoustic (deformation potential) modes for: — $\epsilon_{ac} = 1$meV; -- $\epsilon_{ac} = 2$ meV, *vs.* carrier temperature. The dashed line (- - -) gives the theoretical result for holes in a simple 2D parabolic band (Hess and Sah 1974).

9E HOLE DISTRIBUTIONS IN THE 2D WAVEVECTOR PLANE

The distribution of carriers in the 2D k-space plane, $F(\mathbf{k}) \equiv F(\epsilon, \beta)$, can be readily obtained from the Monte Carlo simulations. Figs. 9.26(a–d) and 9.27(a–d) show $F(\mathbf{k})$ for carriers in bands 1 and 2 respectively, for fields of 1, 5, 10 and 20kVcm^{-1}. The contours on each graph are lines of equal population density $F(\mathbf{k})$, and are each indexed by a number from 1 to 15. The values of $F(\mathbf{k})$ represented by these indices increase in a roughly logarithmic manner, with index 1 representing the lowest value. The fluctuations on the low index contours are statistical in origin, and occur, particularly in the band 2 distributions, because the the actual carrier population at the periphery of the distribution is so low.

In Fig. 9.26a it can be seen that, at $F = 1$kVcm^{-1} the distribution exhibits a fair degree of circular symmetry, with only a small extent of drift in the field direction ($+k_x$). However, a sharp fall-off in the carrier population is already visible at $k \approx 0.075$Å^{-1}, corresponding to the region of strong POP scattering beyond the 1–1 optical emission threshold. At $F = 5$kVcm^{-1} the distribution has been further drifted in the field direction and shows a considerable degree of asymmetry. Moreover, the states on the low k side of the 1–1 optical emission threshold (in the $+k_x$ half-plane) are now markedly *overpopulated*, and the decrease in population above threshold is much steeper. These features correspond to the structure observed on the band 1 energy distribution functions of Fig. 9.11. It is clear that carriers passing the 1–1 optical emission threshold are subject to very efficient scattering into low k states, with very few carriers found beyond the 'pseudo' threshold at $k \approx 0.081$Å^{-1} (see section 7B.2). The 'bunching' (overpopulation) of carriers just below the optical emission threshold is a consequence of the weakness of scattering in this region. Fig. 7.11 shows that the total scattering rate here is smaller than that for states of lower k.

In Figs. 9.26c and d it can be seen that the peak of the carrier distribution moves little as the field is increased, and certainly does not pass beyond the 1–1 optical emission threshold, even at $F = 20$kVcm^{-1}. However, at the higher fields, the distribution spreads to larger wavevectors in all directions, and, in particular, a significant proportion of carriers are now swept across the primary and pseudo-1–1 optical emission thresholds to states of larger k in the $+k_x$ direction.

Fig. 9.28 shows the variation of the band 1 distribution $F(\mathbf{k})$ with k, along a line through $\mathbf{k} = 0$ and parallel to the k_x axis. The 'bunching' effect at $F = 5$kVcm^{-1} (and, to some extent, at $F = 10$kVcm^{-1}) is manifested by the large peak values of the distribution occurring for k just below the threshold at $k \approx 0.07$Å^{-1}. At $F = 20$kVcm^{-1} the peak value of the distribution is much smaller, and a

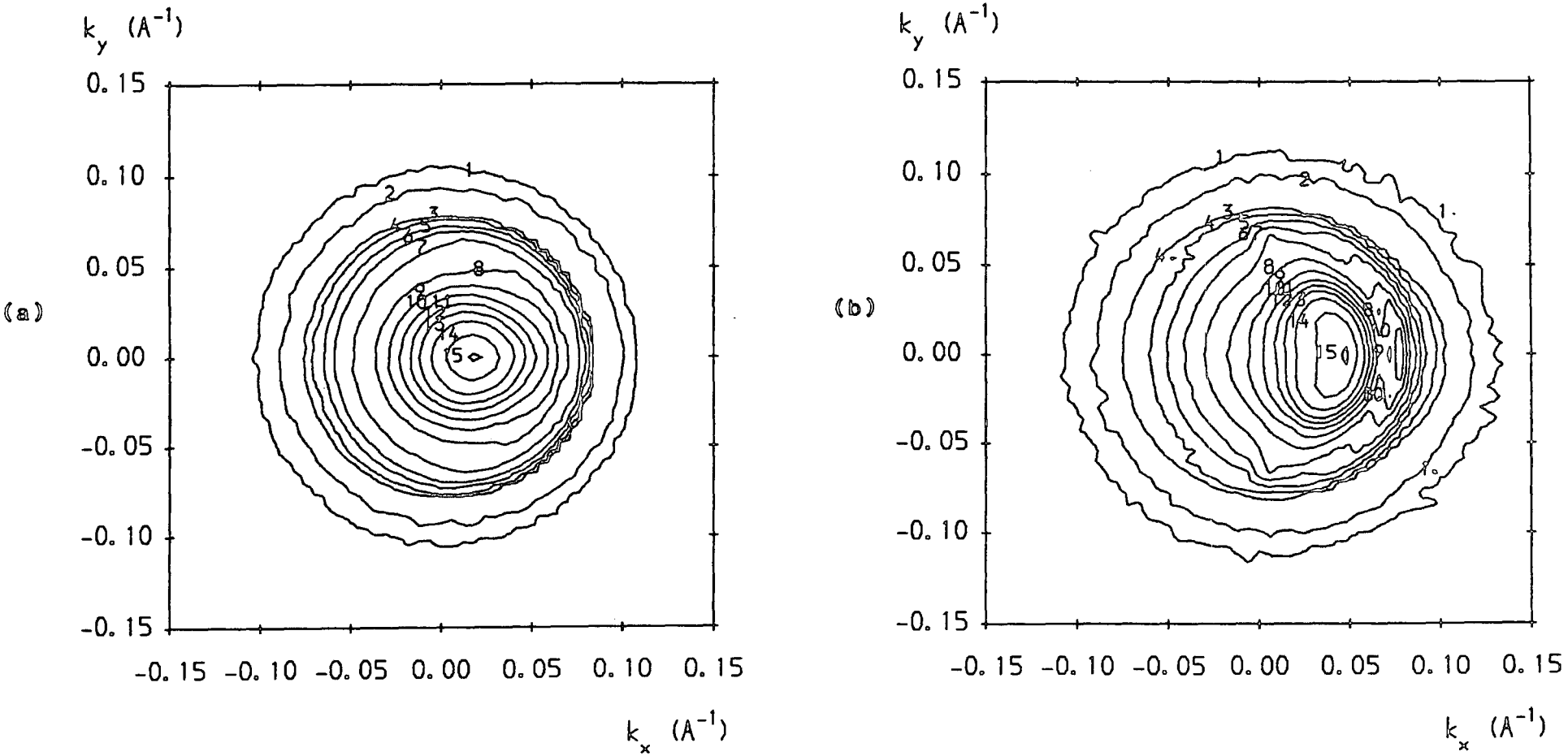

Fig. 9.26(a & b) Hole distributions in 2D k-space. Band 1. (a) $F_x = 1\text{kVcm}^{-1}$; (b) $F_x = 5\text{kVcm}^{-1}$. $T_L = 77\text{K}$; $\epsilon_{\text{ac}} = 1\text{meV}$.

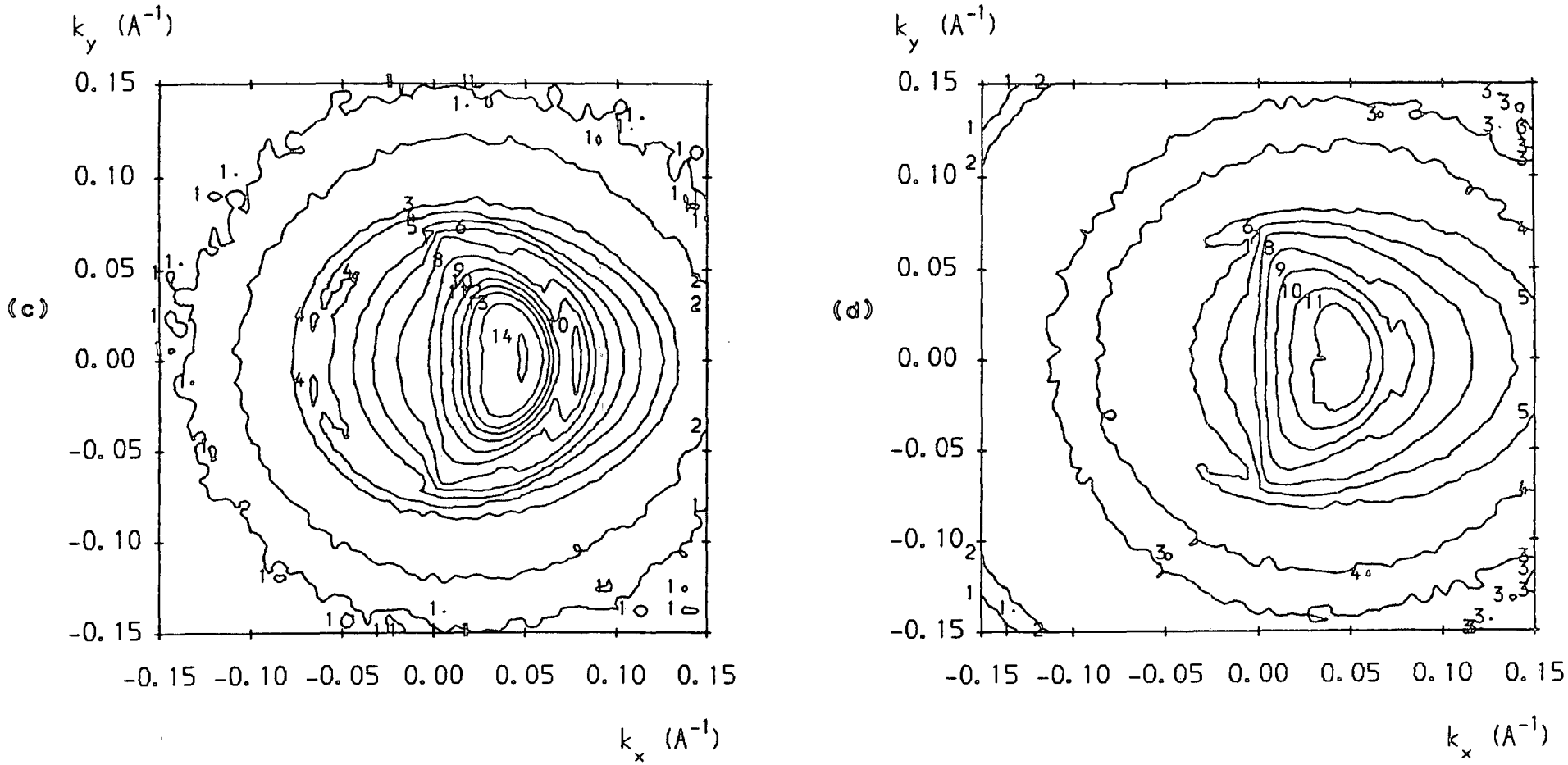

Fig. 9.26(c & d) Hole distributions in 2D k-space. Band 1. (c) $F_x = 10\text{kVcm}^{-1}$; (d) $F_x = 20\text{kVcm}^{-1}$. $T_L = 77\text{K}$; $\epsilon_{ac} = 1\text{meV}$.

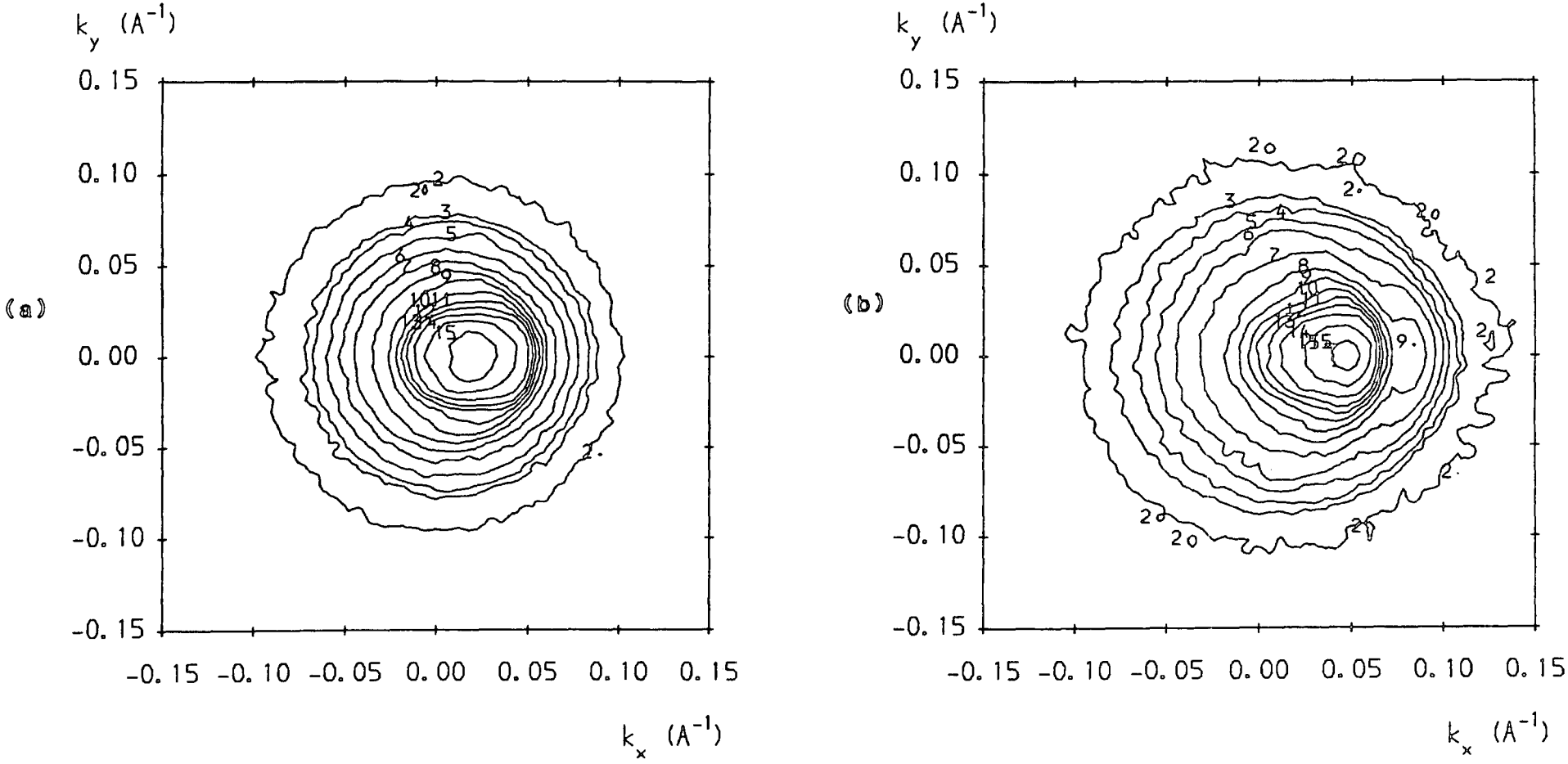

Fig. 9.27(a & b) Hole distributions in 2D k-space. Band 2. (a) $F_x = 1\text{kVcm}^{-1}$; (b) $F_x = 5\text{kVcm}^{-1}$. $T_L = 77\text{K}$; $\epsilon_{ac} = 1\text{meV}$.

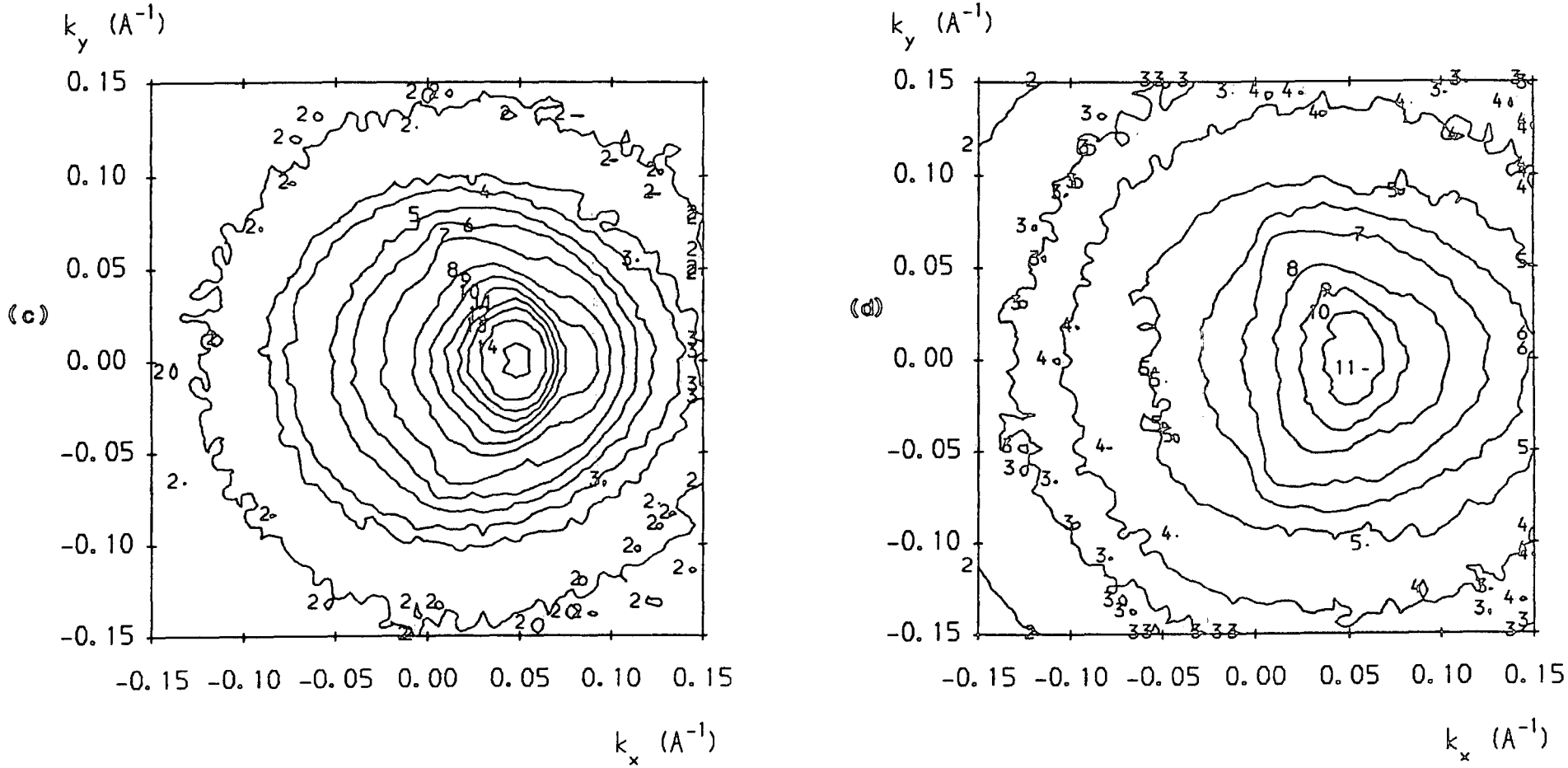

Fig. 9.27(c & d) Hole distributions in 2D k-space. Band 2. (c) $F_z = 10\text{kVcm}^{-1}$; (d) $F_z = 20\text{kVcm}^{-1}$. $T_L = 77\text{K}$; $\epsilon_{\text{ac}} = 1\text{meV}$.

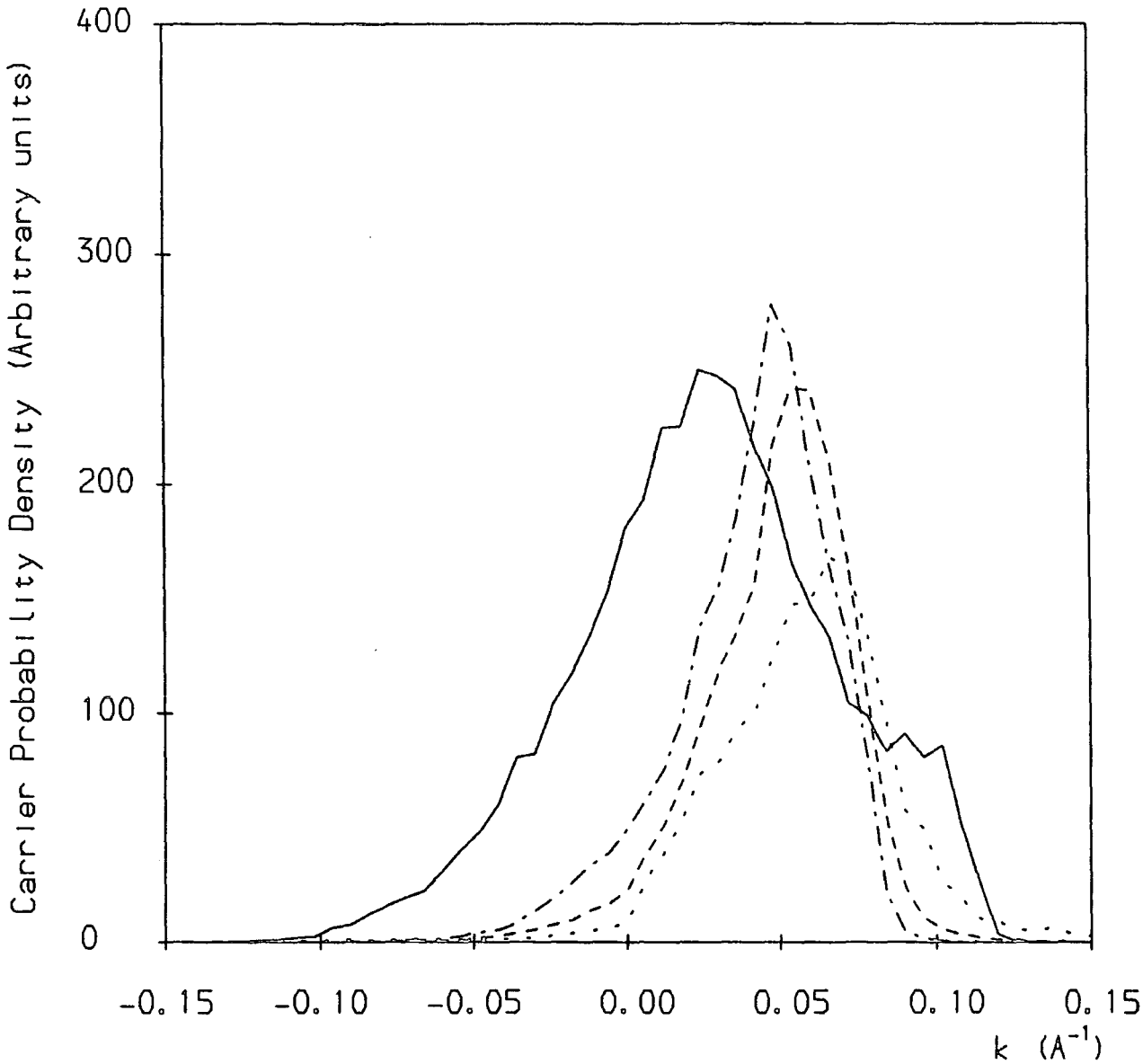

Fig. 9.28 Cross section of the hole distribution in band 1, viewed along a line in k-space parallel to k_x and passing through k = 0. F_x = 1kVcm^{-1} (—); 5kVcm^{-1} (· – ·); 10kVcm^{-1} (- - -), and 20kVcm^{-1} (···).

significant carrier population is evident at larger wavevectors.

The twin protrusions on the trailing edge of the band 1 distributions at large $|k_y|$ — particularly evident for $F = 20\text{kVcm}^{-1}$ — are a further consequence of the weakness of scattering just below the 1–1 optical emission threshold. These features indicate that, in directions perpendicular to the electric field, where the variation of $F(\mathbf{k})$ with k is not dominated by carrier drifting, the carrier population immediately below threshold is actually larger than that for lower values of k. This is a very weak form of the population inversion predicted by Fawcett *et al.* (1970), for electrons in bulk GaAs at states just below the intervalley scattering threshold.

Figs. 9.27(a–d) show that, for band 2, the distribution $F(\mathbf{k})$ retains a higher degree of circular symmetry at all values of electric field considered. At $F = 1\text{kVcm}^{-1}$, a fall-off in the distribution is visible at $k \approx 0.05\text{Å}^{-1}$, corresponding to the threshold for 2–1 optical phonon emission. However, since the POP 2–1em scattering rate is relatively small, states above the threshold are well populated even at low fields.

The difference between the response of the band 1 and band 2 k-space distributions to electric field heating is the key to understanding the field dependence of the band 1 and 2 fractional populations shown in Fig. 9.3. Table 6.3 and Fig. 7.6 show that the 1–2 optical emission threshold lies just beyond the pseudo-threshold for 1–1 optical emission. Now, we have established that, at low fields, very few carriers escape POP 1–1em scattering between the primary and pseudo-thresholds. Therefore, very few carriers are available for scattering into band 2. The 1–2 optical emission threshold is effectively 'hidden' by the region of strong 1–1 optical emission scattering which immediately precedes it in k-space.

Conversely, Figs. 9.27a and b indicate that 2–1 optical emission, although relatively weak, is effective even at low fields, as soon as carriers are accelerated up to the threshold at $k \approx 0.05\text{Å}^{-1}$. Hence a net *repopulation* of band 1, relative to band 2 occurs. This repopulation persists until the field is high enough to sweep carriers in band 1 across the 1–1 pseudo-threshold into states where 1–2 optical emission is allowed. Thus, in Fig. 9.3, repopulation of band 1 is observed for fields up to 3kVcm^{-1}, and the subsequent decrease in the band 1 population is very slow for fields below $10\text{–}12\text{kVcm}^{-1}$.

Finally, we have shown in Figs. 9.29 and 9.30, cross sections of $F(\mathbf{k})$ in bands 1 and 2, along the k_x axis, for the zero field case. Whilst the band 1 distribution has a peak at $\mathbf{k} = 0$, the plot for band 2 exhibits twin peaks, corresponding to diametrically opposite points on the circle of minimum energy (see Fig. 7.3a). Note that the occurrence of these peaks is not a density of states effect; rather, it arises due to the form of the energy dispersion in band 2, and the Maxwellian nature of

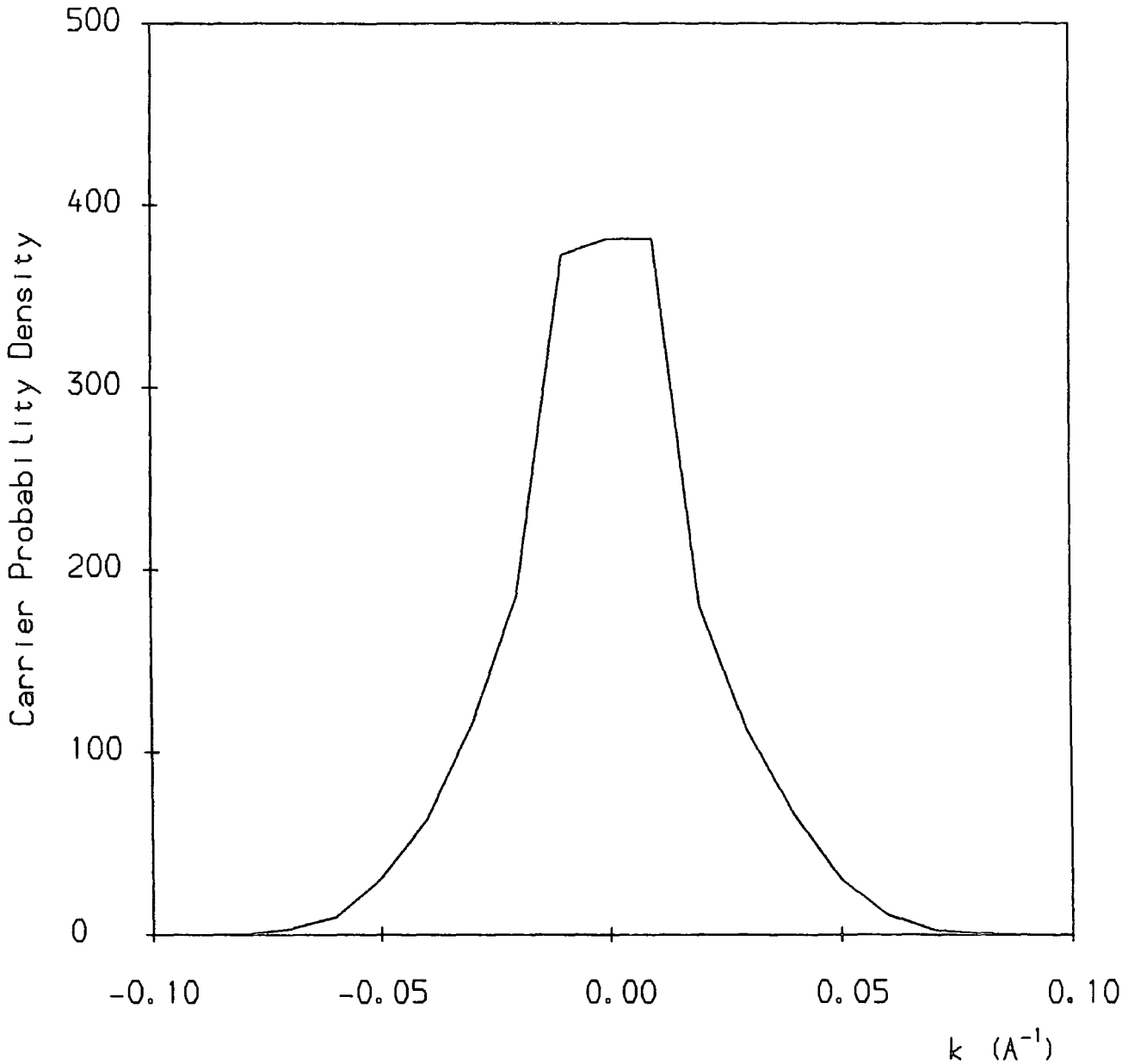

Fig. 9.29 Cross section of the zero field (thermal equilibrium) hole distribution in band 1, viewed along a line in k-space parallel to k_x and passing through $\mathbf{k} = 0$.

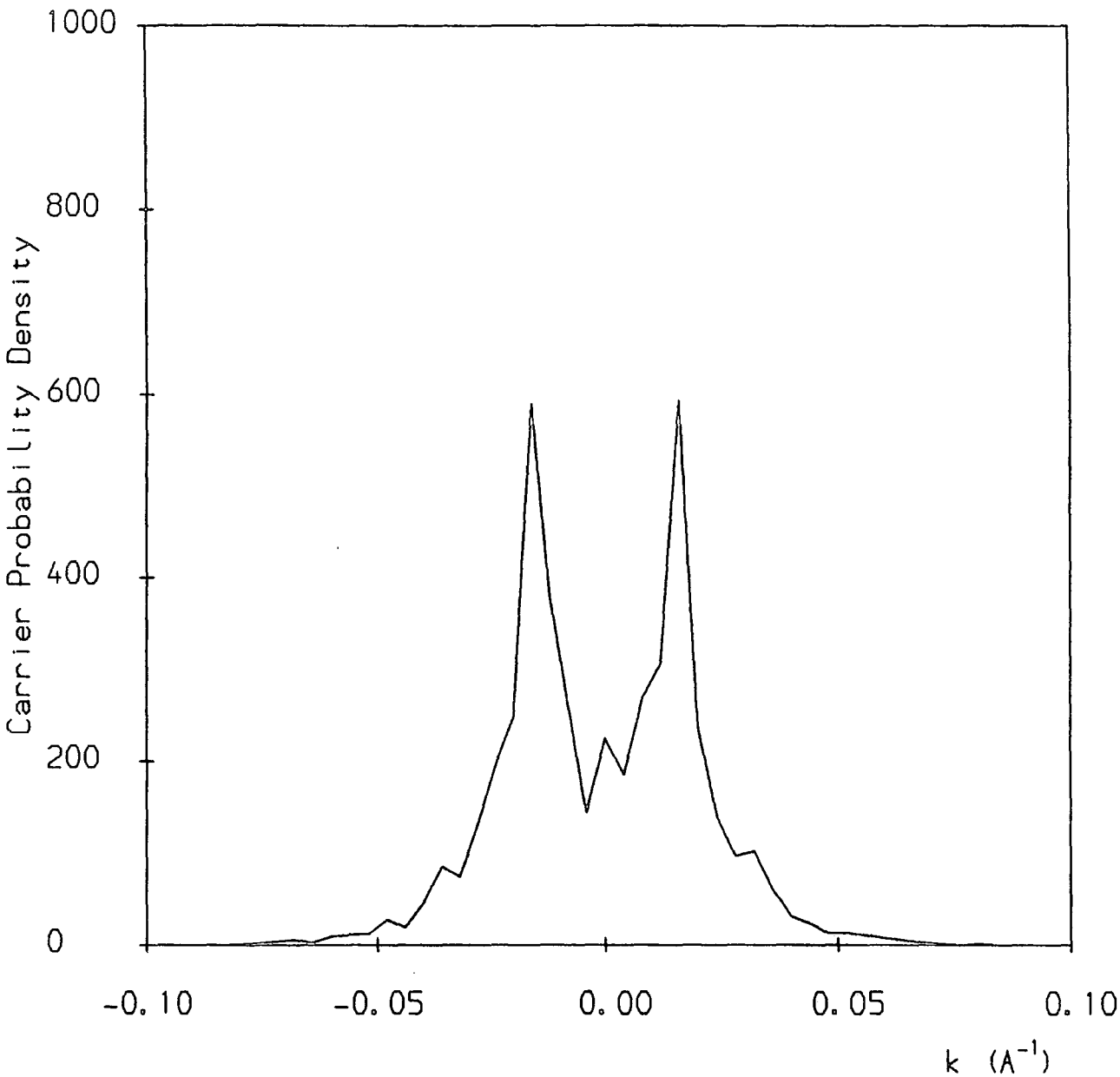

Fig. 9.30 Cross section of the zero field (thermal equilibrium) hole distribution in band 2, viewed along a line in k-space parallel to k_x and passing through $\mathbf{k} = 0$.

the energy distribution function established at zero field (Fig. 9.19).

CHAPTER 10
COOLING OF QUANTUM CONFINED HOLES

10A INTRODUCTION

In Chapter 9 we used our Monte Carlo simulations to examine some of the effects associated with the heating of holes in a GaAs quantum well by an in-plane electric field. In this Chapter we will turn our attention to the problem of hole cooling in a quantum well, and will investigate the time dependent relaxation of a range of non-equilibrium hole distributions. There has been much recent work on carrier cooling in low dimensional semiconductor systems, but in only very few cases have the quantum confined holes been considered. Whilst the cooling of electrons in quantum wells is commonly modelled as a single subband process, hole cooling is clearly a multisubband phenomenon for all but the narrowest of well widths. Our four band model of the GaAs/AlAs quantum well valence band system will allow us to investigate the multisubband aspects of hole cooling. In particular, we may seek answers to several general questions:

(i) How does the energy loss rate of hot holes depend on the number of subbands involved in cooling?

(ii) How does the rate of depopulation of an upper subband depend on the number of subbands beneath it?

Some experimental workers have recently been able to probe the intersubband transitions of electrons in quantum wells. For wide (215Å) GaAs/AlGaAs wells, Oberli *et al.* (1987, 1988) deduced a lifetime in the order of several hundred picoseconds for electrons in the second subband. This long lifetime is associated with the restriction to interband scattering by acoustic phonons only, because the separation of the first and second subbands is less than the optical phonon energy. The same authors also reported much faster scattering in narrower (116Å) wells, where the separation of the first and second subbands exceeded the optical phonon energy. Seilmeier *et al.* (1987) obtained lifetimes of the order of 10ps for electrons in the second subband of narrow (47–51Å) quantum wells. Following on from this work, we may use our four band model of the quantum well valence band system to answer the additional questions, for the case of quantum confined holes:

(iii) is there any evidence of the 'trapping' of carriers in a subband energy minimum,

(iv) and if so, under what conditions does this occur?

Furthermore, we may examine the influence of the peculiarities of the quantum confined valence bandstructure on hole cooling; addressing questions such as:

(v) How do the modifications of the phonon scattering matrix elements caused by band mixing affect hole cooling?

(vi) What is the influence of the unusual features related to band dispersion; *e.g.*, the presence of off-zone-centre band minima and the associated peaks in the density of states?

In order to investigate these points we have carried out time-dependent simulations using three different types of initial conditions:

(a) A 'δ-function' distribution. That is, all carriers occupy states of the same energy in the same band at $t = 0$. The carriers are randomly distributed around a circle of constant energy in 2D k-space.

(*b*) A single-subband heated Maxwellian distribution. All carriers occupy the same band, but have a Maxwellian distribution of energies characterised by a temperature T_c ($> T_L$) at $t = 0$.

(c) A multisubband heated Maxwellian distribution. At $t=0$ carriers are spread over the whole four band system, but have a Maxwellian distribution of energies characterised by a temperature T_c.

Case (a) can be regarded as an idealised model of the carrier distribution resulting from the photoexcitation of free carriers by a suitably narrow-beamwidth laser. In the limit of weak carrier-carrier scattering the distribution will remain essentially monoenergetic until cooling proceeds via phonon scattering.

In a practical situation, carrier populations may be generated at any energy point on the quantum well bandstructure, provided that the laser wavelength can be appropriately tuned. However, for most incident wavelengths, because of the multiplicity of conduction and valence subbands in the well, a number of photoexcited transitions will be possible; thus free carrier populations will be simultaneously generated at several distinct points on the bandstructure. Since the purpose of the work presented in this chapter is the attainment of a general understanding of quantum confined hole cooling, rather than the modelling of a specific set of experimental conditions, we have carried out simulations with just one monoenergetic photoexcited population considered in each case. However, these simulations can still be used to give information on more general forms of the photoexcited distribution, as discussed below.

Case (b) can be regarded as a model of the carrier distribution resulting from photoexcitation in the presence of strong intraband carrier-carrier scattering. This scattering is assumed to occur sufficiently quickly after photoexcitation that the carriers are thermalised, within a given band, after a time considerably shorter than the carrier lifetime for phonon scattering.

Finally, case (c) can be regarded as a model of a photoexcited carrier distribution in the presence of strong intra- and inter-band carrier-carrier scattering; such that the photoexcited population forms a thermalised distribution across the

whole four band system, at an elevated temperature T_c, well within the phonon scattering lifetime.

Regarding case (a), we may also note that the carrier distribution $f(\epsilon, \epsilon', t)$ at any time t, resulting from an initial δ-function distribution at an energy ϵ' is, in a sense, a Greens' function for the carrier cooling problem. That is, $f(\epsilon, \epsilon', t)$ gives, at time t, the response of the system in terms of the energy state occupancy, to an influence at a single energy ϵ'. Thus, it should, in principle, be possible to obtain the time dependent distribution $f(\epsilon, t)$ corresponding to an arbitrary initial distribution $g(\epsilon')$, by evaluating the integral

$$f(\epsilon, t) = \int g(\epsilon') f(\epsilon, \epsilon', t)\, d\epsilon'. \tag{10.1}$$

This theorem is only true in the absence of carrier-carrier scattering, since this process would destroy the superposition property of the distributions $f(\epsilon, \epsilon', t)$. We will not make any explicit use of this principle: however, we will draw on it implicitly, insofar as we will regard the cooling of the δ-function distributions as representative of the cooling of that portion of any arbitrary initial distribution within which a large carrier population is concentrated around the corresponding value of energy.

In all three cases, the initial distributions in the Monte Carlo simulations represent *excess* carrier populations which, in practice, will be superposed on some background carrier density. We will assume that this backgound population is small, and that its effect on carrier cooling can be neglected. Simulations using initial distributions of the types described at (a), (b) and (c) will be labelled by 'δ' (δ-function), 'sM' (single band Maxwellian), and 'mM' (multiband Maxwellian) respectively. Goodnick and Lugli (1988), using a simple effective mass model of quantum confined heavy holes in a Monte Carlo simulation, have suggested that thermalisation of a photoexcited population via (intraband) carrier-carrier scattering occurs within 50fs (for an injected hole density $p_{\text{inj}} \approx 10^{16}\text{cm}^{-3}$). In a previous paper (Lugli and Goodnick 1987), the same authors suggest that interband electron-electron scattering in a GaAs quantum well is very weak (for n_{inj} typically $5 \times 10^{17}\text{cm}^{-3}$). If the latter result is also true for the quantum confined holes, then the simulations using initial distributions of type (b) above may give the most representative picture of 2D hole cooling.

10B TRANSIENT HOLE COOLING SIMULATIONS

In this section we will present results from the δ-, sM- and mM-simulations of quantum confined hole cooling described above. We have carried out δ-simulations using initial monoenergetic distributions located at a variety of significant energy points on the quantum confined valence bandstructure, including the zone centre energy minimum in band 3, and the off-zone-centre minima in bands 2 and 4. Fig. 10.1 shows the position of the initial carrier energies for the various cases on the band dispersion curves. For the sM- and mM-simulations we have taken, for the most part, initial distributions with average energies corresponding to those in the δ cases, to facilitate a direct comparison of the carrier cooling rates. Table 10.1 gives a summary of the exact conditions used in each simulation, for all three categories δ, sM, and mM.

10B.1: Prototype Hole Cooling Simulation

Simulation $\delta 1$: $\epsilon(t{=}0) = 0$, *band 4.*

In this simulation, the initial carrier distribution is monoenergetic at the band 4 minimum. We will use this case as a first example of the δ-category of simulations, to illustrate some of the basic characteristics of hole cooling in the quantum confined system. The example relates well to the photoexcitation picture described in the previous section. For incident light of the appropriate wavelength, a large population of holes will be created at the band 4 minimum, by direct electron transitions to the first conduction subband. Transitions from the lower index valence bands will also occur, but the hole populations thus created will be much smaller than that at the band 4 minimum, because of the very large density of states in that region.

We have carried out simulations using acoustic phonon energies ϵ_{ac} of 1 and 2meV. Figs. 10.2 and 10.3 show the time dependence of the fractional populations $\langle \overline{n} \rangle$ and mean energies $\langle \epsilon \rangle$ in each band, for ϵ_{ac} = 1meV, and Figs. 10.4 and 10.5 show the same parameters for the ϵ_{ac} = 2meV case.

Fig. 10.2 shows that the majority of the carriers are scattered out of band 4 within the first picosecond after excitation, and that depletion of the band is virtually complete after 2ps. Bands 1 and 2 show significant repopulation on the 1ps timescale. The dominant scattering processes during this period are POP 4–1 and 4–2em, and the larger population of band 1 at early times reflects the higher 4–1 scattering rate from states in the band 4 minimum. Band 3 repopulates only very slightly, since the threshold for 4–3 optical emission is some 5meV above the band 4 minimum.

At $t \approx$ 2ps we see on Fig. 10.2 that the repopulation of bands 1 and 2 virtually ceases. Eventually, a very slow increase in the band 1 population is observed,

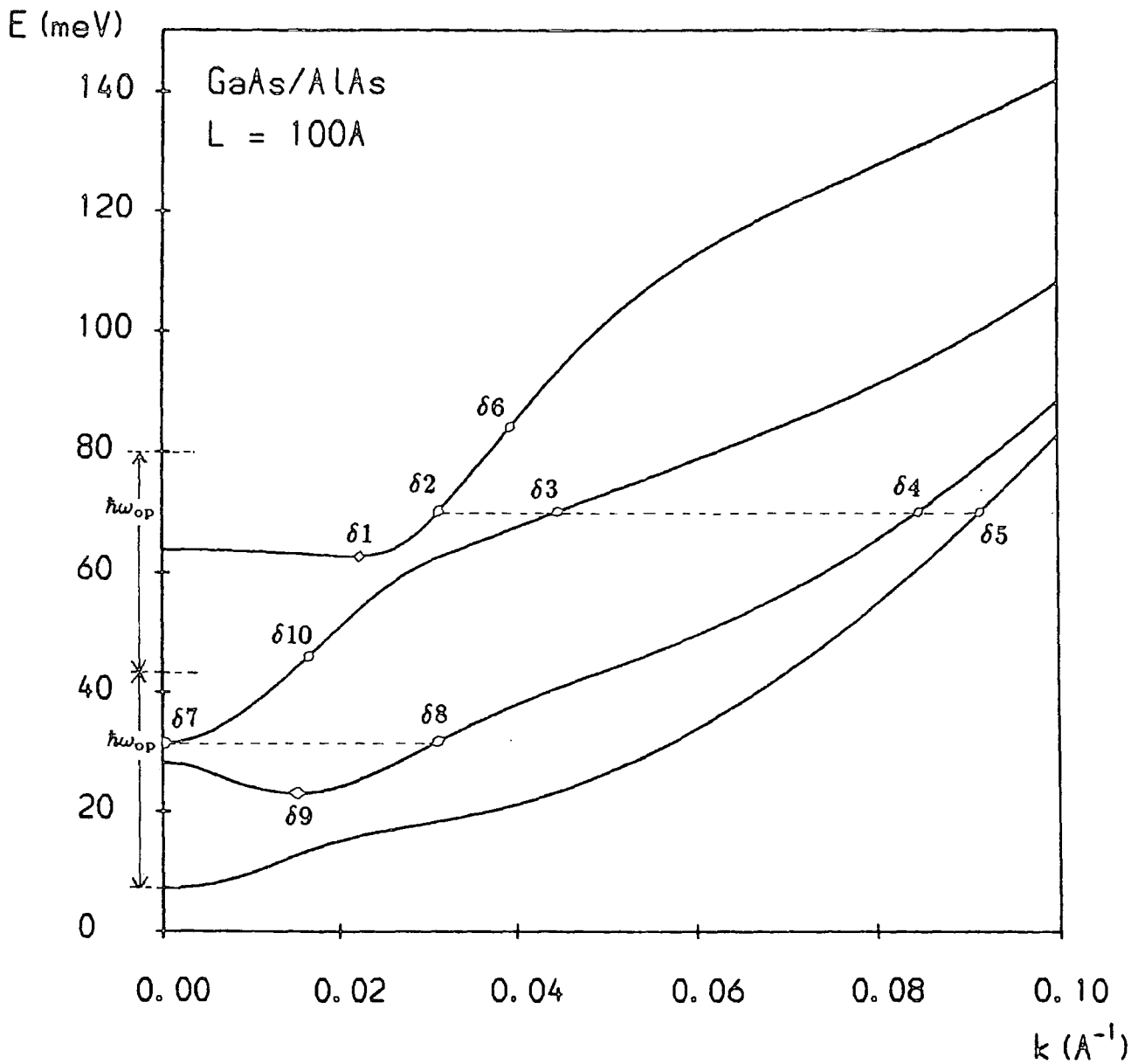

Fig 10.1 In-plane energy dispersion of bands 1...4, showing the locations of the initial monoenergetic carrier distributions used in simulations $\delta 1 \ldots 10$, and the positions of the single and double optical phonon emission thresholds relative to the band 1 minimum.

Simulation	Initial Band (i)	$\epsilon_i(t{=}0)$ meV	$\epsilon_{av}(t{=}0)$ meV relative to band 1	Comments
$\delta 1$	4	0.00	55.55	Band 4 minimum
$\delta 2$	4	7.20	62.75	POP 4–3em threshold + ϵ_{ac}
$\delta 3$	3	38.41	62.75	
$\delta 4$	2	46.85	62.75	
$\delta 5$	1	62.75	62.75	
$\delta 6$	4	21.25	76.80	$2\hbar\omega_{op} + 2\epsilon_{ac}$
$\delta 7$	3	0.00	24.34	Band 3 minimum
$\delta 8$	2	8.44	24.34	
$\delta 9$	2	0.00	15.90	Band 2 minimum
$\delta 10$	3	14.10	38.44	$\hbar\omega_{op} + \epsilon_{ac}$

Table 10.1a: Key to δ-Simulations

Simulation	Initial Band (i)	$T_c(t{=}0)$ K	$\epsilon_i(t{=}0)$ meV	$\epsilon_{av}(t{=}0)$ meV relative to band 1	Comments
sM1	4	132	7.20	62.75	ϵ_{av} as for $\delta 2$–5
sM2	4	222	21.25	76.80	ϵ_{av} as for $\delta 6$
sM3	3	56	6.10	30.44	
mM1		475		62.75	ϵ_{av} as for $\delta 2$–5
mM2		173		24.34	ϵ_{av} as for $\delta 7$

Table 10.1b: Key to sM- and mM-Simulations

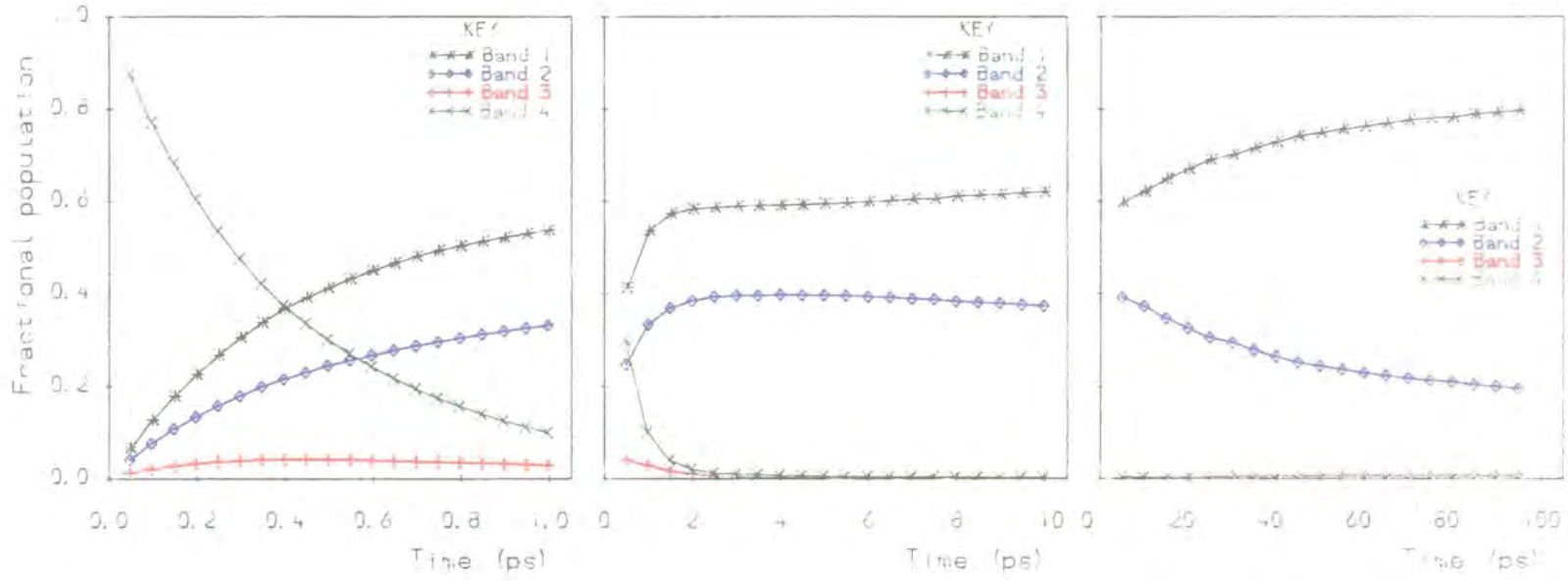

Fig 10.2 Simulation $\delta 1$. Time dependence of the fractional populations in bands 1–4. $T_L = 77\text{K}$; $\epsilon_{ac} = 1\text{meV}$.

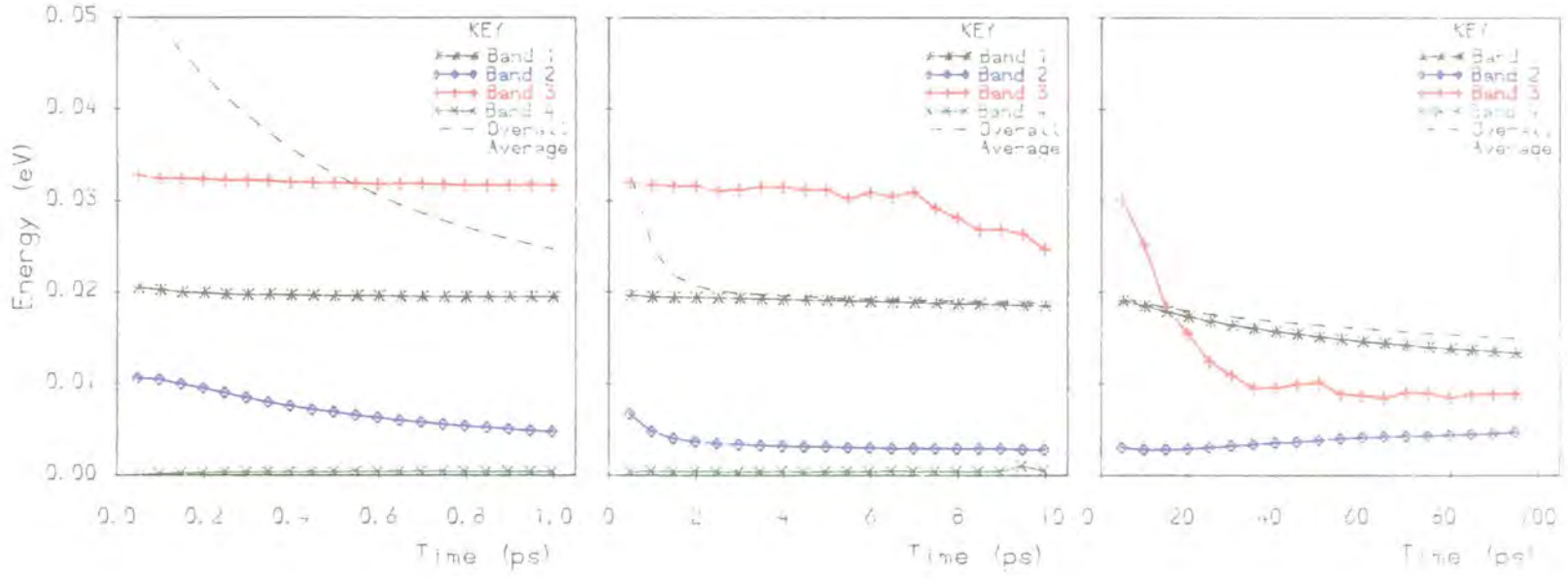

Fig 10.3 Simulation $\delta 1$. Time dependence of the mean hole energies in bands 1–4, and the overall average energy, relative to the band 1 minimum. $T_L = 77\text{K}$; $\epsilon_{\text{ac}} = 1\text{meV}$.

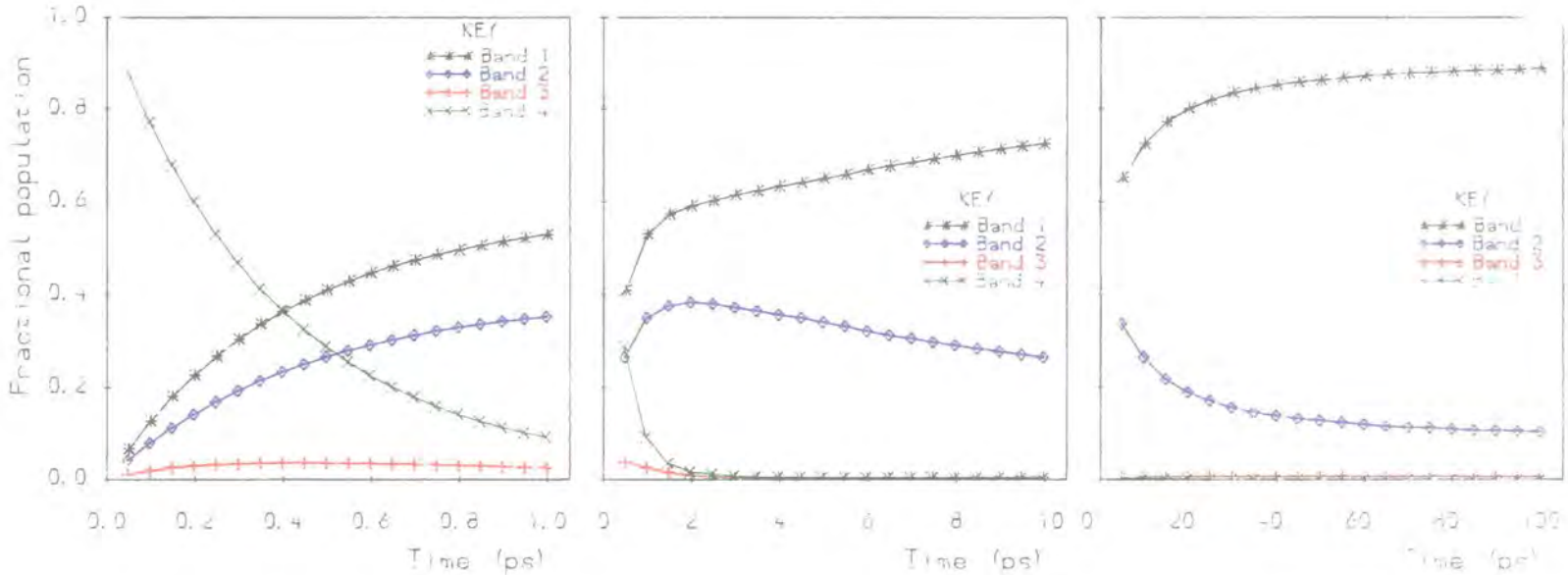

Fig 10.4 Simulation $\delta 1$. Time dependence of the fractional populations in bands 1–4. $T_L = 77\text{K}$; $\epsilon_{\text{ac}} = 2\text{meV}$.

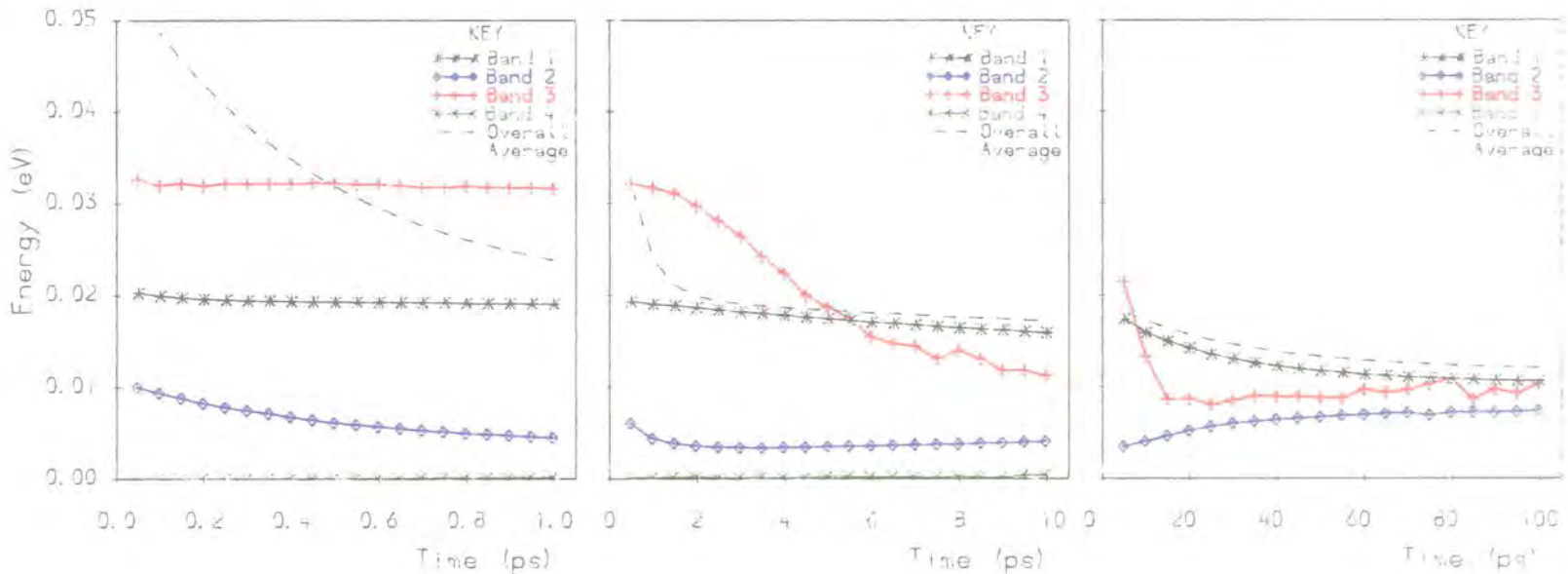

Fig 10.5 Simulation $\delta 1$. Time dependence of the mean energies in bands 1–4, and the overall average energy. $T_L = 77\text{K}$; $\epsilon_{\text{ac}} = 2\text{meV}$.

with a corresponding decrease in the band 2 population. These trends persist through to $t = 100$ps and beyond. Fig. 10.4 shows that, in the $\epsilon_{ac} = 2$meV case, the depopulation of band 2 commences immediately after the maximum in $\langle \overline{n}_2 \rangle$ at $t = 2$ps. The steady state values of $\langle \overline{n}_1 \rangle = 0.87$, $\langle \overline{n}_2 \rangle = 0.13$ at zero field (as obtained from our single particle simulation) are almost attained by $t = 100$ps.

The marked change in $\partial \langle \overline{n} \rangle / \partial t$ at $t = 2$ps in both bands 1 and 2 indicates a transition from 4–1 and 4–2 (POP) scattering to 2–1 scattering. The latter must procede via acoustic phonon modes, since carriers which have scattered from band 4 by the emission of an optical phonon will now lie below the threshold for optical scattering into the band 1 minimum. The slow rate of change of population in bands 1 and 2 exhibited in Figs. 10.2 and 10.4 for all $t > 2$ps is consistent with the activity of interband acoustic modes, which have relatively low scattering rates. Thus we have, already, evidence for the formation of a bottleneck of carriers at a band minimum. Since the threshold for 2–1 optical phonon emission is some 20meV above the band 2 minimum (Table 6.3), carriers scattered from band 4 into low energy states in band 2 cannot escape sufficiently quickly, via the weak acoustic modes, to prevent a significant overpopulation of the band relative to the thermal equilibrium situation.

It is interesting to find that $\partial \langle \overline{n} \rangle / \partial t$ in bands 1 and 2 is so clearly dependent on the value of ϵ_{ac} used in the simulation. There are two reasons for this. Firstly, for $\epsilon_{ac} = 2$meV the probability of carriers returning to band 2 via AC 1–2abs is reduced, and the strength of the competing AC 1–1em process is increased. Secondly, with the higher acoustic phonon energy, that proportion of the carriers scattered out of band 2 by AC 2–1em which still have sufficient energy to be scattered back into the band by AC 1–2em is reduced. In reality, with the acoustic phonon energy continuously variable, the true rates of change of population in bands 1 and 2 are likely to lie somewhere between those depicted in Figs. 10.2 and 10.4. For all the following sets of simulations we have taken $\epsilon_{ac} = 2$meV, which more clearly demonstrates the rôle of acoustic scattering in hole cooling, although we accept that the rates of de-/re-population and the energy loss rates may, in some circumstances, be overestimates of the true values.

Fig. 10.3 shows that after around 5ps the band 3 mean energy begins to destabilise; falling from the hitherto constant value of $\epsilon \approx 32$meV (consistent with scattering of carriers from band 4 by acoustic phonon absorption). This relatively large drop in mean energy is indicative of scattering of carriers to low energy states in band 3 by optical phonon emission. The time delay of 5ps endured before optical scattering takes effect represents the time taken for carriers to migrate up to the optical emission threshold by successive absorption of acoustic phonons. For

ϵ_{ac} = 2meV, Fig. 10.5 shows that this time delay is reduced to around 1ps, in which case a significant proportion of the population formed in the band 3 minimum will have been scattered directly from band 4. In both Figs. 10.3 and 10.5, the overall average energy becomes asymptotic to the band 1 mean energy after around 2ps. This indicates that within t=2ps almost all of the carriers have emitted one optical phonon, giving an average energy for the system close to $\epsilon_{av}(t{=}0) - \hbar\omega_{op}$.

The energy loss rate in an ensemble simulation may be obtained in a similar manner to that described in Section 9D for the steady state case. A record can be obtained, from the simulation, of the number of scattering events of each type occurring during each timestep. If this number is $N(t)$ for a particular process, then the energy loss rate per carrier due to this process at a time $t = t'$ is given by

$$\left\langle \frac{\partial \epsilon}{\partial t} \right\rangle_{t=t'} = \frac{\hbar\omega N(t')}{N_{ens}\, t_{step}} \tag{10.1}$$

where N_{ens} is the ensemble size and t_{step} is the timestep duration. A practical complication arises when estimating the energy loss rates in an ensemble simulation; namely that, for short timesteps, the number of scattering events via certain modes may be so low that the rates obtained from the above equation are subject to large statistical fluctuations. It is for this reason that we have used such a large ensemble size (N_{ens} = 50000) in these simulations; reasonably accurate results for the basic time dependent Monte Carlo estimators $\langle \epsilon(t) \rangle$ and $\langle \overline{n}(t) \rangle$ can be obtained using an ensemble of no more than 20000 particles.

Fig. 10.6 shows the average energy loss rate of the carriers as a function of time, resolved into components for intra- and inter-band scattering via optical and acoustic modes. Only the ϵ_{ac} = 2meV case is shown. The t=0 energy loss rate is approximately 6×10^{-2}eVps^{-1} which corresponds to the steady state rate for $F \approx 8$kVcm^{-1} ($T_c \approx 190$K). As discussed above, energy loss in the first 2–3ps is dominated by interband optical phonon scattering. However, at $t \approx 3$ps a crossover occurs, with energy loss dominated by intraband acoustic scattering thereafter. This acoustic scattering is principally AC 1–1 em (with some PZ 1–1em), as the large population formed in band 1 shifts towards the band minimum. The acoustic energy loss rate here has a maximum value of approximately 2×10^{-4}eVps^{-1}; around twice that observed in the steady state simulations. This confirms that, after the initial phase of carrier scattering out of band 4, the carrier distribution, though far from equilibrium, is concentrated at energies below the lowest (1–1) optical emission threshold. The steep fall-off in the optical energy loss rates over the 2–4ps timescale indicates that, whatever the true values of the acoustic energy loss rates (see Section 9D), these will still form the dominant contribution to the total rate at all later times.

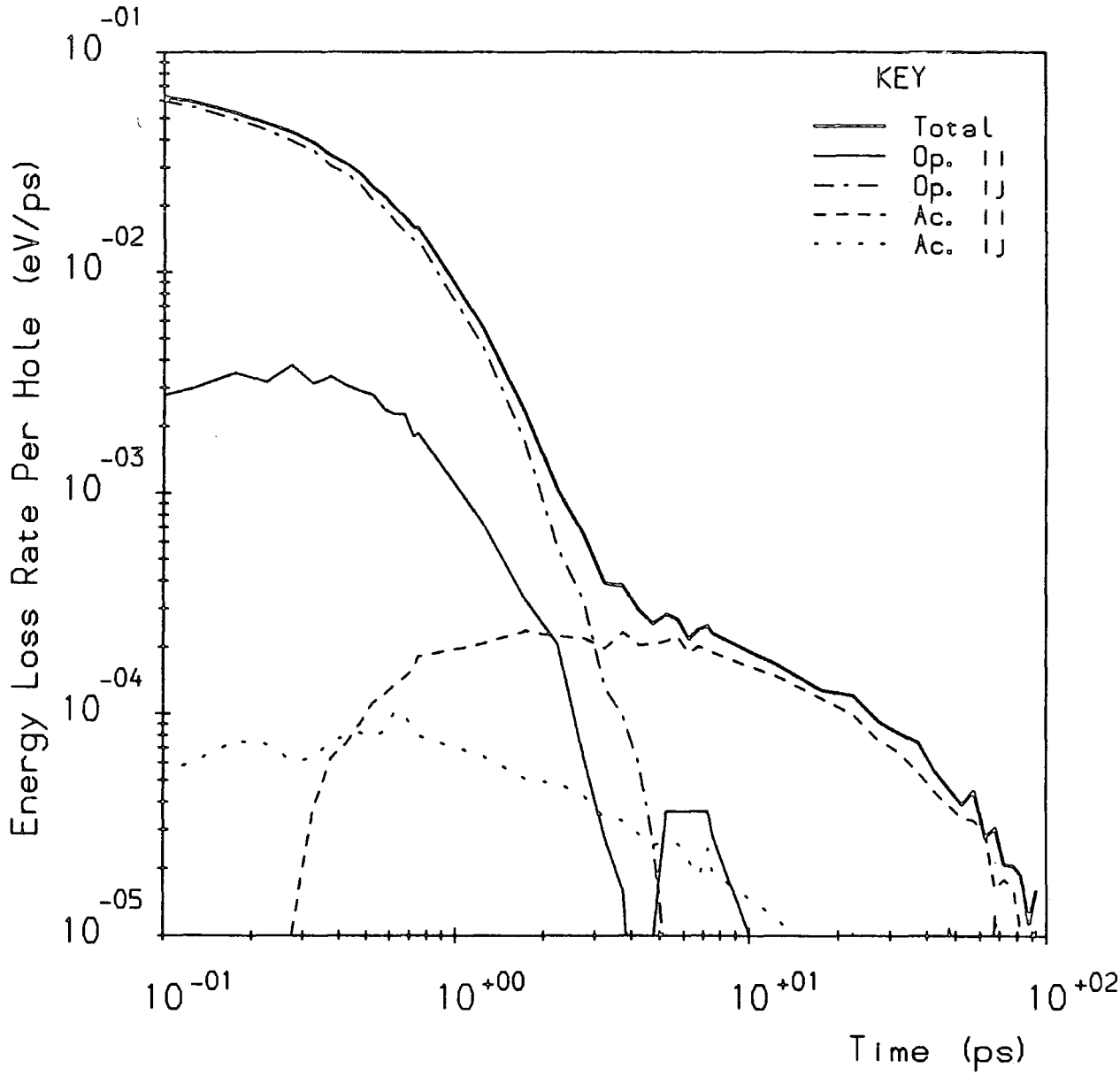

Fig 10.6 Simulation $\delta 1$. Time dependence of the total hole energy loss rate and the component rates due to intraband (ii) and interband (ij) scattering via optical and acoustic modes. $T_L = 77\text{K}$; $\epsilon_{ac} = 2\text{meV}$.

At $t = 100$ps the total energy loss rate is very low, indicating that thermal equilibrium has almost been attained. The lack of any contribution to the energy loss rate from the intraband acoustic modes at early times ($t < 0.3$ps) is a consequence of using an initial distribution in which all the carriers occupy states at the band minimum. Initially, intraband acoustic scattering can only proceed via phonon *absorption*; hence the corresponding energy loss rate is actually negative.

10B.2: Dependence of Hole Cooling on the Number of Subbands present

In this section we will investigate the changes in hole cooling in the quantum well valence band system introduced by varying the number of subbands involved in the cooling process from four down to one. To this end, we have used four sets of simulations, which we will label $\delta 2$–5. These simulations all have a monoenergetic carrier distribution at $t = 0$, with carriers having the *same* energy relative to the band 1 minimum in all four cases, but located in bands 4,3,2 and 1 for $\delta 2$–5 respectively (see Fig. 10.1 and Table 10.1 for details).

Simulation $\delta 2$: $\epsilon(t{=}0) = 7.2\text{meV}$, *band 4;* $\epsilon_{\text{av}} = 62.75\text{meV}$.

The initial energy for this simulation was chosen so that the carrier population in band 4 was located above the threshold for 4–3 scattering via optical phonon emission. The consequent opportunity for strong scattering of carriers into band 3 ensures that cooling in the $\delta 2$ simulations occurs via all four subbands. We will firstly ascertain how this modifies the cooling process with respect to the $\delta 1$ case.

Fig. 10.7 shows $\langle \overline{n}(t) \rangle$, and Fig. 10.8, $\langle \epsilon(t) \rangle$ for the four bands. The principal difference between the $\delta 1$ and $\delta 2$ simulations is that, in the latter case, band 3 aquires a very large population within the first picosecond after photoexcitation, and the populations of bands 1 and 2 during this period are correspondingly reduced. The size of the band 3 population at $t = 1\text{ps}$ reflects the strength of POP 4–3em scattering which, being an inter-anticrossing-band process, has a particularly large matrix element (see section 6C.1). We see on Fig. 10.8 that the mean energy in band 3 is near zero even at the earliest times shown, in contrast to its response in the $\delta 1$ case. This again indicates the rapidity of 4–3 optical scattering. Conversely, the extent of 4–2 optical scattering is considerably reduced. The large value of $\langle \epsilon_2 \rangle$ near $t{=}0$ indicates that most of the carriers in the band occupy high energy states, having been scattered from band 4 via acoustic modes. The overall average energy falls gradually during the first picosecond as the number of carriers which have entered the low energy states via optical scattering increases.

Now, carriers near the band 3 minimum cannot emit an optical phonon: thus, the rate of decay of the large band 3 population after $t = 1\text{ps}$ is expected to be slow. This can be seen on the 10ps timescale of Fig. 10.7. Furthermore, band 2 also experiences overpopulation, but the effect occurs on a much longer timescale than in the $\delta 1$ simulations. We may conclude that band 3, which initially diverts carriers from band 2, subsequently feeds this band, giving rise to the successive occurrence of carrier bottlenecks in the two bands. As a consequence, the fractional populations of the bands have still not converged to their thermal equilibrium values by $t = 100\text{ps}$.

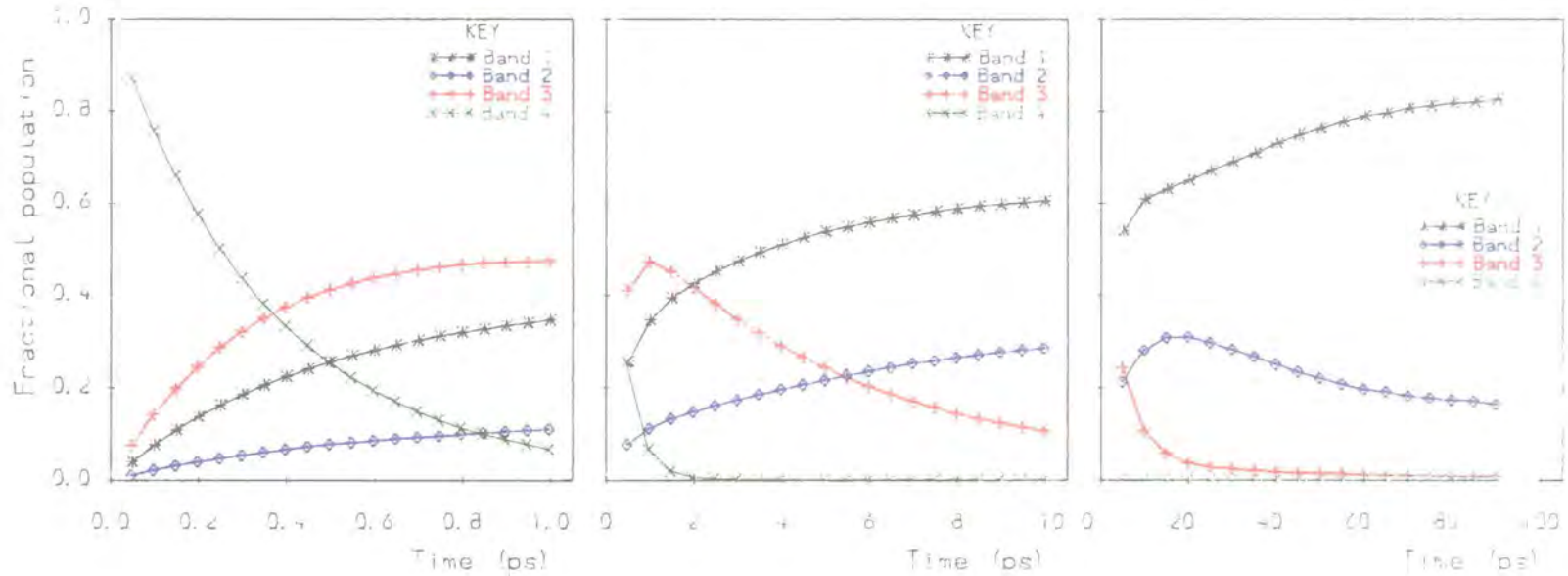

Fig 10.7 Simulation $\delta 2$. Time dependence of the fractional populations in bands 1–4. $T_L = 77\text{K}$; $\epsilon_{ac} = 2\text{meV}$.

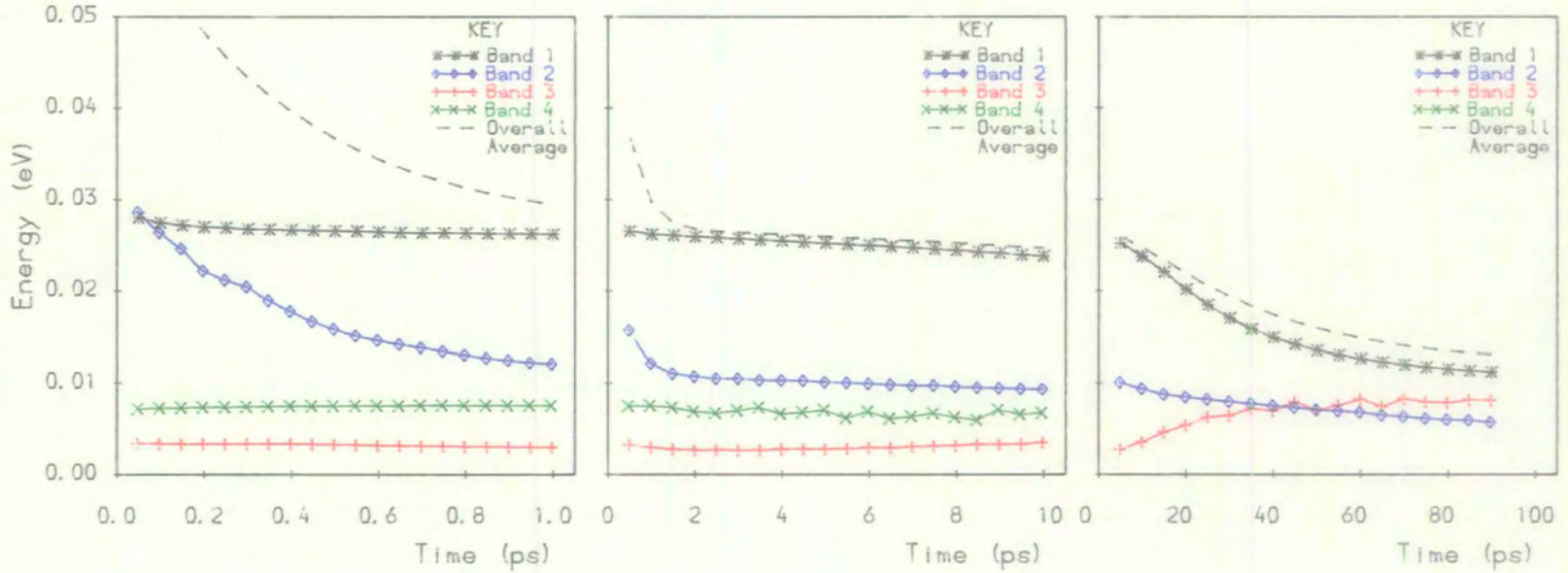

Fig 10.8 Simulation $\delta 2$. Time dependence of the mean energies in bands 1–4, and the overall average energy. $T_L = 77\text{K}$; $\epsilon_{\text{ac}} = 2\text{meV}$.

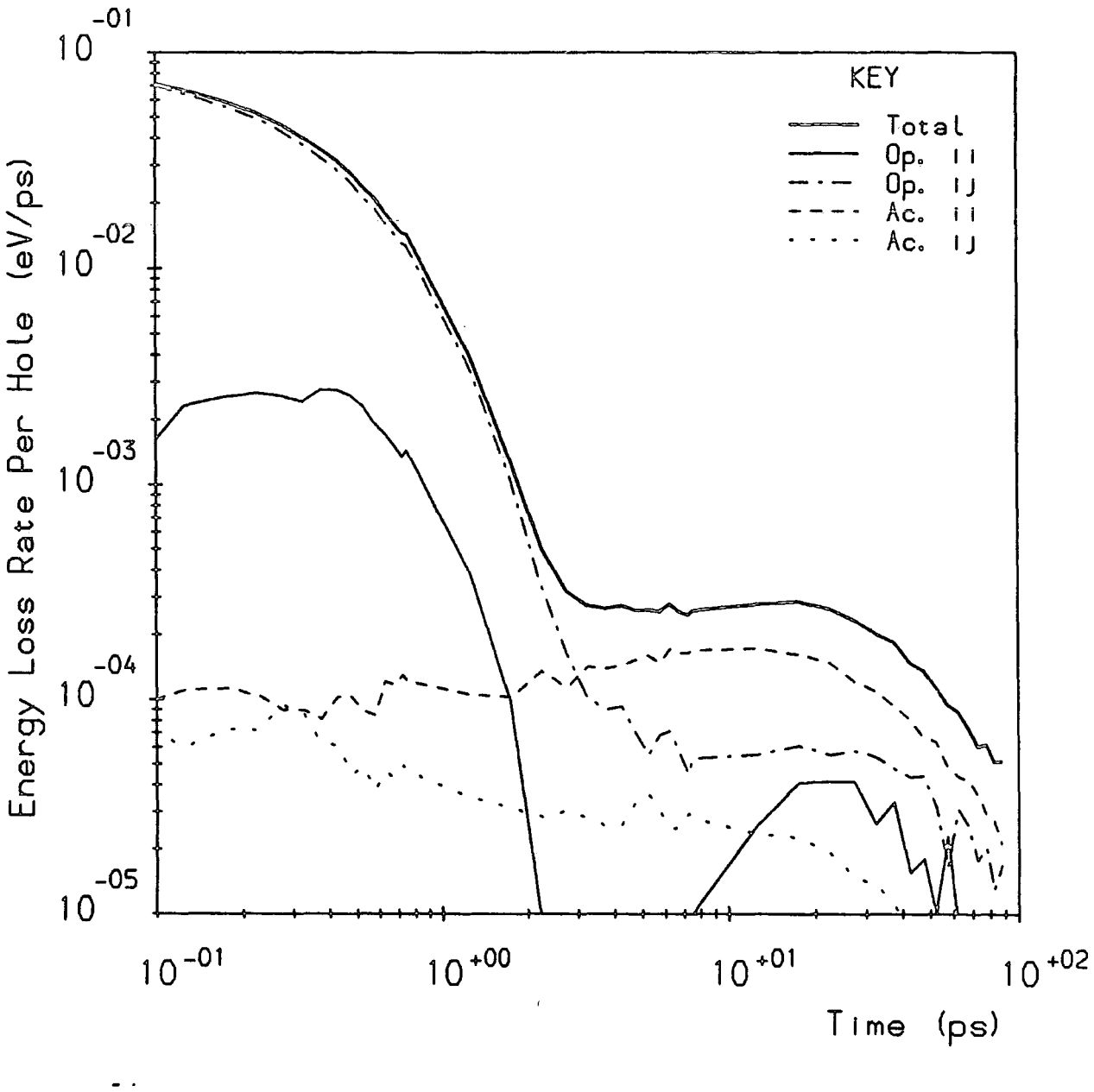

Fig 10.9 Simulation $\delta 2$. Time dependence of the hole energy loss rates. $T_L = 77\text{K}$; $\epsilon_{ac} = 2\text{meV}$.

Fig. 10.9 shows the energy loss rate plot for the $\delta 2$ simulations. It can be seen that the total rate is larger than that for the $\delta 1$ case at early times — due to the strong POP 4–3em scattering — however the rate falls off more quickly. The disappearance of the intraband optical contribution to the energy loss rate between $t = 2$ and 8ps is due to net phonon absorption in band 3 during this period. With reference to Fig. 6.16 we can see that the 3–1 and 3–2 acoustic processes are very weak; hence depopulation of the band 3 minimum must also involve POP 3–3abs. Most of the carriers scattered in this way are subsequently scattered into band 1, where their excess energy is dissipated via POP 1–1em. We may conclude that, after the initial period of fast optical phonon emission, energy loss is delayed due to the accumulation of a large population of carriers in the band 3 minimum where the scattering rate is low. Fig. 10.9 shows that energy dissipation is still measurable at $t = 100$ps, again indicating that thermal equilibrium has not yet been attained.

Simulations $\delta 3$–5: $\epsilon(t{=}0) = 38.41$meV, *band 3;* $\epsilon = 46.85$meV, *band 2;* $\epsilon = 62.75$meV, *band 1;* $\epsilon_{av} = 62.75$meV *throughout.*

In Figs. 10.10–12 we have shown the time dependence of the fractional populations and, in Figs. 10.13–15, the energy loss rate plots for the three cases $\delta 3$–5. Also, in Table 10.2 we have given the values of overall average energy at various times for all four cases $\delta 2$–5. Referring to this table, in conjunction with the energy loss plots, it is clear that in the first 2ps of the simulations when optical scattering is dominant, carrier cooling is fastest for $\delta 5$, then $\delta 4$, $\delta 2$ and lastly, $\delta 3$. However at $t = 10$ps, well within the acoustic dominated cooling regime, whilst carrier cooling in the $\delta 5$ case is still the fastest, the extent of cooling is now very similar for $\delta 2$ and $\delta 3$, with the $\delta 4$ simulation now exhibiting the slowest cooling. This general trend remains unchanged after 100ps.

The period of very fast cooling at early times in the $\delta 5$ case is due to strong POP 1–1em. The $t = 0.1$ps energy loss rate is in excess of 10^{-1}eVps^{-1}, corresponding to the power dissipation of a carrier distribution heated to $T_c \geq 400$K in the steady state (see Fig. 9.24). A high initial cooling rate is also obtained in the $\delta 4$ simulation due to strong intraband (2–2) POP scattering. In contrast, energy loss in the $\delta 3$ case is initially slow, because both intra- and inter-band optical scattering in band 3 are relatively weak. Comparing the four energy loss rate plots (Figs. 10.6 and 10.13–15), we can see that the transition from acoustic to optical phonon dominated cooling occurs after the shortest time (only ≈ 0.7ps) in the $\delta 5$ simulation. However, the intraband acoustic energy loss rate is large (around 2×10^{-4}eVps^{-1} — see comment in previous section) throughout the first 10ps of the simulation, due to the strong AC and PZ 1–1em scattering of the large

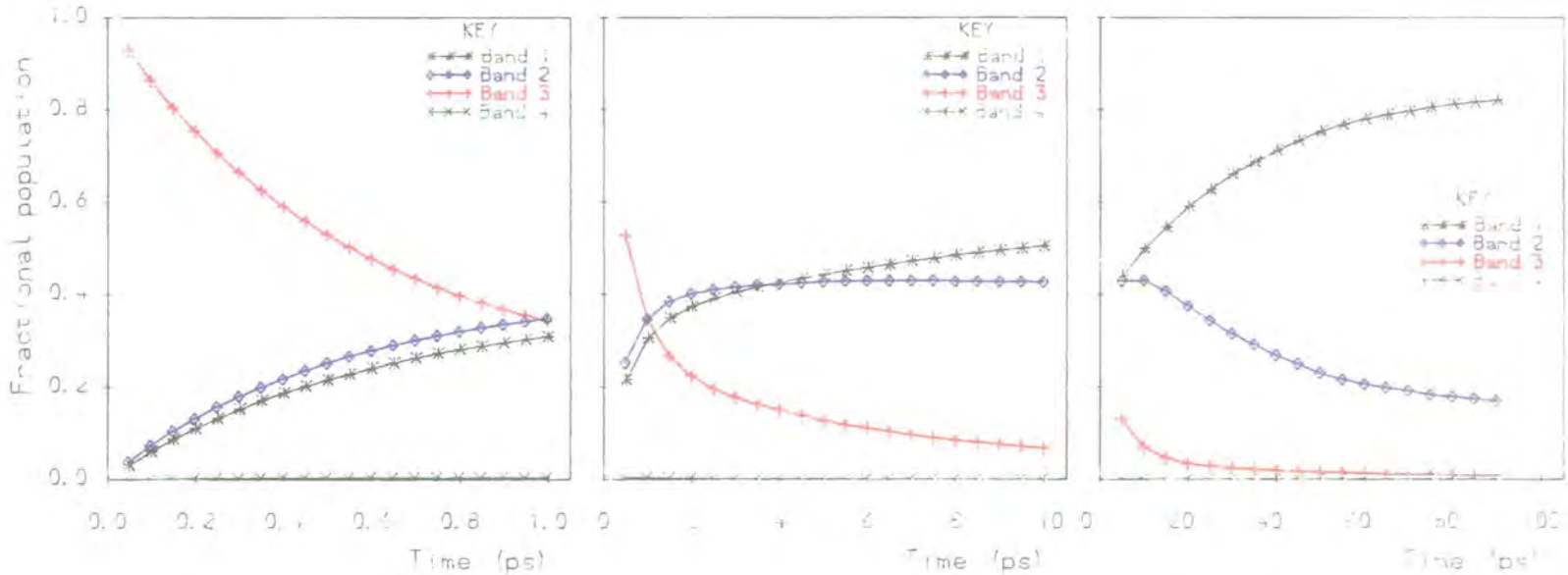

Fig 10.10 Simulation $\delta 3$. Time dependence of the fractional populations in bands 1–4. $T_L = 77\text{K}$; $\epsilon_{ac} = 2\text{meV}$.

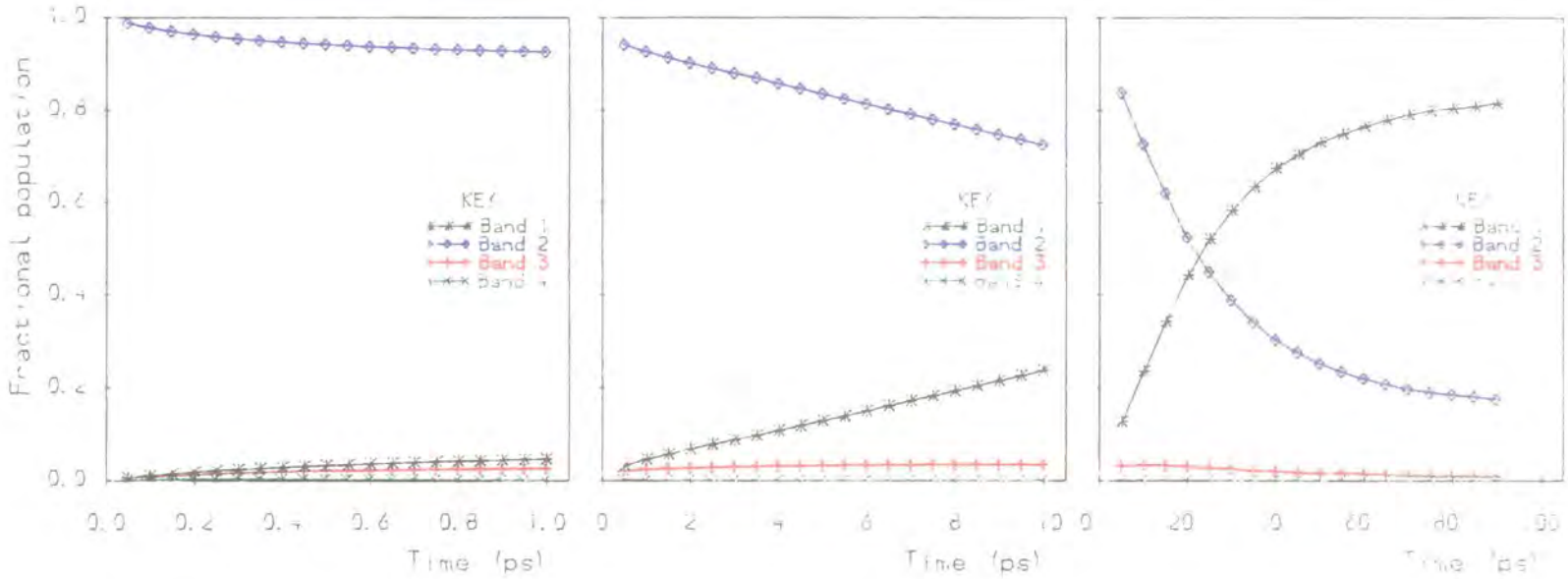

Fig 10.11 Simulation $\delta 4$. Time dependence of the fractional populations in bands 1–4. $T_L = 77\text{K}$; $\epsilon_{\text{ac}} = 2\text{meV}$.

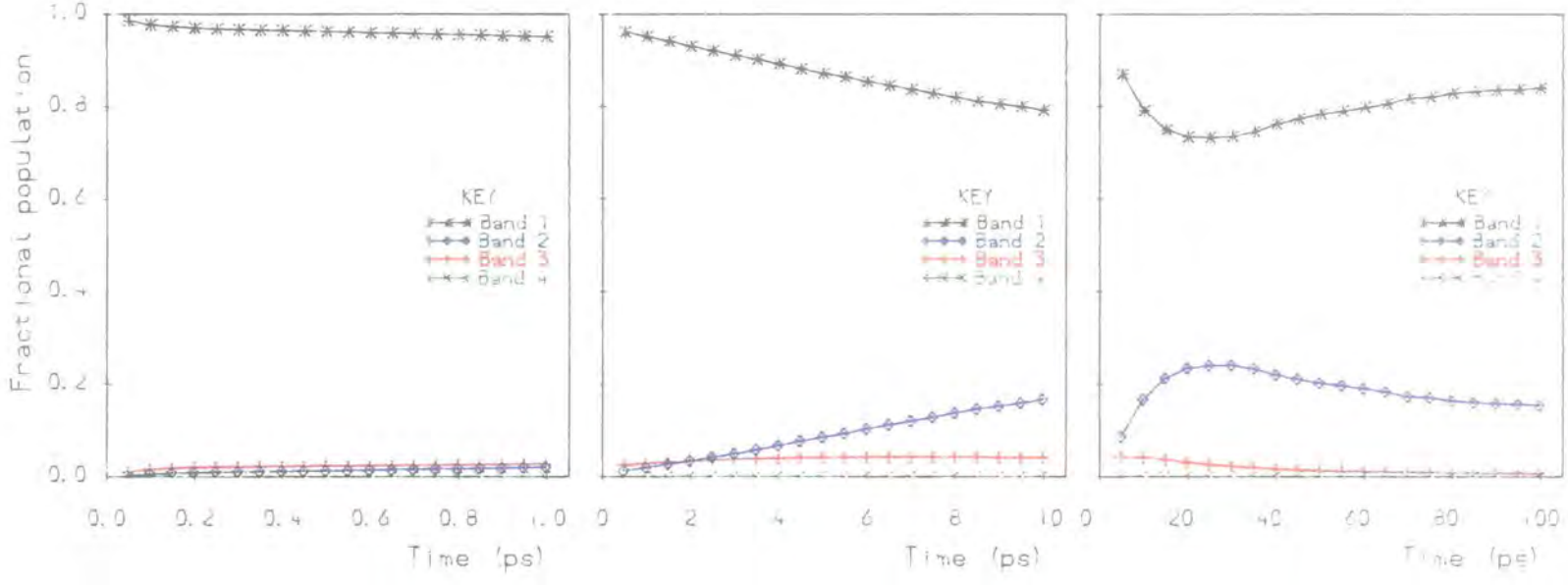

Fig 10.12 Simulation $\delta 5$. Time dependence of the fractional populations in bands 1–4. $T_L = 77\text{K}$; $\epsilon_{ac} = 2\text{meV}$.

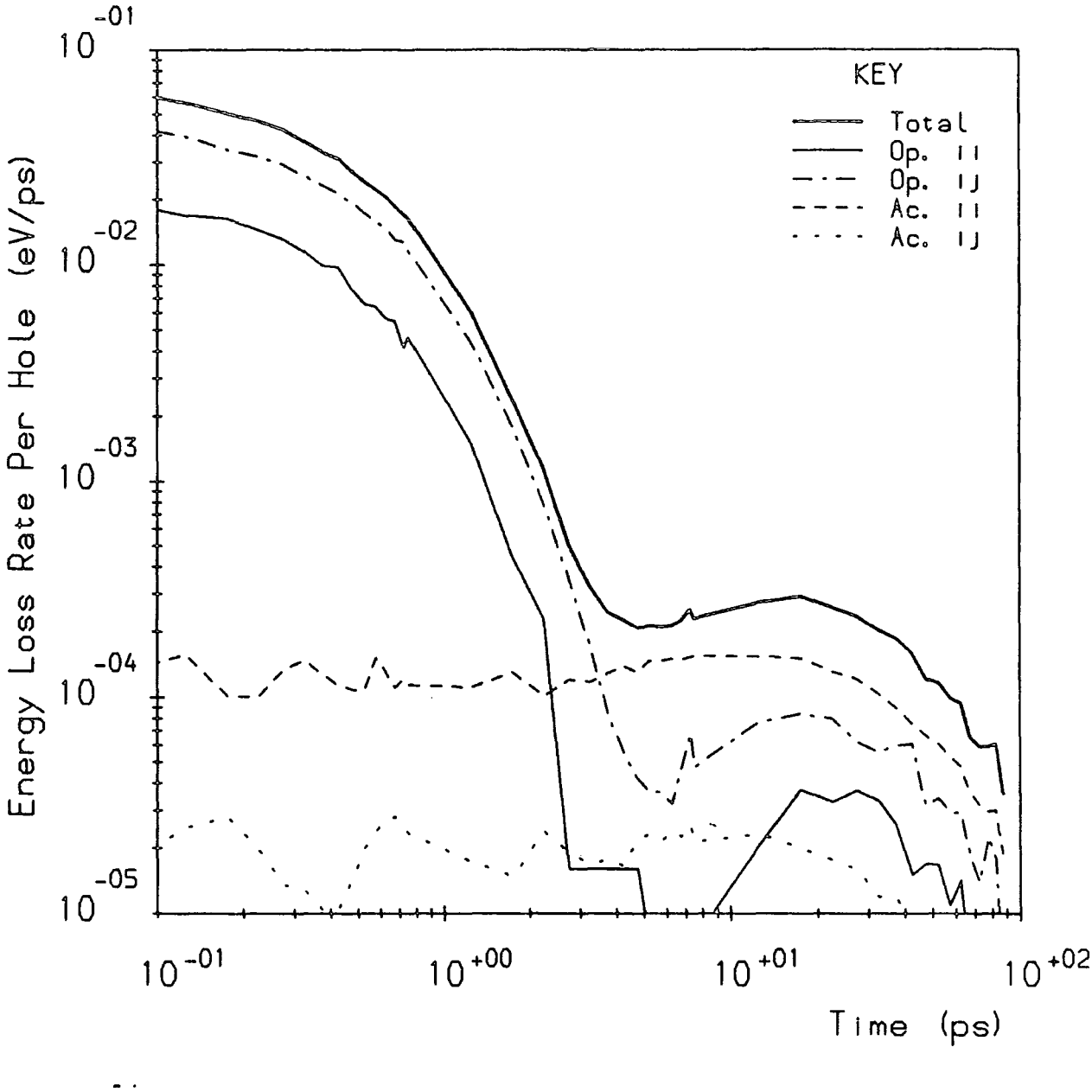

Fig 10.13 Simulation $\delta 3$. Time dependence of the hole energy loss rates. $T_L = 77\text{K}$; $\epsilon_{ac} = 2\text{meV}$.

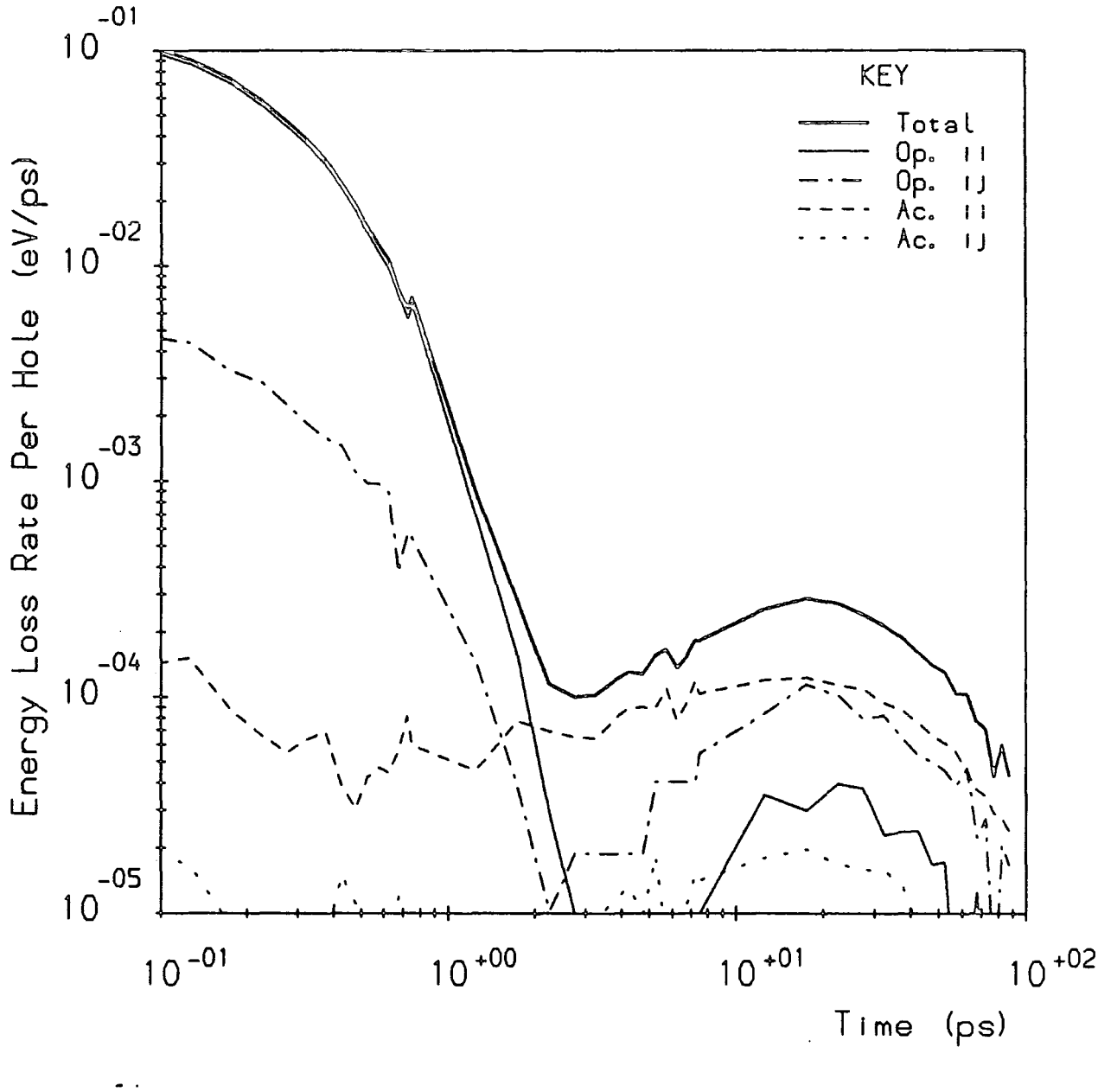

Fig 10.14 Simulation $\delta 4$. Time dependence of the hole energy loss rates. $T_L = 77\text{K}$; $\epsilon_{ac} = 2\text{meV}$.

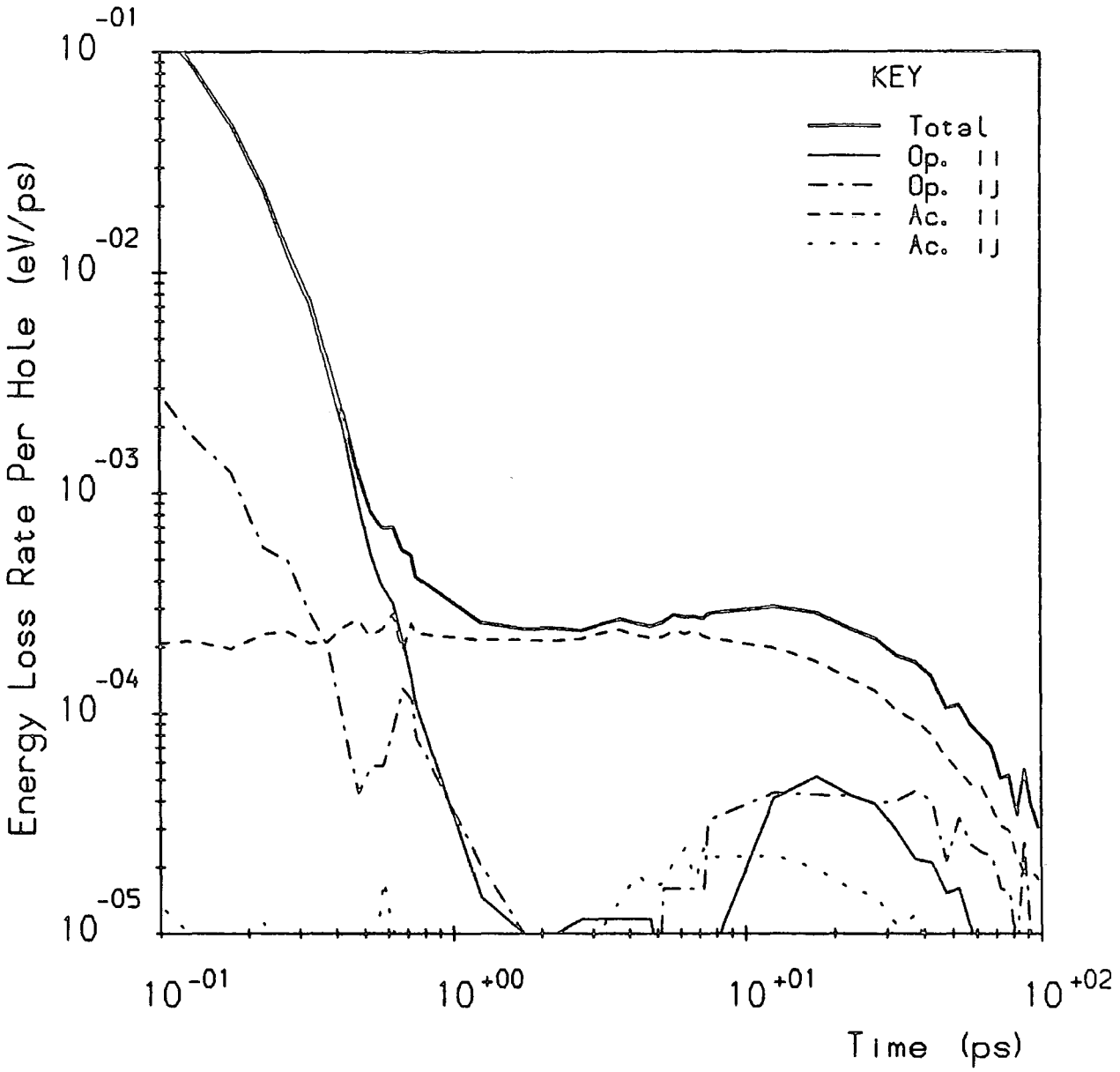

Fig 10.15 Simulation $\delta 5$. Time dependence of the hole energy loss rates. $T_L = 77\text{K}$; $\epsilon_{\text{ac}} = 2\text{meV}$.

t(ps)	ϵ_{av} (meV)					
	$\delta 2$	$\delta 3$	$\delta 4$	$\delta 5$	sM1	mM1
0.0	62.75	62.75	62.75	62.75	62.76	62.77
0.5	36.80	39.85	30.78	26.58	35.80	31.78
1.0	29.40	31.55	27.12	26.35	27.40	24.63
1.5	27.48	28.43	26.69	26.23	24.28	21.84
2.0	26.71	27.18	26.53	26.11	22.84	20.42
2.5	26.53	26.65	26.52	26.03	22.01	19.59
5.0	25.91	25.99	26.29	25.38	20.29	17.68
7.5	25.35	25.43	25.88	24.69	19.31	16.81
10.0	24.72	24.73	25.32	24.07	18.53	16.21
100.0	12.75	12.77	12.87	12.66	12.29	12.04
	thermal equilibrium value: 11.93meV					

Table 10.2: Energy Relaxation in the $\delta 2$–5, sM1 and mM1 Simulations

band 1 population. Hence the total energy loss rate remains higher than that for $\delta 2$–4 within the intermediate (1–10ps) time range. In contrast, the total rate for the $\delta 4$ simulation falls very low during this time interval (Fig. 10.14). This can be ascribed to the relative weakness of AC 2–2em scattering (away from the band 2 minimum), compared with AC 1–1em. Comparing the fractional population plots for the four cases (Figs. 10.4 and 10.10–12), it can be seen that, in the 1–10ps range, by far the lowest band 1 population is obtained in the $\delta 4$ case. This implies that the energy loss rate in the acoustic dominated regime ($t > 1$–3ps) is broadly dependent on the number of carriers present in band 1, since the largest acoustic scattering rates are found here. The remarkably low rate of depopulation of band 2 in the $\delta 4$ case is due to the competition between POP 2–1 and 2–2em, of which the latter is the stronger process. In the $\delta 3$ case, depopulation of band 3 is faster, because intraband optical phonon emission is considerably weaker; however, the depopulation rate is still significantly slower than $\partial\langle\overline{n}_4\rangle/\partial t$ for the $\delta 2$ simulation, where the total optical scattering rate out of the band 4 initial states is considerably larger. Overshoot of the band 2 population can be observed in the $\delta 2$, $\delta 3$ and $\delta 5$ simulations. However, it is clear that carrier trapping (bottlenecking) in band 2 is worst in the $\delta 4$ case, since, after the initial phase of optical scattering, some 90% of the excess carrier population is located in states below the lowest optical emission threshold in band 2. Indeed, because of the relative ineffectiveness of the POP 2–1em process, it could be said that even the high energy $t=0$ population is essentially trapped within the band (though this does not affect the *initial* phase of power dissipation).

We may conclude, from this study of hole cooling via different numbers of subbands, that cooling via just one band is the most efficient route. This is the logical result, since we have seen that the highest scattering rates in the quantum confined valence band system are generally those for the intraband processes for both optical and acoustic modes. For band 1, the principal intraband rates, POP 1–1em and AC 1–1em, are both particularly large for a wide range of energies/wavevectors, compared with those in other bands. Also, in the one band case, cooling is not expected to be inhibited by carrier trapping effects, although a small transient overshoot of the band 2 population in the $\delta 5$ simulation was observed. Concerning multisubband cooling, we found that the overall power loss for cooling via four and three subbands was much the same, due to the extremely fast depopulation of band 4 in the former case. Evidence for carrier trapping in low energy states in bands 3 and 2 was observed in both these cases. Whilst we argued, earlier in this section, that carrier trapping in band 3 formed the larger barrier to the relaxation of the carrier population to thermal equilibrium, because of the small scattering rate near the band minimum: we now find that carrier

trapping is more detrimental to the relaxation rates† when the carrier population is initially generated in band 2, since intraband optical scattering acts to retain the population within the band. It is also clear that, because of the strong intraband acoustic scattering in band 1, the overall energy loss rate for a nonequilibrium carrier population generated in any of the upper bands of the quantum confined system will be governed, to a fair extent, by the efficiency with which carriers can be transferred into band 1, irrespective of the number of intervening bands.

Finally, we may note that, for simulations $\delta 3$–5, in which the initial carrier populations were generated in bands of index 3 or lower, the rôle of the higher index band (4) in carrier relaxation was negligible. This confirms that the neglect of bands of index greater than 4 in simulations such as $\delta 1$ and $\delta 2$ is an entirely reasonable approximation.

† *i.e.*, both the energy loss rates and the rates of de-/re-population of the various bands

10B.3: Cooling of Single- and Multi-band Heated Maxwellian Distributions

Simulation sM1: $T_c = 132K$, *band 4.*

In this simulation, all carriers were initially located in band 4, having a Maxwellian distribution of energies characterised by a carrier temperature of 132K. This value was chosen to give an initial mean energy for the carriers as close as possible to that for the simulations δ2–5. Figs. 10.16–17 show the time dependence of the fractional populations and mean energies for the simulation, and Fig. 10.18 gives the energy loss rates.

The initial (t = 0.1ps) energy loss rate is approximately 7.5×10^{-2}eVps^{-1}, which is greater than that for simulations δ1–3, but less than that for δ4–5. The general form of the energy loss plot bears most resemblance to that for the δ1 simulation. Energy loss at early times is dominated by interband optical scattering; the relative sizes of $\langle\overline{n}_1\rangle$, $\langle\overline{n}_2\rangle$ and $\langle\overline{n}_3\rangle$ after 1ps (Fig. 10.16) reflect the relative strengths of POP 4–1, 4–2 and 4–3em, averaged over the band 4 Maxwellian distribution. We see that POP 4–1em is dominant, as in δ1, with POP 4–3em relatively weak. This is because the majority of carriers in the initial distribution lie below the 4–3 optical emission threshold. The rate of depletion of band 4 over the first picosecond of the simulation is slightly faster than that for the δ1 and δ2 cases.

Fig. 10.19 shows the time evolution of the as-sampled carrier distribution in band 4, within the first picosecond of the simulation. The t=0 distribution is a combination of the T_c = 132K Maxwellian distribution of energies, and the density of states function in band 4. This distribution is rapidly eroded within t = 1ps, with much scattering of carriers out of the upper energy states. The shoulder which develops at $\epsilon \approx$ 36meV corresponds to the 4–4 optical emission threshold. A large population is retained in the band 4 minimum; due to the large density of states there, and also as a result of the weaker scattering below the 4–3 optical emission threshold. This could be construed as a carrier trapping phenomenon in band 4; however, it would only have any significant effect on carrier cooling if *all* interband scattering was dominated by optical, rather than acoustic phonon modes. This will be the case for quantum wells of sufficiently narrow width, as we will discuss in Section 10C.

An important difference between sM1 and the δ-simulations is that, in the former case, optical phonon mediated cooling persists to much later times. A crossover from optical to acoustic phonon dominated cooling occurs at $t \approx$ 6ps in sM1, but both intra- and inter-band optical modes continue to contribute to energy loss beyond this time. Consequently, the overall average energy falls notably faster,

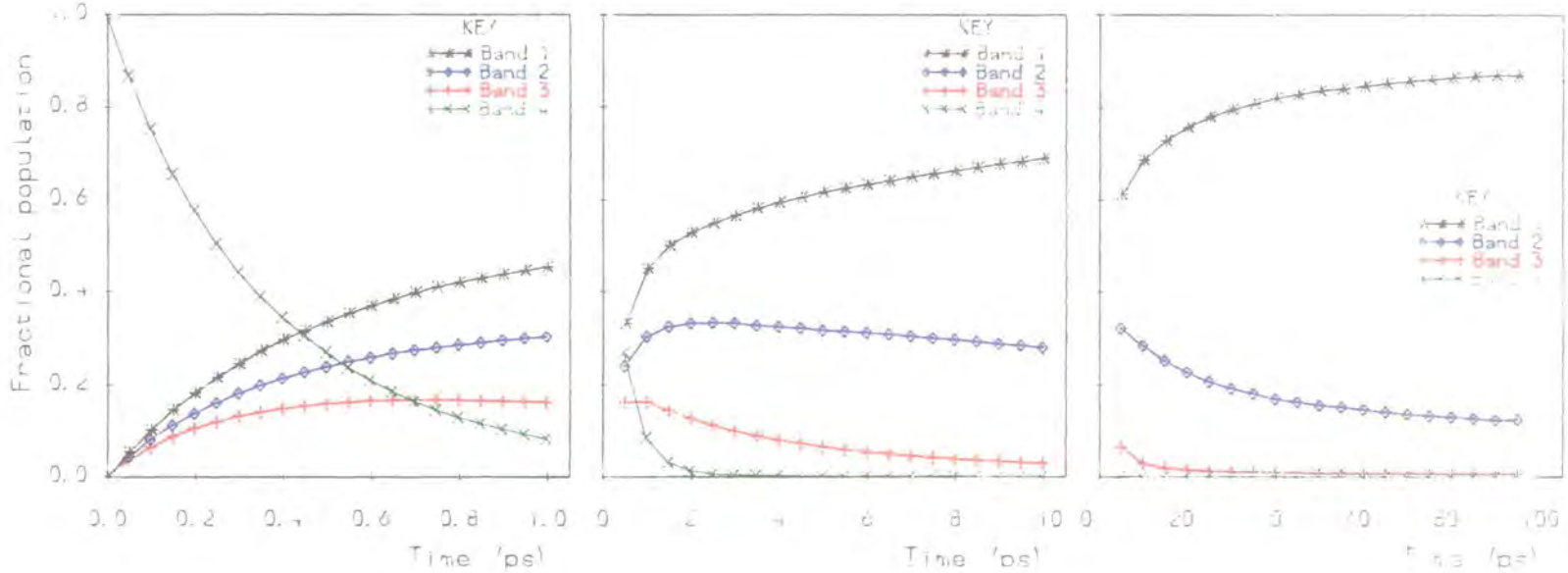

Fig 10.16 Simulation sM1. Time dependence of the fractional populations in bands 1–4. $T_L = 77$K; $\epsilon_{\rm ac} = 2$meV.

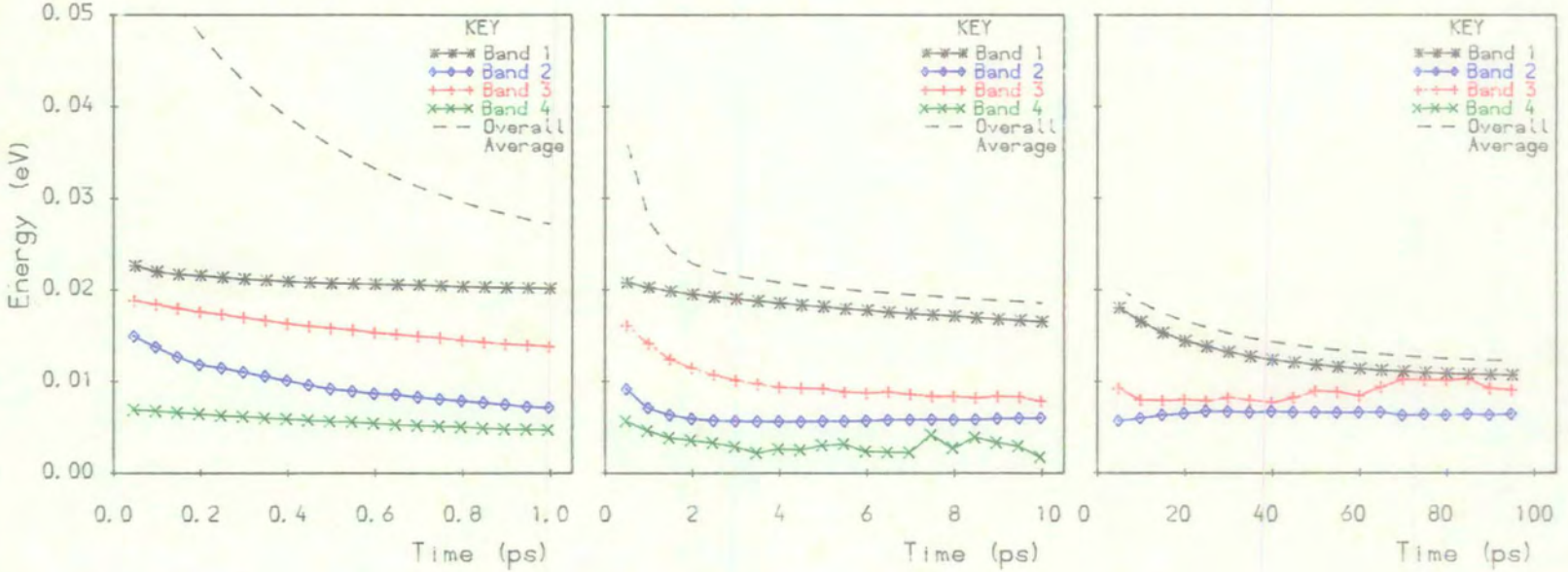

Fig 10.17 Simulation sM1. Time dependence of the mean energies in bands 1–4, and the overall average energy. $T_L = 77\text{K}$; $\epsilon_{\text{ac}} = 2\text{meV}$.

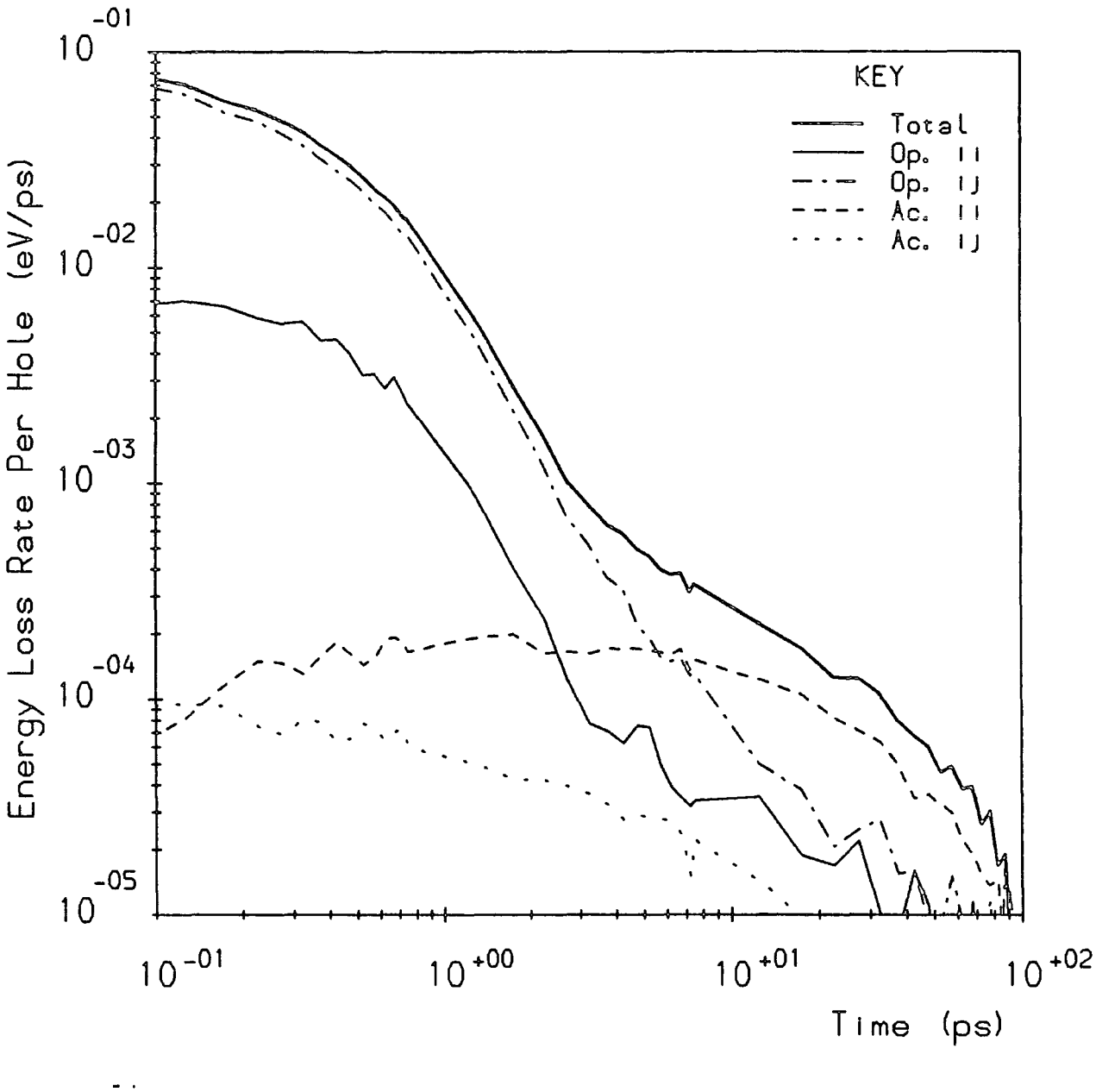

Fig 10.18 Simulation sM1. Time dependence of the hole energy loss rates. $T_L = 77\text{K}$; $\epsilon_{ac} = 2\text{meV}$.

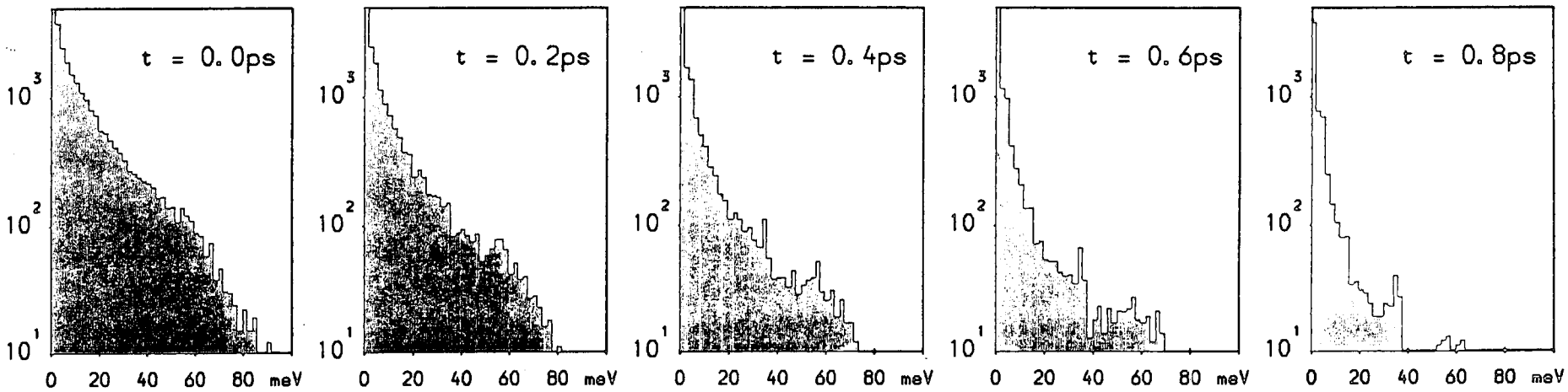

Fig. 10.19 Simulation sM1. Time evolution of the as-sampled hole energy distribution in band 4. $t = 0.0$–0.8ps; $T_L = 77$K; $\epsilon_{ac} = 2$meV.

over the first 10ps of the simulation, than that for $\delta 5$ — the fastest cooling of the four comparative cases $\delta 2$–5. Values of $\langle \epsilon_{av}(t) \rangle$ for simulation sM1 at various times are given in Table 10.2.

Referring to Fig. 10.16, we find that overshoot of the band 2 and 3 populations still occurs, and is on a timescale consistent with that for $\delta 1$, rather than $\delta 2$ (*cf.* Figs. 10.4 and 10.7). A consequence of the spread of energies in the initial sM1 distribution is that part of the carrier population created in band 2 at early times lies above the 2–1 optical emission threshold. Therefore, $\langle \overline{n}_2 \rangle$ is suppressed at early times, relative to $\langle \overline{n}_1 \rangle$, due to POP 2–1em. Hence, only part of the band 2 population is 'trapped'. This is one of the origins of the prolonged contribution of interband optical scattering to the total energy loss rate.

Simulation mM1: $T_c = 475\text{K}$

In this simulation, at $t = 0$ carriers were spread over all four bands in a Maxwellian distribution of energies characterised by $T_c = 475\text{K}$. The carrier temperature was chosen to give an initial distribution with the same overall average energy as that for the simulations $\delta 2$–5 and sM1. The initial average energy corresponds to a temperature of $\langle \epsilon_{av} \rangle / k_B = 728\text{K}$; thus, even in the absence of carrier drifting, the carrier temperatures for non-equilibrium Maxwellian distributions in the quantum well valence band system differ substantially from those expected for a simple 2D band (see Section 9C).

The initial distribution is stochastically generated at the beginning of the Monte Carlo simulation by first allocating carrier energies (relative to the band 1 minimum) according to the Maxwellian probability distribution, and then distributing the carriers between the four bands, in a manner determined by the ratios of the densities of states in each band, at each value of energy concerned. Figs. 10.20 and 10.21 show the time dependence of the fractional populations and mean energies in the four bands, including the initial values. At t=0, the fractional populations decrease with increasing band index; thus, no population inversion exists, contrary to the initial conditions for sM1 and $\delta 1$–4. Fig. 10.21 shows that the mean energies in bands 3 and 4 at $t = 0$ are rather high. This unexpected result can be understood by examining the form of the initial carrier distributions. Figs. 10.22–25 show the as-sampled distributions in bands 1–4 respectively, within the first picosecond of the simulation. The t=0 distributions show that the carrier populations in bands 3 and 4, whilst being smaller than the populations in the lower bands, are nevertheless spread right across the 100meV energy range shown. This is a consequence of the larger densities of states in bands 3 and 4 at high energies, which give rise to population inversion *within* both bands.

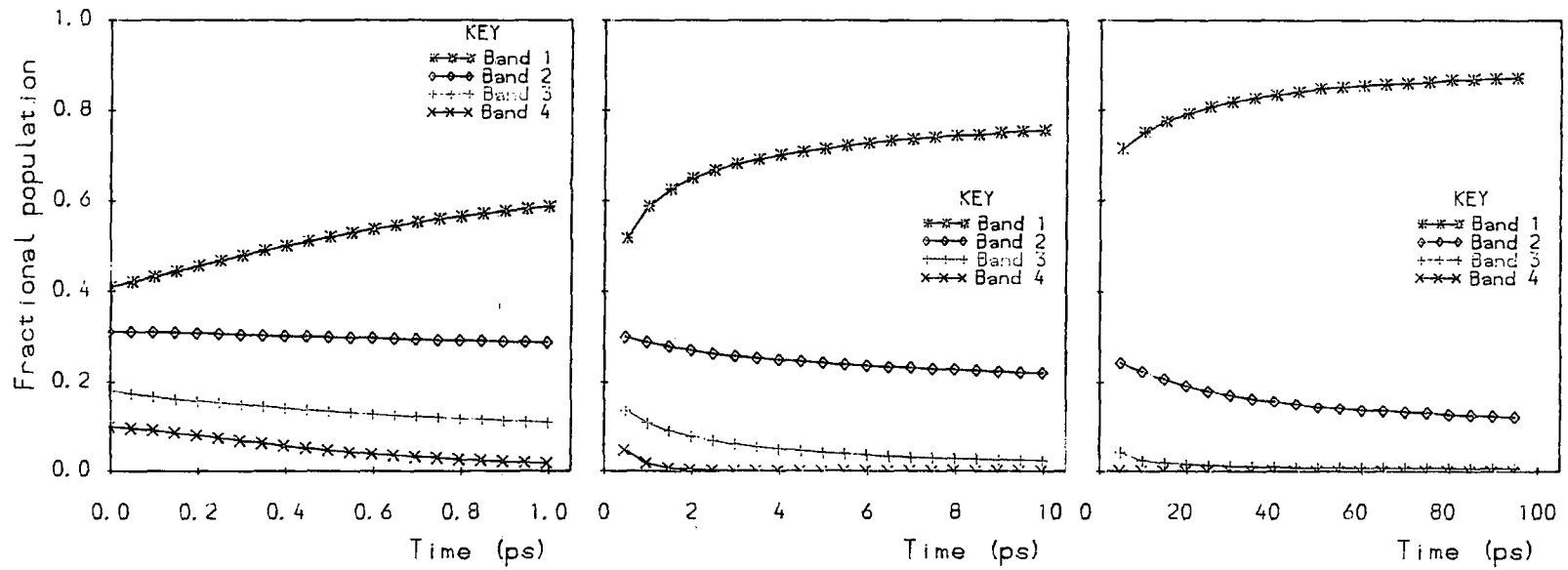

Fig 10.20 Simulation mM1: Time dependence of the fractional populations in bands 1–4. $T_L = 77\text{K}$; $\epsilon_{ac} = 2\text{meV}$.

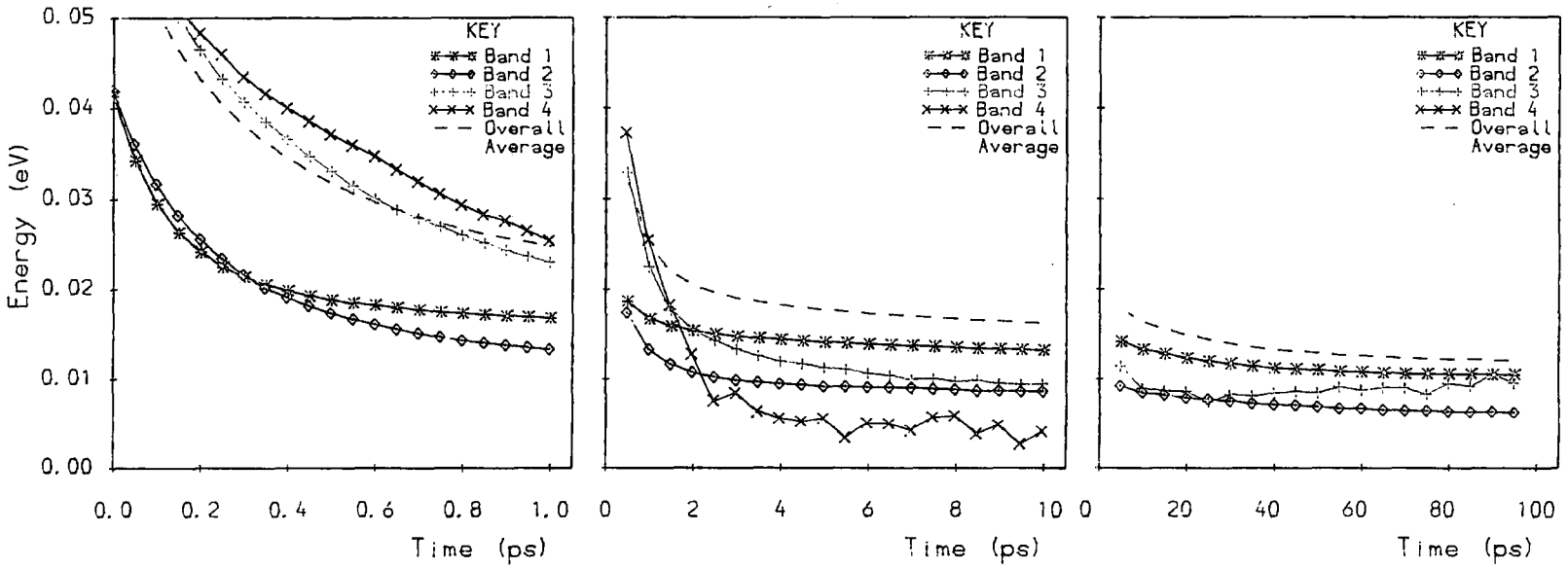

Fig 10.21 Simulation mM1. Time dependence of the mean energies in bands 1–4, and the overall average energy. $T_L = 77\text{K}$; $\epsilon_{\text{ac}} = 2\text{meV}$.

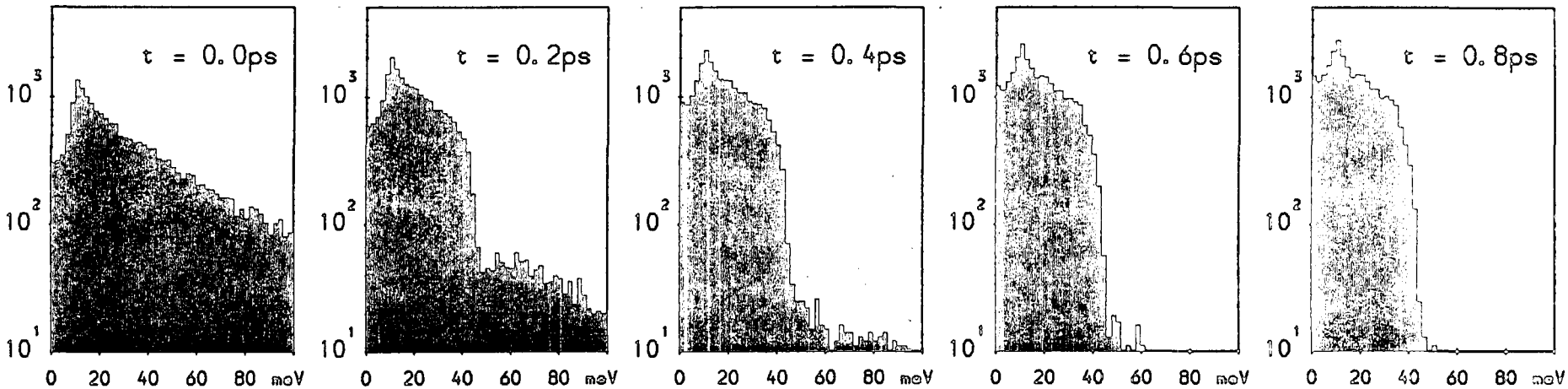

Fig. 10.22 Simulation mM1. Time evolution of the as-sampled hole energy distribution in band 1. $t = 0.0$–0.8ps; $T_L = 77$K; $\epsilon_{ac} = 2$meV.

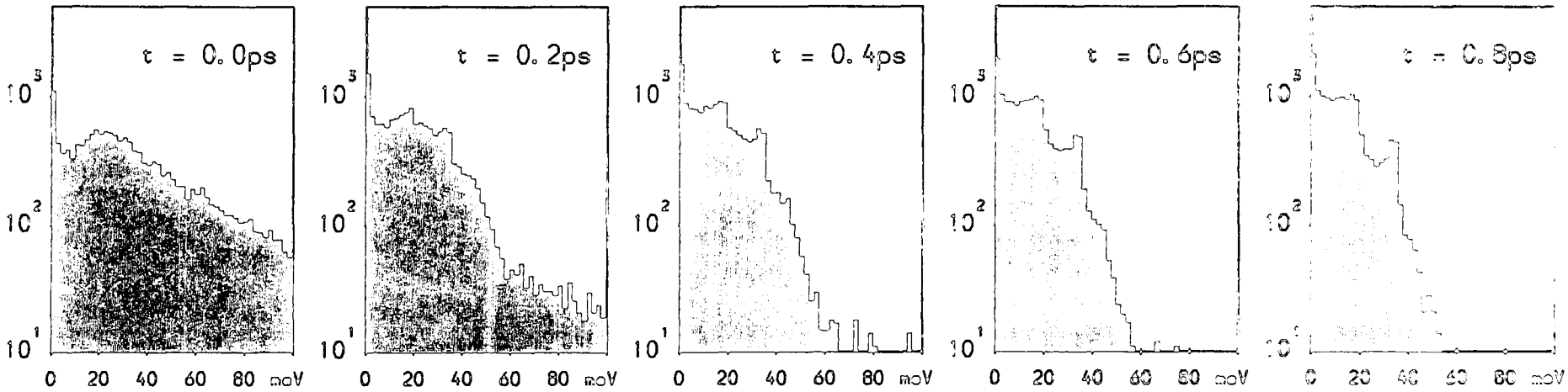

Fig. 10.23 Simulation mM1. Time evolution of the as-sampled hole energy distribution in band 2. $t = 0.0$–0.8ps; $T_L = 77$K; $\epsilon_{ac} = 2$meV.

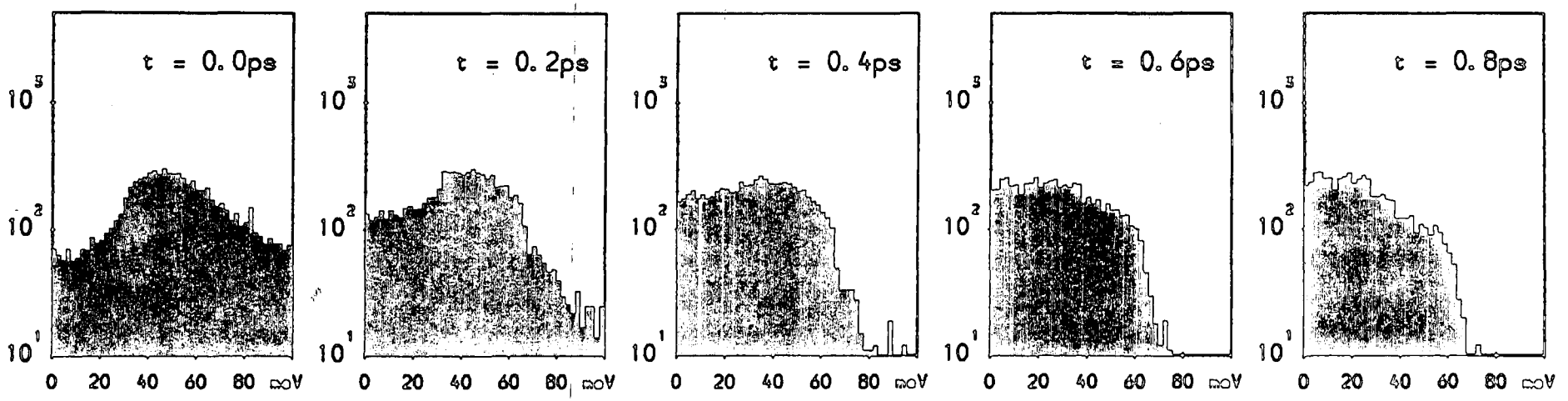

Fig. 10.24 Simulation mM1. Time evolution of the as-sampled hole energy distribution in band 3. $t = 0.0$–0.8ps; $T_L = 77$K; $\epsilon_{ac} = 2$meV.

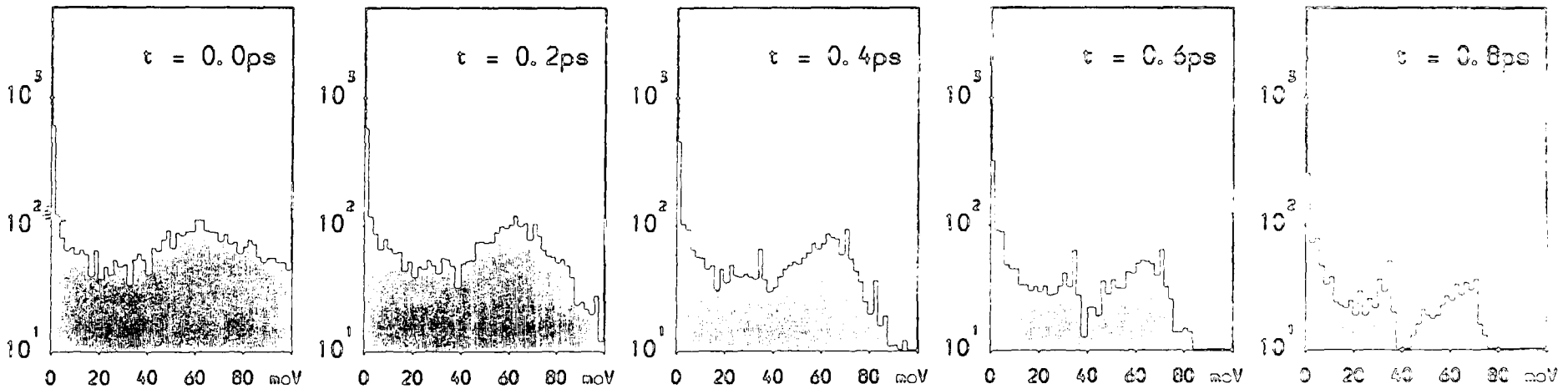

Fig. 10.25 Simulation mM1. Time evolution of the as-sampled hole energy distribution in band 4. $t = 0.0$–0.8ps; $T_L = 77$K; $\epsilon_{ac} = 2$meV.

The four sets of carrier distributions give a very clear picture of the thermalisation process which takes place immediately following the formation of the hot Maxwellian distribution. From Figs. 10.22–24 it may be deduced that strong optical scattering occurs in all the first three bands. The band 1 distribution is significantly modified by POP 1–1em, even after 0.2ps. In band 2, shoulders form in the distribution at approximately 20 and 36meV, corresponding to POP 2–1 and 2–2em respectively. The accumulation of carriers which develops at around $\epsilon = 36$meV within $t = 1$ps is created by POP 2–2abs scattering of carriers from the band 2 minimum. This feature is effectively a 'phonon replica' of the extremely large $\epsilon = 0$ population. Fig. 10.24 depicts the development of a shoulder in the band 3 carrier distribution corresponding to the threshold for successive 3–3 plus 3–2 optical phonon emission, although much depletion of states slightly higher in energy occurs by successive 3–3 optical emission events.

Fig. 10.26 shows the energy loss plot for the mM1 simulation. The initial ($t = 0.1$ps) cooling rate is greater than that for the sM1 simulation, but still less than that for the $\delta 4$ and $\delta 5$ cases. Unlike sM1, the initial phase of cooling here is dominated by the intraband optical modes; principally POP 1–1em. A crossover of the intra- and inter-band optical energy loss rates occurs at $t \approx 0.6$ps, which we attribute to a decay in the intensity of POP 1–1em scattering. The acoustic energy loss rates are low, compared to the previous cases investigated, and decrease with time. Thus, no optical/acoustic crossover is observed; the optical modes remain dominant in power dissipation throughout the timescale shown. Apart from these points, the mM1 energy loss response is broadly similar to that for the sM1 simulation. The strength of intraband optical scattering at early times means that, for $t = 1$ps and beyond, cooling of the mM1 initial distribution is faster than that for both sM1 and $\delta 5$. Values of $\langle \epsilon_{\rm av}(t) \rangle$ are given in Table 10.2.

Looking at the fractional population response of Fig. 10.20, it can be seen that no overshoot of the band 2 population occurs, as has been observed in most of the previous cases. This is principally because the carrier population is more evenly distributed between the bands, with no unusually high concentration at any single location in energy space from which strong interband optical scattering into band 2 may occur. Obviously, the elimination of the carrier 'bottleneck' at the band 2 minimum contributes to the increased efficiency of energy loss in the mM1 simulation. However, it may be argued that, whilst the average energy of the carrier population at $t = 0$ is the same as for simulations sM1 and $\delta 2$–5, the initial distribution of the carriers across the four bands represents a situation less far removed from thermal equilibrium than those cases in which the carriers are initially confined to a single band.

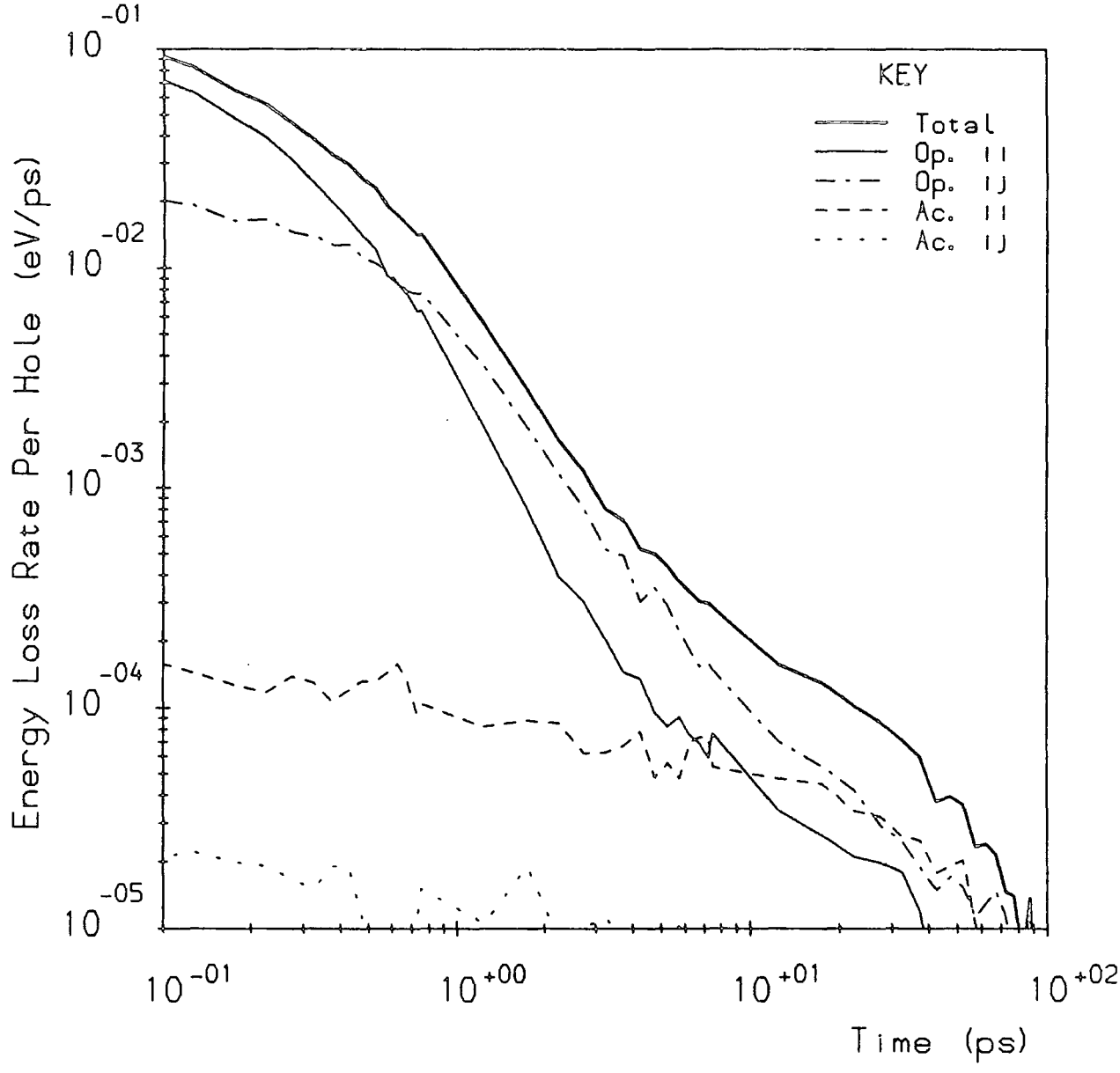

Fig 10.26 Simulation mM1. Time dependence of the hole energy loss rates. $T_L = 77\text{K}$; $\epsilon_{\text{ac}} = 2\text{meV}$.

10B.4: Cooling of a Hole Population above the $2 \times \hbar\omega_{op}$ Threshold

Simulation δ6: $\epsilon(t{=}0) = 21.25\text{meV}$, *band 4.*

The energy of the initial monoenergetic carrier distribution in this simulation was chosen to be just greater than the threshold energy for scattering into the band 1 minimum by the successive emission of two optical phonons. In this case, energy loss, and repopulation of band 1 are expected to be faster than observed for simulations such as δ1 and δ2. Figs. 10.27–28 show the time dependence of the fractional populations and mean energies for the simulation, and Figs. 10.29–30 show the energy loss response.

As expected, the energy loss rate is high ($> 10^{-1}\text{eVps}^{-1}$) in the initial phase of cooling, and is predominantly due to interband optical scattering. Fig. 10.27 shows that depletion of the initial band 4 population is almost complete after 1ps, representing a considerably faster depletion rate than observed in the previous simulations. The population of band 3 rapidly becomes very large ($\langle\overline{n}_3\rangle_{max} = 0.55$ at $t = 0.7$ps), due to strong POP 4–3em (see section 10B.2). Fig. 10.28 shows the band 3 mean energy virtually fixed at 17meV throughout the 1ps timescale. This value corresponds to $\epsilon(t{=}0) - \hbar\omega_{op}$; hence carriers in band 3 at this stage can still scatter out of the band by further optical phonon emission. However, the band 3 population is slow to decay, since the POP 3–1 and 3–2 processes are quite weak.

Conversely, the population in band 2 grows to no more than $\langle\overline{n}_2\rangle \approx 0.16$, just greater than the thermal equilibrium value, before decreasing after only 0.45ps. The detailed breakdown of scattering events for the simulation shows that, within the first picosecond, 4–2 optical emission is more prevalent than 4–1 optical emission, and that there is a good deal of 2–1 optical scattering. Thus, we may conclude that band 2 is initially *re*-populated by POP 4–2em, and then rapidly *de*-populated by POP 2–1em. This serves as an important route by which band 1 is initially repopulated. Fig. 10.28 shows that $\langle\epsilon_1\rangle$ decreases rapidly from around $\hbar\omega_{op}$ at $t = 0.05$ps to below 10meV after 1ps, indicating that most of the carriers in band 1 have emitted two optical phonons by this time.

Looking at the 10 and 100ps timescales on Figs. 10.27–28, it is clear that the population in band 1 rises too high, and that in band 2 falls too low. $\langle\overline{n}_1\rangle$ reaches a maximum value at $t = 15$ps, and then begins to relax. Also, the mean energy in band 1, and the overall average energy fall below their thermal equilibrium values, reaching minimum values at $t = 4.5$ps and $t = 15$ps respectively. Clearly, optical scattering into the low energy states in band 1 is too strong to allow a monotonic relaxation of the system towards thermal equilibrium, and a transient 'overcooling', or 'supercooling' effect occurs. This phenomenon is vividly demonstrated on the energy loss plots of Figs. 10.29–30. The total energy loss rate falls sharply from its

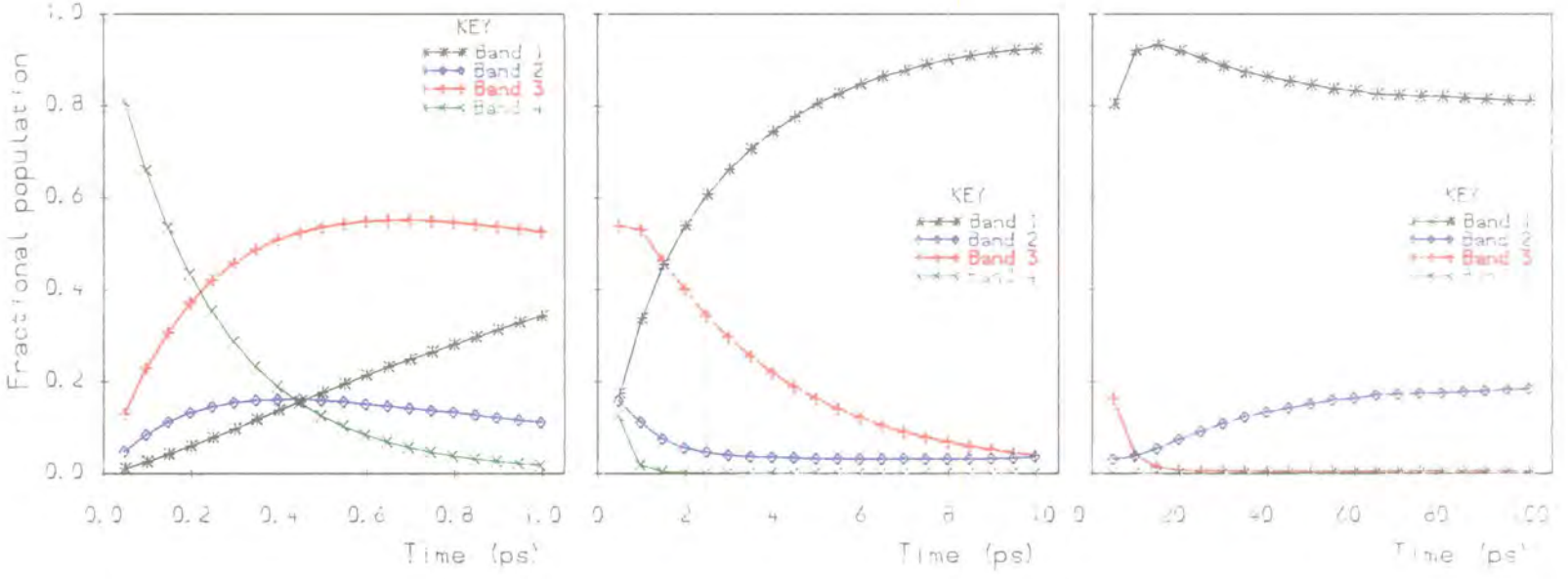

Fig 10.27 Simulation $\delta 6$. Time dependence of the fractional populations in bands 1–4. $T_L = 77\text{K}$; $\epsilon_{\text{ac}} = 2\text{meV}$.

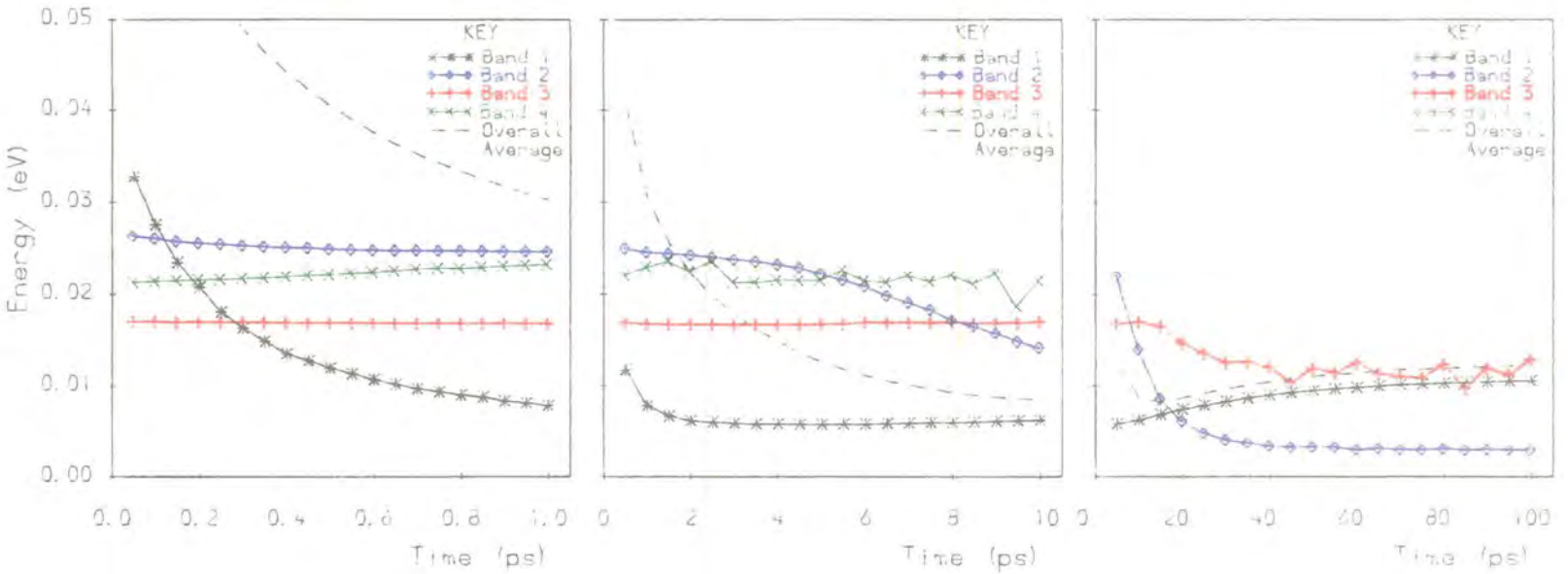

Fig 10.28 Simulation $\delta 6$. Time dependence of the mean energies in bands 1–4, and the overall average energy. $T_L = 77\text{K}$; $\epsilon_{\text{ac}} = 2\text{meV}$.

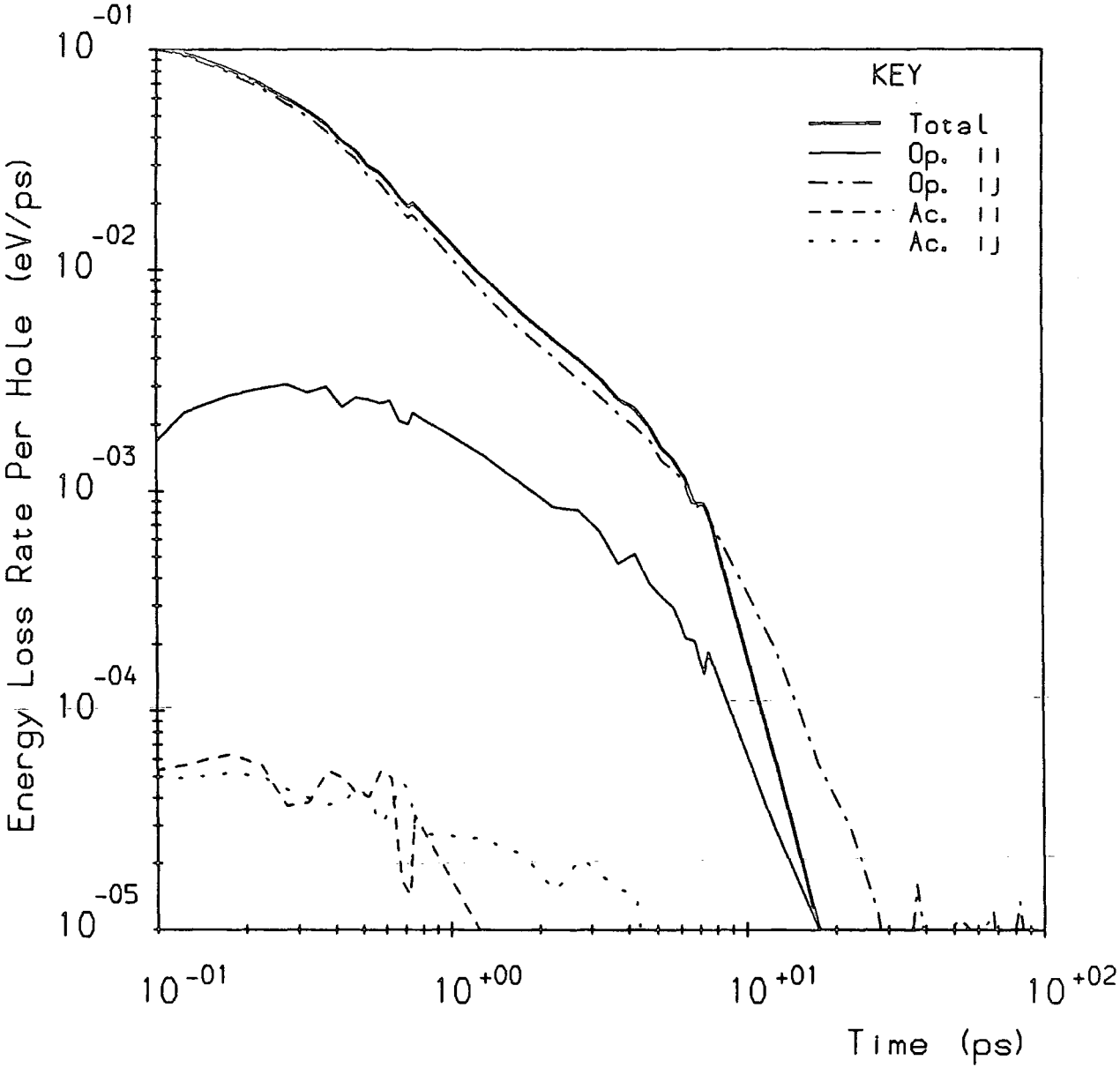

Fig 10.29 Simulation $\delta 6$. Time dependence of the hole energy loss rates. $T_L = 77\text{K}$; $\epsilon_{\text{ac}} = 2\text{meV}$.

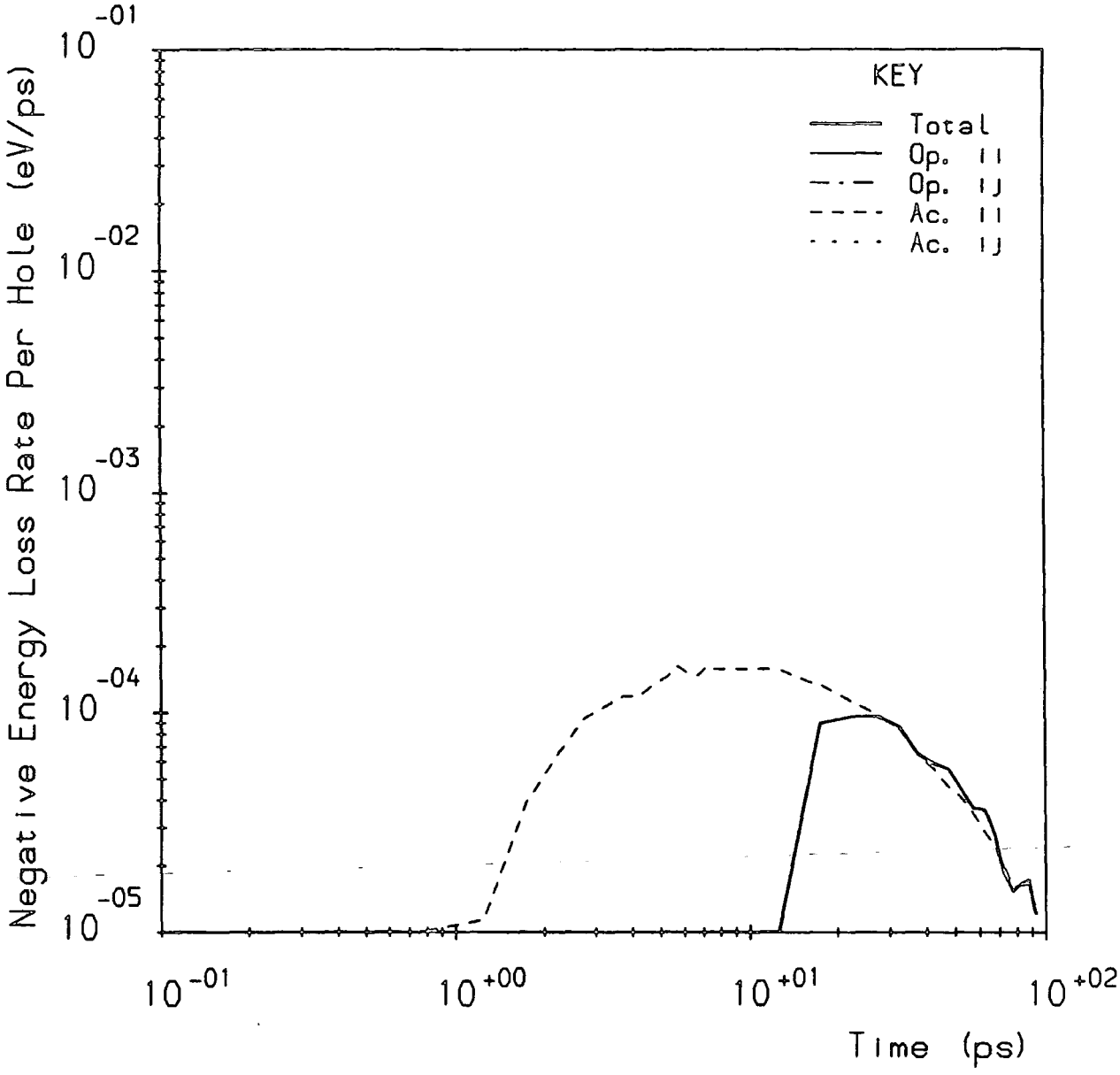

Fig 10.30 Simulation $\delta 6$. Negative portion of the energy loss response. $T_L = 77\text{K}$; $\epsilon_{ac} = 2\text{meV}$.

initial value, and becomes negative for $t > 15$ps. This means that, at all later times, the carrier system is actually absorbing energy from the lattice system. Fig. 10.30 shows the negative portion of the energy loss response. It can be seen that a net absorption of energy from the intraband acoustic phonon modes commences shortly after $t = 1$ps. This corresponds to AC 1–1abs, as the large population created near the band 1 minimum begins to spread upwards in energy.

To complete our understanding of this simulation, we need to know by which route band 2 is repopulated on the 100ps timescale. The breakdown of scattering events produced by the simulation indicates a net amount of AC 1–2abs scattering present for $t \geq 3.5$ps. This is consistent with the decrease in the band 2 energy observed beyond this time. We can deduce that, whilst the upper energy states in band 2 are still being depleted by optical scattering, the low energy states are experiencing *repopulation* by acoustic scattering of carriers immediately above the AC 1–2abs threshold in band 1.

A final point of interest concerning this simulation is that the population of band 2 at $t = 100$ps is, for the *second* time, in excess of its thermal equilibrium value. This rather surprising result signifies the extent of the earlier overpopulation of the low energy states in band 1, and reflects the slowness of the response of the system in the acoustic scattering regime. The subsequent return to the equilibrium population distribution will proceed via AC 2–1 scattering, in which case the equilibrium state may not be attained for a further hundred picoseconds. It should be noted, however, that the energy loss plots of Figs. 10.29–30 show that after 100ps the total energy loss rate is very small, indicating that the system energy is already very close to equilibrium ($\langle \epsilon_{\rm av} \rangle = 12.20$meV compared to the thermal equilibrium value of 11.93meV).

Simulation sM2: $T_{\rm c} = 222$K, *band 4.*

To complete our study of the cooling of carriers above the $2 \times \hbar\omega_{\rm op}$ threshold, we used a simulation having an initial Maxwellian distribution of carriers in band 4, with a mean energy equivalent to that in simulation $\delta 6$. Fig.10.31 shows the energy loss response for this simulation, and Fig. 10.32, the time dependence of the fractional populations. It is clear from Fig. 10.31 that none of the unusual features characterising the $\delta 6$ simulation appear in the present case. The energy loss response is very similar to that of both the sM1 and mM1 simulations, with the optical energy loss components significant for at least 40ps, and no negative contribution to energy loss present. The transient response of the fractional populations is also much the same as in the sM1 and $\delta 1$–2 cases. Overpopulation of band 1 is not observed, and the rate of depopulation of band 1 is somewhat slower than in simulation $\delta 10$. All these observations are not especially surprising,

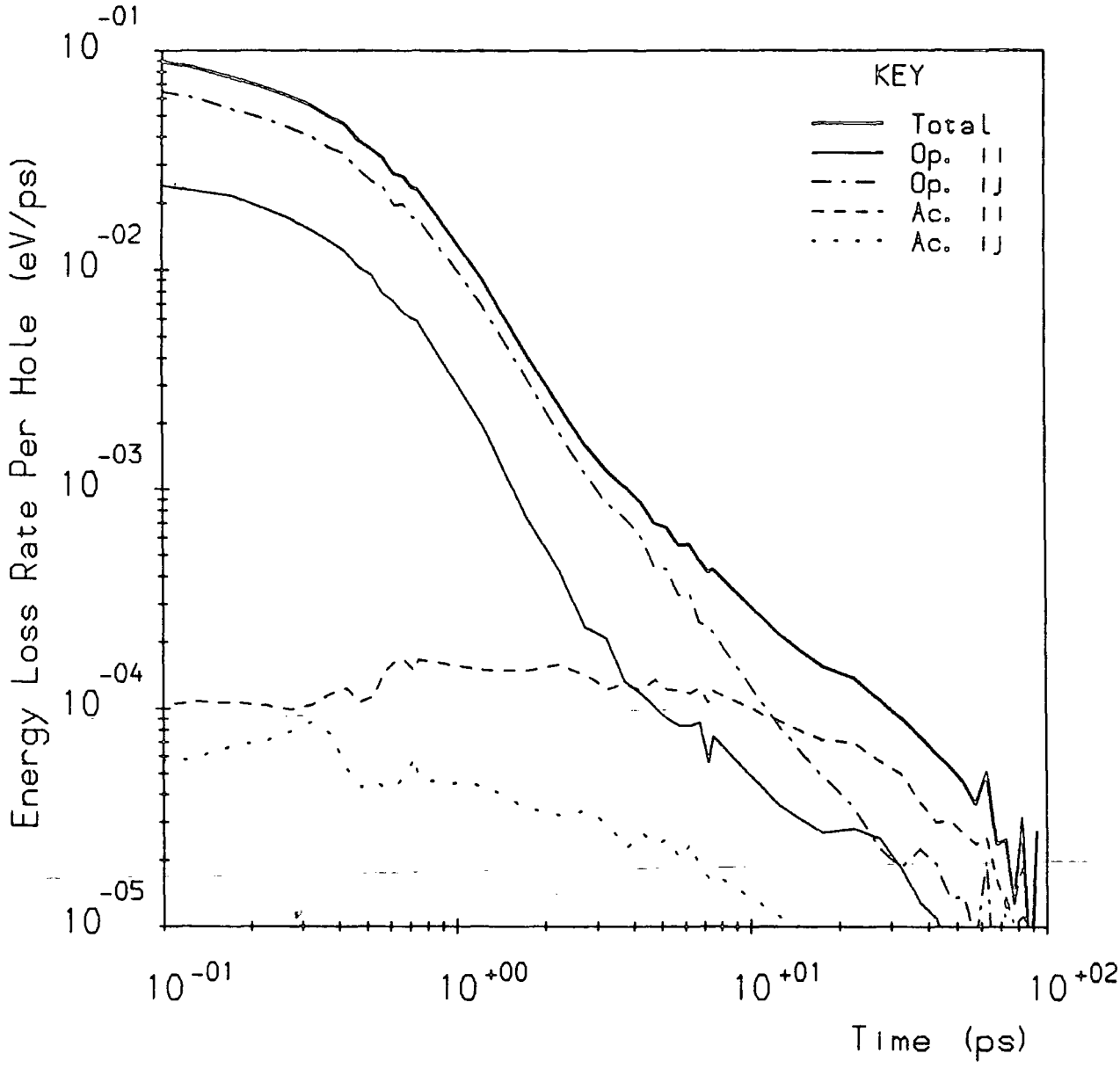

Fig 10.31 Simulation sM2. Time dependence of the hole energy loss rates. $T_L = 77\text{K}$; $\epsilon_{ac} = 2\text{meV}$.

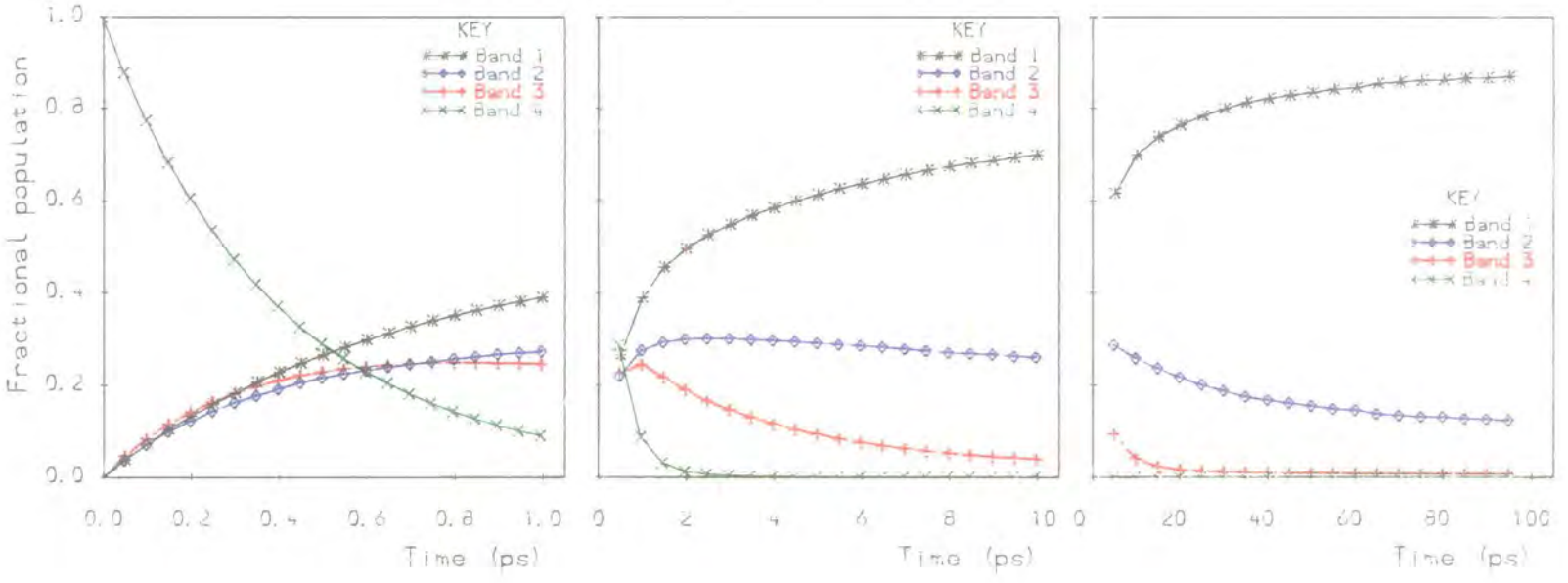

Fig 10.32 Simulation sM2. Time dependence of the fractional populations in bands 1–4. $T_L = 77\text{K}$; $\epsilon_{ac} = 2\text{meV}$.

since, in the Maxwellian distribution, the majority of carriers will occupy low energy states in band 4, with a rather smaller proportion lying above the $2 \times \hbar\omega_{op}$ threshold. We may conclude that the transient 'supercooling' effects described earlier in this section will only be observed when a large population of carriers is concentrated in states close to the relevant optical threshold. A second example of such supercooling will be described in section 10B.7.

10B.5: Cooling of Hole Populations generated in the Lower Bands

Having established that trapping of carriers does occur in states in bands 2 and 3 below the lowest optical phonon emission threshold, we will now proceed to examine, in further detail, the relaxation of carrier populations generated in these regions.

Simulation δ7: $\epsilon(t{=}0) = 0$, *band 3;* $\epsilon_{av} = 24.34$meV.

In this simulation, the initial monoenergetic distribution of carriers was located at the band 3 minimum. Figs. 10.33–34 show the time dependence of the fractional populations and mean energies for the simulation, and Figs. 10.35–36 show the positive and negative portions of the energy loss rates.

Fig. 10.33 shows a rather slow decay of the band 3 population. Indeed, comparison of the 10ps timescale plot with the 1ps plots for simulations $\delta 1$ and $\delta 2$ indicates that the rate of depletion of the low energy states in band 3 is approximately a factor of ten slower than that of low energy states in band 4. Fig. 10.34 shows that $\langle \epsilon_3 \rangle$ increases steadily over the first 10ps of the simulation, and that the overall average energy $\langle \epsilon_{av} \rangle$ also increases, within the first picosecond. Correspondingly, the total energy loss rate is *negative*, for $t \leq 1$ps. Fig. 10.36 shows that the negative components in the energy loss rate are those due to the interband optical and intraband acoustic modes. The intraband acoustic contribution represents 3–3 acoustic phonon absorption, and this involves predominantly piezoelectric coupling, since the intraband PZ matrix elements are so large (see section 6C.2). The interband optical contribution to energy absorption is given by POP 3–1abs scattering, which is of comparable strength to the interband acoustic modes in band 3. Carriers scattered into band 1 by POP 3–1abs very quickly re-emit an optical phonon (POP 1–1em), creating a population in band 1 at an energy equivalent to that of the band 3 minimum.

In the latter part of the simulation, energy loss is dominated by intraband acoustic (AC 1–1em) scattering, as the band 1 population thermalises. The intraband acoustic component of the energy loss rate reaches a maximum value of approximately 2×10^{-4}eVps^{-1}, comparable with the highest values observed for the previous δ-simulations. On Fig. 10.33, a transient overshoot of the band 2 population is observed, with a maximum value occurring at $t = 20$ps. This is a surprising result, since 3–2 scattering in this simulation is very weak. The breakdown of scattering events obtained from the simulation shows net 1–2 acoustic scattering for $t < 20$ps, and net 2–1 acoustic scattering for $t > 20$ps. Therefore, we may deduce that the overpopulation of band 2 is a consequence of the formation of a large population of carriers localised within a very small range of energies in band 1. Such a population develops because the principal routes for scattering

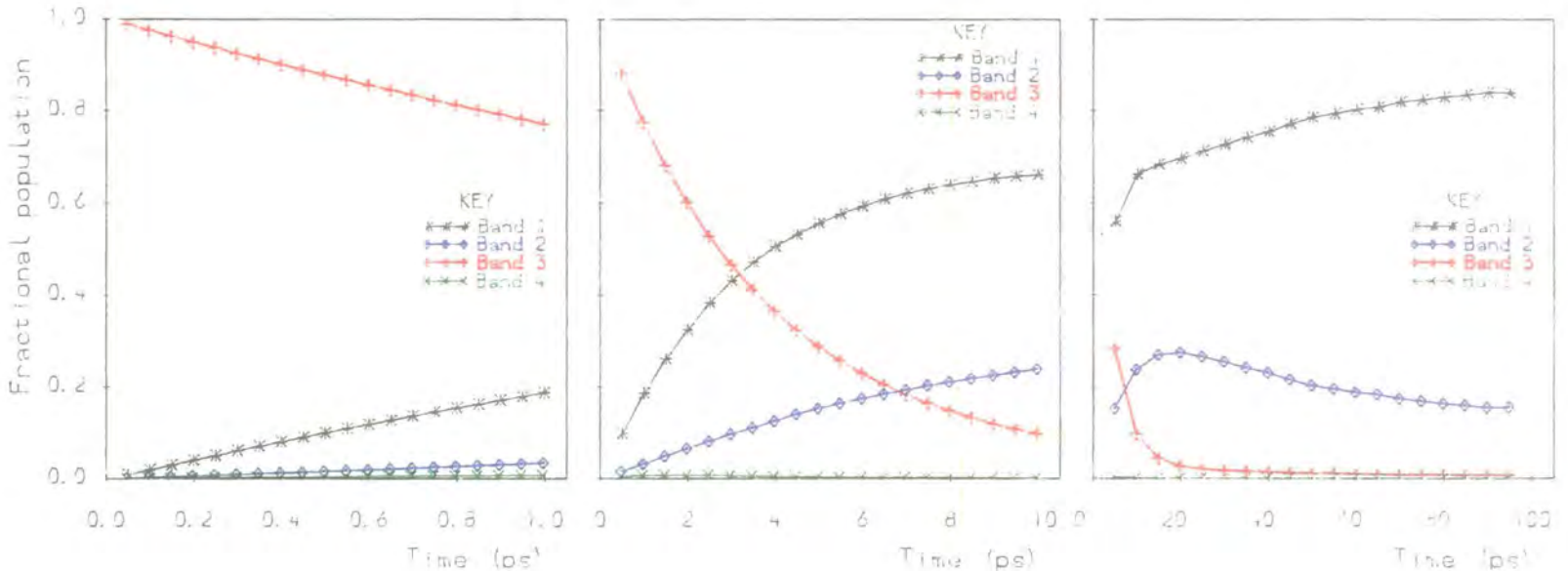

Fig 10.33 Simulation $\delta 7$. Time dependence of the fractional populations in bands 1–4. $T_L = 77\text{K}$; $\epsilon_{ac} = 2\text{meV}$.

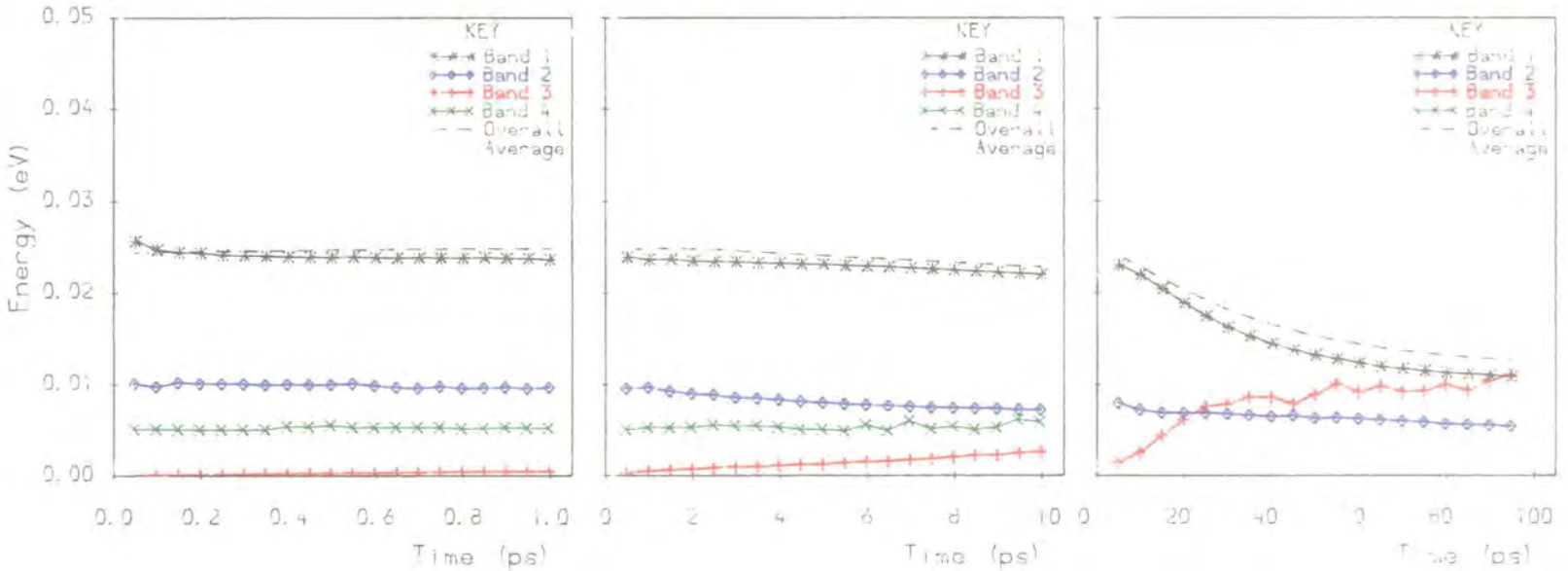

Fig 10.34 Simulation $\delta 7$. Time dependence of the mean energies in bands 1–4, and the overall average energy. $T_L = 77\text{K}$; $\epsilon_{\text{ac}} = 2\text{meV}$.

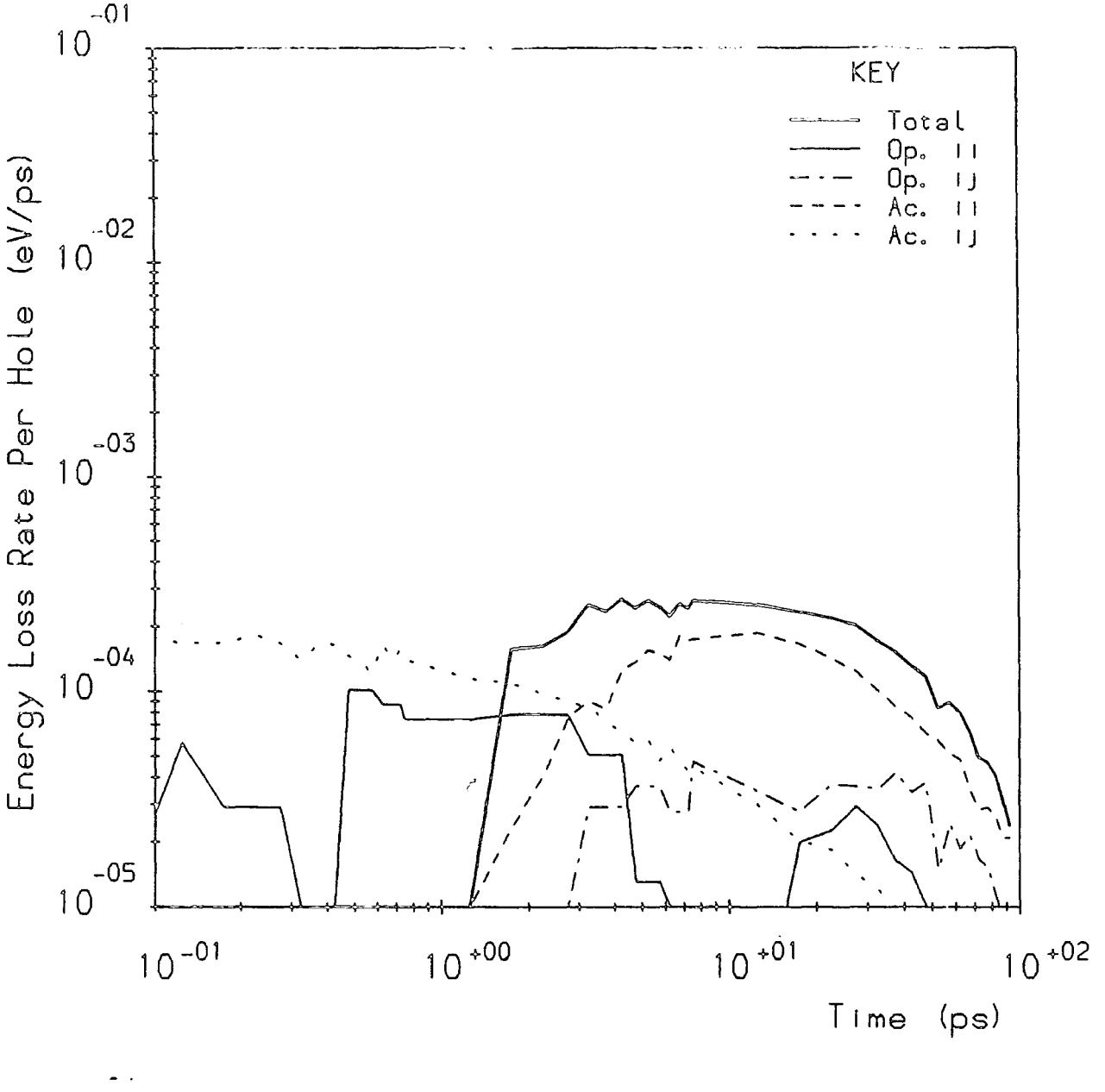

Fig 10.35 Simulation $\delta 7$. Time dependence of the hole energy loss rates. $T_L = 77\text{K}$; $\epsilon_{ac} = 2\text{meV}$.

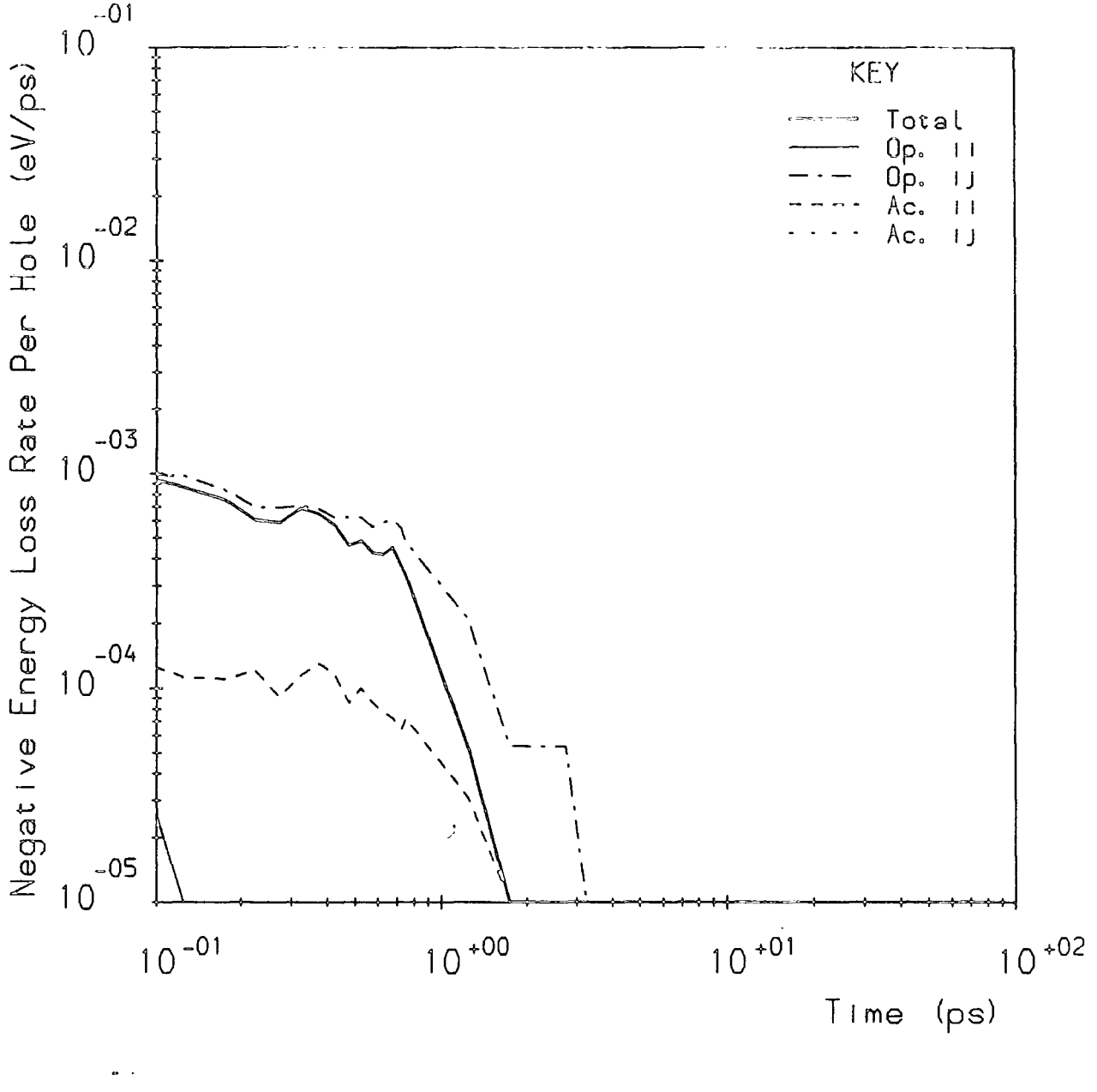

Fig 10.36 Simulation $\delta 7$. Negative portion of the energy loss response. $T_L = 77\text{K}$; $\epsilon_{ac} = 2\text{meV}$.

out of band 3 will all direct carriers to the same region in band 1. If the total rate of scattering into this region exceeds the total intraband acoustic rate, then the population will be forced to relax by the scattering of carriers to other bands. In this case, we would expect the effect to disappear in the presence of intraband carrier-carrier scattering, which would act to thermalise the band 1 population much more efficiently than the intraband acoustic phonon modes.

Simulation δ8: $\epsilon(t{=}0) = 8.44\text{meV}$, *band 2;* $\epsilon_{\text{av}} = 24.34\text{meV}$.

The initial energy, relative to the band 1 minimum, of the carrier distribution in this simulation was chosen to be the same as that for the previous case, $\delta 7$. This will enable us to compare the cooling of carriers in states below the lowest optical phonon emission threshold in bands 2 and 3. We might suspect that cooling would be slower in the band 3 case, since here there are two band minima in which carriers can be trapped.

Fig. 10.37 shows $\langle \overline{n}(t) \rangle$ for each band, and Figs. 10.38–39 show the energy loss rates. In the first picosecond of the simulation, Fig. 10.38 depicts energy loss from the carriers to intraband acoustic phonon modes. This is due to 2–2 acoustic scattering (both AC and PZ) as the carriers relax within band 2. However, there is still a net gain of energy by the carrier system from the lattice (phonon) system over this period. Fig. 10.35 shows that both the intra- and inter-band components of the energy loss rate are initially negative; however, the interband component is significantly smaller than in the $\delta 7$ case. We may also note that the interband acoustic component of the energy loss rate is too small to be shown on Fig. 10.38. It appears that 2–1 acoustic scattering is suppressed by the stronger 2–2 scattering. Consequently, the rates of de-/re-population in the simulation are very slow. Comparing Figs. 10.33 and 10.37 indicates that the depopulation rate of band 2 in the present case is over a factor of ten slower than that of band 3 in simulation $\delta 7$. Thus, contrary to our previous supposition, carrier trapping in the $\delta 8$ case is much more severe than for $\delta 7$. Table 10.3 gives values of the overall average energy at various times for the simulations $\delta 7$ and $\delta 8$, from which it is clear that cooling is slower in the latter case.

Simulation δ9: $\epsilon(t{=}0) = 0$, *band 2.*

Having found that carrier trapping in low energy states in band 2 is so effective, we will now proceed by examining the cooling of a carrier population generated at the energy minimum, where the trapping effect might be expected to be even stronger. Figs. 10.40–41 show the time dependence of the fractional populations and mean energies for this case, and Figs. 10.42–43, the energy loss response.

We see immediately that carrier trapping is *not* as severe as in the $\delta 8$ case. De-

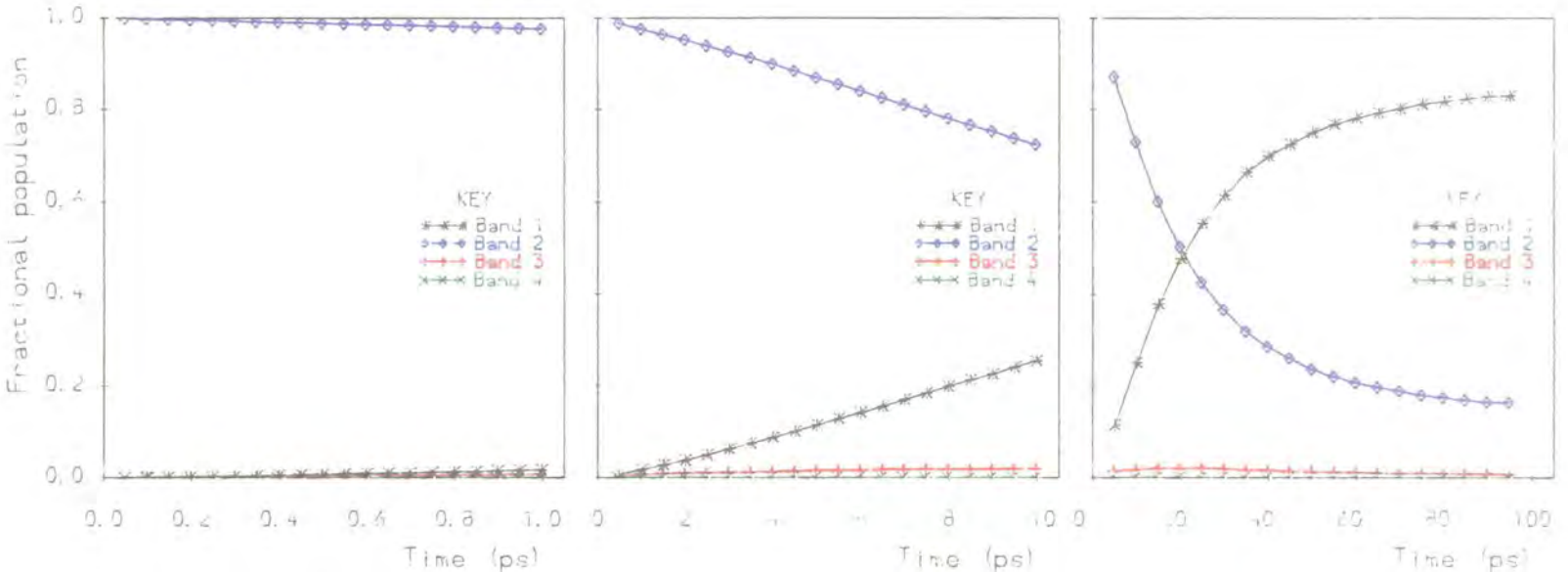

Fig 10.37 Simulation $\delta 8$. Time dependence of the fractional populations in bands 1–4. $T_L = 77\text{K}$; $\epsilon_{\text{ac}} = 2\text{meV}$.

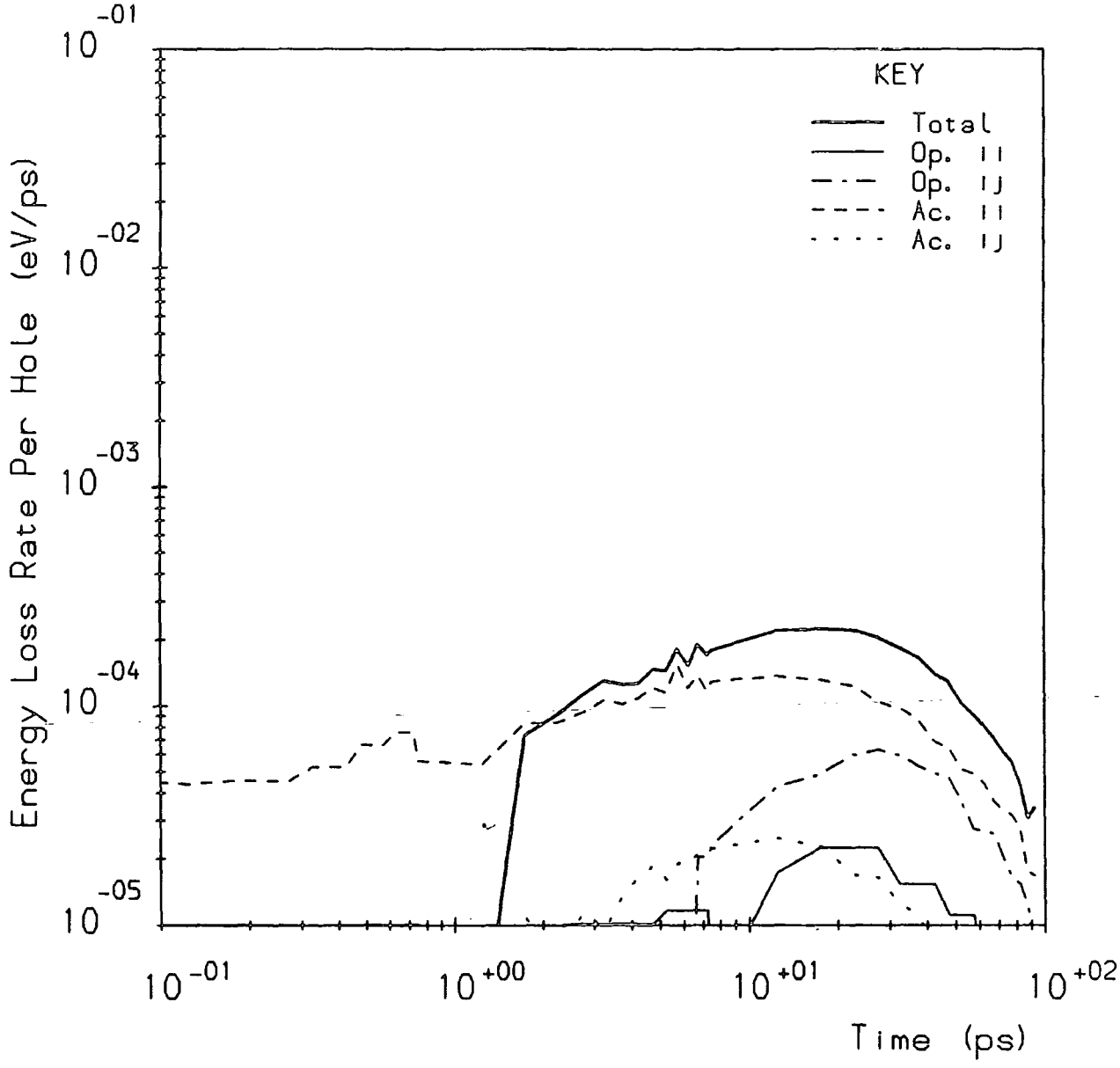

Fig 10.38 Simulation $\delta 8$. Time dependence of the hole energy loss rates. $T_L = 77\text{K}$; $\epsilon_{ac} = 2\text{meV}$.

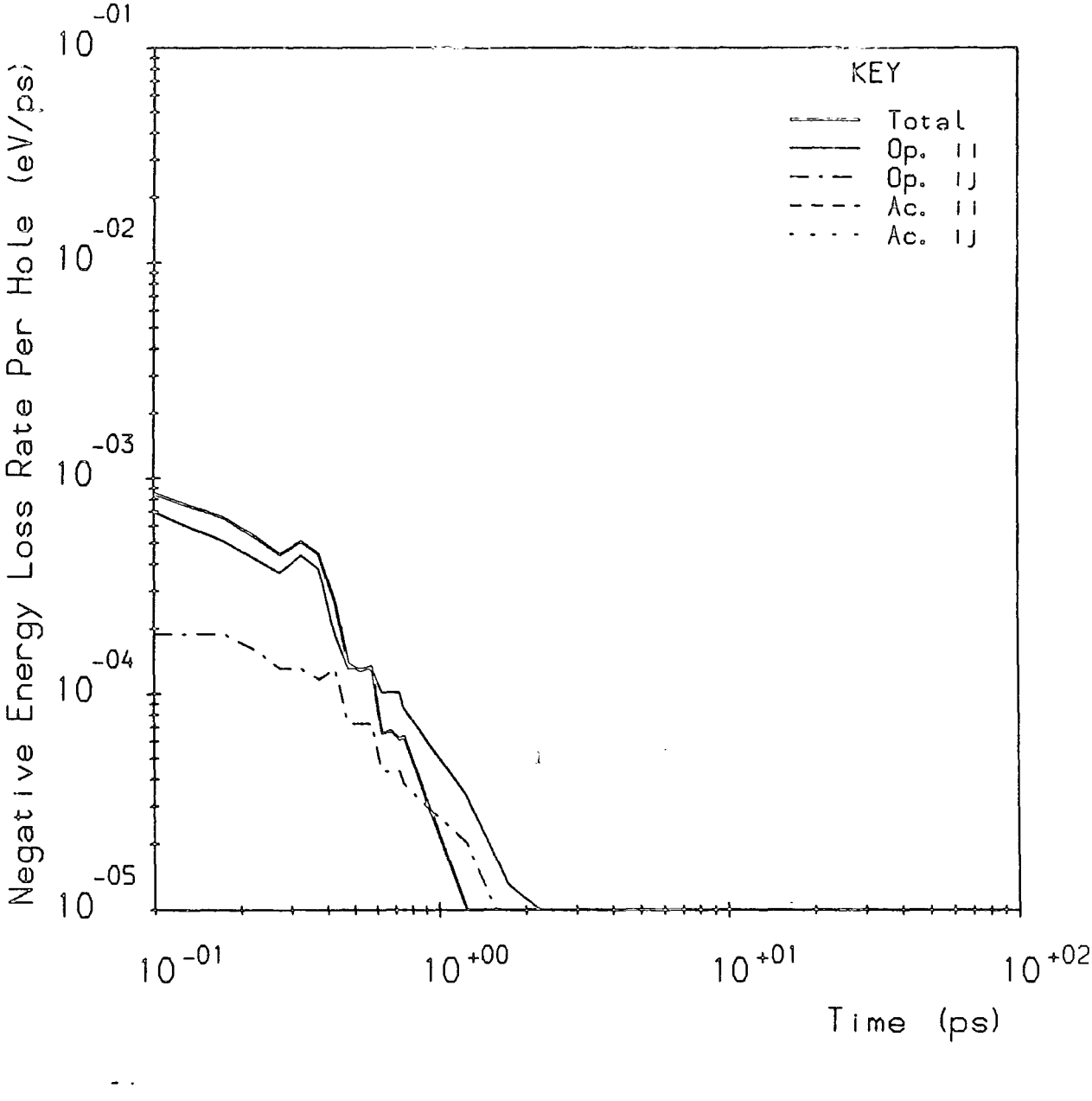

Fig 10.39 Simulation $\delta 8$. Negative portion of the energy loss response. $T_L = 77\text{K}$; $\epsilon_{ac} = 2\text{meV}$.

t(ps)	ϵ_{av} (meV)		
	$\delta 7$	$\delta 8$	mM2
0.0	24.34	24.34	24.34
0.5	24.74	24.64	19.22
1.0	24.87	24.68	17.87
1.5	24.89	24.66	17.22
2.0	24.81	24.63	16.79
2.5	24.76	24.57	16.43
5.0	24.11	24.26	15.65
7.5	23.47	23.82	15.22
10.0	22.87	23.32	14.90
95.0	12.69	12.89	12.00

Table 10.3: Energy Relaxation in the $\delta 7$, $\delta 8$ and mM2 Simulations

population of band 2 in the $\delta 9$ simulation occurs on a 10ps timescale (Fig. 10.40), rather than 100ps as in $\delta 8$ (Fig. 10.37). Although the rate of depopulation of band 2 in the $\delta 9$ simulation is slower than that of band 3 for $\delta 7$, the band 1 population after 10ps is actually greater in the former case, since the population relaxation process involves only two, rather than three bands.

On Fig. 10.43 it can be seen that the contributions to the energy loss rate from the intraband acoustic, and intra- and inter-band optical modes are all negative at early times. These contributions represent AC/PZ 2–2abs, and POP 2–2 and 2–1abs respectively. Also, on Fig. 10.42, it can be seen that the interband acoustic energy loss rate is large from the outset of the simulation. This represents AC 2–1em scattering, which was not observed in the $\delta 8$ case. Its appearance here is due to the much larger matrix element for scattering from states near the band minimum (see Fig. 6.15a). This scattering, together with the POP 2–1abs scattering, provide two effective means of depopulation of band 2 which were not prominent in the $\delta 8$ case. The AC 2–1em scattering persists until $t = 10$ps, and Fig. 10.42 shows a significant contribution to energy loss from intraband optical modes from $t = 0.3$ps onwards, representing optical phonon re-emission by carriers scattered into band 1 by POP 2–1abs.

The initial mean energy of carriers in band 2 is less than the thermal equilibrium value for the band. Therefore, a quantity of carriers equivalent to the thermal equilibrium population ($\langle \overline{n}_2 \rangle = 0.13$) must gain energy by acoustic phonon absorption. This phenomenon can be seen on Fig. 10.41, with the mean energy in band 2 rising over the 100ps timescale, whilst the overall average energy falls. The persistence of AC/PZ 2–2abs also explains the long delay observed before the onset of a net energy loss to intraband acoustic modes, compared to the $\delta 7$ simulation, and the relatively low value of this energy loss component thereafter.

We may summarise the results obtained in this section by saying that carrier trapping, in terms of both reduced energy loss rates and slower population relaxation, is more severe for carriers in the band 3 energy minimum than for carriers in the band 2 minimum. Depopulation of the initially occupied band occurs via interband optical absorption and interband acoustic scattering in both cases, but is more effective for carriers located at the band 2 minimum due to the larger matrix elements for the relevant processes. The population relaxation of carriers initially located in band 3 is also hampered by a transient overpopulation of band 2. However, carrier trapping in band 2 becomes considerably worse if the initial carrier population is located at an energy away from the band minimum, but still below the lowest optical emission threshold. This is due to smaller matrix elements for the key interband scattering processes, and their suppression by

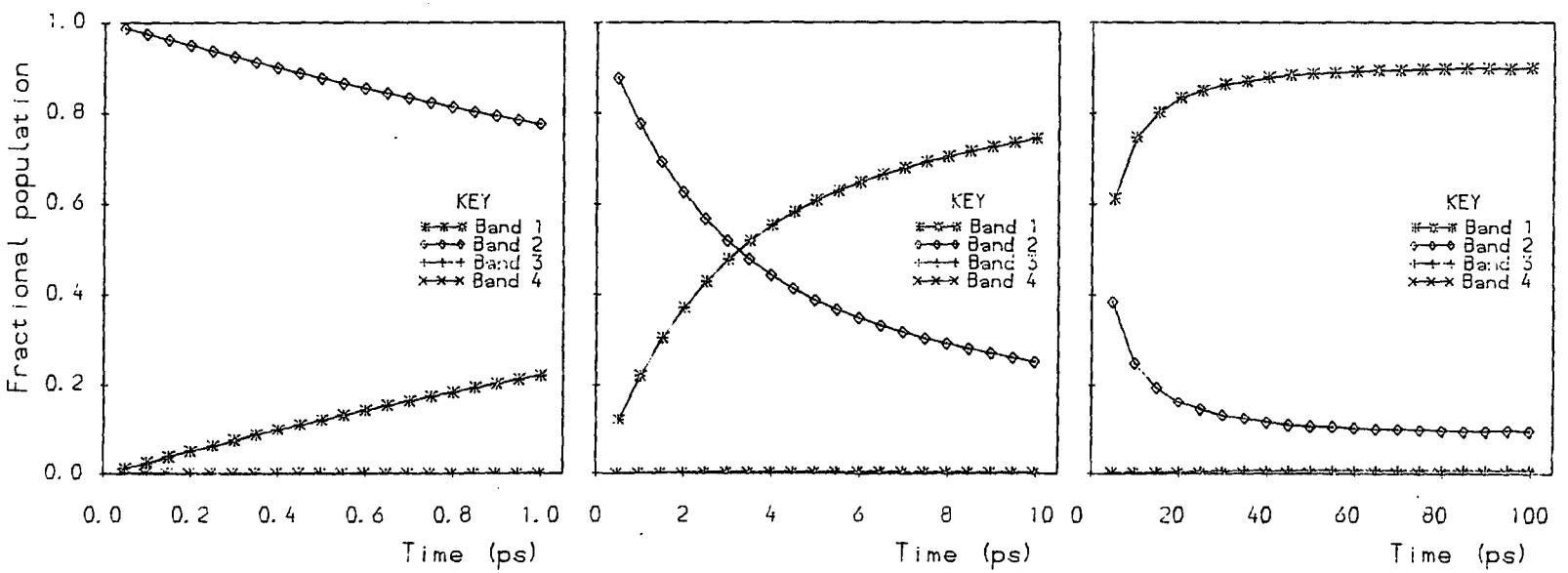

Fig 10.40 Simulation $\delta 9$. Time dependence of the fractional populations in bands 1–4. $T_L = 77\text{K}$; $\epsilon_{ac} = 2\text{meV}$.

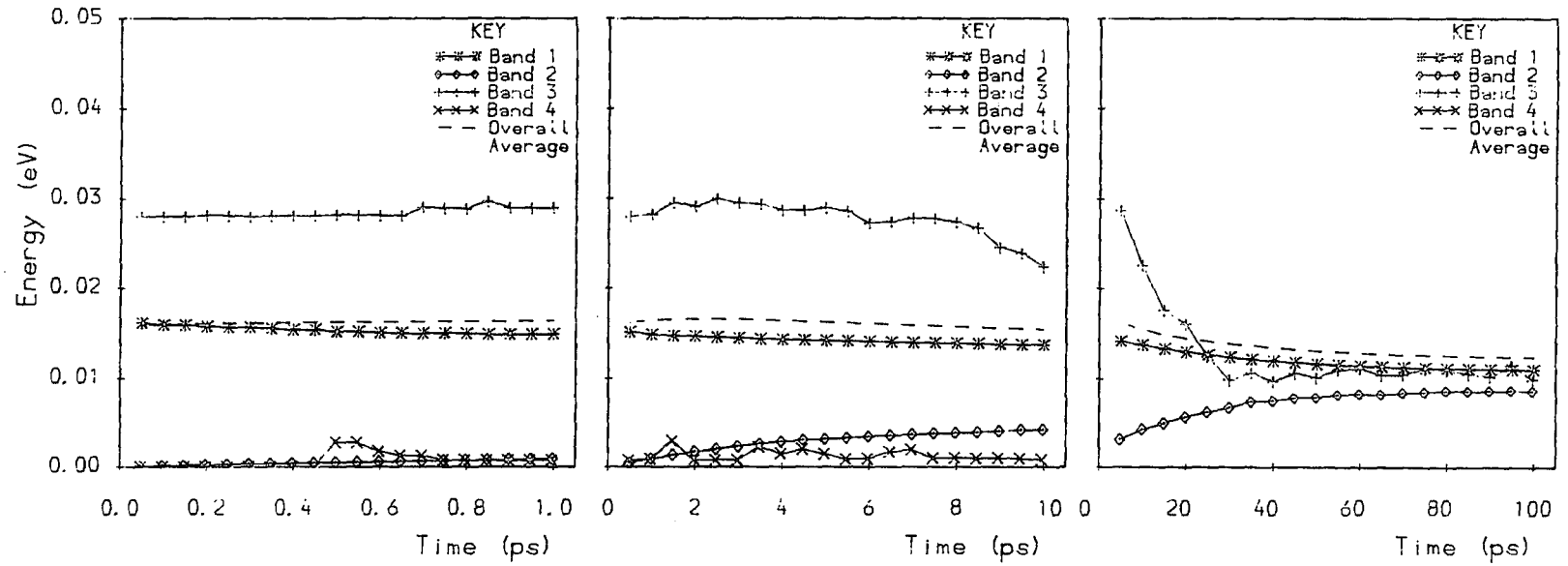

Fig 10.41 Simulation $\delta 9$. Time dependence of the mean energies in bands 1–4, and the overall average energy. $T_L = 77\text{K}$; $\epsilon_{ac} = 2\text{meV}$.

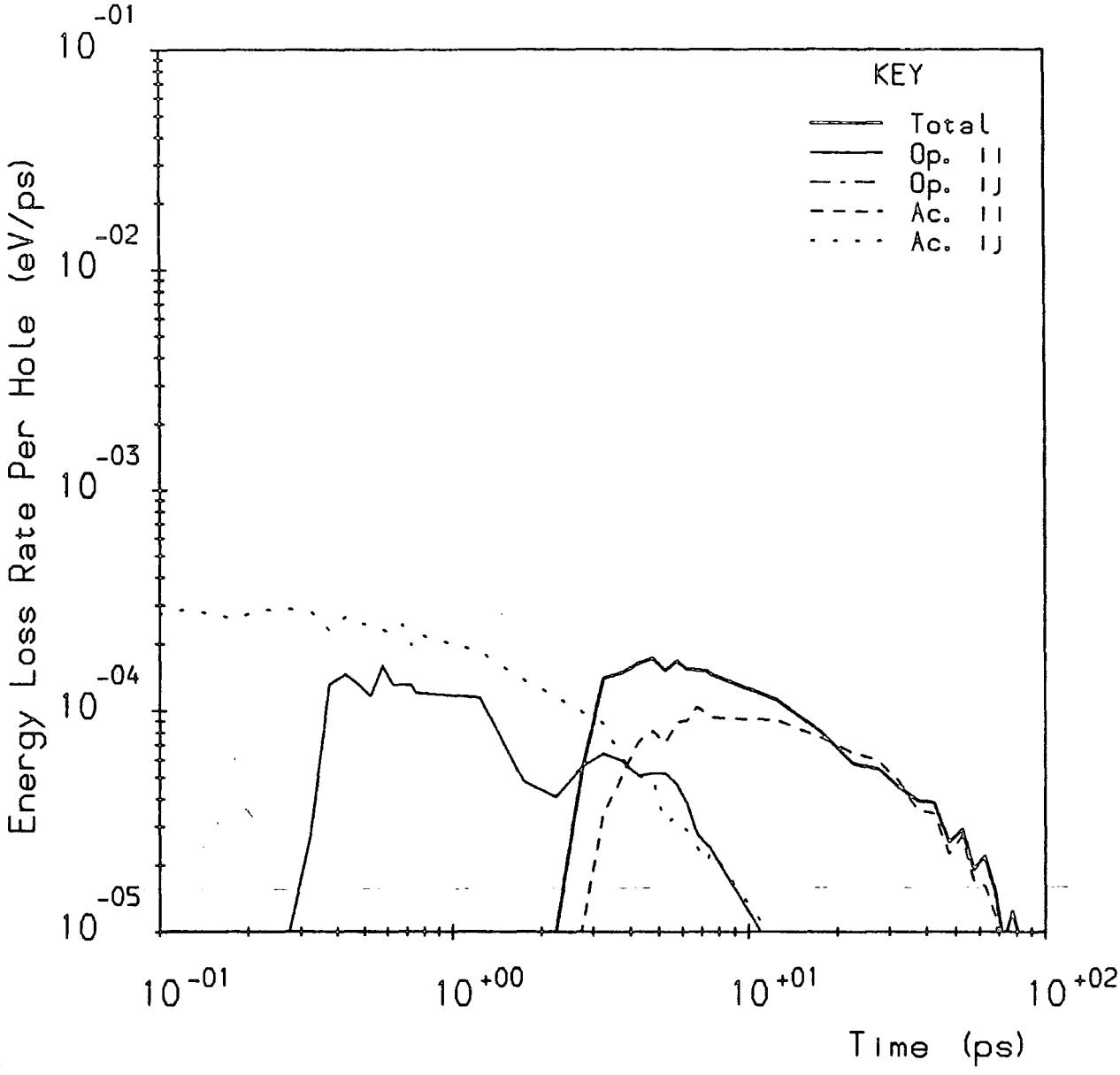

Fig 10.42 Simulation $\delta 9$. Time dependence of the hole energy loss rates. $T_L = 77\text{K}$; $\epsilon_{ac} = 2\text{meV}$.

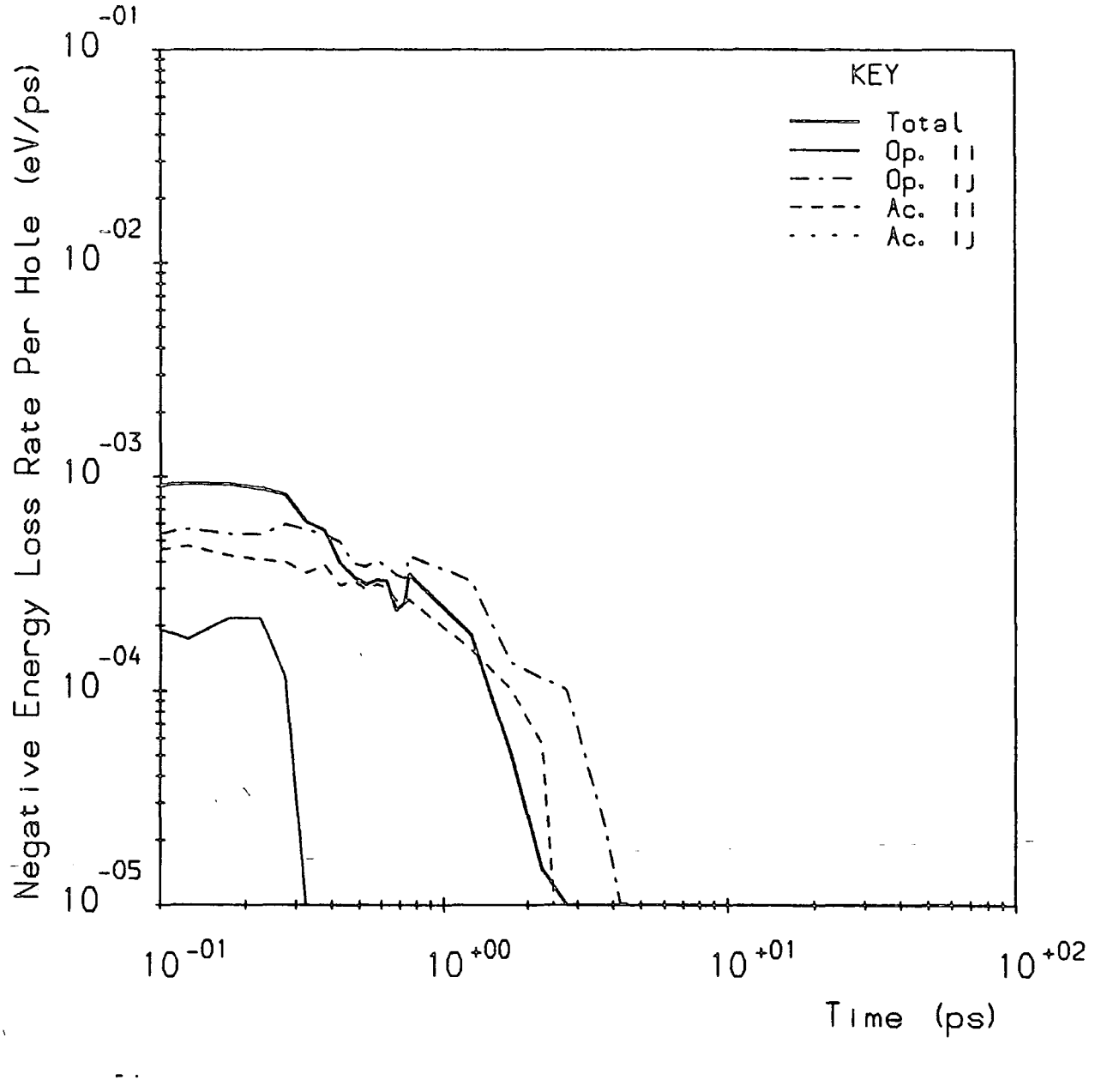

Fig 10.43 Simulation $\delta 9$. Negative portion of the energy loss response. $T_L = 77\text{K}$; $\epsilon_{ac} = 2\text{meV}$.

strong AC/PZ 2–2em scattering into the region of large density of states around the band minimum.

10B.6: Maxwellian Hole Distributions in the Acoustic Dominated Cooling Regime

Simulation sM3: $T_c = 56$K, *band 3.*

The carrier temperature for the initial distribution in this simulation was chosen to give a mean energy in band 3 midway between the band minimum and the lowest optical emission threshold at $\epsilon = 12$meV. Obviously this represents an unusual situation, since the temperature characterising a carrier distribution is expected to be greater than or equal to the lattice temperature, which, in this case, is 77K. However, the distribution used in the sM3 simulation can still be regarded as a model of that resulting from photoexcitation of carriers in band 3 in the presence of a degree of intraband carrier-carrier scattering, which will serve to distribute carriers across a range of energies. We deliberately chose such a low carrier temperature in order to restrict the range of carrier energies to the acoustic dominated cooling regime.

The energy loss plot for the sM3 simulation is shown in Fig. 10.44. The energy loss rate is, at all times, positive, in contrast to the rates for the δ7–9 simulations. However, the intraband optical component is still negative during the first picosecond, indicating that optical phonon absorption by carriers near the band 3 minimum still occurs, as in the δ7 simulation. The large contribution of the interband optical modes to energy loss suggests that some carriers do reach the lowest optical emission threshold in band 3: however, the maximum energy loss rate in this simulation is around a factor of 100 less than that for simulations in which cooling of the entire carrier population is dominated by optical scattering.

The time dependences of the fractional populations for the simulation are shown in Fig. 10.45. Depopulation of band 3 occurs over approximately the same timescale as for the δ7 case, suggesting that the number of carriers reaching the 3–1 optical emission threshold is, indeed, small. Transient overpopulation of band 2 is observed at around 20ps, consistent with the result for δ7. We may conclude that, whilst several similarities exist between carrier cooling in the δ7 and sM3 simulations, both energy loss and the return of the fractional populations to their equilibrium values are faster in the latter case, due to POP 3–1em scattering of the small number of carriers which are able to reach the threshold.

Simulation mM2: $T_c = 173$K

The carrier temperature for the initial multiband Maxwellian distribution in this simulation was chosen to give an overall average carrier energy equivalent to that in the simulations δ7 and δ8. Fig. 10.46 shows the energy loss rates for the simulation, and Fig. 10.47, the fractional population of each of the four bands. The band 1 population at t=0 is high ($\langle \overline{n}_1 \rangle \approx 0.67$), and therefore the simulation cannot

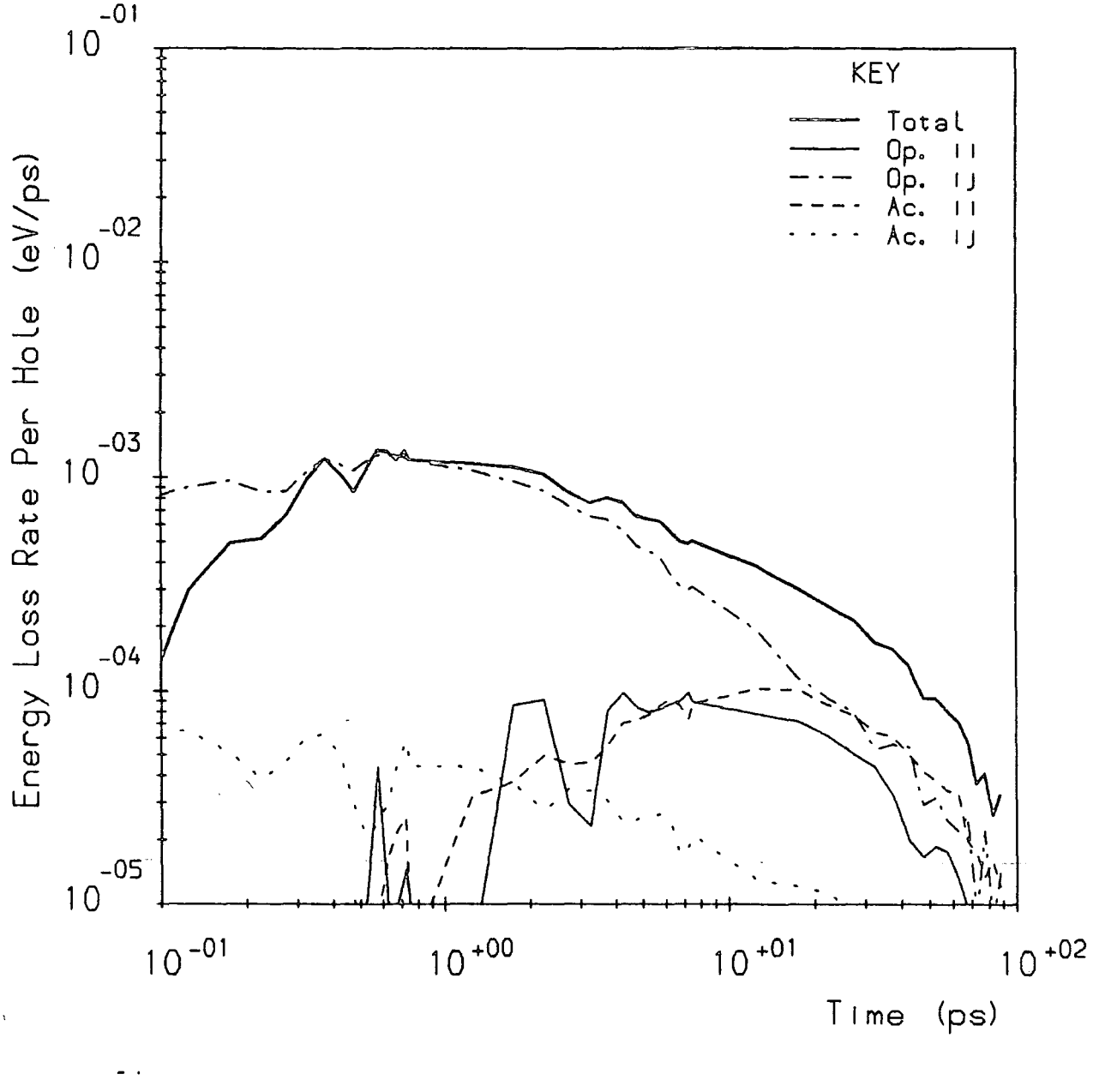

Fig 10.44 Simulation sM3. Time dependence of the hole energy loss rates. $T_L = 77\text{K}$; $\epsilon_{ac} = 2\text{meV}$.

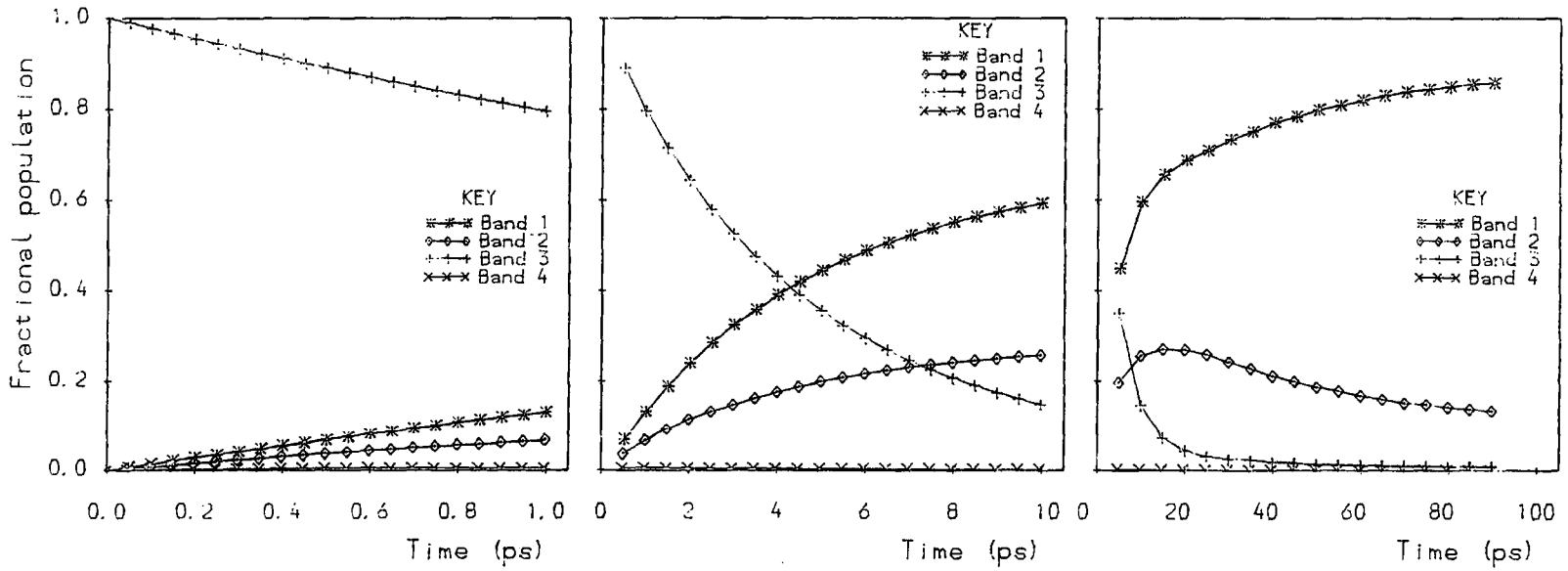

Fig 10.45 Simulation sM3. Time dependence of the fractional populations in bands 1–4. $T_L = 77\text{K}$; $\epsilon_{ac} = 2\text{meV}$.

be expected to bear much resemblance to the $\delta 7$ or $\delta 8$ cases. Population relaxation is quite monotonic, with no overshoot effects, and the fractional populations have virtually attained their thermal equilibrium values within 100ps. Energy loss is dominated by optical scattering, indicating that a fair proportion of the carrier population lies above the lowest optical emission threshold in each of bands 1–3. Indeed, the mM2 energy loss plot is very similar in form to the plots for the sM1 and mM1 simulations, although the initial energy loss rate here is almost a factor of ten smaller. A breakdown of the scattering events occurring in the simulation reveals that the principal scattering processes, in the early stage of the simulation, are (in order of decreasing strength) POP 2–1em, 1–1em and 2–2em. Fig. 10.46 also shows intraband acoustic scattering (principally AC 1–1em) present throughout the simulation, with a weak optical/acoustic energy loss crossover at around 10ps.

Table 10.3 gives values of $\langle \epsilon_{av} \rangle$ at various times in the simulation, for comparison with those for simulations $\delta 7$ and $\delta 8$. We may conclude that carrier cooling, in terms of both energy loss and population relaxation, is significantly faster for the mM2 case. This is mainly due to the large carrier population already present in band 1 at early times, and to the substantial population of carriers in states above the optical emission thresholds in the latter case. Consequently, despite the equivalence of initial average energies for the $\delta 7$, $\delta 8$ and mM2 simulations, the latter is distinct from the two former cases in that energy loss is clearly dominated by optical, rather than acoustic phonon modes.

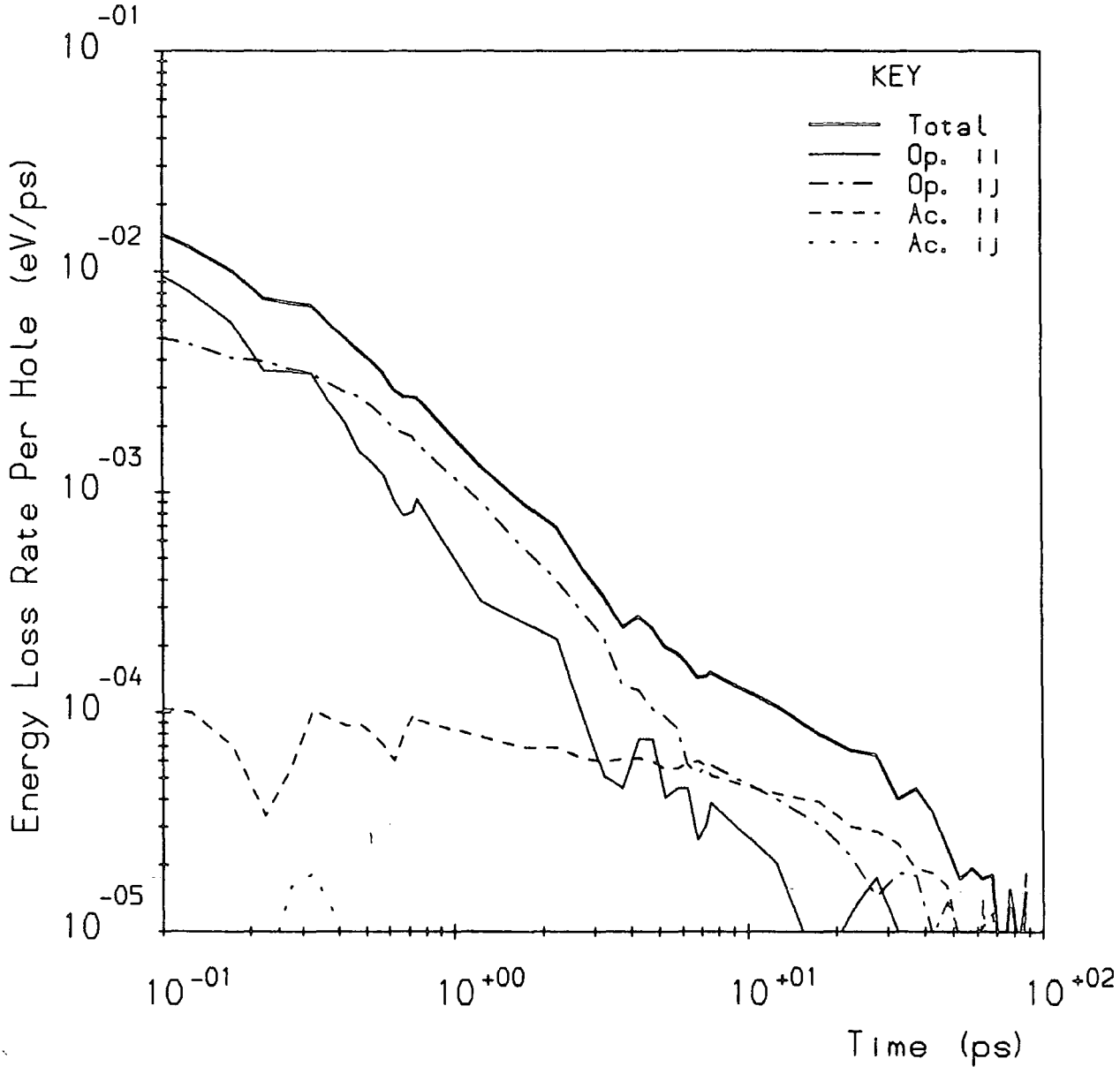

Fig 10.46 Simulation mM2. Time dependence of the hole energy loss rates. $T_L = 77\text{K}$; $\epsilon_{ac} = 2\text{meV}$.

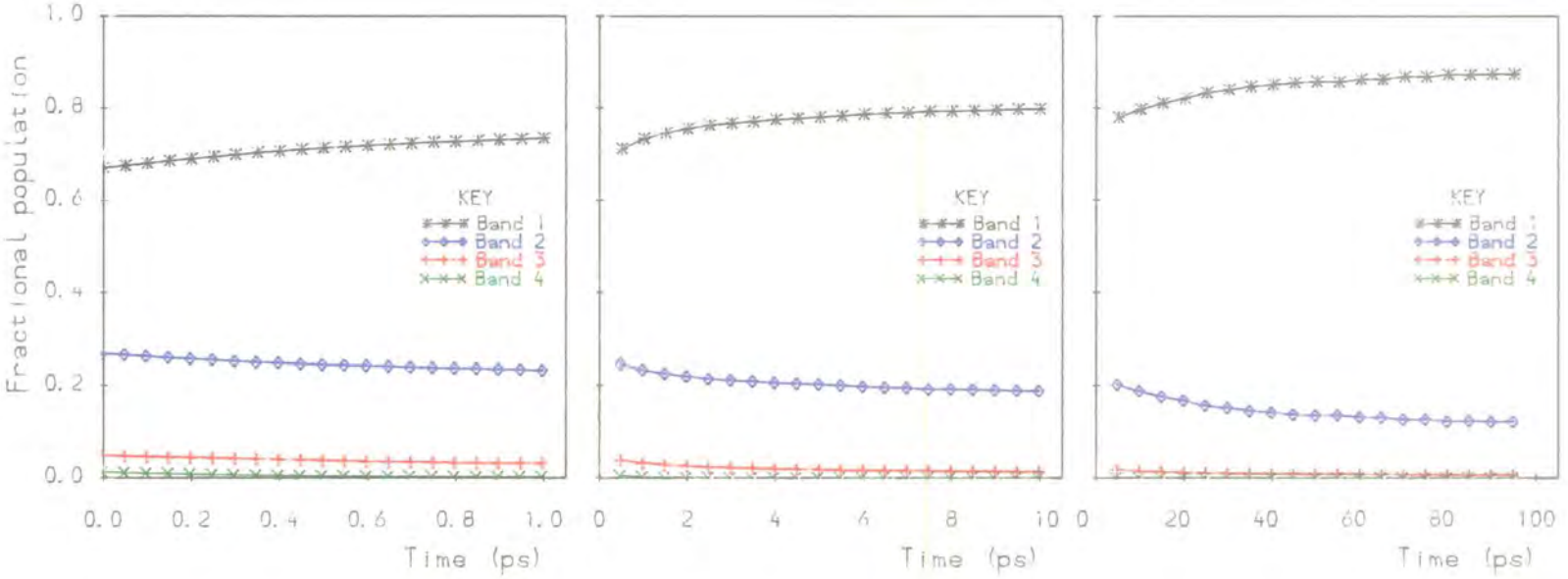

Fig 10.47 Simulation mM2. Time dependence of the fractional populations in bands 1–4. $T_L = 77\text{K}$; $\epsilon_{ac} = 2\text{meV}$.

10B.7: Cooling of a Hole Population at the Lowest Optical Phonon Emission Threshold

Simulation δ10: $\epsilon(t{=}0) = 14.1\text{meV}$, *band 3;* $\epsilon_{\text{av}} = 38.44\text{meV}$

The energy of the initial monoenergetic carrier distribution in this simulation was chosen to be just above (one acoustic phonon energy above) the lowest optical emission threshold in band 3. This will enable us to examine the cooling processes experienced by carriers excited above the threshold. Figs. 10.48–49 show the time dependence of the fractional populations and mean energies for this simulation, and Figs. 10.50–51 show the energy loss rates.

Fig. 10.50 shows that energy loss in the early part of the simulation is almost entirely due to interband optical scattering (POP 3–1em). However, the initial ($t = 0.1$ps) rate is over an order of magnitude lower than that in simulations such as δ1–5, since the POP 3–1em scattering rate is rather small. Fig. 10.48 shows that the population in band 3 decays somewhat more quickly than in simulation δ7: however, the rate of depletion of band 3 in the present case is still almost a factor of ten slower than that of band 4 in the δ1 and δ2 simulations. The population of band 2 remains small throughout the first 10ps of the δ10 simulation; carriers by-pass the band due to the prevalence of 3–1 optical scattering. Consequently, an overpopulation of band 1 occurs, with a maximum value of $\langle \overline{n}_1 \rangle$ attained at $t = 15$ps. This is the same kind of response as was observed in the δ6 simulation, for the cooling of a carrier population generated above the $2 \times \hbar\omega_{\text{op}}$ threshold. Fig. 10.49 shows that the overall average energy falls quite briskly; reaching a minimum value, below that of thermal equilibrium, at $t \approx 15$ps. The band 1 mean energy also falls below its thermal equilibrium value. Clearly, POP 3–1em scattering acts to repopulate the low energy states in band 1 at a rate faster than that at which thermalisation can be achieved by intraband acoustic scattering: thus, as in the δ6 case, a transient 'supercooling' of the carrier system occurs. Correspondingly, the total energy loss rate becomes negative after around 15ps (Figs. 10.50–51). Fig. 10.51 shows that the carrier system is absorbing energy from both intraband acoustic (AC 1–1abs) and intraband optical (POP 1–1abs) phonon modes.

A surprising feature of the energy loss response is the negative contribution from intraband optical modes during the first 0.5ps of the simulation. This represents POP 3–3abs scattering, which indicates that this process is stronger than the various acoustic processes in this region of band 3. Subsequent 3–1 acoustic scattering leads to the formation of a carrier population in the high energy states in band 1, where POP 1–1em, and, to a lesser extent, POP 1–2em are strong. The former process accounts for the large contribution to energy loss from the

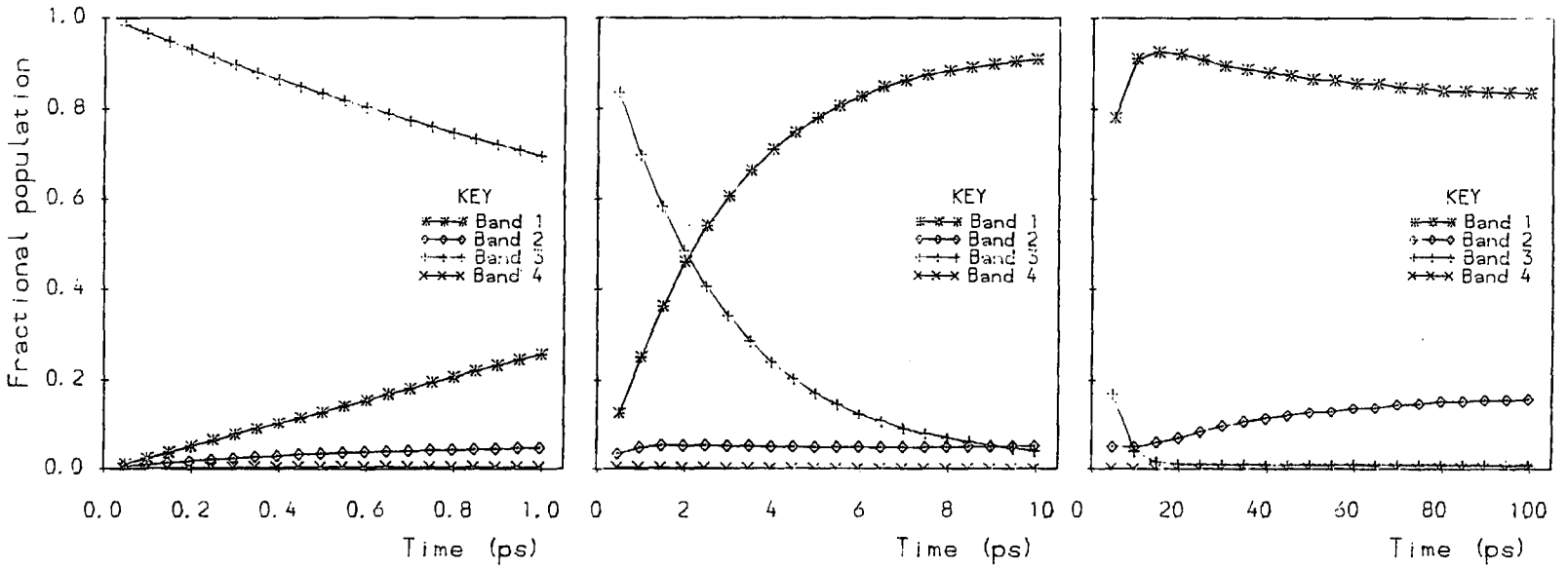

Fig 10.48 Simulation $\delta 10$. Time dependence of the fractional populations in bands 1–4. $T_L = 77\text{K}$; $\epsilon_{ac} = 2\text{meV}$.

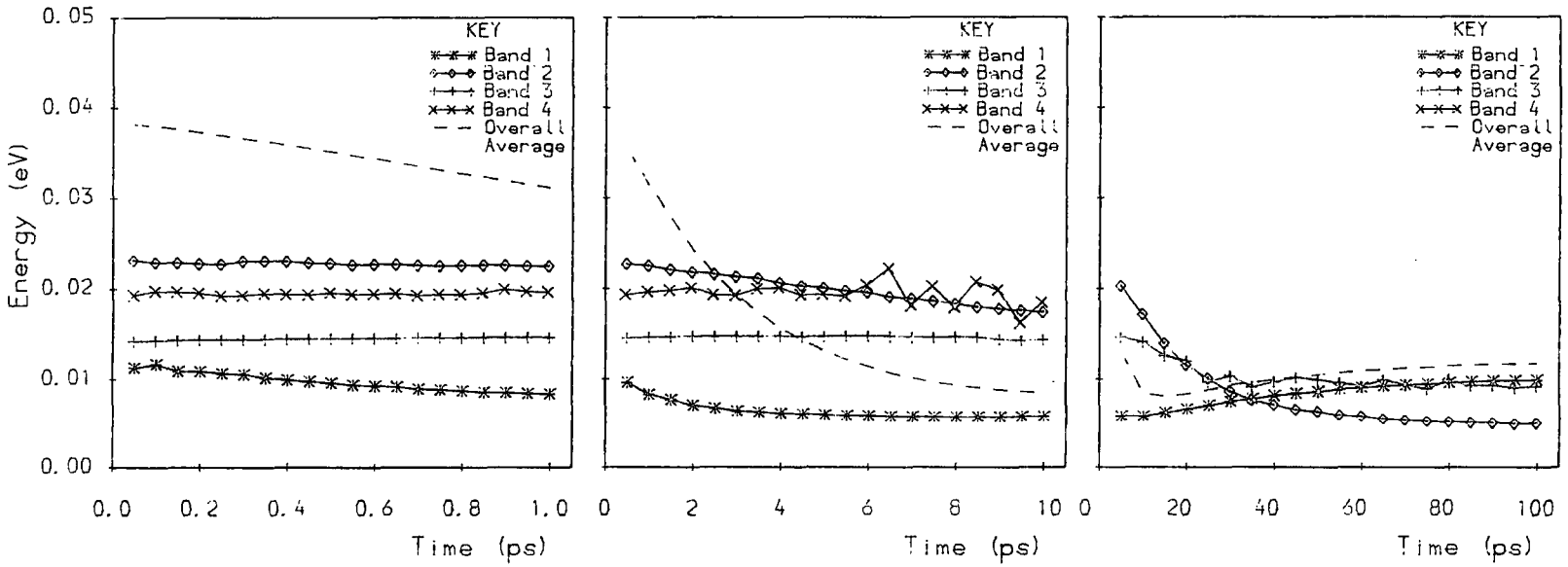

Fig 10.49 Simulation $\delta 10$. Time dependence of the mean energies in bands 1–4, and the overall average energy. $T_L = 77\text{K}$; $\epsilon_{\text{ac}} = 2\text{meV}$.

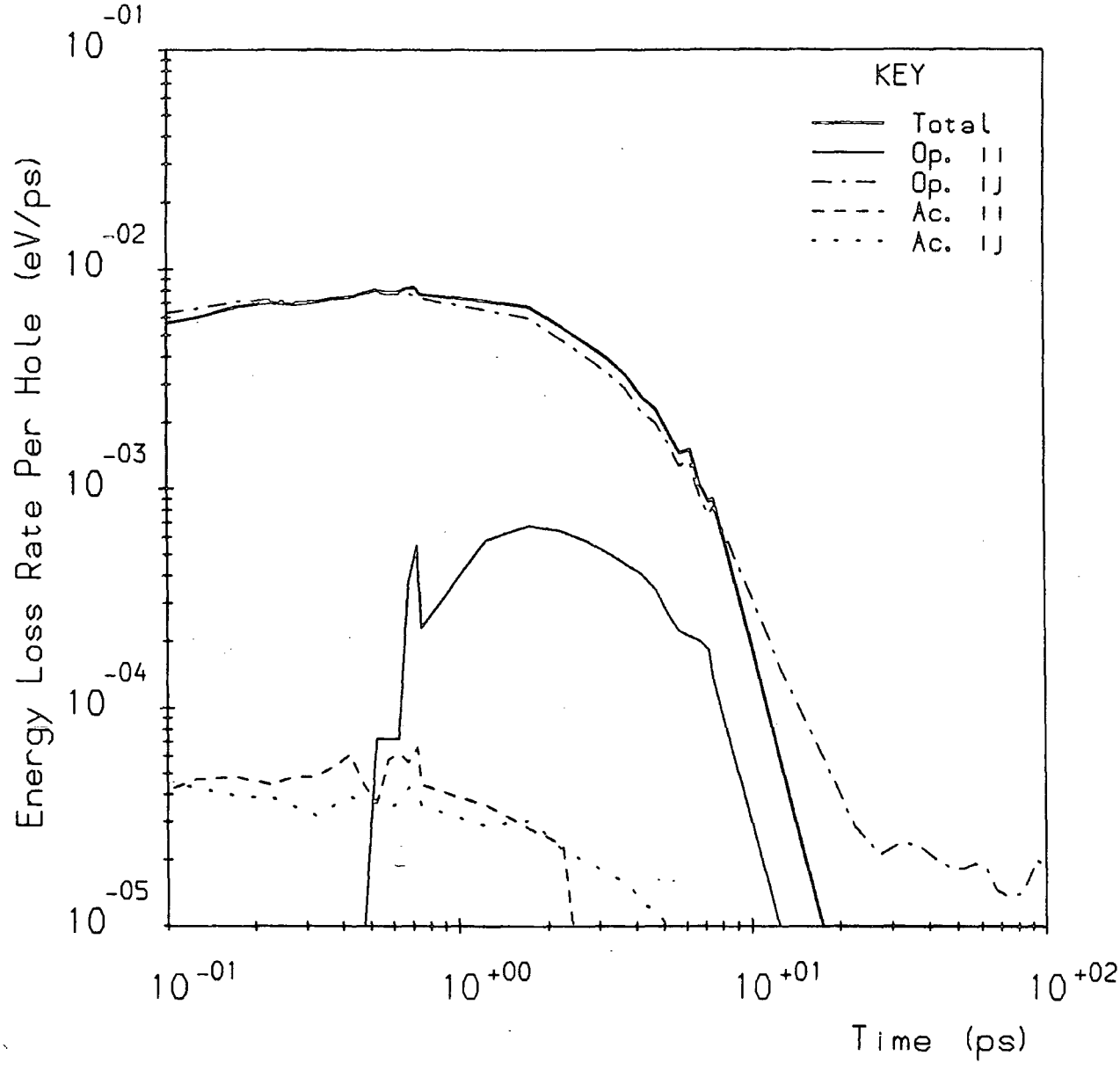

Fig 10.50 Simulation $\delta 10$. Time dependence of the hole energy loss rates. $T_L = 77\text{K}$; $\epsilon_{\text{ac}} = 2\text{meV}$.

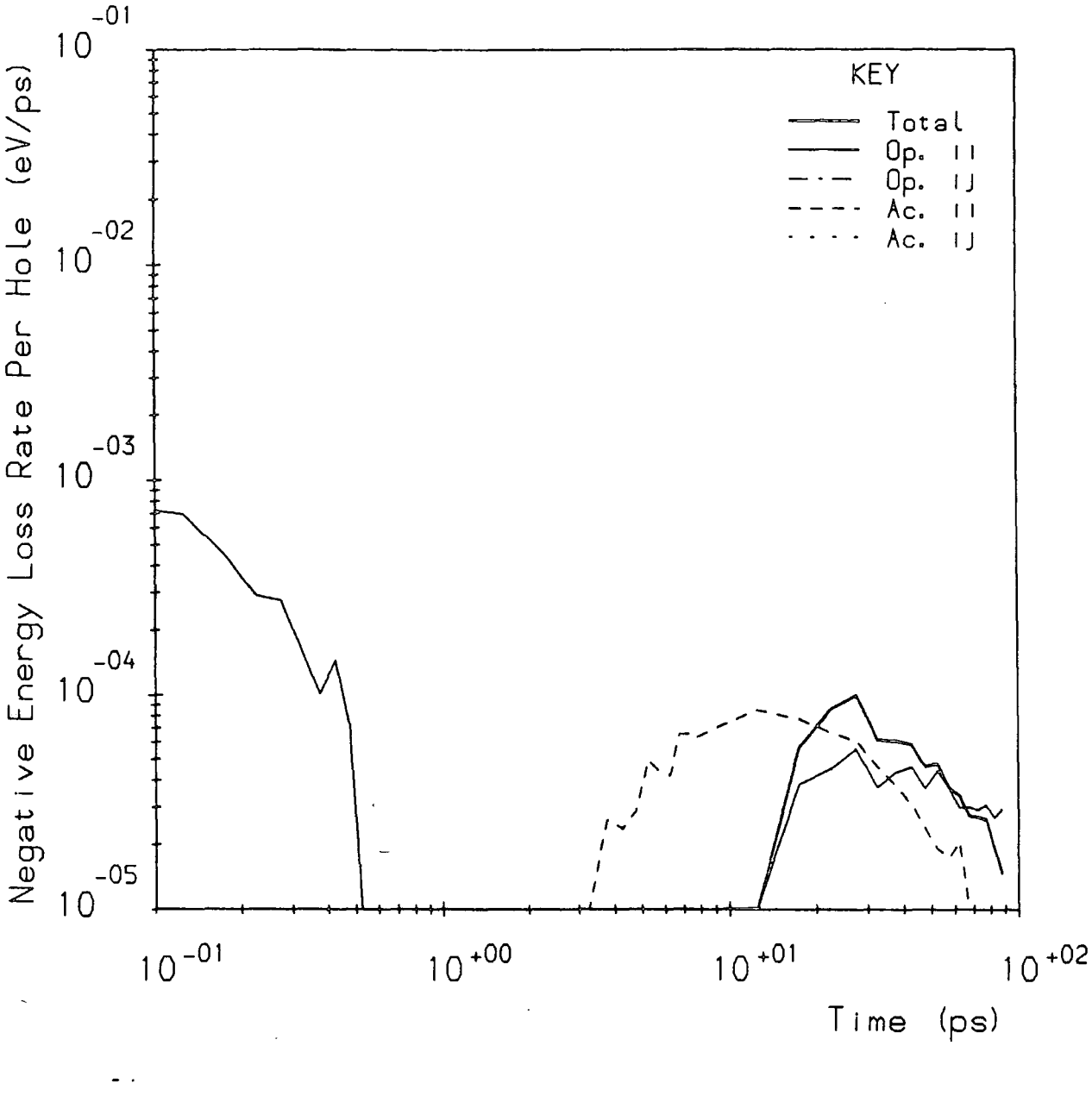

Fig 10.51 Simulation $\delta 10$. Negative portion of the energy loss response. $T_L = 77\text{K}$; $\epsilon_{ac} = 2\text{meV}$.

intraband optical modes after $t = 0.5$ps.

Repopulation of band 2 proceeds via net 1–2 acoustic scattering, and POP 1–2em (represented by the residual contribution of the interband optical modes to energy loss for $t > 15$ps). Although the return of the band 1 and 2 populations and energies to their thermal equilibrium values is somewhat slower than in the $\delta 6$ case, the population of band 2 still rises above its thermal equilibrium value after 100ps, and we predict a shift from net 1–2 to 2–1 acoustic scattering to complete the relaxation process.

10C SUMMARY

Having described, in some detail, simulations of the cooling of a range of quantum confined hole distributions, we are now in a position to take a general overview of our results, and to offer some answers to the questions posed in Section 10A.

Concerning our question (i) of Section 10A, we have seen that hole cooling in the quantum confined valence band system is fastest for an initial distribution located in the lowest band (section 10B.2). In the early phase of cooling ($t < 1$ps), the intraband optical scattering is important, giving faster energy loss for carrier populations generated in both bands 1 and 2, compared to that for equal energy populations in the upper bands, 3 and 4.

However, a crossover from optical to acoustic dominated energy loss was observed in the cooling of the high energy, monoenergetic carrier distributions in all the simulations δ1–5, occurring between $t = 0.7$ and 3.0ps. The importance of acoustic scattering at such early times is not a feature associated with the cooling of *electrons* in quantum wells. It occurs here, firstly, because the optical modes are sufficiently strong as to scatter carriers below the lowest optical phonon emission threshold within a very short time, and secondly, because the intraband acoustic (AC and PZ) scattering rates for the quantum confined holes are also large compared to those for electrons.

Beyond the crossover point, cooling was dominated by AC 1–1em in all cases, and thus was still fastest in the δ5 simulation, where the carrier population was located in band 1 at t=0. We commented in section 10B.2, that an important factor controlling the overall energy loss rate for any non-equilibrium carrier distribution will be the efficiency with which carriers can be scattered into band 1. For this reason, cooling of populations generated in band 4 is relatively fast, since interband optical scattering is quite strong.

Regarding the issue of population relaxation (question (ii) in Section 10A), we observed by far the fastest rates of depopulation in band 4. Assuming the decay of the band 4 populations in simulations δ1 and δ2 to be exponential, during the first picosecond, we may deduce lifetimes for interband scattering of $\tau = 0.37$ and 0.42ps respectively. These values are considerably smaller than those reported by Seilmeier *et al.* (1987) for the lifetimes of quantum confined electrons against intersubband optical phonon scattering. We found that the rate of depopulation of band 3 was typically ten times slower than for band 4, and that for band 2, lesser by a further factor of ten. This was predominantly due to the trapping of carriers in states below the lowest optical emission threshold in both bands 2 and 3 (see questions (iii) and (iv) in Section 10A). The trapping was augmented, in band 3, by the particularly small scattering rates near the band minimum, and

in band 2, by strong intraband scattering (via both optical and acoustic modes). The latter is associated with the large matrix elements for the POP 2–2em and AC 2–2em processes, and also with the extremely large density of states at the band minimum (see questions (v) and (vi) of Section 10A). Indeed, we remarked in section 10B.2, that even high energy populations in band 2 were subject to a carrier trapping effect, due to the suppression of 2–1 optical scattering by strong POP 2–2em.

Obviously, carrier trapping phenomena influence both population relaxation and the energy loss rates. We observed delayed energy loss in the $\delta 2$, compared to the $\delta 1$ simulation, due to the accumulation of a large population in the band 3 minimum in the former case. Also, the bottleneck of carriers which formed in the band 2 minimum in the $\delta 4$ simulation led to particularly low energy loss rates immediately following the optical/acoustic energy loss crossover.

The formation of a residual carrier population around the band 4 minimum was also observed (section 10B.4), due to the large density of states in this region. However, this population has a relatively short lifetime, since interband scattering via optical modes is allowed.

We may conclude that the trapping of carriers is generally associated with the exclusion of interband optical scattering in the various band minima, and this is consistent with the observations of Oberli *et al.* (1987,1988) for quantum confined electrons (see Section 10A). However, for the quantum confined valence band system, carrier trapping is enhanced by features related to band mixing; in particular, the existence of regions of extremely large densities of states at off-zone-centre band minima.

For the cooling of a Maxwellian distribution of carriers (the sM- and mM-simulations), we found that some of the distinctive features observed in the δ cases were somewhat 'smeared out', as we might have expected. Cooling was dominated by optical modes for almost the entire duration of the return to thermal equilibrium; giving rise to faster cooling rates for all but the very early phase of the simulations. Carrier trapping was still observed in the sM-simulations, but not in the mM cases, where most of the carriers are located in band 1 at t=0.

When a large population of carriers was initially located just above an optical phonon emission threshold, we observed the development of an excessively large population in the low energy states in band 1, with a consequent undershoot of both the band 1 mean energy and the overall average energy below their thermal equilibrium values. We described this phenomenon as a transient supercooling of the carrier system. The effect was only observed in the δ-simulations, since, for the sM and mM cases, the spread of carrier energies is too large, with a large

proportion of the initial population located *below* the relevant threshold. However, for any circumstance in which a large population did develop around an optical emission threshold, the supercooling effect should survive even in the presence of intraband carrier-carrier scattering, since this process is elastic, and therefore could not excite the low energy overpopulation in band 1 to higher energy states. Of course, we have not considered Pauli exclusion, which will tend to restrict the extent of overpopulation of any localised range of energy states.

Many of the effects discussed will be dependent on the quantum well width L. Although we have only presented results for one particular width ($L = 100$Å), we may use these results to make same general predictions concerning hole cooling in wells of different sizes. Obviously, if the well width is increased, then the band edges will shift downwards in energy (towards the base of the well). Therefore, for a sufficiently wide well, the band 4 minimum will lie below the lowest optical phonon emission threshold, and carrier trapping will then occur in this band also. As mentioned above, this effect will be enhanced by the large density of states at the band 4 minimum (and throughout the b region of the band), leading to the possibility of even larger carrier lifetimes against interband scattering than in either of bands 2 or 3.

Conversely, if the well width is reduced sufficiently, then, firstly band 3, and subsequently band 2 will rise above the lowest optical emission threshold, thus eliminating carrier trapping effects in these bands. Also, as the well width is reduced, the bands will move further apart in energy; hence the effects of mixing will be diminished. This will eventually shift the minima in bands 2 and 4 back to the zone centre, thus removing the large peaks in the density of states in these regions. Furthermore, the magnitudes of the inter-anticrossing-band matrix elements (see section 6C.1) are likely to be reduced; hence, although interband optical scattering will be more prevalent in cooling, the principal scattering rates will be smaller than for the 100Å case.

CHAPTER 11
CONCLUSIONS

In this chapter, we will first consider the achievements of the work described in this thesis. Secondly, we will discuss some of the approximations involved, and finally, we will make some suggestions for future work.

We have developed, from first principles, a set of Monte Carlo programs to simulate the transport and relaxation of quantum confined holes. As a first example, we considered the specific case of a 100Å GaAs/AlAs lattice matched single quantum well. We have used a 4-band k.p scheme to describe the detailed effects of valence band mixing in the quantum well on the energy band dispersions and hole wavefunctions, and hence on the matrix elements and transition rates for the principal hole-phonon scattering processes. In Chapter 5, we showed how the 4-band k.p scheme could be incorporated in a calculation of the quantum confined hole-phonon scattering rates. In Chapter 6, we presented a comprehensive set of results for the quantum confined hole-phonon scattering matrix elements for acoustic (deformation potential), non-polar optical, polar optical, and piezoelectric phonon modes. We found that, in general, the matrix elements varied markedly with the wavevector of the scattering states, especially for those states located near the so-called anticrossing regions of the bands, whose character is susceptible to the most rapid variation with wavevector. We noted the overall dominance of the intraband matrix elements, especially for acoustic scattering; and for optical phonons, the strength of the transitions between adjacent and anticrossing bands, in which the character of the scattering states showed the closest correlation.

In Chapter 7, we presented results for the quantum confined hole-phonon scattering rates in the first four valence subbands of the GaAs/AlAs quantum well. The rates exhibited distinctive spike-like features, due to the singularities in the density of states at off-zone-centre energy minima in certain subbands. The principal optical phonon emission threshold was not found to be so abrupt as in the case of quantum confined electrons in a parabolic band, but, due to the structure in the density of states, a large polar optical scattering rate was obtained for scattering from states just above the threshold energy. This rate was found to be larger than the principal intraband (heavy hole - heavy hole) polar optical scattering rate for holes in bulk GaAs at the same lattice temperature (Chapter 4).

In Chapter 8, we described some of the computational details of our model, and in Chapter 9, we reported its use in the simulation of the steady state electric field heating of quantum confined holes at a lattice temperature of 77K. We observed a reduction in both the hole drift velocity and the low field hole mobility, compared to the results obtained for bulk GaAs (Chapter 4). This corresponds

to the differences in the 2D and 3D scattering rates described above, and is also in accordance with the experimental predictions of Störmer *et al.* (1984). We obtained energy distributions of holes in the first four subbands of the quantum well. In all cases, the low energy portion of the distribution was modified by structure associated with the density of states, and large carrier populations were observed in the off-zone-centre band minima. Similar structure has also been observed in photoluminescence spectra, such as that of Da Costa *et al.* (1987). Using the high energy tails of the carrier distribution functions, we were able to deduce effective carrier temperatures for holes in each of the four bands. The temperatures in three of the bands were found to be very similar for any given electric field, indicating the importance of interband scattering in carrier thermalisation. In the remaining case (band 3), consistently lower carrier temperatures were observed, although this may be a consequence of the numerical uncertainties associated with the derivation of these temperatures. In all cases, the carrier temperatures were found to be much lower than the values of $\langle \epsilon_{\rm av} \rangle / k_B$ appropriate to carriers in a parabolic band in 2D.

The steady state energy loss rate for the quantum confined holes showed a temperature dependence similar to that predicted for polar optical dominated scattering in a simple 2D band, in accordance with the trend also observed experimentally by Shah *et al.* (1985). Our results deviated from the exponential dependence at low carrier temperatures, due to extremely strong polar optical scattering near its threshold, and due to the non-Maxwellian form of the carrier distribution at low energies.

We also reported, in Chapter 9, the observation of an anomalous repopulation of the lowest subband on electric field heating in the steady state, due to the dissipation of carrier energies by strong intraband polar optical scattering.

In Chapter 10 we studied, in some detail, the cooling of a multisubband system of quantum confined holes of various initial energy distributions. We were able to use our ensemble Monte Carlo program to resolve the energy loss rate into any number of constituent components; in particular we showed, for each simulation, the time dependence of the energy loss rates due to intra- and inter-band scattering by both optical and acoustic phonons.

We observed a number of features: the dominance of intraband scattering; the existence, in many cases, of a crossover between optical and acoustic phonon dominated energy loss after a certain time interval, and the large magnitude of the acoustic energy loss rates compared to those in the steady state. We found evidence for the trapping of carriers in the subband minima — particularly those lying below the optical phonon emission threshold — and saw that this phenomenon

was enhanced by features related to band mixing; especially, the presence of off-zone-centre band minima where the density of states is extremely large.

A transient supercooling of the carrier population was also observed, whenever the initial distribution was concentrated just above an optical phonon emission threshold.

Approximations

Our principal goal of including, in our Monte Carlo simulations, a realistic description of the quantum confined bandstructure and scattering matrix elements has been achieved at the expense of a number of approximations. Firstly, we have assumed the quantum confined bandstructure to be isotropic in the 2D wavevector plane. This approximation was discussed in Chapter 6, and, whilst we would expect some variation in both the band energy dispersions and the scattering matrix elements with direction in k-space, the effects on the results summarised above are not expected to be significant. Secondly, we have assumed, as described in Chapter 5, that the phonon modes in the quantum well have the same form as in the bulk. Whilst this is not the case, the approximation is commonly used; the derivation of quantum confined phonon modes being a major calculation in itself.

Our simulations do not include any form of carrier-carrier scattering. This means that our results will be most appropriate to low carrier density samples. The effects of carrier-carrier scattering were considered in our study of transient hole cooling in Chapter 10, where we described the use of three different categories of initial carrier distributions which we related to the cases of weak carrier-carrier scattering, strong intraband carrier-carrier scattering, and strong intra- and inter-band carrier-carrier scattering. In our simulations of steady state electric field heating, the principal effect of strong carrier-carrier scattering would be to smooth out the structure in the carrier energy distributions, giving a response closer to the Maxwellian form for all values of electric field.

In our simulations we have included neither Pauli exclusion (degeneracy) effects, nor coupled phonon-plasmon scattering. These are, again, both high carrier density effects. We mentioned, in Chapter 10, that the effect of Pauli exclusion would be to inhibit the formation of large carrier populations at localised regions in energy; particularly those associated with the transient supercooling phenomena.

At high carrier densities, the polarisation waves of the lattice become coupled phonon-plasmon modes, rather than simple polar optical phonons. The effect of such modes can be included by the use of a frequency and wavevector dependent dielectric constant with which to screen the polar optical interaction (dynamic screening; see, for example, Shah (1986) and references therein). Such a calculation was considered beyond the scope of this work.

We have not allowed, in our simulations, for any disturbance of the phonon population from its equilibrium value. The generation of non-equilibrium populations of phonons, and subsequent phonon reabsorption by the carriers (hot phonon effects), are phenomena commonly associated with the reduction of the energy loss rate of electrons in both 3D and 2D systems. It has been pointed out that holes, due to their larger effective mass, can interact with phonons of a larger range of wavevectors than can electrons; *i.e.*, the holes can interact with more phonon modes, and hence the probability of a particular mode becoming 'hot' is correspondingly reduced (Shah *et al.* 1985; see also Lyon 1986). The correlation between our results and the experimental results of Shah *et al.* (1985) (even given the difference in the lattice temperatures used) would appear to confirm this suggestion.

We have not allowed for the possibility of real space transfer of holes from the GaAs layer to the AlAs barrier layers. The quantum well barrier height in the valence band is, of course, dependent on the values taken for the band offsets. Assuming that the valence band takes up 40% of the difference between the GaAs and AlAs direct band gaps (Miller *et al.* 1984), the barrier height is around 650meV at T_L=77K (Landolt-Börnstein 1982). In this case, real space transfer should certainly not have any effect on the hole cooling simulations described in Chapter 10, and, for the range of electric fields used, it is unlikely to be significant in the work on electric field heating presented in Chapter 9.

Future Work

As mentioned in Chapter 9, it would be quite possible to use our programs, without modification, to investigate quantum confined hole dynamics at lattice temperatures other than T_L =77K. Of particular interest, however, would be the study of hole cooling at temperatures in the liquid helium range ($T_L \approx 4.2$K), since these are used in a number of experiments on quasi-2D systems. This would require use of the zero-point, rather than the elastic and equipartition approximations, in the calculation of acoustic scattering rates.

The 4-band **k.p** scheme can readily be modified to include strain effects. Therefore, by recalculating the scattering matrix elements, it would be possible to use the same Monte Carlo programs to study hole dynamics in strained layer systems. Similarly, the investigation of hole transport and relaxation in quantum wells of different widths or of different materials systems would also be quite straightforward.

It would certainly be desirable to include some form of carrier-carrier scattering in the simulations. This would allow us to examine the validity of the results presented in Chapters 9 and 10, for a range of carrier densities. It would also be

of interest to enable the disturbance of the phonon populations in the simulations from their equilibrium values. This would allow us to investigate further the suggestion that hot phonon effects are not important for hole energy loss in the steady state. Furthermore, the possible existence of a transient hot phonon effect, as proposed by Kash *et al.* (1985) for the case of photoexcited quantum confined hole cooling, could also be investigated.

Finally, we may note that, having developed a relatively detailed model with which to describe quantum confined hole dynamics, it would not be so difficult a task to incorporate, in the same set of programs, a description of the quantum confined electron system; thus forming a uniquely realistic model for the simulation of carrier photoexcitation and subsequent cooling in a quantum well.

APPENDIX 1
REJECTION TECHNIQUES FOR THE GENERATION OF STOCHASTIC VARIATES

A fundamental feature of the Monte Carlo method is the generation of stochastic variates x according to some specific non-uniform probability distribution $P(x)$. We saw, in Chapter 2, that such a set of stochastic variates could be obtained directly from an algebraic relation involving the random variates r, which were evenly distributed in the range $[0,1]$. However, in many cases the form of the distribution $P(x)$ is too complicated to allow an algebraic determination of the variates x, and one of the so-called rejection techniques must be used instead. In this appendix we will describe two such techniques; the basic rejection technique, and the combined (direct/rejection) technique. Both these methods are discussed in the review article by Jacoboni and Reggiani (1983).

Basic Rejection Technique

Let C be the upper limit of the probability function $P(x)$ in the range of interest $[a,b]$. If r_1 and r_1' are two random numbers obtained from a uniform distribution over $[0,1]$, then a pair of stochastic co-ordinates (x_1, y_1) may be generated, where

$$x_1 = a + (b-a)r_1, \tag{A.1a}$$

$$y_1 = r_1' C. \tag{A.1b}$$

If the point (x_1, y_1) lies below the curve $P(x)$, then x_1 is accepted as a valid choice for x: however, if (x_1, y_1) lies above $P(x)$, then x_1 is rejected, and another pair of co-ordinates (x_2, y_2) are generated. This process is repeated until a point (x_i, y_i) is obtained which lies below the curve. The method is shown graphically in Fig. A.1a. Clearly, the probability of accepting any value x_i is proportional to $P(x_i)$, as required. In Fig. A.1a, the ratio of the area under the curve $P(x)$ to the total area $(b-a)C$ gives a measure of the efficiency of the technique. If this ratio is small, a large percentage of the co-ordinates (x_i, y_i) will be rejected, representing wasted computer processing time. In such cases, the combined technique described below may be used.

Combined (direct/rejection) Technique

In this method, a function $g(x)$ is identified which has values near to, but greater than the probability distribution $P(x)$, everywhere in the required range $[a,b]$. Furthermore, the functional form of $g(x)$ must be sufficiently simple that stochastic values x_i, distributed according to $g(x)$, can be generated by the direct technique described in Chapter 2. Then, the values x_i are accepted as valid choices

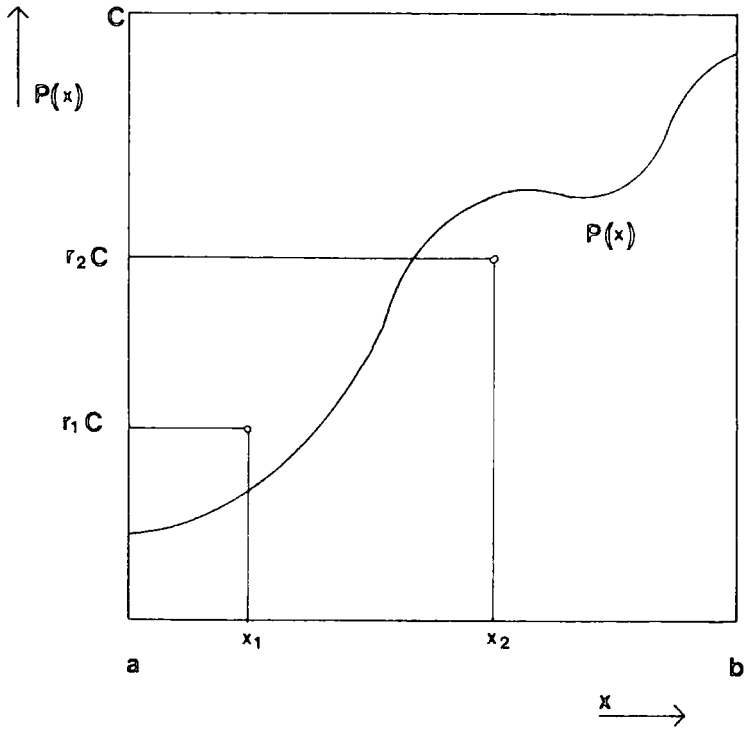

(a)

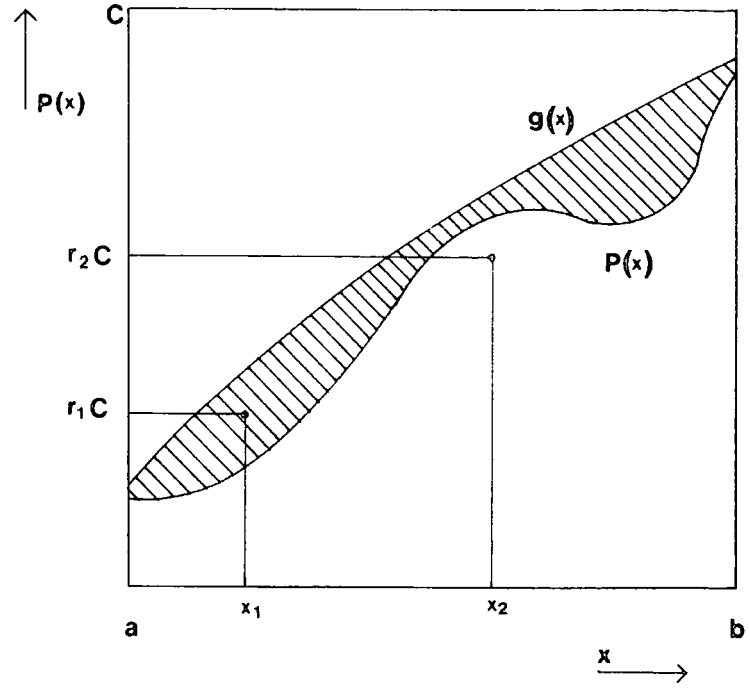

(b)

Fig. A.1 (a) Basic rejection technique, and (b), combined (direct/rejection) technique for the generation of stochastic variates x according to a probability distribution $P(x)$. In each case, the randomly generated co-ordinate $(x_1, r_1 C)$ will be rejected, but $(x_2, r_2 C)$ will be accepted; thus the value x_2 is a valid choice for x.

for the stochastic x (required to be distributed according to $P(x)$), if

$$r_i g(x_i) < P(x_i). \tag{A.2}$$

This process is represented in Fig. A.1b. As before, only the points $(x_i, r_i g(x_i))$ which lie below the curve $P(x)$ give valid choices of x_i. However, in this case all the points generated lie below the curve $g(x)$ by definition; hence only those falling in the hatched area on Fig. A.1b are rejected. For a judicious choice of the function $g(x)$, this can result in a substantial improvement in the efficiency of the method over that for the basic rejection technique.

APPENDIX 2
VALENCE BAND DEFORMATION POTENTIALS

Currently, there exist in the literature, several different methods for defining the deformation potentials associated with phonon scattering in the valence bands of Group IV and III-V semiconductors. Unfortunately, the precise definition of each parameter has not always been made clear, and consequently a degree of confusion over the matter has arisen. In particular, some authors (*e.g.*, Wiley 1975) have preferred to include the effects of the valence band overlap integrals in the definition of the deformation potentials, whereas others (*e.g.*, Costato and Reggiani 1973a) have excluded these effects in their definitions.

In this appendix, we will briefly review some of the definitions of deformation potentials found in the literature, and will give values for the acoustic and optical deformation potentials used in this work, under clearly defined conditions.

Acoustic deformation potentials

As mentioned in Section 3C, in the valence bands of a semiconductor both dilational and shear strains contribute to the acoustic interaction energy, and their effects are properly described by three deformation potentials a, b, and d. However, Lawaetz (1968) has shown that, on taking an average over all directions, a single effective deformation potential Ξ_{eff} can be defined:

$$\Xi_{\text{eff}}^2 = a^2 + \left(\frac{c_l}{c_t}\right)\left(b^2 + \frac{d^2}{2}\right), \tag{A.3}$$

where c_l and c_t are the spherically averaged crystal elastic constants;

$$c_l = \tfrac{1}{5}(3c_{11} + 2c_{12} + 4c_{44}), \tag{A.4a}$$

$$c_t = \tfrac{1}{5}(c_{11} - c_{12} + 3c_{44}), \tag{A.4b}$$

and the c_{ij} are elements of the elastic tensor.

Thus, it appears that Ξ_{eff} is defined to represent the interaction of a carrier with an effective longitudinal mode having the same strength as the actual combination of longitudinal and transverse modes. As such, Ξ_{eff}^2 is intended to be used in conjunction with the longitudinal sound velocity v_l. Therefore, if the mean square sound velocity $\overline{v}^2 = (v_l^2 + 2v_t^2)/3$ is used in the calculation of the acoustic scattering rate, then the corresponding deformation potential (squared) should be:

$$E_{\text{AC}}^2 = \frac{\overline{v}^2}{v_l^2}\Xi_{\text{eff}}^2. \tag{A.5}$$

This is the form suggested by Lawaetz to Wiley (see Wiley 1970), for use in conjunction with his previous work on hole transport (Wiley and DiDomenico 1970).

Costato and Reggiani (1973a), in their calculations of hole-phonon scattering, introduce an acoustic deformation potential E_1, the definition of which also reduces to the above form.

However, in Wiley's paper (Wiley 1970), we also find the relation

$$E^2_{\mathrm{AC,Wiley}} = \left(\frac{\beta+2}{6\beta}\right)\Xi^2_{\mathrm{eff}}, \tag{A.6}$$

where $\beta = c_l/c_t$. This represents the introduction of an extra factor of $1/2$, compared to the definition given in equation (A.5). Equation (A.6) also appears in Wiley's later review of hole transport (Wiley 1975), and is quoted by Adachi (1985) in his survey of material parameters for GaAs and related materials.

Now, Wiley (1975) does say that the deformation potentials described in his review are phenomenological parameters which *include* the effects of the overlap integral $G(\mathbf{k}',\mathbf{k})$. We saw, in Section 3C, that the effect of these overlap integrals in AC and NPO scattering is to reduce the total scattering rates by a factor of two. Thus, the deformation potential E_{AC} introduced in Section 3C, which does *not* include any contribution from the overlap integral $G(\mathbf{k}',\mathbf{k})$, is related to Wiley's deformation potential by

$$E^2_{\mathrm{AC}} = 2E^2_{\mathrm{AC,Wiley}}. \tag{A.7}$$

It would therefore seem that the appearance of the contradictory equations (A.5) and (A.6) in Wiley's original paper (Wiley 1970) is the result either of some typographical error, or of the omission of any reference to the overlap integral contribution.

Costato and Reggiani (1973a) clearly treat the overlap integral term separately in their scattering rate calculation, and this is consistent with the definition of their deformation potential E_1.

In a later paper (Costato *et al.* 1974), yet another form for the valence band acoustic deformation potential is introduced. Costato *et al.* report that this new parameter, E_1^0, is related to Wiley's deformation potential according to $E_1^{0^2} = (9v_l/2\overline{v})E^2_{\mathrm{AC,Wiley}}$, and further, that $E_1^{0^2}$ corresponds to $(9/4)E_1^2$, where E_1 is a deformation potential 'in the formalism of Conwell'. (However, closer inspection shows that, in order to obtain the same expressions for the hole/acoustic phonon scattering matrix element, the true relation between E_1^0 and $E_{\mathrm{AC,Wiley}}$ must be: $E_1^{0^2} = (9v_l^2/2\overline{v^2})E^2_{\mathrm{AC,Wiley}}$.) Now, Conwell (1967) uses the term E_1 in her expression for the acoustic scattering of electrons in Ge, where the overlap integral is unity, and only longitudinal modes contribute. We may eliminate E_1^0 from the two expressions given by Costato *et al.* (making use of our amendment detailed above) to find that $E^2_{\mathrm{AC,Wiley}} = (\overline{v^2}/2v_l^2)E_1^2$. The factor $(\overline{v^2}/v_l^2)$ is associated with the conversion from the case of longitudinal modes only, to that

where a combination of both longitudinal and transverse modes is considered: the remaining factor of 1/2 then reflects the inclusion of the overlap integral $G(\mathbb{k}', \mathbb{k})$ in Wiley's deformation potential. Thus, the work of Costato *et al.* (1974) lends further support to our hypothesis of equation (A.7).

Of course, the advantage of defining a deformation potential which includes the effect of the overlap integral term is that it can be directly compared with the values deduced from experiment. However, the definition of such a deformation potential is clearly not helpful when considering the acoustic scattering of holes in quantum confined systems, where the effect of the carrier wavefunctions on the scattering matrix element cannot be so readily quantified.

We will conclude this discussion of the valence band acoustic deformation potentials by obtaining a value for the parameter E_{AC}, defined in Chapter 3, which *excludes* any contribution from the overlap integral. We thus define

$$E_{\mathrm{AC}}^2 = \frac{\overline{v}^2}{v_l^2}\Xi_{\mathrm{eff}}^2 \tag{A.8}$$

$$= \left(\frac{\beta+2}{3\beta}\right)\Xi_{\mathrm{eff}}^2 \tag{A.9}$$

where $\beta = c_l/c_t$. To obtain a value for Ξ_{eff}, we refer to equations (A.3) and (A.4). Using values given by Adachi (1985) (also Landolt-Börnstein 1982) for c_{11}, c_{12} and c_{44} we obtain, for GaAs, $c_l = 14.032 \times 10^{10}\,\mathrm{Nm}^{-2}$ and $c_t = 4.864 \times 10^{10}\,\mathrm{Nm}^{-2}$. For the deformation potentials a, b and d, Adachi (1985) gives values 2.7eV, -1.7eV and 4.55eV respectively, from which we obtain $\Xi_{\mathrm{eff}} = 6.75\mathrm{eV}$. Then, equation (A.9) gives $E_{\mathrm{AC}} = 5.07\mathrm{eV}$, the value used throughout this work.

Dividing this result by $\sqrt{2}$ gives a value for $E_{\mathrm{AC,Wiley}}$ of 3.59eV, in good agreement with the values given by Wiley (1970, 1975) and Adachi (1985) for GaAs.

Optical deformation potential

The fundamental optical deformation potential is the parameter d_0 derived by Bir and Pikus (1961). It was mentioned in Section 3C that Lawaetz (1968), on averaging the effects of optical strain over all directions, defined a deformation potential constant D_{op}, where

$$D_{\mathrm{op}}^2 = \frac{3}{2}\frac{d_0^2}{a_0^2}. \tag{A.10}$$

This is the form used by Reggiani *et al.* (1977) and Ridley (1988). However, the expression given by Costato and Reggiani (1973a) for the optical deformation potential constant (equation (7) of that reference) does not reduce to the above form.

The matrix element obtained by Lawaetz (1968) for non-polar optical scattering takes the form

$$|\langle \mathbf{k}'|H_{\rm op}|\mathbf{k}\rangle|^2 = \frac{\hbar D_{\rm op}^2}{2\rho V \omega_{\rm op}} \begin{bmatrix} \mathcal{N}_{\rm op} \\ \mathcal{N}_{\rm op}+1 \end{bmatrix}. \tag{A.11}$$

This is in agreement with the result given by Conwell (1967), with $D_{\rm op}$ equivalent to her parameter $D_t K$. Whilst both these workers used for the harmonic oscillator mass M' (see section 3A.1), the total mass of the unit cell, the same result can be deduced from the work of Ridley (1988), who uses the reduced mass $\overline{M}$.

Conwell (1967) also defines an optical deformation potential in a manner analogous to that for acoustic scattering, by writing

$$\langle \mathbf{k}'|H_{\rm op}|\mathbf{k}\rangle|^2 = \frac{\hbar\omega_{\rm op} E_{1,\rm op}^2}{2\rho V v_l^2} \begin{bmatrix} \mathcal{N}_{\rm op} \\ \mathcal{N}_{\rm op}+1 \end{bmatrix}, \tag{A.12}$$

where $E_{1,\rm op}^2 = (v_l^2/\omega_{\rm op}^2)(D_t K)^2$.

Similarly, Wiley and DiDomenico (1970) make use of a phenomenological constant $E_{\rm NPO,Wiley}$ in their calculation of an NPO scattering rate for holes. Their expression for the scattering rate reduces to that of equation (3.80) if

$$E_{\rm NPO,Wiley}^2 = \frac{\overline{v}^2}{\omega_{\rm op}^2} D_{\rm op}^2, \tag{A.13}$$

and this conclusion is explicitly confirmed in the work of Costato *et al.* (1974). The substitution of $\overline{v}^2$ for v_l^2 in equation (A.13) reflects the fact that Costato *et al.* are considering hole scattering, whereas Conwell's work deals with the scattering of conduction electrons, where only longitudinal modes are associated with acoustic scattering.

In his letter concerning the valence band deformation potentials, Wiley (1970) gives the relation

$$E_{\rm NPO,Wiley} = \frac{M_1 + M_2}{2\sqrt{M_1 M_2}} \left(\frac{c_l(\beta+2)}{2\rho\omega_{\rm op}^2 a_0^2 \beta} \right)^{\frac{1}{2}} d_0 \tag{A.14}$$

where $\beta = c_l/c_t$ and M_1 and M_2 are the atomic masses. This reduces to equation (A.13) for the case $M_1 = M_2$, *i.e.*, for elemental semiconductors only. For compound materials, such as GaAs, it is not clear how the above expression relates to any of the other published work.

However, it is clear from the preceding discussion that the term $E_{\rm NPO,Wiley}$, unlike $E_{\rm AC,Wiley}$, does *not* include any contribution from the overlap integral $G(\mathbf{k}', \mathbf{k})$. This is apparent from the definitions of $E_{\rm NPO,Wiley}$ in equations (A.13) and (A.14), and their consistency with the expression given by Conwell for the conduction band

case, where the overlap integral is taken as unity. This discovery becomes even more surprising on noting that equation (A.14) also appears in Wiley's review (1975), where he clearly states that his phenomenological deformation potentials already contain the effects of the term $G(\mathbf{k}', \mathbf{k})$.

In our treatment of NPO scattering in Section 3C there seemed no merit in using any such deformation potential of the form given in equation (A.13). Rather, we preferred to retain the parameter D_{op} as defined in equation (A.10), in a calculation which, as for acoustic scattering, explicitly treats the overlap integral term separately.

Then, taking $d_0 = 41\text{eV}$ (Wiley 1970; Adachi 1985) we obtain, for GaAs, $D_{\text{op}} = 8.88 \times 10^{10}\text{eVm}^{-1}$, the value used throughout this work.

APPENDIX 3
CRITICAL POINTS IN THE VALENCE BAND ENERGY DISPERSIONS

The 2D energy dispersion functions for the quantum confined valence bands may be written in the form $\epsilon(\mathrm{k}) \equiv \epsilon(k_x, k_y)$. Critical points occur in $\epsilon(k_x, k_y)$ when $\nabla_{\mathrm{k}}\epsilon = 0$. These can be maxima, minima or saddle points. The behaviour of $\epsilon(k_x, k_y)$ around a critical point may be examined by expanding the function in a Taylor series, to second order, around the point (k_x, k_y). This gives

$$\epsilon(k_x + s, k_y + t) \approx \epsilon(k_x, k_y) + \left(s\frac{\partial}{\partial k_x} + t\frac{\partial}{\partial k_y}\right)\epsilon(k_x, k_y) + \frac{1}{2}\left(s\frac{\partial}{\partial k_x} + t\frac{\partial}{\partial k_y}\right)^2 \epsilon(k_x, k_y). \tag{A.15}$$

Remembering that $\partial\epsilon/\partial k_x$ and $\partial\epsilon/\partial k_y$ are both zero at the critical point (k_x, k_y), we obtain, after a little algebra, the familiar result (see, for example, Stephenson (1973)):

$$\epsilon(k_x + s, k_y + t) - \epsilon(k_x, k_y) \approx \frac{\epsilon_{xx}}{2}\left[\left(s + \frac{\epsilon_{xy}}{\epsilon_{xx}}t\right) + \frac{\Delta}{\epsilon_{xx}^2}\right], \tag{A.16}$$

where $\Delta = \epsilon_{xx}\epsilon_{yy} - \epsilon_{xy}\epsilon_{yx}$ and $\epsilon_{xx} = \partial^2\epsilon/\partial k_x^2$, $\epsilon_{xy} = \partial^2\epsilon/\partial k_x \partial k_y$ *etc.*

For $\Delta > 0$, the term multiplying ϵ_{xx} on the RHS of equation (A.16) is positive for all s and t. Hence, the point (k_x, k_y) is a maximum for $\epsilon_{xx} < 0$, and a minimum for $\epsilon_{xx} > 0$. If $\Delta < 0$, then the sign of the RHS of equation (A.16) will depend on the values of s and t; this case represents a saddle point in $\epsilon(k_x, k_y)$.

In the isotropic approximation to the quantum confined valence bandstructure, the term Δ may be readily evaluated. With $\epsilon(k_x, k_y)$ independent of the polar angle β in 2D k-space, $\partial\epsilon/\partial\beta \equiv 0$. Hence the first derivatives of $\epsilon(k_x, k_y)$ are simply:

$$\frac{\partial\epsilon}{\partial k_x} = \frac{\partial\epsilon}{\partial k}\cos\beta, \tag{A.17a}$$

$$\frac{\partial\epsilon}{\partial k_y} = \frac{\partial\epsilon}{\partial k}\sin\beta, \tag{A.17b}$$

where k is the 2D radial wavevector, $\cos\beta = \partial k/\partial k_x$ and $\sin\beta = \partial k/\partial k_y$.

The second derivatives of $\epsilon(k_x, k_y)$ are then:

$$\epsilon_{xx} = \frac{\partial^2\epsilon}{\partial k_x \partial k}\frac{\partial k}{\partial k_x} + \frac{\partial\epsilon}{\partial k}\frac{\partial^2 k}{\partial k_x^2}, \tag{A.18a}$$

$$\epsilon_{xy} = \frac{\partial^2\epsilon}{\partial k_x \partial k}\frac{\partial k}{\partial k_y} + \frac{\partial\epsilon}{\partial k}\frac{\partial^2 k}{\partial k_x \partial k_y}, \tag{A.18b}$$

$$\epsilon_{yx} = \frac{\partial^2\epsilon}{\partial k_y \partial k}\frac{\partial k}{\partial k_x} + \frac{\partial\epsilon}{\partial k}\frac{\partial^2 k}{\partial k_y \partial k_x}, \tag{A.18c}$$

$$\epsilon_{yy} = \frac{\partial^2\epsilon}{\partial k_y \partial k}\frac{\partial k}{\partial k_y} + \frac{\partial\epsilon}{\partial k}\frac{\partial^2 k}{\partial k_y^2}. \tag{A.18d}$$

At a critical point, $\partial\epsilon/\partial k = 0$, and so the second terms on the RHS of each of equations (A.18a–d) will be zero. The second derivatives then reduce to:

$$\epsilon_{xx} = \frac{\partial^2\epsilon}{\partial k^2}\cos^2\beta, \tag{A.19a}$$

$$\epsilon_{xy} = \frac{\partial^2\epsilon}{\partial k^2}\sin\beta\cos\beta, \tag{A.19b}$$

$$\epsilon_{yx} = \frac{\partial^2\epsilon}{\partial k^2}\sin\beta\cos\beta, \tag{A.19c}$$

$$\epsilon_{yy} = \frac{\partial^2\epsilon}{\partial k^2}\sin^2\beta, \tag{A.19d}$$

from which it can be seen that $\Delta = 0$. This condition holds for all values of β in the expressions for ϵ_{xx}, ϵ_{xy} *etc.* above; hence, for $k_x \neq 0$, $k_y \neq 0$, we have a continuous ring of critical points, with $\Delta = 0$ throughout (see Van Hove 1953).

Before referring to equation (A.16), we must check the individual values of ϵ_{xx}, ϵ_{xy} *etc.*, since, if these were all simultaneously zero at a critical point, the equation could not be used and the inclusion of higher order terms in the expansion of $\epsilon(k_x, k_y)$ would be necessary. However, on examining equations (A.19a–d) we find that the four second derivatives are never simultaneously zero. We may then conclude that, since $\epsilon_{xx} \geq 0$ for all β, equation (A.16) indicates that the behaviour of $\epsilon(k_x, k_y)$ resembles that around a minimum at every point on the ring (see also Fig. 7.3). In section 7A.2 we have conducted a further examination of the behaviour of the density of states around such a continuous ring of critical points.

REFERENCES

Adachi S. 1985 *J. Appl. Phys.* 58 R1

Alberigi Quaranta A., Jacoboni C. and Ottaviani G. 1971 *Rivista del Nuovo Cimento* 1 445

Babiker M. 1986 *J. Phys. C: Solid State Phys.* 19 L339

Babiker M. and Ridley B. K. 1986 *Superlatt. Microstruct.* 2 287

Babiker M., Ghosal A. and Ridley B. K. 1989 *Superlatt. Microstruct.* 5 133

Bardeen J. and Shockley W. 1950 *Phys. Rev.* 80 72

Bassani F. and Parravicini G. P. 1975 *Electronic States and Optical Transitions in Solids* Pergamon, Oxford.

Bir G. L. and Pikus G. E. 1961 *Sov. Phys. Solid State* 2 2039

Birman J. L., Lax M. and Loudon R. 1966 *Phys. Rev.* 145 620

Born M. and Huang K. 1954 *Dynamical Theory of Crystal Lattices* Clarendon, Oxford.

Borsari V. and Jacoboni C. 1972 *Phys. Stat. Sol. (b)* 54 649

Brennan K. and Hess K. 1984 *Phys. Rev. B* 29 5581

Briggs S. and Leburton J. P. 1988 *Phys. Rev. B* 38 8163

Callen H. B. 1949 *Phys. Rev.* 76 1394

Canali C., Jacoboni C., Nava F., Ottaviani G. and Alberigi Quaranta A. 1975 *Phys. Rev. B* 12 2265

Chamberlain M. P. 1987 *MSc Thesis* Essex University, unpublished.

Chang Y. C. and Schulman J. N. 1983 *Appl. Phys. Lett.* 43 536

Chang Y. C. and Schulman J. N. 1985 *Phys. Rev. B* 31 2069

Colak S., Eppenga R. and Schuurmans M. F. H. 1987 *IEEE J. Quantum Elec.* QE-23 960

Conwell E. M. 1967 *Solid State Physics, Supplement 9* Academic, New York.

Costato M., Jacoboni C. and Reggiani L. 1972 *Phys. Stat. Sol. (b)* 52 461

Costato M. and Reggiani L. 1973a *Phys. Stat. Sol. (b)* 58 471

Costato M. and Reggiani L. 1973b *Phys. Stat. Sol. (b)* 59 47

Costato M., Gagliani G., Jacoboni C. and Reggiani L. 1974 *J. Phys. Chem. Sol.* 35 1605

Da Costa J. A. P., Taylor R. A., Turberfield A. J., Ryan J. F. and Wang W. I. 1987 in *Proceedings of the 18th International Conference on the Physics of Semiconductors, Stockholm, 1986* ed. O. Engström. World Scientific, Singapore. p1327.

Dalal V. L., Dreeben A. B. and Triano A. 1971 *J. Appl. Phys.* 42 2864

Dingle R. 1975 in *Festkörperprobleme XV (Advances in Solid State Physics)* ed. H. J. Queisser. Pergamon/Vieweg, Braunschweig. p21.

Dingle R., Störmer H. L., Gossard A. C. and Wiegmann W. 1978 *Appl. Phys. Lett.* 33 665

Dresselhaus G., Kip A. F. and Kittel C. 1955 *Phys. Rev.* 98 368

Eppenga R., Schuurmans M. F. H. and Colak S. 1987 *Phys Rev. B* 36 1554

Fawcett W. and Rees H. D. 1969 *Phys. Lett* 28A 731

Fawcett W., Boardmann A. D. and Swain S. 1970 *J. Phys. Chem. Sol.* 31 1963

Ferry D. K. 1977 *Solid State Comm.* 22 127

Ferry D. K. 1978 *Surf. Sci.* 75 86

Fröhlich H. 1937 *Proc. Roy. Soc. A* 160 230

Goodnick S. M. and Lugli P. 1988 *Phys. Rev. B* 38 10135

Hammar C. 1971 *Phys. Rev. B* 4 417

Hammersley J. M. and Handscomb D. C. 1964 *Monte Carlo Methods* Methuen, London.

Hammersley J. M. and Mauldon J. G. 1956 *Proc. Camb. Phil. Soc.* 52 476

Hammersley J. M. and Morton K. W. 1956 *Proc. Camb. Phil. Soc.* 52 449

Harrison W. A. 1956 *Phys. Rev.* 104 1281

Hess K. 1979 *Appl. Phys. Lett.* 35 484

Hess K., Morkoç H., Shichijo H. and Streetman B. G. 1979 *Appl. Phys. Lett.* 35 469

Hess K. and Sah C. T. 1974 *Phys. Rev. B* 10 3375

Hinckley J. M. and Singh J. 1988 *Appl. Phys. Lett.* 53 785

Hockney R. W. and Eastwood J. W. 1981 *Computer Simulation Using Particles* McGraw-Hill, Maidenhead.

Holway L. H., Steele S. R. and Alderstein M. G. 1979 *Proceedings of the 7th Biennial Cornell Electrical Engineering Conference* Cornell Univ. Press, Ithaca, N.Y. p199.

Hutson A. R. 1961 *J. Appl. Phys.* 32 (Suppl.) 2287

Jacoboni C. and Reggiani L. 1983 *Rev. Mod. Phys.* 55 645

Jones H. 1975 *The Theory of Brillouin Zones and Electronic States in Crystals* (2nd, revised edn.) North-Holland, Amsterdam.

Kash K., Shah J., Block D., Gossard A. C. and Wiegmann W. 1985 *Physica* 134B 189

Kelsall R. W., Taylor R. I., Wood A. C. G. and Abram R. A. 1989 *Superlatt. Microstruct.* **5** 207

Kirton M. J. 1987 private communication

Kittel C. 1963 *Quantum Theory of Solids* Wiley, New York.

Kurosawa T. 1966 *J. Phys. Soc. Japan* **21** (Suppl.) 424

Landolt-Börnstein 1982 *Numerical Data and Functional Relationships in Science and Technology* ed. O. Madelung, vol. III/17a. Springer-Verlag, Berlin.

Law A. M. and Kelton W. D. 1982 *Simulation Modeling and Analysis* McGraw-Hill, New York. Chapter 11.

Lawaetz P. 1968 *Phys. Rev.* **174** 867

Leo K., Rühle W. W. and Ploog K. 1988 *Phys. Rev. B* **38** 1947

Lugli P. and Goodnick S. M. 1987 *Phys. Rev. Lett.* **59** 716

Lyon S. A. 1986 *J. Lumin.* **35** 121

Mason B. A. and Das Sarma S. 1987 *Phys. Rev. B* **35** 3890

Mason W. P. 1950 *Piezoelectric Crystals and their Application to Ultrasonics* Van Nostrand, New York.

Mears A. L. and Stradling R. A. 1971 *J. Phys. C: Solid State Physics* **4** L22

Meyer H. J. G. 1958 *Phys. Rev.* **112** 298

Miller R. C., Kleinman D. A. and Gossard A. C. 1984 *Phys. Rev. B* **29** 7085

Miller R. C. and Kleinman D. A. 1985 *J. Lumin.* **30** 520

Miller R. C., Gossard A. C., Sanders G. D., Chang Y. C. and Schulman J. N. 1985 *Phys. Rev. B* **32** 8452

NAG (Numerical Algorithms Group) 1987 *The NAG Fortran Library Manual* Mark 12 (vol. 6). NAG, Oxford.

Ninno D., Gell M. A. and Jaros M. 1986 *J. Phys. C: Solid State Physics* **19** 3845

Oberli D. Y., Wake D. R., Klein M. V., Klem J., Henderson T. and Morkoç H. 1987 *Phys. Rev. Lett.* **59** 696

Oberli D. Y., Wake D. R., Klein M. V., Henderson T. and Morkoç H. 1988 *Solid State Elec.* **31** 413

Phillips J. C. 1956 *Phys. Rev.* 104 1263

Pikus G. E. and Bir G. L. 1960 *Sov. Phys. Solid State* **1** 1502

Price P. J. 1968 in *Proceedings of the 9th International Conference on the Physics of Semiconductors* ed. S. M. Ryvkin. Nauka, Leningrad. p753.

Price P. J. 1970 *IBM J. Res. Dev.* **14** 12

Price P. J. 1979 in *Semiconductors and Semimetals* vol. 14, ed. R. K. Willardson and A. C. Beer. Academic, New York. p249.

Price P. J. 1981 *Ann. Phys.* 133 217

Price P. J. 1982 *J. Appl. Phys.* 53 6863

Rees H. D. 1968 *Phys. Lett.* 26A 416

Rees H. D. 1969 *J. Phys. Chem. Sol.* 30 643

Reggiani L., Canali C., Nava F. and Ottaviani G. 1977 *Phys. Rev. B* 16 2781

Riddoch F. A. and Ridley B. K. 1983 *J. Phys C: Solid State Physics* 16 6971

Riddoch F. A. and Ridley B. K. 1985 *Physica* 134B 342

Ridley B. K. 1982 *J. Phys C: Solid State Physics* 15 5899

Ridley B. K. 1988 *Quantum Processes in Semiconductors* 2nd edn. Clarendon, Oxford.

Rockett P. I. 1987 *IEE Proc.* 134 Pt. I 101

Rode D. L. 1970 *Phys. Rev. B* 2 1012

Rühle W. W., Polland H. J., Bauser E., Ploog K. and Tu C. W. 1988 *Solid State Electron.* 31 407

Sanders G. D. and Chang Y. C. 1985 *Phys. Rev. B* 31 6892

Sanders G. D. and Chang Y. C. 1987 *Phys. Rev. B* 35 1300

Schuurmans M. F. H. and t'Hooft G. W. 1985 *Phys. Rev. B* 31 8041

Seilmeier A., Hübner H. J., Abstreiter G., Weimann G. and Schlapp W. 1987 *Phys. Rev. Lett.* 59 1345

Seitz F. 1948 *Phys. Rev.* 73 549

Shah J. 1978 *Solid State Electron.* 21 43

Shah J. 1986 *IEEE J. Quantum Electron.* QE-22 1728

Shah J., Pinczuk A., Gossard A. C. and Wiegmann W. 1985 *Phys. Rev. Lett.* 54 2045

Sham L. J. and Ziman J. M. 1963 *Solid State Phys.* 15 221

Stephenson G. 1973 *Mathematical Methods for Science Students* 2nd edn. Longman, London.

Störmer H. L., Gossard A. C., Wiegmann W., Blondel R. and Baldwin K. 1984 *Appl. Phys. Lett.* 44 139

Taylor R. I. 1987 unpublished

Van Hove L. 1953 *Phys. Rev.* 89 1189

Wiley J. D. 1970 *Solid State Comm.* 8 1865

Wiley J. D. 1971 *Phys. Rev. B* 4 2485

Wiley J. D. 1979 in *Semiconductors and Semimetals* vol. 10, ed. R. K. Willardson and A. C. Beer. Academic, New York. p91.

Wiley J. D. and DiDomenico M. 1970 *Phys. Rev. B* 2 427

Wood A. C. G 1987 unpublished

Yorston R. 1986 *J. Comp. Phys.* 64 177

Ziman J. M. 1960 *Electrons and Phonons* Clarendon, Oxford.

Zook J. D. 1964 *Phys. Rev.* 136A 869

Zschauer K. H. 1973 in *Proceedings of the 4th International Symposium on GaAs and Related Compounds, Boulder, 1972* Institute of Physics, London. p6.

HOLE TRANSPORT AND RELAXATION IN THE VALENCE BANDS OF A GaAs / AlAs QUANTUM WELL

R. W. Kelsall, R. I. Taylor*, A. C. G. Wood, and R. A. Abram

Applied Physics Group,
School of Engineering and Applied Science,
University of Durham,
South Road,
Durham, DH1 3LE, UK.

(Received 8 August, 1988)

We have developed a new Monte Carlo model of hole transport and relaxation in the valence bands of a GaAs/AlAs quantum well. The model includes realistic energy bands and phonon scattering matrix elements calculated using a 4-band k.p scheme. We demonstrate the use of the model in the investigation of the steady state electric field heating, and transient energy relaxation of a two dimensional hole gas.

1. Introduction

There has been much recent interest in the dynamics of electrons in GaAs based semiconductor heterostructures. Advanced MOCVD and MBE fabrication techniques have enabled the growth of high quality quantum well and superlattice devices, whilst the development of sub-picosecond lasers has enabled detailed spectroscopic studies of fast transient transport and relaxation. However, there has, as yet, been little attention directed towards the behaviour of holes in these devices. The effect of quantum confinement on the valence band system is clearly much more complicated than for the conduction band, and the consequences for hole transport are not yet understood. Most theoretical models of quasi two dimensional (2D) transport in semiconductors are based on a single, parabolic subband model, but neither the assumption of parabolicity, nor that of single subband occupancy holds good for the case of holes. The purpose of this paper is to describe a realistic Monte Carlo model of 2D hole transport and relaxation. We have considered the particular case of a 100Å GaAs/AlAs lattice matched single quantum well, and we have chosen a 4-band k.p model[1] to describe the quantum confined valence band system. This method gives accurate results for the energies and wavefunctions of the valence band states, but involves much less computational effort than the more usual pseudopotential or variational bandstructure calculations.

2. Bandstructure

In a quantum well, considerable mixing of heavy and light hole states occurs. This gives rise to a set of valence subbands which have markedly non parabolic energy dispersions in the plane of the well. We have used the 4-band k.p scheme to obtain energies for the first four subbands in a 100Å GaAs/AlAs quantum well. Fig. 1 shows the valence bandstructure in the plane of the well. Anisotropy was found to be relatively small (less than 10% in band 1 in the range of the figure), and the bandstructure was treated as isotropic throughout the work described. Repulsion (anticrossing) effects between adjacent bands can be clearly seen. These are accompanied by an exchange of character of the associated states. In particular, bands 2 and 4 have regions of negative effective mass near the zone centre, with energy minima at non zero values of in-plane wavevector. The densities of states of these bands diverge at the energy minima, though the effect is expected to be damped somewhat by band anisotropy.

* Present address; Plessey Research Caswell Limited, Allen Clark Research Centre, Towcester, Northants., UK.

0749-6036/89/020207+05 $02.00/0

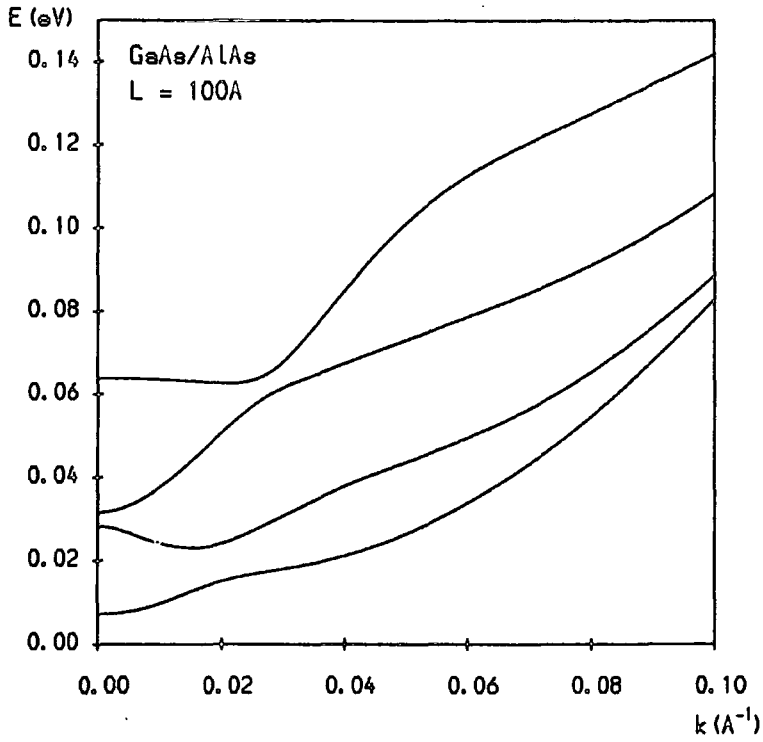

Fig. 1 Energy dispersion of the first four valence subbands in the (100) direction of a 100Å GaAs/AlAs quantum well. The growth direction is (001).

3.-Matrix Elements

A method for calculating the matrix elements for the scattering of electrons by phonons in a quantum well has been described by Price[2] and Ridley[3], where it is assumed that the electronic wavefunctions can be written as the product of a single Bloch function and a sinusoidal envelope function. However the hole wavefunctions in the quantum well, for any non-zero in-plane wavevector, contain significant contributions from a number of bulk states, and cannot be accurately represented in such a simple form. We have used the 4-band k.p method to calculate realistic hole wavefunctions for the first four valence subbands, and used these to calculate the matrix elements for hole-phonon scattering.

The matrix elements are given by terms like

$$F_{mn}(q) = \int_{-\infty}^{\infty} A(\mathbf{q}) |I_{mn}(\mathbf{q})|^2 dq_z \qquad (1)$$

where

$$I_{mn}(\mathbf{q}) = \int \psi_m^*(\mathbf{r}) \psi_n(\mathbf{r}) exp(i\mathbf{q}.\mathbf{r}) d\mathbf{r} \qquad (2)$$

with m and n the subband indices,
$\mathbf{q}$ is the phonon wavevector and q_z its component in the well direction.

$A(\mathbf{q}) = 1$ for deformation potential and non polar optical scattering,

$A(\mathbf{q}) = \frac{1}{q^2}$ for unscreened polar optical and piezoelectric scattering, and

$A(\mathbf{q}) = \frac{q^2}{(q^2 + q_0^2)^2}$ for screened polar optical and piezoelectric scattering, with q_0 the reciprocal screening length.

Fig. 2a shows the matrix elements obtained for intraband (1-1) and interband (1-2) polar optical phonon absorption, compared with that given by a simple 1-band effective mass calculation. It can be seen that the mixed character of the quantum well valence states has an important effect on scattering. For the intraband process, for small wavevectors, the initial and final hole states lie on opposite sides of the anticrossing region of the band. The small k initial states are heavy hole like, whilst the large k final states are light hole like,

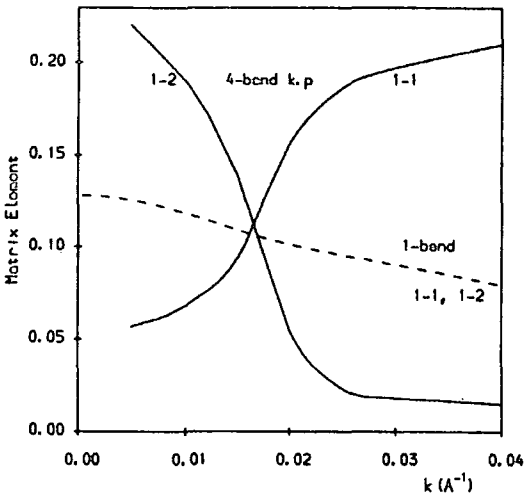

Fig. 2(a) Matrix elements for polar optical phonon scattering, integrated over all scattering angles, and shown in dimensionless form $\frac{1}{4L}\int_0^{2\pi} F_{mn}d\beta$. The full curves are the results of 4-band k.p calculations for band 1–band 1 and band 1–band 2 scattering, whilst the broken curve shows simple 1-band effective mass results for the same two cases.

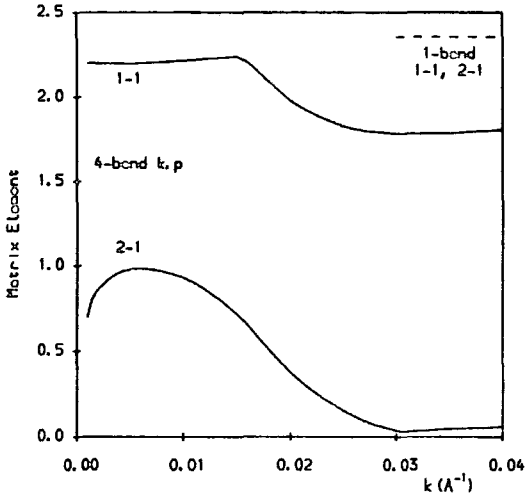

Fig. 2(b) Matrix elements for deformation potential scattering in dimensionless form, $L/4\ F_{mn}(q)$. Full curves, 4-band k.p calculations; broken curve, 1-band effective mass results, for band 1–band 1 and band 2–band 1 scattering.

hence the matrix element is small. As the wavevector of the initial state traverses the anticrossing region, the state becomes increasingly light hole like, so the matrix element increases. For the interband process, the converse is true. The large k states in band 2 are heavy hole like, and for scattering from the small k band 1 states, the matrix element is large. As the wavevector of the band 1 state passes the anticrossing region, the matrix element decreases. The result for the 1-band model shows only the variation in matrix element due to the $1/q^2$ dependence.

result which is independent of wavevector, and represents an upper limit for the 4-band matrix elements.

4. Scattering Rates

The scattering rates are calculated from Fermi's Golden Rule

$$P_{if} = \frac{2\pi}{\hbar} \sum_{\substack{\text{final} \\ \text{states}}} |M|^2 \delta(E_f - E_i) \tag{3}$$

and are of the form

$$P(k)_{\substack{abs \\ em}} = C \times \int\int k'dk'd\beta \frac{1}{\omega_q} \begin{bmatrix} N_q \\ N_q + 1 \end{bmatrix} F_{mn}(q)\delta_{k',k\pm q}\delta[E(k') - E(k) \mp \hbar\omega_q] \tag{4}$$

Fig. 2b shows intraband and interband matrix elements obtained for deformation potential scattering. These are calculated in an isotropic, elastic approximation (assuming that initial and final states have the same wavevector). This means that the wavefunctions of initial and final states for intraband scattering are virtually identical, and the matrix elements are always much larger than for interband scattering. This remains true even when the initial and final states are displaced by a typical acoustic phonon energy. The 1-band calculation gives, in the elastic approximation, a

where N_q is the phonon occupation number, $q^2 = k^2 + k'^2 - 2kk'cos\beta$, k and k' are the wavevectors of the initial and final states, and β is the scattering angle.

For optical phonon scattering, ω is assumed independent of q, and the phonon energy $\hbar\omega$ is taken as 35.4meV for both LO and TO phonons. The acoustic rates are calculated in the elastic and energy equipartition approximations, which give a very good approximation to the total (absorption + emission) rate at 77K, the lattice temperature concerned. For unscreen-

ed piezoelectric scattering, a finite result cannot be obtained for the scattering rate, since the matrix element contains a term in $1/q^3$, which always leads to a divergence. Therefore, the matrix elements for piezoelectric scattering were calculated assuming weak screening, with a screening length appropriate to a free hole density of 5×10^{16} cm^{-3}. Under these conditions, the effect of screening on the polar optical scattering rates is expected to be negligible, and these rates were calculated for the unscreened case.

Scattering rates were calculated for intraband and interband polar optical, non-polar optical, deformation potential and piezoelectric processes in and between all four bands. For scattering into bands 2 and 4, there is a range of energies in which the final state for scattering has two possible values of k'. These cases must be treated separately, giving a total of 144 possible scattering processes.

5. Monte Carlo Model

We have developed both steady state and ensemble Monte Carlo programs to simulate 2D hole dynamics. The valence band system is modelled by the four subband dispersion curves, as described in section 2, with the derived group velocities and densities of states. These, and the matrix elements for the 144 scattering processes, are tabulated against wavevector and are loaded into the simulation as data. For polar optical and piezoelectric scattering the matrix elements are also tabulated against scattering angle, to enable the stochastic scattering angles generated in the Monte Carlo algorithm to be chosen from the correct distribution for each process. An energy dissipation scheme is included for acoustic (deformation potential and piezoelectric) scattering, in which a stochastic phonon wavevector, q, and energy, $\hbar v_s q$, are generated upon each scattering event, and the ratio of absorption to emission events weighted according to the ratio $N_q/N_q + 1$.

The steady state program simulates 500,000 scattering events (including self scatterings), and the ensemble program simulates 20,000 electrons in parallel. In both programs, an electric field can be applied in the plane of the quantum well.

6. Results

Steady state Monte Carlo simulations were performed for a range of electric fields, at a lattice temperature of 77K. In all cases, most of the holes (80-90%) were located in band 1, with very few ($< 0.5\%$ for $F \leq 10$ kVcm^{-1}) in band 4. Fig. 3 shows the steady state distribution of hole energies over all four bands,

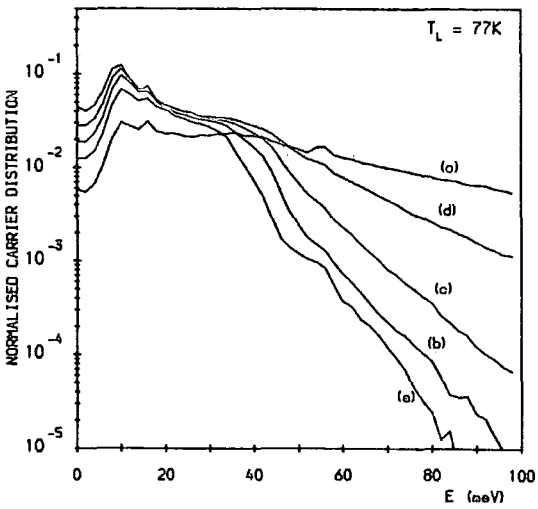

Fig. 3 Steady state distribution of hole energies over all four bands, for in plane electric fields of (a) 1.0, (b) 2.5, (c) 5.0, (d) 10.0, and (e) 20.0 kVcm^{-1} Energies are measured relative to the band 1 minimum.

for five values of electric field. At low energies, the distribution is dominated by the form of the density of states in band 1, and the structure at 16meV represents the contribution from the large density of states at the band 2 minima. For low fields, the distribution has a definite shoulder at the optical phonon energy (35meV), which becomes less prominent as the distribution is heated. At high energies, the distribution is

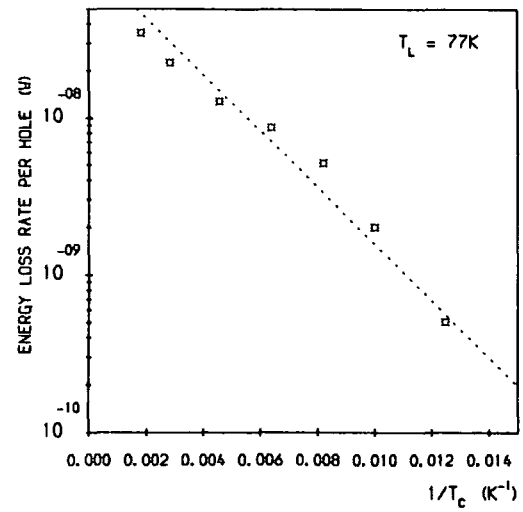

Fig. 4 Energy loss rate per hole vs. $1/T_C$, as calculated from steady state Monte Carlo simulations. The dotted line indicates a fit to the points with slope $\hbar\omega_{op}$.

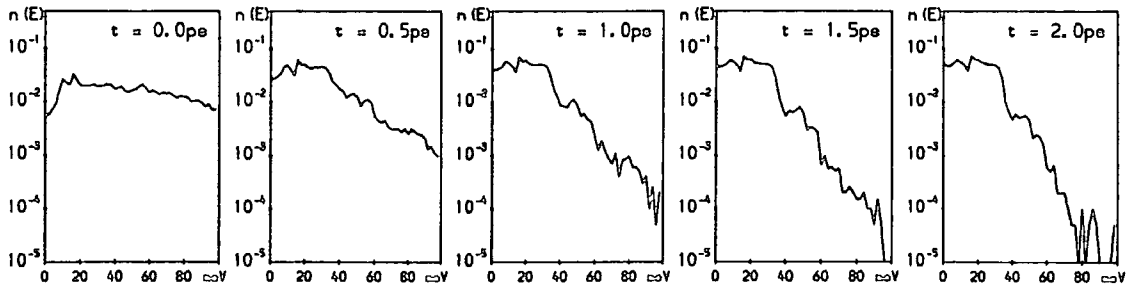

Fig. 5 Time evolution of the hole energy distribution, $F = 0.0$, $T_L = 77K$. The initial distribution of energies is Maxwellian, with $T_C = 500K$.

Maxwellian for all the cases shown, and a carrier temperature can readily be defined. For a Maxwellian distribution of carriers in a simple 2D band, the carrier temperature is given by $\overline{E}/k_B$, where $\overline{E}$ is the mean energy. In this system however, the obtained values of $\overline{E}/k_B$ were typically a factor of two larger than the carrier temperatures, T_C, derived from the energy distributions, indicating the influence of non-parabolicity and multiple band occupancy. The power supplied by the electric field is eFv_d, where v_d is the average drift velocity, and in the steady state, this is equivalent to the energy loss rate per hole. In Fig. 4, we have plotted this energy loss rate against the inverse carrier temperature. For a single, parabolic, 2D band, the rate of energy loss due to optical phonon emission is expected to depend on[4] $exp(-\hbar\omega_{op}/k_BT_C)$. Despite the complexities of the valence band system, our data appear to follow this trend, with the dotted line of slope $\hbar\omega_{op}$ showing a good fit to the points. This result is in concordance with experimental work[5] on hot holes in 2D, in which the energy loss rate was also found to follow a simple exponential law[6].

An ensemble Monte Carlo simulation was performed, at 77K, in which the supplied initial distribution of energies was Maxwellian, with a carrier temperature of 500K. Fig. 5 shows the time evolution of this distribution, with zero applied field. Again, the density of states structure is clearly reflected in the form of the distribution at low energies, but with significant repopulation of states in the band 1 energy minima as the distribution cools. The graphs show the development of three shoulders in the distribution, at 35meV, 51meV, and 60meV, due to optical emission into bands 1, 2, and 3, respectively. Consequently, the high energy tails of these distributions do not appear Maxwellian, and it is not clear whether a single carrier temperature can be defined.

7. Conclusion

We have demonstrated the use of a detailed Monte Carlo model, based on a 4-band k.p bandstructure scheme, to simulate hole transport and relaxation in a quantum well. The complicated nature of the 2D valence band system is reflected in the hole energy distributions obtained in both steady state electric field and transient relaxation simulations. The results show the importance of using a realistic model to describe 2D hole dynamics, and also allow its description in terms of simple experimental parameters.

Acknowledgments — RWK and ACGW acknowledge tenure of SERC studentships, the latter holding a CASE studentship with Plessey Research Caswell Limited. RIT acknowledges financial support from SERC for the period of this work.

References

1. M. F. H. Schuurmans and G. W. 't Hooft, Physical Review B **31**, 8041 (1985)
2. P. J. Price, Annals of Physics **133**, 217 (1981)
3. B. K. Ridley, Journal of Physics C: Solid State Physics, **15**, 5899 (1982)
4. S. A. Lyon, Journal of Luminescence **35**, 121 (1986)
5. J. Shah, A. Pinczuk, A. C. Gossard, and W. Wiegmann, Physical Review Letters **54**, 2045 (1985)
6. It should be noted that the lattice temperature used in the experiments of Ref. 5 was much lower than that considered here.